Evaluating Coordinative Binding, Biological activity, and Catalysis of Redox-Active Azothioformamide Metal Systems

A Dissertation

Presented in Partial Fulfillment of the Requirements for the

Degree of Doctor of Philosophy

with a

Major in Chemistry

in the

College of Graduate Studies

University of Idaho

by

Rabina Nuchhe Pradhan

Approved by:

Major Professor: Kristopher V. Waynant, Ph.D.

Committee Members: Ray von Wandruszka, Ph.D.; I. Francis Cheng, Ph.D.

James G. Moberly, Ph.D.

Department Administrator: Ray von Wandruszka, Ph.D.

December 2023

Abstract

Redox active Azothioformamide (ATF) ligands dissolve and/or coordinate various transition metal and metal salts to form unique ligand:metal coordination complexes. Single crystal X-ray diffraction and UV-Vis titration studies have indicated that ATF ligands form 1:1 μ-X halogen-bridged dimers from copper(I) halides, and 2:1 ligand:metal complexes from Copper(I) salts containing non-coordinative counterions (BF_4^-, PF_6^-). When ATFs are appended with electron-donating moieties there is an increased binding association which was confirmed by DFT calculations to show more exergonic interactions while electron-withdrawing moieties provided weaker binding association interactions. Furthermore, the preference of 2:1 non-linear binding model over 1:1 binding model were then studied. The findings, supported by crystal structures and UV-Vis binding studies, were further substantiated through computational evaluations of potential mechanisms, elucidating the unique 2:1 binding regime. These insights into the binding mechanisms and coordination strengths of substituted ATF ligands pave the way for their application as catalyst for metal-catalyzed reactions and biological applications. Notably it was found that non-complexed ATF compounds have limited activity, while ATF-metal coordination complexes exhibit varying effects against microbes, highlighting their potential in antimicrobial applications. Furthermore, the feasibility of Cu(I)-ATF complexes as a catalyst for the insertion of CO_2 into C-H alkyne bonds was also studied and it was found out that Cu(I) complexes, both 2:1 and 2:2 dimers with ATF ligand having electron donating group gave high yield. Overall, through comprehensive exploration of binding affinity and coordination intricacies, the potential of ATF ligands in diverse applications from catalysis to biological activity to metal recycling was studied.

Acknowledgments

The completion of this doctoral dissertation marks a significant milestone in my academic journey, and I am deeply grateful for the invaluable support and contributions of many individuals that have accompanied me on this path.

Foremost, I would like to express my sincere gratitude to my advisor, Dr. Waynant for the opportunity given to work under his guidance. I would like to thank him for his encouragement, guidance, and research training throughout my Ph.D. research. The research knowledge and skills I have learned from him are the most valuable achievements of my Ph.D. degree. His mentorship has not only shaped my academic growth but has also inspired me to strive for excellence in every aspect of my work.

I am very thankful to the members of my dissertation committee, Dr. Ray von Wandruszka, Dr. I Francis Cheng, and Dr. James G. Moberly for their gracious acceptance to serve on my committee and their careful evaluation of my work. Their thoughtful feedback and insights have been instrumental in refining the quality of this dissertation. I would also want to extend my sincere thanks to our collaborators, Dr. Mark F. Roll (University of Idaho), Dr. Zacharian M. Heiden (Washington State University), Dr. Elliot B. Hulley (University of Wyoming) and Dr. Kenneth Cornell (Boise State University). Their guidance and support have been very helpful in my research Journey.

I also appreciate Dr. Alexender Blumenfeld for helping me analyze my NMR spectra and Dr. Lee Deobald for running mass spectroscopy on my samples. I would also like to acknowledge to both past and current members of the Waynant Group - Dr. Abdulakeem Osumah, Dr.Moubani Chakraborty, Skyler Oneida, and Laxmi Tiwari. I deeply appreciate each one of them for their invaluable contributions throughout my Ph.D. days.

Dedication

I wholeheartedly dedicate this Ph.D. to my parents, Bishoram Nuchhe Pradhan, and Ram Keshari Nuchhe Pradhan, and my husband Dipak Koirala. Their love, encouragement, and belief in my aspirations have been the pillars of strength throughout my academic journey.

Table of Contents

Abstract ii

Acknowledgments iii

Dedication iv

List of Tables viii

List of Figures ix

List of Abbreviations xiv

Statement of Contribution xivi

Chapter 1: Introduction 1

1.1 Introduction to Redox-Active ligands 1

1.2 Synthesis and crystal structure of ATF ligand 2

1.3 Coordination of ATF ligand with metal precursors 5

1.4 Tuning the binding affinity of ATF ligand 7

1.5 References 10

Chapter 2: Substitution effects on binding interactions of redox-active arylazothioformamide ligands and copper(I) salts 15

2.1 Introduction 16

2.2 Materials and Methods 18

2.3 Results 24

2.4 Discussion 31

2.5 References 37

Chapter 3: Synthesis of an N, N-diethyl-tert-butylazothioformamide ligand and coordination studies with Copper(I) salts 39

3.1 Introduction 40

3.2 References 48

Chapter 4: Evaluating Coordinative Binding Mechanisms through Experimental and Computational Studies of Methoxy-substituted Arylazothioformamide Copper(I) Complexes. 52

4.1 Introduction 53

4.2 Results and Discussion 54

4.3 Conclusion 71

4.4 Experimental 72

4.5 References 79

Chapter 5: Evaluation of Azothioformamides and Their Copper(I) and Silver(I) Complexes for Biological Activity. 82

5.1 Introduction 83

5.2 Results 85

5.3 Discussion 93

5.4 Conclusion 95

5.5 Experimental 96

5.6 References 106

Chapter 6: Catalytic Carboxylation of Terminal Alkynes with Copper(I) Azothioformamide complexes. 112

6.1 Introduction 112

6.2 Results and Discussion 115

6.3 Conclusion 127

6.4 Experimental 128

6.5 References 137

Chapter 7: Conclusions and Future Directions 140

7.1 Future Directions 141

7.2 References 146

Appendix I 148

Appendix II 199

Appendix III 242

Appendix IV 301

Appendix V 332

List of Tables

Table 2.1: Bond Distances and Angles for 1,4-Heterodiene units of Substituted ATF ligands from Single Crystal X-Ray Diffraction.....26

Table 2.2: Gibb's Energy, Association Constant, and Substituent Ratio from DFT Modeling 29

Table 2.3: 2:1 H:G models fit of CuBr, CuI, and $[(CH_3CN)_4Cu(I)]BF_4$ with ATF ligands using Bindfit 33

Table 3.1: Bond distances for *t*-butyl ATF and coordination complexes 43

Table 3.2: Key Bond Angles and torsion angle of SCNN of ligand and Coordination Complexes.....44

Table 3.3: Binding Models of the t-butyl-ATF ligand to Cu(I) salts.....46

Table 4.1: Key Bond Distances for Complexes 11-19 in Angstroms (Å) 59

Table 4.2: Key coordination bond angles of 2:1 Complexes 62

Table 5.1: IC_{50} values for monomeric ATF Compounds.....89

Table 5.2: IC_{50} values for Methoxy ATF (6c) series compounds.....90

Table 5.3: IC_{50} values for Fluoro ATF (6e) series compounds.....91

Table 5.4: IC_{50} values for Trifluoro methyl ATF (6f) series compounds.....92

Table 5.5: IC_{50} values for Cyano ATF (6g) series compounds 93

Table 6.1: Initial Screening of Cu(I) catalysts for CO_2 insertions.....118

Table 6.2: Screening of Reaction Conditions with catalyst 12 at 4 mol% 119

List of Figures

Figure 1.1: Top: Traditional unreactive ligands in an oxidative addition reaction where metal changes oxidation state. Bottom: Redox-active ligands functioning as an electron reservoir in an oxidative addition reaction thereby keeping the metal in the same oxidation state. 1

Figure 1.2: Different ways of redox-active ligands expanding the reactivity of metal center...2

Figure 1.3: Synthesis of ATF ligand, photographic image of ATF crystals, and X-ray crystal structure shown at 50% probability 3

Figure 1.4: Reductive pathways and frontier molecular orbitals of ATF (HOMO), rotated transition state ATF* (HOMO), $[ATF\cdot]^{1-}$ (SOMO), and $[ATF\cdot\cdot]^{2-}$ (HOMO) 4

Figure 1.5: Coordination of ATF ligands with various copper and silver sources 6

Figure 2.1: Asymmetric units of X-ray crystal structures for ligands 5a-d. A) ligand 5a; B) 5b where the asymmetric unit displayed two similar but unique structures; C) 5c; D) 5d.....25

Figure 2.2: UV-visible absorbance spectra (left axes) and coefficient of determination (R^2) (right axes) of ATF ligands 1, 5a-d. For clarity, only every 5th data point from dilution curves are shown. Error bars are the standard error between replicate samples 30

Figure 2.3: UV-visible spectra of Cu(I)Br titrations with ATF ligands 1, 5a-d. For clarity, only every 5th data point from titration curves are shown. Error bars are the standard error between triplicate samples 31

Figure 2.4: Binding isotherms of ligands 1, 5a-d, at comparable wavelengths for the titration of Cu(I)Br. Error bars are the standard error between triplicate samples 32

Figure 2.5: Hammett plot of ATF ligands 1, 5a-d for $[(CH_3CN)_4Cu]BF_4$ complexes. Each substituent was normalized to ATF ligand 1 (Ka_1^0). 35

Figure 3.1: Synthesis of ligand 2 and X-ray crystal structure shown at 50% probability 41

Figure 3.2: Reaction and structures of coordination complexes formed from reacting 2 with various Cu(I) salts 41

Figure 3.3: X-ray crystal structures of 3a and 3b coordination complexes, both as 1:1 μ-X dimers.....42

Figure 3.4: X-ray crystal structure of coordination complex 4 as a distorted tetrahedron in a 2:1 ligand: metal arrangement (shown at 50% probability) and with the counterion BF_4^- in the foreground.....42

Figure 3.5: UV-Vis Titration spectra of Cu(I)Br into t-butyl-ATF; inset-binding isotherm ...45

Figure 4.1: Comparative coordinative investigations of ATF (1a/b) with Cu^I halide and non-coordinative BF_4 salts produce either μ-X 1:1 dimer complexes (2a/b or 3a/b) or 2:1 complexes 4a/b.....54

Figure 4.2: Synthesis of MeO ATF ligands (6, 8, and 10) with crystal structure of ortho-MeOATF (8). Thermal ellipsoid plot drawn at the 50% probability level. Hydrogen atoms have been omitted for clarity 55

Figure 4.3: Coordination complexes and found crystal structures when mixing ligand 6 (para-MeO ATF) with Cu^I salts 57

Figure 4.4: Synthesis and X-ray crystal structures from mixing ortho-MeOATF (8) or meta-MeOATF (10) with Cu^I salts 61

Figure 4.5: UV-Vis Binding isotherms for para-, ortho-, and meta-MeOATF complexes with Cu^IBr as representative ligand-metal salt complex (average of triplicate trials) at 414 nm 65

Figure 4.6: Computational investigations of found crystal structures 11 and 12 and comparisons to potential exo-X and halogen-bridged μ-X, and μ-X “butterfly” dimers (20 - 23) 66

Figure 4.7: Mechanism 1 for A_2B_2 formation; dimerization via AB + AB 67

Figure 4.8: Mechanism 2 of A_2B_2 formation utilizing the AB+B pathway.....68

Figure 4.9: Mechanism 3, formation of UV-Vis invisible B_2 in solution followed by sequential ligand additions.....69

Figure 4.10: Exergonic mechanism of Mechanism 3 binding when starting from the solvated metal salt dimer.....70

Figure 5.1: Various SCNN functional groups. Bioactivity has been investigated in thiosemicarbazones, thiosemicarbazides, and isothiosemicarbazones, but not in azothioformamides.....83

Figure 5.2: One pot synthesis of ATF compounds from various alkyl and phenylhydrazine/phenylhydrazine HCl salts and the various substitutions and yields. ATF 6g was synthesized through a two-step process with added TEA base to give an increased yield 85

Figure 5.3: X-ray crystal structures of ATF 6g and ATF 6h shown at 50% probability level. 6g hydrogens are omitted for clarity; 6h hydrogens are included to indicate the Z = 8 (two structures of the unit cell) 86

Figure 5.4: Synthesis of metal(I) salt complexes. Dimeric 1:1 complex was found predominantly with copper(I) halides in a variety of conformations including an exo-X, 7c; symmetric μ-X dimers, 7e, 7f, 8f; asymmetric μ-X dimers 8c, 8e, 7g; and unsolved structure of 8g; while 2:1 structure was isolated from metal salts with non-coordinative counteranions (9c-9g, 10c-10g and 11c-11g). X-ray crystal structures of 7g and 9g are shown at 50% probability.....88

Figure 5.5: A. Antimicrobial activity of ATF metal complexes against MRSA (strain BAA-44) cells. B. Antiproliferative activity of ATF metal complexes against human carcinoma (A549) cells 90

Figure 6.1: ATF ligands 1a-e react with copper (0) to create Copper (II) complexes (i.e., 3c) with singly reduced ligands as seen previously or with Copper(I) salts to produce neutral coordination complexes (i.e., 2c, 4c) for catalytic screening of CO_2 insertion 113

Figure 6.2: General reaction scheme for CO_2 insertion into terminal alkynes to create propiolates followed by creation of acids or esters; and the decarboxylation of propiolates creates homodiynes. 114

Figure 6.3: Various structures of Copper(I) ATF complexes. All structures are adapted from single crystal X-ray diffraction at 50% probability level..... 116

Figure 6.4: DFT-derived free energies indicating the speciation of $[Cu(L)_2]^+$ and $[(L)Cu(\mu\text{-}I)]_2$ in DMSO under standard state conditions per mole of copper catalyst.....120

Figure 6.5: Free Energy coordinate diagrams of proposed mechanistic steps starting from DMSO bound resting state to the coordinated acetylene, acetylide formation, and CO_2 insertion 121

Figure 6.6: Equilibrium between eta-2 acetylene and acetylide 123

Figure 6.7: Free energy difference and equilibrium between propiolate protonation and acetylene deprotonation 124

Figure 6.8: Proposed catalytic mechanism for the formation of propiolates starting from $[Cu(p\text{-}MeOATF)(OSMe_2)]^+$ arising from either $[Cu(p\text{-}MeOATF)_2]^+$ or $[Cu(p\text{-}MeOATF)(\mu\text{–}I)_2]_2$ as pre-catalysts 125

Figure 6.9: Substrate scope for CO_2 insertion via optimized conditions.....126

Figure 6.10: Expansion of CO_2 insertions towards esterification to create 8b. Decarboxylation to homodiyne was also observed due to the low carboxylation energy barrier 127

Figure 7.1: Synthesis of ATFs with different amide substituents 141

Figure 7.2: Synthesis scheme for AAF, ACT, ADT, and PCT.....142

Figure 7.3: Synthesis scheme for Triazole through click reaction.....143

List of Abbreviations

ATF	Azothioformamide
Aq.	Aqueous
Bn	Benzyl
D	Doublet
DCM	Dichloromethane
DIPEA	Diisopropylethylamine
DMAP	4-dimethylaminopyridine
DMF	*N*,*N*-dimethylformamide
DMSO	dimethyl sulfoxide
Et	Ethyl
Equiv	Equivalents
FTIR	Fourier transform infrared
H	Hours
HRMS	high resolution mass spectrometry
Hz	Hertz
IR	Infrared
mL	Milliliter
M	Multiplet
M	Molar
Me	Methyl
m	*Meta*

m.p	melting point
NMR	nuclear magnetic resonance
O	Ortho
P	Para
Ph	Phenyl
i-Pr	Isopropyl
Q	Quartet
R_f	relative to front
S	Singlet
r.t	Room temperature
SEM	scanning electron microscopy
SM	starting material
T	Triplet
TEA	Triethylamine
THF	Tetrahydrofuran
TLC	thin layer chromatography

Statement of Contribution

In the collaborative effort documented in this dissertation, I, along with multiple researchers played a pivotal role in advancing our knowledge on Azothioformamide (ATF) ligand system through extensive research. Dr. Kristopher V. Waynant, being a principal investigator, provided the vision and leadership shaping the overall trajectory of the research projects. As a key researcher, my responsibilities were diverse including various critical aspects of research. I carried out the literature review, formulated research questions and developed conceptual frameworks for all the research projects. Moreover, I also conducted design and synthesis of most of the ATFs and complexes for diverse applications, data analysis and interpretation, as well as playing a significant part in drafting and editing manuscripts.

The collaborative team effort involved valuable contributions from individuals like Kaylaa, Garrett, Nicholas, and Laxmi, who were instrumental in synthesizing various additional ATFs and complexes. Vincent played a key role in conducting UV-Vis titrations, data analysis, and Abu contributed to electrochemical experiments. Caleb, Kyle, and Nathan assisted in running biological studies.

Furthermore, computational insights provided by Dr. Zacharian M. Heiden and Dr. Elliot B. Hulley added depth to our research, positioning it within the broader academic landscape. Dr Kenneth Cornell's expertise was pivotal in designing and implementing experiments to test ATF ligands and their complexes for biological activity. Finally, Dr. James G. Moberly and Dr. Mark Roll contributed their statistical analysis expertise, refining our research design and methodology. The combined efforts of this collaborative team have significantly enhanced our understanding of ATF ligand system, opening avenues for further exploration and applications.

Chapter 1: Introduction

1.1 Introduction to Redox-Active Ligands

Coordination chemistry is a pivotal branch of organometallic chemistry that delves into the study of coordination compounds, wherein metal atoms/ions are enveloped by a ligand sphere.[1,2] This field serves as the nexus connecting various scientific disciplines, from fundamental chemistry to catalysis, materials science, and bioinorganic chemistry.[3,4,5] At the heart of coordination chemistry lies an intriguing class of compounds, the redox-active ligands.[6] This ligand class stands out because of their ability to delocalize, take on, and/or provide electrons to the metal center influencing the oxidation states of both the metal centers and the ligands and thus altering the reactivity of the complexes.[7,8] This unique property consequently creates two distinct scenarios: 1) ligand centered redox processes that occur independently or; 2) synergistic redox interactions resulting in the changes in both the ligand and metal oxidation states as shown in **Figure 1.1**.[9]

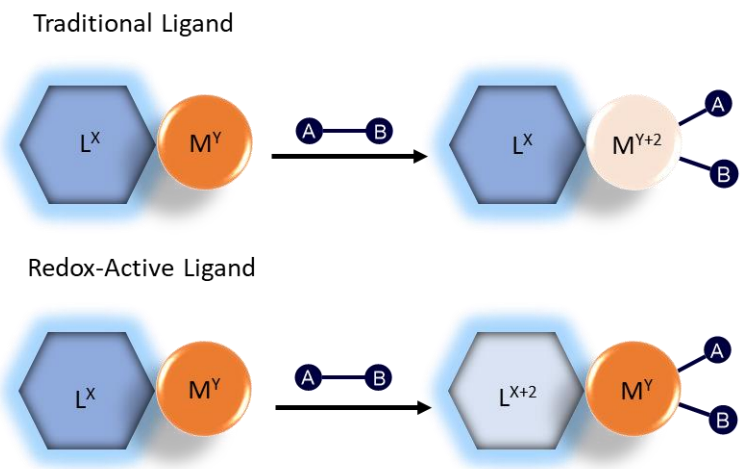

Figure 1.1: Top: Traditional unreactive ligands in an oxidative addition reaction where metal changes oxidation state. Bottom: Redox-active ligands functioning as an electron reservoir in an oxidative addition reaction thereby keeping the metal in the same oxidation state.[9]

Redox-active ligands can enhance metal reactivity through several mechanisms, as depicted in **Figure 1.2**, where: A) they serve as electron reservoirs, B) alter the Lewis acidity of the metal; C) produce ligand-centered radicals that participate in both bond formation and cleavage processes, or D) transfer a lone electron to the substrate, potentially serving as a redox active entity itself.[8,10] This ability influences the electronic structure of coordination complexes allowing chemists to engineer materials with specific properties to be used in catalysis, material sciences, and various other scientific disciplines.[7,12,13]

One notable family of redox-active ligands is the azothioformamides (ATFs), which exhibit three possible redox states (neutral, singly reduced and doubly reduced).[14,15] This property offers versatility and control over the redox behavior of coordination complexes making ATFs intriguing class among wide range of redox-active ligands.

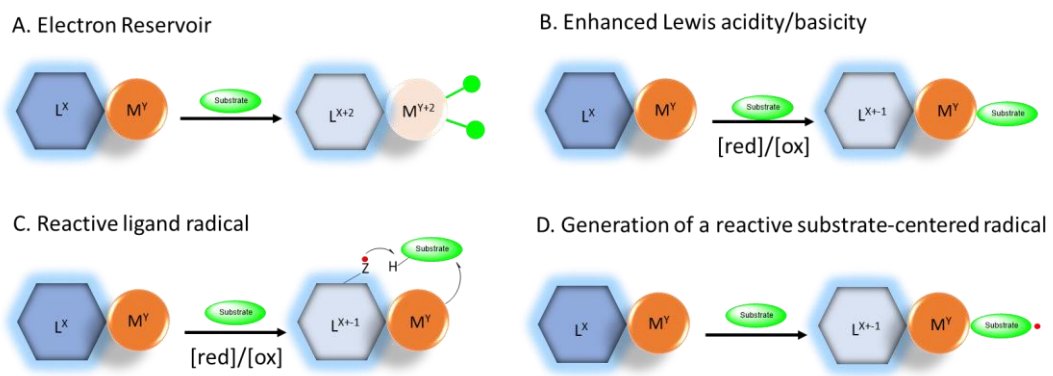

Figure 1.2: Different ways of redox-active ligands expanding the reactivity of metal center. [9]

1.2 Synthesis and Crystal structure of ATF Ligand

The ATF ligand was first synthesized in the late 1970s through a one-pot reaction scheme starting from phenylhydrazine (shown in **figure 1.3**).[16,17] The first crystal structure of the ATF ligand was reported 40 years later, in 2017, by the Waynant group.[15] Crystallographic

analyses revealed an interesting conformation where the thiocarbonyl group rotated away from the diazo phenyl π-system, forming an angle of 83.5 degrees between them. This observation is of significance as creating a bidentate ligand requires the thiocarbonyl group to rotate into same plane as the diazophenyl group.

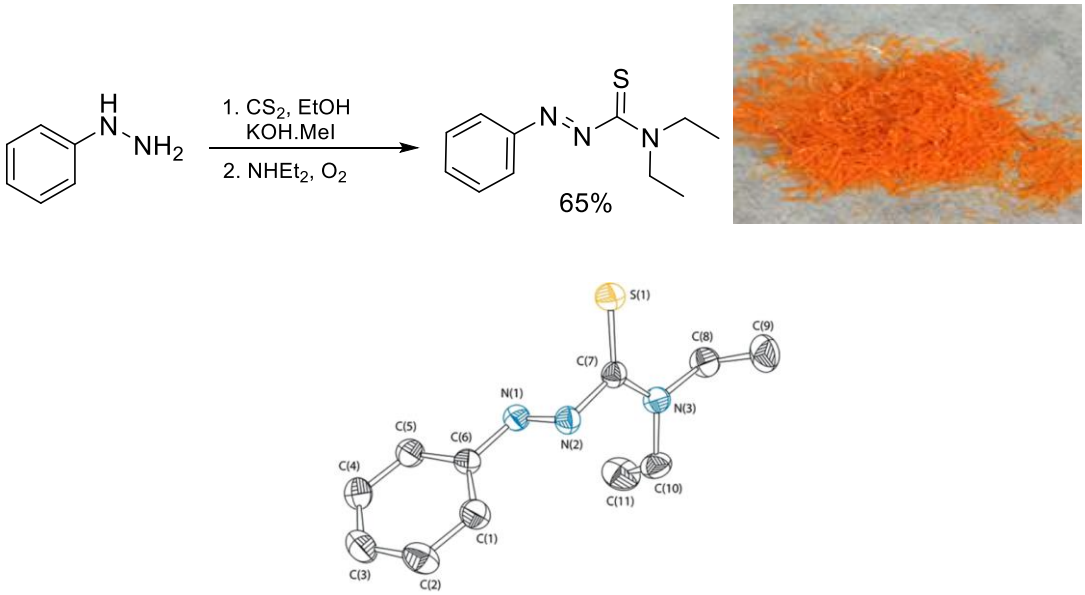

Figure 1.3: Synthesis of ATF ligand, photographic image of ATF crystals, and X-ray crystal structure shown at 50% probability.

Further computational analysis using B3LYP/6-31G* was chosen over five other DFT functional methods to determine the activation energy for the rotation of the thiocarbonyl group into the plane of the diazo phenyl group and the molecular parameters of the singly $[ATF\cdot]^{1-}$ and doubly reduced $[ATF\cdot\cdot]^{2-}$ as the structural parameters yielded by B3LYP best matched the experimental data. The analysis revealed that the rotation of the thiocarbonyl group into the plane of the diazo phenyl group requires an energy input of 3.4 kcal/mol relative to the unrotated ATF ligand found in the crystal structure. This transition state structure (ATF*) of the rotated ATF produced only a slight increase in the distance between C(7)–N(3) and C(7)–N(2), with increments of 0.01 and 0.02 Å, respectively, compared to the corresponding

distances observed in the ATF ligand itself. However, the reduction of ATF to $[ATF\cdot]^{1-}$ results in the elongation of N(3)–C(7) bond by nearly 0.05 Å. Furthermore, both the C(7)–S(1) and N(2)–N(1) bond lengths undergo an increase upon reduction, suggesting the presence of partial double bond character, illustrated in **figure 1.4**.

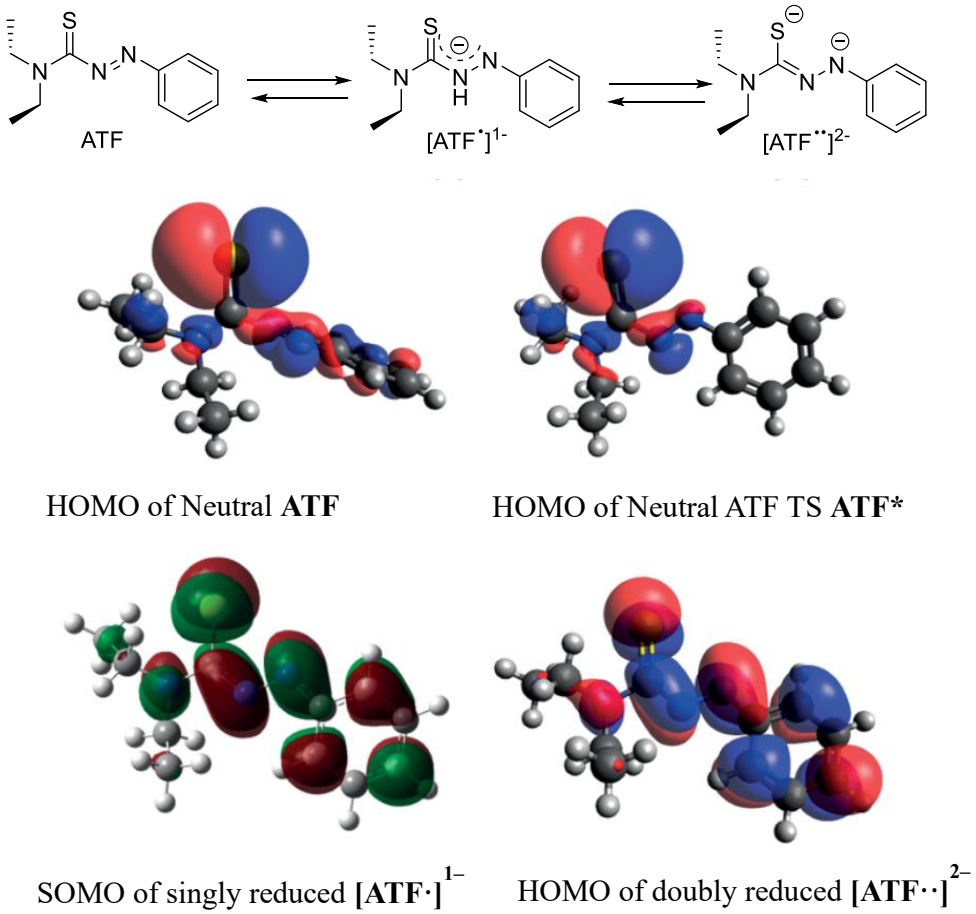

Figure 1.4: Reductive pathways and frontier molecular orbitals of ATF (HOMO), rotated transition state ATF* (HOMO), $[ATF\cdot\ ]^{1-}$ (SOMO), and $[ATF\cdot\cdot]^{2-}$ (HOMO)

The addition of the second electron to form doubly reduced $[ATF\cdot\cdot]^{2-}$ leads to the further lengthening of the C(7)-S(1) and N(1)-N(2) bonds, with increments of 0.09 Å and 0.14 Å, respectively, as compared to ATF. Notably, not all bonds exhibit lengthening upon addition of electrons to ATF. The introduction of one or two electrons to ATF actually results in a

contraction of the C(7)–N(2) distance by 0.07 Å and 0.12 Å, relative to the corresponding in ATF. This contraction implies the presence of partial double bond character in $[ATF\cdot]^{1-}$ and double bond character in $[ATF\cdot\cdot]^{2-}$ structure. This observation strongly suggests a unique coordination mechanism where either the diazophenyl or thiocarbonyl group initiates coordination with the metal center as the first step. Subsequently, the remaining group undergoes a rotational transition, ultimately achieving the desired bidentate coordination.[17]

1.3 Coordination of ATF ligand with metal Precursors

Azothioformamide ligand dissolves and coordinates solid zerovalent transition metals including copper (Cu), palladium (Pd), platinum (Pt), and nickel (Ni) through azothiocarbonyl 1,3-heterodiene moiety.[17,18] This interaction results in the induction of redox activity and substantial enhancements in molar extinction coefficients, magnifying them by factors ranging from 4000 to 8000-fold. ATFs oxidatively dissolve and coordinate zerovalent copper to form a 2:1 coordination complex as shown in **figure 1.5**. These complexes were first isolated by Krebs and Bechgaard through the crystallization process involving the dissolution of copper wire in a concentrated THF solution of ATF ligand.[16]

According to their report, the recovered species was likely either Cu(I) atom coordinated with one singly reduced ligand and one neutral ligand [Cu(I) $(ATF\cdot^{1})$ (ATF)] or an antiferromagnetically coupled [Cu(I) $(ATF\cdot)^{2}$] complex.[19] Later Waynant group suggested that actual complex reported by Krebs and Bechgaard is mostly likely the ferromagnetic complex as the bond length and angles in this complex closely resemble those of $[ATF\cdot]^{1-}$ rather than $[ATF\cdot\cdot]^{2-}$ calculated through computational analysis.[15] This indicates that the copper center in this complex is in +2 oxidation state, coordinated with two singly reduced ligands. A similar modelling approach was utilized with other metal complexes previously

reported (Ni, Pd, Pt), and all aligned with the model of a M^{2+} metal ion coordinated with two singly reduced ligands.

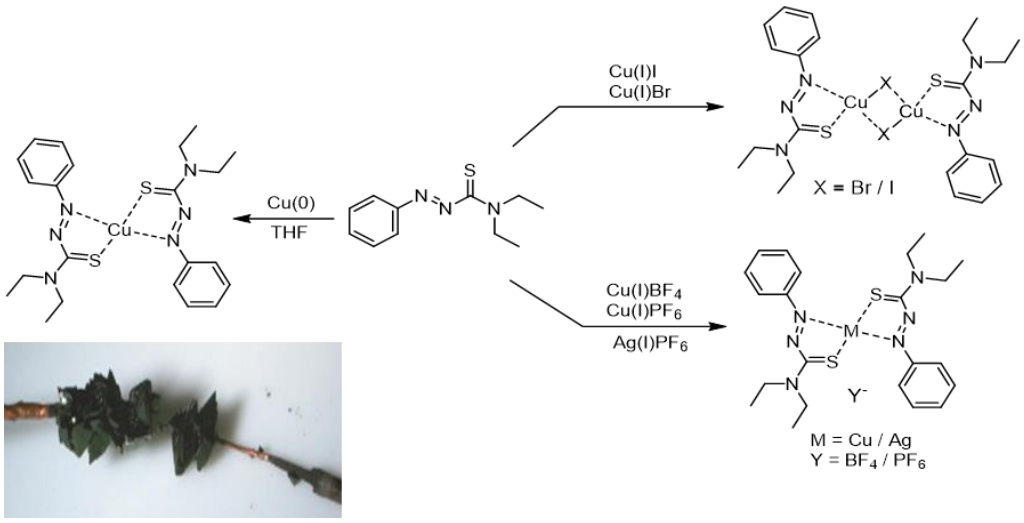

Figure 1.5: Coordination of ATF ligands with various copper and silver sources.

The redox activity of ATF ligands, however, is contingent upon the specific metal with which they interact. While these ligands exhibit redox activity when binding to zerovalent copper Cu (0), their behavior diverges when coordinating with Cu(I) and Ag(I) salts.[15,20] ATF upon coordination with copper(I) halides (CuI, CuBr), forms dimeric complex containing ATF ligands bridged by halogen as in fig 1.5. The formation of a dimeric bridged Cu(I) halide species has been previously observed and documented.[21] With Copper(I) and Silver(I) salt having non coordinating counter anions like BF_4 and PF_6, crystalline 2:1 complex with respective non-coordinative counterions was isolated. Both 1:1 and 2:1 complex had ATF ligands in neutral state and copper in +1 oxidation states as indicated through their crystal structure and computational analysis.

1.4 Tuning the binding affinity of ATF ligand

The metal dissolution property of ATF ligands has been successfully utilized to remove and extract late transition metals (Cu, Pd) nanoparticles and catalyst from polymeric materials.[17,18] However, despite the inherent simplicity of the ATF ligand structure and the promise of diverse applications, particularly in material purification, metal recycling, catalysis and biological applications, further investigations have been relatively limited. So, the next frontier is tuning the binding affinity by focusing on altering the electronic properties of the ATF ligand system. This can be achieved by introducing substituents, ranging from strong electron-donating to strong electron-withdrawing groups, in the para position of the aromatic ring within ATF ligand or even replacing phenyl ring by weakly electron donating alkyl group. This adjustment has proven to be valuable for modulating the donor strength of ligands. For e.g., the donor strength of bifunctional pyridine-cyclopentadienyl ligands was altered systematically by the introduction of donating groups in the para-position of the pyridine.[22] Similarly, to enhance the selective catalytic ethylene tri/tetramerization, N-substituted PNP ligands $Ph^2PN(R)$, was synthesized with the different electron-withdrawing or -donating group.[23] The objective is to examine and understand how these modifications impact binding affinity of ATF ligands with various metals and metal salts, opening new avenues for future enhancements in predicting binding interactions.

Moreover, there is also a compelling need to delve further into evaluating coordinative binding mechanisms towards the formation of diverse metal complexes. This exploration necessitates a multifaceted approach that combines experimental investigations with computational studies, offering complete understanding of the underlying processes. Experimental studies will involve the synthesis and characterization of various metal

complexes using a range of ligands, including those with substituents designed to modulate their electron-donating properties. These experiments will unveil the nuances of how different metal or metal salts interact with ligands under varying conditions, shedding light on the thermodynamics and kinetics of complex formation. Crystallography, UV-Vis spectroscopy and computational methods will be invaluable tools in elucidating the structure and electronic features of these complexes.[24,25] This knowledge will not only advance fundamental understanding on how these complexes form, but also inform the design of novel ligands and complexes for their use in catalysis, biological exploration and beyond.

Azothioformamide ligand possess unique N=N–C=S 1,3-heterodiene backbone, sharing structural similarities with biologically active thiosemicarbazones, thiosemicarbazides, and isothiosemicarbazones. These compounds and their metal complexes have displayed a wide spectrum of biological properties, including antineoplastic, antimycobacterial, antibacterial, antifungal, antiviral, and antimalarial activities.[26-30] Despite these promising attributes, ATF ligand and its metal complexes have remained relatively underexplored in the field of biological research. Recognizing this knowledge gap, the next project will be designed to address voids comprehensively. The project will involve an in-depth investigation into the biological activity of ATF ligands themselves, as well as their copper(I) and silver(I) complexes. A diverse library of ATF ligands along with their copper and silver complexes, will be synthesized, each with specific modifications to explore the impact of structural variations on biological activities.

The final project then explores catalysis using this unique ligand class. ATF ligands produce unique coordination complexes with copper(I) salts. Copper(I) catalysis has been well-established and extensively studied in the field of synthetic chemistry and is known for

its versatility and the diverse range of reactions it can catalyze.[31,32] Numerous copper catalyzed reactions such as Ullman coupling, Chan-Lam coupling, amination, carboxylation of terminal alkynes, click reaction has been frequently used in organic synthesis.[33-36] To explore potential of these complexes as a catalyst, different copper(I) complexes can be synthesized using a series of monosubstituted ligands and these complexes were investigated and will be reported on their catalytic activity in carbon dioxide (CO_2) insertion reaction as this reaction is well described and their mechanism is previously reported.[35,37] The rationale behind using the monosubstituted ligand lies in the desire to tailor the properties of copper(I) complexes for specific catalytic reactions of interest. By introducing different substitution or modifications to ATF ligands, electronic and steric properties can be tuned, which, in turn, impact catalytic activity of the resulting copper (I) complexes. Understanding how specific ligand modifications influence catalytic performance of these complexes is essential in designing more efficient and selective catalysts for the transformations.

1.5 References

1. Constable, E.C., What's in a Name? —A Short History of Coordination Chemistry from Then to Now. *Chemistry* **2019**,*1*, 126-163.

2. Birk, J.P.; Foster, J., Coordination Compounds. *Journal of Chemical Education* **1993,** 70 (6), 460.

3. Elsevier, C.J.; Reedjik, J.; Walton, P.H.; Ward, M.D., Ligand design in coordination chemistry: approaches to new catalysts, new materials, and a more sustainable environment. *Dalton Trans.* **2003**, (10), 1869-1880.

4. Liu,P.; Qin, R.; Fu, G.; Zheng, N, Surface Coordination Chemistry of Metal Nanomaterials. *Journal of the American Chemical Society* **2017,** 139 (6), 2122-2131.

5. Haas, K. L.; Franz, K.J., Application of metal coordination chemistry to explore and manipulate cell biology. *Chem Rev*. **2009**, 109 (10):4921-4960.

6. Steuer, L.; Kaifer, E.; Himmel H. J., On the metal–ligand bonding in dinuclear complexes with redox-active guanidine ligands. *Dalton Trans.,* **2021**, 50, 9467.

7. Chirik, P. J., Preface: Forum on Redox-Active Ligands. *Inorg. Chem.* **2011**, 50, 20, 9737–9740.

8. Hoffman, J.M.; Oliver, A.G.; Brown, S.N., The Metal or the Ligand? The Preferred Locus for Redox Changes in Oxygen Atom Transfer Reactions of Rhenium Amidodiphenoxides. *J. Am. Chem. Soc.* **2017**, 139, 12, 4521–4531.

9. Broere, D.L.; Plessiusa, R.; van der Vlugt, I. J., New avenues for ligand-mediated processes – expanding metal reactivity by the use of redox-active catechol, o-aminophenol and o-phenylenediamine ligands. *Chem. Soc. Rev.***, 2015,** 44**,** 7010-7010.

10. Dzik W.I.; Zhang X.P.; de Bruin B., Redox Noninnocence of Carbene Ligands: Carbene Radicals in (Catalytic) C−C Bond Formation. *Inorg. Chem.* **2011**,50,20, 9896–9903.

11. Storr, T.; Mukherjee, R., Preface for the Forum on Applications of Metal Complexes with Ligand-Centered Radicals. *Inorg. Chem.* **2018**, 57, 16, 9577–9579.

12. Bowen Ding, B.; Solomon, M. B.; Leong, C.F.; D'Alessandro, D.M., Redox-active ligands: Recent advances towards their incorporation into coordination polymers and metal-organic frameworks. *Coordination Chemistry Reviews* **2021**,439, 213891.

13. Pakpour, F.; Safaei E.; Azami, S.M.; Wojtczak, A.; Kaldunska K., The role of a redox-active non-innocent ligand in additive-free C-C Glaser-Hay and Suzuki coupling reactions by an *o*-aminophenol palladium(ii) complex. *RSC Adv*. **2023**,13(5):3278-3289.

14. Bechgaard K., Nonplanar electron-transfer complexes .1. Chemistry of 5 Ni-N2s2z complexes derived from nickel-Bis-N,N-diethylphenylazothioformamide. *Acta Chem Scand A.* **1974**; A 28(2):185–193

15. Johnson N.A.; Wolfe S.R.; Kabir, H.; Andrade, G. A.; Yap,G.P.; Heiden, Z.M.; Moberly, J.M.; Roll, M.F.; Waynant, K.V. Deconvoluting the innocent vs. non-innocent behavior of N, N-diethylphenylazothioformaide ligands with copper sources. *Eur J Inorg Chem.* **2017**, 47, 5576–5581.

16. Bechgaard K., Nonplanar electron-transfer complexes .2. chemistry of 4 Cu-N2s2z complexes derived from copper-Bis-N,N-diethylphenylazothioformamide. *Acta Chem Scand A.* **1977**,31(8):683–688.

17. Nielsen, K. T.; Bechgaard, K.; Krebs, F. C., Removal of palladium nanoparticles from polymer materials. *Macromolecules* **2005,** *38* (3), 658-659.

18. Nielsen, K. T.; Bechgaard, K.; Krebs, F. C., Effective removal and quantitative analysis of Pd, Cu, Ni, and Pt catalysts from small-molecule products. *Synthesis-Stuttgart* **2006,** (10), 1639-1644.

19. Nielsen, K. T.; Harris, P.; Bechgaard, K.; Krebs, F. C., Structural study of four complexes of the M-N2S2 type derived from diethylphenylazothioformamide and the metals palladium, platinum, copper and nickel. *Acta Crystallographica Section B-Structural Science* **2007,** *63*, 151-156.

20. Groner, V. M.; Larson, G. E.; Kan, Y.; Roll, M. F.; Moberly, J. G.; Waynant, K. V., The synthesis and crystal structure of bis-[3,3-diethyl-1-(phenyl-imino-kappaN)thio-urea-

kappaS]silver hexa-fluorido-phosphate. *Acta Crystallogr E Crystallogr Commun* **2019,** *75* (Pt 9), 1394-1398.

21. Lobana, T.S.; R.; Butcher, R.J.; Castineiras, A.; Bermejo, E.; Bharatam P.V.; Bonding Trends of Thiosemicarbazones in Mononuclear and Dinuclear Copper(I) Complexes: Syntheses, Structures, and Theoretical Aspects. *Inorg. Chem.* **2006**, 45, 4, 1535–1542.

22. Hansen, H.B.; Wadepohl, H.; Enders, M., The Stronger the Better: Donor Substituents Push Catalytic Activity of Molecular Chromium Olefin Polymerization Catalysts. *Chem. Eur. J.* **2021**, 27, 11084–1109.

23. Liu, R.; Yang, W.; Li, X; Feng L., Chromium-Based Complexes Bearing N-Substituted Diphosphinoamine Ligands for Ethylene Oligomerization. *ACS Omega* **2022**, 7 (40), 35933-35941.

24. Brynn Hibbert, D.; Thordarson, P., The death of the Job plot, transparency, open science and online tools, uncertainty estimation methods and other developments in supramolecular chemistry data analysis. *Chem Commun (Camb)* **2016,** *52* (87), 12792-12805.

25. Vaillancourt, F.H.; Barbosa, C.J.; Spiro, T.G.; Bolin, J.T.; Blades, M.W.; Turner, R.F.; Eltis, L.D., Definitive Evidence for Monoanionic Binding of 2,3-Dihydroxybiphenyl to 2,3-Dihydroxybiphenyl 1,2-Dioxygenase from UV Resonance Raman Spectroscopy, UV/Vis Absorption Spectroscopy, and Crystallography. *J. Am. Chem. Soc.* **2002**, 124, 11, 2485–2496.

26. Bajaj, K.; Buchanan, R. M.; Grapperhaus, C. A., Antifungal activity of thiosemicarbazones, bis(thiosemicarbazones), and their metal complexes. *Journal of Inorganic Biochemistry* **2021,** *225*, 111620.

27. Rogalewicz, B.; Climova, A.; Pivovarova, E.; Sukiennik, J.; Czarnecka, K.; Szymański, P.; Szczesio, M.; Gas, K.; Sawicki, M.; Pitucha, M.; Czylkowska1, A., Antitumor Activity and Physicochemical Properties of New Thiosemicarbazide Derivative and Its Co(II), Ni(II), Cu(II), Zn(II) and Cd(II) Complexes. *Molecules* **2022**, 27(9):2703.

28. Pavan, F. R.; Maia, P. I. D.; Leite, S. R. A.; Deflon, V. M.; Batista, A. A.; Sato, D. N.; Franzblau, S. G.; Leite, C. Q. F., Thiosemicarbazones, semicarbazones, dithiocarbazates and hydrazide/hydrazones: Anti-Mycobacterium tuberculosis activity and cytotoxicity. *Eur J Med Chem* **2010,** *45* (5), 1898-1905.

29. Venkatachalam, T. K.; Bernhardt, P. V.; Noble, C. J.; Fletcher, N.; Pierens, G. K.; Thurecht, K. J.; Reutens, D. C., Synthesis, characterization and biological activities of semicarbazones and their copper complexes. *Journal of Inorganic Biochemistry* **2016**,162, 295–308.

30. El-Shazly R. M.; Al-Hazmi G. A., "Synthesis and spectroscopic characterization of cobalt (II) thiosemicarbazone complexes. *Journal of Coordination Chemistry* **2006**, 845–859.

31. Gawande, M. B.; Goswami, A.; Felpin‖, F. X.; Asefa T.; Huang, X.; Silva, R.; Zou, X.; Zboril, R.; and Varma, R. S., Cu and Cu-Based Nanoparticles: Synthesis and Applications in Catalysis. *Chem. Rev.* **2016**, 116, 6, 3722–3811.

32. Baig, N. B. R.; Varma, R. S., Copper Modified Magnetic Bimetallic Nano-Catalysts Ligand Regulated Catalytic Activity. *Curr. Org. Chem.* **2013**, 17, 2227– 2237.

33. Mondal, J.; Biswas, A.; Chiba, S.; Zhao, Y., Cu^0 Nanoparticles Deposited on Nanoporous Polymers: A Recyclable Heterogeneous Nanocatalyst for Ullmann Coupling of Aryl Halides with Amines in Water. *Sci. Rep.* **2015**, 5, 8294.

34. Kessler, M. T.; Robke, S.; Sahler, S.; Prechtl, M. H. G. Ligand-Free Copper(I) Oxide Nanoparticle-Catalysed Amination of Aryl Halides in Ionic Liquids. *Catal. Sci. Technol.* **2014**, 4, 102– 108.

35. Gooßen, L. J.; Rodríguez, N.; Manjolinho, F.; Lange, P. P., Synthesis of Propiolic Acids via Copper-Catalyzed Insertion of Carbon Dioxide into the C-H Bond of Terminal Alkynes. *Advanced Synthesis & Catalysis* **2010,** *352* (17), 2913-2917.

36. Nandivada, H.; Jiang, X. W.; Lahann, J. Click chemistry: Versatility and Control in the Hands of Materials Scientists. *Adv. Mater.* **2007**, 19, 2197– 2208.

37. Yu, D.; Zhang, Y., Copper- and copper–*N*-heterocyclic carbene-catalyzed C─H activating carboxylation of terminal alkynes with CO_2 at ambient conditions. *Proceedings of the National Academy of Sciences* **2010,** *107* (47), 20184-20189.

Chapter 2: Substitution effects on the binding interactions of redox-active arylazothioformamide ligands and copper(I) salts

Chapter 2 is an adaptation of published manucript:

Pradhan, R.; Groner, V. M.; Gutman, K. L.; Heiden, Z. M.; Roll, M. F.; Moberly, J. G.; Waynant, K. V., *Supramol Chem* **2020**, *32* (8), 466-478.

Abstract

The straightforward synthesis of redox-active arylazothioformamide (ATF) ligands allows for electronic diversity as to measure the weak-binding interactions of transition metal salts in supramolecular coordination complexes. A small library of para-substituted ATFs was created with varied electronic components to evaluate how electron-donating and electron-withdrawing groups alter binding association constants. Following full characterization, including single-crystal X-ray diffraction, UV-Vis titration studies were performed using copper(I) salts to assess the Host:Guest binding. Simultaneously, substitutions were evaluated computationally by modelling the Gibbs' Free Energy change of the rotational barriers from ligand crystal structures to the predicted metal coordinating species and the various complexes. The multi-model association calculations and experimental measurements interplay to help limit error propagations and reliably predict the more accurate binding models. Through a thorough investigation it was found that experimentally, each ligand supports a 2:1 binding model yet may employ unique binding mechanisms to achieve that model.

Keywords: Host: Guest; arylazothioformamide; substitution effects

2.1 Introduction

Redox-active arylazothioformamide (ATF) coordination complexes with late transition metals were first reported in the late 1970s [1,2] and then again in the early 2000s for use as material purification agents [3–5]. ATF has been shown to bind through the 1,4-azothiocarbonyl heterodiene moiety to various late transition metals (Cu, Pd, Pt, Ni) resulting in significant increases (4,000 to 8,000 fold) in extinction coefficient, thus allowing for detection of low levels of the metal:ligand complex by UV-Vis spectroscopy and the ability to assess coordination.

With a simple structure, as shown in **Scheme 2.1**, the non-substituted ATF ligand 1 has been shown to bind to Cu(I) salts in both 1:1 dimers (2) and 2:1 (3) arrangements, depending on the counter anion, yet exhibits no redox-activity in forming these complexes[6]. By modifying the electronics of the system, the redox-activity and binding association of the ligand may be affected, altering association constants, and potentially inducing redox activity in the ligand and potentially oxidizing the Cu(I) to Cu (II). X-ray crystal structures of the metal:ligand coordination complexes of 1 with the various Cu(I) salts serve as starting points for computational modelling of both the rotation of the 1,4 azothiocarbonyl heterodiene into binding coordination and of the energy differences between the neutral and the singly reduced forms of the ligand.[7] With Cu(I) halides the complexes crystalized as μ-X 2:2 dimers yet with non-coordinative counter anions the crystal stoichiometry was 2:1.[6] Extending the information from crystallography, computational modelling provides predictions for H:G interactions and strengthening or weakening of chemical alterations prior to coordination or synthesis. The simplicity of the ATF structure lends itself to both computational and synthetic substitution approaches.

Herein, a small library of para-substituted ATF ligands, which range from strong electron donating to strong electron withdrawing, were prepared, crystallized, and evaluated to explore substitution effects on Cu(I) coordination. Crystal structures were adapted into computational models to predict Gibb's free energy changes and experimental UV-Vis titration studies were performed with various Cu(I) salts to validate binding association predictions. Both 1:1 and 2:1 binding models were assessed to compare computational expectations. Our hypothesis is that the addition of electron-donating substituents in the para-position will increase binding association while electron-withdrawing moieties will decrease binding or induce an oxidation event of the transition metal. The null hypothesis would predict no correlation between electronic substituents and binding affinity.

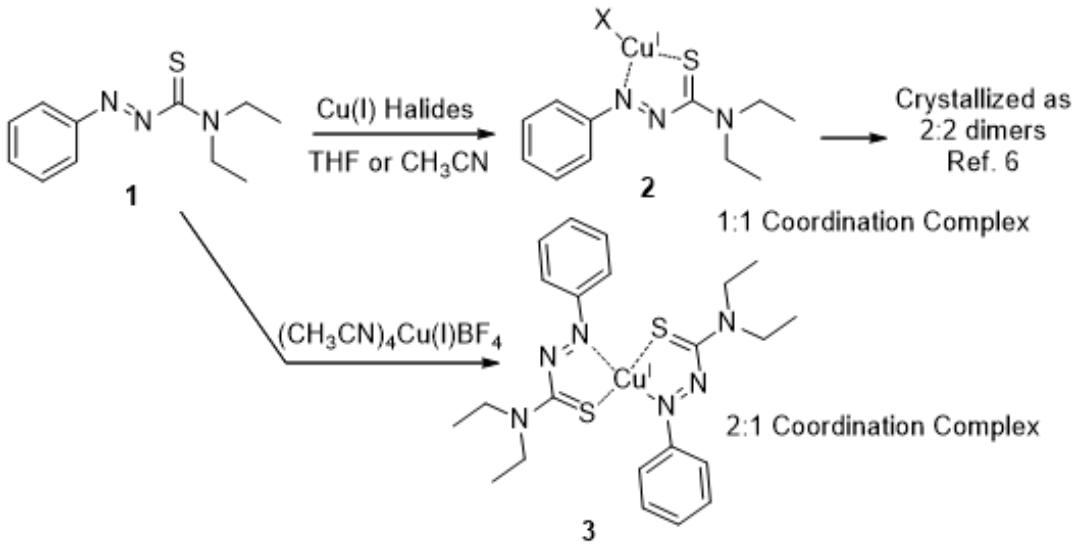

Scheme 2.1: Binding interactions seen with arylazothioformamide ligand 1 and various Cu(I) salts.

2.2 Materials and Methods

Experimental Procedures

***N,N*-diethyl-2-phenyldiazothioformamide (1)**: Ethanol (75 mL) was placed in a 200 mL 3-neck round bottom flask and degassed with nitrogen for 0.5 h. Phenylhydrazine (3.95 mL, 0.04 mol) was added followed by a dropwise addition of carbon disulfide (2.76 mL, 0.045 mol) and the solution was stirred for 0.5 h in which a precipitate formed. Potassium hydroxide (2.7 g, 0.048 mol) dissolved in degassed ethanol (25 mL) was then quickly poured into the mixture and the mixture immediately dissolved and turned light orange. This solution was stirred for 0.5 h after which methyl iodide (2.8 mL, 0.045 mol) was added in one aliquot and the mixture that had turned cloudy turned from maroon to a light yellow. This solution was stirred for 1 h and then ethanol and carbon disulphide were removed via rotary evaporation. Diethylamine (40 mL) was then added, and the mixture was stirred at reflux overnight (thiosemicarbazone by NMR) before the reflux column and heat were removed. Oxygen in the form of air was then bubbled into the solution at room temperature for 2-4 hrs. After concentrating onto silica, column chromatography using 9:1 hexane: ethyl acetate yielded 6.0 grams of a dense red oil (68%). This oil was subjected to recrystallization using 20:1 heptane: ethyl acetate to receive orange needles. Physical data matched that of previous reports[6, 8].

***N,N*-diethyl-2-(4-methoxyphenyl)diazothioformamide (5a)**: 75 mL of ethanol was degassed under nitrogen flow in a flame-dried round bottom fitted with a magnetic stirrer for one hour. 4-methoxyphenylhydrazine•HCl (30.00 mmol, 5.821 g) was added and allowed to dissolve forming a dark purple solution. Carbon disulphide (34.2 mmol, 2.06 mL) was added dropwise and allowed to stir for 0.5 hour. Potassium hydroxide (2.36 g, 42.0 mmol) dissolved in degassed ethanol (25 mL) was then quickly poured into the mixture and stirred the solution

was stirred for 0.5 h. Following, methyl iodide (33.60 mmol, 2.09 mL) was added in one aliquot. The solution was stirred for 1 h before concentrating with a rotary evaporator to produce an orange solid. The flask was then fitted with a reflux condenser and put under inert nitrogen flow. Diethylamine (40 mL) was added, and the solution was refluxed for 48 h. The resulting dark red solution was then opened to the air, allowed to cool to RT, and continued to stir for 2 h. The solution was then washed with brine and extracted with ethyl acetate to afford a dark red oil. The resulting red liquid was concentrated via rotary evaporator and purified using flash column chromatography 7:3 hexane: ethyl acetate forming 4.693 g (62%) of orange solid. The resulting solid was recrystallized with 7:3 hexane: ethyl acetate to form dark red crystal. ^{1}H NMR (300 MHz, Chloroform-d) δ 7.89 (d, J = 9.0 Hz, 2H), 6.99 (d, J = 9.0 Hz, 2H), 4.03 (q, J = 7.1 Hz, 2H), 3.90 (s, 3H), 3.55 (q, J = 7.2 Hz, 2H), 1.40 (t, J = 7.1 Hz, 3H), 1.18 (t, J = 7.2 Hz, 3H). ^{13}C NMR (125 MHz, $CDCl_3$) δ 195.0 164.3, 147.0, 126.7, 115.3, 56.5, 48.8, 45.9, 14.6, 12.3. FTIR(cm^{-1}): 2974,1579, 1419, 1259,1145, 775. Elemental Analysis: $C_{12}H_{17}N_3OS$ (251.35) (Calculated) C, 57.74; H, 6.756; N, 16.42 (Found) C, 57.34; H, 6.82; N, 16.72; mp: 93˚C.

***N,N*-diethyl-2-(p-tolyl)diazothioformamide (5b)**: 50 mL of ethanol and *p*-methylphenylhydrazine HCl (25.90 mmol, 4.11 g) were added to a flame-dried round-bottom flask and allowed to degas for 1.5 h under nitrogen flow. While under nitrogen, carbon disulphide (29.53 mmol, 2.25 ml) was added dropwise, and the solution was allowed to stir under ambient conditions for an additional 0.5 h. Potassium hydroxide (32.37 mmol, 1.82 g) dissolved in degassed ethanol (20 mL) was then added into the mixture dropwise in a single aliquot and allowed to stir under nitrogen for 0.5 h resulting in the formation of a thick off-white liquid. Methyl iodide (29.01 mmol, 1.8 ml) was then added to the solution and stirred

under nitrogen for 1 h. The resulting liquid was then concentrated with a rotary evaporator to afford a white paste. The flask was then equipped with a reflux condenser and put under nitrogen flow. Diethylamine (35 mL) was added and the mixture was refluxed under nitrogen for 48 h. The solution was cooled to ambient temperatures then exposed to air and allowed to stir for 2 h. The resulting red liquid was concentrated via rotary evaporator and purified using flash column chromatography 4:1 hexane: ethyl acetate forming 4.32 g (77 %) of orange solid. The resulting solid was subjected to recrystallization from the slow evaporation of acetonitrile to afford diffracting crystals. ^{1}H NMR (300 MHz, Chloroform-d) δ 7.97 (d, *J* = 8.3 Hz, 2H), 7.79 (d, *J* = 8.4 Hz, 2H), 4.03 (q, *J* = 7.3 Hz, 2H), 3.50 (q, *J* = 7.2 Hz, 2H), 1.54 (s, 3H), 1.42 (t, *J* = 7.1 Hz, 3H), 1.20 (t, *J* =7.2 Hz, 3H). ^{13}C NMR (126 MHz, $CDCl_3$) δ 195.2 (C=S), 150.9, 144.5, 130.8, 124.5, 48.7, 45.9, 22.5, 14.6, 12.3. FTIR (cm^{-1}): 2931, 1512, 1431, 1078, 782, 702. Elemental Analysis: (calculated) $C_{12}H_{17}N_3S$ (235.35) C, 61.24; H, 7.28; N, 17.85; (found) C, 61.24; H, 7.28; N, 17.85; S, 13.62. mp: 84˚C.

***N,N*-diethyl-2-(4-fluorophenyl)diazothioformamide (5c)**: 50 mL of ethanol and *p*-fluorophenylhydrazine HCl (24.29 mmol, 3.95 g) was added to a flame-dried round-bottom flask equipped with a magnetic stirrer and allowed to degas for 1.5 h under nitrogen flow. While under nitrogen, carbon disulphide (27.69 mol, 2.65 ml) was added dropwise to the flask and the solution was allowed to stir under ambient conditions for 0.5 h. Potassium hydroxide (1.63 g, 29.02 mol) dissolved in degassed ethanol (20 mL) was then added and allowed to stir under nitrogen for 0.5 h. Methyl iodide (27.20 mmol, 1.7 ml) was then added to the solution and stirred under nitrogen for 1 h. The resulting liquid was then concentrated with a rotary evaporator to afford an off-white paste. The flask was then equipped with a reflux condenser and put under nitrogen flow upon 30 mL of diethylamine was then added and the mixture was

heated to reflux under nitrogen for 48 h. The solution was cooled to ambient temperature, opened to air, and allowed to stir for 2 h. The resulting red liquid was concentrated via rotary evaporator and purified using flash column chromatography 4:1 hexane: ethyl acetate forming 4.16 g (72 %) of red solid. The resulting solid was subjected to recrystallization using slow evaporation of acetonitrile to afford diffracting dark red crystals. ^{1}H NMR (300 MHz, Chloroform-*d*) δ 7.91 (t, 2H), 7.19 (t, 2H), 4.03 (q, *J* = 7.1, 2H), 3.51 (q, *J* = 7.2 2H), 1.41 (t, *J* = 7.2 Hz, 3H), 1.18 (t, *J* = 7.2 Hz, 3H). ^{13}C NMR (75 MHz, $CDCl_3$) δ 194.6 (C=S), 165. (d, $J_{C\text{-}F}$ = 225 Hz), 149.2 (d $J_{C\text{-}F}$ = 3 Hz), 126.6 d $J_{C\text{-}F}$ = 9 Hz), 117.15 (d $J_{C\text{-}F}$ = 22 Hz), 48.6, 46.0, 14.6, 12.2. FTIR (cm^{-1}): 2984, 1500, 1422,1220,1140,1078,706. Elemental Analysis: (calculated) $C_{11}H_{14}FN_3S$ (239.09) C, 55.21; H 5.90; N, 17.56; (Found) C, 55.21; H, 5.90; N, 17.56; mp: 82˚C.

***N,N*-diethyl-2-(4-(trifluoromethyl)phenyl)diazothioformamide (5d)**: 75 mL of ethanol was degassed under nitrogen flow in a flame-dried round bottom fitted with a magnetic stirrer for 1 h in which *p*-(trifluoromethyl)-phenylhydrazine•HCl (4.25 g, 19.2 mmol) was added and stirred for 0.5 h. Carbon disulphide (1.32 mL, 21.88 mmol) was added dropwise and the solution stirred for 0.5 h. Potassium hydroxide (1.29 g, 232.01 mmol) dissolved in degassed ethanol (25 mL) was then added dropwise in one portion aliquot and the solution stirred for 0.5 h before the addition of methyl iodide (1.33 mL, 21.48 mmol). The solution was stirred for an additional 1 h before concentrating with a rotary evaporator. The flask was then fitted with a reflux condenser and put under nitrogen flow. Diethylamine (40 mL) was added, and the solution was refluxed for 48 h. The resulting dark red solution was then allowed to cool before being open to the air and stirred for an additional 2 h. The solution was then washed with brine and extracted with ethyl acetate to afford a dark red liquid. The resulting oil from rotary

evaporation was purified using flash column chromatography 7:3 hexane: ethyl acetate yielding 0.71 g (13 %) of red solid. The solid was recrystallized via slow evaporation with tetrahydrofuran (THF) to form diffracting crystals. ^{1}H NMR (300 MHz, Chloroform-*d*) δ 7.97 (d, *J* = 8.3 Hz, 2H), 7.79 (d, *J* = 8.4 Hz, 2H), 4.03 (q, *J* = 7.3 Hz, 2H), 3.50 (q, *J* = 7.2 Hz, 2H), 1.42 (t, *J* = 7.1 Hz, 3H), 1.19 (t, *J* = 7.0 Hz, 3H). ^{13}C NMR (126 MHz, $CDCl_3$) δ 193.5(C=S), 153.7, 133.8 (q, $J_{C\text{-}F}$ = 33 Hz), 126.7 (q, $J_{C\text{-}F}$ = 3.8 Hz), 123.81, 123.7 (q, $J_{C\text{-}F}$ = 273 Hz), 48.6, 46.0, 14.5, 12.2. FTIR (cm^{-1}): 2982, 1581, 1434, 1316, 1159, 1079, 773. Elemental Analysis; $C_{12}H_{14}F_3N_3S$ (289.32) (Calculated) C, 49.86; H, 4.96; N, 14.39; (Found) C, 49.82; H, 4.88; N, 14.52; mp: 93˚C.

Determination of pure species molar extinction coefficients

Before binding studies, all ligands and guests were diluted in triplicate to obtain molar extinction coefficients of the pure species. Dilution curves were produced by preparing a stock solution of ATF (or substituted ATF) dissolved in HPLC grade acetonitrile to 0.1125 mM. Starting with pure species at this stock concentration, the absorbance spectra were measured using a ThermoFisher GENESYS 60S UV-Vis Spectrophotometer or a Thermo Scientific Evolution UV-Vis Spectrophotometer. Dilutions were performed in succession by adding 40 μL aliquots of acetonitrile to 1.2 mL of stock ATF using a micropipette, gently mixing, and measuring the absorbance spectra after each aliquot addition, this was repeated 30 times until a final volume of 2.0 mL was achieved. The same dilution procedure described was performed for all ligands and Cu(I) salts, Cu(I)Br, Cu(I)I, and $[(CH_3CN)_4Cu(I)]BF_4$, dissolved in acetonitrile. Molar extinction coefficients were evaluated from linear absorbance regions which observed Beer–Lambert behavior.

Determination of H:G binding constants and molar extinction coefficients

UV-Vis spectroscopic titration studies of ATF ligands 1, 5a-d, and Cu(I) salts were prepared as follows: ligand solutions were prepared to 1.45×10^{-4} M in acetonitrile. A 1.2 mL of ATF solution was added to a quartz cuvette for spectroscopic evaluation. Titrations were performed with Cu(I) halide salts utilizing 1.35 mM stock solutions in acetonitrile and sequentially adding 13 μL (roughly 0.1 equivalent of guest) until reaching a guest concentration of three equivalents (a final volume of 2.0 mL). $[(CH_3CN)_4Cu(I)]BF_4$ salt titrations were performed in the same manner as above to final 1.5 equivalents. Each titration was performed in triplicate. Following data acquisition, the average of each ligand and copper salt spectra was evaluated using non-complexing absorbance models to evaluate wavelength regions where complexation may occur. Additionally, the first-derivative averaged absorbance spectra of ATF ligands 1, 5a-5d with each copper salt were summed over concentration at each wavelength to identify regions of common maxima (or minima) and compared to absorbance spectra and mixing models to select wavelengths for calculating binding association constant information. First derivative analysis showed maxima with all copper salts for a specific ATF ligand 1, 5a-c at wavelengths of 348, 414, 367, 352 nm, respectively. First derivative analysis for ligand 5d gave an inflection point at a non-zero value of 324 nm, and this was used for further analyses (see Figure S14). For each replicate, absorbance values from four additional wavelengths (−4, −2, +2, +4 nm of maxima) were used to predict binding behavior for ATF ligands 1, 5a-d. Binding association constants were calculated utilizing nonlinear binding regression models for 1:1 and 2:1 statistical, full, additive, and non-cooperative models in Bindfit® [9,10].

Computational studies

All structures were fully optimized without symmetry constraints using the B3LYP functional as implemented in Gaussian 09 using the 6–31 G** basis set for C, H, N, S, Br, B, F, and P and the Stuttgart basis set with effective core potentials for all metal and iodine atoms. To verify the validity of the chosen method, other DFT functionals were used: B3LYP-D3, B3P86, B3PW91, M11, and wB97XD, but B3LYP gave structural parameters that best matched the experimental structures. The ultrafine integration grid was employed in all calculations, which ensured the stability of the optimization procedure for the investigated molecules. Each stationary point was confirmed by a frequency calculation at the same level of theory to be a real local minimum on the potential energy surface. More accurate electronic energies were computed for the optimized geometries using the larger 6–311++G (d, p) basis set. All reported free energies are for tetrahydrofuran solution at the standard state (T = 298.15 K, P = 1 atm, 1 mol/L concentration of all species in THF) as modelled by a polarized continuum model. The energy values given in the manuscript correspond to solvent corrected Gibbs free energies that are based on B3LYP/ 6-311++G(d,p) electronic energies and all corrections calculated at the B3LYP/6-31 G(d) level.

2.3 Results

Synthesis and X-ray crystal structures

Substituted ATF ligands were synthesized based on various electron-donating or electron-withdrawing groups following known one-pot procedures [4,6]. Preparation was straightforward from commercially available phenylhydrazine HCl salts (4a-d) as shown in **Scheme 2.2**. Ligand yields varied with all but the strongly electron-withdrawing CF_3

substituted ligand (5d) providing a modest one-pot yield. Attempts to isolate the xanthate ester intermediate to optimize the reaction for 5d only sparingly increased the yield. All ligands were purified through column chromatography and recrystallized through evaporative concentration from tetrahydrofuran or acetonitrile yielding diffracting crystals of X-ray quality as shown in **Figure 2.1**.

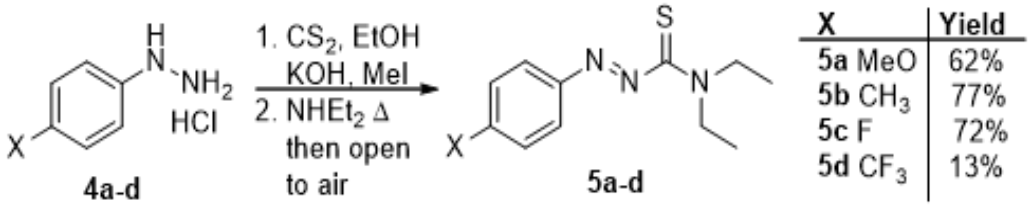

Scheme 2.2: One Pot Synthesis of variably substituted ATF ligands 5a-d.

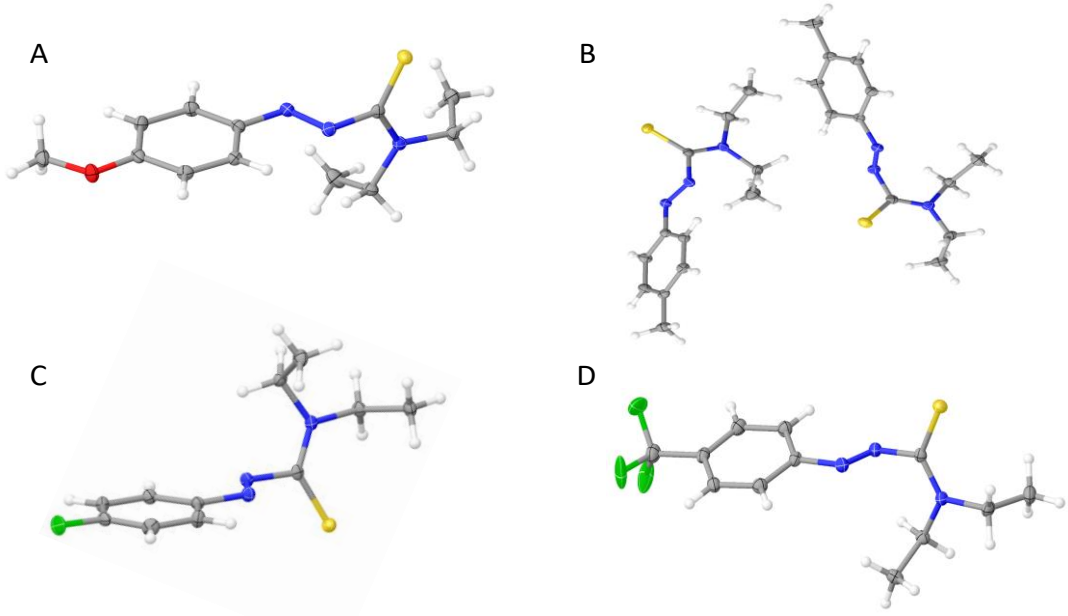

Figure 2.1: Asymmetric units of X-ray crystal structures for ligands 5a-d. A) ligand 5a; B) 5b where the asymmetric unit displayed two similar but unique structures; C) 5c; D) 5d.

Table 2.1 provides bond lengths and torsional angles of the 1,4- azothiocarbonyl heterodiene units of the synthesized and recrystallized ligands 5a-d. Comparisons of bond

distances for the N=N, N–C, and C=S and bond angles of the heterodiene from the previously reported ATF crystal structure of 1 show very little difference and indicate that the substituents on the phenyl ring have little influence on the asymmetric unit ligand structure before coordination. As seen above in Figure 2.1, MeO-ATF derivative, 5a, when in crystalline form, displays both of its ethyl groups in the same direction instead of the lower energy staggered conformation. This same phenomenon was seen when non-substituted 1 was crystallized with silver(I) and dense crystal packing was argued to induce this higher energy state [11]. Full crystallization parameters and tables can be found in Appendix I.

Table 2.1: Bond Distances and Angles for 1,4-Heterodiene units of Substituted ATF ligands from Single Crystal X-Ray Diffraction.

Ligand	Bond Distances from XRD Data (in Å)			Bond Angles from XRD		
	N=N	N-C	C=S	S1-C1-N1	C1-N1-N2	N1-N2-C2
5a MeO-ATF	1.257(7)	1.435(8)	1.670(6)	117.74	113.89	114.72
5b Me-ATF†	1.252(4)	1.440(1)	1.663(3)	118.28	112.40	114.07
	1.250(9)	1.435(9)	1.665(0)	119.20	112.77	114.52
1 ATF*	1.244(0)	1.440(0)	1.662(0)	117.8	114.3	114.42
5c F-ATF	1.252(0)	1.435(8)	1.667(4)	118.09	114.36	114.15
5d CF_3-ATF	1.254(0)	1.445(0)	1.663(0)	116.43	110.81	114.54

*These values were obtained from previous report.[11]

†Note that the Z' for this crystal is 2 and two independent but similar structures were found in the asymmetric unit cell.

Computational modelling

For association to occur, the ligands must rotate from their lowest energy *s*-trans crystalline state into an *s*-cis 1,4-azothiocarbonyl configuration. In the previous report, non-substituted ATF ligand 1 was modelled to require 3.3 kcal/mol to attain a binding configuration

in a neutral transition state. The rotational energy barriers of the para-substituted ATF analogues 5a-d as neutral transition states were modelled, and these values are shown in Table S2. As predicted, the electron-donating substituted ligands 5a and 5b require less energy for rotation compared with unsubstituted and the strong electron-withdrawing CF_3 substituted ligand 5d has a predicted larger energy of rotation than nonsubstituted. This rotation is illustrated in **Scheme 2.3** with representative examples of 1, 5b, and 5d rotating into coordination as 1′, 5b’, and 5d’ respectively. Interestingly, computational predictions suggested that *p*-fluoro substituted derivative 5c to be similar to the unsubstituted ligand 1 and perhaps the small size of the fluorine atom and the slightly donating resonance contribution of the halogen provides this slight decrease in energy to overcome the rotational barrier.

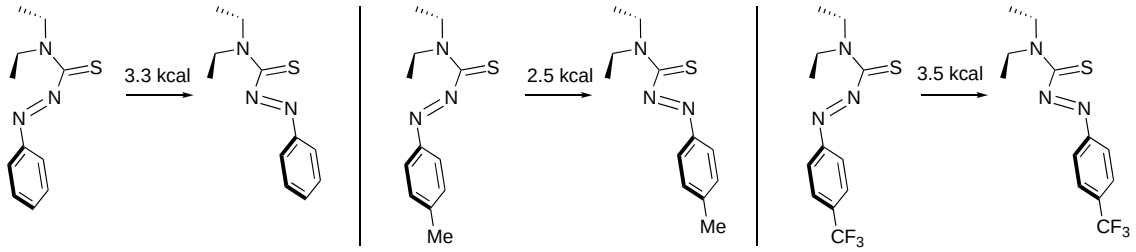

Scheme 2.3: Representative examples of the calculated energy of rotation for the crystalline structures from s-trans to adopt the s-cis configuration.

Following the rotational energy models, metal to ligand associations were modelled utilizing a 6–311 G++G(d,p) basis set as to obtain free energies and subsequently calculate equilibrium constants to compare these values with those found with titration experiments. Shown in **Scheme 2.4** is a representative example for the variant ATF ligands, shown is ligand 5c associating to a Cu(I)Br and Cu(I)I with loss of an acetonitrile in a 1:1 coordination yielding structure 6 and 7 respectively, and 5c undergoing both 1:1 coordination to give 8 while continuing in the two-step model for 2:1 coordination and predicted structure 9 (Full binding

diagrams can be found in the Appendix I (Figures A1.2-A1.6). Table 2.2 displays the binding energies and calculated K values for these coordination complexes to both 1:1 and predicted 2:1 coordination complex. For the 1:1 case there were two obvious trends for the association constants: 1) that stronger electron-donating substituents (5a, 5b) released more exothermic energy upon complexation and thus larger equilibrium constants and stronger associations than non-substituted 1 and electron-withdrawing substituted ATFs (5c, 5d); 2) when comparing Cu(I)Br and Cu(I)I, the less electronegative and larger iodide atom was slightly more exothermic and therefore increased the binding association constants of these salts.

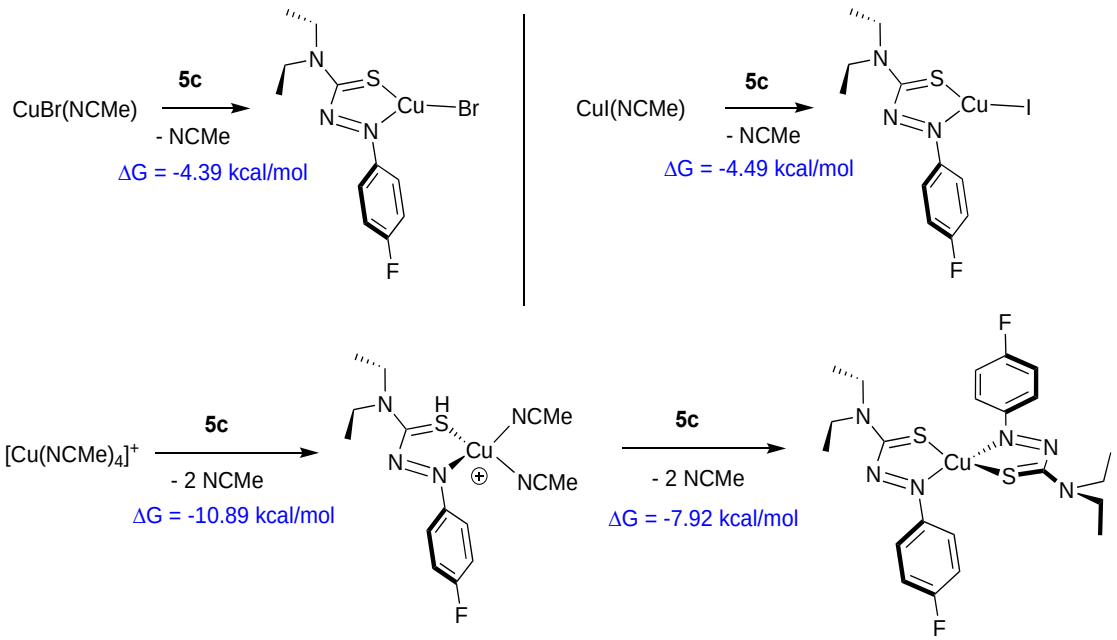

Scheme 2.4: Representative example of ligand 5c when bound to the various Cu(I) salts. Computationally calculated Gibbs free energy values for the 1:1 binding and 2:1 binding event.

For the predicted 2:1 association, the binding energy for the first ligand addition can be modelled separately from the second ligand association. Expectedly, the first association was multiple orders of magnitude larger in energy than the second but both being more appreciable than a predicted 1:1 interaction providing ample delivery of a 2:1 coordination complex as a favorable interaction. Again, when comparing 5ad, the trend of electron-donating groups

increasing the association constant was observed with the 5a being the strongest and CF_3 substituent 5d being predicted to be the weakest bound neutral species.

From the energies associated with predicted 1:1 binding, equilibrium constants were calculated as potential guidelines for experimental data. **Table 2.2** displays the equilibrium constants (Keq) for the various ligands when coordinated.

Table 2.2: Gibb's Energy, Association Constant, and Substituent Ratio from DFT Modeling						
CuBr				CuI		
Sub.	□G (kcal/mol)	K_{a1}	K_{a1i}/K_{aATF}	□G (kcal/mol)	K_{a1}	K_{a1i}/K_{aATF}
ATF	-4.5	2.00E+03	1.0	-4.6	2.36E+03	1.0
MeO	-6.82	1.00E+05	50.0	-6.9	1.15E+05	48.7
Me	-5.47	1.03E+04	5.2	-5.57	1.22E+04	5.2
F	-4.39	1.66E+03	0.8	-4.49	1.96E+03	0.8
CF_3	-3.59	4.29E+02	0.2	-3.64	4.67E+02	0.2
$(CH_3CN)_4CuBF_4$ (Addition of first ligand)				$(CH_3CN)_4CuBF_4$ (Addition of second ligand)		
Sub.	□G (kcal/mol)	K_{a1}	K_{a1i}/K_{aATF}	□G (kcal/mol)	K_{a2}	K_{ai}/K_{a2ATF}
ATF	-10.7	7.04E+07	1.0	-8.2	1.03E+06	1.0
MeO	-12.52	1.52E+09	21.6	-10.87	9.38E+07	91.1
Me	-11.38	2.22E+08	3.2	-10.32	3.71E+07	36.0
F	-10.89	9.70E+07	1.4	-7.92	6.44E+05	0.6
CF_3	-10.14	2.73E+07	0.4	-6.59	6.81E+04	0.1

Binding coordination studies

Supramolecular binding association constants are the most commonly included calculable feature when reporting H:G interactions [12,13]. Non-linear association models (isotherms) have seen increased use in recent years over the classic linear regression methods (i.e.Benesi-Hildebrand) [14,15]. All pure species of ligands show a high degree of linearity

near the 200–500 nm range as seen in **Figure 2.2** with coefficient of determination (R^2) greater than 0.99. Ligand hosts show virtually no signal in the latter portions of the visible spectrum, even at elevated concentrations.

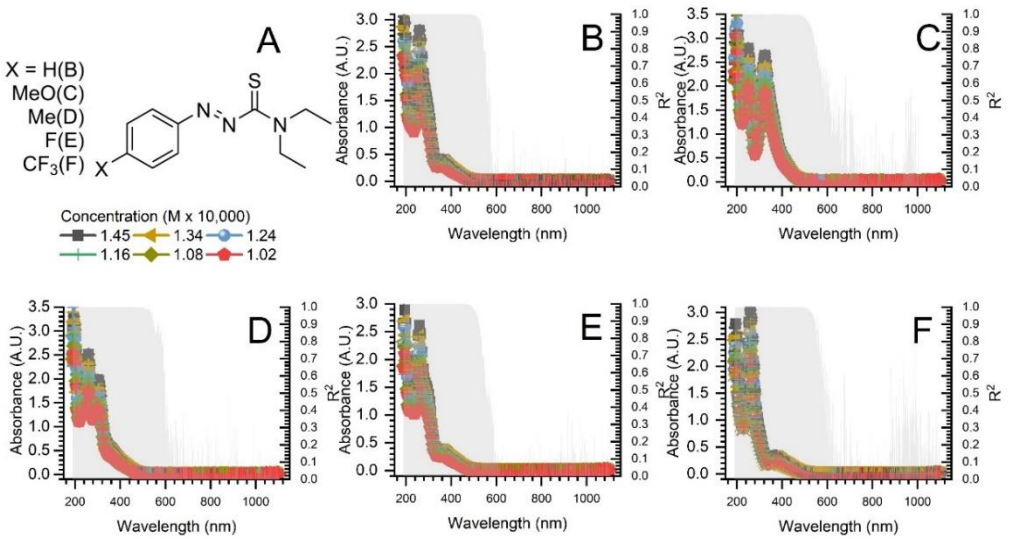

Figure 2.2: UV-visible absorbance spectra (left axes) and coefficient of determination (R^2) (right axes) of ATF ligands **1, 5a-d**. For clarity, only every 5th data point from dilution curves are shown. Error bars are the standard error between replicate samples.

Figure 2.3 illustrates absorbance spectra of ATF ligands 1, 5a-d when titrated with Cu(I)Br (similar spectra of Cu(I)I and $[(CH_3CN)_4Cu(I)]BF_4$ salt titrations are shown in Appendix II Figure A1.14-S15). Titration studies resulted in the formation of observable shifts in the absorbance spectra that differ from the pure ligand absorbance spectra and most likely indicate an ATF-Cu complex. Ligands with more electron-donating groups (5a-b) show pronounced peak shifts in the 250–400 nm range towards lower energy in the 300–500 nm wavelengths.

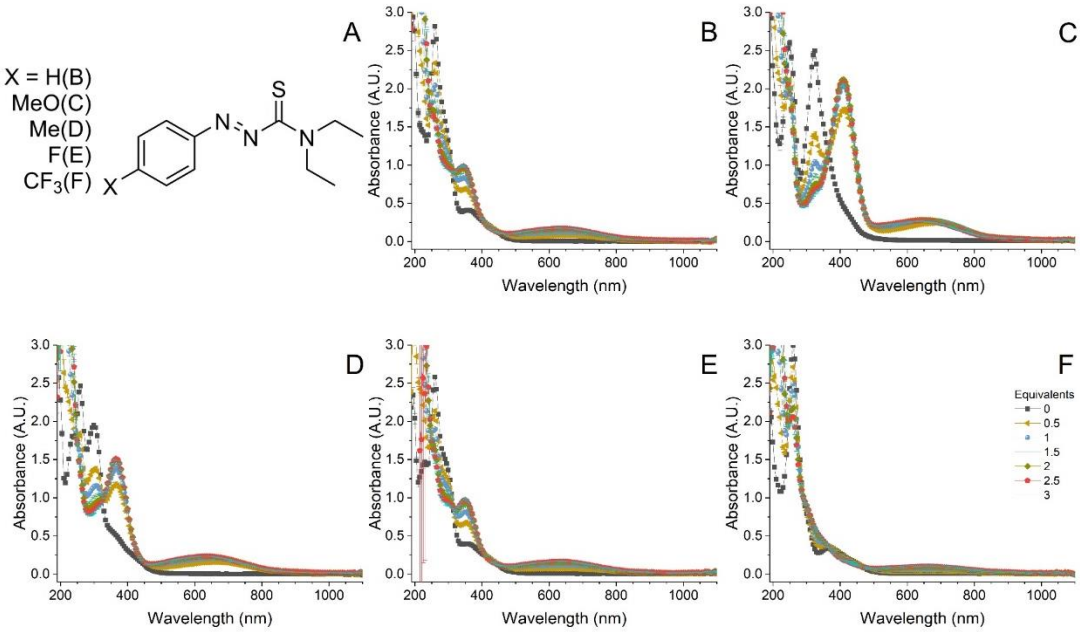

Figure 2.3: UV-visible spectra of Cu(I)Br titrations with ATF ligands **1, 5a-d**. For clarity, only every 5th data point from titration curves are shown. Error bars are the standard error between triplicate samples.

Ligand 1 and 5c, present very similar spectra. Ligand 5d shows the least pronounced absorbance response to increasing Cu(I) salt concentrations and the lowest molar extinction coefficients of 1, 5a-d ligands evaluated. Shown in **Figure 2.4** are isotherms associated with Cu(I) bromide and the ligand library. The compiled isotherms indicate that the electron-donating substituents, ligands 5a-b, result in a higher binding association constant compared to non-substituted ligand 1 or electron-withdrawing substituted (ATF ligands 5c-d) and was observed in Cu(I)I and $[(CH_3CN)_4Cu(I)]BF_4$ (additional isotherms can be found in ESI Figures Appendix `1.15-1.16). Bindfit values for 2:1 H:G coordination are presented in **Table 2.3**.

2.4 Discussion

Electron-donating species produced higher molar extinction coefficients compared to electron withdrawing groups in the order 5a>5b>1≈5c>5d (see Figure 2.4). This relationship

was observed regardless of guest species introduced. Through X-ray diffraction of ligand 1, 5a-d crystals, no substantial variance in bond distance and bond angles was observed, suggesting differences in binding with guests are driven by electronic interaction from substituents.

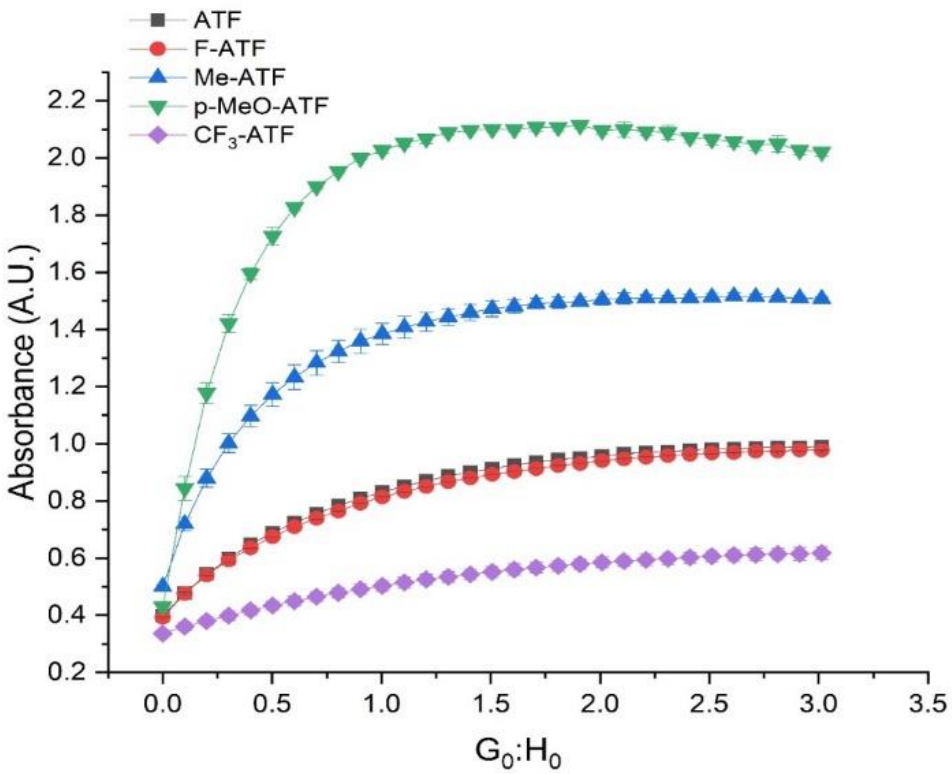

Figure 2.4: Binding isotherms of ligands 1, 5a-d, at comparable wavelengths for the titration of Cu(I)Br. Error bars are the standard error between triplicate samples.

Table 2.2 shows a similar trend in the predicted H:G DFT models. Copper halides with ligands were expected to fit a 1:1 model based on DFT from Johnson et al. [6], because the addition of another host was predicted to result in a positive ΔG for 2:1 and 2:2 μ-X dimers and as a 2:1 H: G for $(CH_3CN)_4Cu(I)BF_4$ complexes of ATF ligand 1, 5a-d. In all cases using Bindfit to predict interactions, 1:1 model was a poor fit (data not shown).

Table 2.3: 2:1 H:G models fit of CuBr, CuI, and $[(CH_3CN)_4Cu(I)]BF_4$ with ATF ligands 1, 5a-d using Bindfit.

Guest	Host	K_{A1} ± % K_{A1}		K_{A2} ± % K_{A2}		RMS	Cov ratio	SSR	BIC
CuBr	*Full*								
	CF_3-ATF	1,525	± 0.9916	1.53E-06	± 0.5912	1.25E-03	0.29	4.35E-04	718.75
	F-ATF	6,172	± 2.8801	1,961	± 3.2027	3.13E-03	0.78	4.55E-03	481.89
	ATF	1,224	± 0.7002	6,075	± 0.3840	2.57E-03	0.28	3.08E-03	521.37
	Me-ATF	2,386	± 0.8028	26,295	± 0.3826	4.72E-03	0.15	1.04E-02	398.67
	MeO-ATF	4,724	± 0.8361	27,113	± 0.2503	9.81E-03	0.24	4.48E-02	251.01
	Additive								
	CF_3-ATF	35,151	± 2.3478	737	± 3.0097	1.72E-03	0.55	8.29E-04	673.75
	F-ATF	6,064	± 10.2267	2,104	± 11.4615	3.51E-03	0.99	5.73E-03	478.47
	ATF	13,279	± 3.3472	1,078	± 5.1132	4.76E-03	0.95	1.05E-02	417.14
	Me-ATF	5,360	± 2.9528	14,940	± 1.5508	1.03E-02	0.73	4.93E-02	261.33
	MeO-ATF	14,994	± 2.4613	17,569	± 0.7819	1.67E-02	0.70	1.29E-01	164.19
	Non-cooperative								
	CF_3-ATF	1,475	± 0.0567	369	-	1.30E-03	0.31	4.71E-04	712.10
	F-ATF	6,610	± 0.1542	1,653	-	3.13E-03	0.79	4.57E-03	482.75
	ATF	3,400	± 0.0777	850	-	2.86E-03	0.34	3.79E-03	501.50
	Me-ATF	15,479	± 0.3012	3,870	-	8.55E-03	0.50	3.40E-02	280.09
	MeO-ATF	20,441	± 0.3516	5,110	-	1.68E-02	0.71	1.31E-01	143.81
	Statistical								
	CF_3-ATF	7,259	± 0.2513	1,815	-	2.33E-03	1.00	1.52E-03	613.88
	F-ATF	7,105	± 0.1807	1,776	-	3.53E-03	1.00	5.80E-03	478.68
	ATF	7,639	± 0.2386	1,910	-	4.88E-03	1.00	1.11E-02	413.49
	Me-ATF	16,177	± 0.4329	4,044	-	1.21E-02	1.00	6.76E-02	230.69
	MeO-ATF	30,735	± 0.5608	7,684	-	1.99E-02	1.00	1.84E-01	129.80
CuI	*Full*								
	CF_3-ATF	2,775	± 1.6250	3.80E-07	± 0.9934	6.79E-03	0.47	1.29E-02	376.90
	F-ATF	1,320	± 0.5462	1,843	± 0.267	2.35E-03	0.18	2.57E-03	539.58
	ATF	1,383	± 0.5410	6,303	± 0.2807	2.61E-03	0.20	3.17E-03	518.28
	Me-ATF	2,584	± 0.5287	10,440	± 0.1974	4.11E-03	0.15	7.85E-03	426.77
	MeO-ATF	13,127	± 0.9403	7,552	± 0.2332	1.22E-02	0.19	6.87E-02	207.72
	Additive								
	CF_3-ATF	75,684	± 9.1424	761	± 9.4111	8.86E-03	0.13	2.19E-02	343.10
	F-ATF	20,333	± 1.6901	494	± 4.9552	4.23E-02	6.95	8.33E-03	440.78
	ATF	15,840	± 3.1540	1,230	± 4.3587	5.55E-03	0.81	1.43E-02	386.19
	Me-ATF	9,573	± 3.5462	6,552	± 1.7957	1.00E-02	0.48	4.69E-02	266.21
	MeO-ATF	30,542	± 4.0668	12,614	± 1.0236	2.71E-02	0.48	3.43E-01	65.45
	Non-cooperative								
	CF_3-ATF	2,649	± 0.2803	662	-	6.94E-03	0.50	1.35E-02	373.72
	F-ATF	1,862	± 4.3824e-2	466	-	2.44E-03	0.19	2.77E-03	533.20
	ATF	3,873	± 0.0657	968	-	2.96E-03	0.26	4.08E-03	494.25
	Me-ATF	8,005	± 0.1352	2,001	-	6.32E-03	0.36	1.86E-02	341.13
	MeO-ATF	17,817	± 0.2093	4,454	-	1.27E-02	0.21	7.55E-02	199.53
	Statistical								
	CF_3-ATF	8,037	± 0.8082	2,009	-	9.86E-03	1.00	2.71E-02	322.96
	F-ATF	7,104	± 0.2567	1,776	-	5.61E-03	1.00	1.46E-02	385.35
	ATF	8,740	± 0.2333	2,185	-	5.80E-03	1.00	1.56E-02	378.62
	Me-ATF	15,934	± 0.3738	3,984	-	1.05E-02	1.00	5.11E-02	258.95
	MeO-ATF	39,504	± 0.8176	9,876	-	2.76E-02	1.00	3.53E-01	63.74
$(CH_3CN)_4CuBF_4$	*Full*								
	CF_3-ATF	814	± 4.0641	42,849	± 2.9122	1.48E-03	0.81	6.12E-04	684.31
	F-ATF	1,416	± 1.0626	14,895	± 0.6924	1.30E-03	0.38	7.91E-04	658.48
	ATF	1,926	± 1.7418	8,724	± 1.0016	3.23E-03	0.70	4.69E-03	478.67
	Me-ATF	3,851	± 0.6787	10,853	± 0.2868	2.72E-03	0.23	3.44E-03	510.08
	MeO-ATF	12,099	± 2.3260	19,799	± 0.5936	1.89E-02	0.35	1.57E-01	124.08
	Additive								
	CF_3-ATF	1,055	± 10.9097	25,633	± 7.2082	1.60E-03	0.95	7.16E-04	688.57
	F-ATF	3,372	± 4.2548	9,883	± 3.2144	1.78E-03	0.71	1.47E-03	615.91
	ATF	5,710	± 8.9435	6,810	± 6.4410	3.68E-03	0.90	6.09E-03	472.40
	Me-ATF	10,337	± 3.1608	12,487	± 1.5671	4.65E-03	0.68	1.00E-02	421.90
	MeO-ATF	31,974	± 7.9417	28,292	± 1.9562	2.97E-02	0.91	4.11E-01	47.03
	Non-cooperative								
	CF_3-ATF	6,620	± 0.6060	1,655	-	1.56E-03	0.89	6.76E-04	675.75
	F-ATF	7,731	± 0.0942	1,933	-	1.75E-03	0.68	1.42E-03	600.94
	ATF	6,764	± 0.1264	1,691	-	3.49E-03	0.81	5.47E-03	464.63
	Me-ATF	12,496	± 0.0978	3,124	-	3.88E-03	0.47	7.00E-03	439.63
	MeO-ATF	20,483	± 0.3363	5,121	-	2.20E-02	0.50	2.26E-01	89.00
	Statistical								
	CF_3-ATF	6,739	± 0.6404	1,685	-	1.65E-03	1.00	7.56E-04	684.34
	F-ATF	11,742	± 0.1496	2,935	-	2.11E-03	1.00	2.07E-03	582.75
	ATF	13,216	± 0.2197	3,304	-	3.87E-03	1.00	6.74E-03	463.53
	Me-ATF	23,330	± 0.2202	5,833	-	5.64E-03	1.00	1.48E-02	383.99
	MeO-ATF	57,224	± 1.0159	14,306	-	3.11E-02	1.00	4.51E-01	39.13

Full, additive, noncooperative, and statistical 2:1 H: G models were evaluated against spectroscopic data for copper halide and BF_4 species (shown in Table 2.3); each model fits reasonably well, though some results were likely nonphysical. Non-coordinative $[CH_3CN)_4Cu(I)]BF_4$ species show equivalent absorbance values for spectra compared to

halides at half the equivalent concentration, suggesting a 2:1 additive or statistical model from spectroscopic observations. DFT modelling predicted that a ‘full model, in addition to additive or statistical, could describe binding of host with $[(CH_3CN)_4Cu(I)]BF_4$ as the H: G complex with its non-coordinating counter ion was able to accept a second host with a predicted negative ΔG. For $[(CH_3CN)_4Cu(I)]BF_4$ complexes, full or additive models ranked more favorably using Bayesian-Information-Criterion (BIC) though this trend decreased with increasing electron-donating substitution towards full or noncooperative models. While still predicted to be 2:1 in nature, $[(CH_3CN)_4Cu(I)]BF_4$ complexes with electron withdrawing substituents favor asymmetric (full, additive) models while more electron-donating substituents favor more symmetric (non-cooperative, statistical) models and this symmetry is supported by DFT predictions (Appendix I Figures A1.2-1.6). The hypothesis that electronic structure influences binding strength, with more electron withdrawing groups showing weaker binding while electron-donating groups show stronger binding, was supported in full, additive, and statistical models for KA1, shown in the Hammett plot (Figure 2.5) and some KA2 models (Appendix I Fig. A1.28). As association constants, KA1 and KA2, for both non-cooperative and statistical models are related by a scalar of 4, if KA1 was significant for these models, KA2 showed identical result.

Each of these models showed significantly different slopes from zero (p-value < 0.03) and were of high correlation (adjusted R2 > 0.77). DFT models for $[(CH_3CN)_4Cu(I)]BF_4$ complexes with 1, 5a-d displayed similar correlations (adj. R2 ≈ 0.69) but were not significant at the 0.05 level (p-value of 0.052). Copper halide data fit reasonably well with different 2:1 model but did not show the same features as $[(CH_3CN)_4Cu(I)]BF_4$ complexes.

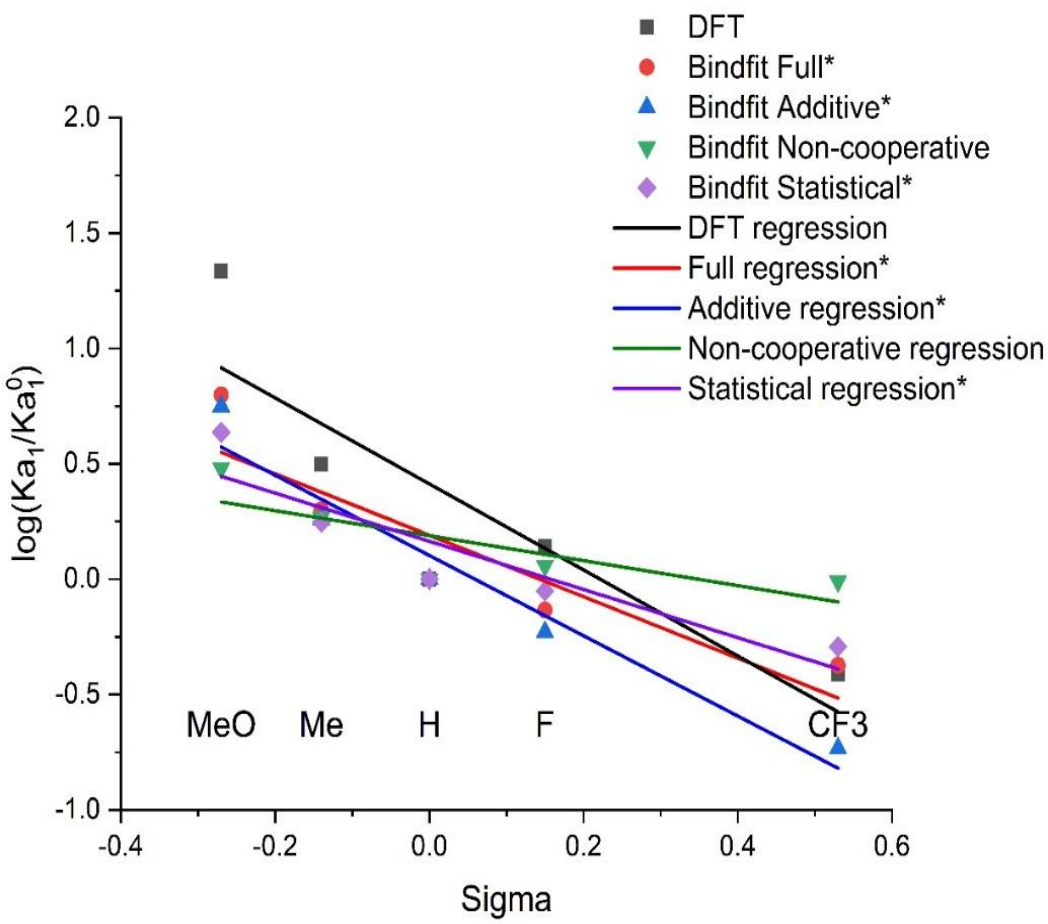

Figure 2.5: Hammett plot of ATF ligands 1, 5a-d for $[(CH_3CN)_4Cu]BF_4$ complexes. Each substituent was normalized to ATF ligand 1 (Ka_1^0). All models show similar trend of increasingly electron donating substituents showing increased binding affinity. Slopes for models with an asterisk are significantly different than zero at a 0.05 level.

BIC for full (asymmetric) or non-cooperative (symmetric) models was ranked identically with both halide species. Non-cooperative and statistical models match the closest to our substituent hypothesis pattern with electron-withdrawing groups showing weaker coordination than electron donating groups. The ambiguity of the asymmetric and symmetric predictions may suggest that a different binding mechanism may be occurring. Regression models of Hammett plots for Cu(I)Br complexes showed DFT and non-cooperative models as significantly different than zero (p-value <0.035), while only DFT models were significantly

different than zero (p-value ≈ 0.031) for Cu(I)I complexes, though trends followed the substituent hypothesis (except additive with CuI). By synthesizing and investigating a small library of substituted redox-active ATF ligands it was found that electron- donating moieties resulted in more exothermic interactions, larger extinction coefficients, and an increased predicted binding association. Electron-withdrawing moieties provided weaker binding association interactions and no evidence of a reduction event as indicated by spectral shift. Computational predicted association values followed similar trends with a relative strength of coordination is of the order MeO-ATF > Me-ATF > ATF ≈ F-ATF > CF_3-ATF for para-substituted species. Overall, computational models and crystal structures of ligands can provide valuable predictive information for experimental studies, even if absolute values disagree. Understanding H:G interactions with metal centers contributes to both catalyst design, organic synthesis, and quantitative analysis. A better understanding of how substitution impacts binding will allow for future refinements in computational tools for predicting binding interactions.

2.5 References

1. Bechgaard, K., Nonplanar Electron-Transfer Complexes .2. Chemistry of 4 Cu-N2s2z Complexes Derived from Copper-Bis-N,N-Diethylphenylazothioformamide. *Acta Chem Scand A* **1977,** *31* (8), 683-688.

2. Bechgaard, K., Nonplanar Electron-Transfer Complexes .1. Chemistry of 5 Ni-N2s2z Complexes Derived from Nickel-Bis-N,N-Diethylphenylazothioformamide. *Acta Chem Scand A* **1974,** *A 28* (2), 185-193.

3. Nielsen, K. T.; Bechgaard, K.; Krebs, F. C., Removal of palladium nanoparticles from polymer materials. *Macromolecules* **2005,** *38* (3), 658-659.

4. Nielsen, K. T.; Bechgaard, K.; Krebs, F. C., Effective removal and quantitative analysis of Pd, Cu, Ni, and Pt catalysts from small-molecule products. *Synthesis-Stuttgart* **2006,** (10), 1639-1644.

5. Nielsen, K. T.; Harris, P.; Bechgaard, K.; Krebs, F. C., Structural study of four complexes of the M-N2S2 type derived from diethylphenylazothioformamide and the metals palladium, platinum, copper and nickel. *Acta Crystallogr B* **2007,** *63* (Pt 1), 151-6.

6. Johnson, N. A.; Wolfe, S. R.; Kabir, H.; Andrade, G. A.; Yap, G. P. A.; Heiden, Z. M.; Moberly, J. G.; Roll, M. F.; Waynant, K. V., Deconvoluting the Innocent vs. Non-Innocent Behavior of N,N-diethylphenylazothioformaide Ligands with Copper Sources. *European Journal of Inorganic Chemistry* **2017,** (47), 5576-5581.

7. Guo, J.-Y.; Minko, Y.; Santiago, C. B.; Sigman, M. S., Developing Comprehensive Computational Parameter Sets to Describe the Performance of Pyridine-Oxazoline and Related Ligands. *ACS Catalysis* **2017,** *7* (6), 4144-4151.

8. Nielsen, K. T.; Bechgaard, K.; Krebs, F. C., Effective Removal and Quantitative Analysis of Pd, Cu, Ni, and Pt Catalysts from Small-Molecule Products. *Synthesis* **2006,** (10), 1639-1644.

9. Brynn Hibbert, D.; Thordarson, P., The death of the Job plot, transparency, open science and online tools, uncertainty estimation methods and other developments in supramolecular chemistry data analysis. *Chem Coomun* **2016,** *52* (87), 12792-12805.

10. Available from: http://supramolecular.org. Accessed June 10th, 2020.

11. Groner, V. M.; Larson, G. E.; Kan, Y.; Roll, M. F.; Moberly, J. G.; Waynant, K. V., The synthesis and crystal structure of bis-[3,3-diethyl-1-(phenyl-imino-kappaN)thio-urea-kappaS]silver hexa-fluorido-phosphate. *Acta Crystallogr E Crystallogr Commun* **2019,** *75* (Pt 9), 1394-1398.

12. Steed, J. W.; Atwood, J. L., *Supramolecular chemistry*. 2nd ed.; Wiley: Chichester, UK, **2009**; p xxvi, 970 p., 8 p. of plates.

13. Cragg, P. J., Supramolecular Chemistry: From Biological Inspiration to Biomedical Applications. *Supramolecular Chemistry: From Biological Inspiration to Biomedical Applications* **2010**, 1-260.

14. Hargrove, A. E.; Zhong, Z. L.; Sessler, J. L.; Anslyn, E. V., Algorithms for the determination of binding constants and enantiomeric excess in complex host : guest equilibria using optical measurements. *New J Chem* **2010**, 34 (2), 348-354.

15. Thordarson, P., Determining association constants from titration experiments in supramolecular chemistry. *Chemical Society Reviews* **2011,** *40* (3), 1305-1323.

Chapter 3: Synthesis of an N, N-diethyl-tert-butylazothioformamide ligand and coordination studies with Copper(I) salts

Chapter 3 is an adaptation of published manuscript:

Pradhan, R.; Groner, V. M.; Johnson, N. A.; Zhang, Q.; Roll, M. F.; Moberly, J. G.; Waynant, K. V., *Inor. Chem. Commun.* **2021**, *124*, 108393.

Abstract

Redox-active azothioformamides ligands rapidly coordinate to transition metals and are excellent substrates for monitoring host–guest binding interaction mechanisms as they can exhibit unique coordination complexes while producing an increase in extinction coefficient upon addition of metal salt. Herein, an alkyl derivative, N,N-diethyl-*t*-butylazothioformamide, was synthesized and fully characterized, including X-ray crystallography. Crystalline coordination complexes were prepared with various copper(I) salts (CuBr, CuI and $[(CH_3CN)_4Cu]BF4$ producing both 1:1 μ-X dimers from copper(I) halides and a distorted tetrahedral 2:1 species with non-coordinative tetrafluoroborate salt. Bond distances and angles suggest neutrally bound alkyl azothioformamide ligands with copper(I), indicating no redox activity upon binding. UV–Vis titration studies with copper(I) salts and subsequent data evaluation with both 1:1 and 2:1 non-linear regression binding models suggest inconsistent mechanisms with copper(I) salts.

Keywords: Copper(I) azothioformamide; Crystal structures; UV–Visible spectroscopy; Supramolecular binding interactions

3.1 Introduction

The redox-active 1,3-heterodiene S = C–N = N, α-azothiocarbonyl, motif is the key feature of copper metal binding in the azothioformamide (ATF) system. A similar chelating motif is found in thiosemicarbazones and thiosemicarbazides ligand systems [1–3]. While copper(I) coordinated thiosemicarbazones, isothiosemicarbazones, and thiosemicarbazides have been investigated extensively in coordination chemistry, catalysis, and for potential health benefits, including anticancer, antifungal, and antimicrobial activity [4–11], the azothioformamide (ATF) has seen less attention. Aryl azothioformamide (aryl- ATF) ligands were first reported in the 1970 s as capable of coordinatively dissolving a series of zerovalent late transition metals commonly used in catalysis, specifically Pd, Pt, Ni, and Cu [12,13]. Dissolution using these redox-active ligands resulted in oxidation at the metal center yielding divalent metals coupled to two singly reduced aryl-ATF ligands and was later used to successfully remove both Pd and Cu from polymeric materials [14,15]. The divalent metal oxidation was recently validated through in-depth experimental and computational studies comparing crystal structural data of divalent metal–ligand complexes to that of non-reduced ligands in monovalent copper(I) coordination complexes [16]. In this same report, the crystal structure of the aryl-ATF displayed a distorted p-orbital system with thiocarbonyl out of the plane with the diazophenyl group.

In the presence of copper(I) salts, the aryl-ATF produced a rapid increase in the extinction coefficient, as seen in UV–Vis spectroscopy, forming 1:1 μ-X dimer crystalline material from copper(I) halides similar to what have been found for copper(I) halides in non-polar solvents [17]. Whereas 2:1 ligand to metal complexes formed from copper(I) salts

contain non-coordinative counterions (BF_4, PF_6). This rapid increase in absorption is attributed to the rotation and resulting pi-system alignment for metal binding to occur [17].

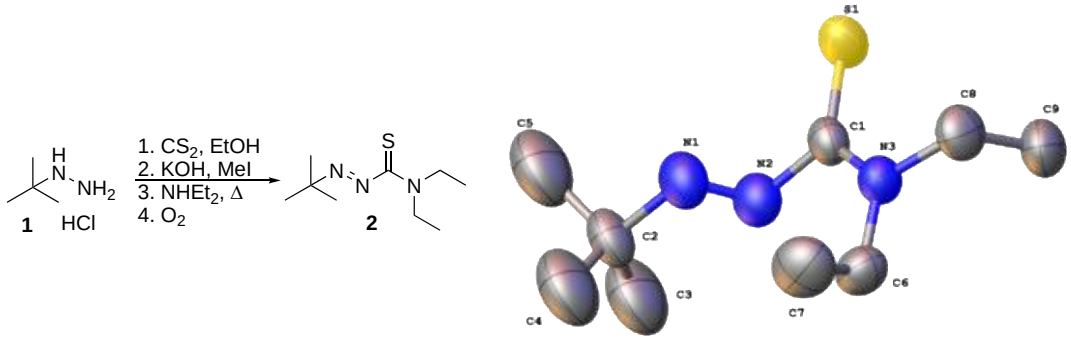

Figure 3.1: Synthesis of ligand 2 and X-ray crystal structure shown at 50% probability.

A more recent report noted that *para*-substituted aryl-ATF derivatives with either electron-donating or electron-withdrawing groups coordinated to copper(I) salts with varying degrees of binding strength [18]. An increase in binding affinity was seen when electron-donating substituents were added. Redox events were not observed. These observations gave impetus to explore the synthesis, potential binding affinities, and prospective redox activity of a weakly electron -donating alkyl azothioformamide ligand derivative.

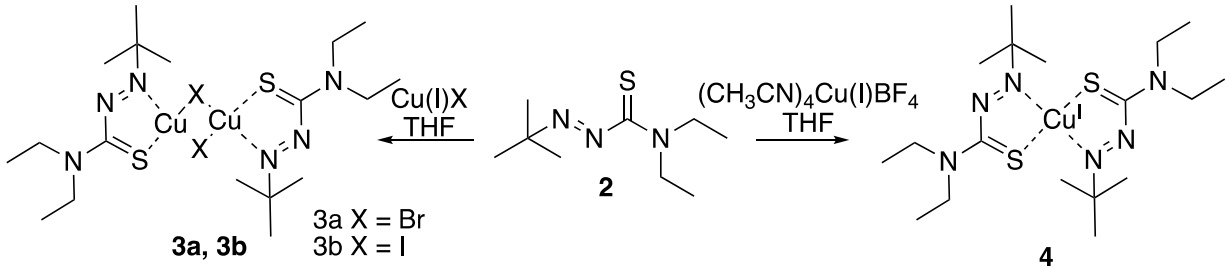

Figure 3.2: Reaction and structures of coordination complexes formed from reacting 2 with various Cu(I) salts.

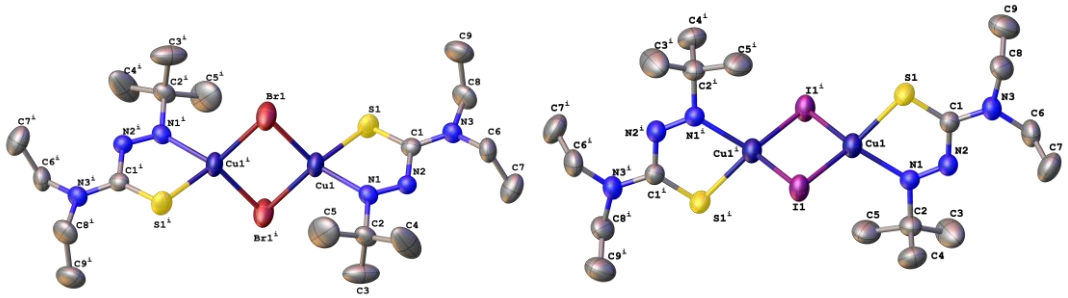

Figure 3.3: X-ray crystal structures of 3a and 3b coordination complexes, both as 1:1 μ-X dimers.

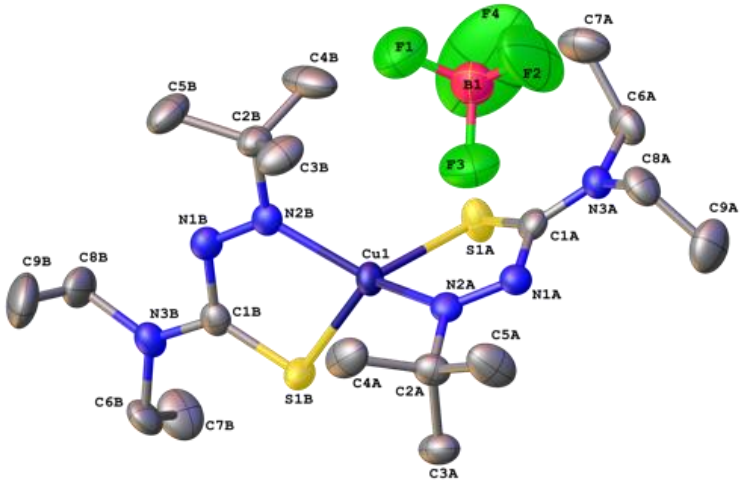

Figure 3.4: X-ray crystal structure of coordination complex 4 as a distorted tetrahedron in a 2:1 ligand: metal arrangement (shown at 50% probability) and with the counterion BF_4^- in the foreground.

Alkyl derivative N, N-diethyl-*tert*-butyl-azothioformamide (2, *t*-Bu- ATF) was synthesized from *t*-butylhydrazine HCl, 1, using the known one-pot procedure [16] (**Figure 3.1**) in 54% yield. Briefly, carbon disulfide is added to a degassed ethanolic mixture of alkyl hydrazine when KOH, is slowly added, followed by methyl iodide to create the xanthate ester. Following the removal of ethanol, the mixture is charged with diethylamine and refluxed for 16 h before opening to air and allowing for oxidization of the azo group. Following column

chromatography, ligand 2 recrystallized from acetonitrile (Full procedure and characterization data can be found inAppendix).

Table 3.1: Bond distances for *t*-butyl ATF and coordination complexes

Structure	N=N	N–C	C=S	Cu–N	Cu–S	Cu–Cu
2	1.181 Å	1.470 Å	1.647 Å	-	-	-
3a	1.251 Å	1.440 Å	1.678 Å	2.011 Å	2.331 Å	3.069 Å
3b	1.244 Å	1.439 Å	1.667 Å	2.071 Å	2.329 Å	3.009 Å
4	1.25 Å	1.442 Å	1.686 Å	1.9965 Å	2.297 Å	
	1.252 Å	1.440 Å	1.685 Å	1.9935 Å	2.292 Å	

Ligand 2 was dissolved in THF and mixed with monovalent copper salts (CuBr, CuI, and $[(CH_3CN)_4Cu]BF_4$]) at room temperature (RT) to evaluate for coordinative complexation (**Figure 3.2**). The three copper salts formed complexes in good yields. High-quality single crystals were obtained through solvent evaporation at room temperature. The crystal structures of these complexes were revealed through single-crystal X-ray diffraction analyses. As shown in **Figure 3.3** and **Figure 3.4**, the copper(I) halides formed 1:1 μ-X dimers and the $[(CH_3CN)_4Cu]BF_4$] salt leads to the formation of a 2:1 tetrahedral complex. Compound 3a and compound 4 crystallized in the monoclinic crystal system, the space group *P21/c* (NO. 14) was suggested by the unique pattern of systematic absences and was confirmed by the successful solution and refinement of the structures. Interestingly, compound 3b was crystallized in the triclinic crystal system with a space group of *P*1 (NO. 2).

A comparison of N = N, N–C, and C = S bond lengths for the complexes are shown in **Table 3.1** alongside ligand 2 for comparison. Upon complexation, an elongation of N = N and C = S bond distances was noted, yet the C–N bond is relatively unchanged. Both Cu–N and

Cu–S bonds were slightly shorter in the 2:1 structure 4 than that of the μ-X dimers (3a/ 3b) as the distorted tetrahedron at the copper(I) center allows the *tert*-butyl groups to elongate and not form strong steric interactions (space fill representations are provided in Appendix II **Figure A2.3**).

Table 3.2: Key Bond Angles (°) and torsion angle of SCNN of ligand and Coordination Complexes

	S1–C1–N1	C1–N1=N2	Cu–N2=N1	N1–Cu–S1	C1–S1–Cu	Cu1–X–Cu2	SCNN torsion angle
2	117.6	113.6	-	-	-	-	-79.27
3a	123	114.71	122.73	83.71	94.16	77.95	14.77
3b	123.7	112.6	122.2	82.6	95.97	70.26	2.41
4	122.47	114.42	121.29	85.02	92.61	-	-19.35
	123.27	114.85	122.16	85.03	94.26	-	2.68

The Cu–Cu distances were measured at 3.069 for 3a, and 3.009 Å for 3b in the halide dimers, which are significantly longer than those reported in aryl- ATFs and μ-X complexes elsewhere possessing more potent steric interactions [19–23]. For the same reason, the Cu (1)–X–Cu (2) bond angles in 3a (77.95◦) and 3b (70.26◦), are wider than that of the phenyl analog (66.48◦) [16] **Table 3.2**.

Ligand 2 was titrated against copper(I) salts: CuBr, CuI, and $[(CH_3CN)_4Cu]BF_4]$, in acetonitrile, a region of increasing extinction coefficient with a linear response in the UV–Vis absorbance spectrum was seen around 510 nm. Binding studies were performed on wavelengths near 510 nm (λ □ 4 nm, λ □ 2 nm, λ, λ + 2 nm, λ + 4 nm) using the Bindfit® program [24], the binding isotherms were calculated with both 1:1 and full, additive, non-cooperative, and statistical 2:1 non-linear regression binding models [25,26]. UV–Vis spectra

for CuBr and binding isotherm are shown in **Figure 3.5**. Binding association constants, errors, and the sum of square residuals (SSR), and Bayesian information criterion (BIC) for all the copper(I) salts are shown in **Table 3.3**. BIC was calculated to distinguish the more accurate model based on the various parameters, degrees of freedom, and the sum of least square regressions [27].

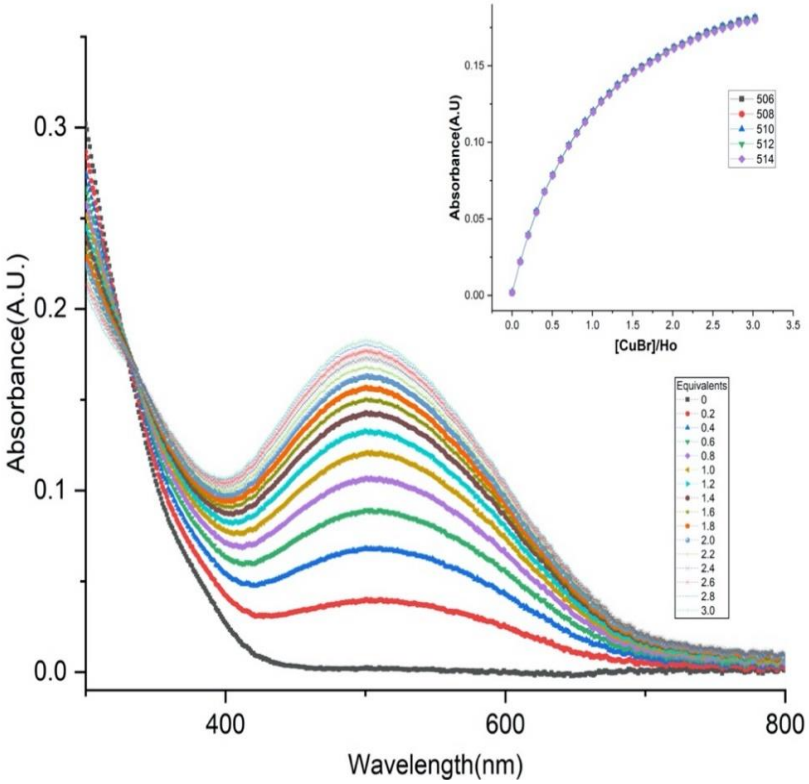

Figure 3.5: UV-Vis Titration spectra of Cu(I)Br into t-butyl-ATF; inset-binding isotherm.

Based solely on BIC (lowest number), the 2:1 full model are the best predictors for the three copper(I) salts. Although the crystal structures predicted a 1:1 bind, both halide 1:1 model showed a higher error and larger BIC compared to other models. However, the 2:1 full model for copper(I)-halides are inconsistent with each other as K12 binding association for CuBr is 224,194 M□ 1 while CuI is 21 M□ 1.

Table 3.3: Binding Models of the t-butyl-ATF ligand to Cu(I) salts

Guest	Binding Model		Association Constant 1:1 H:G		Association Constant 2:1 H:G		SSR	BIC
			K11	Error %	K12	Error %		
Cu(I)Br	1 to 1		6,347	0.43	-	-	3.09E-03	-5,440
	2 to 1	Full	83	0.14	224,194	0.95	2.84E-04	-6,450
		Non-Cooperative	3,088	0.20	772	-	1.52E-03	-5,677
		Additive	1,489	4.41	2,027	8.05	1.34E-03	-5,822
		Statistical	3,038	0.20	760	-	1.54E-03	-5,762
Cu(I)I	1 to 1		13,393	0.61	-	-	2.13E-03	-5,612
	2 to 1	Full	4,336	0.63	21	1.05	3.62E-04	-6,338
		Non-Cooperative	2,581	0.09	645	-	3.74E-04	-6,329
		Additive	6,780	2.26	639	8.52	1.47E-03	-5,777
		Statistical	4,554	0.26	1,139	-	1.52E-03	-5,768
$Cu(I)BF_4$	1 to 1		19,484	0.84	-	-	3.30E-03	-5,408
	2 to 1	Full	1,216	0.42	89,878	1.36	1.74E-04	-6,678
		Non-Cooperative	3,850	0.10	963	-	2.55E-04	-6,507
		Additive	1,927	4.22	2,124	7.34	7.85E-04	-6,070
		Statistical	4,230	0.18	1,058	-	8.07E-04	-6,063

Based on the similarity in crystal structure, it is expected that their binding behavior would be similar and association values are inconsistent with previously published results on similar derivatives with rapid exchange and weak binding [18]. Likewise, additive models show elevated errors in association constants and SSR compared to other binding models, eliminating them from the selection. Symmetric models (non-cooperative and statistical) of halides have the lowest error which is consistent with previous studies. Of the two models,

non-cooperative did not reflect observations of the isotherm profiles as CuI was expected to bind stronger than CuBr. The expected increase in ligand binding with CuI over CuBr was due, in part, to the increased Cu-I bond distance and decreased electronegativity of the iodine atom. The 2:1 model fits may not reflect binding (as suggested by crystal structure) and a more extensive binding mechanism for these alkyl-ATF species has potential. The $[(CH_3CN)_4Cu]BF_4$ models were observed to follow similar trends as halides, with additive and 1:1 showing large errors and the full model giving unreasonably large K12 association constants. Both non-cooperative and statistical models better approximate the experimental observations, with non-cooperative presenting a lower overall error and BIC of the valid models. BIC can be a useful tool in model selection but needs to be tempered with common sense. In summary, N,N-diethyl-*tert*-butyl-azothioformamide ligand, 2, represents the first of a novel alkyl class of ATF ligand and displays many similar properties to the aryl-ATFs when combined with copper(I) salts. Binding mechanisms of alkyl-ATF ligands may be more complex than anticipated and warrants further exploration of possible coordination complexes, reactivity, and non-innocence as a redox-active species with other metals and oxidations states.

3.2 References

1. Casas, J. S.; Garcia-Tasende, M. S.; Sordo, J., Main group metal complexes of semicarbazones and thiosemicarbazones. A structural review. *Coordin Chem Rev* **2000,** *209*, 197-261.

2. Donaruma, L. G.; Kitoh, S.; Walsworth, G.; Depinto, J. V.; Edzwald, J. K., Polymeric Ligands .9. Oxidation-Reduction Properties of Some Polymeric Thiosemicarbazides Containing Copper Ions. *Macromolecules* **1979,** *12* (3), 435-438.

3. Arion, V. B., Coordination chemistry of S-substituted isothiosemicarbazides and isothiosemicarbazones. *Coordin Chem Rev* **2019,** *387*, 348-397.

4. Khan, A.; Jasinski, J. P.; Smolenski, V. A.; Hotchkiss, E. P.; Kelley, P. T.; Shalit, Z. A.; Kaur, M.; Paul, K.; Sharma, R., Enhancement in anti-tubercular activity of indole based thiosemicarbazones on complexation with copper(I) and silver(I) halides: Structure elucidation, evaluation and molecular modelling. *Bioorg Chem* **2018,** *80*, 303-318.

5. Lobana, T. S.; Rekha; Butcher, R. J.; Castineiras, A.; Bermejo, E.; Bharatam, P. V., Bonding trends of thiosemicarbazones in mononuclear and dinuclear copper(I) complexes: Syntheses, structures, and theoretical aspects. *Inorg Chem* **2006,** *45* (4), 1535-1542.

6. de Lima, R. L.; Teixeira, L. R. D.; Carneiro, T. M. G.; Beraldo, H., Nickel(II), copper(I) and copper(II) complexes of bidentate heterocyclic thiosemicarbazones. *J Brazil Chem Soc* **1999,** *10* (3), 184-188.

7. Lobana, T. S.; Kumari, P.; Castineiras, A.; Butcher, R. J., Metal derivatives of thiosemicarbazones: crystal and molecular structures of mono- and di-nuclear copper(I) complexes with N1-substituted thiosemicarbazones. *J Coord Chem* **2009,** *62* (11), 1754-1765.

8. Lobana, T. S.; Sharma, R.; Sharma, R., Metal derivatives of thiosemicarbazones: crystal structure of [chloro bis(triphenylphosphino) (thiophene-2-carbaldehyde thiosemicarbazone) copper(I)] complex. *J Coord Chem* **2009,** *62* (9), 1468-1475.

9. Palanimuthu, D.; Shinde, S. V.; Somasundaram, K.; Samuelson, A. G., In Vitro and in Vivo Anticancer Activity of Copper Bis(thiosemicarbazone) Complexes. *J Med Chem* **2013,** *56* (3), 722-734.

10. Rogolino, D.; Gatti, A.; Carcelli, M.; Pelosi, G.; Bisceglie, F.; Restivo, F. M.; Degola, F.; Buschini, A.; Montalbano, S.; Feretti, D.; Zani, C., Thiosemicarbazone scaffold for the design of antifungal and antiaflatoxigenic agents: evaluation of ligands and related copper complexes. *Sci Rep-Uk* **2017,** *7*.

11. Ibrahim, A. B. M.; Farh, M. K.; Mayer, P., Copper complexes of new thiosemicarbazone ligands: Synthesis, structural studies and antimicrobial activity. *Inorg Chem Commun* **2018,** *94*, 127-132.

12. Bechgaard, K., Nonplanar Electron-Transfer Complexes .2. Chemistry of 4 Cu-N2s2z Complexes Derived from Copper-Bis-N,N-Diethylphenylazothioformamide. *Acta Chem Scand A* **1977,** *31* (8), 683-688.

13. Nielsen, K. T.; Harris, P.; Bechgaard, K.; Krebs, F. C., Structural study of four complexes of the M-N2S2 type derived from diethylphenylazothioformamide and the metals palladium, platinum, copper and nickel. *Acta Crystallogr B* **2007,** *63*, 151-156.

14. Nielsen, K. T.; Bechgaard, K.; Krebs, F. C., Effective removal and quantitative analysis of Pd, Cu, Ni, and Pt catalysts from small-molecule products. *Synthesis-Stuttgart* **2006,** (10), 1639-1644.

15. Nielsen, K. T.; Bechgaard, K.; Krebs, F. C., Removal of palladium nanoparticles from polymer materials. *Macromolecules* **2005,** *38* (3), 658-659.

16. Johnson, N. A.; Wolfe, S. R.; Kabir, H.; Andrade, G. A.; Yap, G. P. A.; Heiden, Z. M.; Moberly, J. G.; Roll, M. F.; Waynant, K. V., Deconvoluting the Innocent vs. Non-innocent Behavior of N,N-diethylphenylazothioformamide Ligands with Copper Sources. *Eur J Inorg Chem* **2017,** *2017* (47), 5576-5581.

17. Kitagawa, S.; Munakata, M., Binuclear Copper(I) Complexes Which Reversibly React with Co .1. Di-Mu-Halogeno-Bis(2,2'-Bipyridine)Dicopper(I) and Its Derivatives. *Inorg Chem* **1981,** *20* (7), 2261-2267.

18. Pradhan, R.; Groner, V. M.; Gutman, K. L.; Heiden, Z. M.; Roll, M. F.; Moberly, J. G.; Waynant, K. V., Substitution effects on the binding interactions of redox-active arylazothioformamide ligands and copper(I) salts. *Supramolecular Chemistry* **2020**, 1-13.

19. Kim, Y.-E.; Kim, J.; Park, J. W.; Park, K.; Lee, Y., σ-Complexation as a strategy for designing copper-based light emitters. *Chem Commun* **2017,** *53* (19), 2858-2861.

20. Hueting, R.; Christlieb, M.; Dilworth, J. R.; Garcia Garayoa, E.; Gouverneur, V.; Jones, M. W.; Maes, V.; Schibli, R.; Sun, X.; Tourwe, D. A., Bis(thiosemicarbazones) as bifunctional chelators for the room temperature 64-copper labeling of peptides. *Dalton Trans* **2010,** *39* (15), 3620-32.

21. Beloglazkina, E. K.; Majouga, A. G.; Mironov, A. V.; Yudina, A. V.; Moiseeva, A. A.; Lebedeva, M. A.; Khlobystov, A. N.; Zyk, N. V., Synthesis, X-ray crystallography and electrochemistry of three novel copper complexes with imidazole-containing hydantoin and thiohydantoins. *Polyhedron* **2013,** *63*, 15-20.

22. Stoffels, A. L. E.; Haanstra, W. G.; Driessen, W. L.; Reedijk, J., [Cu4(ddtp)2Br4], a Unique Tetranuclear Copper(I) Complex with Bridging Thioethers and Bridging Bromides. *Angewandte Chemie International Edition in English* **1990,** *29* (12), 1419-1420.

23. Belicchi-Ferrari, M.; Bisceglie, F.; Buluggiu, E.; Pelosi, G.; Tarasconi, P., Synthesis, characterization and crystal structure of triphenylphosphine copper(I) methylpyruvate thiosemicarbazones. *Polyhedron* **2009,** *28* (6), 1160-1168.

24. Nitsch, J.; Kleeberg, C.; Frohlich, R.; Steffen, A., Luminescent copper(I) halide and pseudohalide phenanthroline complexes revisited: simple structures, complicated excited state behavior. *Dalton Trans* **2015,** *44* (15), 6944-60.

25. www.supramolecular.org.

26. Thordarson, P., Determining association constants from titration experiments in supramolecular chemistry (vol 40, pg 1305, 2011). *Chem Soc Rev* **2011,** *40* (12), 5922-5923.

27. Brynn Hibbert, D.; Thordarson, P., The death of the Job plot, transparency, open science and online tools, uncertainty estimation methods and other developments in

supramolecular chemistry data analysis. *Chem Commun (Camb)* **2016,** *52* (87), 12792-12805.

Chapter 4: Evaluating Coordinative Binding Mechanisms through Experimental and Computational Studies of Methoxy-substituted Arylazothioformamide Copper(I) Complexes.

Chapter 4 is an adaptation of published manuscript:

Pradhan, R.; Groner, V. M.; Gutman, K. L.; Larson, G. E.; Kan, Y. W.; Zhang, Q.; Heiden, Z. M.; Roll, M. F.; Moberly, J. G.; Waynant, K. V., *Eur J Inorg Chem* **2022**, (33).

Abstract

Redox-active arylazothioformamide (ATF) ligands, when reacted with Cu^I salts, coordinate to form a variety of 1:1 dimers and 2:1 ligand-metal complexes through a N=N–C=S chelation motif. In this study, monosubstituted (*ortho/meta/para*) methoxy regioisomers of ATF were synthesized and evaluated with Cu^I halide and BF_4 salts. UV-Vis binding association studies revealed a 2:1 binding association model against all species producing a *para* >> *ortho* > *meta* pattern across the methoxy substitution range. To understand why the 2:1 non-linear binding model was preferred over a 1:1 model for Cu^I halide salt dimers (i.e., A_2B_2), a series of mechanisms were computed indicating that metal salt dimers (i.e., $B + B \rightarrow B_2$) or ligand-metal salt-metal salt- (i.e., $AB + B \rightarrow AB_2$) interactions provide favorable pathways. Combined, the data substantiate the 2:1 binding association mechanistically even as the substitution pattern, steric bulk, and electronics alter the coordination strength of the ligands to the Cu^I center.

Keywords: Coordination chemistry; complex formation; arylazothioformamide; UV-Vis titration; Single crystal X-ray diffraction

4.1 Introduction

Coordination chemistry sits at the interface of ligand design, catalyst development, and coordinative binding dynamics.[1] Rational design of ligands and experiments can help deduce binding mechanisms when complex formations are non-trivial.[2,3] Many ligands have been identified as redox-active and can induce oxidation state changes, acting as either "innocent" or "non-innocent", which can complicate or complement the structures and association constants of the predicted structures.[4] One such redox-active ligand series, the azothioformamide (ATF), is capable of oxidatively dissolving late transition metals (Cu^0, Pd^0, Pt^0, Ni^0) to create 2:1 coordination complexes as metals oxidize to M^{II} species and ligands singly reduce.[5-7] Subsequently, these ligands have been utilized for oxidative metal dissolution and removal of copper(0) and palladium(0) nanoparticles from various materials.[8,9]

While redox-active with Cu^0, ATFs have shown no further redox activity with Cu^I salts. Coordinative investigations of Cu^I halides, both Cu^IBr and Cu^{II}, and non-coordinating $[(CH_3CN)_4Cu^I](BF_4)$ with ATF ligands (1a/b) in organic solvents produced 1:1 μ-X halogen-bridged dimers (2a/b) and (3a/b) from halide salts (i.e., 2:2 complexes), and 2:1 complexes (4a/b) with non-coordinative tetrafluoroborate counterions, respectively. All complexes (2a/b), (3a/b), and (4a/b) exhibited unchanged oxidation states of both the ligands (neutral) and metal (1+).[10,11] Follow-up investigations on a series of para-substituted ATFs with varying electron-donating or withdrawing strength monitored through UV-Vis binding association studies found that the presence of electron-donating groups (para-EDGs) produce stronger binding affinities than para-EWGs.[12] Additionally, the binding association values for all complexes gave less error when fit to all types of 2:1 non-linear binding models (Full, Additive, Non-Cooperative, and Statistical) with higher error found in the 1:1 non-linear binding model.13-15 While 2:1

binding is obvious for the coordination complexes resulting from $[(CH_3CN)_4Cu^I](BF_4)$ salt due to non-coordinative counterions (i.e., 4a/b), a 2:1 association was not expected for the found 1:1 dimers (2:2 complexes, i.e., 2a/b, 3a/b) from Cu^I halides: Cu^IBr and Cu^{II}; and warranted further investigation.

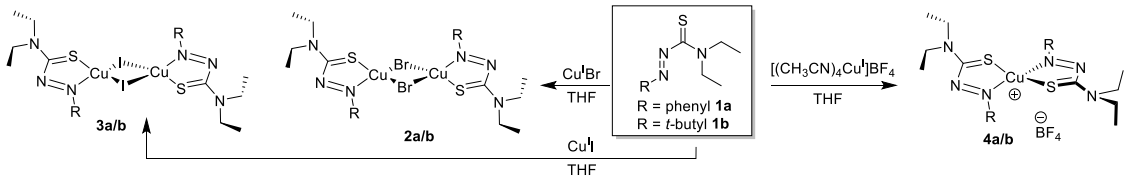

Figure 4.1: Comparative coordinative investigations of ATF (1a/b) with Cu^I halide and non-coordinative BF_4 salts produce either μ-X 1:1 dimer complexes (2a/b or 3a/b) or 2:1 complexes 4a/b

Herein is an exploration of the coordination complexes formed when reacting Cu^I salts with a series of synthesized monosubstituted electron-donating ortho-, meta-, and para-methoxy ATF ligands and how found crystal structures and UV-Vis binding studies, alongside a computational evaluation of potential mechanisms, justify the unique 2:1 binding regime. With insight into the binding mechanisms and coordination strengths of substituted ATF ligands, how they react with metal salts and the resulting ligand-metal complexes they form, their use as both metal dissolution agents and as ligands for metal-catalyzed reactions can be further explored.

4.2 Results and Discussion

Synthesis

Ligand 6 was prepared as described previously from para-methoxyphenyl hydrazine HCl (5).12 Monosubstituted N,N-diethyl-ortho-methoxyphenylazothioformamide (ortho-MeOATF, 8) and N,N-diethyl-meta-methoxyphenylazothioformamide (meta-MeOATF, 10)

ligands were synthesized in a similar manner using known one-pot procedure starting from the corresponding methoxyphenylhydrazine HCl salts (7 and 9), as shown in **Figure 4.2** (Full experimental protocols can be found in the electronic supporting information, Appendx III).

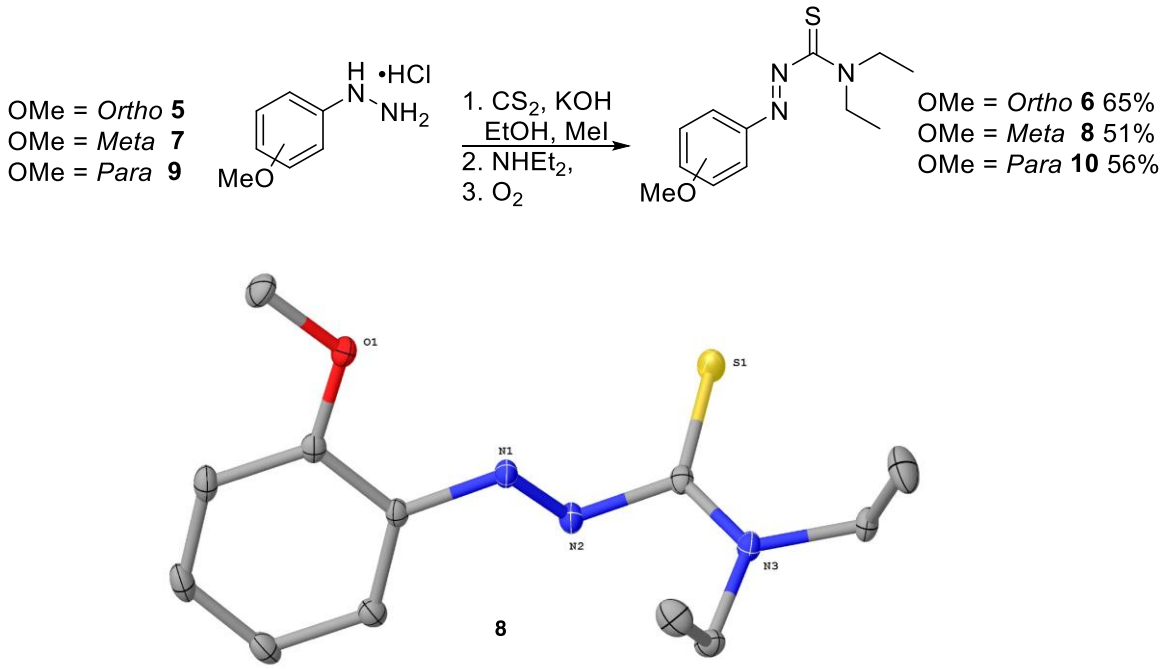

Figure 4.2: Synthesis of MeOATF ligands (6, 8, and 10) with crystal structure of *ortho*-MeOATF (8). Thermal ellipsoid plot drawn at the 50% probability level. Hydrogen atoms have been omitted for clarity.

After purification, a single crystal X-ray structure was obtained for ortho-MeOATF ligand (8), however (10) was isolated as an oil. Interestingly, the X-ray crystal structure of (8) displays the diethyl group in the less favorable syn direction similar to that of crystalline para-MeOATF (6).[12] In addition to full characterization, a thorough UV-Vis titration (representative examples in Appendix III Figure A3.26-3.28) and coordinative crystallization study were undertaken to compare the complexes formed as all three ATF ligands were reacted with Cu^{I} salts.

Ligand Complexation and Crystallization Studies

Complexes were prepared by dissolving each ligand in THF, acetonitrile, or chloroform followed by addition of salt (Cu^IBr, Cu^II, or $[(CH_3CN)_4Cu^I](BF_4)$) in either a 2:1 or 1:1 stoichiometric ratio, respectively, and then gently heating to encourage solvation and /or simply allowing each solution to evaporatively concentrate and recover crystalline material. X-ray crystal structures (11-13) were obtained from mixing Cu^I salts with para-methoxy ATF (6) as shown in **Figure 4.3** (Diffraction data can be found in Appendix III Table A3.2). Firstly, in contrast to structures (2a/b) and (3a/b), ligand (6) when mixed with an equimolar amount of Cu^IBr gave dimeric exo-Br structure (11) in 44% yield. This monoclinic exo-Br complex (11) crystallized in a C_{2c} space group where all bond distances and bond angles are identical for each 6•CuBr pair (a true 1:1 dimer). The diethyl groups in the thioformamide were displayed in a syn direction with minimal short contacts found in the larger crystalline lattice. This diethyl group orientation is the same as seen previously in ligands 6 and 8.[12] Key bond distances for complexes (11-13) (C_1=S; C_1–N_1, N_1=N_2, Cu–S_1, Cu–N_2, Cu–X, And Cu–Cu) are shown in Table 4.1. To note is the extended C_1=S_1 bond distance in (11) of 1.712 Å over (2a) of 1.684 Å, which is rationalized as each sulfur atom in the dimer being coordinated to both Cu atoms in this exo-Br structure vs. one Cu atom (as in (μ-Br)-2a). Exo-Br structures like (11) have precedent with anti-tuberculosis Ag(I) and Cu(I) thiosemicarbazone complexes,[16, 17] yet are novel for the ATF ligand class. Additionally, a single water molecule was found in the crystal structure for (11), but with minimal short contacts, suggesting either slightly wet THF or possibly hydrated Cu^IBr salt.

Crystalline (μ-I) iodide-bridged dimer (12), shaped as a butterfly, was found from allowing Cu^II to react with (6) in THF and sequentially decanting yielding the crystalline

complex in 69% yield. This “butterfly” feature has been previously seen with $Cu^{I}I$ complexes bridged by P^N ligands and reported to provide both decreased Cu–Cu bond distance and unique photophysical properties.[18-20]

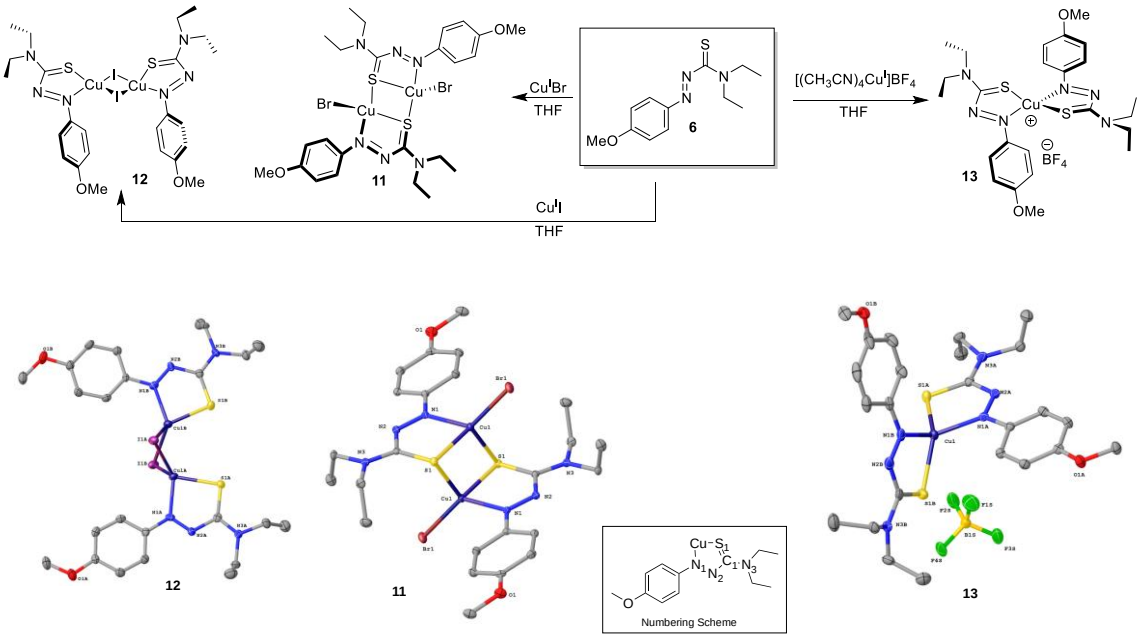

Figure 4.3: Coordination complexes and found crystal structures (11-13) when mixing ligand 6 with Cu^{I} salts. A numbering scheme is provided for reference. Thermal ellipsoids are shown at 50% probability. Hydrogens have been removed for clarity. H_2O molecule has been removed from (11).

As the stability of this butterfly system was unusual, as opposed to known symmetric (μ-I) dimers, i.e., (3b), and others,[21] additional crystallization experiments were explored including: 1) premixing equimolar solutions of $[(CH_3CN)_4Cu^{I}](BF_4)$ and tetrabutylammonium iodide (TBAI) in CH_3CN prior to the addition of a CH_3CN solution of 1.0 equivalent of (6) and; 2) mixing synthesized $(NBu_4)_2Cu_2I_4$, which itself adopts a (μ-I) dimeric structure, and then adding this mixture to the ligand solution resulting in a 2:1 stoichiometric THF solution of (6).[22] In both cases, the unit cells from the crystalline material collected were of (μ-I)-

butterfly complex (12). Apart from these halide salt structural particularities, when $[(CH_3CN)_4Cu](BF_4)$ was mixed directly with two equivalents of (6) in THF, the crystalline material (13) was afforded in 89% yield which displayed a 2:1 distorted tetrahedral structure comparable to the non-substituted ATF 2:1 species (4a/b) in regard to bond distances and bond angles indicating that non-coordinating counterions had little effect on the general crystal formation. Continuing, crystallization studies of Cu^I salts with ortho-MeOATF and meta-MeOATF gave structures (14-19) as shown in Figure 4.4 (Full X-ray data is available for these complexes in Appendix III, Tables A3.2 and A3.3) with bond distances noted in **Table 4.1**. Complex (14), which proved difficult to crystallize, produced a most unique 1:1 dimer complex with only one sulfur atom of the dimer coordinating with both Cu atoms at distances of 2.365 and 2.422 Å allowing for a Cu – Cu distance of 2.770 Å.The proximity of the *ortho*-methoxy groups to the metal center contributed significantly to (14) as seen in the O-Cu distances at 2.586 Å and 2.685 Å. While lengthened in complex (11), S_1=C_1 bonds are held at 1.671 and 1.696 Å in (14) again showing less of a dimeric influence and more influence from the methoxy oxygen. Additionally, the phenyl rings in this complex align with the 1,3-heterodiene displaying torsion angles of 21.18˚ and 23.12˚ between the Cu-N_2-C_2-C_3 atoms and 10.89˚ and 10.21˚ between the Cu-O_1-C_3-C_2 atoms, respectively, of the *ortho*-substituted 2:2 system. This added coordination by the methoxy groups has a profound effect on the weakened binding association values, as seen in the UV-Vis titration results (Figure 4.5). Symmetric exo-Br species (17) from meta-MeOATF crystallized in a P21/c space group, and in contrast to (14), this complex exhibited an exo-Br with noted less influence from the methoxy group on the coordination center than its ortho counterpart. Noticeable is the lengthened Cu–Cu distance to

2.825 Å and the extended C1=S1 bond 1.706 Å due to the coordination of each sulfur atom to both Cu atoms.

Table 4.1: Key Bond Distances for Complexes 11-19 in Angstroms (Å).

Complex	S_1=C_1	C_1–N_2	N_1=N_2	S_1–Cu	N_1–Cu	Cu–X	Cu–Cu	Cu–O_{1A}	Cu–O_{2A}
11	1.712	1.419	1.277	2.320 2.405	2.038	X = Br 2.351, 2.405	2.763		
12	1.685/ 1.686	1.422/ 1.426	1.265/ 1.272	2.316/ 2.301	2.050/ 2.060	X = I 2.596, 2.623/ 2.621, 2.645	2.643		
13	1.699 1.696	1.416 1.417	1.278 1.273	2.289	2.005 2.014				
14	1.671	1.413	1.268	2.297	2.078	X = Br 2.41	2.77	2.685	2.588
	1.696	1.406	1.268	2.422 2.365	2.031	X = Br 2.353			
15	1.678	1.416	1.271	2.326	2.111	X = I 2.589, 2.648	3.024	2.702	2.702
16	1.692 1.692	1.414 1.415	1.272 1.275	2.271 2.277	2.01 2.006			2.787 2.770	2.796 2.808
17	1.706	1.418	1.267	2.335 2.388	2.033	X = Br 2.344	2.825		
18	1.682	1.422	1.267	2.306	2.064	X = I 2.599, 2.603	2.919		
19	1.687	1.427	1.276	2.277 2.261	1.986				

For this series of exo-Br structures (11, 14, and 17) we see the C1=S1 bond lengthen as the methoxy moves further from the Cu center (ortho < meta < para). The ortho- and meta-MeOATF $Cu^{I}I$ series of complexes were found as monoclinic (μ-I) dimers. Ortho-MeOATF complex (15), crystallized in a P21/c space group, aligning methoxy oxygens inwards towards the copper atoms of the complex at distances of 2.702 Å. The torsion angle of the methoxyphenyl ring with the 1,3-heterodiene (O-C3-C2-N2) was -1.62˚ providing a stronger internal coordination to the Cu center. The Cu–Cu distance was measured at 3.024 Å, much larger than the distance of para-MeOATF "butterfly" dimer complex (12) and of meta-MeOATF complex (18).

Interestingly, symmetric (μ-I) 1:1 dimer (18) was found when $Cu^{I}I$ was mixed with meta-MeOATF. Key attributes to this structure are the distorted tetrahedral at the copper centers in a P21/n space group contrasting the "butterfly" (μ-I) dimer (12) and rationalized due to the potential steric interactions of meta-methoxy components if in a butterfly conformation. Cu–Cu distance was found to be 2.919 Å, larger than the sum of the calculated van der Waals radius of copper. Neither ortho nor meta $Cu^{I}I$ complexes (15 and 18) formed a "butterfly" conformation and the Cu–Cu bonds lengths for this series grew as the methoxy unit moved closer to the metal center with (15, ortho as 3.024 Å, 18, meta as 2.919 Å and 12, para as 2.644 Å). Coordination complexes from $[(CH_3CN)_4Cu^{I}](BF_4)$, (13, 16, 19), produced expected 2:1 species with analogous bond distances and angles. Complex (16), from *ortho*-MeOATF (8), gave two similar but unique complexes in the unit cell (only one shown in Figure 4.4). In each, central Cu atom is bound in a 2:1 distorted tetrahedral complex in a C2/c space group containing close contacts to the oxygen atoms in the ortho-methoxy units (2.787, 2.770; 2.796, 2.808 Å).

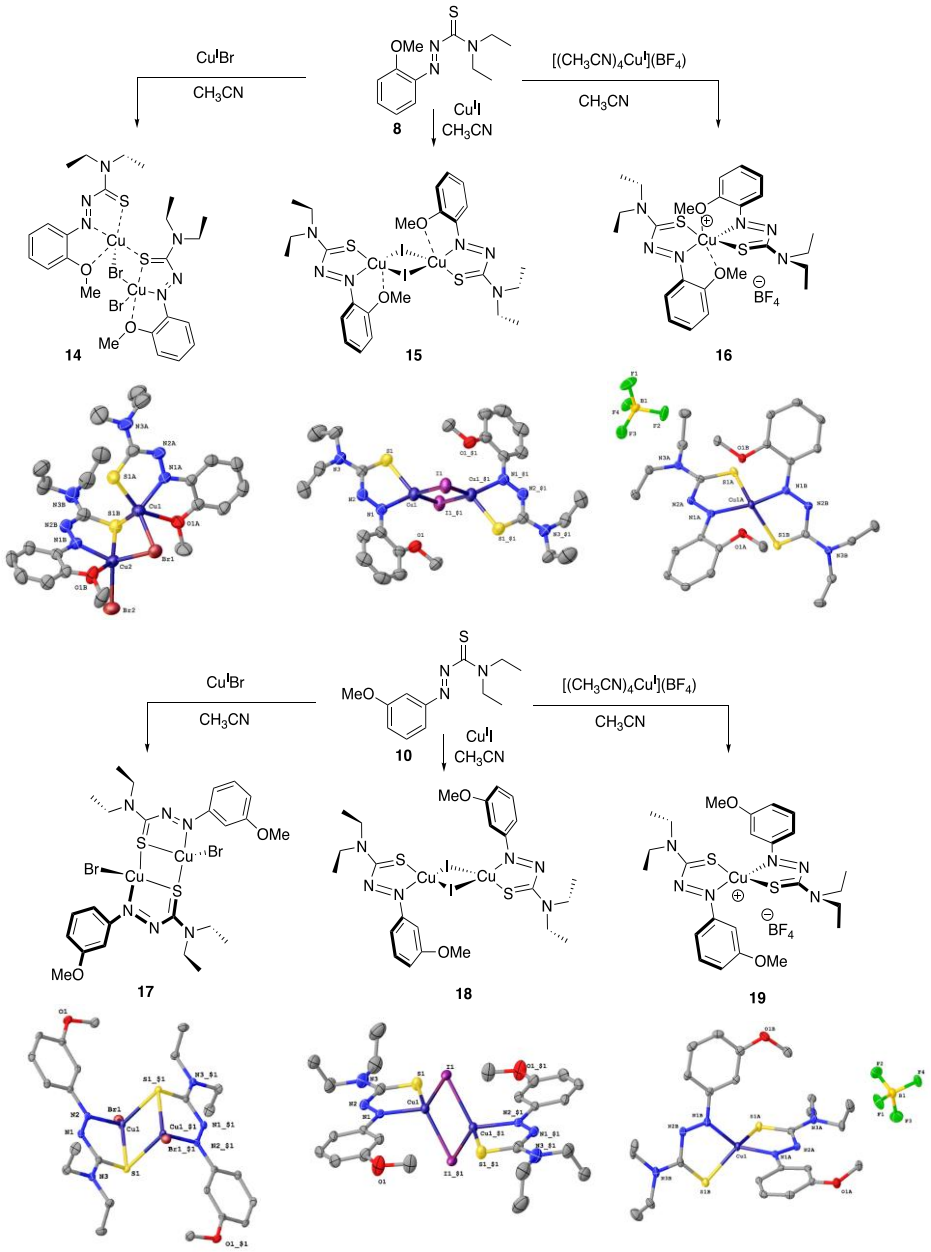

Figure 4.4: Synthesis and X-ray crystal structures of (14 - 19) from mixing ortho-MeOATF (8) or meta-MeOATF (10) with Cu^I salts. All thermal ellipsoid plots drawn at the 50% probability level. Hydrogen atoms have been omitted for clarity. For (15), two chloroform molecules have been removed for clarity.

Species (19) from mixing (10) with $[(CH_3CN)_4Cu^I](BF_4)$ in CH_3CN, formed as crystalline material in a P-1 space group in 65% yield. Complex (13) crystallized with a single

THF molecule in the unit cell but with no coordination or contacts with copper. Distorted tetrahedral bond angles were 84.69˚ and 84.82˚ for N_1–Cu_1–S_1 and N_2–Cu_2–S_2, 125.46˚ and 123.71˚ for S_1–Cu–S_2 and N_1–Cu–N_2, respectively as shown in **Table 4.2**. Similar angles were found for (19) yet (16) produced a much wider N_1-Cu-N_2 bond angle of 139.90˚ due to the proximal *ortho*-methoxy group.

Table 4.2: Key coordination bond angles of 2:1 Complexes

Complex	N_1–Cu_1–S_1	N_2–Cu_1–S_2	S_1–Cu–S_2	N_1–Cu–N_2
13	84.69(5)	84.92(5)	125.46(2)	123.71(7)
16	85.35(6)	85.28(6)	125.84(3)	139.90(8)
19	85.68(5)	85.53(5)	127.16(2)	129.70(7)

Comparatively, the *ortho*- and *meta*- complexes from Cu^IX salts had slightly longer Cu – Cu distances over the *para*-MeOATF complexes as the only key crystallographic difference between the systems. The differences in complexation patterns of complexes from halide salts (11, 12, 14, 15, 17 and 18) over previously found (2a/b) and (3a/b), despite the similarity of ligands suggests that the coordination mechanism(s) may be more complex than simple dimerization from concentration (i.e., the associations are 1:1 in solution, yet dimerize to 2:2 when slow evaporation is used as a crystallization technique).

The strikingly dissimilar symmetry of compound (12) merits closer examination. It can be readily noted that the Cu–Cu distance is the shortest of all the structures obtained thus far in these studies of ATF derivatives. A planar (μ-I)-Cu–I geometry would appear to be favored from a purely electrostatic standpoint, pushing the copper cations as far apart as possible. In

this case, the non-planar geometry does not appear to be driven by steric bulk based on consideration of close contacts (per CCDC Mercury). Speculatively, the configuration could suggest a “cuprophilic” attraction between copper centers, bringing the cations closer together. Such a possibility has been previously explored, due to the short Cu–Cu distances found in complexes including biological systems.[24,25] Recently, a survey of interatomic distances by Alvarez explicitly investigated the Group 11 metals and calculated a clear peak for Cu–Cu distances of 2.64 Å (FWHM ~ 0.5 Å per S9 in the Alvarez), which are assigned to covalent bonding. Thus, these complexes may be of interest for delineating "cuprophilic" behavior over dimerization.

UV-Vis Titration Results

Binding association values for the ligands were fit to both 1:1 and the four 2:1 binding association types (Full, Additive, Non-cooperative, and Statistical) and these fits can be found in Appendix III Table A3.4. Representative UV-Vis titration spectral data of each salt with the these ligands can be found in Appendix III Figures A3.26-A3.28. Binding association data was calculated over a series of wavelengths (410, 412, 414, 416, 418 nm) in triplicate and all values were used to calculate binding association values and errors. Binding association values for *para*-,[12] *ortho*-, and *meta*- are shown and include the (μ-I) complex $(NBu_4)_2Cu_2I_4$ titrations. To note are that binding association values across all 2:1 types for $(NBu_4)_2Cu_2I_4$ complex were comparable to the Cu^II, indicating the likely rapid formation of dimeric Cu^II ($[(CH_3CN)_2Cu_2I_2]$) in solution and subsequent addition of the ATF ligands. Cu^II is known to form coordination polymers in organic solutions and so the idea of a second Cu^II addition was a possibility, and the modelled exergonic complex favors this second binding event. However, the minimal error associated with the 2:1 types and the relatively low concentrations of metal

salts and ligands make this less likely for these particular systems while providing support of why coordination polymers of $Cu^{I}X$ do form in more concentrated systems.[26] UV-Vis generated binding isotherms for representative $Cu^{I}Br$ with various MeOATF complexes are shown in **Figure 4.5**.

Ortho-MeOATF, (8), when titrated against Cu^{I} salts gave binding association constants that were ~3x weaker compared to *para*-MeOATF (6), which are attributed to steric influences from methoxy group oxygen atoms coordinating to the Cu^{I} center, affording a slower dimeric association. *Meta*-MeOATF (10) produced similar binding trends as *ortho*-MeOATF (8) indicating that the steric effect of the coordinating methoxy group in (8) to weaken the association compares well with the reduced donating ability of the *meta* substitution pattern in (10). Bayesian Information Criteria (BIC) was used to compare between association model types. BIC allows for evaluating models with a different number of parameters by penalizing models with additional parameters.[27] The magnitude of the change in BIC comparing 2:1 models suggest that a full model type ($K_1 \neq 4K_2$ and $\delta_{\Delta}AB_2 \neq 2\delta_{\Delta}AB$) best predicts binding, except for $Cu^{I}I$ for *para*-MeOATF (6) or $(Cu^{I}I_2)_2$ for *para*-MeOATF (6) and *meta*-MeOATF (10) where a non-cooperative model type fits as well. These binding results, low errors, computational comparisons (see below) and statistical values (RMS, BIC, see Appendix III Table A3.4) lead to the suggested mechanisms of formation for all complexes being of 2:1 type binding association.

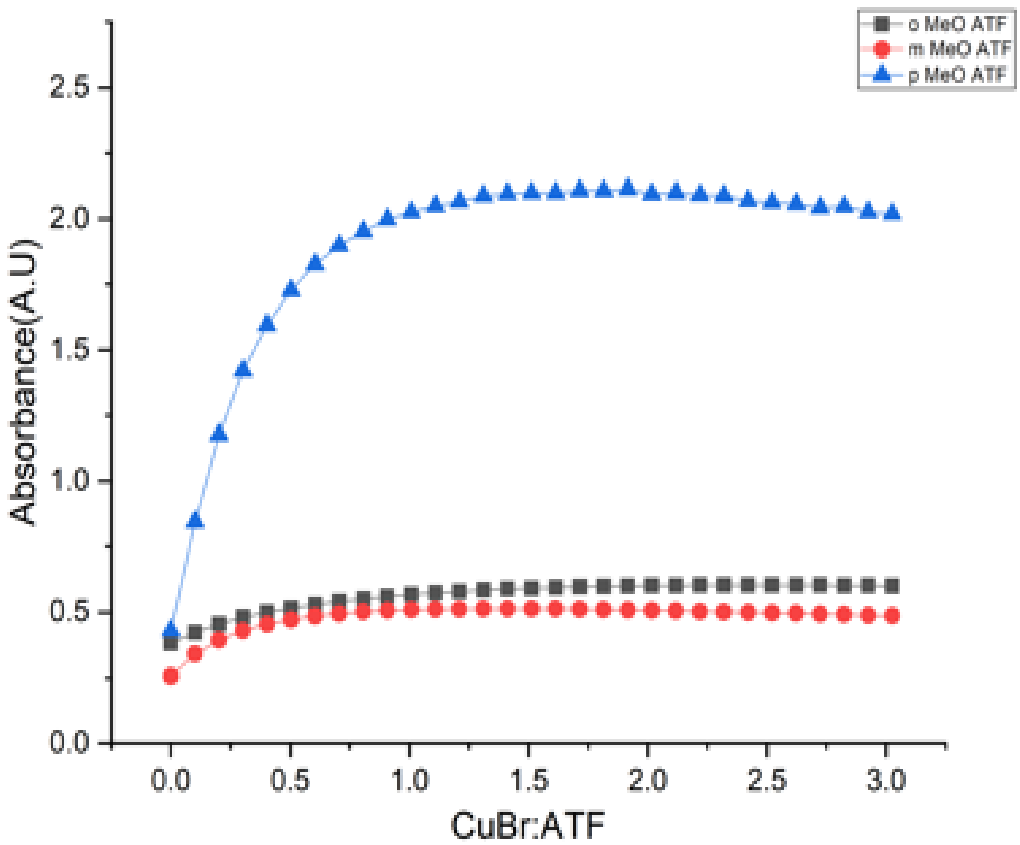

Figure 4.5: UV-Vis Binding isotherms for para-, ortho-, and meta-MeOATF complexes with $Cu^{I}Br$ as representative ligand-metal salt complex (average of triplicate trials) at 414 nm. All UV-Vis measurements were performed in acetonitrile with beginning ligand concentrations of 1.45 x 10^{-4} M. Binding trends indicate that para-substituted methoxy ATFs have a much stronger binding association constant than ortho which is closer to meta indicating a weakened electronic effect on the dimerization.

Computational Studies

Mechanistic investigations commenced with the modelling of found complexes (i.e., (11) and (12)) using B3LYP/6-311G++(d,p)//B3LYP/6-31G(d,p) to predict the single point energy and geometry optimizations of the isolated structures and other possible structures (either (*exo*-X and halogen-bridged symmetric μ-X dimer;, or μ-X "butterfly" dimer) as shown

in Figure 4.6 as to describe each found complex as thermodynamically or kinetically favored. The computations were run in various solvents (e.g., THF and acetonitrile) as triplets.

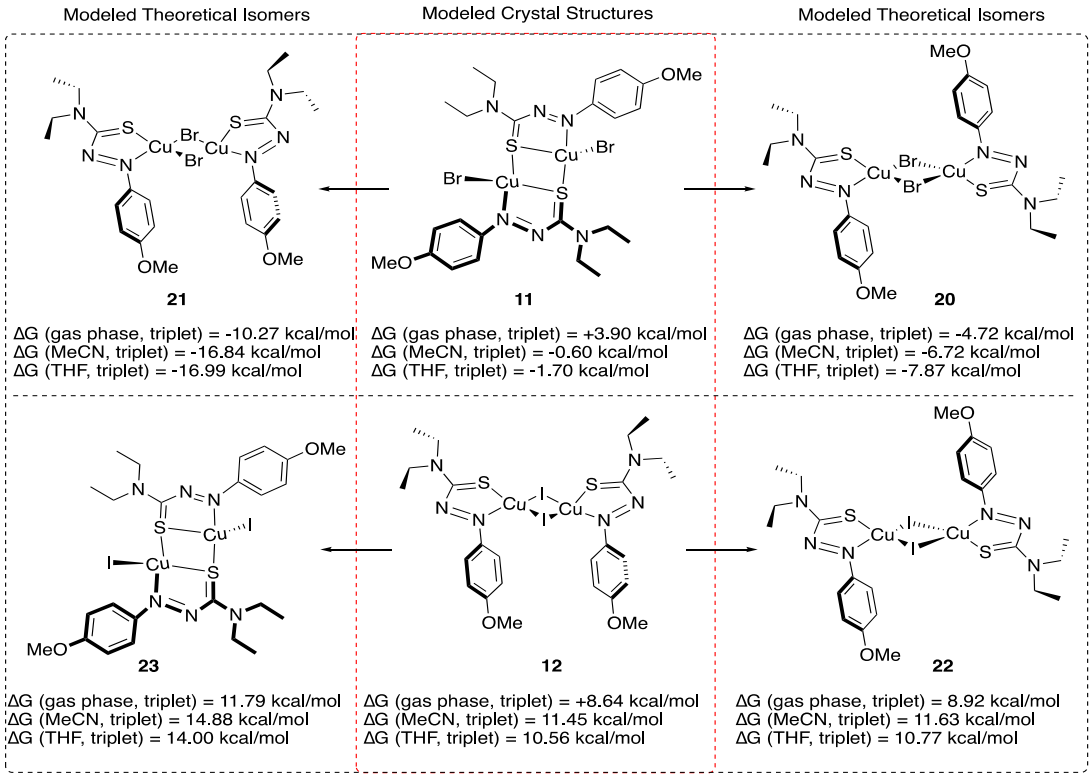

Figure 4.6: Computational investigations of found crystal structures 11 and 12 and comparisons to potential exo-X and halogen-bridged μ-X, and μ-X "butterfly" dimers (20 - 23).

For example, the *exo*-Br structure (11) was higher in energy by ~9 kcal/mol over the computed (μ-X) dimeric structure (20) and ~14 kcal/mol higher than the computed butterfly dimer (21). As isolated *exo-Br* structure (11) exhibited the highest energy in all scenarios it is most likely a kinetic product. However, isolated butterfly dimer (12) from $Cu^{I}I$ resulted in the lowest energy structure when modelled against computed isomers (i.e., symmetric μ-I dimer (*22*) and *exo*-I (23) and assumed a thermodynamic product. Calculations and orbital diagram of all *para*-MeOATF Cu^{I} halide systems are provided (See Appendix III, Figures A3.1-A3.11).

Further DFT investigations provided mechanistic insight into the formation of the found crystalline structures (and the other possible structures as shown in ESI Figures S12-S25).

Mechanistically, the formation of 1:1 dimers (2:2 complexes 11, 12, 14, 15, 17, and 18) warrants further attention. Dimers can be generated through three potential complexation pathways as shown in Figures 3.7-3.10, using complex (12) as example, and labelled Mechanisms 1-3 below. All mechanisms begin with acetonitrile solvated Cu^{I} halides (i.e., 24) as UV-Vis titration studies were performed with dissolved salts in acetonitrile.

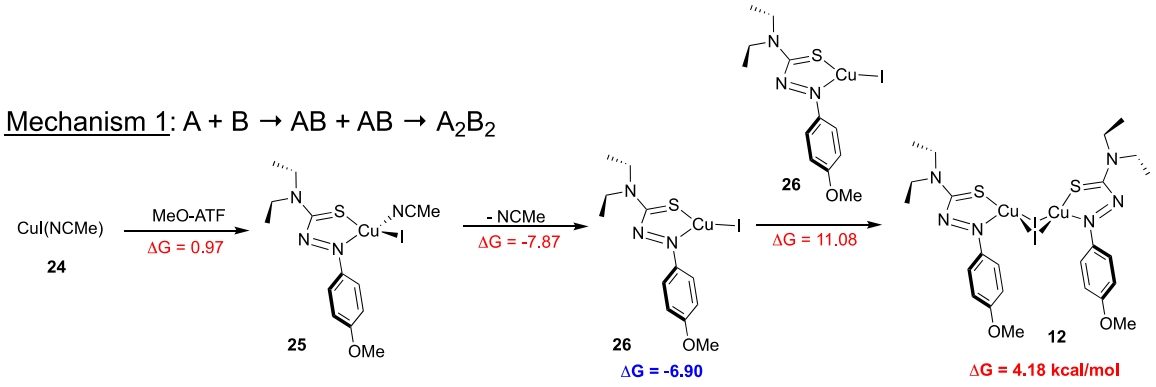

Figure 4.7: Mechanism 1 for A_2B_2 formation; dimerization via AB + AB.

Mechanism 1, **Figure 4.7**, depicts simple dimerization of Ligand (A) and Metal Salt (B) complex AB formed from an A + B → AB + AB → A_2B_2 pathway. Starting from an endergonic coordination of ligand (6) to (24) creates compound (25) which then undergoes an exergonic (-7.87 kcal/mol) loss of the acetonitrile yielding an AB complex (26) which is followed by a subsequent endergonic (11.08 kcal/mol) dimerization step with another metal-ligand (26) pair to yield (12). Initially, this dimerization mechanism was hypothesized to be a result of evaporative concentration of a 1:1 association mechanism, and at high concentrations, a minor energetic obstacle in the formation of crystalline material. Yet, as the crystalline dimer material forms minutes after addition and UV-Vis studies show 2:1 binding at low

concentrations, indicates a kinetic product and this mechanism, while slightly uphill, is absolutely a possibility.

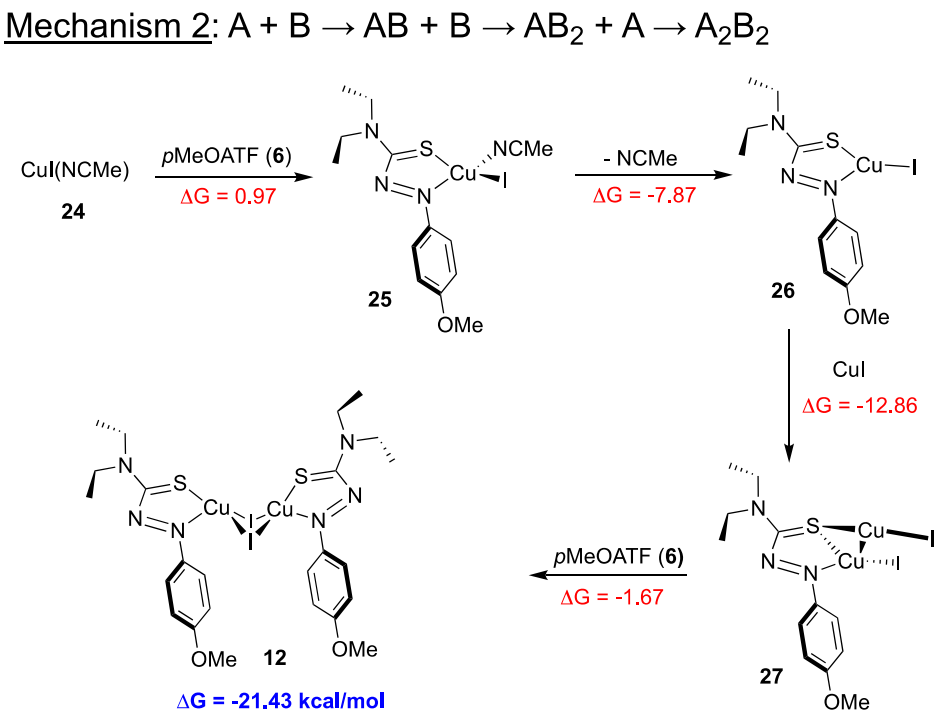

Figure 4.8: Mechanism 2 of A_2B_2 formation utilizing the AB+B pathway.

Mechanism 2, as shown in **Figure 4.8**, begins with the initial favorable AB formation of (26) followed by an exergonic second addition of metal salt (Cu^I salt) giving (27) followed by second addition of ligand through the pathway (A + B → AB + B → AB_2 + A → A_2B_2) to yield (12). This mechanism is the most exergonic as each step following the 1:1 complexation event has a negative ΔG. The only issue is that this pathway is the result of a three individual binding events as AB, AB_2 and A_2B_2 species are all expected to be spectroscopically active. The low errors associated with all 2:1 binding model types make this scenario difficult to justify unless the second coordination to a metal salt, the formation of AB_2 (27), does not cause a major fluctuation in spectroscopic response or if the final ligand addition is incredibly fast. This mechanistic evaluation, however, depicts the substantial and favorable nature of Cu^IX

addition and one can see how multi-unit coordination polymers of $Cu^{I}I$ can form in concentrated solutions capitalizing on this style of mechanism and high concentrations of metal salt.

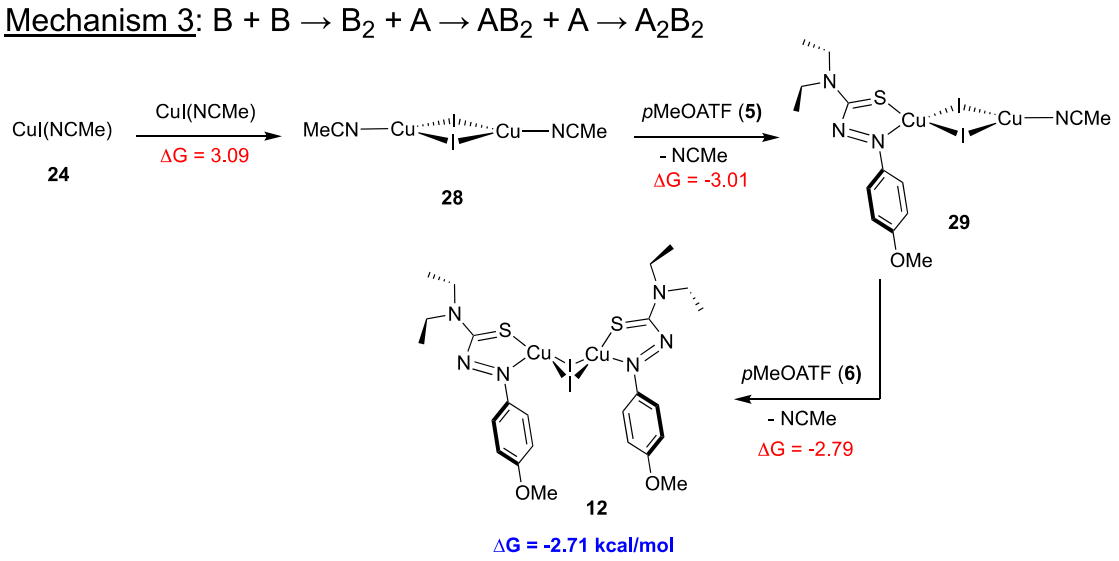

Figure 4.9: Mechanism 3, formation of UV-Vis invisible B_2 in solution followed by sequential ligand additions.

Furthermore, as shown in **Figure 4.9**, Mechanism 3, depicts two metal salts associating first to create a spectroscopically (UV-Vis) invisible B_2 dimer, essentially the $[(CH_3CN)Cu^{I}(\mu\text{-}I)]_2$ species (28), followed by the sequential addition of ligands ($B + B \rightarrow B_2 + A \rightarrow AB_2 + A \rightarrow A_2B_2$), providing an exergonic and rational pathway to a 2:1 binding association model.

Finally, binding isotherms and association values with synthesized $(NBu_4)_2Cu_2I_4$ salts (Appendix III Table A3.4, Figure A3.18, A3.19 A3.23 and A3.24) show relatively similar binding association constants from $Cu^{I}I$ titrations over three of the four 2:1 binding type models.[22] As shown in **Figure 4.10**, mechanism 3 is hypothesized to be the most plausible scenario to create the isolated complex (12) and was corroborated by the experiments

mentioned above where various in-situ $Cu^{I}I$ species, presumably $[(CH_3CN)Cu^{I}(\mu\text{-}I)]_2$, were formed.

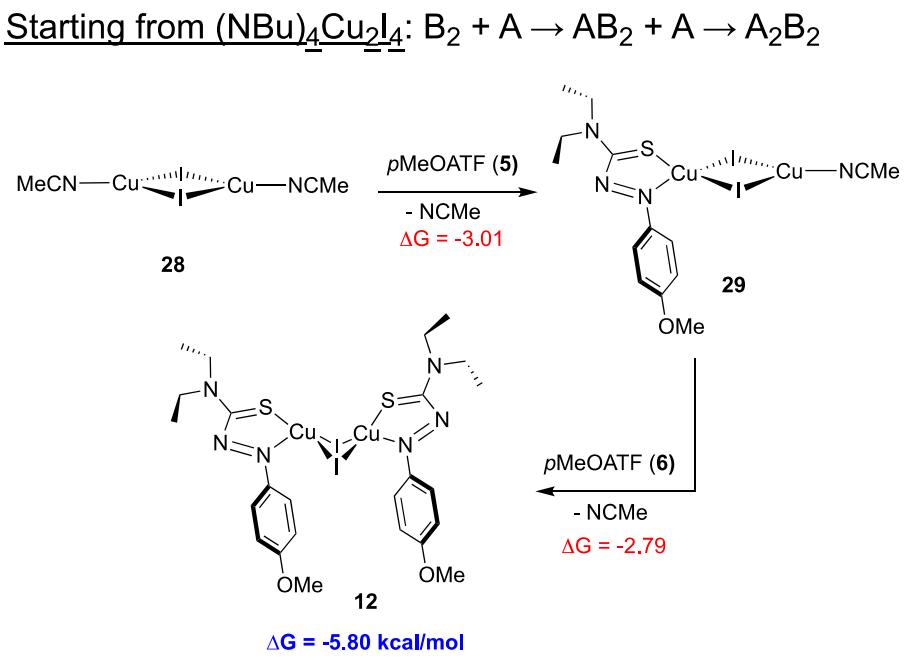

Figure 4.10: Exergonic mechanism of Mechanism 3 binding when starting from the solvated metal salt dimer (28).

It should be noted that, while plausible for the formation of (12), mechanism 3 is not exergonic for all substituted MeOATF-copper salt species. For example, *exo*-Br dimer (11), owing to the two Cu-S interactions for each ligand of the dimer, and the C_{2c} symmetry aligns more favorably with mechanism 1 (Figure in Appendix III). Compound (14) with only one copper atom interacting with each sulfur atom of the two ATF ligands in the dimer suggests mechanism 2 over others. Lastly, the formation of all 2:1 ligand – metal species, (13, 16, and 19) follows the exergonic A + B → AB + A → A_2B mechanism.

4.3 Conclusion

In this study, the electron-donating methoxy monosubstituted *ortho*, *meta*, and *para* monosubstituted ATF ligands (6, 8, and 10) were synthesized and their coordination to Cu^I salts was evaluated experimentally using UV-Vis titration binding data, through computational modelling, and following critical review of isolated X-ray crystal structures. All complexes, no matter the substitution pattern, fit 2:1 non-linear binding association isotherms with less error than 1:1 models. While these model fits were obvious for the 2:1 complexes derived from $[(CH_3CN)_4]Cu^IBF_4$ (13, 16, 19), for the Cu^IX 1:1 dimer complexes to exhibit a 2:1 binding association revealed the possibility of more complex binding mechanisms. Mechanisms arising from an AB_2 species, forming from either $B_2 + A \rightarrow AB_2$ or $AB + B \rightarrow AB_2$ were both modeled as potential mechanisms over a simple dimerization pattern. *Exo*-Br species (11, 14, and 17) suggest $AB + B \rightarrow AB_2$ mechanism which is complimented by an extra Cu-S interaction and, in some cases, (14), with limited symmetry. The (μ-I) and (μ-I)-butterfly dimers (12, 15, and 18) from Cu^II were rationalized to undergo an initial Cu^II dimerization creating a $(CH_3CN)_2Cu_2I_2$ species in solution which then bound MeOATF ligands sequentially ($B_2 + A \rightarrow AB_2 + A \rightarrow A_2B_2$) as additional experiments $(NBu_4)_2Cu_2I_4$ titration and unit cells from TBAI/$[(CH_3CN)_4Cu^I](BF_4)$ mix) were performed to give further support to this theory. The μ-I halogen-bridged "butterfly" dimer (12) was unique in this regard as the crystal uniformity and stronger modelled energetics over the *exo*-X species or symmetric μ-X species from both *ortho* and *meta*-MeOATF species suggest a weak cuprophilicity of the two copper atoms. The binding strength of the *ortho* and *meta*-MeOATF ligands was compromised and significantly lower than the *para*-MeOATF. This was seen through the extended Cu – Cu distances in this series of complexes and attributed to the potential influence of the methoxy group to coordinate

or provide steric hindrance for dimerization. Ultimately, the binding studies suggest that *para*-MeOATF Cu^{I} complexes have stronger binding associations than *ortho* and *meta* and the shortened Cu – Cu bond distance (< 2.7 Å), suggestive of cuprophilicity, may promote μ-I halogen-bridged "butterfly" dimer complexes as seen in 12 over other potential orientations. Overall, the investigation into coordinative complexes of ligand regioisomers led to a critical evaluation of potential binding association mechanisms and how sterics and electronics influence binding. These key factors will drive ligand selection for future metal dissolution and catalysis studies.

4.4 Experimental

General methods and experimental procedures for the synthesis of ligands 6, 8, and 10, NMR spectral data for all ligands and complexes and X-ray crystallography parameters can be found in the Electronic Supporting information (ESI). All crystal structures have been submitted to the CCDC and are identified by their CCDC codes.

Synthetic procedures

[Cu•6(exo-Br)]$_2$ (11): To *para*-MeOATF (**6**) (200 mg, 0.79 mmol) dissolved in 5 mL of anhydrous THF in a 2-dram vial was added $Cu^{I}Br$ (113 mg, 0.79 mmol). The solution had a rapid color change from light orange to dark blue and was heated with a heat gun to promote solvation and then decanted into another 2-dram vial and allowed to slowly concentrate over 3-5 days to yield 137 mg (44%) of dark blue crystals. ^{1}H NMR (500 MHz, Chloroform-d) δ 8.58 (d, *J* = 8.6 Hz, 2H), 7.06 (d, *J* = 8.6 Hz, 2H), 4.20 – 4.07 (m, 4H), 3.95 (s, 3H), 1.48 (t, *J* = 7.1 Hz, 4H), 1.43 (t, *J* = 7.1 Hz, 3H). ^{13}C NMR (126 MHz, $CDCl_3$) δ 195.19, 164.35, 147.12, 126.79, 115.27, 56.54, 48.76, 45.95, 14.62, 12.32. FTIR (ATR, cm^{-1}): 2978, 1592, 1436, 1297,

1154, 847, 705. Elem. Anal.: $C_{24}H_{34}Cu_2Br_2N_6O_2S_2$ (789.6) (Calcd) C, 36.51; H, 4.34; N, 10.64; (Found) C, 36.20; H, 4.27; N, 9.74. mp: 183˚C. **CCDC 2169093**

[Cu•6(μ-I)]$_2$ (12): To *para*-MeOATF (**6**) (100 mg, 0.398 mmol) dissolved in 5 mL of anhydrous THF was added $Cu^{I}I$ (76 mg, 0.398 mmol). After rapid color change from light orange to dark green the solution was decanted into another 2-dram vial and allowed to concentrate via evaporation at room temperature over 3-5 days to afford 121 mg of dark green crystals (69%). ^{1}H NMR (500 MHz, Chloroform-d) δ 8.80 (d, *J* = 9.2 Hz, 2H), 7.06 (d, *J* = 9.2 Hz, 2H), 4.13 – 4.07 (m, 4H), 1.46 (t, *J* = 7.2 Hz, 3H), 1.39 (t, *J* = 7.2 Hz, 3H). ^{13}C NMR (126 MHz, $CDCl_3$) δ 187.77, 166.01, 146.01, 130.43, 115.41, 56.27, 50.21, 47.50, 15.13, 11.40. FTIR (ATR, cm^{-1}): 2970, 1596, 1435, 1297, 1154, 838, 709. Elem. Anal.: $C_{24}H_{34}Cu_2I_2N_6O_2S_2$ (883.6) (Calcd) C, 32.62; H, 3.88; N, 9.51 (Found) C, 32.66; H, 3.67; N, 8.81; mp: 164˚C. **CCDC 2169094**

[Cu•6$_2$]BF$_4$ (13): To *para*-MeOATF (**6**) (100 mg, 0.398 mmol) in 5 ml of anhydrous THF in a 2-dram vial was added $[(CH_3CN)_4Cu^{I}]BF_4$ (63 mg, 0.199 mmol). After rapid color change from light orange to dark blue, the solution was decanted into another 2-dram vial and allowed to concentrate via evaporation at room temperature to afford 208 mg (80%) of crystals. ^{1}H NMR (500 MHz, Chloroform-d) δ 8.11 (d, *J* = 9.2 Hz, 2H), 7.00 (d, *J* = 9.2 Hz, 2H), 4.27 (q, *J* = 7.2 Hz, 2H), 4.10 (q, *J* = 7.2 Hz, 2H), 3.91 (s, 3H), 1.53 – 1.45 (m, 6H). ^{13}C NMR (126 MHz, $CDCl_3$) δ 186.84, 167.43, 145.38, 130.00, 116.33, 56.74, 50.85, 48.72, 15.02, 11.23. FTIR (ATR, cm^{-1}): 2981, 1592, 1438, 1271, 1141, 844, 705. Elemental Analysis: $C_{24}H_{34}CuBF_4N_6O_2S_2$ (653.04) (Calculated) C, 44.14; H, 5.25; N, 12.87 (Found) C, 44.25; H, 5.25; N, 12.30; mp: 134 ˚C. **CCDC 2169095**

[Cu•(8)Br]$_2$ (14): To *ortho*-MeOATF (**8**) (59 mg, 0.235 mmol) dissolved in 5 ml of acetonitrile in a 2-dram vial was added $Cu^{I}Br$ (34 mg, 0.235 mmol). After rapid color change light orange to dark green the solution was decanted into another 2-dram vial and allowed to slowly concentrate via evaporation at room temperature collecting 45 mg solid material (49%). ^{1}H NMR (300 MHz, Chloroform-d) δ 7.75 (d, *J* = 8.1 Hz, 1H), 7.53 (t, *J* = 7.8 Hz, 1H), 7.07 (t, *J* = 10.3 Hz, 2H), 4.11 (q, *J* = 7.1 Hz, 4H), 3.90 (s, 3H), 1.46 – 1.40 (m, 6H). ^{13}C NMR (126 MHz, CDCl3) δ 186.32, 158.04, 139.97, 137.51, 124.28, 121.89, 113.48, 56.34, 51.04, 48.30, 15.04, 11.44. FTIR (ATR, cm^{-1}): 2974, 1590, 1436, 1273, 1144, 838, 755. Elem. Anal.: $C_{24}H_{34}Cu_2Br_2N_6O_2S_2$ (789.6) (Calcd) C, 36.51; H, 4.34; N, 10.64; (Found) C, 35.98; H, 4.04; N, 9.56. mp: 150˚C. **CCDC 2169096**

[Cu•(8)I]$_2$ (15): To *ortho*-MeOATF (**8**) (30 mg, 0.12 mmol) dissolved in 5 mL of acetonitrile in a 2-dram vial was added $Cu^{I}I$ (23 mg, 0.12 mmol). After rapid color change from light orange to dark green the solution was decanted into another 2-dram vial and allowed to concentrate via evaporation at room temperature over 3-5 d to yield 38 mg solid material (72%). A portion of this material was recrystallized in $CHCl_3$. ^{1}H NMR (300 MHz, Chloroform-d) δ 7.89 (d, *J* = 8.2 Hz, 1H), 7.53 (t, *J* = 7.6 Hz, 1H), 7.10 (d, *J* = 8.4 Hz, 1H), 7.01 (t, J = 7.7 Hz, 1H), 4.09 (s, 3H), 4.02 (q, *J* = 6.3 Hz, 4H), 1.42 (t, *J* = 7.1 Hz, 3H), 1.36 (t, *J* = 7.1 Hz, 3H). ^{13}C NMR (126 MHz, $CDCl_3$) δ 186.76, 158.13, 140.84, 136.48, 124.14, 121.34, 113.44, 56.41, 50.40, 47.61, 14.88, 11.49. FTIR (ATR, cm^{-1}): 2978, 1588, 1435, 1287, 1154, 849, 755. Elem. Anal.: $C_{24}H_{34}Cu_2I_2N_6O_2S_2$ (883.6) (Calculated) C, 32.62; H, 3.88; N, 9.51 (Found) C, 32.70; H, 3.79; N, 8.38; mp: 152˚C. **CCDC 2169097**

[Cu•(8)$_2$]BF$_4$ (16): To *ortho*-MeOATF (**8**) (77 mg, 0.31 mmol) in 5 mL of acetonitrile in a 2-dram vial was added $[(CH_3CN)_4Cu^{I}]BF_4$ (48 mg, 0.153 mmol). After rapid color change from

light orange to dark green the solution was decanted into another 2-dram vial and slowly concentrated via evaporation at room temperature to yield 70 mg of crystals (69%). ^{1}H NMR (300 MHz, Chloroform-d) δ 7.73 (d, *J* = 7.8 Hz, 1H), 7.53 (t, *J* = 7.8 Hz, 1H), 6.98 (t, *J* = 7.2 Hz, 2H), 4.15 (q, *J* = 7.2, 6.5 Hz, 2H), 4.01 (q, *J* = 7.1 Hz, 2H), 3.64 (s, 3H), 1.45 (t, *J* = 5.3 Hz, 3H), 1.41 (t, *J* = 5.3 Hz, 3H). 13C NMR (126 MHz, $CDCl_3$) δ 186.51, 157.76, 140.59, 137.63, 123.76, 122.23, 113.79, 55.79, 50.99, 48.60, 14.89, 11.01. FTIR (ATR, cm^{-1}): 2980, 1588, 1443, 1289, 1160, 850, 758. Elemental Analysis: $C_{24}H_{34}CuBF_4N_6O_2S_2$ (653.04) (Calculated) C, 44.14; H, 5.25; N, 12.87; (Found) C, 44.34; H, 5.23; N, 12.34; mp: 135˚C. **CCDC 2169098**

[Cu•10(*exo*-Br)]$_2$ (17): To *meta*-MeOATF (**10**) (59 mg, 0.235 mmol) dissolved in 5 ml of acetonitrile was added $Cu^{I}Br$ (34 mg, 0.235 mmol) in a 2-dram vial. The solution was decanted into another vial and allowed to slowly concentrate via evaporation to form 41 mg of crystals (44 %). ^{1}H NMR (500 MHz, Chloroform-d) δ 8.41 (s, 1H), 8.20 (d, *J* = 7.8 Hz, 1H), 7.47 (t, *J* = 8.1 Hz, 1H), 7.24 (d, *J* = 8.4 Hz, 1H), 4.15 – 4.09 (m, 4H), 3.99 (s, 3H), 1.48 (t, *J* = 7.2 Hz, 3H), 1.42 (t, *J* = 7.2 Hz, 3H). ^{13}C NMR (126 MHz, $CDCl_3$) δ 187.28, 160.95, 152.49, 130.71, 122.98, 119.13, 112.32, 56.37, 51.16, 48.08, 15.15, 11.16. FTIR (ATR, cm^{-1}): 2979, 1598, 1434, 1257, 1169, 857, 792. Elem. Anal.: $C_{24}H_{34}Cu_2Br_2N_6O_2S_2$ (789.6) (Calcd) C, 36.51; H, 4.34; N, 10.64; (Found) C, 36.95; H, 4.24; N, 9.57; mp: 171 ˚C. **CCDC 2169099**

[Cu•10(μ-I)]$_2$ (18): To *meta*-MeOATF (**10**) (30 mg, 0.12 mmol) dissolved in 5 mL of acetonitrile in a 2-dram vial was added CuII (23 mg ,0.12 mmol). After rapid color change, the solution was decanted into another 2-dram vial and allowed to concentrate via evaporation at room temperature to afford 33 mg of crystalline material (72 %). ^{1}H NMR (500 MHz, Chloroform-d) δ 8.44 (s, 1H), 8.16 (d, *J* = 7.9 Hz, 1H), 7.44 (t, *J* = 8.1 Hz, 1H), 7.21 (d, *J* =

8.1 Hz, 1H), 4.10 – 4.05 (m, 4H), 4.00 (s, 3H), 1.47 (t, *J* = 7.2 Hz, 3H), 1.38 (t, *J* = 7.2 Hz, 3H). ^{13}C NMR (126 MHz, CDCl3) δ 187.95, 160.68, 152.78, 130.30, 122.19, 118.27, 112.35, 56.39, 50.10, 47.37, 15.04, 11.27. FTIR (ATR, cm^{-1}): 2976, 1600, 1433, 1257, 1167,855, 705. Elem. Anal.: $C_{24}H_{34}Cu_2I_2N_6O_2S_2$ (883.6) (Calcd) C, 32.62; H, 3.88; N, 9.51; (Found) C, 31.75; H, 3.65; N, 8.39; mp: 163˚C. **CCDC 2169100**

[Cu•(10)$_2$]BF$_4$ (19): To *meta*-MeO ATF (**10**) (77 mg, 0.30 mmol) dissolved in 5 mL of acetonitrile in a 2-dram vial was added [(CH$_3$CN)$_4$Cu^I]BF$_4$ (48 mg, 0. 15 mmol). After rapid color change, the solution was decanted into another 2-dram vial and left to concentrate via evaporation at room temperature to afford 65 mg of crystals (65%). ^{1}H NMR (500 MHz, Chloroform-*d*) δ 7.64 (d, *J* = 7.7 Hz, 1H), 7.47 (s, 1H), 7.40 (t, *J* = 8.1 Hz, 1H), 7.16 (d, *J* = 7.7 Hz, 1H), 4.30 (q, *J* = 7.1 Hz, 2H), 4.13 (q, *J* = 7.1 Hz, 2H), 3.79 (s, 3H), 1.51 (t, *J* = 7.2 Hz, 3H), 1.47 (t, *J* = 7.2 Hz, 3H). ^{13}C NMR (126 MHz, CDCl$_3$) δ 186.82, 160.92, 151.93, 131.27, 123.32, 121.10, 108.71, 55.97, 51.21, 49.11, 15.16, 11.04. FTIR (ATR, cm^{-1}): 2976, 1598, 1446, 1278, 1154, 836, 702. Elem. Anal.: $C_{24}H_{34}CuBF_4N_6O_2S_2$ (653.04) (Calcd) C, 44.14; H, 5.25; N, 12.87; (Found) C, 45.06; H, 5.28; N, 12.15. mp: 135˚C. **CCDC 2169101**

UV-Vis Titrations

UV-Vis spectroscopic titration studies of ATF ligands 6, 8 and 10 with Cu^I salts were prepared as follows: ligand solutions were prepared to 1.45 x 10^{-4} M in acetonitrile. 1.2 mL of ATF solution was added to a quartz cuvette. Titrations were performed with CuI halide salts and [N(Bu$_4$)$_2$(μ-I)-Cu$_2$I$_4$] utilizing 1.35 mM stock solutions in acetonitrile and sequentially adding 13 μL (roughly 0.1 equivalent of metal salt) until reaching a metal salt concentration of three equivalents (a final volume of 2.0 mL); [(CH$_3$CN)$_4$Cu^I]BF$_4$ salts titrations were performed in the same manner as above to a final 1.5 equivalents. Each titration was performed

in triplicate. Following data acquisition, each spectra series was evaluated using non-complexing absorbance models to evaluate wavelength regions where complexation may occur. Binding association constants were calculated utilizing non-linear binding regression models in OriginLab® and Bindfit.

The data that support the findings of this study are openly available in the University of Idaho RCDS data repository at https://doi.org/10.7923/2Z54-2V65 (Pradhan et al. 2022).[28]

X-ray Crystallography

X-ray diffraction data for all compounds was collected at 100 K on a Bruker D8 Venture using MoKα-radiation (λ=0.71073 Å). Data have been corrected for absorption using SADABS[29] area detector absorption correction program. Using Olex2[30], the structure was solved with the SHELXT[31] structure solution program using Direct Methods and refined with the SHELXL[32] refinement package using least squares minimization. Further individual crystal experimental data is provided in the electronic supporting information.

Computational Details

All structures were fully optimized without symmetry constraints using the B3LYP functional as implemented in Gaussian 09 using the 6-31G** basis set for C, H, N, S, Br, B, F, and P and the Stuttgart basis set with effective core potentials for all metal and iodine atoms. To verify the validity of the chosen method, other DFT functionals were used: B3LYP-D3, B3P86, B3PW91, M11, and wB97XD, but B3LYP gave structural parameters that best matched the experimental structures. The ultrafine integration grid was employed in all calculations, which ensured the stability of the optimization procedure for the investigated molecules. Each stationary point was confirmed by a frequency calculation at the same level

of theory to be a real local minimum on the potential energy surface. More accurate electronic energies were computed for the optimized geometries using the larger 6-311++G(d,p) basis set. All reported free energies are for tetrahydrofuran solution at the standard state (T = 298 K, P = 1 atm, 1 mol/L concentration of all species in THF) as modeled by a polarized continuum model. The energy values given in the manuscript correspond to solvent-corrected Gibbs free energies that are based on B3LYP/6-311++G(d,p) electronic energies and all corrections calculated at the B3LYP/6-31G(d) level.

4.5 References

1. Elsevier, C.J.; Reedjik, J.; Walton, P.H.; Ward, M.D., *Dalton Trans.* **2003**, (10), 1869-1880.

2. Lamm, J.H.; Niermeier, P.; Mix, A.; Chmiel, J.; Neumann, B.; Stammler, H. G.; Mitzel, N.W., *Angew. Chem. Int. Ed.* **2014**, *53* (30) 7938-42.

3. Sakata, Y.; Tamiya, M.; Okada, M.; Akine, S., *J. Amer. Chem. Soc.* **2019**, *141* (39), 15597-15604.

4. Szaloki, G.; Croue, V.; Carre, V.; Aubriet, F.; Aleveque, O.; Levillian, E.; Allain, M.; Arago, J.; Orti, E.; Goeb, S.; Salle, M., *Angew. Chem. Int. Ed.* **2017**, *56* (51), 16272-16276.

5. Bechgaard, K., *Acta Chem Scand A* **1977**, *31* (8), 683-688.

6. Hazell, R. G., *Acta Chem Scand A* **1976**, *30* (5), 322-326.

7. Bechgaard, K., *Acta Chem Scand A* 1974, *A 28* (2), 185-193.

8. Nielsen, K. T.; Bechgaard, K.; Krebs, F. C., *Macromolecules* **2005**, *38* (3), 658-659.

9. Nielsen, K. T.; Bechgaard, K.; Krebs, F. C., *Synthesis-Stuttgart* **2006**, (10), 1639-1644.

10. Johnson, N. A.; Wolfe, S. R.; Kabir, H.; Andrade, G. A.; Yap, G. P. A.; Heiden, Z .M.; Moberly, J. G.; Roll, M. F.; Waynant, K. V. *Eur. J. Inor. Chem.* **2017** (47) 5576-5581.

11. Pradhan, R.; Groner, V. G.; Johnson, N. A.; Zhang, Q.; Roll, M. F.; Moberly, J. G.; Waynant, K. V., *Inor. Chem. Commun.* **2021**, *124*, 108393.

12. Pradhan, R.; Groner, V. M.; Gutman, K. L.; Heiden, Z. M.; Roll, M. F.; Moberly, J. G.; Waynant, K. V., *Supramol Chem* **2020**, *32* (8), 466-478.

13. Thordarson, P., *Chem Soc Rev* **2011**, *40* (3), 1305-23.

14. Brynn Hibbert, D.; Thordarson, P., *Chem Commun (Camb)* **2016**, *52* (87), 12792-12805.

15. von Krbek, L. K. S.; Schalley, C. A.; Thordarson, P., *Chem Soc Rev* **2017**, *46* (9), 2622-2637.

16. Khan, A.; Paul, K.; Singh, I.; Jasinski, J. P.; Smolenski, V. A.; Hotchkiss, E. P.; Kelley, P. T.; Shalit, Z. A.; Kaur, M.; Banerjee, S.; Roy, P.; Sharma, R., *Dalton Trans* **2020**, *49* (47), 17350-17367.

17. Sharma, R.; Lobana, T. S.; Castineiras, A.; Butcher, R. J.; Akitsu, T., *Polyhedron* **2019**, *158*, 449-457.

18. Mondal, R.; Lozada, I. B.; Davis, R. L.; Williams, J. A. G.; Herbert, D. E., *Inorganic Chemistry* **2018**, *57* (9), 4966-4978.

19. Zink, D. M.; Bächle, M.; Baumann, T.; Nieger, M.; Kühn, M.; Wang, C.; Klopper, W.; Monkowius, U.; Hofbeck, T.; Yersin, H.; Bräse, S., *Inorganic Chemistry* **2013**, *52* (5), 2292-2305.

20. Zink, D. M.; Volz, D.; Baumann, T.; Mydlak, M.; Flügge, H.; Friedrichs, J.; Nieger, M.; Bräse, S., *Chem Mater* **2013**, *25* (22), 4471-4486.

21. Zeng, C.; Wang, N.; Peng, T.; Wang, S., *Inorganic Chemistry* **2017**, *56* (3), 1616-1625.

22. Nekkanti, S.; Veeramani, K.; Sujana Kumari, S.; Tokala, R.; Shankaraiah, N., *RSC Advances* **2016**, *6* (105), 103556-103566.

23. Barth, E. R.; Golz, C.; Knorr, M.; Strohmann, C., *Acta Crystallogr E Crystallogr Commun* **2015**, *71* (Pt 11), m189-90.

24. Cotton, F. A.; Feng, X. J.; Timmons, D. J., *Inorganic Chemistry* **1998**, *37* (16), 4066-4069.

25. Sugiura, T.; Yoshikawa, H.; Awaga, K., *Inorganic Chemistry* **2006**, *45* (19), 7584-7586.

26. Alvarez, S., *Dalton Trans* **2013**, *42* (24), 8617-8636.

27. Schwarz, G. *Ann Statist* **1978**, 6(2), 461-464.

28. Pradhan, R., Groner, V., Gutman, K. L., Larson, G. E., Kan, Y., Zhang, Q., Heiden, Z., Roll, M., Moberly, J., & Waynant, K. (**2022**). Data from: Evaluating Coordinative Binding Mechanisms through Experimental and Computational Studies of Methoxy-substituted Arylazothioformamide Copper(I) Complexes [Data set]. University of Idaho.

29. Haming, L.; Sheldrick, G. M., Sadabs.,*Acta Crystallogr A* **1999**, *55*, 206-206.

30. Dolomanov, O. V.; Bourhis, L. J.; Gildea, R. J.; Howard, J. A. K.; Puschmann, H., *J Appl Crystallogr* **2009**, *42*, 339-341.

31. Sheldrick, G. M., *Acta Crystallogr A* **2015**, *71*, 3-8.

32. Sheldrick, G. M., *Acta Crystallographica Section C-Structural Chemistry* **2015**, *71*, 3-8.

Chapter 5: Evaluation of Azothioformamides and Their Copper(I) and Silver(I) Complexes for Biological Activity.

Chapter 5 is an adaptation of published manuscript:

Pradhan, R.; Tiwari, L.; Groner, V.M.; Leach, C.; Lusk, K.; Harrison,N. S.; Cornell, K.A.; Waynant, K.V., *Journal of Inorganic Biochemistry*, **2023**, 246, 112294.

Abstract

Redox-active azothioformamides (ATFs) contain an NNCS 1,3-heterodiene motif typically found in other molecular subclasses that exhibit a wide range of cytotoxic and anti-neoplastic effects, either alone or as chelation complexes with various metals. For this study, a small library of ATF compounds was synthesized and tested across a range of microbes, fungi, and cancer cell lines for biological activity, both alone and as metal chelates of copper(I) and silver(I) salts. Alone, the ATF compounds exhibited little antimicrobial activity, but all inhibited the cell growth of A549 lung carcinoma cells (IC_{50} values of 1-6 μM). As copper(I) and silver(I) coordination complexes, several of the ATFs showed antimicrobial activity against gram positive Staphylococcus aureus and Bacillus subtilis cells (IC_{50} ~ 5-20 μM) and the fungi Candida albicans (IC_{50} ~ 8-12 μM); as well as cytotoxicity against both lung carcinoma A549 cells and lymphoblastic leukemia K562 cells.

Keywords: azothioformamide, Copper(I) complexes, Silver(I) complexes, antineoplastic, antimicrobial

5.1 Introduction

The metal chelating and redox-active azothioformamide (ATF), (1), contains an N=N–C=S 1,3-heterodiene backbone like the biologically active thiosemicarbazones, (2), thiosemicarbazides, (3), and isothiosemicarbazones, (4), species, as shown in **Figure 5.1**. While thiosemicarbazones, thiosemicarbazides, and isothiosemicarbazones and a variety of their metal(I) and metal(II) complexes have been extensively explored for biological activity, ATF compounds have seen very limited exploration, with most studies in transition metal oxidative dissolution and coordination[1-4], trace metal removal[5, 6], or in the determination of binding association values with various metal(I) salts.[2, 7-10]

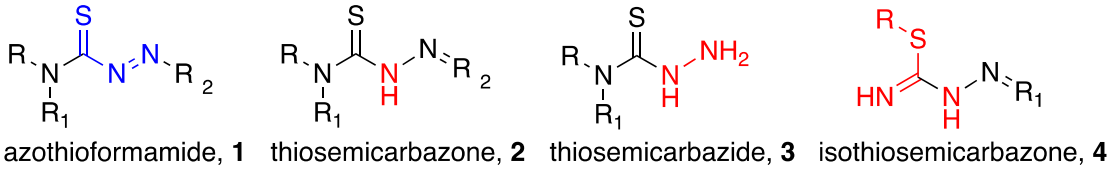

Figure 5.1: Various SCNN functional groups. Bioactivity has been investigated in thiosemicarbazones, thiosemicarbazides, and isothiosemicarbazones, but not in azothioformamides.

There are numerous reports highlighting the biological activity of thiosemicarbazones, (2), stemming from early work that explored their use as antiviral agents.[11-14] Both thiosemicarbazones and their metal complexes have shown antineoplastic, antimycobacterial, antibacterial, antifungal, antiviral, and antimalarial properties.[15-25] The thiosemicarbazones, (2), appear to exert their antineoplastic effects through the chelation of iron that is essential for cell proliferation. This mechanism is thought to work through inhibition of the diferric iron center in ribonucleotide reductase (RNR) enzyme responsible for the production of deoxyribonucleotides, amongst other pathways.[26] Metal complexes of thiosemicarbazides, 3,

have been reported to express antineoplastic properties by inhibition of epithelial growth factor receptor (EGFR) kinase.[27] Isothiosemicarbazones, (4), and resultant metal complexes have also shown antineoplastic, antiproliferative and antimycobacterial properties.[28-31] Due to their known antimicrobial properties as both free metal ions and in various metal complexes, copper(I) and silver(I) were selected for ATF chelation.[32, 33] Copper(I), while generally accepted as the form most common in the bioinorganic community, has seen relatively few examples as an anticancer agent due to poor stability.[34, 35] Key examples of copper(I) anticancer agents and silver(I) antimicrobial and anticancer agents have been those stabilized by phosphino ligands with most thiosemicarbazone derivatives bound to metal(II).[35, 36] An anthrahydrazone copper(I) complex has indicated anticancer reactivity through a reactive oxygen species pathway.[37] Both copper(I) and silver(I) coordinate as tetrahedrons to ATF ligands without an oxidation state change, in either the ligand or the metal, which, we believe, will indicate whether increases or decreases in antimicrobial activity versus the base ligand extends from metal chelation, or in the case of weakly binding ATF ligands, metal ion release. The exact mechanism of cell death due to copper ions is unknown while many potential mechanisms mention the infiltration of metal ions into the cell or the generation of reactive oxygen species through copper ion reduction.[38]

To the best of our knowledge ATFs and ATF:metal chelates have not been subjected to any preliminary screening. Therefore, this study was designed to give a broad overview of the antibiotic and antiproliferative activity of a small library of ATF ligands, and their metal(I) salt complexes of copper(I) and silver(I).

5.2 Results

Synthesis of ATF ligands and complexes

ATF ligands (6a-6h) were synthesized from an efficient one-pot four-step process as shown in **Figure 5.2** using known procedures from commercially available alkylhydrazine, phenylhydrazine, or *para*-substituted phenylhydrazine HCl salts (5a-5h).[7-10] Due to low yields, ATF (6g), was subjected to an alternative procedure where xanthate ester was isolated prior to reflux. After collecting, a higher boiling toluene solvent with 1.5 equivalents of diethylamine and added triethylamine base was used to give an increased yield in the two-step process.

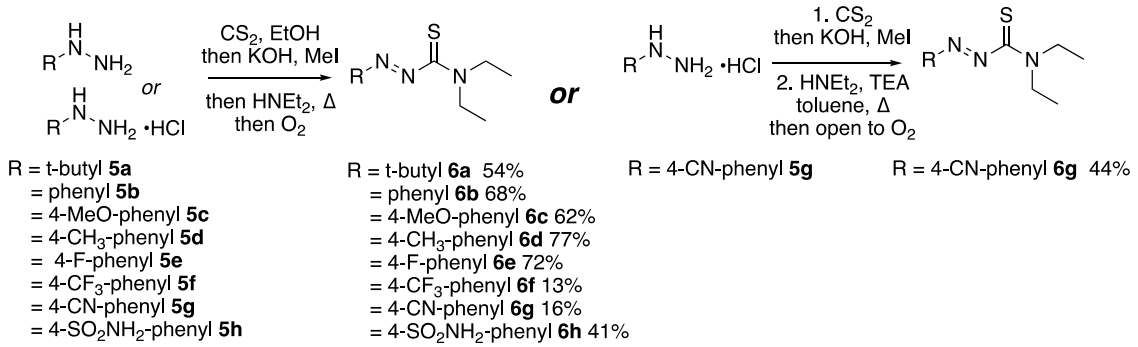

Figure 5.2: One pot synthesis of ATF compounds 6a-h from various alkyl and phenylhydrazine/phenylhydrazine HCl salts 5a-h and the various substitutions and yields. ATF 6g was synthesized through a two-step process with added TEA base to give an increased yield.

Like thiosemicarbazone/thiosemicarbazide systems, ATFs bind to a wide variety of transition metals creating both symmetric and asymmetric coordination complexes which could play a role in their antineoplastic behavior. The ATF series shown consists of a variety of *para*-substituted substituents from strongly electron-donating (6c) to strong electron-withdrawing properties (6f). Previous reports have shown lower ATF binding association values to metal salts when ATFs were appended with electron withdrawing groups (*para*-substituted -F (6e), -CF_3, (6f)).[8] Moderately electron-withdrawing ATFs (6g) and (6h) were

newly synthesized for this study and full experimental and characterization data is provided in the Appendix IV including single crystal X-ray diffraction information. The X-ray crystal structures are shown in **Figure 5.3**. Sulfonamide ATF, 6h, crystallized as perpendicular pairs with a Z = 8 in the unit cell. The major differences in these two structures are the *N,N'*-diethylamide component, where one structure has the diethyl group staggered and the other has the diethyl eclipsed. In solution, these two rotamers must exist in equilibrium as the spectroscopic data (^{1}H and ^{13}C NMR, see Appendix IV) suggest one pure compound. The bond lengths of ligands 6g and 6h for C_1=S_1 are 1.6616 and 1.664(3)/1.667(3) Å, for C_1-N_2 1.4543 and 1.432(4)/1.443(4) Å, finally the N_1=N_2 were 1.2379 and 1.250(3)/1/250(3) Å, respectively, which correlate well with known bond lengths of previously published ATF ligands.[7, 8] Furthermore, dihedral angles for the $S_1C_1N_1N_2$ coordination motif of 6g and 6h were measured at 61.50˚ and 63.68˚/70.79˚ respectively indicating that the heterodiene is not in conjugation prior to metal chelation.

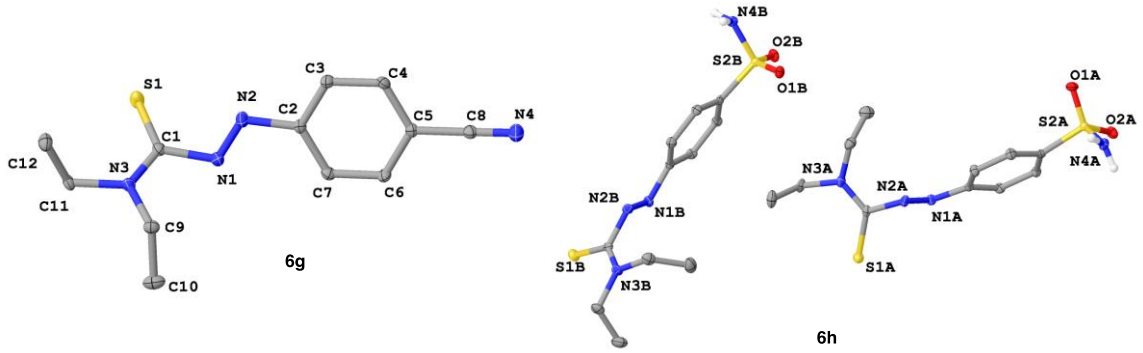

Figure 5.3: X-ray crystal structures of ATF 6g and ATF 6h shown at 50% probability level. 6g hydrogens are omitted for clarity; 6h hydrogens are included to indicate the Z = 8 (two structures of the unit cell).

ATF ligands complex with copper(I) halide salts to produce binding association constants calculated in a range from 10^3 - 10^6 M^{-1} based on the substitution pattern with

electron-donating substituents yielding stronger binding than ATFs with electron-withdrawing substituents.[8] A series of ATFs (6c, 6e, 6f, and 6g) were selected for both strong (6c) and weak (6e, 6f, 6g) binding and mixed with copper(I) and silver(I) salts to produce a library of coordination complexes. Two copper(I) halides (CuBr and CuI) and two copper salts with non-coordinating counterions $[(CH_3CN)_4Cu^I](PF_6)$ and $[(CH_3CN)_4Cu^I](BF_4)$ were investigated along with Ag^IPF_6. In general, the Cu(I) halide species form 2:2 dimeric complexes and $[(CH_3CN)_4Cu^I](PF_6)$, $[(CH_3CN)_4Cu^I](BF_4)$, and Ag^IPF_6 form 2:1 ligand to metal complexes as shown in Figure 5.4. All complexes have been fully characterized and many have yielded single crystal X-ray diffraction structures. Characterization data can be found in the Appendix IV. Through the examination of single crystal X-ray diffraction data, a multitude of structures were isolated including *exo*-halide dimer 7c, symmetric μ-halide dimers (7e, 7f, and 8f), asymmetric μ-halide dimers (8c, 8e, and 7g), single crystal X-ray diffraction data for (7g) is included in Appendix IV. Compound (8g) did not produce X-ray quality crystals after exhaustive recrystallization efforts. Metal salts with stable non-coordinative counterions (BF_4 and PF_6) yielded 2:1 ligand:metal complexes (X-ray structure of (9g) is shown in Figure 5.4). Crystal structures of the –CN appended copper(I) complexes 7g and 9g gave bond distances for the chelating C_1=S_1 bond as 1.687/1.683 and 1.699/1.694 Å; C_1–N_2 as 1.430/1.432 and 1.431/1.428 Å; and N_2–N_1 as 1.266/1.269 and 1.272/1.261 Å, respectively. Torsion angles of the $S_1C_1N_1N_2$ motif in these structures were measured at 8.71˚/-9.48˚ for 7g and 11.16˚/13.80˚ for 9g indicating significantly more conjugation of the heterodiene into the metallocycles. The Cu_{1A}–Cu_{1B} distance for 7g was 2.786 Å. All complexes were isolated in yields over 50% and following characterization were moved forward for biological evaluation against a series of common microbes and various cancer cell lines.

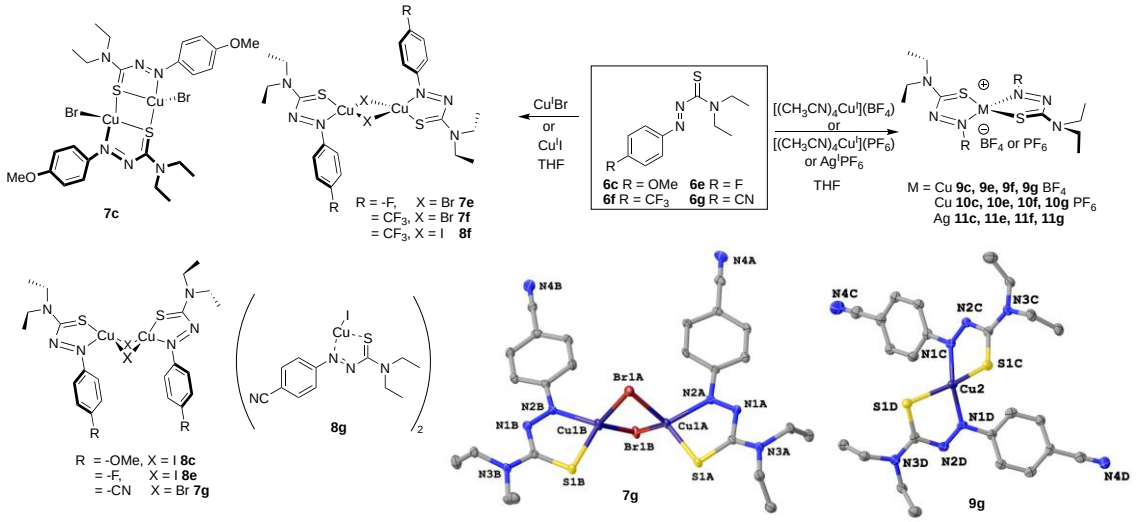

Figure 5.4: Synthesis of metal(I) salt complexes. Dimeric 1:1 complex was found predominantly with copper(I) halides in a variety of conformations including an exo-X, 7c; symmetric μ-X dimers, 7e, 7f, 8f; asymmetric μ-X dimers 8c, 8e, 7g; and unsolved structure of 8g; while 2:1 structures were isolated from metal salts with non-coordinative counteranions (9c-9g, 10c-10g and 11c-11g). X-ray crystal structures of 7g and 9g are shown at 50% probability.

ATF Biological Activity

The antimicrobial activity of the ATF series (6a-6h) was examined using established disk diffusion[39] and antibiotic microdilution[40] assays. A panel of microbial species were tested that included gram-positive bacteria: methicillin resistant *Staphylococcus aureus* (MRSA, ATCC BAA-44), *Bacillus subtilis* (ATCC 23857); gram-negative bacteria: *Chromobacteria violaceum* (ATCC 12472), *E. coli* O157:H7 (ATCC 43894), *Pseudomonas aeruginosa* (ATCC 47085); and the fungal pathogen *Candida albicans* (ATCC 10231). The results of disk diffusion assay sensitivity and minimum inhibitory concentration tests can be found in ESI figures (S1 - S2, Table S1). However, none of the initial ATF compounds (6a-6h) showed antimicrobial activity by either the disk diffusion or the microdilution assay (IC_{50}'s > 50μM)

(**Table 5.1**). Thus, there is no indication that these ATFs by themselves have any significant antibacterial or antifungal properties.

Table 5.1: IC_{50} values for monomeric ATF Compounds.

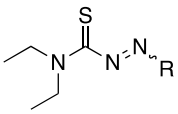	**Compound IC_{50}, µM (± SEM)**							
			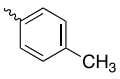	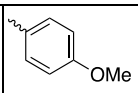	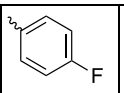	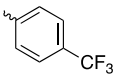	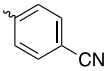	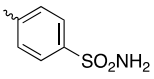
	6a	**6b**	**6d**	**6c**	**6e**	**6f**	**6g**	**6h**
Microbe: *B. subtilis*	>50	>50	>50	>50	>50	>50	>50	>50
S. aureus	>50	>50	>50	>50	>50	>50	>50	>50
Chr. violaceum	>50	>50	>50	>50	>50	>50	>50	>50
E. coli	>50	>50	>50	>50	>50	>50	>50	>50
Ps. aeruginosa	>50	>50	>50	>50	>50	>50	>50	>50
C. albicans	>50	>50	>50	>50	>50	>50	>50	>50
Cell line: *A549*	5 (2)	6 (2)	5 (2)	6 (2)	1 (0.4)	5 (1)	1 (1)	5 (2)
K562	>100	>100	>100	>100	>100	>100	>100	>100

The antiproliferative activity of these parental ATFs were also examined against two cancer cell lines: the adherent A549 human lung adenocarcinoma line (ATCC CRM-CCL-185); and the non-adherent K562 human chronic myelogenous leukemia line (ATCC CCL-243) using an established resazurin reduction assay.[42]

As can be seen in Table 5.1, mixed results were noted: A549 cells were found to be sensitive to all the ATF compounds (IC_{50}'s = 1-6 µM), while K562 cells were insensitive (IC_{50}'s > 100 µM). The results of antimicrobial studies of metal salt coordination complexes based on the structures of monomer (6c, 6e, 6f, and 6g) are further presented in **Tables 5.2-5.5**, with representative antimicrobial growth inhibition curves shown in **Figure 5.5**.

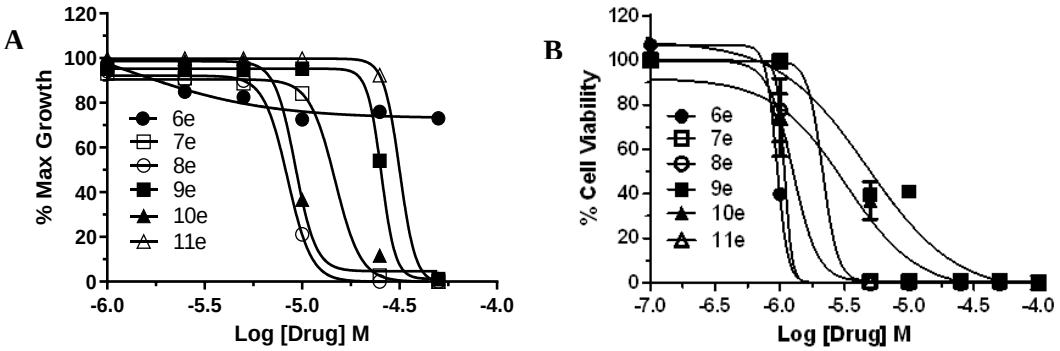

Figure 5.5: A. Antimicrobial activity of ATF metal complexes against MRSA (strain BAA-44) cells. B. Antiproliferative activity of ATF metal complexes against human carcinoma (A549) cells.

Table 5.2: IC_{50} values for 6c series compounds.

	Compound IC_{50}, µM (± SEM)				
	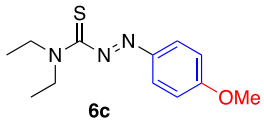 6c	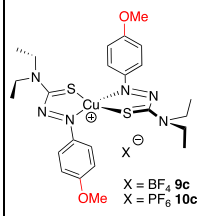 X = BF_4 9c, X = PF_6 10c	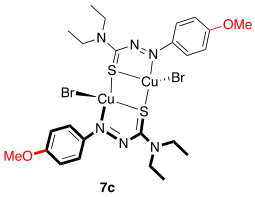 7c	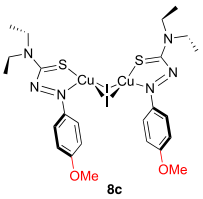 8c	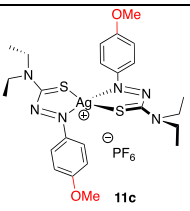 11c
	9c	10c	7c	8c	11c
Microbe: *B. subtilis*	16.8 (2.4)	13.1 (3.5)	5.7 (0.1)	9.4 (1.5)	7.7 (2.1)
S. aureus	6.2 (0.8)	7.9 (1.1)	4.8 (0.8)	11.3 (1.7)	11.8 (1.0)
Chr. violaceum	>50	>50	>50	>50	>50
E. coli	>50	>50	>50	>50	49.2 (2.0)
Ps. aeruginosa	>50	>50	>50	>50	26.3 (5.2)
C. albicans	11.7 (2.6)	>50	8.5 (0.7)	9.3 (2.9)	>50
Cell line: *A549*	3.5 (3)	2.1 (2)	3.6 (4)	10 (1.2)	5 (6.3)
K562	2 (1)	2 (1)	2 (1)	2.3 (1)	16.5 (5)

As can be seen in the tables, the gram-positive bacteria (*S. aureus*, *B. subtilis*) were generally more susceptible to inhibition by the metal salt coordination complexes with IC_{50}

values in the low to medium micromolar (5-50 µM) range. Conversely, gram-negative bacteria (*Chr. violaceum*, *E. coli*, *Ps. aeruginosa*) and the yeast (*Candida albicans*) were generally not inhibited by the metal coordination complexes. There were some exceptions, particularly with compounds based on the structure of (6c, 6e, 6f, and 6g) that contained silver(I) ion complexes (11c, 11e, 11f, 11g). These complexes generally exerted antimicrobial effects on both gram-positive and gram-negative bacteria, and occasionally (11g) against Candida albicans.

Table 5.3: IC_{50} values for 6e series compounds.

	Compound IC_{50}, µM (± SEM)				
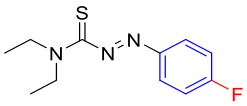 **6e**	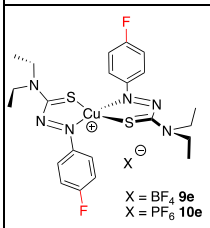 X = BF_4 **9e** X = PF_6 **10e**	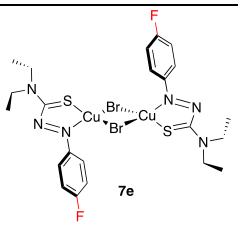 **7e**	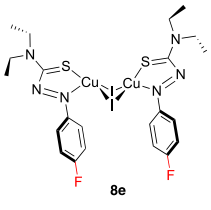 **8e**	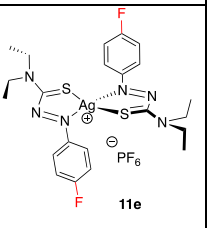 **11e**	
	9e	10e	7e	8e	11e
Microbe: *B. subtilis*	>50	24.2 (0.9)	>50	21.1 (1.2)	15.5 (2.2)
S. aureus	20.1 (3.9)	7.3 (2.7)	14.0 (4.0)	7.7 (2.3)	32.7 (1.0)
Chr. violaceum	>50	>50	>50	>50	12.8 (4.0)
E. coli	>50	>50	>50	>50	20.2 (4.5)
Ps. aeruginosa	>50	>50	>50	>50	16.4 (3.4)
C. albicans	>50	>50	>50	>50	>50
Cell line: *A549*	4.5 (0.4)	4.7 (2)	4.5 (3)	1.4 (0.4)	1.4 (0.3)
K562	9 (1)	4 (1)	10 (1.2)	4 (1)	2.5 (1.5)

More striking results were seen when testing the complexes for antiproliferative activity against the two cancer cell lines (**Figure 5.5**, **Tables 5.2-5.5)**. Here, most of the compounds exhibited IC_{50} values against both cancer cell lines (A549, K562) that were in the low micromolar range (2-10 µM). While the complexes did not show improved activity against

the A549 carcinoma cells (relative to the parental (6a-6h) series), they were uniformly more active against the K562 leukemia cells. In addition, unlike the observations made regarding their improved antimicrobial activity, the silver(I) containing complexes (11c, 11f, 11g) were generally less active against both mammalian cancer cell types. The exception to this was seen with complex (11e), which exerted among the most potent antiproliferative activity (IC_{50}'s 1.4-2.5 µM) against the two cancer cells lines (**Table 5.3**).

Table 5.4: IC_{50} values for 6f series compounds.

	Compound IC_{50}, µM (± SEM)				
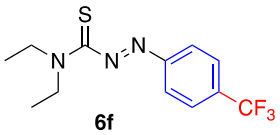 **6f**	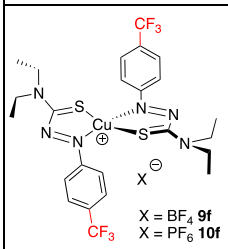 X = BF_4 **9f** X = PF_6 **10f**	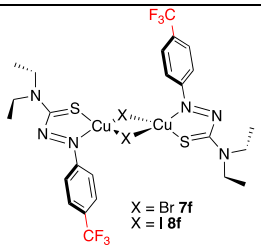 X = Br **7f** X = I **8f**	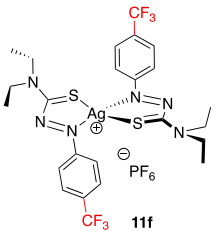 **11f**		
	9f	10f	7f	8f	11f
Microbe: *B. subtilis*	>50	>50	>50	21.9 (2.2)	5.8 (1)
S. aureus	>50	>50	>50	7.3 (2.6)	10.5 (0.6)
Chr. violaceum	>50	>50	>50	>50	9.8 (3.8)
E. coli	>50	>50	>50	>50	14.0 (2.3)
Ps. aeruginosa	>50	>50	>50	>50	13.7 (2.0)
C. albicans	>50	>50	>50	>50	>50
Cell Line: *A549*	33 (5)	39 (5)	47 (6)	1.4 (0.3)	44 (20)
K562	20.7 (3.4)	29 (5.2)	26.3 (4.8)	2 (1)	26.5 (11.5)

Table 5.5: IC_{50} values for 6g series compounds

	Compound IC_{50}, µM (± SEM)				
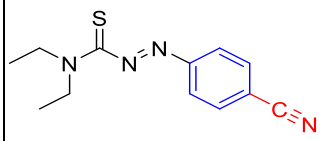 **6g**	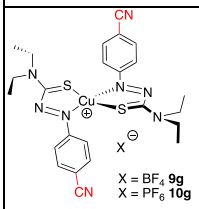 X = BF_4 **9g** X = PF_6 **10g**	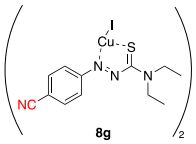 **8g**	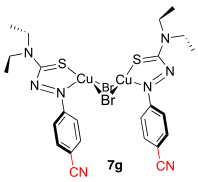 **7g**	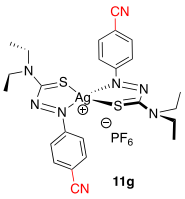 **11g**	
	9g	10g	8g	7g	11g
Microbe: *B. subtilis*	43.2 (2.5)	45.5 (2.5)	>50	26.2 (3.1)	21.4 (4.0)
S. aureus	7.2 (0.7)	16.0 (4.0)	>50	10.9 (0.9)	6.4 (1.7)
Chr. violaceum	>50	>50	>50	>50	19.4 (1)
E. coli	>50	>50	>50	>50	13.0 (0.3)
Ps. aeruginosa	>50	>50	>50	>50	24.1 (4.6)
C. albicans	>50	>50	>50	>50	22.3 (2.8)
Cell Line: *A549*	8.6 6)	1.4 (0.3)	7.2 (2)	2.7 (1.5)	9.5 (1.5)
K562	8.3 (3)	6.5 (1)	44 (4)	7.5 (1.5)	9.5 (1.5)

5.3 Discussion

Non-complexed ATF compounds showed no appreciable cytotoxic activity against a panel of gram-positive and gram-negative bacteria, yeast, and the human leukemia K562 cell line. The adherent human lung carcinoma A549 cells appeared uniquely sensitive with low micromolar IC_{50} values (1-6 µM) exerted by all the parent ATF compounds. However, the mechanism of this selectivity is unknown. Perhaps the parent ATF compounds are complexing an essential ion or interacting with a cell surface biomolecule on these cells that alters their growth or metabolism. Such potential mechanisms will be explored in future follow-up investigations.

The ATF-metal coordination complexes showed highly variable effects against the microbial strains that were tested. Generally, gram-positive cells were more sensitive to these complexes suggesting that its exposed peptidoglycan cell and associated synthetic machinery may be interacting with at least some of these compounds. The Cu(I) and Ag(I) ATF complexes showed a higher level of activity against gram-positive cell lines and with the more electron-withdrawing group (EWG) appended ATFs. In many instances the added EWG groups were reported to have lower binding association values to the metal salts and the release of metal alone could have provided the cytotoxicity especially for (11e, 11f, and 11g) with a cytotoxic Ag(I) metal center. The gram-negative bacterial strains and the yeast *Candida* were mostly insensitive to the ATF complexes, except for the ATF-silver(I) ion complexes (11c, 11e, 11f, and 11g). Gram-negative bacteria have an outer cell membrane that reduces their sensitivity to many of the antibiotics like β-lactams that target cell wall biosynthesis. The cell walls of yeasts are surface accessible, but are cellulosic rather than peptidoglycan based, and thus yeasts are similarly insensitive to β-lactams and other antibacterial agents targeting cell wall biosynthesis. The broader sensitivity of the microbes to the ATF-silver(I) ion complexes suggests a role for the silver(I) ion specifically in the antimicrobial activity. Silver(I) ions interact with sulfhydryl (-SH) and other functional groups found on proteins and are known to exert antimicrobial activity.[42] Perhaps this indicates that the ATF-silver(I) ion complexes are leaching Ag^+ ions that subsequently interact with microbial biomolecules to inhibit essential functions in the microbes.

In the cancer cell line antiproliferative studies, the ATF-complexes were mostly less potent against the human lung carcinoma A549 line than the parent free ATF compounds. This suggests that the transport processes or surface interactions available to the free ATFs show

reduced activity against the complexes. Conversely, the K562 leukemia cells showed no sensitivity to the parental ATF compounds but were potently inhibited by many of the ATF complexes. Interestingly, the K562 leukemia cells were particularly sensitive to the (7c-10c) series. This series contains a ligand with the strongest binding constants, which may allude to a mechanism of action involving the release of Cu(I) ions. Overall, IC_{50} values are broadly comparable to the anti-neoplastic properties of Cu(II) thiosemicarbazones.[21]

5.4 Conclusion

A broad biological screen of ATFs and their Cu(I) and Ag(I) coordination complexes for antimicrobial and anticancer cell activity was performed in this study. The ATF series varied in phenyl substitutions of electron-donating groups or electron-withdrawing groups and overall, the entire ATF library was relatively inactive against a series of microbial strains yet highly active against the A549 human cancer cell line with multiple low μM IC_{50} hits from compounds (6e and 6g). The mechanism of action may be due to the metal chelation ability of the ATF, and this may explain why metal coordinated ATF salts when tested provided slightly lower activities – due to competition of their metal center with cellular metals. Small degrees of inhibition of K562 cells were scattered throughout the series of complexes as seen in IC_{50} values (> 2μM) of (8f), and the (9c-f) series. Silver(I) complexes were, in general, more active than copper on the bacterial strains with activity increasing from electron-withdrawing group appended ATF complexes. The increased activity is proposed to be due to higher Ag(I) concentrations from the weakly coordinating ATF ligands and the known antimicrobial effects of free Ag^+ cations. Further studies will more closely investigate the mechanism of activity against microbes, A549 cells and other cancer cell lines.

5.5 Experimental

General Methods

^{1}H and ^{13}C NMR experiments were performed on either a Bruker AVANCE 300 MHz or 500 MHz instrument and samples were obtained in *d*-chloroform, $CDCl_3$, referenced to 7.26 ppm for ^{1}H and 77.16 ppm for ^{13}C, or Acetonitrile-d_3, CD_3CN, referenced to 1.93 ppm for ^{1}H and 1.4 and 117.7 ppm for ^{13}C. Coupling constants (*J*) are in Hz. The multiplicities of the signals are described using the following abbreviations: s = singlet, br s = broad singlet, d = doublet, t = triplet, q = quartet, dd = doublet of doublets, dq = doublet of quartets, m = multiplet, app = apparent. Infrared spectra were obtained on a Thermo Scientific Nicolet 380 FT-IR spectrometer as thin films on ZnSe ATR attachment and peaks are reported in cm^{-1}. Reaction progress was monitored by thin-layer chromatography on silica gel plates (60-F254), observed under UV light. Column chromatography was performed using silica gel (particle size 40–63 µm). Methyl iodide was purchased from EMD Millipore, 4-cyanophenylhydrazine hydrochloride and 4-sulfonamidophenylhydrazine hydrochloride were purchased from AK Scientific, *N*, *N*-diethylamine and carbon disulfide were purchased from Alfa-Aesar and used without further purification. Ag(I)PF_6, Cu(I) halides, and $[(CH_3CN)_4Cu^{I}](BF_4)/(PF_6)$ salts were purchased from Acros, Sigma–Aldrich, Alfa–Aesar, and AK Scientific and used without further purification.

Complete synthetic procedures for ATF compounds (6a-f) as well as complexes (7c, 8c, 9c, 10c, 7e, 8e, 9e, 10e, 7f, 8f, 9f, and 10f) can be found in previous reports.[7-10, 43]

Synthetic Procedures

***N,N*-diethyl-2-(4-cyanophenyl) diazothioformamide (6g)**: 70 mL of ethanol and 4-cyanophenyl hydrazine • HCl (4.24 g, 25 mmol) were added to a flame-dried round-bottom flask equipped with a magnetic stirrer and allowed to degas for 30 minutes under nitrogen flow. While under nitrogen, carbon disulfide (1.71 ml, 28.5 mmol) was added dropwise by needle to the flask and allowed to stir under ambient conditions for an hour. Potassium hydroxide (1.96 g, 35 mmol) dissolved in degassed ethanol (25 mL) was then added via cannula and allowed to stir under nitrogen for 30 minutes. Methyl iodide (1.74 ml, 28 mmol) was then added to the solution and allowed to stir under nitrogen for 1 hour. The liquid was then concentrated with a rotary evaporator and the flask with resulting paste was then equipped with condenser and put under nitrogen flow. Diethylamine (40 mL) was then added by needle and the mixture was allowed to reflux under nitrogen for 48 hours (forming a solution). The solution was cooled to ambient temperature and then exposed to air and allowed to stir for 2 hours. The resulting orange liquid was concentrated via rotary evaporator and purified using flash column chromatography 7:3 hexanes: ethyl acetate forming .797 g (16%) of red solid. The resulting solid was subjected to recrystallization using acetonitrile to afford a diffracting crystal.

Alternatively, xanthate ester intermediate can be isolated prior to diethylamine addition. The recovered paste (as described above under similar conditions) was purified with flash column chromatography (7:3 hexanes: ethyl acetate) to recover 1.561g (7 mmol) of xanthate ester intermediate. The xanthate ester product was dissolved in 15 mL of toluene, and triethylamine (1.46 mL, 10.5 mmol) was added to the solution followed by diethylamine (1.08 mL, 10.5 mmol). The solution was refluxed under nitrogen for 48 hours and then cooled to

room temperature, opened to air, and allowed to stir for 24 hours. The resulting orange liquid was washed with brine and dried over anhydrous $MgSO_4$ followed by concentration via a rotary evaporator and purified using flash column chromatography (7:3 hexanes: ethyl acetate) giving the product as a red solid in an overall 44% yield. The resulting solid was subjected to recrystallization using slow evaporation of acetonitrile. ^{1}H NMR (300 MHz, Chloroform-*d*) δ 7.95 (d, *J* = 8.6 Hz, 2H), 7.82 (d, *J* = 8.6 Hz, 2H), 4.03 (q, *J* = 7.2 Hz, 2H), 3.48 (q, *J* = 7.2 Hz, 2H), 1.41 (t, *J* = 7.2 Hz, 3H), 1.19 (t, *J* = 7.2 Hz, 3H). ^{13}C NMR (75 MHz, Chloroform-*d*) δ 193.643, 154.231, 133.951, 124.446, 118.511, 116.244, 48.367, 45.767, 14.290, 11.973. FTIR (ATR, cm^{-1}): 2977, 2229, 1517, 1441, 1283, 1163, 1079, 835. Anal Calcd for $C_{12}H_{14}N_4S$: C, 58.51; H, 5.73; N, 22.74; Found: C, 59.07; H, 5.56; N, 22.36. MP: 147°C. CCDC # **2244039**

***N,N*-diethyl-2-(4-Sulfonamidephenyl) diazothioformamide (6h)**: 70 mL of ethanol was degassed under nitrogen flow in a flame-dried round bottom fitted with a magnetic stirrer for one hour. 4-sulfonamidophenylhydrazine•HCl (5.6 g, 25 mmol) was then added followed by dropwise addition of carbon disulfide (1.71 mL, 28.5 mmol) stirred for an hour. Potassium hydroxide (1.96 g, 35 mmol) dissolved in degassed ethanol (20 mL) was then quickly poured into the mixture and was left to stir at room temperature for 30 minutes. Methyl iodide (28 mmol, 1.74 mL) was added by syringe. The solution was allowed to stir for one hour and carbon disulfide and ethanol was removed by rotary evaporator producing an orange solid. The flask was then fitted to a reflux condenser and put under nitrogen flow. Diethylamine (40 mL) was added via cannula and heated to reflux for 48 hours. The resulting dark red solution was then allowed to cool and stir under ambient conditions for 2 hours. The solution was then washed with brine and extracted with ethyl acetate to afford a red liquid. The resulting red liquid was concentrated via rotary evaporator and purified using flash column chromatography

(4:1 hexane: ethyl acetate) yielding 0.87 g (41 %) of orange solid. ^{1}H NMR (300 MHz, Chloroform-*d*) δ 8.07 (d, *J* = 8.7 Hz, 2H), 7.96 (d, *J* = 8.7 Hz, 2H), 4.02 (q, *J* = 7.2 Hz, 2H), 3.49 (q, *J* = 7.2 Hz, 2H), 1.41 (t, *J* = 7.2 Hz, 3H), 1.18 (t, *J* = 7.2 Hz, 3H). ^{13}C NMR (75 MHz, $CDCl_3$) δ 193.92, 154.43, 146.03, 128.57, 124.76, 48.74, 46.23, 14.62, 12.27. FTIR (ATR, cm^{-1}); 3313, 3218, 2981, 1516, 1431, 1050. Anal. Calcd for $C_{11}H_{16}N_4O_2S_2$: C, 43.98; H, 5.37; N, 18.65; Found: C, 43.46; H, 5.12; N, 17.78; MP: 128°C. CCDC # **2244041**

Synthesis of metal Coordination complexes

Bis[(*N*,*N*-diethyl-2-(4-cyanophenyl) diazothioformamide)CuBr] (7g): To *para*-Cyano ATF (6g) (98 mg, 0.40 mmol) dissolved in 5 mL of anhydrous acetonitrile in a 2-dram vial was added Cu(I)Br (57 mg, 0.40 mmol). The solution had a rapid color change from light red to dark blue and was heated with a heat gun to promote solvation and then poured into another vial and allowed to slowly concentrate over 3-5 days to yield dark blue solid. The solid was recrystallized with acetonitrile to obtain 144 mg of dark blue crystals (92%). ^{1}H NMR (300 MHz, Acetonitrile-d_3) δ 8.73 (d, *J* = 8.4 Hz, 2H), 7.96 (d, *J* = 8.5 Hz, 2H), 4.06 (q, *J* = 7.3 Hz, 2H), 3.97 (q, *J* = 7.2 Hz, 2H), 1.41 (t, *J* = 7.1 Hz, 3H), 1.34 (t, *J* = 7.1 Hz, 3H).^{13}C NMR (126 MHz, $CDCl_3$) δ 185.888, 153.519, 133.770, 127.490, 117.839, 116.864, 51.302, 47.816, 14.751, 10.661. FTIR (ATR, cm^{-1}): 2972, 2230, 1522, 1437, 1283, 1165, 1053, 830. Anal. Calcd for $C_{24}H_{28}Cu_2Br_2N_8S_2$: C, 36.98; H, 3.62; N, 14.37; Found: C, 36.81; H, 4.300; N, 14.13 MP: 153°C. CCDC # **2244038**

Bis[(*N*,*N*-diethyl-2-(4-cyanophenyl) diazothioformamide)CuI] (8g): To *N*,*N*-diethyl-2-(4-cyanophenyl) diazothioformamide (6g) (98 mg, 0.40 mmol) dissolved in 10 mL of anhydrous acetonitrile was added Cu(I)I (76 mg, 0.40 mmol). After a rapid color change from light orange to dark blue the solution was decanted into another 2-dram vial and allowed

to concentrate via evaporation at room temperature over 3-5 d to afford a dark blue solid. After repeated washes with hexanes to remove any unreacted ligand, 170 mg (97%) of product was collected. ^{1}H NMR (300 MHz, Chloroform-*d*) δ 8.81 (d, *J* = 8.5 Hz, 2H), 7.89 (d, *J* = 8.5 Hz, 2H), 4.15 – 4.05 (m, 4H), 1.52 (t, *J* = 7.1 Hz, 3H), 1.41 (t, *J* = 7.1 Hz, 3H). ^{13}C NMR (126 MHz, $CDCl_3$) δ 186.551, 153.495, 133.886, 127.392, 118.112, 117.190, 50.760, 47.962, 15.100, 11.071. FTIR (ATR, cm^{-1}): 2979, 2225, 1506, 1458, 1338, 1108, 1081, 844. Anal. Calcd for $C_{24}H_{28}Cu_2I_2N_8S_2$: C, 33.00; H, 3.23; N, 12.83; Found: C, 33.02; H, 2.781; N, 12.76 MP: 182°C.

[(*N,N*-diethyl-2-(4-cyanophenyl) diazothioformamide)$_2$Cu](BF$_4$) (9g): To *N,N*-diethyl-2-(4-cyanophenyl) diazothioformamide, (6g) (98 mg, 0.40 mmol) in 5 ml of anhydrous THF in a 2-dram vial was added [$(CH_3CN)_4Cu^I$](BF4) (62 mg, 0.20 mmol). After a rapid color change from light red to dark blue, the solution was decanted into another 2-dram vial and allowed to concentrate via evaporation at room temperature to afford a dark blue solid. This solid was washed repeatedly with hexanes to give 158 mg (61% yield) of complex. ^{1}H NMR (500 MHz, Chloroform-*d*) δ 8.26 (d, *J* = 8.4 Hz, 2H), 7.82 (d, *J* = 8.6 Hz, 2H), 4.34 (q, *J* = 7.1 Hz, 2H), 4.11 (q, *J* = 7.2 Hz, 2H), 1.53 – 1.48 (m, 6H). ^{13}C NMR (126 MHz, Chloroform-*d*) δ 186.11, 152.78, 134.54, 127.04, 117.66, 117.39, 51.41, 49.46, 14.94, 10.69. FTIR (ATR, cm^{-1}): 2982, 2226, 1530, 1431, 1284, 1152, 1035, 850. Anal. Calcd for $C_{24}H_{28}CuBF_4N_8S_2$: C, 44.83; H, 4.39; N, 17.43; Found: C, 44.05; H, 3.889; N, 16.58 MP: 155°C. CCDC# **2244040**

[(*N,N*-diethyl-2-(4-cyanophenyl) diazothioformamide)$_2$Cu](PF$_6$) (10g): To *N,N*-diethyl-2-(4-cyanophenyl) diazothioformamide (6g) (98 mg, 0.40 mmol) dissolved in 5 ml of acetonitrile was added [$(CH_3CN)_4Cu^I$](PF_6) (75 mg, 0.20 mmol). The solution was poured into another vial and allowed to slowly concentrate via solvent evaporation to form a dark blue

solid. The solid was repeatedly washed with hexanes to give 155 mg (55%) of complex. ^{1}H NMR (300 MHz, Acetonitrile-d_3) δ 8.09 (d, J = 8.0 Hz, 2H), 7.91 (d, J = 8.7 Hz, 2H), 4.27 – 4.15 (m, 4H), 1.44 (t, J = 7.1 Hz, 3H), 1.41 (t, J = 7.2 Hz, 3H). ^{13}C NMR (75 MHz, CD_3CN) δ 187.394, 152.279, 134.569, 127.881, 119.727, 117.030, 51.503, 49.507, 15.028, 11.436. FTIR (ATR, cm^{-1}): 2988, 2227, 1525, 1432, 1312, 1164, 1076, 827. Anal. Calcd for $C_{24}H_{28}CuPF_6N_8S_2$: C, 41.11; H, 4.03; N, 15.98; Found: C, 41.74; H, 3.987; N, 15.85. MP: 188°C.

[(*N*,*N*-diethyl-2-(4-cyanophenyl) diazothioformamide)$_2$Ag](PF$_6$) (11g): To *N*,*N*-diethyl-2-(4-cyanophenyl) diazothioformamide (6g) (98 mg, 0.40 mmol) in 5 ml of acetonitrile in a 2-dram vial was added Ag(I)PF_6 (50 mg, 0.20 mmol). After a rapid color change from light red to dark red, the solution was decanted into another 2-dram vial and allowed to concentrate via evaporation at room temperature to afford a dark red solid. The solid was washed repeatedly with hexanes to give 149 mg (50%) of complex. ^{1}H NMR (500 MHz, Chloroform-d) δ 8.11 (s, 2H), 7.84 (d, J = 6.4 Hz, 2H), 4.14 (s, 2H), 3.94 (s, 2H), 1.49 (t, J = 7.2 Hz, 3H), 1.33 (t, J = 7.2 Hz, 3H). ^{13}C NMR (126 MHz, $CDCl_3$) δ 188.937, 152.622, 133.819, 125.595, 123.931, 117.666, 50.783, 47.740, 14.382, 11.218. FTIR (ATR, cm^{-1}): 2981, 2229, 1532, 1443, 1290, 1166, 1074, 830. Anal. Calcd for $C_{24}H_{28}AgPF_6N_8S_2$: C, 38.67; H, 3.79; N, 15.03; Found: C, 37.36; H, 3.853; N, 14.11 MP: 112°C

[(*N*,*N*-diethyl-2-(4-methoxyphenyl) diazothioformamide)$_2$Ag](PF$_6$) (11c): To *N*,*N*-diethyl-2-(4-methoxyphenyl) diazothioformamide (6c) (221 mg, 0.88 mmol) in 10 ml of acetonitrile in a 2-dram vial was added Ag(I)PF_6 (111 mg, 0.44 mmol). After rapid color change from light red to dark red, the solution was stirred for 30 minutes and allowed to concentrate via evaporation at room temperature to afford a red solid. The solid was washed repeatedly with

hexanes to give 231 mg (70%) of complex. ^{1}H NMR (300 MHz, Chloroform-d) δ 7.89 (d, *J* = 9.1 Hz, 2H), 6.95 (d, *J* = 9.1 Hz, 2H), 4.15 (q, *J* = 7.1 Hz, 2H), 4.02 (q, *J* = 7.2 Hz, 2H), 3.89 (s, 3H), 1.46 (t, *J* = 7.2 Hz, 3H), 1.31 (t, *J* = 7.1 Hz, 3H). ^{13}C NMR (75 MHz, $CDCl_3$) δ 189.85, 167.12, 146.08, 129.21, 116.2, 57.14, 51.36, 48.27, 15.50, 12.13. FTIR (ATR, cm^{-1}): 2972, 1597, 1423, 1271, 1141. Anal. Calcd for $C_{24}H_{34}AgPF_6O_2N_6S_2$: C, 38.15; H, 4.54; N, 11.12; Found: C, 38.52; H, 4.34; N, 11.01. MP: 163°C.

[(*N*,*N*-diethyl-2-(4-fluorophenyl) diazothioformamide)$_2$Ag]PF$_6$ (11e): To *N*,*N*-diethyl-2-(4-fluorophenyl) diazothioformamide (6e) (198 mg, 0.83 mmol) in 10 ml of acetonitrile in a 2-dram vial was added Ag(I)PF_6 (100 mg, 0.415 mmol). After rapid color change from light red to dark red, the solution was stirred for 30 minutes and allowed to concentrate via evaporation at room temperature to afford a red solid. The solid was washed repeatedly with hexanes to give 198 mg (66 %) of red complex. ^{1}H NMR (300 MHz, Chloroform-*d*) δ 7.98 – 7.84 (m, 2H), 7.25 – 7.10 (m, 2H), 3.98 (q, *J* = 7.2 Hz, 2H), 3.52 (q, *J* = 7.2 Hz, 2H), 1.36 (t, *J* = 7.1 Hz, 3H), 1.15 (t, *J* = 7.2 Hz, 3H). ^{13}C NMR (75 MHz, $CDCl_3$) δ 193.57, 167.59 (d, $J_{C\text{-}F}$ =254 Hz), 148.65, 126.55 (d, $J_{C\text{-}F}$ =10 Hz), 117.04 (d, $J_{C\text{-}F}$ =23 Hz), 48.58, 45.87, 14.21, 11.79. FTIR (ATR, cm^{-1}): 2979, 1500, 1441, 1218, 1139, 1077. Anal. Calcd for $C_{22}H_{28}AgPF_8N_6S_2$: C, 36.12; H, 3.86; N, 11.49; Found: C, 38.91; H, 3.77; N, 11.06. MP: 167 °C.

[(*N*,*N*-diethyl-2-(4-trifluoromethylphenyl) diazothioformamide)$_2$Ag](PF$_6$) (11f): To *N*,*N*-diethyl-2-(4-trifluoromethylphenyl) diazothioformamide (6f) (225 mg, 0.74 mmol) in 5 ml of acetonitrile in a 2-dram vial was added Ag(I)PF_6 (94 mg, 0.37 mmol). After rapid color change from light red to dark red, the solution was stirred for 30 minutes and allowed to concentrate via evaporation at room temperature to afford 0.22 (72 %) mg of red complex. ^{1}H NMR (500 MHz, Acetonitrile-d_3) δ 8.68 (d, *J* = 8.4 Hz, 2H), 7.90 (d, *J* = 8.3 Hz, 2H), 4.08 (q, *J* = 7.1 Hz,

2H), 4.01 (q, J = 7.1 Hz, 2H), 1.41 (t, J = 7.1 Hz, 3H), 1.34 (t, J = 7.1 Hz, 3H). ^{13}C NMR (126 MHz, CD_3CN) δ 186.57, 154.57, 135.46, 128.10 (q, $J_{C\text{-}F}$ = 4 Hz), 127.93 (q, $J_{C\text{-}F}$ = 34 Hz), 125.93 (q, $J_{C\text{-}F}$ = 274 Hz), 51.88, 49.10, 14.85, 10.77. FTIR (ATR, cm^{-1}); 2953, 1704, 1416, 1320, 1062. Anal. Calcd for $C_{24}H_{28}AgPF_{12}N_6S_2$: C, 34.67; H, 3.39; N, 10.11; Found: C, 34.81; H, 2.96; N, 9.45; MP: 171 °C.

Antimicrobial Assays

Disk diffusion assay: Fifty micrograms of each ATF or ATF-metal ion complex were diluted with 100% ethanol and impregnated into paper disks and applied to the surface of Mueller Hinton agar (for bacteria) or Yeast-Potato-Dextrose agar (YPD, for yeast) plates evenly inoculated with a dilution of overnight microbial culture (diluted to a 0.5 McFarland standard)[30]. Plates were incubated overnight (30 - 37 ºC, depending on species), and the clearing zone surrounding the disk measured with a ruler as an indicator of antimicrobial activity. Standard antimicrobial disks (ampicillin, oxacillin, amphotericin B) were used as controls. All assays were repeated a minimum of three times. Images of representative disk diffusion results can be seen in Appendix (Figure A4.1) with results summarized in Appendix (Table A4.1).

Antimicrobial microdilution assay: Antimicrobial assays were conducted using microdilution assays in 96-well assay plates[31]. The concentration of compounds tested ranged from 1 – 50 µM. Plates were incubated overnight at 30-37 ºC (depending on species), and the culture turbidity measured at 24 hr. using a multiwell spectrophotometer set to 600 nm. Individual drug concentrations were tested in triplicate, with all assays repeated 2-4 times. The minimal inhibitory concentration (MIC) was recorded as the lowest tested concentration of

drug that showed no evidence of growth (absorbance values within 10% of background). The percentage of maximal growth was calculated from the equation:

$$\% \text{ max growth} = \frac{[\text{mean test}_{A600} - \text{mean bkg}_{A600}]}{[\text{mean max}_{A600} - \text{mean bkg}_{A600}]} \times 100$$

Mean absorbance values were plotted as a function of compound concentration using GraphPad Prism (ver 6) software. The MIC values (in micromolar, µM) are found in Table S2. The mean concentration of drug required to inhibit 50% of the growth (IC_{50}) was calculated from nonlinear fits of the data (± standard error on the mean, SEM) using GraphPad Prism.

Mammalian cell antiproliferation assay: Antiproliferation assays were conducted using a standard assay that follows the conversion of resazurin to fluorescent resorufin (Alamar Blue assay). Briefly, 5000 cells were dispensed in each well of a 96-well assay plate. The plates are incubated in complete media (DMEM or RPMI depending on the cell type) containing 10% cosmic calf serum and pen/strep for 24 hr. in a humidified 5% CO_2 atmosphere at 37 ºC. Drug stocks (10-20 mM) were prepared in 100% ethanol and dilutions created in DMEM or RPMI. Solvent controls consisted of dilutions of ethanol into biological medium. Drugs were added to cells at a final concentration of 1-100 µM, and the plates reincubated for 48 hr. Equivalent dilutions of ethanol were tested on cells and demonstrated no inhibition of cellular growth (data not shown). Resorufin was then added to the wells to a final concentration of 0.01% and the plates returned to the incubator for 24 hr. Metabolically active cells convert the resorufin to fluorescent resorufin, which is detected using a multiwell fluorimeter (Ex. 530 nm / Em. 590 nm). Individual drug concentrations were tested 3-5 times, with all assays repeated 2-3 times. The percent cell viability was calculated from the equation:

$$\% \text{ cell viability} = \frac{[\text{mean test}_{590nm} - \text{mean bkg}_{590nm}]}{[\text{mean untreated}_{590nm} - \text{mean bkg}_{590nm}]} \times 100$$

The mean concentration of drug required to inhibit 50% of cell proliferation (IC_{50}) was calculated from nonlinear fits of the data (± standard error on the mean, SEM) using GraphPad Prism.

5.6 References

1. Nielsen, K. T.; Harris, P.; Bechgaard, K.; Krebs, F. C., Structural study of four complexes of the M-N2S2 type derived from diethylphenylazothioformamide and the metals palladium, platinum, copper and nickel. *Acta Crystallographica Section B-Structural Science* **2007,** *63*, 151-156.

2. Bechgaard, K., Nonplanar Electron-Transfer Complexes .2. Chemistry of 4 Cu-N2s2z Complexes Derived from Copper-Bis-N,N-Diethylphenylazothioformamide. *Acta Chem Scand A* **1977,** *31* (8), 683-688.

3. Bechgaard, K., Nonplanar Electron-Transfer Complexes .1. Chemistry of 5 Ni-N2s2z Complexes Derived from Nickel-Bis-N,N-Diethylphenylazothioformamide. *Acta Chem Scand A* **1974,** *A 28* (2), 185-193.

4. Groner, V. M.; Larson, G. E.; Kan, Y.; Roll, M. F.; Moberly, J. G.; Waynant, K. V., The synthesis and crystal structure of bis-[3,3-diethyl-1-(phenyl-imino-kappaN)thio-urea-kappaS]silver hexa-fluorido-phosphate. *Acta Crystallogr E Crystallogr Commun* **2019,** *75* (Pt 9), 1394-1398.

5. Nielsen, K. T.; Bechgaard, K.; Krebs, F. C., Removal of palladium nanoparticles from polymer materials. *Macromolecules* **2005,** *38* (3), 658-659.

6. Nielsen, K. T.; Bechgaard, K.; Krebs, F. C., Effective removal and quantitative analysis of Pd, Cu, Ni, and Pt catalysts from small-molecule products. *Synthesis-Stuttgart* **2006,** *10*, 1639-1644.

7. Johnson, N. A.; Wolfe, S. R.; Kabir, H.; Andrade, G. A.; Yap, G. P. A.; Heiden, Z. M.; Moberly, J. G.; Roll, M. F.; Waynant, K. V., Deconvoluting the Innocent vs. Non-Innocent Behavior of N,N-Diethylphenylazothioformamide Ligands with Copper Sources. *European Journal of Inorganic Chemistry* **2017**, *47*, 5576-5581.

8. Pradhan, R.; Groner, V. M.; Gutman, K. L.; Heiden, Z. M.; Roll, M. F.; Moberly, J. G.; Waynant, K. V., Substitution effects on the binding interactions of redox-active arylazothioformamide ligands and copper(I) salts. *Supramolecular Chemistry* **2020**, *32* (8), 466-478.

9. Pradhan, R.; Groner, V. M.; Johnson, N. A.; Zhang, Q.; Roll, M. F.; Moberly, J. G.; Waynant, K. V., Synthesis of an N, N-diethyl-tert-butylazothioformamide ligand and coordination studies with Copper(I) salts. *Inorganic Chemistry Communications* **2021**, *124*, 108393.

10. Pradhan, R.; Groner, V. M.; Gutman, K. L.; Larson, G. E.; Kan, Y.; Zhang, Q.; Heiden, Z. M.; Roll, M. F.; Moberly, J. G.; Waynant, K. V., Evaluating Coordinative Binding Mechanisms through Experimental and Computational Studies of Methoxy-Substituted Arylazothioformamide Copper(I) Complexes. *European Journal of Inorganic Chemistry* **2022**, *33*, e202200421.

11. Thompson, R. L.; Price, M. L.; Minton, S. A., Jr., Protection of mice against vaccinia virus by administration of benzaldehyde thiosemicarbazone. *Proceedings of the Society for Experimental Biology and Medicine* **1951,** *78* (1), 11-13.

12. Thompson, R. L.; Davis, J.; Russell, P. B.; Hitchings, G. H., Effect of Aliphatic Oxime and Isatin Thiosemicarbazones on Vaccinia Infection in the Mouse and in the Rabbit. *Proceedings of the Society for Experimental Biology and Medicine* **1953,** *84* (2), 496-499.

13. Bauer, D. J., The antiviral and synergic actions of isatin thiosemicarbazone and certain phenoxypyrimidines in vaccinia infection in mice. *British Journal of Experimental Pathology* **1955,** *36* (1), 105-114.

14. Slack, R.; Wooldridge, K. R. H.; McFadzean, J. A.; Squires, S., A New Antiviral Agent : 4-Bromo-3-methylisothiazole-5-carboxaldehyde thiosemicarbazone, M and B 7714. *Nature* **1964,** *204* (4958), 587-587.

15. Mohamed, N. A.; Mohamed, R. R.; Seoudi, R. S., Synthesis and characterization of some novel antimicrobial thiosemicarbazone O-carboxymethyl chitosan derivatives. *International Journal of Biological Macromolecules* **2014**, *63*, 163-169.

16. Aly, M. M.; Mohamed, Y. A.; El-Bayouki, K. A. M.; Basyouni, W. M.; Abbas, S. Y. Synthesis of some new 4(3H)-quinazolinone-2-carboxaldehyde thiosemicarbazones and their metal complexes and a study on their anticonvulsant, analgesic, cytotoxic and

antimicrobial activities - Part-1. *European Journal of Medicinal Chemistry* **2010**, *45* (8), 3365-3373.

17. Kulandaivelu, U.; Padmini, V. G.; Suneetha, K.; Shireesha, B.; Vidyasagar, J. V.; Rao, T. R.; Jayaveera, K. N.; Basu, A.; Jayaprakash, V., Synthesis, Antimicrobial and Anticancer Activity of New Thiosemicarbazone Derivatives. *Archiv der Pharmazie* **2011,** *344* (2), 84-90.

18. Yu, Y.; Kalinowski, D. S.; Kovacevic, Z.; Siafakas, A. R.; Jansson, P. J.; Stefani, C.; Lovejoy, D. B.; Sharpe, P. C.; Bernhardt, P. V.; Richardson, D. R. Thiosemicarbazones from the Old to New: Iron Chelators That Are More Than Just Ribonucleotide Reductase Inhibitors. *Journal of Medicinal Chemistry* **2009**, *52* (17), 5271-5294.

19. Agarwal, R. K.; Singh, L.; Sharma, D. K. Synthesis, spectral, and biological properties of copper(II) complexes of thiosemicarbazones of Schiff bases derived from 4-aminoantipyrine and aromatic aldehydes. *Bioinorganic Chemistry Applications* **2006**, *2006*, 59509.

20. Pavan, F. R.; Maia, P. I. D.; Leite, S. R. A.; Deflon, V. M.; Batista, A. A.; Sato, D. N.; Franzblau, S. G.; Leite, C. Q. F., Thiosemicarbazones, semicarbazones, dithiocarbazates and hydrazide/hydrazones: Anti-Mycobacterium tuberculosis activity and cytotoxicity. *European Journal of Medicinal Chemistry* **2010**, *45* (5), 1898-1905.

21. Singh, N. K.; Kumbhar, A. A.; Pokharel, Y. R.; Yadav, P. N., Anticancer potency of copper(II) complexes of thiosemicarbazones. *Journal of Inorganic Biochemistry* **2020,** *210*, 111134.

22. Bajaj, K.; Buchanan, R. M.; Grapperhaus, C. A., Antifungal activity of thiosemicarbazones, bis(thiosemicarbazones), and their metal complexes. *Journal of Inorganic Biochemistry* **2021**, *225*, 111620.

23. Bisceglie, F.; Bacci, C.; Vismarra, A.; Barilli, E.; Pioli, M.; Orsoni, N.; Pelosi, G., Antibacterial activity of metal complexes based on cinnamaldehyde thiosemicarbazone analogues. *Journal of Inorganic Biochemistry* **2020**, *203*, 110888.

24. Matesanz, A. I.; Caballero, A. B.; Lorenzo, C.; Espargaro, A.; Sabate, R.; Quiroga, A. G.; Gamez, P., Thiosemicarbazone Derivatives as Inhibitors of Amyloid-beta Aggregation: Effect of Metal Coordination. *Inorganic Chemistry* **2020**, *59* (10), 6978-6987.

25. Pahontu, E.; Julea, F.; Rosu, T.; Purcarea, V.; Chumakov, Y.; Petrenco, P.; Gulea, A., Antibacterial, antifungal and in vitro antileukaemia activity of metal complexes with thiosemicarbazones. *Journal of Cellular and Molecular Medicine* **2015**, *19* (4), 865-878.

26. Kalinowski, D. S.; Quach, P.; Richardson, D. R., Thiosemicarbazones: the new wave in cancer treatment. *Future Medicinal Chemistry* **2009**, *1* (6), 1143-1151.

27. Zhang, H. J.; Qian, Y.; Zhu, D. D.; Yang, X. G.; Zhu, H. L., Synthesis, molecular modeling and biological evaluation of chalcone thiosemicarbazide derivatives as novel anticancer agents. *European Journal of Medicinal Chemistry* **2011**, *46* (9), 4702-4708.

28. Graur, V.; Usataia, I.; Bourosh, P.; Kravtsov, V.; Garbuz, O.; Hureau, C.; Gulea, A., Synthesis, characterization, and biological activity of novel 3d metal coordination compounds with 2-acetylpyridine N4-allyl-S-methylisothiosemicarbazone. *Applied Organometallic Chemistry* **2021**, *35* (4), e6172.

29. Munaretto, L. S.; Ferreira, M.; Gouvea, D. P.; Bortoluzzi, A. J.; Assuncao, L. S.; Inaba, J.; Creczynski-Pasa, T. B.; Sa, M. M., Synthesis of isothiosemicarbazones of potential antitumoral activity through a multicomponent reaction involving allylic bromides, carbonyl compounds and thiosemicarbazide. *Tetrahedron* **2020**, *76* (23), 131231.

30. Balan, G.; Burduniuc, O.; Usataia, I.; Graur, V.; Chumakov, Y.; Petrenko, P.; Gudumac, V.; Gulea, A.; Pahontu, E. Novel 2-formylpyridine 4-allyl-S-methylisothiosemicarbazone and Zn(II), Cu(II), Ni(II) and Co(III) complexes: Synthesis, characterization, crystal structure, antioxidant, antimicrobial and antiproliferative activity. *Applied Organometallic Chemistry* **2020**, *34* (3), e5423.

31. Cocco, M. T.; Congiu, C.; Onnis, V.; Pellerano, M. L.; De Logu, A., Synthesis and antimycobacterial activity of new S-alkylisothiosemicarbazone derivatives. *Bioorganic and Medicinal Chemistry* **2002,** *10* (3), 501-506.

32. Salah, I.; Parkin, I. P.; Allan, E. Copper as an antimicrobial agent: recent advances. *RSC Advances* **2021**, *11* (30), 18179-18186.

33. Chernousova, S.; Epple, M. Silver as Antibacterial Agent: Ion, Nanoparticle, and Metal. *Angewandte Chemie International Edition* **2013**, *52* (6), 1636-1653.

34. Santini, C. Pellei, M.; Esposito, G.; Gandin, V.; Porchia, M.; Tisato, F.; Marzano, C. Advances in Copper Complexes as Anticancer agents. *Chemistry Reviews* **2014**, *225* (1), 815-862.

35. Gandin, V.; Ceresa, C.; Esposito, G.; Indraccolo, S.; Porchia, M.; Tisato, F.; Santini, C.; Pellei, M.; Marzano, C. Therapeutic potential of the phosphino Cu(I) complex (hydroCuP) in the treatment of solid tumors. *Scientific Reports* **2017**, *7*, 13936.

36. Berners-Price, S.J.; Johnson, R.K.; Giovenella, A.J.; Faucette, L.; Mirabelli, C.K.; Sadler, P.J. Antimicrobial and Anticancer activity of tetrahedral, chelated, diphosphine silver(I) complexes: comparison with copper and gold. *Journal of Inorganic Biochemistry* **1988**, *33* (4) 285 – 295.

37. Liu, R.-X.; Luo, R.-Y.; Tang, M.-T.; Liu, Y.-C.; Chen, Z.-F.; Liang, H. The first copper(I) complex of anthrahydrazone with potential ROS scavenging activity showed significant *in vitro* anticancer activity by inducing apoptosis and autophagy. *Journal of Inorganic Chemistry* 2021, *218*, 111390.

38. Ge, E.J.; Bush, A.I.; Casini, A.; Cobine, P.A.; Cross, J.R.; DeNicola, G.M.; Dou, Q.P.; Franz, K.J.; Gohil, V.M.; Gupta, S.; Kaler, S.G.; Lutsenko, S.; Mittal, V.; Petris, M.J.; Polishchuk, R.; Ralle, M.; Schilsky, M.L.; Tonks, N.K.; Vahdat, L.T.; Van Aelst, L.; Xi, D.; Yuan, P.; Brady, D.C.; Chang, C.J. Connecting copper and cancer: from transition metal signalling to metalloplasia. *Nature Reviews Cancer* **2022**, *22*, 102-113.

39. Andrews, J. M.; BSAC Working Party on Susceptibility testing ft. BSAC standardized disc susceptibility testing method. *Journal of Antimicrobial Chemotherapy* **2001,** *48 Suppl 1*, 43-57.

40. *Clinical and Laboratory Standards Institute (CLSI). Methods for Dilution Antimicrobial Susceptibility Tests for Bacteria that Grow Aerobically.* 11th ed.; **2018**.

41. O'Brien, J.; Wilson, I.; Orton, T.; Pognan, F., Investigation of the Alamar Blue (resazurin) fluorescent dye for the assessment of mammalian cell cytotoxicity. *European Journal of Biochemistry* **2000**, *267* (17), 5421-5426.

42. Feng, Q. L.; Wu, J.; Chen, G. Q.; Cui, F. Z.; Kim, T. N.; Kim, J. O., A mechanistic study of the antibacterial effect of silver ions on Escherichia coli and Staphylococcus aureus. *Journal of Biomedical Materials Research* **2000**, *52* (4), 662-668.

43. Pradhan, R.; Gutman, K. L.; Mas Ud, A.; Hulley, E. B.; Waynant, K. V., Catalytic Carboxylation of Terminal Alkynes with Copper(I) Azothioformamide Complexes. *Organometallics* **2023**, *42* (5), 362-371.

Chapter 6: Catalytic Carboxylation of Terminal Alkynes with Copper(I) Azothioformamide complexes.

Chapter 6 is an adaptation of published manuscript:

Pradhan, R.; Gutman, K. L.; Mas Ud, A.; Hulley, E. B.; Waynant, K. V., *Organometallics* **2023**, *42* (5), 362-371.

Abstract

Redox-active azothioformamide (ATF) ligands produce coordination complexes with Cu(I) salts. A series of monosubstituted ligands were used to synthesize Cu(I) complexes and investigated for the catalytic insertion of carbon dioxide into terminal alkynes. The optimal catalytic conditions were found using phenylacetylene with 4 mol% of a halogen-bridged (μ-I)-*para*-substituted [(*p*-MeOATF-Cu(I)I)]$_2$ dimer with three equivalents of Cs_2CO_3 as base in DMSO under 1 atm of CO_2 at 40 ˚C for 24 h followed by treatment with HCl. A variety of aryl and alkyl substrates were evaluated giving yields from 47% - 99%. The reaction was computationally deconstructed, and a series of likely intermediates and associated energies are provided along with a proposed mechanism. Additionally, it was found that the conditions were suitable for one-pot esterification.

Keywords: azothioformamide, CO_2 insertion, alkyne C-H addition, propiolic acids

6.1 Introduction

Arylazothioformamide (ATF) ligands are unique as they readily undergo a redox event in the presence of zerovalent late transition metals which can oxidatively dissolve to create metal:ligand coordination complexes.[1] Initial examples of ATF based coordinative dissolution

were from copper(0) and $Ni(CO)_4$ yet various forms of zerovalent palladium and platinum have also been investigated.[2, 3] Each of these metals oxidizes to a M^{2+} oxidation state while the ATF ligand singly reduces to radical anions creating neutral 2:1 ligand to metal complexes as shown in **Figure 6.1** where ATF 1c promotes the formation of a copper(II) complex containing two singly reduced ATF ligands (3c). This property was highlighted to remove unwanted copper and palladium metals from polymeric materials.[4,5] Following metal dissolution studies, a series of investigations of mixing ATF and substituted ATF ligands with copper(I) salts yielded example structures 2c and 4c providing key differences that both confirm the radical anion species 3c from zerovalent copper and highlight the neutral coordination of the redox-active ligand with copper(I).[6-8] Using a similar strategy, a variety of copper(I) coordination complexes have been synthesized, and some confirmed by X-ray crystallography and their binding association constants reported, however, catalysis has yet to be explored with this unique ligand class.

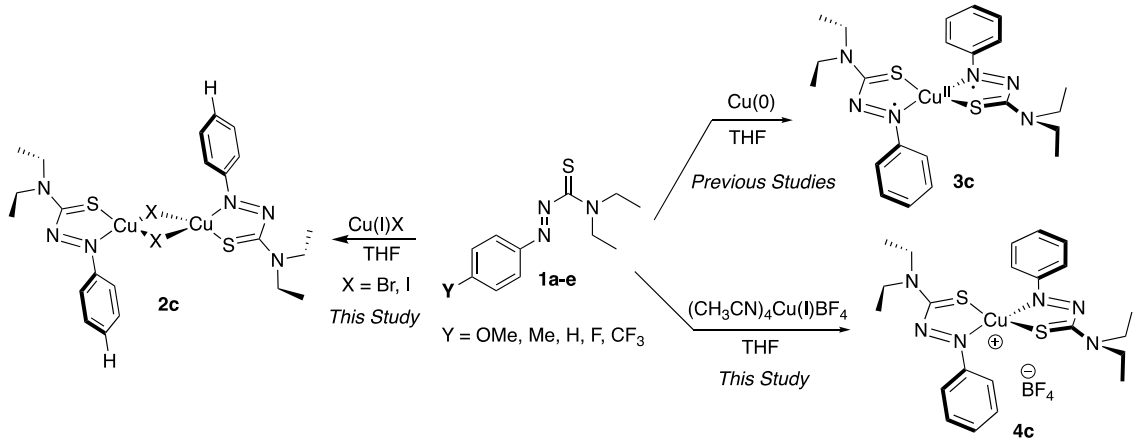

Figure 6.1: ATF ligands 1a-e react with copper (0) to create Copper (II) complexes (i.e., 3c) with singly reduced ligands as seen previously or with Copper(I) salts to produce neutral coordination complexes (i.e., 2c, 4c) for catalytic screening of CO_2 insertion.

Copper-catalyzed CO_2 insertion reactions at terminal alkynes was chosen as an entry point for the investigation of these metal:ligand systems as the reactions are well described and their mechanisms previously reported.[9-15] Simultaneously, by exploring the reductive insertion of CO_2, both experimentally and through DFT calculations, provides insight into the copper(I) catalyzed propiolic acid decarboxylation process. Silver(I) systems have been both utilized and computationally modeled for CO_2 insertion and decarboxylation into terminal alkynes noting that the addition of a coordinative metal salt allows for a significant (~10 kcal/mol) lowering of the energy required for terminal acetylene deprotonation.[16, 17]

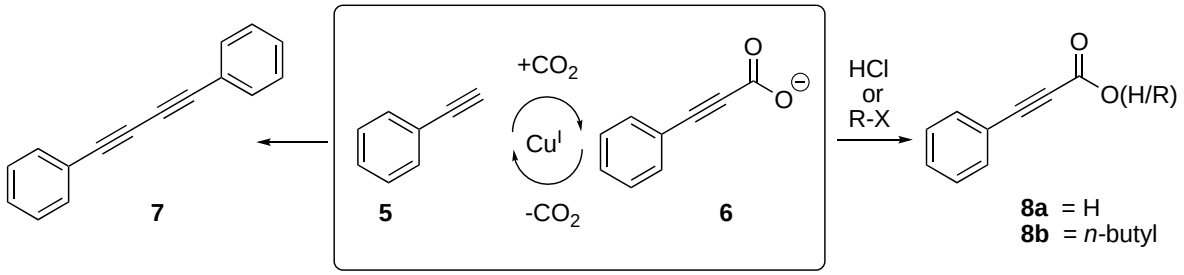

Figure 6.2: General reaction scheme for CO_2 insertion into terminal alkynes to create propiolates followed by creation of acids or esters; and the decarboxylation of propiolates creates homodiynes.

Beginning with phenylacetylene (5) under 1 atm of CO_2, multiple copper(I)ATF complexes were investigated to create phenylpropiolate (6) and work-up with $HCl_{(aq)}$ or upon the addition of an alkyl halide afforded either carboxylic acid (8a) or ester (8b), respectively. The energetics of these reactions and the intermediates, as calculated by DFT, suggest that not only would the conditions undergo successful formation of (6), but that (6), under such mild catalytic conditions and with low energetic thresholds for insertion, can, in the absence of CO_2 undergo decarboxylative homodiyne coupling to create cross-coupled Glaser-Hay product (7).[18,19] As ATFs are known to oxidatively dissolve zerovalent metals, the complexes formed

from metal salts provide insight into the dissolution products and the potential reactions that can be accomplished. Herein, a variety of conditions were screened and analyzed to introduce the ATF series as a unique ligand for the copper catalyzed CO_2 insertion.

6.2 Results and Discussion

ATF ligands were synthesized in a known one-pot procedure and with various electron donating and electron withdrawing substituents in the *para*-position, specifically -OMe (1a), -CH_3 (1b), -F (1d), and -CF_3 (1e).[7] Copper(I) coordination complexes were readily prepared from mixing the copper(I) salt with a solution of the ligand and then purifying the resulting complex through decantation or washing with non-polar solvents following evaporative concentration. Complexes were isolated as either 1:1 dimers (i.e., 2:2 complexes) as seen in 12-19 or as 2:1 complexes as in 20-27. Single crystal X-ray diffraction (XRD) structures were obtained for all copper(I) halide structures and the tetrafluoroborate copper(I) 2:1 salts. The hexafluorophosphate salts (24-27) gave similar spectroscopic evidence as the tetrafluoroborates and did not undergo XRD. Some substitutions allowed for deviations in overall structural complexes and less symmetry than those found in 2c, 3c and 4c above. Representative structures from crystal data are shown below in **Figure 6.3**, XRD data is provided (in ESI) for compounds 13-15, 17-19, and 21-23 with 12, 16, and 20 appearing in a previous report.[20]

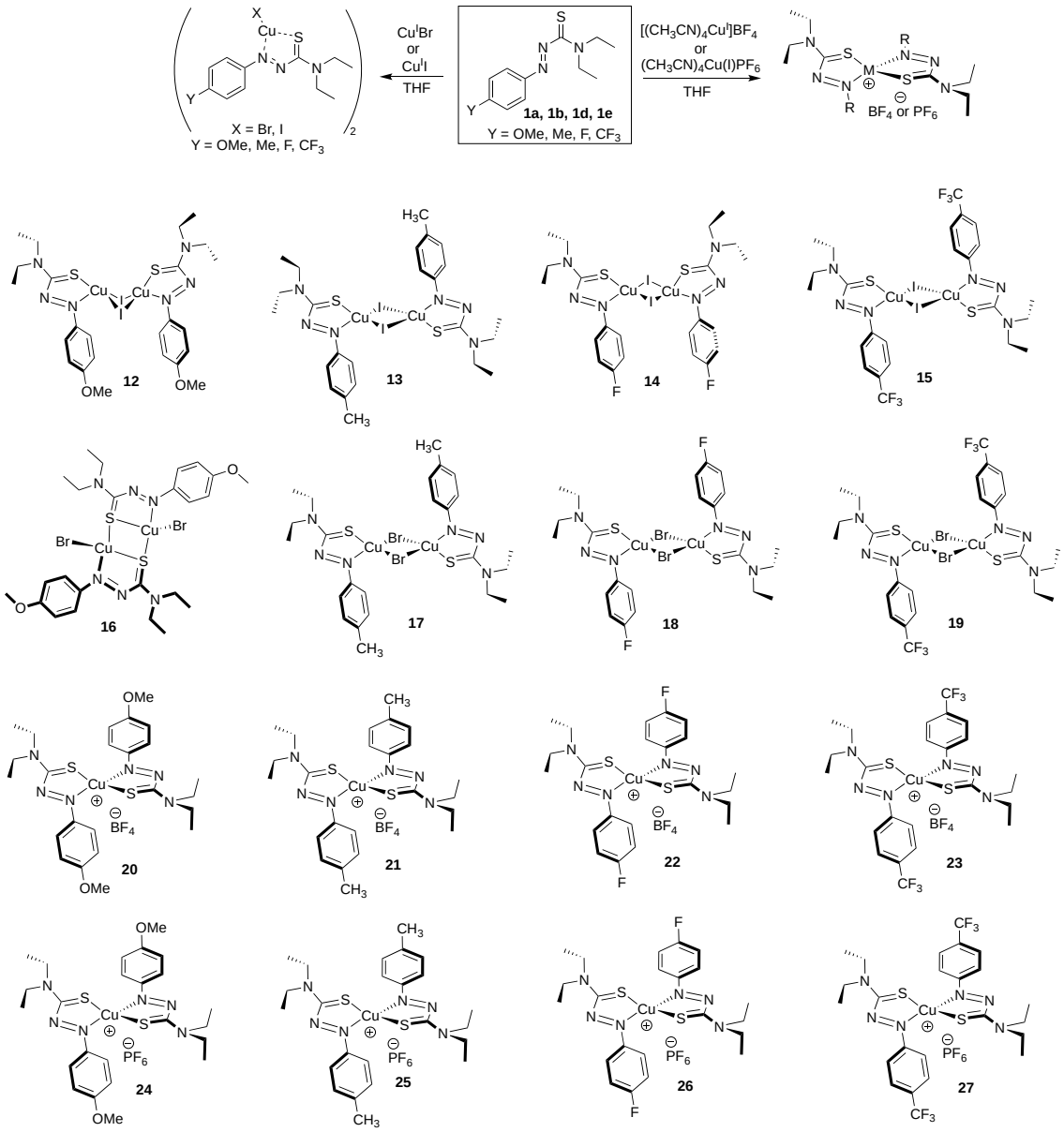

Figure 6.3: Various structures of Copper(I) ATF complexes. All structures are adapted from single crystal X-ray diffraction at 50% probability level. Compound 21 co-crystallized with one water molecule (see Appendix V).

Catalyst Screening

Initial transformations of phenylacetylene (5) to propiolic acid (8a) were tested at 4 mol % complex loading under 1 atm CO_2 in the presence of Cs_2CO_3 as base, DMSO as solvent,

and run at 40˚C, similar to reported conditions.[9,21-23] As seen in **Table 6.1** (entries 1-17), 16 ATF•Cu(I) complexes (compounds 12-27) were screened as well as copper(I) salts without ligand (entries 18-21), and Cs_2CO_3 alone (entry 22 as there are many reports on the cesium effect, especially in polar aprotic solvents like DMF/DMSO[24]). As indicated in Table 6.1, overall higher yields were obtained with copper(I) complexes containing ligands with electron-donating groups (Entries 1-3, 6,7, 10, 14, and 15) as opposed to ligands with electron withdrawing substitutions producing much lower yields (entries 4, 5, 8, 9, 12, 13, 16 and 17). This correlates to a previous study of weak binding of metal(I) salts with electron withdrawing group appended ATF ligands.[7] Yields of electron-withdrawing group substituted complexes were similar to copper(I) salts alone (entries 18-21). Overall, 4 mol % of the (μ-I)-bis(N,N'-diethyl-*para*-methoxyphenylazothioformamide) copper(I) complex (12) produced the highest yield (Entry 1) of all catalysts screened and was chosen for continued investigations. To note, complex (12) at 4 mol % is 8 mol % in copper(I). Catalyst (12) was tested at lower loading conditions (entry 2) which, while successful, took longer times to reach completion, and 92 % yield after 24 h.

Reaction Conditions Screening

DMSO was the highest yielding solvent when investigated against DMF and CH_3CN. DMSO is believed to coordinate and interrupt the μ-X dimerization / coordination of the ligand in these complexes to allow for copper to associate to the alkyne (see computational data below). For the optimized base, as shown in **Table 6.2**, three equivalents of Cs_2CO_3 (entries 2 and 3) performed overwhelmingly better than other inorganic bases tested (entries 6 and 7) and this correlated with similar results from silver(I) CO_2 insertion catalysis.[16]

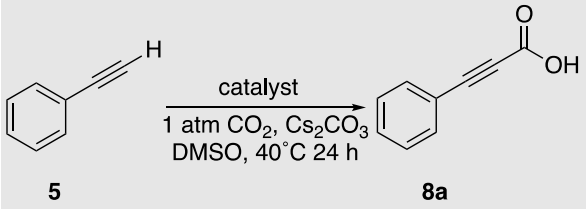

Table 6.1: Initial Screening of Cu(I) catalysts for CO_2 insertions

Entry	Catalyst	Compound ID	Mol% of Cu	Yield (8a)
1	(*p*-MeOATF-CuI)$_2$	12	8	99%
2	(*p*-MeOATF-CuI)$_2$	12	4	92%
3	(*p*-Me-ATF-CuI)$_2$	13	8	77%
4	(*p*-F-ATF-CuI)$_2$	14	8	49%
5	(*p*-CF$_3$-ATF-CuI)$_2$	15	8	46%
6	(*p*-MeOATF-CuBr)$_2$	16	8	65%
7	(*p*-Me-ATF-CuBr)$_2$	17	8	62%
8	(*p*-F-ATF-CuBr)$_2$	18	8	44%
9	(*p*-CF$_3$-ATF-CuBr)$_2$	19	8	23%
10	[(*p*-MeOATF)$_2$Cu]BF$_4$	20	4	73%
11	[(*p*-Me-ATF)$_2$Cu]BF$_4$	21	4	52%
12	[(*p*-F-ATF)$_2$Cu]BF$_4$	22	4	51%
13	[(*p*-CF$_3$-ATF)$_2$Cu]BF$_4$	23	4	41%
14	[(*p*-MeOATF)$_2$Cu]PF$_6$	24	4	79%
15	[(*p*-Me-ATF)$_2$Cu]PF$_6$	25	4	67%
16	[(*p*-F-ATF)$_2$Cu]PF$_6$	26	4	63%
17	[(*p*-CF$_3$-ATF)$_2$Cu]PF$_6$	27	4	57%
18	[(CH$_3$CN)$_4$Cu]PF$_6$	-	4	38%
19	Cu(I)I	-	4	44%
20	Cu(I)Br	-	4	44%
21	[(CH$_3$CN)$_4$Cu(I)]BF$_4$	-	4	43%
22	None	-	-	17%

The reaction did not proceed in the presence of 1.5 equivalents triethylamine or with diisopropylethylamine (entries 8 and 9) and only slightly with DBU. DBU was modeled (shown below) to bind strongly to the copper(I). As opposed to DBU, triethylamine appears to facilitate the deprotonation to form copper acetylide, as expected from precedent in copper(I) mediated deprotonation of alkynes in Sonogashira reactions, yet the second role of the base in these reactions is to coordinate to the newly formed propiolate ion prior to work-up.

Table 6.2: Screening of Reaction Conditions with catalyst 12 at 4 mol%

Entry	Catalyst	Base (equiv.)	Solvent	Temp (˚C)	Yield/%(8a)
1	12	Cs_2CO_3 (3)	DMF	40	81
2	12	Cs_2CO_3 (3)	CH_3CN	40	20
3	12	Cs_2CO_3 (3)	DMSO	40	99
4	12	Cs_2CO_3 (2)	DMSO	40	81
5	12	Cs_2CO_3 (1)	DMSO	40	65
6	12	K_2CO_3 (3)	DMSO	40	18
7	12	K_3PO_4 (3)	DMSO	40	22
8	12	K_2CO_3 (3) + TEA (1.5)	DMSO	40	0
9	12	DIPEA (3)	DMSO	40	0
10	12	DBU (3)	DMSO	40	15
11	12	Cs_2CO_3 (3)	DMSO	RT	63
12	12	Cs_2CO_3 (3)	DMSO	60	71

Triethylamine was titrated into phenylpropiolic acid in d_6-DMSO (as monitored by NMR) to form a triethylammonium complex yet upon addition of a copper(I) salt (Cu(I)I), the solution began to rapidly decarboxylate forming phenylacetylene (confirmed by ^{1}H NMR). This phenomenon occurred at a slower rate in the presence of Cs_2CO_3 suggesting that, in addition to deprotonating the alkyne (following Cu(I) coordination), the role of Cs_2CO_3 was to

serve as a more stable counterion to the propiolate due to its increased solubility in DMSO. Increasing the temperature of the reaction increased decarboxylative homodiyne coupling side product and lowered the yield of propiolic acid.

Computational Data and Mechanism

Metal-catalyzed alkyne carboxylation has been the subject of prior experimental and computational studies and many features of previous systems apply to this study.[14, 21-23] The steps most relevant to this work include (1) binding of the alkyne to an available copper(I) binding site, (2) deprotonation of the bound alkyne, (3) insertion of CO_2 giving C-C bond formation, and (4) loss of the nascent carboxylate *via* transmetallation with inorganic base.

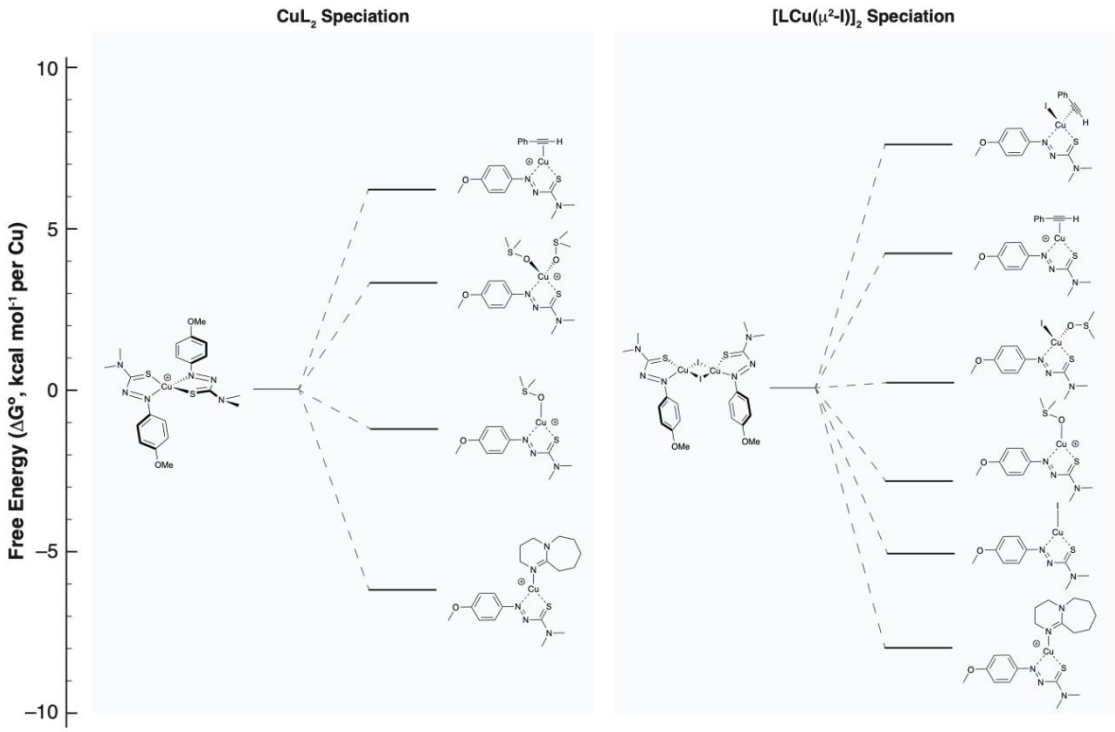

Figure 6.4: DFT-derived free energies indicating the speciation of $[Cu(L)_2]^+$ and $[(L)Cu(\mu\text{-}I)]_2$ in DMSO under standard state conditions per mole of copper catalyst.

Some of these steps are outside the scope of this report – for example, the involvement of Cs^+ in deprotonation and transmetallation reactions is complex and depends greatly on the speciation and aggregation of the Cs^+ salts. As such, DFT studies focused more on (1) identifying the likely resting state of the catalyst and (2) estimating the free energy of potential intermediates to rule out deactivation pathways. Since monometallic $[(L)_2Cu]^+$ and bimetallic $[(L)Cu(\mu\text{-}X)]_2$ compounds are both active as precatalysts (L = *p*-MeOATF), the speciation of these complexes in DMSO was investigated first (**Figure 6.4**).

To hasten calculations and minimize rotamer complications while maintaining catalytic relevance, truncation of the system was restricted by replacing the ethyl groups in *p*-MeOATF ligands with methyl groups. For the bis(ligand) complex $[(L)_2Cu]^+$ we examined the species related to dissociation of an *p*-MeOATF ligand and binding of solvent and substrates, whereas studies of the dimeric complex $[(L)Cu(\mu\text{-}I)]_2$ included monomer-dimer equilibria and iodide dissociation (Figure 6.4). We also explored the possibility that DBU binds to Cu species during catalysis.

Under standard-state conditions, dissociation of *p*-MeOATF (1a) from the bis(ligand) complex $[Cu(L)_2]^+$ yields the mono-solvated $[Cu(L)(OSMe_2)]^+$ and is slightly favored (–1.17 kcal/mol), but formation of other solvates (e.g., $[Cu(L)(OSMe_2)_2]^+$ and $[Cu(L)(S(O)Me_2)]^+$) are endergonic. Substitution with phenylacetylene is also thermodynamically uphill (+6.18 kcal/mol); the alkyne complex is thus unlikely to be the resting state of the catalyst. Catalytic conditions (~0.015 mM [Cu], DMSO solvent) are such that $[Cu(L)(OSMe_2)_2]^+$ will dominate the speciation equilibria, so this is the likely resting state when $[Cu(L)_2]^+$ is employed as a precatalyst. For dimeric $[(L)Cu(\mu\text{-}I)]_2$ the case is similar, wherein dissociation to monomeric derivatives $[Cu(L)(OSMe_2)]^+$ and Cu(L)I is favorable (– 2.99 kcal/mol and – 5.32 kcal/mol,

respectively). Although the neutral iodide complex Cu(L)I is predicted to be slightly more favorable under standard conditions, the dilute conditions (and low [I^-]) under which catalysis is performed would likely render $[Cu(L)(OSMe_2)]^+$ to be the favored species. Thus, for both systems ($[Cu(L)_2]^+$ and $[(L)Cu(\mu\text{-}I)]_2$), DFT calculations suggest that the monosolvated cation $[Cu(L)(OSMe_2)]^+$ will predominate under catalytic conditions. This is not the case when DBU is employed as a terminal base, as the DGº for binding of DBU to copper is 5.0 kcal/mol more favorable than that for DMSO, and this is likely the origin for the poorer catalytic performance in the presence of DBU.

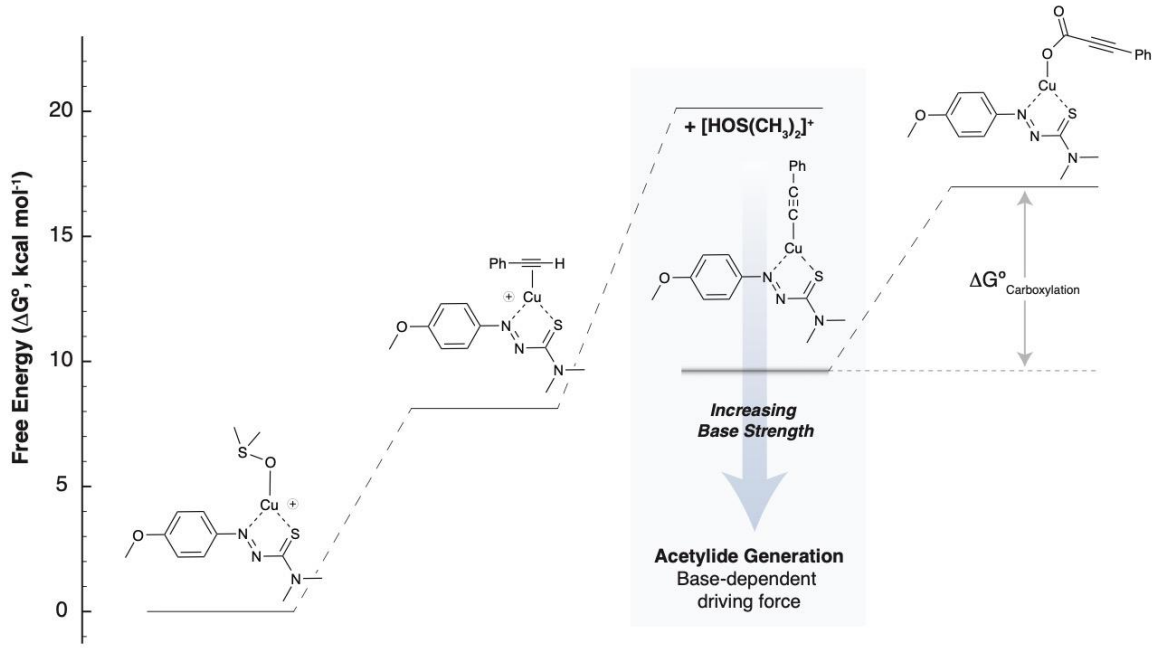

Figure 6.5: Free Energy coordinate diagrams of proposed mechanistic steps starting from DMSO bound resting state to the coordinated acetylene, acetylide formation, and CO_2 insertion.

With the probable resting state in mind, efforts then focused on calculating the intermediates involved in the C–H activation and CO_2 insertion steps (**Figure 6.5**). A full investigation of the transition states was not employed in this study since the nature of the

deprotonation step has not been elucidated experimentally, and whether the barriers for ligand substitution and CO_2 insertion will be rate-limiting depend greatly on this step.

Ligand substitution by phenylacetylene yields the h^2-alkyne complex (+ 7.36 kcal/mol) which can then be deprotonated by an exogenous base to yield the acetylide. The *kinetic* base for this step could be free ligand (particularly when $[Cu(L)_2]^+$ is used as a pre-catalyst), CsO_2CCPh product (particularly as the reaction progresses), or solvated cesium carbonate clusters. Since the calculated free energy of carboxylation for the acetylide is substantial (DG° = 7.35 kcal/mol), the kinetic base is unlikely to be the solvent itself, as this would result in the carboxylate lying 27 kcal/mol above the catalyst resting state and result in catalytic rates far lower than observed. Using protonation of DMSO as a free-energy benchmark, however, we can approximate the pK_a of the alkyne intermediate and estimate an upper-limit for the free energy of the acetylide intermediate under reaction conditions. For the simple proton transfer reaction between the alkyne complex and DMSO (yielding O-protonated $DMSO(H)^+$) as shown in **Figure 6.6** where the reaction is endergonic by 12.7 kcal/mol, indicative of a pK_a(DMSO) of 9.3

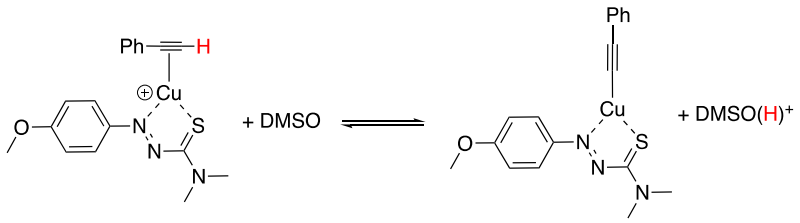

Figure 6.6: Equilibrium between eta-2 acetylene and acetylide.

Calculating *accurate* pK_a values is notoriously difficult, thus we interpret this value to be an *estimate* when predicting the driving force with other bases. For example, in the case of DBU (pK_a = 13.9 in DMSO), deprotonation of the h^2-alkyne complex would be exergonic by

6.3 kcal/mol, and the carboxylate formed after CO_2 insertion would only be 8.4 kcal/mol above the proposed resting state $[Cu(L)(OSMe_2)]^+$. The final step, removal of the nascent carboxylate and regeneration of $[Cu(L)(OSMe_2)]^+$, seems likely to be affected by solvated cesium carbonate clusters. It is conceivable that the propiolic acid could be produced directly from $Cu(L)(O_2CC{\equiv}CPh)$ through protonation by phenylacetylene as shown in **Figure 6.7**, but this step is predicted to be sufficiently endergonic that it would be inconsistent with observed rates.

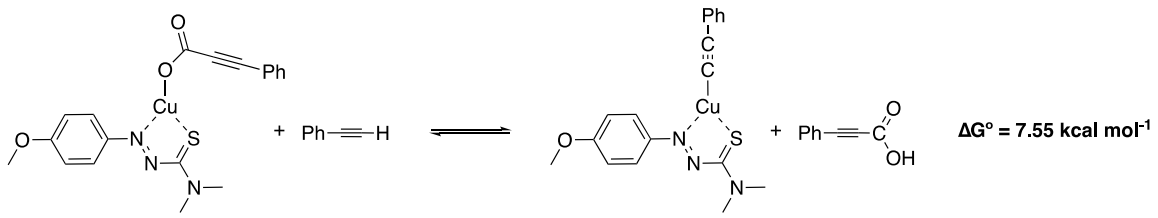

Figure 6.7: Free energy difference and equilibrium between propiolate protonation and acetylene deprotonation.

In short, we propose a catalytic cycle based on the $[Cu(p\text{-MeOATF})(OSMe_2)]^+$ resting state as shown in **Figure 6.8.**

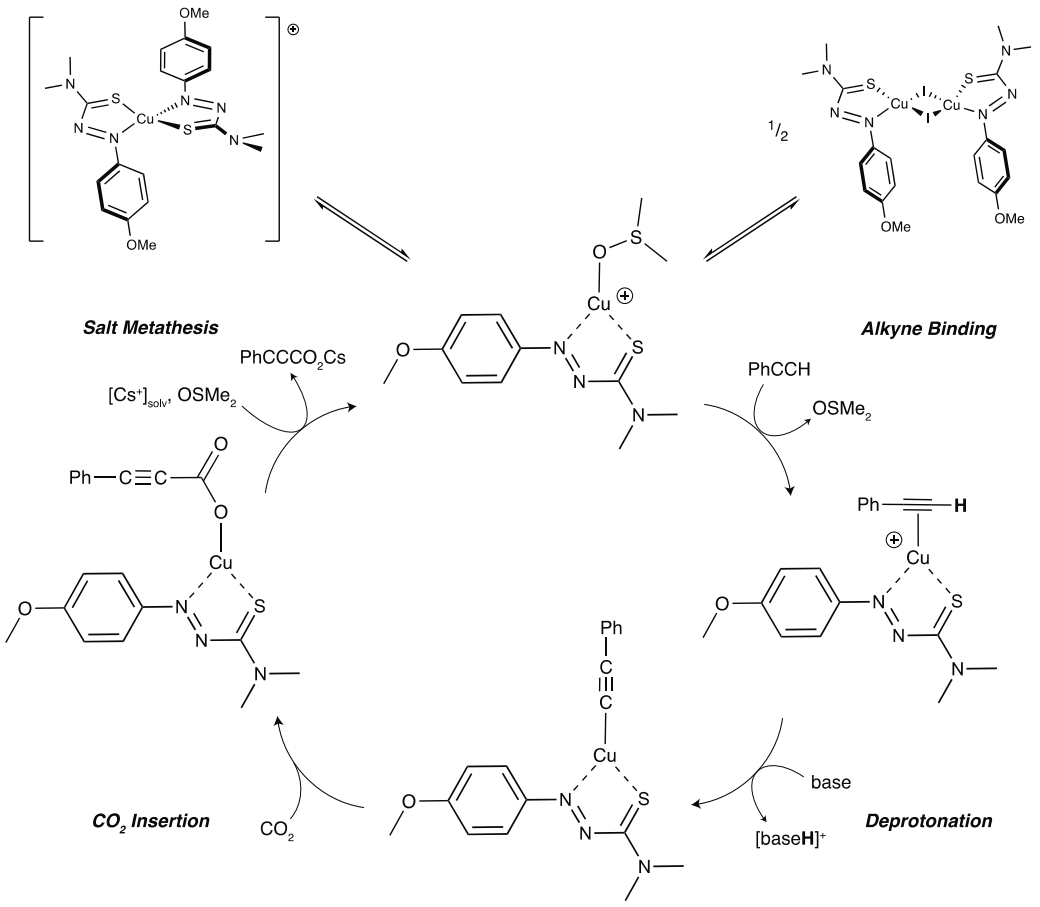

Figure 6.8: Proposed catalytic mechanism for the formation of propiolates starting from [Cu(p-MeOATF)(OSMe$_2$)]$^+$ arising from either [Cu(p-MeOATF)$_2$]$^+$ or [Cu(p-MeOATF)(μ–I)$_2$]$_2$ as pre-catalysts.

Scope of phenylacetylenes

With the optimized conditions (Table 6.2, entry 3), a series of aryl and alkyl acetylenes were examined as shown in Figure 6.9. Most aryl substrates, ortho-, meta-, and para-substituted, proceeded in good to excellent yields ranging from 67% to 99%. However, 2-ethynylpyridine, 41, gave a low yield which may be indicative of a nitrogenous coordination equilibrium that slows catalysis as described above with DBU. Lastly, looking at a complex pharmaceutical, ethynyl estradiol carboxylates, yielding product 47, at a modest yield of 38%.

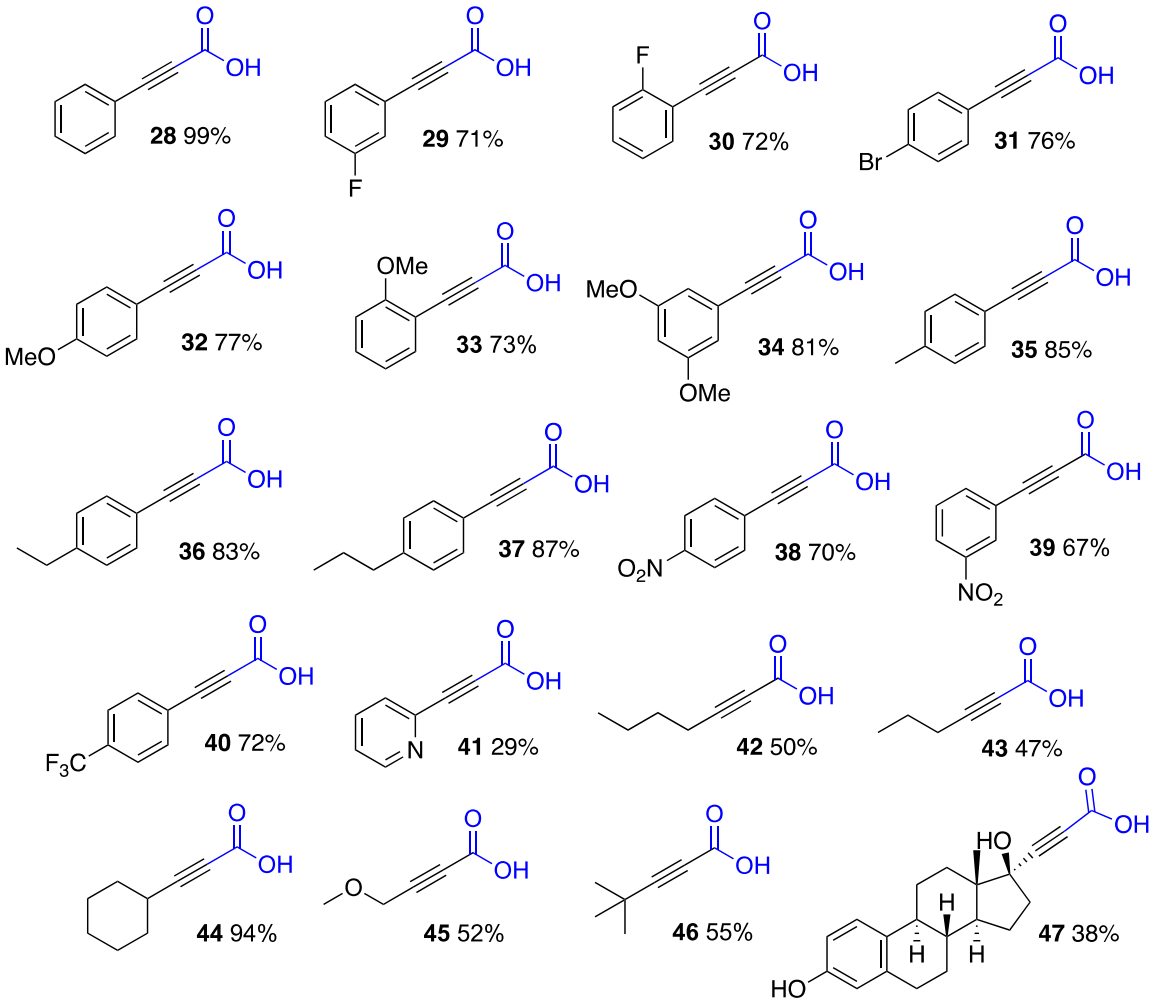

Figure 6.9: Substrate scope for CO_2 insertion via optimized conditions.

Expansion to Esterification

The variability and utility of these reaction conditions was tested in one-pot esterification. Esterification of phenylacetylene using butyl iodide as alkylating agent proceeded well, affording ester 8b in 83% yield. For this reaction modification, after 21 hours, the reaction was cooled to rt, and following addition of 1.2 equivalents of butyl iodide, the reaction was returned to 40 ˚C for an additional 3 hours as shown in Figure 6.10. Decarboxylative homodiyne coupling was also found when starting from phenylpropiolic acid (8a) without CO_2 atmosphere, and previously described[25] to give (7) in a reasonable 62% yield.

This reaction worked both under N_2 and in air, suggesting multiple potential oxidants and oxidative coupling mechanisms are currently being pursued. This is mentioned as CO_2 insertion reaction conditions were kept at low temperatures (i.e., 40 ˚C) as to limit the formation of homodiyne byproduct.

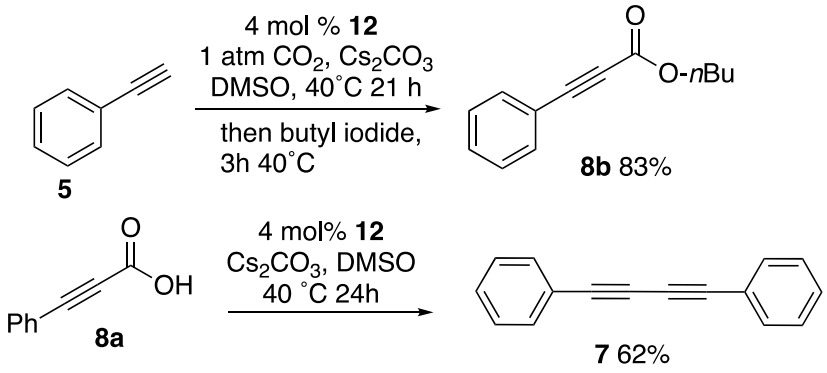

Figure 6.10: Expansion of CO_2 insertions towards esterification to create 8b. Decarboxylation to homodiyne 7 was also observed due to the low carboxylation energy barrier.

6.3 Conclusion

Copper(I) azothioformamide complexes were investigated for insertion of CO_2 into C_{sp}-H alkyne bonds to form propiolic acids. It was found that Cu(I) complexes, both 2:1 and 2:2 dimers with ATF substituted with electron-donating groups, especially complex (12), produced the highest yields per mol% of Cu. DFT calculations were invaluable towards a proposed mechanism, catalytic resting state, and indicating the need for an inorganic base. The substrate scope showed that while tolerant of many common substitutions on phenylacetylenes, the yields of alkyl and non-aryl aromatic CO_2 insertions can be improved. The reactions conditions allow for esterification with addition of alkyl halides. Overall, ATF complexes offer a new ligand option for copper(I) catalysis.

6.4 Experimental

Synthesis of coordination complexes 12, 16, and 20 appear in a previous report.[20]

Synthesis of coordination complexes

(μ-I)-[Cu(*p*-tolyl-ATF)I]$_2$ (13): To *N*,*N*-diethyl-2-(*p*-tolyl)azothioformamide (72 mg, 0.31 mmol) dissolved in 5 mL of acetonitrile was added Cu(I)I (59 mg, 0.31 mmol). After rapid color change from light orange to dark blue the solution was decanted into another 2-dram vial and allowed to concentrate via evaporation at room temperature over 3-5 days to afford dark blue crystals. After washing with hexanes 80 mg (61%) was collected. ^{1}H NMR (300 MHz, Chloroform-*d*) δ 8.40 (d, *J* = 8.2 Hz, 4H), 7.34 (d, *J* = 8.2 Hz, 4H), 4.18 (q, *J* = 7.2 Hz, 4H), 4.10 (q, *J* = 7.1 Hz, 4H), 2.44 (s, 6H), 1.51 – 1.40 (m, 12H). ^{13}C NMR (75 MHz, $CDCl_3$) δ 188.11, 150.13, 148.41, 131.68, 127.95, 51.34, 48.86, 23.00, 15.85, 11.90. FTIR (ATR, cm^{-1}): 2966, 1513, 1426, 1075, 779. Elem Anal. for $C_{24}H_{34}I_2Cu2N_6S_2$ Calcd: C, 33.85; H, 4.02; N, 9.87; Found: C, 34.04; H, 3.79; N, 8.97. MP: 170°C. **CCDC 2215318**

(μ-I)[Cu(*p*-fluorophenyl-ATF)I]$_2$ (14): To *N*,*N*-diethyl-2-(4-fluorophenyl)azothioformamide (50 mg, 0.21 mmol) dissolved in 5 mL of acetonitrile was added Cu(I)I (40 mg, 0.21 mmol). After rapid color change from light orange to dark blue the solution was decanted into another 2-dram vial and allowed to concentrate via evaporation at room temperature over 3-5 days to afford 53 mg (61%) of dark blue crystals. ^{1}H NMR (500 MHz, Chloroform-*d*) δ 8.84 (d, *J* = 9.1 Hz, 4H), 7.25 (d, *J* = 8.0 Hz, 4H), 4.16 – 4.06 (m, 8H), 1.48 (t, *J* = 7.2 Hz, 6H), 1.39 (t, *J* = 7.2 Hz, 6H). ^{13}C NMR (126 MHz, $CDCl_3$) δ 186.67, 167.83 (d, $J_{C\text{-}F}$ =259 Hz), 148.06, 129.89 (d, $J_{C\text{-}F}$ = 11 Hz),117.30 (d, $J_{C\text{-}F}$ = 23 Hz), 50.45, 47.72, 15.17, 11.24. FTIR (ATR, cm^{-1}): 2980,

1493, 1431, 1232, 1142, 1072, 702. Elem Anal. for $C_{22}H_{28}I_2F_2Cu_2N_6S_2$ Calcd: C, 30.74; H, 3.28; N, 9.78; Found: C, 31.01; H, 3.09; N, 9.42. MP: 182°C. **CCDC 2215325**

(μ-I)[Cu(*p*-trifluoromethylphenyl-ATF)I]$_2$ (15): To *N*,*N*-diethyl-2-(4-(trifluoromethyl) phenyl)azothioformamide (30 mg, 0.10 mmol) dissolved in 5 mL of anhydrous THF was added Cu(I)Br (19 mg, 0.10 mmol). After rapid color change from light orange to dark blue the solution was decanted into another 2-dram vial and allowed to concentrate via evaporation at room temperature over 3-5 days to afford 33 mg (69%) of dark blue crystals.^{1}H NMR (500 MHz, Chloroform-*d*) δ 8.83 (d, *J* = 8.2 Hz, 4H), 7.85 (d, *J* = 8.2 Hz, 4H), 4.15 – 4.09 (m, 8H), 1.49 (t, *J* = 7.1 Hz, 6H), 1.39 (t, *J* = 7.1 Hz, 6H). ^{13}C NMR (126 MHz, $CDCl_3$) δ 186.42, 153.46, 135.91 (q, $J_{C\text{-}F}$ = 33 Hz), 127.09 (q, $J_{C\text{-}F}$ = 3 Hz), 124.84 (q, $J_{C\text{-}F}$ = 267 Hz), 118.95, 50.43, 47.64, 15.12, 11.09. FTIR (ATR, cm^{-1}); 2986, 1520,1433, 1320, 1124, 1063. Elem Anal. for $C_{24}H_{28}I_2Cu_2F_6N_6S_2$ Calcd: C, 30.04; H, 2.94; N, 8.76; Found: C, 30.31; H, 2.79; N, 8.79. MP: 173 °C. **CCDC 2215324**

(μ-Br)-[Cu(*p*-tolyl-ATF)Br]$_2$ (17): To *N*,*N*-diethyl-2-(*p*-tolyl)azothioformamide (60 mg, 0.26 mmol) dissolved in 5 mL of acetonitrile was added Cu(I)Br (37 mg, 0.26 mmol). After rapid color change from light orange to dark blue the solution was decanted into another 2-dram vial and allowed to concentrate via evaporation at room temperature over 3-5 days to afford dark blue crystals. After washing the crystals with hexanes, 49 mg (51%) was collected. ^{1}H NMR (300 MHz, Chloroform-*d*) δ 8.45 (d, *J* = 8.2 Hz, 4H), 7.35 (d, *J* = 8.2 Hz, 4H), 4.22 – 4.05 (m, 8H), 1.51 – 1.39 (m, 12H). ^{13}C NMR (75 MHz, $CDCl_3$) δ 188.08, 150.18, 148.26, 131.62, 127.99, 51.27, 48.76, 23.00, 15.84, 11.91. FTIR (ATR, cm^{-1}); 2971, 1527,1425, 1073, 782. Elem Anal. for $C_{24}H_{34}Br_2Cu_2N_6S_2$ Calcd: C, 38.05; H, 4.52; N, 11.09; Found: C, 38.43; H, 4.29; N, 10.73. MP: 148°C. **CCDC 2215317**

(μ-Br)[Cu(*p*-fluorophenyl-ATF)Br]$_2$ (18): To *N*,*N*-diethyl-2-(4-fluorophenyl) azothioformamide (33 mg, 0.14 mmol) dissolved in 5 mL of acetonitrile was added Cu(I)Br (20 mg, 0.14 mmol). After rapid color change from light orange to dark blue the solution was allowed to concentrate via evaporation at room temperature over 3-5 days to afford 29 mg (54%) of dark blue crystals. ^{1}H NMR (300 MHz, Chloroform-*d*) δ 8.79 (d, *J* = 7.5 Hz, 4H), 7.30 (d, *J* = 8.5 Hz, 4H), 4.12 (q, *J* = 6.9 Hz, 8H), 1.50 – 1.39 (m, 12H). ^{13}C NMR (126 MHz, $CDCl_3$) δ 187.34, 168.07(d, $J_{C\text{-}F}$ =260 Hz), 147.84, 130.12(d, $J_{C\text{-}F}$ =10 Hz), 117.57(d, $J_{C\text{-}F}$ =23 Hz), 50.91, 47.91, 15.08, 11.08. FTIR (ATR, cm^{-1}): 2986, 1492, 1429, 1227, 1154, 1070, 701. Elem Anal. for $C_{22}H_{28}Br_2F_2Cu_2N_6S_2$ Calcd: C, 34.52; H, 3.69; N, 10.98; Found: C, 34.90; H, 3.62; N, 10.23. MP: 180°C. **CCDC 2215319**

(μ-Br)[Cu(*p*-trifluoromethylphenyl-ATF)Br]$_2$ (19): To *N*,*N*-diethyl-2-(4-(trifluoromethyl) phenyl)azothioformamide (20 mg, 0.07 mmol) dissolved in 5 mL of anhydrous THF was added Cu(I)Br (10 mg, 0.07 mmol). After rapid color change from light orange to dark blue the solution was decanted into another 2-dram vial and allowed to concentrate via evaporation at room temperature over 3-5 days to afford 21 mg (67%) of dark blue crystals.^{1}H NMR (500 MHz, Acetonitrile-d_3) δ 8.68 (d, *J* = 8.4 Hz, 4H), 7.90 (d, *J* = 8.3 Hz, 4H), 4.08 (q, *J* = 7.1 Hz, 4H), 4.01 (q, *J* = 7.1 Hz, 4H), 1.41 (t, *J* = 7.1 Hz, 6H), 1.34 (t, *J* = 7.1 Hz, 6H). ^{13}C NMR (126 MHz, CD_3CN) δ 186.57, 154.57, 135.46 (q, $J_{C\text{-}F}$ = 33 Hz), 128.10 (q, $J_{C\text{-}F}$ = 4 Hz), 127.93, 125.93 (q, $J_{C\text{-}F}$ = 274 Hz), 51.88, 49.10, 14.85, 10.77. FTIR (ATR, cm^{-1}); 2980, 1518,1431, 1325, 1122, 1060. Elem. Anal. for $C_{24}H_{28}Br_2Cu_2F_6N_6S_2$ Calcd: C, 33.3; H, 3.26; N, 9.71; Found: C, 33.4; H, 3.71; N, 9.69. MP: 157 °C. **CCDC 2215320**

[(*p*-tolyl-ATF)$_2$Cu](BF$_4$) (21): To *N*,*N*-diethyl-2-(*p*-tolyl)azothioformamide (38 mg, 0.16 mmol) dissolved in 5 mL of acetonitrile was added $[(CH_3CN)_4]BF_4$ (26 mg, 0.08 mmol). After

rapid color change from light orange to dark blue the solution was decanted into another 2-dram vial and allowed to concentrate via evaporation at room temperature over 3-5 days to afford 61 mg (59%) of dark blue crystals. ^{1}H NMR (500 MHz, Acetonitrile-d_3) δ 7.96 (d, J = 8.0 Hz, 4H), 7.34 (d, J = 8.0 Hz, 4H), 4.28 (q, J = 7.1 Hz, 4H), 4.14 (q, J = 7.0 Hz, 4H), 2.48 (s, 6H), 1.45 – 1.42 (m, 12H). ^{13}C NMR (126 MHz, CD_3CN) δ 187.72, 150.29, 148.86, 131.45, 128.06, 51.54, 49.49, 21.81, 15.15, 11.46. FTIR (ATR, cm^{-1}): 2985, 1534, 1429, 1151, 823. Elem Anal. for $C_{24}H_{34}CuBF_4N_6S_2$ Calcd: C, 46.41; H, 5.52; N, 13.53; Found: C, 46.61; H, 5.02; N, 12.71. MP: 155°C. **CCDC 2215323**

[(*p*-fluorophenyl-ATF)$_2$Cu](BF$_4$) (22): To *N*,*N*-diethyl-2-(4-fluorophenyl)azothioformamide (78 mg, 0.33 mmol) dissolved in 10 mL of acetonitrile in a 4-dram vial was added $[(CH_3CN)_4Cu](BF_4)$ (51 mg, 0.165 mmol). After rapid color change from light orange to dark blue the solution was decanted into a 2-dram vial and allowed to concentrate via evaporation at room temperature over 3-5 days to afford 50 mg (49%) of dark blue crystals. ^{1}H NMR (300 MHz, Chloroform-*d*) δ 8.16 (d, J = 9.1 Hz, 4H), 7.20 (d, J = 8.4 Hz, 4H), 4.33 (q, J = 7.1 Hz, 4H), 4.11 (q, J = 7.1 Hz, 4H), 1.53 – 1.45 (m, 12H). ^{13}C NMR (75 MHz, $CDCl_3$) δ 187.23, 169.93 (d, $J_{C\text{-}F}$ =254 Hz),148.22, 130.24 (d, $J_{C\text{-}F}$ =10 Hz), 118.89 (d, $J_{C\text{-}F}$ =23 Hz), 51.92, 49.89, 15.77, 11.60. FTIR (ATR, cm^{-1}): 2982, 1493, 1436, 1234, 1141, 1033,707. Elem Anal. for $C_{22}H_{28}CuBF_6N_6S_2$ Calcd: C, 42.01; H, 4.49; N, 13.36; Found: C, 41.61; H, 4.59; N, 13.31. MP: 178°C. **CCDC 2215321**

[(*p*-trifluoromethylphenyl-ATF)$_2$Cu](BF$_4$) (23): To *N*,*N*-diethyl-2-(4-(trifluoromethyl) phenyl)azothioformamide (46 mg, 0.16 mmol) dissolved in anhydrous THF was added $[(CH_3CN)_4Cu](BF_4)$ (51 mg, 0.16 mmol). After rapid color change from light orange to dark blue the solution was allowed to concentrate via evaporation at room temperature over 3-5

days to afford 76 mg (64%) of dark blue crystals. ^{1}H NMR (500 MHz, Chloroform-*d*) δ 8.22 (d, *J* = 8.4 Hz, 4H), 7.77 (d, *J* = 8.4 Hz, 4H), 4.36 (q, *J* = 7.2 Hz, 4H), 4.12 (q, *J* = 7.2 Hz, 4H), 1.56 – 1.44 (m, 12H). ^{13}C NMR (126 MHz, $CDCl_3$) δ 186.31, 152.74, 136.54(q, $J_{C\text{-}F}$ = 34 Hz), 127.85 (q, $J_{C\text{-}F}$ = 4 Hz), 126.58 (q, $J_{C\text{-}F}$ = 274 Hz), 122.24, 51.55, 49.52, 15.07, 10.82. FTIR (ATR, cm^{-1}); 2984, 1532,1436, 1317, 1122, 1061. Elem Anal. for $C_{22}H_{28}CuBF_{10}N_6S_2$ Calcd: C, 39.54; H, 3.87; N, 11.53; Found: C, 40.32.; H, 3.65; N, 12.45. MP: 163°C. **CCDC 2215322**

[(*p*-methoxyphenyl-ATF)$_2$Cu](PF$_6$) (24): To *N*,*N*-diethyl-2-(4-methoxyphenyl) azothioformamide (157 mg, 0.62 mmol) dissolved in 5 mL of acetonitrile was added $[(CH_3CN)_4Cu](PF_6)$ (110 mg, 0.31 mmol). After rapid color change from light orange to dark green the solution was allowed to concentrate via evaporation at room temperature over 3-5 days to afford 115 mg (52%) of dark green crystals. ^{1}H NMR (300 MHz, Chloroform-*d*) δ 8.08 (d, *J* = 8.9 Hz, 4H), 6.96 (d, *J* = 9.1 Hz, 4H), 4.24 (q, *J* = 7.1 Hz, 4H), 4.08 (q, *J* = 7.1 Hz, 4H), 3.86 (s, 6H), 1.50 – 1.41 (m, 12H). ^{13}C NMR (75 MHz, $CDCl_3$) δ 187.76, 167.92, 146.01, 130.45, 116.87, 57.30, 51.48, 49.36, 15.71, 11.78. FTIR (ATR, cm^{-1}); 2986, 1593, 1437, 1262, 1142. Elem Anal. for $C_{24}H_{34}CuPF_6O_2N_6S_2$ Calcd: C, 40.53; H, 4.82; N, 11.82; Found: C, 41.02; H, 7.87; N, 11.85. MP: 168°C.

[(*p*-tolyl-ATF)$_2$Cu](PF$_6$) (25): To *N*,*N*-diethyl-2-(*p*-tolyl)azothioformamide (372 mg, 1.58 mmol) dissolved in 15 mL of acetonitrile was added $[(CH_3CN)_4](PF_6)$ (294 mg, 0.79 mmol). After rapid color change from light orange to dark blue the solution was allowed to concentrate via evaporation at room temperature over 3-5 days to afford 832 mg (74%) of dark blue crystals. ^{1}H NMR (300 MHz, Chloroform-*d*) δ 7.94 (d, *J* = 7.8 Hz, 4H), 7.27 (d, *J* = 7.7 Hz, 4H), 4.28 (q, *J* = 7.1 Hz, 4H), 4.10 (q, *J* = 7.1 Hz, 4H), 2.36 (s, 6H), 1.52 – 1.43 (m, 12H). ^{13}C NMR (75 MHz, $CDCl_3$) δ 187.52, 149.81, 149.67, 132.06, 127.35, 51.77, 49.67, 22.90, 15.80,

11.64. FTIR (ATR, cm^{-1}): 2981, 1523,1429, 1087, 722. Elem Anal. for $C_{24}H_{34}CuPF_6N_6S_2$ Calcd: C, 42.44; H, 5.05; N, 12.37; Found: C, 42.29; H, 5.70; N, 12.26. MP: 166°C.

[(*p*-fluorophenyl-ATF)$_2$Cu](PF$_6$) (26): To *N*,*N*-diethyl-2-(4-fluorophenyl)azothioformamide (373 mg, 1.58 mmol) dissolved in 15 mL of acetonitrile was added $[(CH_3CN)_4](PF_6)$ (294 mg, 0.79 mmol). After rapid color change from light orange to dark blue the solution was allowed to concentrate via evaporation at room temperature over 3-5 days to afford 782 mg (72%) of dark blue crystals.^{1}H NMR (300 MHz, Chloroform-*d*) δ 8.22 (d, *J* = 8.3 Hz, 4H), 7.77 (d, *J* = 8.1 Hz, 4H), 4.43 – 4.31 (m, 4H), 4.18 – 4.06 (m, 4H), 1.56 – 1.47 (m, 12H). ^{13}C NMR (75 MHz, $CDCl_3$) δ 180.63, 167.85 (d, $J_{C\text{-}F}$ =260 Hz),150.54, 131.17(d, $J_{C\text{-}F}$ =11 Hz), 117.72 (d, $J_{C\text{-}F}$ =23 Hz), 51.92, 49.89, 15.77, 11.60. FTIR (ATR, cm^{-1}): 2987, 1494, 1436, 1233, 1141, 1074, 708. Elem Anal. for $C_{22}H_{28}CuPF_8N_6S_2$ Calcd: C, 38.45; H, 4.11; N, 12.23; Found: C, 38.38; H, 3.93; N, 11.45. MP: 174°C.

[(*p*-trifluoromethylphenyl-ATF)$_2$Cu](PF$_6$) (27): To *N*,*N*-diethyl-2-(4-(trifluoromethyl) phenyl)azothioformamide (450 mg, 1.58 mmol) dissolved in 15 mL of acetonitrile was added $[(CH_3CN)_4Cu](PF_6)$ (294 mg, 0.79 mmol). After rapid color change from light orange to dark blue the solution was allowed to concentrate via evaporation at room temperature over 3-5 days to afford 721 mg (58%) of dark blue crystals. ^{1}H NMR (300 MHz, Chloroform-*d*) δ 8.22 (d, *J* = 8.4 Hz, 4H), 7.77 (d, *J* = 8.4 Hz, 4H), 4.36 (q, *J* = 7.2 Hz, 4H), 4.12 (q, *J* = 7.2 Hz, 4H), 1.56 – 1.47 (m, 12H). ^{13}C NMR (75 MHz, $CDCl_3$) δ 194.24, 154.42, 134.75 (q, $J_{C\text{-}F}$ = 33 Hz), 127.46 (q, $J_{C\text{-}F}$ = 4 Hz), 126.28 (q, $J_{C\text{-}F}$ = 271Hz), 124.49, 48.62, 46.04, 14.51, 12.21. FTIR (ATR, cm^{-1}); 2984, 1592,1434, 1316, 1127, 1063. Elem Anal. for $C_{22}H_{28}CuPF_{12}N_6S_2$ Calcd: C, 36.62; H, 3.59; N, 10.68; Found: C, 37.41; H, 3.89; N, 11.02. MP:173°C.

General procedure for the synthesis of propiolic acids

(μ-I)[Cu(*p*-methoxyphenyl-ATF)I)]$_2$ complex (12) (35 mg, 0.04 mmol) and cesium carbonate (977 mg, 3.0 mmol) were added to a flame-dried and carbon dioxide flushed round-bottom flask equipped with a magnetic stirrer. Under carbon dioxide atmosphere, terminal alkyne (1 mmol) and anhydrous DMSO (5 mL) were added to the flask. Carbon dioxide in the form of balloon was introduced at ambient pressure and the mixture was stirred at 40 ˚C for 24 hrs. After such time the reaction mixture was cooled to room temperature, quenched with water, and filtered. The filtrate was then acidified with aqueous 6M HCl (20 mL) and extracted with diethyl ether (4 x 10 mL). The combined organic layers were washed with brine and then dried with anhydrous Na_2SO_4. The solvent was removed under reduced pressure to yield target propiolic acid product. Characterization data for compounds 28-47 can be found in the ESI.

General procedure for the synthesis of ester *n*-Butyl 3-phenylpropiolate

(μ-I)[Cu(*p*-methoxyphenyl-ATF)I)]$_2$ complex (12) (70 mg, 0.08 mmol) and cesium carbonate (1.95 g, 6.0 mmol) were added to a flame dried, carbon dioxide flushed round-bottom flask equipped with a magnetic stirrer. Under carbon dioxide atmosphere, phenylacetylene (204 mg, 2.0 mmol) and anhydrous DMSO (10 mL) were added. Carbon dioxide in the form of balloon was introduced at ambient pressure and the mixture was stirred at 40 ˚C for 21 h and then cooled to room temperature. *n*-Iodobutane was added dropwise, and the reaction was returned to 40˚C for 3 h. After such time the reaction mixture was cooled to room temperature where saturated brine (30 mL) was added along with aqueous HCl (1M, 12 ml). The acidified mixture was extracted with DCM (3 x 10 mL), dried with Na_2SO_4 and concentrated. Purification by column chromatography using 20:1 hexane and ethyl acetate

afforded 335 mg of the ester as a colorless oil (83% yield). ^{1}H NMR (300 MHz, Chloroform-*d*) δ 7.55 (d, *J* = 6.7 Hz, 2H), 7.45 – 7.38 (m, 1H), 7.37 – 7.30 (m, 2H), 4.22 (t, *J* = 6.7 Hz, 2H), 1.72 – 1.63 (m, 2H), 1.47 – 1.37 (m, 2H), 0.94 (t, *J* = 7.3 Hz, 3H). ^{13}C NMR (75 MHz, $CDCl_3$) δ 154.94, 133.75, 131.41, 129.40, 120.55, 86.79, 81.65, 66.68, 31.34, 19.89, 14.44. This data matched that of known *n*-butyl 3-phenylpropiolate.[13]

Procedure for homodiyne coupling

1,4-Diphenyl buta-1,3-diyne (7): (μ-I)[*p*-methoxyphenyl-ATF-CuI]$_2$ complex 12 (14 mg, 0.016 mmol) and cesium carbonate (390 mg, 1.2.0 mmol) were added to aflame-dried round-bottom flask equipped with a magnetic stirrer. 3-phenylpropiolic acid (58 mg, 0.4 mmol) and anhydrous DMSO (5 mL) were added sequentially into the flask. The reaction mixture was stirred at 40˚C for 24 hours. After 24 hours, the reaction mixture was cooled to room temperature and extracted with ethyl acetate (2 x 10 mL) and the product was purified by column chromatography using hexanes to afford 25 mg of pure compound (62% yield). ^{1}H NMR (300 MHz, Chloroform-*d*) δ 7.57 – 7.52 (m, 4H), 7.39 – 7.32 (m, 6H). ^{13}C NMR (75 MHz, $CDCl_3$) δ 133.39, 130.08, 129.33, 122.72, 82.45, 74.84. Matching that of previously reported.[27]

Computational methods

Calculations were performed with the Gaussian16 software package.[26]The B3LYP functional was used in conjunction with the 6-31G(d,p) (H, C, N, O, and S) and SDD (Cu, with ECP) basis sets using ultrafine integration grids.[27] The CPCM solvation model was used to calculate thermodynamic parameters in DMSO.[28] Frequency calculations were performed on

all minimized structures to confirm the absence of imaginary frequencies and evaluate thermodynamics.

6.5 References

1. Nielsen, K. T.; Harris, P.; Bechgaard, K.; Krebs, F. C., Structural study of four complexes of the M-N2S2 type derived from diethylphenylazothioformamide and the metals palladium, platinum, copper and nickel. *Acta Crystallogr B* **2007,** *63* (Pt 1), 151-6.
2. Bechgaard, K., Nonplanar Electron-Transfer Complexes .1. Chemistry of 5 Ni-N2s2z Complexes Derived from Nickel-Bis-N,N-Diethylphenylazothioformamide. *Acta Chem Scand A* **1974,** *A 28* (2), 185-193.
3. Bechgaard, K., Nonplanar Electron-Transfer Complexes .2. Chemistry of 4 Cu-N2s2z Complexes Derived from Copper-Bis-N,N-Diethylphenylazothioformamide. *Acta Chem Scand A* **1977,** *31* (8), 683-688.
4. Nielsen, K. T.; Bechgaard, K.; Krebs, F. C., Effective removal and quantitative analysis of Pd, Cu, Ni, and Pt catalysts from small-molecule products. *Synthesis-Stuttgart* **2006,** (10), 1639-1644.
5. Nielsen, K. T.; Bechgaard, K.; Krebs, F. C., Removal of palladium nanoparticles from polymer materials. *Macromolecules* **2005,** *38* (3), 658-659.
6. Johnson, N. A.; Wolfe, S. R.; Kabir, H.; Andrade, G. A.; Yap, G. P. A.; Heiden, Z. M.; Moberly, J. G.; Roll, M. F.; Waynant, K. V., Deconvoluting the Innocent vs. Non-Innocent Behavior of N,N-Diethylphenylazothioformamide Ligands with Copper Sources. *Eur J Inorg Chem* **2017,** (47), 5576-5581.
7. Pradhan, R.; Groner, V. M.; Gutman, K. L.; Heiden, Z. M.; Roll, M. F.; Moberly, J. G.; Waynant, K. V., Substitution effects on the binding interactions of redox-active arylazothioformamide ligands and copper(I) salts. *Supramol Chem* **2020,** *32* (8), 466-478.
8. Pradhan, R.; Groner, V. M.; Johnson, N. A.; Zhang, Q.; Roll, M. F.; Moberly, J. G.; Waynant, K. V., Synthesis of an N, N-diethyl-tert-butylazothioformamide ligand and coordination studies with Copper(I) salts. *Inorg Chem Commun* **2021,** *124*.
9. Goußen, L. J.; Rodríguez, N.; Manjolinho, F.; Lange, P. P., Synthesis of Propiolic Acids via Copper-Catalyzed Insertion of Carbon Dioxide into the C-H Bond of Terminal Alkynes. *Advanced Synthesis & Catalysis* **2010,** *352* (17), 2913-2917.
10. Li, H.-R.; He, L.-N., Construction of C–Cu Bond: A Useful Strategy in CO_2 Conversion. *Organometallics* **2020,** *39* (9), 1461-1475.

11. Fukue, Y.; Oi, S.; Inoue, Y., Direct Synthesis of Alkyl 2-Alkynoates from Alk-1-ynes, CO_2, and Bromoalkanes Catalyzed by Copper(I) or Silver(I) Salt. *J Chem Soc Chem Comm* **1994,** (18), 2091-2091.
12. Zhang, W.-Z.; Li, W.-J.; Zhang, X.; Zhou, H.; Lu, X.-B., Cu(I)-Catalyzed Carboxylative Coupling of Terminal Alkynes, Allylic Chlorides, and CO_2. *Org Lett* **2010,** *12* (21), 4748-4751.
13. Inamoto, K.; Asano, N.; Kobayashi, K.; Yonemoto, M.; Kondo, Y., A copper-based catalytic system for carboxylation of terminal alkynes: synthesis of alkyl 2-alkynoates. *Org Biomol Chem* **2012,** *10* (8), 1514-1516.
14. Yu, D.; Zhang, Y., Copper- and copper–*N*-heterocyclic carbene-catalyzed C─H activating carboxylation of terminal alkynes with CO_2 at ambient conditions. *Proceedings of the National Academy of Sciences* **2010,** *107* (47), 20184-20189.
15. Yang, L.; Yuan, Y.; Wang, H.; Zhang, N.; Hong, S., Theoretical insights into copper(I)–NHC-catalyzed C–H carboxylation of terminal alkynes with CO_2: the reaction mechanisms and the roles of NHC. *RSC Advances* **2014,** *4* (61), 32457-32466.
16. Liu, C.; Luo, Y.; Zhang, W.; Qu, J.; Lu, X., DFT Studies on the Silver-Catalyzed Carboxylation of Terminal Alkynes with CO_2: An Insight into the Catalytically Active Species. *Organometallics* **2014,** *33* (12), 2984-2989.
17. Goußen, L. J.; Linder, C.; Rodríguez, N.; Lange, P. P.; Fromm, A., Silver-catalysed protodecarboxylation of carboxylic acids. *Chem Commun* **2009,** (46), 7173-7175.
18. Su, L. B.; Dong, J. Y.; Liu, L.; Sun, M. L.; Qiu, R. H.; Zhou, Y. B.; Yin, S. F., Copper Catalysis for Selective Heterocoupling of Terminal Alkynes. *J Am Chem Soc* **2016,** *138* (38), 12348-12351.
19. Jover, J.; Spuhler, P.; Zhao, L. G.; McArdle, C.; Maseras, F., Toward a mechanistic understanding of oxidative homocoupling: the Glaser-Hay reaction. *Catal Sci Technol* **2014,** *4* (12), 4200-4209.
20. Pradhan, R.; Groner, V. M.; Gutman, K. L.; Larson, G. E.; Kan, Y. W.; Zhang, Q.; Heiden, Z. M.; Roll, M. F.; Moberly, J. G.; Waynant, K. V., Evaluating Coordinative Binding Mechanisms through Experimental and Computational Studies of Methoxy-Substituted Arylazothioformamide Copper(I) Complexes. *Eur J Inorg Chem* **2022,** *2022* (33).

21. Yu, D. Y.; Zhou, F.; Lim, D. S. W.; Su, H. B.; Zhang, Y. G., NHC-Ag/Pd-Catalyzed Reductive Carboxylation of Terminal Alkynes with CO2 and H-2: A Combined Experimental and Computational Study for Fine-Tuned Selectivity. *Chemsuschem* **2017,** *10* (5), 836-841.
22. Hu, L. F.; Gao, H.; Hu, Y. L.; Lv, X. Y.; Wu, Y. B.; Lu, G., Origins of regio- and stereoselectivity in Cu-catalyzed alkyne difunctionalization with CO2 and organoboranes. *Org Chem Front* **2022,** *9* (4), 1033-1039.
23. Dijkstra, G.; Kruizinga, W. H.; Kellogg, R. M., An Assessment of the Causes of the Cesium Effect. *J Org Chem* **1987,** *52* (19), 4230-4234.
24. Liu, D.-X.; Li, F.-L.; Li, H.-X.; Gong, W.-J.; Gao, J.; Lang, J.-P., Efficient and Reusable CuI/1,10-Phenanthroline-Catalyzed Oxidative Decarboxylative Homocoupling of Arylpropiolic Acids in Aqueous DMF. *Eur J Org Chem* **2014,** *2014* (22), 4817-4822.
25. Frisch, M. J.; Trucks, G. W.; Schlegel, H. B.; Scuseria, G. E.; Robb, M. A.; Cheeseman, J. R.; Scalmani, G.; Barone, V.; Petersson, G. A.; Nakatsuji, H.; Li, X.; Caricato, M.; Marenich, A. V.; Bloino, J.; Janesko, B. G.; Gomperts, R.; Mennucci, B.; Hratchian, H. P.; Ortiz, J. V.; Izmaylov, A. F.; Sonnenberg, J. L.; Williams; Ding, F.; Lipparini, F.; Egidi, F.; Goings, J.; Peng, B.; Petrone, A.; Henderson, T.; Ranasinghe, D.; Zakrzewski, V. G.; Gao, J.; Rega, N.; Zheng, G.; Liang, W.; Hada, M.; Ehara, M.; Toyota, K.; Fukuda, R.; Hasegawa, J.; Ishida, M.; Nakajima, T.; Honda, Y.; Kitao, O.; Nakai, H.; Vreven, T.; Throssell, K.; Montgomery Jr., J. A.; Peralta, J. E.; Ogliaro, F.; Bearpark, M. J.; Heyd, J. J.; Brothers, E. N.; Kudin, K. N.; Staroverov, V. N.; Keith, T. A.; Kobayashi, R.; Normand, J.; Raghavachari, K.; Rendell, A. P.; Burant, J. C.; Iyengar, S. S.; Tomasi, J.; Cossi, M.; Millam, J. M.; Klene, M.; Adamo, C.; Cammi, R.; Ochterski, J. W.; Martin, R. L.; Morokuma, K.; Farkas, O.; Foresman, J. B.; Fox, D. J. *Gaussian 16 Rev. B.01*, Wallingford, CT, 2016.
26. Zhao, Y.; Truhlar, D. G., A new local density functional for main-group thermochemistry, transition metal bonding, thermochemical kinetics, and noncovalent interactions. *J Chem Phys* **2006,** *125* (19), 194101.
27. Mennucci, B.; Tomasi, J.; Cammi, R.; Cheeseman, J. R.; Frisch, M. J.; Devlin, F. J.; Gabriel, S.; Stephens, P. J., Polarizable continuum model (PCM) calculations of solvent effects on optical rotations of chiral molecules. *J Phys Chem A* **2002,** *106* (25), 6102-6113.

Chapter 7: Conclusions and Future Directions

This dissertation encompasses a comprehensive investigation into the fine tuning, versatile properties, and potential applications of azothioformamide (ATF) ligands and their metal salts in various areas of coordination chemistry, biological activity, catalysis, and the potential for enabling selective precious metal recovery processes.

The study began with an in-depth exploration of the impact of substituents on the binding affinity of ATF ligands. Through comprehensive UV-Vis binding association studies, computational analysis and crystallography, it was observed that the presence of electron-donating groups (*para*-EDGs) leads to stronger binding affinities, while *para*-electron-withdrawing groups (*para*-EWGs) result in weaker binding or potentially induce an oxidation event of the transition metal.

The study further delved into coordination of ATF ligands with metals salts, particularly cu(I) salts. It was revealed that the binding association values for these complexes exhibit lower errors when fit into various 2:1 non-linear binding model (including Full, Additive, Non-Cooperative, and Statistical), as opposed to the 1:1 non-linear binding model, which yielded higher errors. To understand the underlying mechanism, different coordination complexes were formed by reacting Cu(I) salts with a series of synthesized monosubstituted electron-donating ATF ligands. By scrutinizing crystal structures, conducting UV-Vis binding studies, and employing computational evaluations of potential mechanisms, unique 2:1 binding behavior was elucidated, and different pathways were proposed. This fundamental understanding helps on rationale design of ATF ligands and complexes for use in catalysis and biological exploration and beyond.

Further study then explored the applications of this novel ATF ligands class and its complexes in biological research and catalysis. A diverse library of ATF ligands along with their copper and silver complexes were synthesized to investigate the biological activity. It was found that non-complexed ATF compounds had limited activity, while ATF-metal coordination complexes exhibit varying effects against microbes. Furthermore, the feasibility of Copper(I)-ATF complexes as a catalyst for the insertion of CO_2 into C-H alkyne bonds was also studied and it was found out that Cu(I) complexes, both 2:1 and 2:2 dimers with ATF ligand having electron donating group gave high yield.

In conclusion, this dessertion has provided an in-depth and comprehensive exploration of ATF ligands, their versatile properties and their potential applications in coordination chemistry, biological research, and catalysis. These diverse avenues explored shed light on promising potential of ATF ligands.

7.1 Future Directions

The central objective of this research was to create a sustainable process in which we can utilize a synthesized ligand to dissolve a zerovalent metal (or metal salt) into a specific coordination complex. These complexes, in turn, serve as a catalyst for the transformation we desire and then following that transformation, to be able to remove that ligand from the metal and recover both for later use. So far, our research has moved from 1) Tuning binding affinity of ATF ligands; 2) investigations of binding, binding mechanisms and 3) catalytic and biological potential of these systems. As we move forward, our research trajectory continues to evolve. Future directions include:

7.1.1 Exploring modification on the Amide side of ATF ligand system

After the promising results of tuning binding affinity of ATF ligands, through modification on aryl ring of ATF ligands system, research will shift towards exploring modifications on amide side with different heterocyclic secondary amines (as in Fig 7.1). This work may involve updating the existing one pot procedure to two-step process, where xanthate esters intermediate is first isolated before refluxing it with an amine.[1] This precise method offers means to finely tune the secondary amine component in ATF ligand system. This shift in focus aims to further elevate the binding affinity of ATF ligands, potentially unlocking even greater potential for their applications.

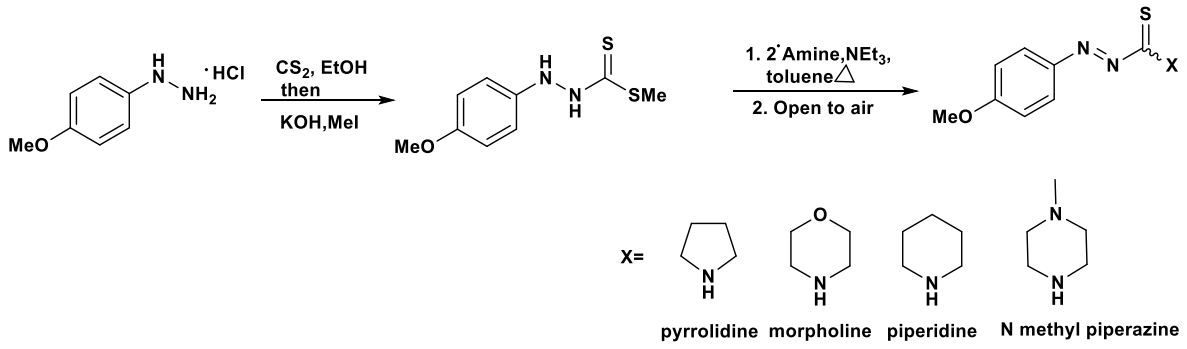

Figure 7.1: Synthesis of ATFs with different amide substituents.

7.1.2 Identifying key structural characteristics within the ATF ligand system that govern dissolution of metals

ATF ligands have demonstrated their ability to dissolve and coordinate a broad spectrum of transition metals.[2,3] However, beyond these established capabilities, an unexplored avenue of research lies in identifying the essential characteristics within the chemical structure of ATF ligands that govern the dissolution of metals. It involves deciphering the specific structural features, functional groups, or ligand motifs within ATF molecule that serve as a key

driver in the dissolution of wide range of metals. To achieve this the synthesis of diverse ligands using established procedure should be conducted with structural variations to the ATF ligand system as in (fig 7.2).[4-7] This expansion also represents a substantial broadening of our research scope. The structural variants include: Arylazothioformamide (AAF) where thioamide group in ATF ligands is replaced by amide moiety. The substitution of sulfur with oxygen in the ligand structure can significantly impact its reactivity and dissolution properties. Arylcarbothiamide (ACT) represents ATF variant with primary amide group. Aryldiazenylthione (ADT), in this modification, the thioamide component is removed, but N=N-C=S structure is retained. This unique feature preserves the 1,3 heterodiene backbone with sulfur and nitrogen ligating site. Investigating ADT allows us to discern the significance of this specific structural motif. Pyridinylcarbothioamide (PCT) represents a variant where the azo group is removed, but the conjugated 1,3 heterodiene feature is retained, incorporating soft sulfur and hard nitrogen ligating sites. This structural alteration validates the role of the azo group in ATF ligand. This expansion of our research will unveil the intricate relationships between ligand structure and metal dissolution.

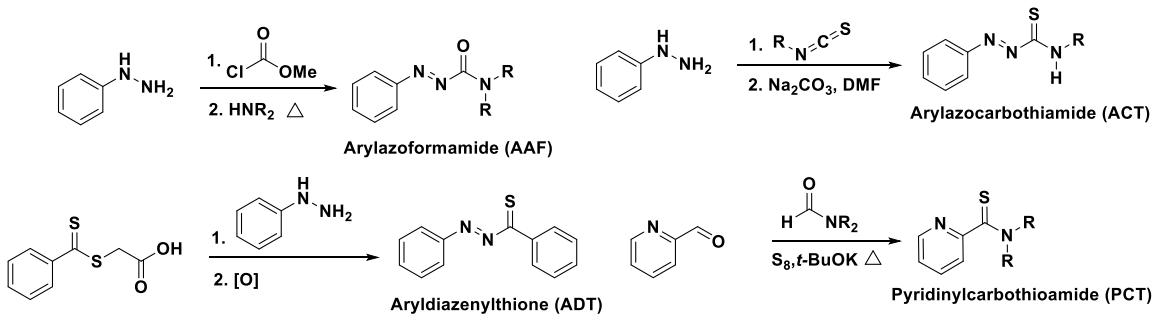

Figure 7.2: Synthesis scheme for AAF, ACT, ADT, and PCT.

7.1.2 Further explore catalysis using ATF-Copper(I) in context of Click chemistry

Moreover, considering the remarkable catalytic potential of ATF-Cu(I) complexes in facilitating the transformation of terminal alkyne to propiolic acid through the insertion of carbon dioxide,[8] there is an exciting opportunity for further exploration of their catalytic activity in context of the copper catalyzed azide alkyne cyclo addition, commonly known as click reaction (as in fig 7.3). The click reaction has been highly valuable and widely used chemical transformation in synthesis of different drug, material science and bioconjugation.[9,10]

Following work will first focus on exploring the potential of ATF-Cu(I) complexes as a catalyst for click reaction. This will include experimentation with different reaction conditions to identify the optimal parameters for achieving excellent yields. Additionally, there is a need to investigate the compatibility of these conditions with a variety of substrates, probing where the catalytic system exhibits tolerance to different functional groups. Alongside experimental work, there is a need to mechanistically study the aspect of the click reactions. This will help understand the underlying mechanism and pathways for the product formation.

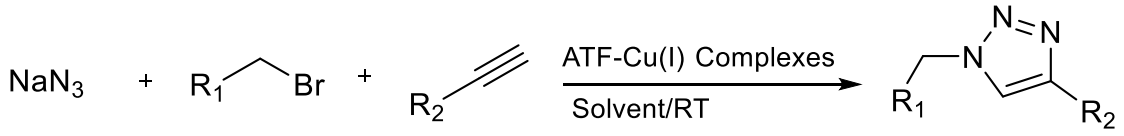

Figure 7.3: Synthesis scheme for Triazole through click reaction.

One of the persistent challenges in metal-catalyzed reactions, including click reaction is the presence of residual amount of the catalyst or metal in the final product.[11,12] This is undesirable, especially in applications such as pharmaceuticals and material science. The next future directions would be to try to mitigate this problem by using ATF ligands. The hypothesis driving this investigation is the unique property of ATF ligands i.e. Its ability to effectively

dissolve solid metals. Therefore, it's reasonable to postulate that the use of ATF ligand in click reaction, would lead to the reduction of amount of residual copper in the final product. Hence, the amount of residual copper in the final product generated by two methods: the standard click reaction conditions and the click reaction conditions using extra ATF ligands will be compared. This comparison analysis can be conducted through a precise analytical technique called Inductively Coupled Plasma Mass Spectrometry which allows for the accurate identification of copper traces in the sample.

7.2 References

1. Pradhan, R.; Tiwari, L.; Groner, V.M.; Leach, C.; Lusk, K.; Harrison,N. S.; Cornell, K.A.; Waynant, K.V., Evaluation of azothioformamides and their copper(I) and silver(I) complexes for biological activity. *Journal of Inorganic Biochemistry* **2023**, 246, 112294.

2. Nielsen, K. T.; Bechgaard, K.; Krebs, F. C., Effective removal and quantitative analysis of Pd, Cu, Ni, and Pt catalysts from small-molecule products. *Synthesis-Stuttgart* **2006**, (10), 1639-1644.

3. Nielsen, K. T.; Bechgaard, K.; Krebs, F. C., Removal of palladium nanoparticles from polymer materials. *Macromolecules* **2005**, 38 (3), 658-659.

4. Zhu, B.; Yang, T.; Gu, Y.; Zhu, S.; Zhua G.; Chang J., Enantioselective organocatalytic amination of 2-perfluoroalkyl-oxazol-5(2H)-ones towards the synthesis of chiral N, O-aminals with perfluoroalkyl and amino groups. *Org. Chem. Front.* **2021**,8, 4160-4165.

5. Pasyukov, D.V.; Chernenko, A.Y.; Lavrentev, I.V.; Baydikova, V.A.; Minyaev, M. E.; Starovoytova, O. A., Chernyshev, V. M, Dimroth rearrangement “thiadiazole-triazole”: synthesis and exploration of 3-sulfanyl-1,2,4-triazolium salts as NHC-proligands. *Russ Chem Bull* **2022**,71, 993–1008.

6. Ahmad, A.H.; Jalal, Z.A.; Salim, S.S.; Firas, A.F.; Abadleh M. Mohammed, A.M.; Qasem, A.M.; Mustafa, E.M., Thiophene Ring-opening Reactions III: One-Pot Synthesis and Antitumor Activity of 1,3,4-Thiadiazoline–Benzothiazolo[3,2-*b*] pyridazine Hybrids. *Current Organic Synthesis* **2022**, 19,2.

7. Peng, L.; Ma, L.; Ran, Y.; Chen, Y.; Zeng, Z., Metal-free three-component synthesis of thioamides from β-nitrostyrenes, amines and elemental sulfur. *Tetrahedron Lett* **2021**, *74, 153092.*

8. Pradhan, R.; Gutman, K. L.; Mas Ud, A.; Hulley, E. B.; Waynant, K. V., Catalytic Carboxylation of Terminal Alkynes with Copper(I) Azothioformamide Complexes. *Organometallics* **2023**, *42* (5), 362-371.

9. Moses, J.E., and Moorhouse, A.D.,The growing applications of click chemistry. *Chem. Soc. Rev.* **2007**, 36, 1249–1262.

10. New, K.; Brechbiel, M.W., Growing applications of "click chemistry" for bioconjugation in contemporary biomedical research. *Cancer Biother Radiopharm*. **2009**, 24,3, 289-302.
11. Reginato, G.; Sadler, P.; Wilkes, R. D., Scaling up Metal Scavenging Operations for Pharmaceutical Pilot Plant Manufactures. *Org. Process Res. Dev.* **2011**, *15* (6), 1396– 1405.
12. Neumann, S.; Biewend, M.; Rana, S.; Binder, W.H., The CuAAC: Principles, Homogeneous and Heterogeneous Catalysts, and Novel Developments and Applications. *Macromol. Rapid Commun*.**2020**, 41, 1900359.

Appendix I

Supporting Information for Chapter 2: Substitution effects and binding interactions of redox-active arylazothioformamide ligands and copper(I) salts.

General Methods

1H and 13C NMR experiments were performed on either a Bruker 300 or Bruker AVANCE 500 MHz instrument and samples were obtained in $CDCl_3$ (referenced to 7.28 ppm for 1H and 77.16 ppm for 13C). Coupling constants (*J*) are in Hz. The multiplicities of the signals are described using the following abbreviations: s=singlet, br s=broad singlet, d=doublet, t=triplet, dd=doublet of doublets, dq=doublet of quartets, dsep=doublet of septets; t=triplet of triplets, m=multiplet, app=apparent. Infrared spectra were obtained on a Thermo Scientific Nicolet 380 FT-IR spectrometer as thin films on ZnSe disks and peaks are reported in cm−1. Reaction progress was monitored by thin-layer chromatography on silica gel plates (60-F254), observed under UV light. Column chromatography was performed using silica gel (particle size 40–63 μm). Methyl iodide was purchased from EMD Millipore, 4-methoxyphenylhydrazine hydrochloride, 4- trifluoromethylphenylhydrazine hydrochloride, 4-fluorphenylhydrazine, and 4- methylphenylhydrazine were purchased from AK Scientific, N,N-Diethylamine and CS2 were purchased from Alfa-Aesar and used without further purification. Cu(I) halides were purchased from both Acros and AK Scientific, (CH3CN)4Cu(I)BF4 was purchased from Sigma-Aldrich and used without further purification. A ThermoFisher Genesys UV-Vis spectrophotometer or a Thermo Scientific Evolution 220 UV-Vis spectrophotometer was utilized with quartz cuvettes for the titration experiments. HPLC grade Acetonitrile was purcahsed from Fisher Scientific.

Computational Details

All structures were fully optimized without symmetry constraints using the B3LYP functional as implemented in Gaussian 09 using the 6-31G** basis set for C, H, N, S, Br, B, F, and P and the Stuttgart basis set with effective core potentials for all metal and iodine atoms. To verify the validity of the chosen method, other DFT functionals were used: B3LYP-D3, B3P86, B3PW91, M11, and wB97XD, but B3LYP gave structural parameters that best matched the experimental structures. The ultrafine integration grid was employed in all calculations, which ensured the stability of the optimization procedure for the investigated molecules. Each stationary point was confirmed by a frequency calculation at the same level of theory to be a real local minimum on the potential energy surface. More accurate electronic energies were computed for the optimized geometries using the larger 6-311++G(d,p) basis set. All reported free energies are for tetrahydrofuran solution at the standard state (T = 298 K, P = 1 atm, 1 mol/L concentration of all species in THF) as modeled by a polarized continuum model. The energy values given in the manuscript correspond to solvent-corrected Gibbs free energies that are based on B3LYP/6-311++G(d,p) electronic energies and all corrections calculated at the B3LYP/6-31G(d) level.

Calculated Rotational Energies

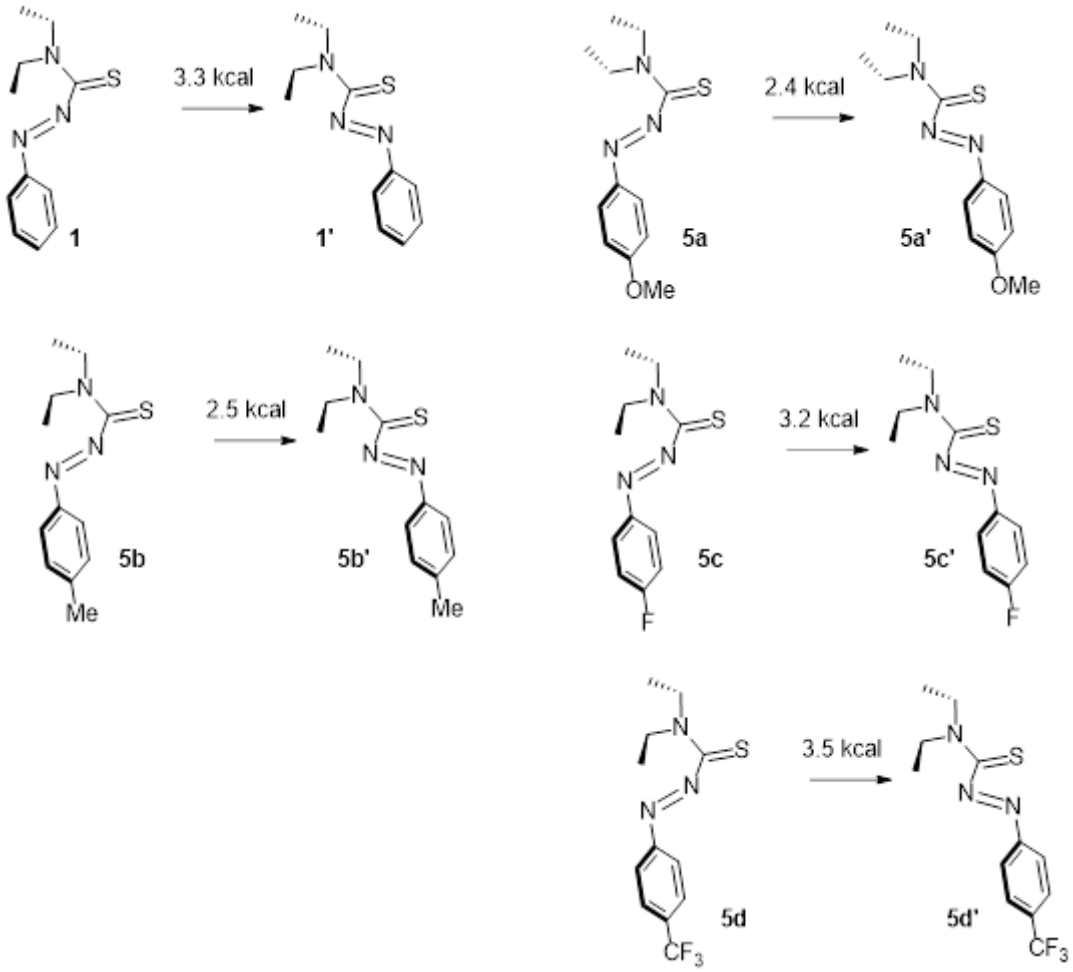

Figure A1.1: Rotational energies calculated for ligands 1, 5a-d at 6-311g++ basis level.

Table A1.1: Equilibrium Calculations of Rotational Energy from Modelling

Ligand	Energy (kcal/mol)	K_{eq}	Ratio to **1**
1	3.3	3.80E-03	1.00
5a	2.4	1.74E-02	4.57
5b	2.5	1.47E-02	3.86
5c	3.2	4.50E-03	1.18
5d	3.5	2.71E-03	0.71

Calculated Association Energies

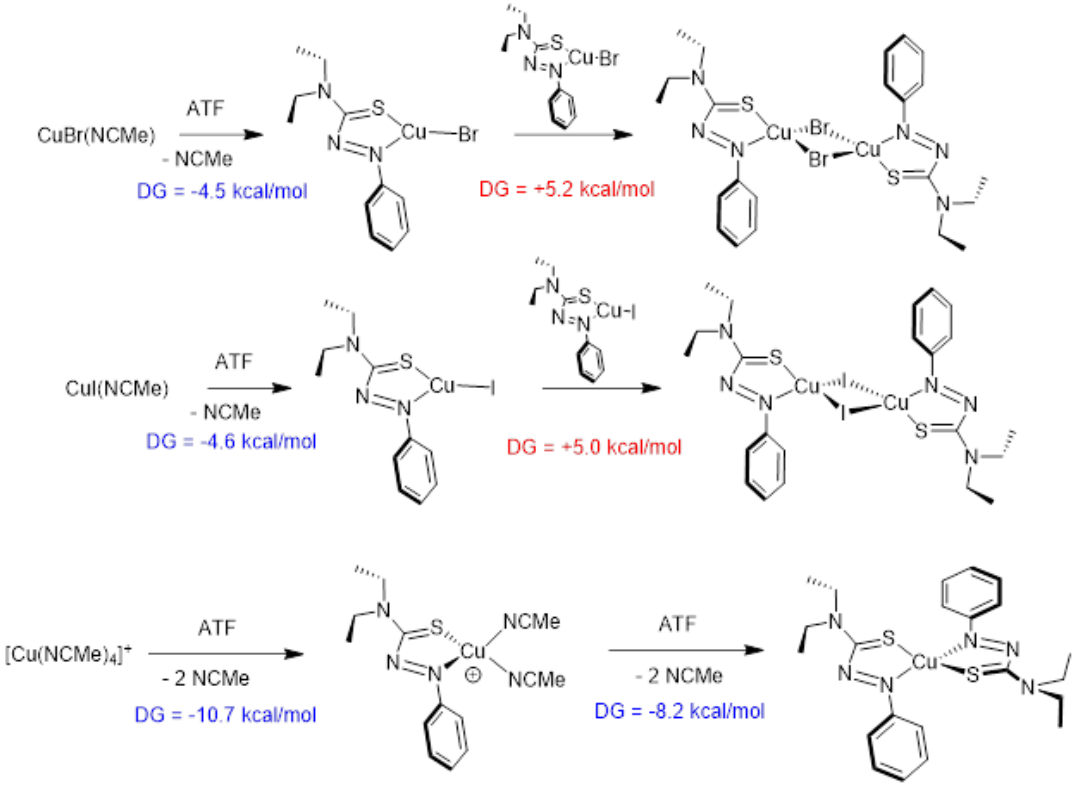

Figure A1.2: calculated energies of association for both 1:1 and 2:1 species. These species in ref. 7 crystallized to give dimers with the copper(I) halides.

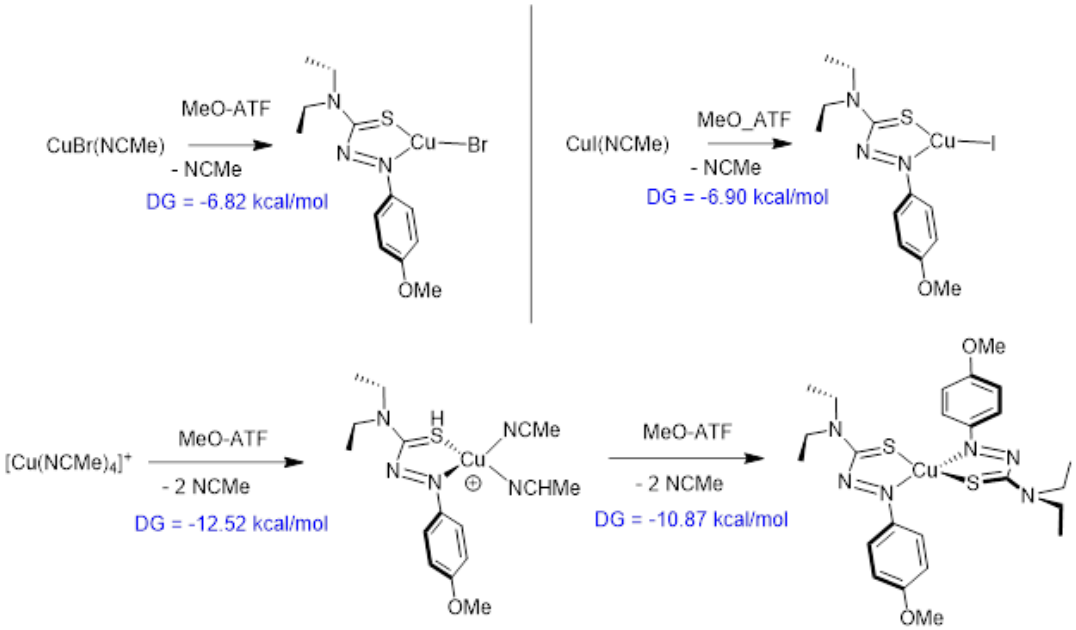

Figure A1.3: calculated association energies for ligand 5a with various copper(I) salts.

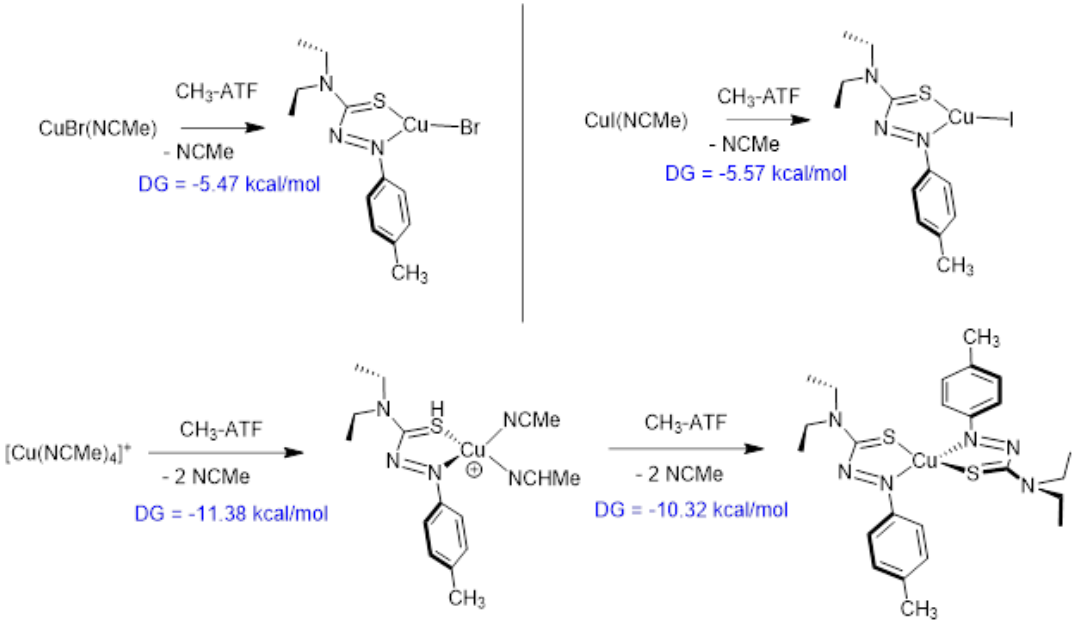

Figure A1.4: calculated association energies for ligand 5b with various copper(I) salts.

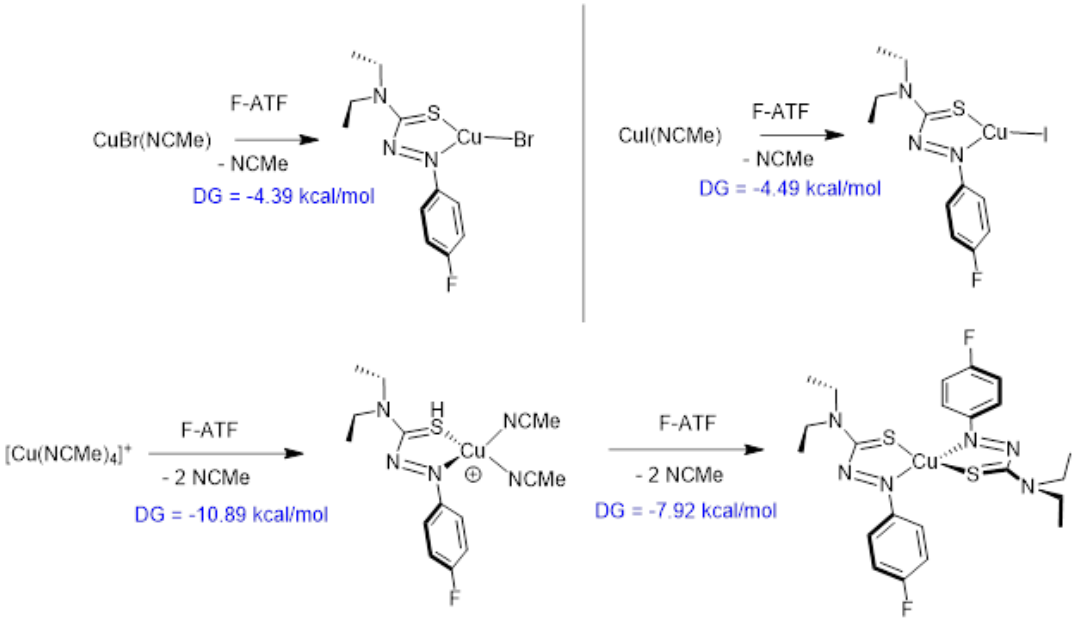

Figure A1.5: calculated association energies for ligand 5c with various copper(I) salts.

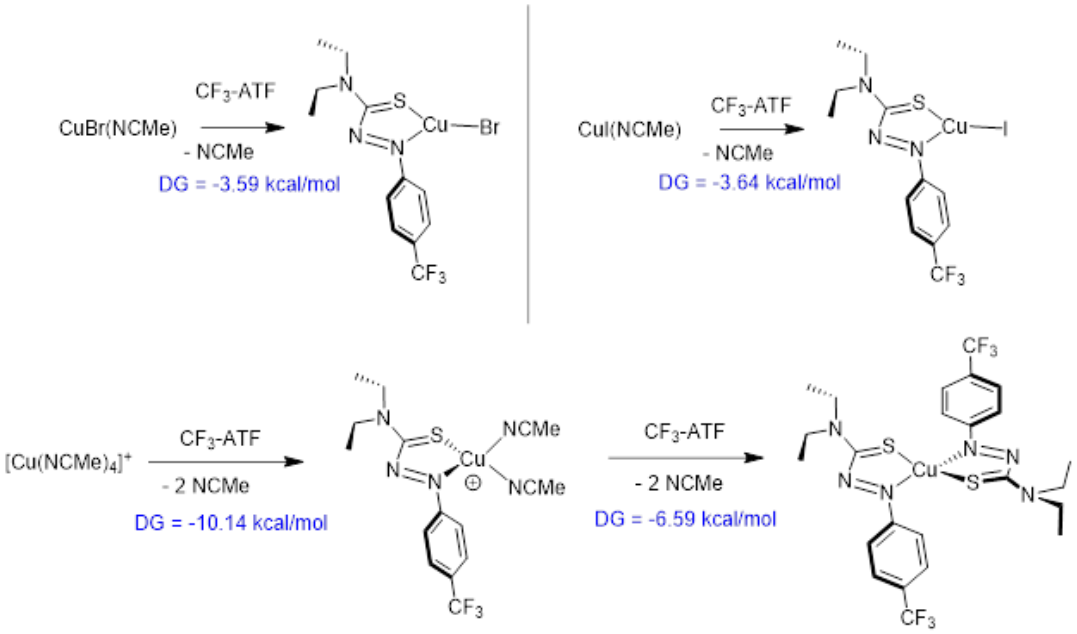

Figure A1.6: Calculated association energies for ligand 5d with various copper(I) salts.

Syntheses and Crystallization procedures

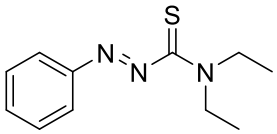

N,N-diethyl-2-phenyldiazothioformamide (1) : Ethanol (75 mL) was placed in a 200 mL 3-neck round bottom flask and degassed with nitrogen for 0.5 h. Phenylhydrazine (3.95 mL, 0.04 mol) was added followed by a dropwise addition of carbon disulphide (2.76 mL, 0.045 mol) and the solution was stirred for 0.5 h in which a precipitate formed. Potassium hydroxide (2.7 g, 0.048 mol) dissolved in degassed ethanol (25 mL) was then quickly poured into the mixture and the mixture immediately dissolved and turned light orange. This solution was stirred for 0.5 h-after which methyl iodide (2.8 mL, 0.045 mol) was added in one aliquot and the mixture that had turned cloudy turned from maroon to a light yellow. This solution was stirred for 1 h and then ethanol and carbon disulphide were removed via rotary evaporation. Diethylamine

(40 mL) was then added and the mixture was stirred at reflux overnight (thiosemicarbazone by NMR) before the reflux column and heat were removed. Oxygen in the form of air was then bubbled into the solution at room temperature for 2-4 hrs. After concentrating onto silica, column chromatography using 9:1 hexane: ethyl acetate yielded 6.0 grams of a dense red oil (68%). This oil was subjected to recrystallization using 20:1 heptane: ethyl acetate to receive orange needles. Physical data matched that of previous reports.[7]

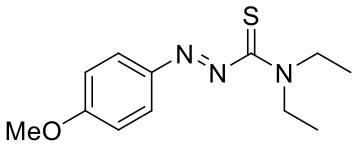

N,N-diethyl-2-(4-methoxyphenyl)diazothioformamide (5a) : 75 mL of ethanol was degassed under nitrogen flow in a flame-dried round bottom fitted with a magnetic stirrer for one hour. 4-methoxyphenylhydrazine•HCl (30.00 mmol, 5.821 g) was added and allowed to dissolve forming a dark purple solution. Carbon disulphide (34.2 mmol, 2.06 mL) was added dropwise and allowed to stir for 0.5 hour. Potassium hydroxide (2.36 g, 42.0 mmol) dissolved in degassed ethanol (25 mL) was then quickly poured into the mixture and stirred the solution was stirred for 0.5 h. Following, methyl iodide (33.60 mmol, 2.09 mL) was added in one aliquot. The solution was stirred for 1 h before concentrating with a rotary evaporator to produce an orange solid. The flask was then fitted with a reflux condenser and put under inert nitrogen flow. Diethylamine (40 mL) was added and the solution was refluxed for 48 h. The resulting dark red solution was then opened to the air, allowed to cool to RT, and continued to stir for 2 h. The solution was then washed with brine and extracted with ethyl acetate to afford a dark red oil. The resulting red liquid was concentrated via rotary evaporator and purified using flash column chromatography 7:3 hexane: ethyl acetate forming 4.693 g (62%) of orange

solid. The resulting solid was recrystallized with 7:3 hexane: ethyl acetate to form dark red crystal. ^{1}H NMR (300 MHz, Chloroform-d) δ 7.89 (d, J = 9.0 Hz, 2H), 6.99 (d, J = 9.0 Hz, 2H), 4.03 (q, J = 7.1 Hz, 2H), 3.90 (s, 3H), 3.55 (q, J = 7.2 Hz, 2H), 1.40 (t, J = 7.1 Hz, 3H), 1.18 (t, J = 7.2 Hz, 3H). ^{13}C NMR (125 MHz, $CDCl_3$) δ 195.0 164.3, 147.0, 126.7, 115.3, 56.5, 48.8, 45.9, 14.6, 12.3. FTIR(cm^{-1}): 2974,1579, 1419, 1259,1145, 775. Elemental Analysis: $C_{12}H_{17}N_3OS$ (251.35) (Calculated) C, 57.74; H, 6.756; N, 16.42 (Found) C, 57.34; H, 6.82; N, 16.72; mp: 93˚C.

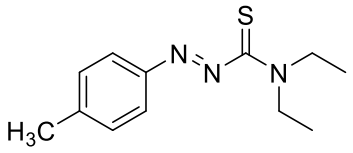

N,N-diethyl-2-(p-tolyl)diazothioformamide (5b**)**: 50 mL of ethanol and p-methylphenylhydrazine HCl (25.90 mmol , 4.11 g) were added to a flame-dried round-bottom flask and allowed to degas for 1.5 h under nitrogen flow. While under nitrogen, carbon disulphide (29.53 mmol, 2.25 ml) was added dropwise and the solution was allowed to stir under ambient conditions for an additional 0.5 h. Potassium hydroxide (32.37 mmol, 1.82 g) dissolved in degassed ethanol (20 mL) was then added into the mixture dropwise in a single aliquot and allowed to stir under nitrogen for 0.5 h resulting in the formation of a thick off-white liquid. Methyl iodide (29.01 mmol, 1.8 ml) was then added to the solution and stirred under nitrogen for 1 h. The resulting liquid was then concentrated with a rotary evaporator to afford a white paste. The flask was then equipped with a reflux condenser and put under nitrogen flow. Diethylamine (35 mL) was added and the mixture was refluxed under nitrogen for 48 h. The solution was cooled to ambient temperatures then exposed to air and allowed to stir for 2 h. The resulting red liquid was concentrated via rotary evaporator and purified using

flash column chromatography 4:1 hexane: ethyl acetate forming 4.32 g (77 %) of orange solid. The resulting solid was subjected to recrystallization from the slow evaporation of acetonitrile to afford diffracting crystals. ^{1}H NMR (300 MHz, Chloroform-d) δ 7.97 (d, J = 8.3 Hz, 2H), 7.79 (d, J = 8.4 Hz, 2H), 4.03 (q, J = 7.3 Hz, 2H), 3.50 (q, J = 7.2 Hz, 2H), 1.54 (s, 3H), 1.42 (t, J = 7.1 Hz, 3H), 1.20 (t, J =7.2 Hz, 3H). ^{13}C NMR (126 MHz, $CDCl_3$) δ 195.2 (C=S), 150.9, 144.5, 130.8, 124.5, 48.7, 45.9, 22.5, 14.6, 12.3. FTIR (cm^{-1}): 2931, 1512, 1431, 1078, 782, 702. Elemental Analysis: (calculated) $C_{12}H_{17}N_3S$ (235.35) C, 62.03; H, 7.479; N, 17.82; (found) C, 61.24; H, 7.28; N, 17.85; S, 13.62. mp: 84˚C.

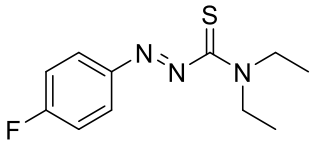

N,N-diethyl-2-(4-fluorophenyl)diazothioformamide (5c): 50 mL of ethanol and p-fluorophenylhydrazine HCl (24.29 mmol, 3.95 g) was added to a flame-dried round-bottom flask equipped with a magnetic stirrer and allowed to degas for 1.5 h under nitrogen flow. While under nitrogen, carbon disulphide (27.69 mol, 2.65 ml) was added dropwise to the flask and the solution was allowed to stir under ambient conditions for 0.5 h. Potassium hydroxide (1.63 g, 29.02 mol) dissolved in degassed ethanol (20 mL) was then added and allowed to stir under nitrogen for 0.5 h. Methyl iodide (27.20 mmol, 1.7 ml) was then added to the solution and stirred under nitrogen for 1 h. The resulting liquid was then concentrated with a rotary evaporator to afford an off-white paste. The flask was then equipped with a reflux condenser and put under nitrogen flow upon 30 mL of diethylamine was then added and the mixture was heated to reflux under nitrogen for 48 h. The solution was cooled to ambient temperature, opened to air, and allowed to stir for 2 h. The resulting red liquid was concentrated via rotary

evaporator and purified using flash column chromatography 4:1 hexane: ethyl acetate forming 4.16 g (72 %) of red solid. The resulting solid was subjected to recrystallization using slow evaporation of acetonitrile to afford diffracting dark red crystals. ^{1}H NMR (300 MHz, Chloroform-d) δ 7.91 (t, 2H), 7.19 (t, 2H), 4.03 (q, J = 7.1, 2H), 3.51 (q, J = 7.2 2H), 1.41 (t, J = 7.2 Hz, 3H), 1.18 (t, J = 7.2 Hz, 3H). ^{13}C NMR (75 MHz, $CDCl_3$) δ 194.6 (C=S), 165. (d, J_{C-F} = 225 Hz), 149.2 (d J_{C-F} = 3 Hz), 126.6 d J_{C-F} = 9 Hz), 117.15 (d J_{C-F} = 22 Hz), 48.6, 46.0, 14.6, 12.2. FTIR (cm^{-1}): 2984, 1500, 1422,1220,1140,1078,706. Elemental Analysis: (calculated) $C_{11}H_{14}FN_3S$ (239.09) C, 56.41; H 6.242; N, 17.48; (Found) C, 55.21; H, 5.90; N, 17.56; mp: 82˚C.

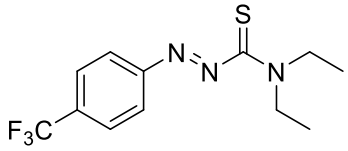

N,N-diethyl-2-(4-(trifluoromethyl)phenyl)diazothioformamide (5d): 75 mL of ethanol was degassed under nitrogen flow in a flame-dried round bottom fitted with a magnetic stirrer for 1 h in which p-(trifluoromethyl)-phenylhydrazine•HCl (4.25 g, 19.2 mmol) was added and stirred for 0.5 h. Carbon disulphide (1.32 mL, 21.88 mmol) was added dropwise and the solution stirred for 0.5 h. Potassium hydroxide (1.29 g, 232.01 mmol) dissolved in degassed ethanol (25 mL) was then added dropwise in one portion aliquot and the solution stirred for 0.5 h before the addition of methyl iodide (1.33 mL, 21.48 mmol). The solution was stirred for an additional 1 h before concentrating with a rotary evaporator. The flask was then fitted with a reflux condenser and put under nitrogen flow. Diethylamine (40 mL) was added and the solution was refluxed for 48 h. The resulting dark red solution was then allowed to cool before being open to the air and stirred for an additional 2 h. The solution was then washed with brine

and extracted with ethyl acetate to afford a dark red liquid. The resulting oil from rotary evaporation was purified using flash column chromatography 7:3 hexane: ethyl acetate yielding 0.71 g (13 %) of red solid. The solid was recrystallized via slow evaporation with tetrahydrofuran (THF) to form diffracting crystals. ^{1}H NMR (300 MHz, Chloroform-d) δ 7.97 (d, J = 8.3 Hz, 2H), 7.79 (d, J = 8.4 Hz, 2H), 4.03 (q, J = 7.3 Hz, 2H), 3.50 (q, J = 7.2 Hz, 2H), 1.42 (t, J = 7.1 Hz, 3H), 1.19 (t, J = 7.0 Hz, 3H). ^{13}C NMR (126 MHz, $CDCl_3$) δ 193.5(C=S), 153.7, 133.8 (q, J_{C-F} = 33 Hz), 126.7 (q, J_{C-F} = 3.8 Hz), 123.81, 123.7 (q, J_{C-F} = 273 Hz), 48.6, 46.0, 14.5, 12.2. FTIR (cm^{-1}): 2982, 1581, 1434, 1316, 1159, 1079, 773. Elemental Analysis; $C_{12}H_{14}F_3N_3S$ (289.32) (Calculated) C, 49.86; H, 4.96; N, 14.39; (Found) C, 49.82; H, 4.88; N, 14.52; mp: 93˚C.

Cyclic Voltammetry

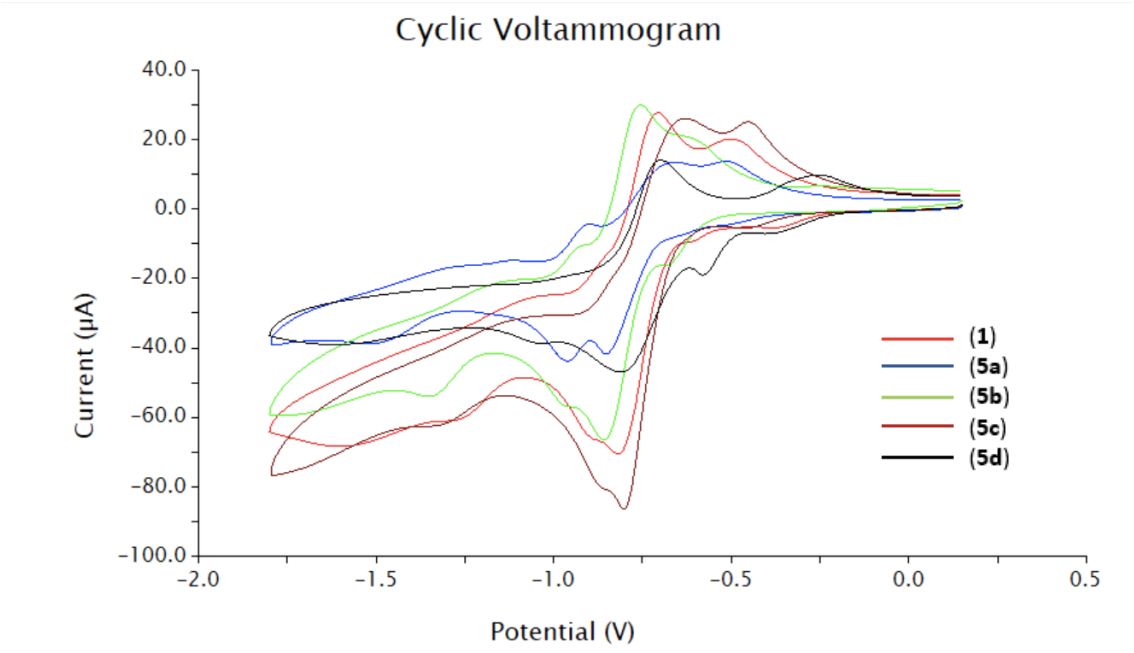

Figure A1.7: Overlay of the cyclic voltammograms for ligands 1, 5a-d.

Table A1.2: Electrochemical Potentials of the ATF ligands				
Ligand	**First reduction potential Epc_1(V)**	**Second reduction potential Epc_2(V)**	**First oxidation potential Epa_1(V)**	**Second oxidation Potential Epa_2(V)**
1	-0.8	-1.25	-0.75	-0.45
5a	-0.85	-0.95	-0.9	-0.5
5b	-0.85	-1.35	-0.8	-0.6
5c	-0.8	-1.3	-0.6	-0.4
5d	-0.6	-0.85	-0.7	-0.25

Electrochemistry was used to check for significant reduction potential differences and the possibility of a reduction event in any of the ligands. ATF ligands **1**, **5a-d** were prepared as 20 mM solutions in 1.0 mM of recrystallized $N(Bu)_4PF_6$ electrolyte in acetonitrile and bubbled with nitrogen for 0.5 h and then evaluated for their redox potential using Pine Research WaveNow potentiostat run at a scan rate of 50 mV/s**.** All CV are in 1 mM solution of different ATFs with NBu_4PF_6 (supporting electrolyte) and acetonitrile (solvent) and run after purging with N2 (>1hr). Scan rate 50 mV/S. Working electrode - Glassy carbon; Counter electrode - Graphite rod; All potentials measured vs Ag/AgCl.

X-Ray Crystal Data

X-ray diffraction data were collected at 100 K on a Bruker D8 Venture using MoKα-radiation (λ=0.71073 Å). Data have been corrected for absorption using SADABS[1] area detector absorption correction program. Using Olex2[2], the structure was solved with the SHELXT[3] structure solution program using Direct Methods and refined with the SHELXL[4] refinement package using least squares minimization. All non-hydrogen atoms were refined with anisotropic thermal parameters. Hydrogen atoms of the investigated structure were

located from difference Fourier maps but finally their positions were placed in geometrically calculated positions and refined using a riding model. Isotropic thermal parameters of the placed hydrogen atoms were fixed to 1.2 times the *U* value of the atoms they are linked to (1.5 times for methyl groups). Calculations and refinement of structures were carried out using APEX3[5], SHELXTL[6], and Olex2 software.

***N,N*-diethyl-2-(4-methoxyphenyl)diazothioformamide** (5a) :Crystallographic Data for **5a** $C_{12}H_{17}N_3OS$ (*M* =251.34 g/mol): triclinic, space group P-1 (no. 2), *a* = 6.7366(5) Å, *b* = 7.3334(5) Å, *c* = 14.8540(11) Å, *α* = 95.174(3)°, *β* = 100.290(3)°, *γ* = 113.795(2)°, *V* = 649.82(8) Å^3, *Z* = 2, *T* = 100 K, μ(MoKα) = 0.238 mm^{-1}, *Dcalc* = 1.285 g/cm^3, 2Θmax = 55.06° 21809 reflections collected, 2986 unique (R_{int} = 0.0325, R_{sigma} = 0.0198), R_1 = 0.0313 (I > 2σ(I)), wR_2 = 0.0806 (all data).

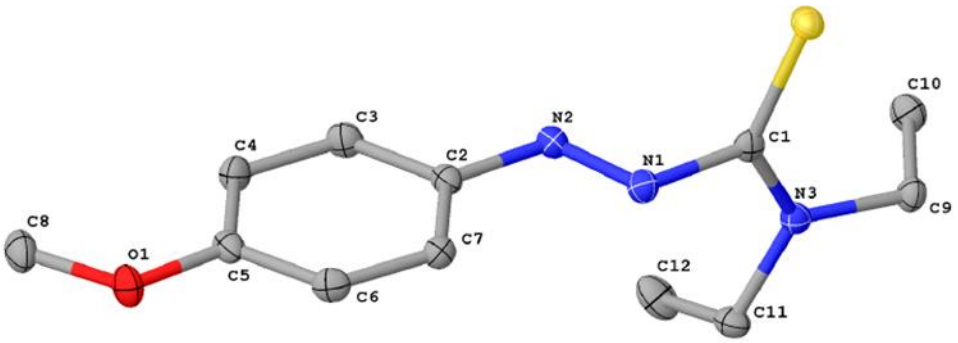

Table A1.3: Crystal data and structure refinement for 5a.	
Identification code	5a
Empirical formula	$C_{12}H_{17}N_3OS$
Formula weight	251.34
Temperature/K	100

Crystal system	triclinic
Space group	P-1
a/Å	6.7366(5)
b/Å	7.3334(5)
c/Å	14.8540(11)
α/°	95.174(3)
β/°	100.290(3)
γ/°	113.795(2)
Volume/$Å^3$	649.82(8)
Z	2
ρ_{calc}g/cm^3	1.285
μ/mm^{-1}	0.238
F(000)	268.0
Crystal size/mm^3	0.28 × 0.11 × 0.06
Radiation	MoKα (λ = 0.71073)
2Θ range for data collection/°	6.172 to 55.06
Index ranges	$-8 \leq h \leq 8$, $-9 \leq k \leq 9$, $-19 \leq l \leq 19$
Reflections collected	21809
Independent reflections	2986 [R_{int} = 0.0325, R_{sigma} = 0.0198]
Data/restraints/parameters	2986/0/157

Goodness-of-fit on F^2	1.042
Final R indexes [I>=2σ (I)]	R_1 = 0.0313, wR_2 = 0.0764
Final R indexes [all data]	R_1 = 0.0387, wR_2 = 0.0806
Largest diff. peak/hole / e $Å^{-3}$	0.40/-0.17

Table A1.4: Fractional Atomic Coordinates ($\times 10^4$) and Equivalent Isotropic Displacement Parameters ($Å^2 \times 10^3$) for 5a. U_{eq} is defined as 1/3 of of the trace of the orthogonalised U_{IJ} tensor.

Atom	***x***	***y***	***z***	**U(eq)**
S1	11888.4(5)	6634.4(4)	8644.7(2)	16.99(9)
O1	-398.0(15)	2614.9(14)	4619.7(6)	21.1(2)
N1	7603.5(16)	4202.3(15)	7906.6(7)	15.0(2)
N2	7403.6(16)	3616.5(15)	7059.3(7)	14.9(2)
N3	9473.1(16)	2893.0(15)	8941.1(7)	13.6(2)
C1	9651.4(19)	4426.3(18)	8498.8(8)	13.6(2)
C2	5407.6(19)	3429.6(17)	6458.9(8)	14.2(2)
C3	5057(2)	2610.0(19)	5530.8(9)	17.4(2)
C4	3125(2)	2300.5(18)	4886.4(9)	17.7(2)
C5	1554(2)	2848.0(18)	5180.2(8)	16.1(2)
C6	1919(2)	3703.7(18)	6111.6(9)	16.8(2)
C7	3824.1(19)	3991.2(17)	6749.7(8)	14.8(2)
C8	-886(2)	1738(2)	3663.6(9)	22.4(3)

C9	11377(2)	3021.8(18)	9654.4(8)	16.2(2)
C10	12991(2)	2406(2)	9256.0(9)	19.9(3)
C11	7405(2)	983.2(18)	8717.3(9)	17.2(2)
C12	7384(2)	-561(2)	7955.5(10)	24.9(3)

Table A1.5: Anisotropic Displacement Parameters ($Å^2 \times 10^3$) for 5a. The Anisotropic displacement factor exponent takes the form: $-2\pi^2[h^2a^{*2}U_{11}+2hka^*b^*U_{12}+\ldots]$.

Atom	U_{11}	U_{22}	U_{33}	U_{23}	U_{13}	U_{12}
S1	15.38(15)	14.54(15)	18.53(16)	3.84(11)	2.02(11)	4.54(11)
O1	17.1(4)	25.5(5)	19.6(5)	3.2(4)	-1.6(3)	10.7(4)
N1	14.6(5)	16.2(5)	15.2(5)	3.6(4)	2.8(4)	7.6(4)
N2	13.3(5)	14.8(5)	16.0(5)	2.3(4)	2.9(4)	5.5(4)
N3	13.0(5)	14.6(5)	13.7(5)	2.1(4)	2.8(4)	6.7(4)
C1	14.1(5)	16.2(5)	12.6(5)	1.0(4)	4.1(4)	8.6(4)
C2	12.8(5)	13.2(5)	15.9(6)	3.6(4)	2.4(4)	5.2(4)
C3	15.9(6)	19.7(6)	18.4(6)	2.3(5)	4.9(5)	9.2(5)
C4	19.0(6)	18.3(6)	14.0(6)	0.7(4)	2.7(5)	7.1(5)
C5	14.2(5)	14.3(6)	18.2(6)	5.9(4)	0.8(4)	5.4(5)
C6	16.6(6)	17.4(6)	19.9(6)	4.6(5)	5.6(5)	9.8(5)
C7	16.1(6)	14.3(5)	14.5(6)	2.7(4)	3.9(4)	7.0(5)
C8	21.3(6)	21.7(6)	19.7(6)	4.8(5)	-2.5(5)	7.6(5)

C9	16.6(6)	19.3(6)	13.5(6)	4.2(4)	1.6(4)	9.0(5)
C10	16.8(6)	23.1(6)	21.7(6)	4.7(5)	2.9(5)	10.8(5)
C11	14.3(6)	15.3(6)	21.1(6)	5.4(5)	4.9(5)	4.9(5)
C12	19.7(6)	17.3(6)	31.9(8)	-2.7(5)	0.7(5)	5.9(5)

Table A1.6: Bond Lengths for 5a

Atom	**Atom**	**Length/Å**		**Atom**	**Atom**	**Length/Å**
S1	C1	1.6706(12)		C2	C3	1.3918(17)
O1	C5	1.3615(14)		C2	C7	1.4075(17)
O1	C8	1.4271(16)		C3	C4	1.3925(17)
N1	N2	1.2577(14)		C4	C5	1.3953(18)
N1	C1	1.4358(15)		C5	C6	1.4022(17)
N2	C2	1.4223(15)		C6	C7	1.3791(16)
N3	C1	1.3277(15)		C9	C10	1.5210(17)
N3	C9	1.4750(15)		C11	C12	1.5209(18)
N3	C11	1.4794(15)				

Table A1.7: Bond Angles for 5a

Atom	**Atom**	**Atom**	**Angle/°**		**Atom**	**Atom**	**Atom**	**Angle/°**
C5	O1	C8	117.85(10)		C7	C2	N2	124.34(11)

N2	N1	C1	113.89(10)		C2	C3	C4	120.56(11)
N1	N2	C2	114.72(10)		C3	C4	C5	119.14(11)
C1	N3	C9	120.58(10)		O1	C5	C4	124.71(11)
C1	N3	C11	121.61(10)		O1	C5	C6	114.83(11)
C9	N3	C11	117.78(9)		C4	C5	C6	120.46(11)
N1	C1	S1	117.64(8)		C7	C6	C5	120.25(11)
N3	C1	S1	127.27(9)		C6	C7	C2	119.56(11)
N3	C1	N1	114.74(10)		N3	C9	C10	113.51(10)
C3	C2	N2	115.63(10)		N3	C11	C12	112.98(10)
C3	C2	C7	120.02(11)					

Table A1.8: Hydrogen Atom Coordinates (Å×10^4) and Isotropic Displacement Parameters (Å^2×10^3) for 5a.

Atom	***x***	***y***	***z***	**U(eq)**
H3	6145	2259	5335	21
H4	2879	1724	4255	21
H6	849	4087	6304	20
H7	4067	4564	7381	18
H8A	-2338	1642	3343	34
H8B	-928	381	3617	34
H8C	275	2590	3374	34

H9A	10800	2137	10102	19
H9B	12199	4431	10001	19
H10A	13593	3290	8821	30
H10B	12202	998	8928	30
H10C	14217	2534	9763	30
H11A	6109	1291	8518	21
H11B	7240	385	9286	21
H12A	7602	38	7397	37
H12B	5946	-1758	7810	37
H12C	8589	-958	8169	37

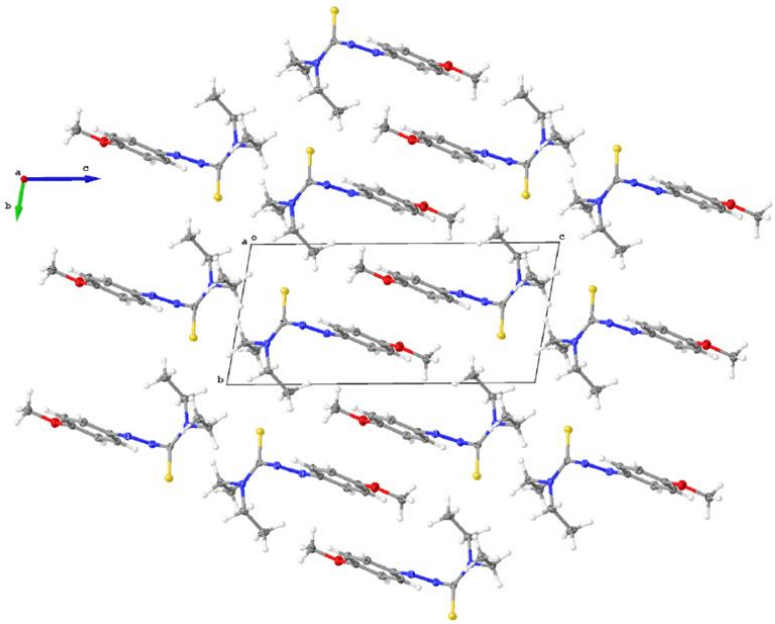

Figure A1.8: packing structure of N,N-diethyl-2-(4-methoxyphenyl)diazothioformamide (5a) ***N,N*-diethyl-2-(p-tolyl)diazothioformamide** (5b): Crystallographic Data for **5b** $C_{12}H_{17}N_3S$ (M =235.34 g/mol): monoclinic, space group C2/c (no. 15), a = 18.6399(18) Å, b = 7.2897(7) Å, c = 38.772(4) Å, β = 102.768(2)°, V = 5138.0(9) Å^3, Z = 16, T = 100 K, μ(MoKα) = 0.230 mm^{-1}, *Dcalc* = 1.217 g/cm^3, 2Θmax = 63.214°, 44407 reflections collected, 8579 unique (R_{int} = 0.0397, R_{sigma} = 0.0359), R_1 = 0.0494 (I > 2σ(I)), wR_2 = 0.1103 (all data).

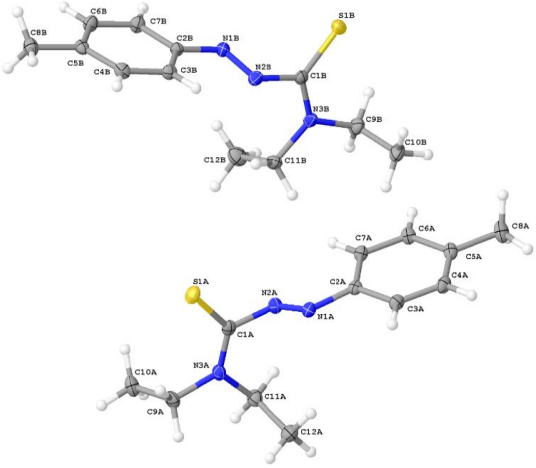

Table A1.9: Crystal data and structure refinement for 5b	
Identification code	UI_KW10(Me-ATF)
Empirical formula	$C_{12}H_{17}N_3S$
Formula weight	235.34
Temperature/K	100
Crystal system	monoclinic
Space group	C2/c
a/Å	18.6399(18)
b/Å	7.2897(7)
c/Å	38.772(4)
α/°	90
β/°	102.768(2)
γ/°	90
Volume/Å^3	5138.0(9)
Z	16
ρ_{calc}g/cm^3	1.217
μ/mm^{-1}	0.230
F(000)	2016.0
Crystal size/mm^3	0.61 × 0.42 × 0.35
Radiation	MoKα (λ = 0.71073)

2Θ range for data collection/°	5.384 to 63.214
Index ranges	$-27 \leq h \leq 27$, $-10 \leq k \leq 10$, $-57 \leq l \leq 56$
Reflections collected	44407
Independent reflections	8579 [R_{int} = 0.0397, R_{sigma} = 0.0359]
Data/restraints/parameters	8579/0/295
Goodness-of-fit on F^2	1.128
Final R indexes [I>=2σ (I)]	R_1 = 0.0494, wR_2 = 0.1038
Final R indexes [all data]	R_1 = 0.0698, wR_2 = 0.1103
Largest diff. peak/hole / e $Å^{-3}$	0.40/-0.27

Table A1.10: Fractional Atomic Coordinates ($\times 10^4$) and Equivalent Isotropic Displacement Parameters ($Å^2 \times 10^3$) for 5b. U_{eq} is defined as 1/3 of of the trace of the orthogonalised U_{IJ} tensor.

Atom	***x***	***y***	***z***
S1A	5149.8(2)	7849.0(5)	5636.2(2)
N1A	5799.9(6)	8971.4(16)	6284.5(3)
N2A	6317.1(6)	7852.8(16)	6375.4(3)
N3A	5889.7(6)	10977.6(17)	5832.0(3)
C1A	5645.2(7)	9359.3(19)	5911.2(3)
C2A	6480.5(7)	7414.5(18)	6743.0(3)
C3A	7159.2(7)	6575.6(19)	6870.8(4)
C4A	7381.3(8)	6185.5(19)	7229.8(4)

C5A	6929.4(8)	6583.8(19)	7462.0(4)
C6A	6239.8(8)	7383.7(19)	7325.6(4)
C7A	6013.9(7)	7802.0(19)	6970.6(3)
C8A	7165.0(9)	6149(2)	7850.4(4)
C9A	5751.6(8)	11626(2)	5463.5(4)
C10A	5051.7(9)	12758(2)	5369.0(4)
C11A	6323.3(8)	12209(2)	6102.5(4)
C12A	7145.4(8)	11863(2)	6156.9(4)
S1B	4110.9(2)	-104.8(5)	6909.8(2)
N1B	3915.8(6)	1002.4(16)	6237.1(3)
N2B	3232.2(6)	1191.3(16)	6155.8(3)
N3B	4612.0(6)	2937.8(17)	6652.3(3)
C1B	4222.1(7)	1400(2)	6602.7(3)
C2B	2905.2(7)	795.6(18)	5794.5(3)
C3B	3277.7(7)	-4.6(19)	5557.5(4)
C4B	2908.5(8)	-259.4(19)	5209.0(4)
C5B	2174.5(8)	262.2(18)	5090.2(3)
C6B	1811.1(8)	1031(2)	5333.9(4)
C7B	2171.2(8)	1290(2)	5684.3(4)
C8B	1786.3(9)	19(2)	4708.8(4)

C9B	4988.2(8)	3516(2)	7009.2(4)
C10B	5779.8(8)	2854(2)	7102.8(4)
C11B	4669.2(8)	4180(2)	6358.8(4)
C12B	4052.5(9)	5584(2)	6284.6(4)

Table A1.11: Anisotropic Displacement Parameters ($Å^2 \times 10^3$) for 5b. The Anisotropic displacement factor exponent takes the form: $-2\pi^2[h^2a^{*2}U_{11}+2hka^*b^*U_{12}+\ldots]$.

Atom	**U_{11}**	**U_{22}**	**U_{33}**	**U_{23}**	**U_{13}**	**U_{12}**
S1A	18.22(16)	23.33(18)	19.94(16)	-5.30(13)	2.20(13)	-0.04(14)
N1A	17.2(5)	17.2(5)	15.7(5)	-0.2(4)	3.4(4)	2.2(4)
N2A	14.6(5)	17.5(5)	16.4(5)	-1.0(4)	2.2(4)	0.6(4)
N3A	17.8(6)	20.8(6)	12.7(5)	-0.6(4)	3.0(4)	0.7(5)
C1A	11.6(6)	20.0(6)	16.3(6)	-0.9(5)	4.2(5)	4.1(5)
C2A	15.3(6)	12.1(6)	15.8(6)	-2.1(4)	2.1(5)	0.0(5)
C3A	15.5(6)	16.0(6)	20.1(6)	-1.5(5)	3.4(5)	1.7(5)
C4A	16.1(6)	15.9(6)	22.8(7)	-0.6(5)	-0.2(5)	3.1(5)
C5A	22.4(7)	13.4(6)	16.5(6)	-1.7(5)	-0.4(5)	0.5(5)
C6A	21.2(7)	16.4(6)	17.3(6)	-2.7(5)	4.7(5)	2.7(5)
C7A	15.2(6)	15.5(6)	15.9(6)	-2.0(5)	1.7(5)	2.4(5)
C8A	32.0(8)	23.7(7)	19.0(7)	0.7(6)	0.5(6)	7.4(6)
C9A	25.2(7)	25.3(7)	13.6(6)	1.3(5)	6.1(5)	0.4(6)

C10A	32.1(8)	26.9(8)	18.8(7)	3.8(6)	1.6(6)	5.3(7)
C11A	24.4(7)	19.9(7)	16.6(6)	-2.0(5)	3.0(5)	-1.6(6)
C12A	23.2(7)	29.1(8)	25.3(7)	0.2(6)	1.2(6)	-6.2(6)
S1B	18.78(17)	27.10(19)	22.47(16)	8.49(14)	4.78(13)	-0.39(14)
N1B	15.2(5)	18.4(6)	17.1(5)	-1.2(4)	2.9(4)	-1.6(4)
N2B	14.8(5)	18.4(6)	15.9(5)	1.0(4)	2.4(4)	-0.1(4)
N3B	15.1(5)	22.4(6)	14.4(5)	-1.1(4)	2.5(4)	-3.0(5)
C1B	11.1(6)	21.2(7)	16.1(6)	0.9(5)	3.6(5)	1.9(5)
C2B	15.4(6)	15.2(6)	13.3(5)	0.1(5)	2.5(5)	-0.8(5)
C3B	15.7(6)	16.5(6)	19.5(6)	0.2(5)	4.8(5)	2.1(5)
C4B	22.1(7)	16.2(6)	17.9(6)	-1.4(5)	6.8(5)	2.0(5)
C5B	21.6(7)	13.1(6)	15.0(6)	-0.1(5)	3.0(5)	-1.4(5)
C6B	15.7(6)	21.9(7)	19.7(6)	-0.9(5)	2.7(5)	1.8(5)
C7B	16.9(6)	22.5(7)	17.3(6)	-2.4(5)	4.8(5)	2.1(5)
C8B	29.1(8)	18.7(7)	16.5(6)	-1.1(5)	0.6(5)	1.4(6)
C9B	22.1(7)	31.5(8)	16.1(6)	-4.5(6)	2.1(5)	-6.8(6)
C10B	23.7(7)	23.8(7)	25.9(7)	0.6(6)	-4.3(6)	-4.5(6)
C11B	19.9(7)	22.7(7)	17.9(6)	1.0(5)	6.8(5)	-3.8(6)
C12B	31.5(8)	24.6(8)	29.5(8)	4.4(6)	8.0(7)	3.2(7)

Table A1.12: Bond Lengths for 5b.

Atom	Atom	Length/Å		Atom	Atom	Length/Å
S1A	C1A	1.6633(14)		S1B	C1B	1.6650(14)
N1A	N2A	1.2524(16)		N1B	N2B	1.2509(16)
N1A	C1A	1.4402(17)		N1B	C1B	1.4359(17)
N2A	C2A	1.4263(17)		N2B	C2B	1.4282(17)
N3A	C1A	1.3249(19)		N3B	C1B	1.3268(19)
N3A	C9A	1.4725(17)		N3B	C9B	1.4680(18)
N3A	C11A	1.4780(18)		N3B	C11B	1.4766(18)
C2A	C3A	1.3939(19)		C2B	C3B	1.3959(18)
C2A	C7A	1.3978(18)		C2B	C7B	1.3879(19)
C3A	C4A	1.3909(19)		C3B	C4B	1.3866(19)
C4A	C5A	1.393(2)		C4B	C5B	1.397(2)
C5A	C6A	1.404(2)		C5B	C6B	1.3955(19)
C5A	C8A	1.5062(19)		C5B	C8B	1.5065(19)
C6A	C7A	1.3816(18)		C6B	C7B	1.3891(19)
C9A	C10A	1.519(2)		C9B	C10B	1.518(2)
C11A	C12A	1.521(2)		C11B	C12B	1.518(2)

TableA1.13: Bond Angles for 5b.

Atom	Atom	Atom	Angle/°		Atom	Atom	Atom	Angle/°
N2A	N1A	C1A	112.40(11)		N2B	N1B	C1B	112.77(11)
N1A	N2A	C2A	114.07(11)		N1B	N2B	C2B	114.52(11)
C1A	N3A	C9A	121.00(12)		C1B	N3B	C9B	120.76(12)
C1A	N3A	C11A	122.60(11)		C1B	N3B	C11B	122.48(11)
C9A	N3A	C11A	116.39(12)		C9B	N3B	C11B	116.72(12)
N1A	C1A	S1A	118.28(10)		N1B	C1B	S1B	119.20(10)
N3A	C1A	S1A	127.70(10)		N3B	C1B	S1B	127.14(11)
N3A	C1A	N1A	113.88(12)		N3B	C1B	N1B	113.52(11)
C3A	C2A	N2A	115.47(11)		C3B	C2B	N2B	124.30(12)
C3A	C2A	C7A	120.44(12)		C7B	C2B	N2B	115.30(11)
C7A	C2A	N2A	124.08(12)		C7B	C2B	C3B	120.40(12)
C4A	C3A	C2A	119.44(12)		C4B	C3B	C2B	119.03(12)
C3A	C4A	C5A	121.03(13)		C3B	C4B	C5B	121.61(12)
C4A	C5A	C6A	118.50(13)		C4B	C5B	C8B	120.99(12)
C4A	C5A	C8A	121.22(13)		C6B	C5B	C4B	118.21(12)
C6A	C5A	C8A	120.28(13)		C6B	C5B	C8B	120.80(13)
C7A	C6A	C5A	121.27(13)		C7B	C6B	C5B	120.99(13)
C6A	C7A	C2A	119.29(12)		C2B	C7B	C6B	119.74(12)

N3A	C9A	C10A	111.43(11)		N3B	C9B	C10B	111.76(12)
N3A	C11A	C12A	111.95(12)		N3B	C11B	C12B	112.25(11)

Table A1.14: Hydrogen Atom Coordinates (Å×10^4) and Isotropic Displacement Parameters (Å^2×10^3) for 5b.

Atom	***x***	***y***	***z***	**U(eq)**
H3A	7467.47	6272.87	6714.07	21
H4A	7848.47	5638.72	7317.89	23
H6A	5922.48	7642.21	7480.37	22
H7A	5546.55	8347.18	6882.08	19
H8AA	7120.95	7252.72	7988.7	39
H8AB	7677.5	5732.73	7904.3	39
H8AC	6849.74	5180.42	7910.98	39
H9AA	5709.3	10557.06	5302.72	25
H9AB	6173.05	12378.39	5430.12	25
H10A	4983.59	13201.39	5125.23	40
H10B	5089.55	13807.29	5530.08	40
H10C	4630.44	11997.42	5390.54	40
H11A	6172.53	12023.92	6329.36	25
H11B	6216.99	13499.32	6028.94	25
H12A	7291.74	11974.6	5930.13	40

H12B	7259.43	10624.58	6251.83	40
H12C	7414.71	12765.17	6323.92	40
H3B	3776.97	-369.3	5633.9	20
H4B	3161.02	-801.99	5047.17	22
H6B	1309.96	1381.47	5258.89	23
H7B	1915.99	1803.88	5847.97	22
H8BA	1680.48	1225.17	4597.4	33
H8BB	1324.46	-646.68	4696.11	33
H8BC	2101.31	-678.65	4584.6	33
H9BA	4721.06	3021.96	7183.01	28
H9BB	4980.01	4871.39	7023.69	28
H10D	6054.09	3405.55	6940.69	39
H10E	5790.54	1514.81	7082.18	39
H10F	6005.8	3214.03	7346.12	39
H11C	4656.04	3445.68	6142.67	24
H11D	5147.63	4827.45	6418.06	24
H12D	4129.36	6425.12	6098.97	42
H12E	4049.95	6279.24	6500.69	42
H12F	3580.16	4953.37	6206.42	42

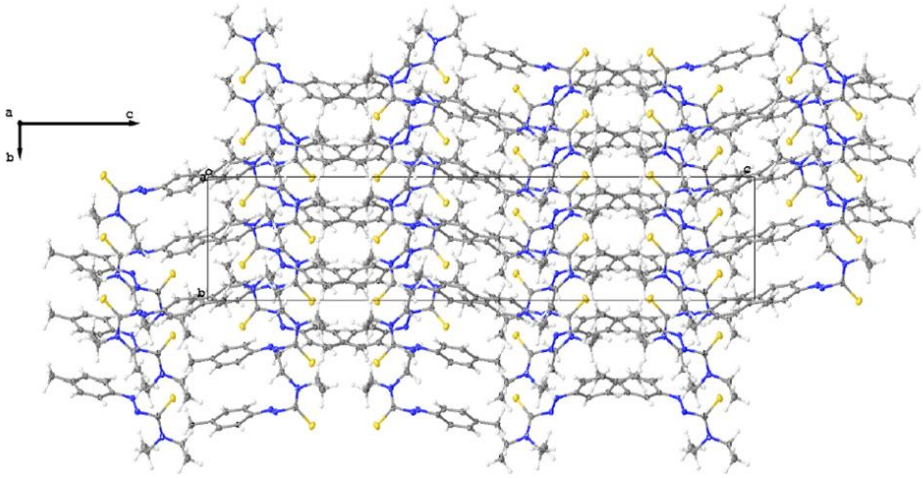

Figure A1.9: packing structure of N,N-diethyl-2-(p-tolyl)diazothioformamide (5b).

***N,N*-diethyl-2-(4-fluorophenyl)diazothioformamide** (5c): Crystallographic Data for **5c** $C_{11}H_{14}FN_3S$ (M =239.31 g/mol): triclinic, space group P-1 (no. 2), a = 6.8978(3) Å, b = 7.1664(4) Å, c = 13.3406(6) Å, α = 75.671(2)°, β = 88.061(2)°, γ = 67.920(2)°, V = 590.79(5) Å^3, Z = 2, T = 100 K, μ(MoKα) = 0.263 mm^{-1}, $Dcalc$ = 1.345 g/cm^3, 2Θmax = 55.062°, 14688 reflections measured, 2716 unique (R_{int} = 0.0437, R_{sigma} = 0.0311), R_1 was 0.0359 (I > 2σ(I)), wR_2 was 0.0800 (all data).

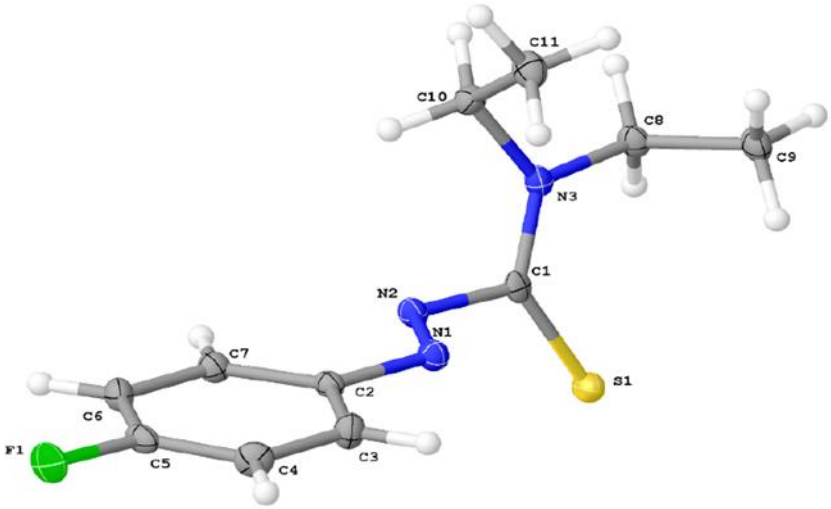

Table A1.15: Crystal data and structure refinement for 5c.	
Identification code	UI_KW12 (F-ATF)
Empirical formula	$C_{11}H_{14}FN_3S$
Formula weight	239.31
Temperature/K	100
Crystal system	triclinic
Space group	P-1
a/Å	6.8978(3)
b/Å	7.1664(4)
c/Å	13.3406(6)
α/°	75.671(2)
β/°	88.061(2)
γ/°	67.920(2)
Volume/Å^3	590.79(5)
Z	2
ρ_{calc}g/cm^3	1.345
μ/mm^{-1}	0.263
F(000)	252.0
Crystal size/mm^3	0.26 × 0.23 × 0.21
Radiation	MoKα (λ = 0.71073)

2Θ range for data collection/°	6.318 to 55.062
Index ranges	$-8 \leq h \leq 8$, $-9 \leq k \leq 9$, $-17 \leq l \leq 17$
Reflections collected	14688
Independent reflections	2716 [R_{int} = 0.0437, R_{sigma} = 0.0311]
Data/restraints/parameters	2716/0/147
Goodness-of-fit on F^2	1.043
Final R indexes [I>=2σ (I)]	R_1 = 0.0359, wR_2 = 0.0744
Final R indexes [all data]	R_1 = 0.0494, wR_2 = 0.0800
Largest diff. peak/hole / e $Å^{-3}$	0.35/-0.22

Table A1.16: Fractional Atomic Coordinates ($\times 10^4$) and Equivalent Isotropic Displacement Parameters ($Å^2 \times 10^3$) for 5c. U_{eq} is defined as 1/3 of of the trace of the orthogonalised U_{IJ} tensor.

Atom	***x***	***y***	***z***	**U(eq)**
S1	7894.4(6)	1978.8(6)	1607.7(3)	16.60(11)
F1	-1166.3(15)	1992.6(15)	6025.0(7)	24.6(2)
N1	4215.0(19)	3715.8(19)	2370.0(9)	14.2(3)
N2	4679.1(19)	3327(2)	3318.7(10)	15.1(3)
N3	5299.6(19)	6010.9(19)	1165.0(9)	13.6(3)
C1	5806(2)	4052(2)	1710.2(11)	13.2(3)
C2	3117(2)	2931(2)	3973.7(11)	13.4(3)
C3	3582(2)	2518(2)	5032.3(12)	18.7(3)

C4	2144(2)	2162(3)	5735.5(12)	19.9(3)
C5	274(2)	2263(2)	5345.7(12)	17.3(3)
C6	-219(2)	2629(2)	4302.3(12)	18.2(3)
C7	1225(2)	2964(2)	3607.1(12)	16.0(3)
C8	6656(2)	6554(2)	360.9(11)	16.2(3)
C9	8526(2)	6843(3)	779.3(12)	18.7(3)
C10	3408(2)	7721(2)	1349.2(12)	16.2(3)
C11	3857(3)	8813(3)	2104.0(12)	20.1(3)

Table A1.17: Anisotropic Displacement Parameters ($Å^2 \times 10^3$) for 5c. The Anisotropic displacement factor exponent takes the form: $-2\pi^2[h^2a^{*2}U_{11}+2hka^*b^*U_{12}+\ldots]$.

Atom	U_{11}	U_{22}	U_{33}	U_{23}	U_{13}	U_{12}
S1	15.35(19)	15.06(19)	18.94(19)	-4.02(14)	3.76(14)	-5.69(14)
F1	22.0(5)	28.8(5)	23.8(5)	-3.8(4)	11.7(4)	-13.1(4)
N1	14.2(6)	15.3(6)	14.0(6)	-3.0(5)	2.2(5)	-7.2(5)
N2	14.7(6)	16.2(6)	14.8(6)	-3.7(5)	2.3(5)	-6.5(5)
N3	13.2(6)	16.2(6)	12.6(6)	-3.2(5)	1.2(5)	-7.3(5)
C1	13.9(7)	18.4(7)	11.3(7)	-5.1(6)	-0.8(5)	-9.4(6)
C2	13.7(7)	12.0(7)	14.7(7)	-3.3(5)	3.7(5)	-5.3(6)
C3	14.9(7)	23.6(8)	17.9(8)	-3.9(6)	1.4(6)	-8.4(6)
C4	22.0(8)	22.8(8)	13.1(7)	-2.7(6)	2.5(6)	-7.8(7)

C5	16.9(7)	14.2(7)	20.2(8)	-3.1(6)	9.0(6)	-6.7(6)
C6	14.0(7)	18.9(8)	23.0(8)	-4.3(6)	2.3(6)	-8.2(6)
C7	16.4(7)	16.6(7)	15.6(7)	-3.5(6)	1.3(6)	-7.3(6)
C8	17.5(7)	18.5(8)	13.0(7)	-1.7(6)	3.1(6)	-9.0(6)
C9	16.9(8)	21.0(8)	20.6(8)	-4.4(6)	4.6(6)	-10.7(6)
C10	12.9(7)	15.8(7)	17.9(7)	-2.6(6)	1.2(6)	-4.2(6)
C11	19.5(8)	22.8(8)	21.3(8)	-9.0(6)	7.4(6)	-10.1(7)

Table A1.18: Bond Lengths for 5c.

Atom	**Atom**	**Length/Å**		**Atom**	**Atom**	**Length/Å**
S1	C1	1.6674(15)		C2	C3	1.392(2)
F1	C5	1.3576(17)		C2	C7	1.399(2)
N1	N2	1.2520(17)		C3	C4	1.392(2)
N1	C1	1.4371(18)		C4	C5	1.377(2)
N2	C2	1.4312(18)		C5	C6	1.381(2)
N3	C1	1.3284(19)		C6	C7	1.384(2)
N3	C8	1.4752(18)		C8	C9	1.525(2)
N3	C10	1.4798(19)		C10	C11	1.521(2)

Table A1.19: Bond Angles for 5c.

Atom	Atom	Atom	Angle/°		Atom	Atom	Atom	Angle/°
N2	N1	C1	114.36(12)		C7	C2	N2	124.03(13)
N1	N2	C2	114.15(12)		C2	C3	C4	119.92(14)
C1	N3	C8	120.33(12)		C5	C4	C3	117.87(14)
C1	N3	C10	122.00(12)		F1	C5	C4	118.17(14)
C8	N3	C10	117.66(12)		F1	C5	C6	118.18(14)
N1	C1	S1	118.09(11)		C4	C5	C6	123.65(14)
N3	C1	S1	127.48(11)		C5	C6	C7	118.20(14)
N3	C1	N1	114.02(13)		C6	C7	C2	119.70(14)
C3	C2	N2	115.35(13)		N3	C8	C9	114.14(12)
C3	C2	C7	120.62(14)		N3	C10	C11	112.80(12)

Table A1.20: Hydrogen Atom Coordinates (Å×10^4) and Isotropic Displacement Parameters (Å^2×10^3) for 5c.

Atom	*x*	*y*	*z*	U(eq)
H3	4880.1	2477.99	5274.76	22
H4	2442.87	1859.84	6461.05	24
H6	-1514.25	2649.99	4067.79	22
H7	931.97	3214.64	2884.51	19
H8A	5801.22	7858.33	-147.43	19

H8B	7180	5442.13	-11.67	19
H9A	9332.97	7228	201.96	28
H9B	9421.41	5538.75	1258.32	28
H9C	8025.78	7947.21	1146.34	28
H10A	2339.54	7151.47	1626.42	19
H10B	2819	8752.99	680.41	19
H11A	4882.44	9418.21	1824.06	30
H11B	4422.93	7803.6	2771.29	30
H11C	2555.99	9918.91	2202.7	30

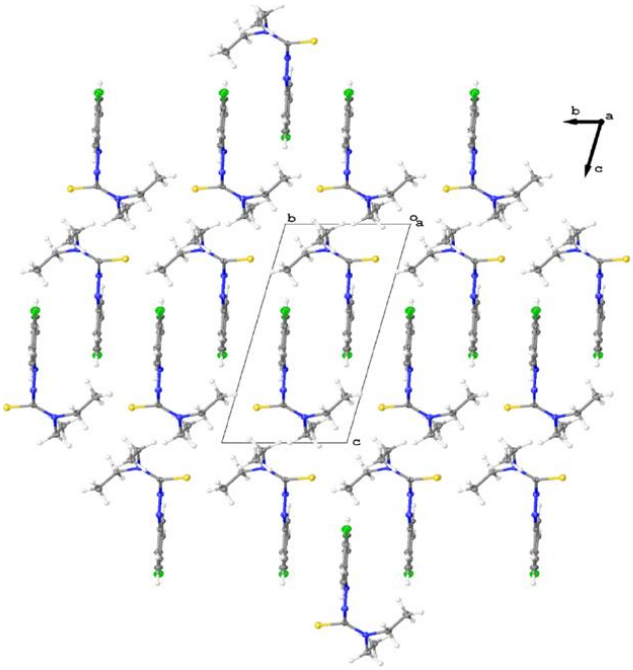

Figure A1.10: packing structure of N,N-diethyl-2-(4-fluorophenyl)diazothioformamide (5c)

***N,N*-diethyl-2-(4-(trifluoromethyl)phenyl)diazothioformamide** (5d):Crystallographic Data for **5d** $C_{12}H_{14}F_3N_3S$ (M =289.32 g/mol): orthorhombic, space group Fdd2 (no. 43), a =

25.783(2) Å, *b* = 26.989(2) Å, *c* = 7.7745(6) Å, *V* = 5409.8(7) Å^3, *Z* = 16, *T* = 100 K, μ(MoKα) = 0.264 mm^{-1}, *Dcalc* = 1.421 g/cm^3, 2Θmax = 55.11°, 17920 reflections collected, 3104 unique (R_{int} = 0.0253, R_{sigma} = 0.0208), R_1 = 0.0271 (I > 2σ(I)), wR_2 = 0.0657 (all data).

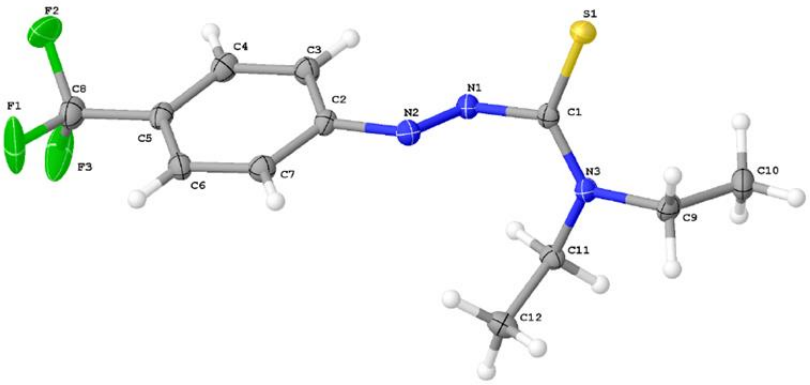

Table A1.21: Crystal data and structure refinement for 5d.	
Identification code	UI_KW1 (KG-26)
Empirical formula	$C_{12}H_{14}F_3N_3S$
Formula weight	289.32
Temperature/K	100
Crystal system	orthorhombic
Space group	Fdd2
a/Å	25.783(2)
b/Å	26.989(2)
c/Å	7.7745(6)
α/°	90
β/°	90
γ/°	90
Volume/Å^3	5409.8(7)
Z	16
ρ_{calc}g/cm^3	1.421
μ/mm^{-1}	0.264
F(000)	2400.0
Crystal size/mm^3	0.28 × 0.21 × 0.08
Radiation	MoKα (λ = 0.71073)

2Θ range for data collection/°	6.038 to 55.11
Index ranges	$-33 \leq h \leq 32$, $-34 \leq k \leq 28$, $-10 \leq l \leq 10$
Reflections collected	17920
Independent reflections	3104 [R_{int} = 0.0253, R_{sigma} = 0.0208]
Data/restraints/parameters	3104/56/231
Goodness-of-fit on F^2	1.046
Final R indexes [I>=2σ (I)]	R_1 = 0.0271, wR_2 = 0.0641
Final R indexes [all data]	R_1 = 0.0301, wR_2 = 0.0657
Largest diff. peak/hole / e $Å^{-3}$	0.25/-0.13
Flack parameter	0.000(18)

Table A1.22: Fractional Atomic Coordinates ($\times 10^4$) and Equivalent Isotropic Displacement Parameters ($Å^2 \times 10^3$) for 5d. U_{eq} is defined as 1/3 of of the trace of the orthogonalised U_{IJ} tensor.

Atom	***x***	***y***	***z***	**U(eq)**
S1	5729.5(2)	3234.1(2)	9110.2(6)	18.37(12)
F1	7778.7(15)	3414(3)	-782(5)	51.1(13)
F2	8241(3)	3708(2)	1243(8)	51.4(14)
F3	8284(3)	2939(2)	636(11)	51.7(17)
N1	6412.0(6)	2824.3(6)	7007.6(19)	16.6(3)
N2	6304.0(6)	2940.1(6)	5487(2)	17.6(3)
N3	5755.8(6)	2293.8(6)	7966(2)	15.6(3)

C1	5945.4(7)	2748.9(6)	8003(2)	14.7(4)
C2	6745.4(7)	3040.6(7)	4422(2)	16.5(4)
C3	7246.5(8)	3124.9(7)	5030(3)	20.0(4)
C4	7641.9(8)	3211.4(7)	3863(3)	21.5(4)
C5	7533.6(8)	3209.7(6)	2101(3)	18.7(4)
C6	7032.9(8)	3130.5(7)	1502(3)	19.8(4)
C7	6636.7(8)	3053.2(7)	2672(3)	19.8(4)
C8	7962.9(9)	3297.8(8)	835(3)	25.4(4)
C9	5281.9(8)	2167.4(7)	8932(3)	20.4(4)
C10	5399.8(9)	1985.8(8)	10739(3)	27.1(5)
C11	6014.7(8)	1879.3(7)	7066(2)	16.8(4)
C12	5792.1(8)	1784.9(8)	5283(3)	22.6(4)
F1A	7871(8)	3647(6)	-210(30)	32(4)
F2A	8427(5)	3405(11)	1670(20)	54(4)
F3A	8070(8)	2917(5)	-90(30)	31(4)
F1B	8022(5)	3740(3)	401(19)	40(3)
F2B	8427(3)	3134(5)	1461(13)	40.1(19)
F3B	7888(4)	3006(5)	-579(12)	51(3)

Table A1.23: Anisotropic Displacement Parameters ($Å^2 \times 10^3$) for 5d. The Anisotropic displacement factor exponent takes the form: $-2\pi^2[h^2a^{*2}U_{11}+2hka^*b^*U_{12}+\ldots]$.

Atom	U_{11}	U_{22}	U_{33}	U_{23}	U_{13}	U_{12}
S1	19.6(2)	17.2(2)	18.3(2)	-3.59(18)	1.86(19)	-0.72(18)
F1	33.5(18)	98(4)	21.9(17)	21(2)	6.9(15)	-11(3)
F2	50(3)	50(3)	54(3)	-19(2)	27(2)	-35(2)
F3	48(4)	37(3)	70(5)	26(3)	42(3)	23(3)
N1	17.1(8)	17.0(7)	15.7(8)	0.1(6)	1.9(6)	-1.1(6)
N2	19.1(9)	17.9(7)	15.9(8)	0.6(6)	0.4(7)	-0.6(6)
N3	15.4(8)	16.2(7)	15.3(7)	-0.1(6)	1.9(6)	-0.4(6)
C1	13.6(9)	18.2(8)	12.5(8)	1.9(7)	-1.9(7)	-0.2(7)
C2	16.4(9)	15.1(8)	18.1(10)	2.5(7)	2.6(7)	0.5(7)
C3	19.7(10)	22.3(9)	18.0(10)	1.3(7)	-0.2(8)	-0.9(8)
C4	17.3(9)	21.4(9)	25.8(11)	1.9(8)	1.5(8)	-1.0(8)
C5	19.7(10)	13.6(8)	22.9(10)	1.6(7)	6.8(8)	1.3(7)
C6	24.4(10)	18.6(9)	16.6(9)	0.7(7)	3.4(8)	0.5(7)
C7	18.7(9)	20.0(9)	20.8(10)	-0.4(8)	0.0(8)	-0.3(8)
C8	23.9(11)	24.0(10)	28.3(11)	2.2(8)	8.6(9)	0.5(8)
C9	17.6(10)	20.4(8)	23.3(10)	-0.2(8)	5.9(8)	-3.8(7)
C10	34.7(12)	25.0(10)	21.7(10)	2.1(8)	10.3(9)	-3.2(9)
C11	18.4(10)	15.5(8)	16.6(10)	-0.4(7)	0.4(7)	2.6(7)

C12	24.5(11)	23.7(10)	19.7(10)	-5.2(8)	-2.5(8)	2.4(8)
F1A	36(11)	26(6)	35(9)	20(6)	15(6)	13(7)
F2A	23(5)	84(11)	54(6)	-9(9)	15(4)	-16(7)
F3A	31(12)	20(4)	43(10)	2(5)	27(6)	4(5)
F1B	44(8)	21(3)	55(8)	12(4)	28(5)	0(3)
F2B	24(3)	56(6)	40(5)	15(4)	17(3)	15(4)
F3B	34(5)	88(8)	30(4)	-17(5)	18(3)	-12(4)

Table A1.24: Bond Lengths for 5d.

Atom	**Atom**	**Length/Å**		**Atom**	**Atom**	**Length/Å**
S1	C1	1.6630(18)		C4	C5	1.398(3)
F1	C8	1.380(4)		C5	C6	1.389(3)
F2	C8	1.357(4)		C5	C8	1.500(3)
F3	C8	1.283(4)		C6	C7	1.384(3)
N1	N2	1.254(2)		C8	F1A	1.267(13)
N1	C1	1.445(2)		C8	F2A	1.392(13)
N2	C2	1.433(2)		C8	F3A	1.283(14)
N3	C1	1.323(2)		C8	F1B	1.248(8)
N3	C9	1.474(2)		C8	F2B	1.366(7)
N3	C11	1.478(2)		C8	F3B	1.366(8)

C2	C3	1.394(3)		C9	C10	1.519(3)
C2	C7	1.389(3)		C11	C12	1.522(3)
C3	C4	1.384(3)				

Table A1.25: Bond Angles for 5d.

Atom	**Atom**	**Atom**	**Angle/°**		**Atom**	**Atom**	**Atom**	**Angle/°**
N2	N1	C1	110.81(15)		F2	C8	F1	102.1(4)
N1	N2	C2	114.54(16)		F2	C8	C5	111.5(2)
C1	N3	C9	120.67(16)		F3	C8	F1	106.5(4)
C1	N3	C11	123.10(16)		F3	C8	F2	107.6(4)
C9	N3	C11	116.12(15)		F3	C8	C5	115.8(3)
N1	C1	S1	116.43(13)		F1A	C8	C5	113.7(8)
N3	C1	S1	128.23(14)		F1A	C8	F2A	107.7(11)
N3	C1	N1	115.28(16)		F1A	C8	F3A	106.1(10)
C3	C2	N2	124.83(18)		F2A	C8	C5	111.2(6)
C7	C2	N2	114.20(17)		F3A	C8	C5	113.4(6)
C7	C2	C3	120.96(18)		F3A	C8	F2A	104.0(10)
C4	C3	C2	119.19(19)		F1B	C8	C5	114.8(5)
C3	C4	C5	119.64(19)		F1B	C8	F2B	107.3(7)
C4	C5	C8	119.7(2)		F1B	C8	F3B	110.5(8)

C6	C5	C4	120.98(18)		F2B	C8	C5	111.2(4)
C6	C5	C8	119.35(19)		F2B	C8	F3B	103.0(6)
C7	C6	C5	119.25(19)		F3B	C8	C5	109.4(5)
C6	C7	C2	119.92(19)		N3	C9	C10	112.35(17)
F1	C8	C5	112.3(2)		N3	C11	C12	112.77(15)

Table A1.26: Hydrogen Atom Coordinates (Å×10^4) and Isotropic Displacement Parameters (Å^2×10^3) for 5d.

Atom	***x***	***y***	***z***	**U(eq)**
H3	7316	3123	6230	24
H4	7985	3272	4257	26
H6	6963	3129	302	24
H7	6291	3009	2280	24
H9A	5089	1907	8303	25
H9B	5056	2464	9002	25
H10A	5624	1693	10678	41
H10B	5075	1899	11322	41
H10C	5577	2248	11384	41
H11A	5979	1575	7766	20
H11B	6389	1954	6961	20
H12A	5865	2070	4540	34

H12B	5416	1736	5368	34
H12C	5952	1488	4791	34

TableA1.27: Atomic Occupancy for 5d							
Atom	***Occupancy***		**Atom**	***Occupancy***		**Atom**	***Occupancy***
F1	0.529(4)		F2	0.529(4)		F3	0.529(4)
F1A	0.173(4)		F2A	0.173(4)		F3A	0.173(4)
F1B	0.298(4)		F2B	0.298(4)		F3B	0.298(4)

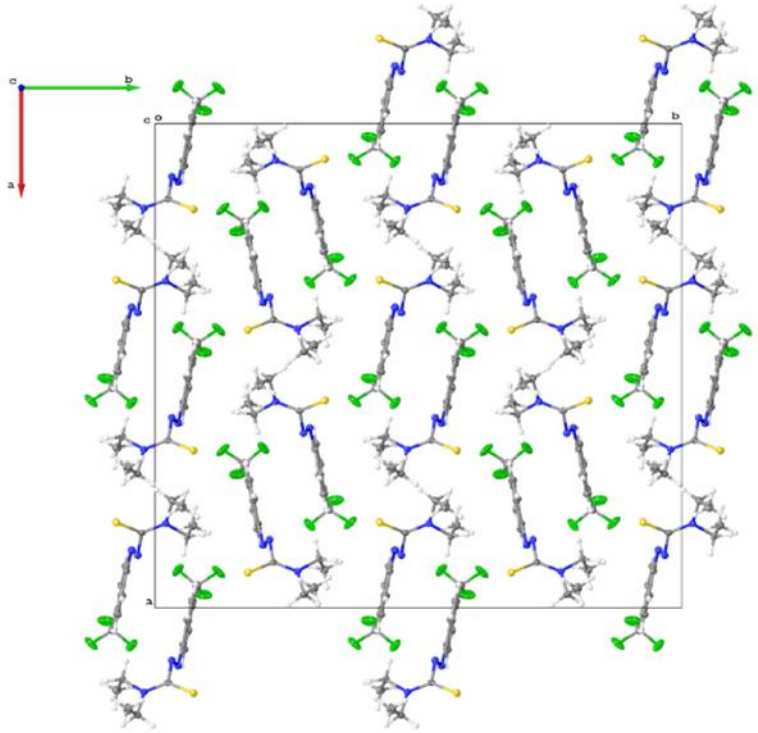

Figure A1.11: Packing structure of N,N-diethyl-2-(4-trifluorophenyl)diazothioformamide (5d)

UV-Vis Data:

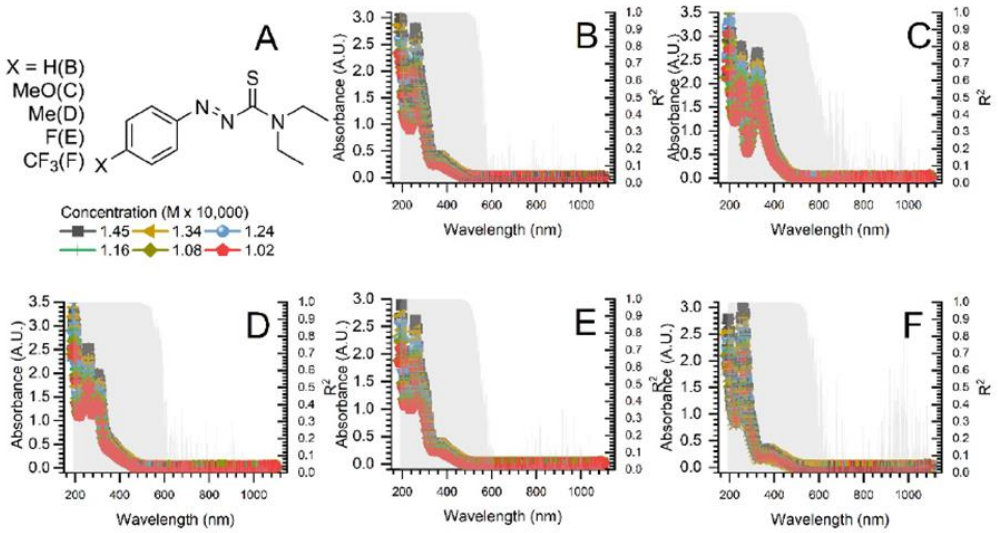

Figure A1.12: ATF ligand dilution graphs to calculate extinction coefficients of ligands before titration studies. Linearity (r2) shown in gray. A) structure and key of ligands; b) 1; c) 5a; d) 5b; e) 5c; f) 5d.

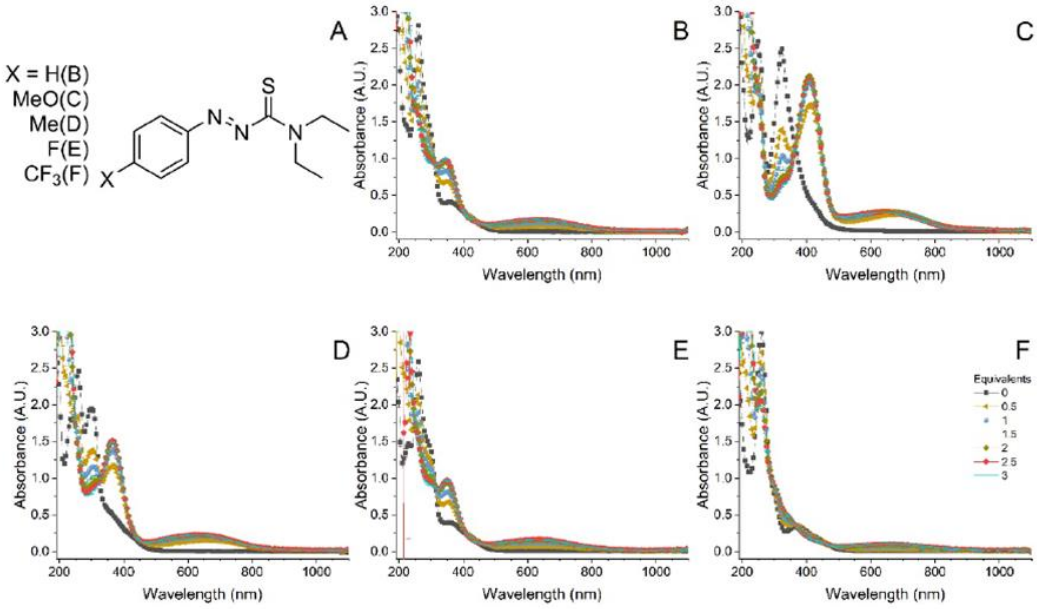

Figure A1.13: ATF ligand uv-vis titration experiments with 0-3 equivalents of cu(I)Br. A) structure and key of ligands; b) 1; c) 5a; d) 5b; e) 5c; f) 5d.

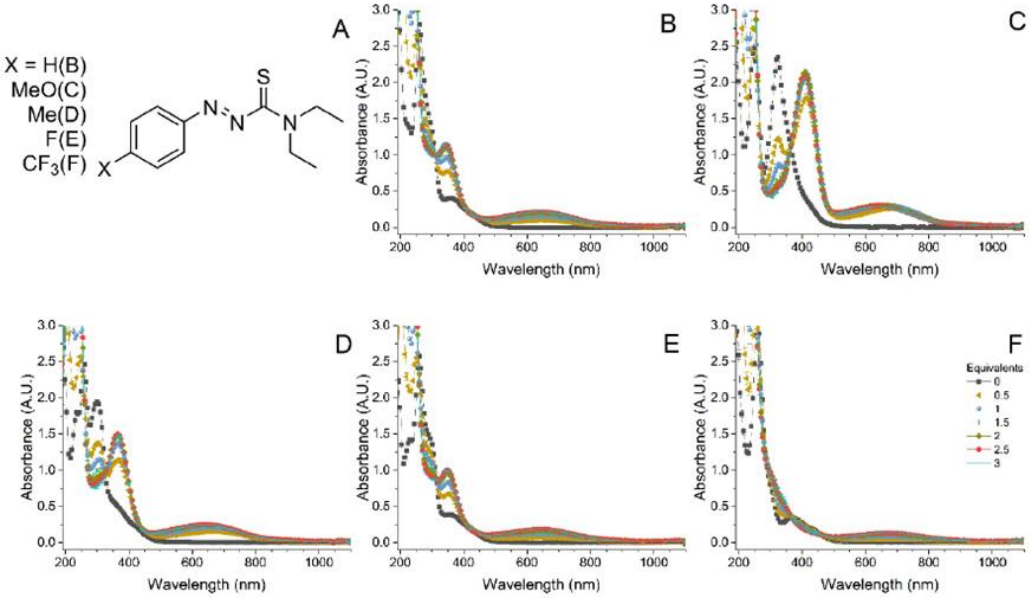

Figure A1.14: ATF ligand UV-vis titration experiments with 0-3 equivalents of cu(I)I. A) structure and key of ligands; b) 1; c) 5a; d) 5b; e) 5c; f) 5d.

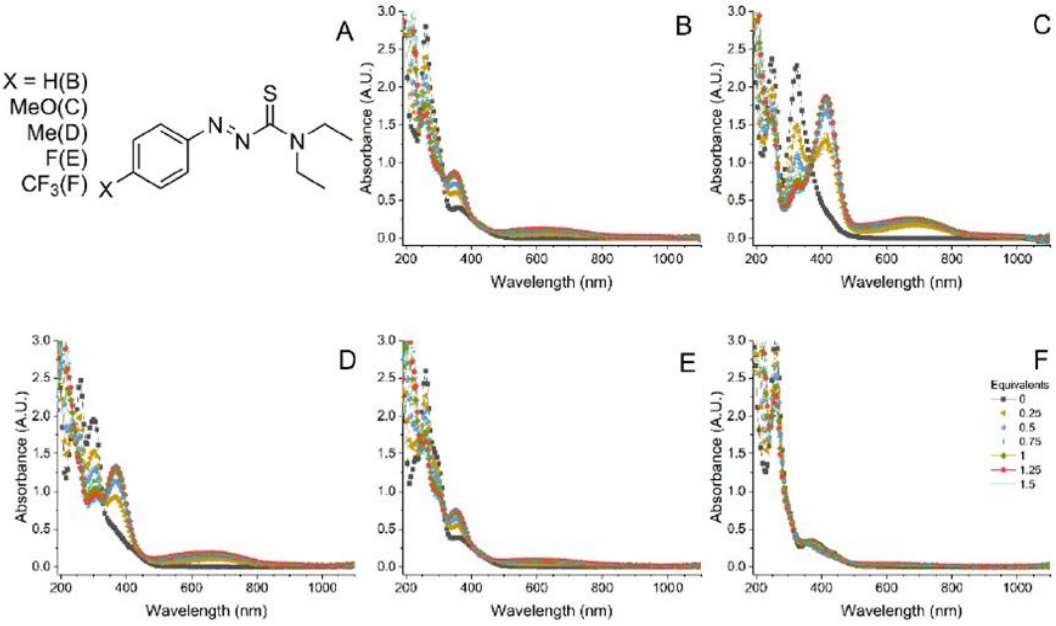

Figure A1.15: ATF ligand UV-vis titration experiments with 0-3 equivalents of $(CH_3CN)4Cu(I)BF_4$. A) structure and key of ligands; b) 1; c) 5a; d) 5b; e) 5c; f) 5d.

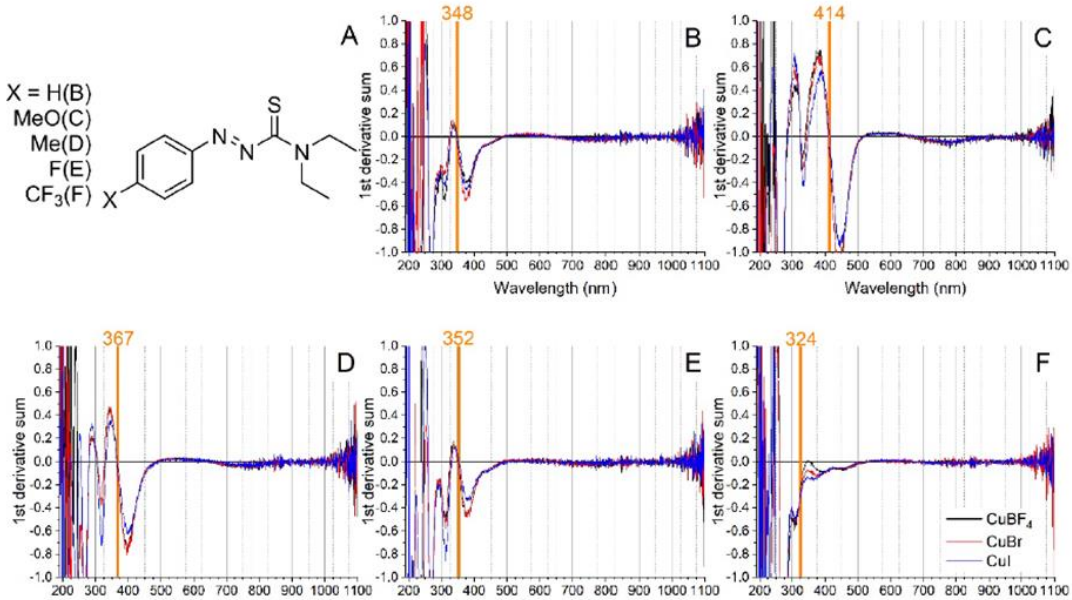

Figure A1.16: Spectral data illustrating the wavelengths chosen for binding comparison utilizing the sum of the first derivative method for the various Cu(I) salts. A) structure and key of ligands; b) 1; c) 5a; d) 5b; e) 5c; f) 5d.

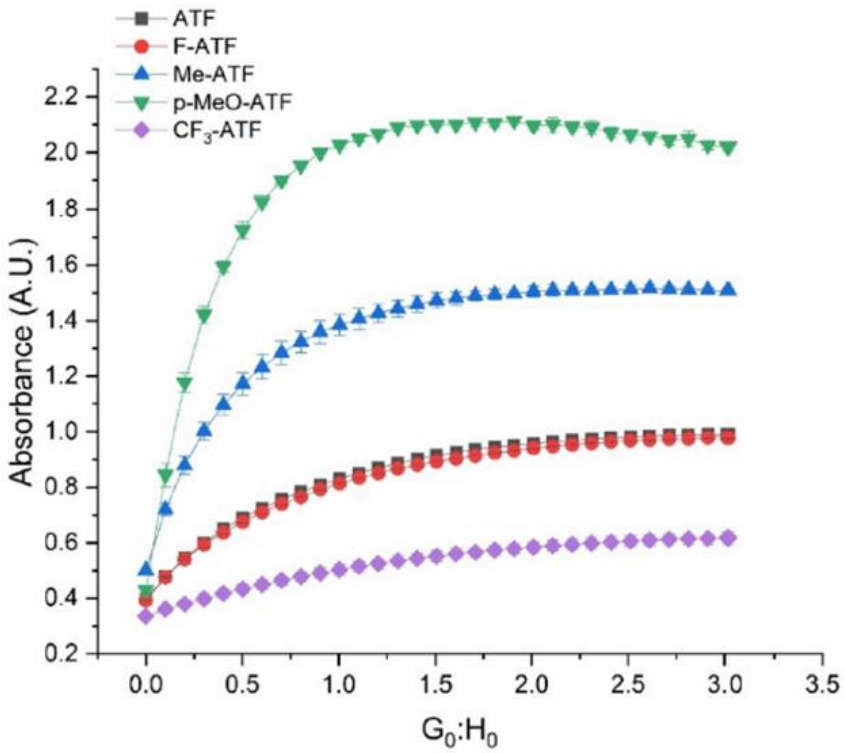

Figure A1.17: Binding isotherms for ligands 1, 5a-d, with copper(I) bromide.

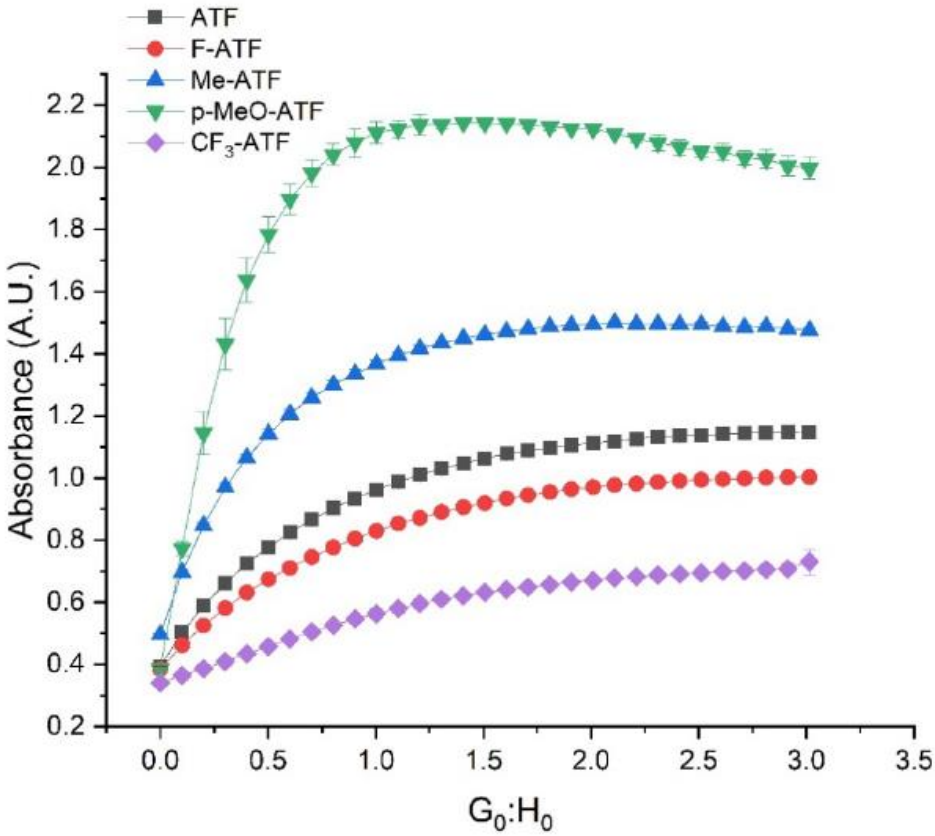

Figure A1.18: Binding isotherms for ligands 1, 5a-d, with copper(I) iodide

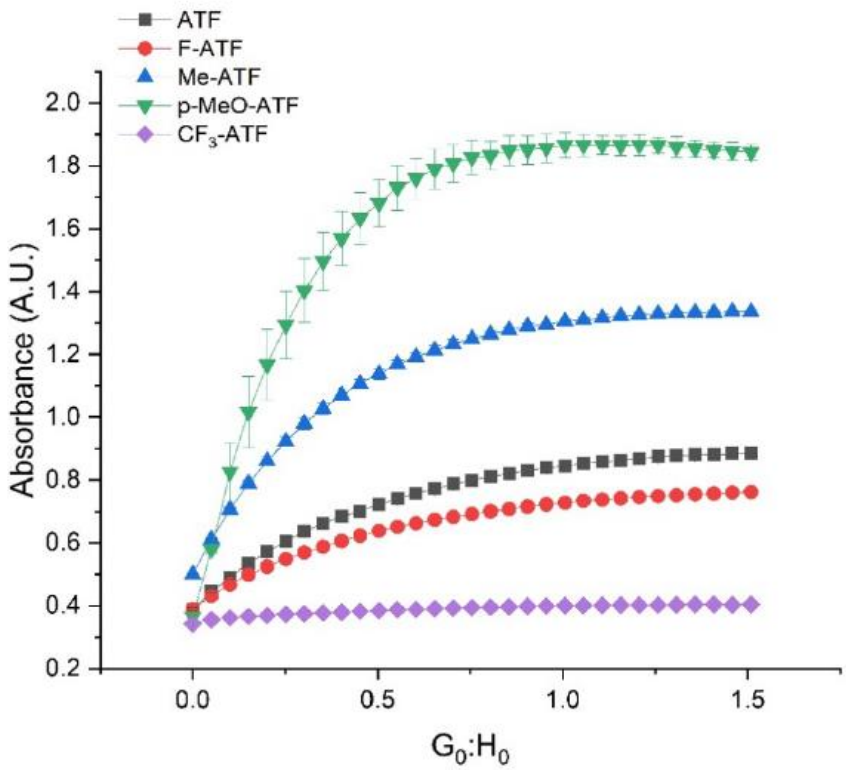

Figure A.19: Binding isotherms for ligands 1, 5a-d, with tetrakis(acetonitrile) Cu(I) tetrafluoroborate.

Table A1.28: H:G models fit with Bindfit

Cu(I) species	Sub.	Ka (M^{-1})	Std Err (M^{-1})	ϵ_{HG} ($M^{-1}cm^{-1}$)	K_{a1i}/K_{aATF}	Std Err
CuBr	ATF	13,350	351	9,697	1.0	0.0
	MeO	277,946	238,003	17,730	20.8	17.8
	Me	67,215	15,289	13,014	5.0	1.1
	F	11,609	352	9,792	0.9	0.0
	CF_3	2,310	11	8,821	0.2	0.0
CuI	ATF	16,834	591	11,153	1.0	0.0
	MeO	343,617	360,854	17,970	20.4	21.4
	Me	68,761	13,253	12,826	4.1	0.8
	F	11,084	158	10,285	0.7	0.0
	CF_3	1,964	31	11,875	0.1	0.0
$(CH_3CN)_4$ $CuBF_4$	ATF	28,151	2,513	9,319	1.0	0.1
	MeO	33,973	9,571	23,778	1.2	0.4
	Me	32,976	5,643	14,774	1.2	0.2
	F	26,379	2,180	7,691	0.9	0.1
	CF_3	25,794	3,514	3,221	0.9	0.2

Appendix II

Supporting Information for Chapter 3: Synthesis of an N,N-diethyl-t-butylazothioformamide ligand and Coordination studies with Copper(I) salts.

General Methods

^{1}H and ^{13}C NMR experiments were performed on a Bruker AVANCE 300 or 500 MHz instrument and samples were obtained in $CDCl_3$ (referenced to 7.28 ppm for ^{1}H and 77.16 ppm for ^{13}C). Coupling constants (*J*) are in Hz. The multiplicities of the signals are described using the following abbreviations: s=singlet, br s=broad singlet, d=doublet, t=triplet, dd=doublet of doublets, dq=doublet of quartets, dsep=doublet of septets; t=triplet of triplets, m=multiplet, app=apparent. Infrared spectra were obtained on a Thermo Scientific Nicolet 380 FT-IR spectrometer as thin films on ZnSe disks and peaks are reported in cm^{-1}. Reaction progress was monitored by thin-layer chromatography on silica gel plates (60-F254), observed under UV light. Column chromatography was performed using silica gel (particle size 40–63 μm). Methyl iodide was purchased from EMD Millipore, t-butylhydrazine hydrochloride was purchased from AK Scientific, N,N-Diethylamine and CS_2 were purchased from Alfa-Aesar and used without further purification. Cu(I) halides were purchased from both Acros and AK Scientific, $(CH_3CN)_4Cu(I)BF_4$ was purchased from Sigma-Aldrich and used without further purification. Acetonitrile (HPLC grade) was purchased from Fischer Scientific. A ThermoFisher Genesys UV-Vis spectrophotometer was utilized with quartz cuvettes for titration experiments.

Synthetic Procedures

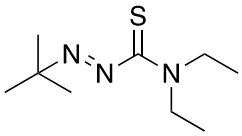

N,N-diethyl-*t*-butylazothioformamide (2): 75 mL of ethanol and t-butyl hydrazine•HCl (5.046 g, 40.5 mmol) was added to a flame-dried round-bottom flask equipped with a magnetic stirrer and allowed to degas for 1.5 hours under nitrogen flow. While under nitrogen, CS_2 (2.8 ml, 46.17 mmol) was added dropwise by needle to the flask and allowed to stir under ambient conditions for 30 minutes. Potassium hydroxide (4.14g, 56.7 mmol) dissolved in 25 mL of degassed ethanol was then added by needle to the flask and allowed to stir under nitrogen for 30 minutes. Methyl iodide (2.82 ml, 45.36 mmol) was then added to the solution and allowed to stir under nitrogen for 1 hour. The resulting liquid was then concentrated with a rotary evaporator. The flask with the resulting paste was then equipped with a condensing column and put under nitrogen flow. 40 mL of diethylamine was added by needle and the solution was allowed to reflux under nitrogen for 48 hours. The solution was cooled to ambient temperatures then opened to air and allowed to stir for 2 hours. The resulting orange liquid was concentrated via rotary evaporator and purified using flash column chromatography 7:3 hexane: ethyl acetate forming 4.36 g (53.5 %) of yellow solid. The resulting solid was subjected to recrystallization using acetonitrile as solvent. ^{1}H NMR (300 MHz, $CDCl_3$) δ 3.92 (q, *J* = 7.2 Hz, 2H), 3.39 (q, *J* = 7.2 Hz, 2H), 1.35 (t, *J* = 7.1 Hz, 3H), 1.30 (s, 9H), 1.11 (t, *J* = 7.2 Hz, 3H). ^{13}C NMR (75 MHz, $CDCl_3$) δ 195.9(C=S), 70.1, 48.7, 45.4, 14.4, 12.2. Elemental Analysis; $C_9H_{19}N_3S$ (201.13); (Calculated) C, 53.58; H, 9.52; N, 20.93. (Found) C, 53.69; H, 9.51; N, 20.87. FTIR (cm^{-1}) = 2976, 1424, 1160, 1090, 830. M.p. 44 ˚C. **CCDC 2034875**.

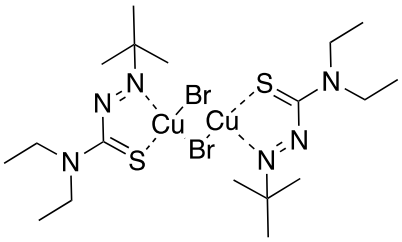

[Cu•2(μ-Br)]$_2$ 3a: Ligand **2** (0.11 g, 0.55 mmol) was dissolved in 5 ml of anhydrous THF and Cu(I)Br (0.079g, 0.55 mmol) was added. The solution was heated to promote solvation and was poured into another vial and allowed to slowly concentrate over 2 d forming dark blue crystals (62%). ^{1}H NMR (300 MHz, $CDCl_3$) δ 4.12 (q, J = 7.3 Hz, 4H), 1.66 (s, 9H), 1.51 – 1.44 (m, 3H), 1.41 – 1.35 (m, 3H). ^{13}C NMR (75 MHz, CDCl3) δ 190.54(C=S), 48.73, 29.73, 15.73, 11.74. Elemental Analysis; $C_{18}H_{38}Br_2Cu_2N_6S_2$ (689.56); (Calculated) C, 31.35; H, 5.55, N, 12.19 (Found); C, 31.35; H, 5.55; N, 12.19. FTIR (cm^{-1}) = 2980, 1432, 1281, 1155, 1094, 780. M. p. 169 ˚C. **CCDC 2034876**

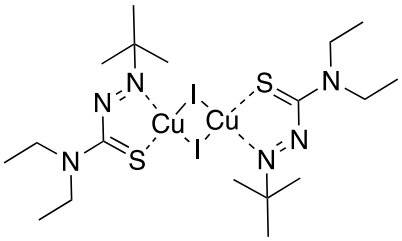

[Cu•2(μ-I)]$_2$ 3b: Anhydrous THF (5 ml) was added to a vial **2** (0.1 g, 0.49 mmol) and Cu(I)I (0.094g ,0.49 mmol). The solution was allowed to concentrate at room temperature over 3-5 d to afford dark blue crystals (55%). ^{1}H NMR (300 MHz, $CDCl_3$) δ 4.06 (q, *J* = 7.1 Hz, 4H), 1.74 (s, 9H), 1.44 (t, *J* = 7.2 Hz, 3H), 1.33 (t, *J* = 7.2 Hz, 3H). ^{13}C NMR (75 MHz, $CDCl_3$) δ 187.69(C=S), 74.78, 50.75, 47.84, 30.65, 15.66, 11.85. Elemental Analysis. $C_{18}H_{38}Cu_2I_2N_6S_2$ (783.56); (Calculated) C, 27.59; H 4.89, N, 10.73 (Found); C, 27.59; H, 4.89; N, 10.73. FTIR (cm^{-1}) = 2878, 1428, 1289, 1155, 1076, 784. M.p. 178 ˚C. **CCDC 2034877**

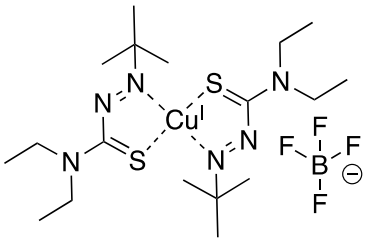

[Cu•2$_2$]BF$_4$ (4): t butyl ATF ligand **2** (0.10 g, 0.49 mmol) and [(CH$_3$CN)$_4$Cu(I)]BF$_4$ (0.075 g, 0.24 mmol) were mixed in 10 ml of THF. After rapid color change from light orange to dark blue, the solution was decanted into another vial and the solvent slowly evaporated at room temperature to afford crystals (69%). ^{1}H NMR (300 MHz, CDCl$_3$) δ 4.22 (q, *J* = 7.4 Hz, 2H), 4.12 (q, *J* = 7.4 Hz, 2H), 1.54 – 1.48 (m, 12H), 1.43 (t, *J* = 7.3 Hz, 3H). ^{13}C NMR (75 MHz, CDCl$_3$) δ 187.14, 74.29, 51.68, 49.42, 29.71, 15.61, 11.49. Elemental Analysis. C$_{18}$H$_{38}$CuBF$_4$N$_6$S$_2$ (553.01); Calculated C, 46.37, H 8.22, N, 18.03 (Found); C, 46.37; H, 8.22; N, 18.03. FTIR (cm^{-1}) = 2983, 1441, 1293, 1102, 1044, 792. M.p. 132 ˚C. **CCDC 2034878.**

^{1}H NMR and ^{13}C NMR Spectra

N,N-diethyl-*t*-butylazothioformamide (2)

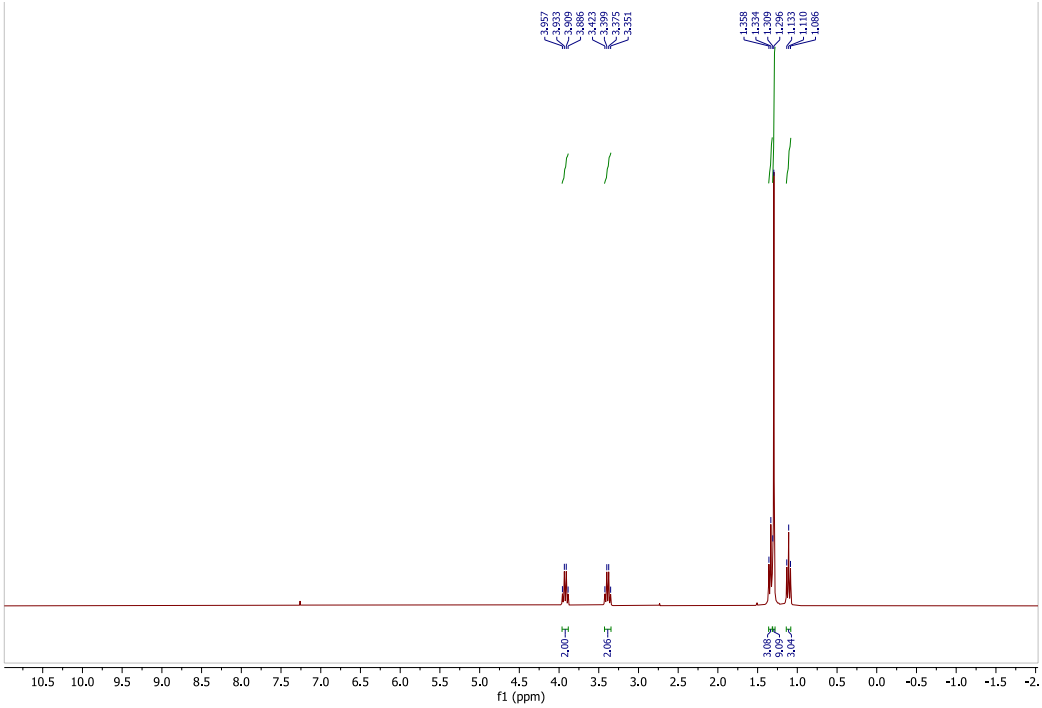

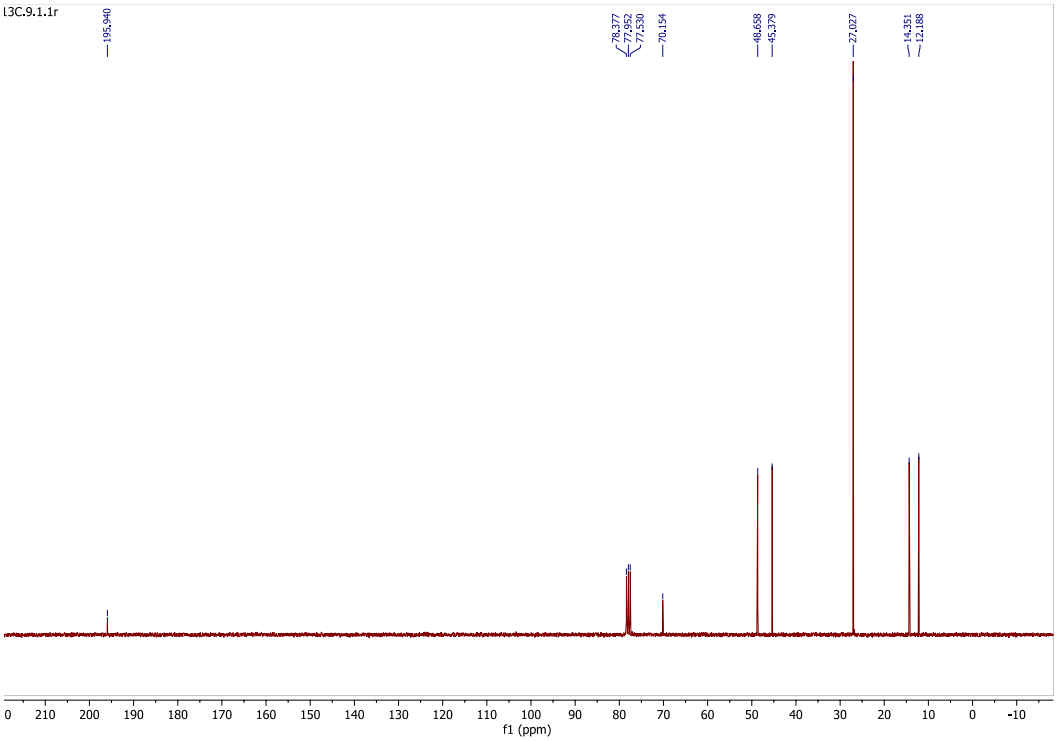

[Cu•2(μ-Br)]$_2$ 3a

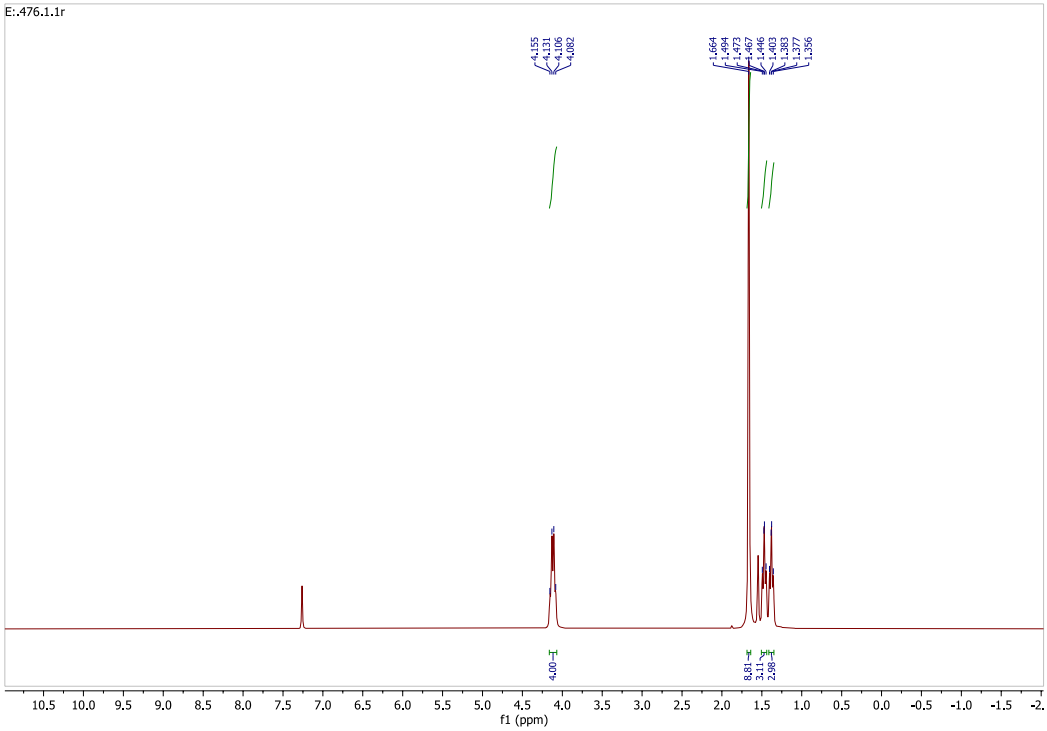
E:.476.1.1r
4.155
4.131
4.106
4.082
1.664
1.494
1.473
1.467
1.446
1.403
1.383
1.377
1.356
4.00
8.81
3.11
2.08
f1 (ppm)

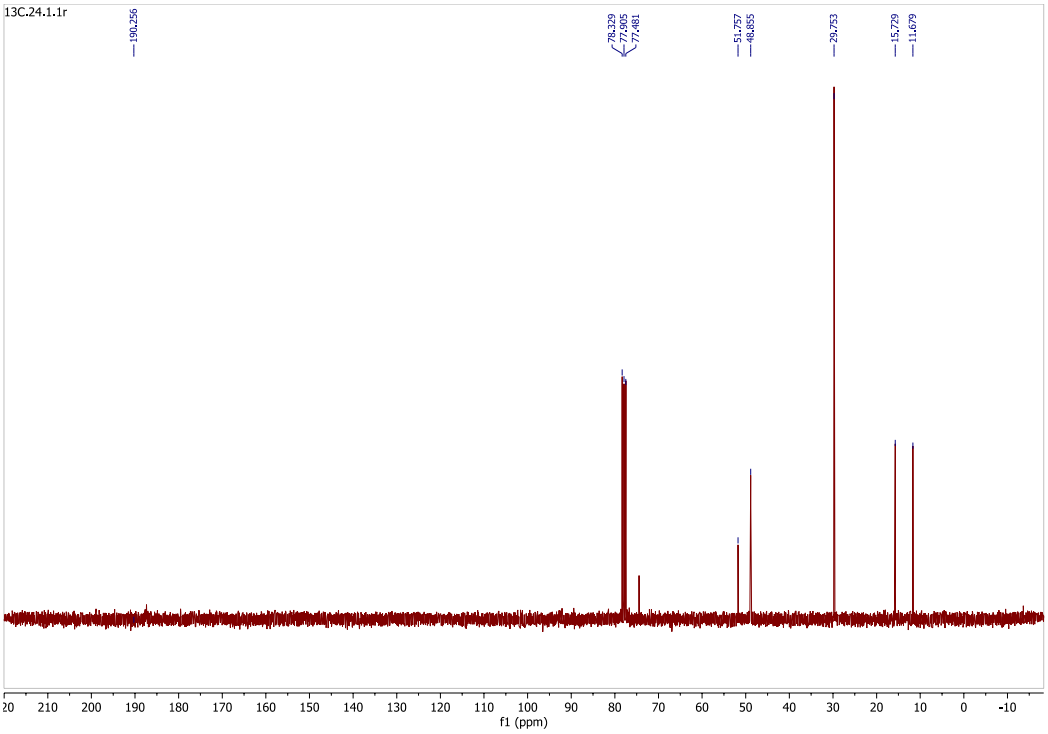
13C.24.1.1r
190.256
78.329
77.905
77.481
51.757
48.855
29.753
15.729
11.679
f1 (ppm)

[Cu•2(μ-I)]$_2$ 3b

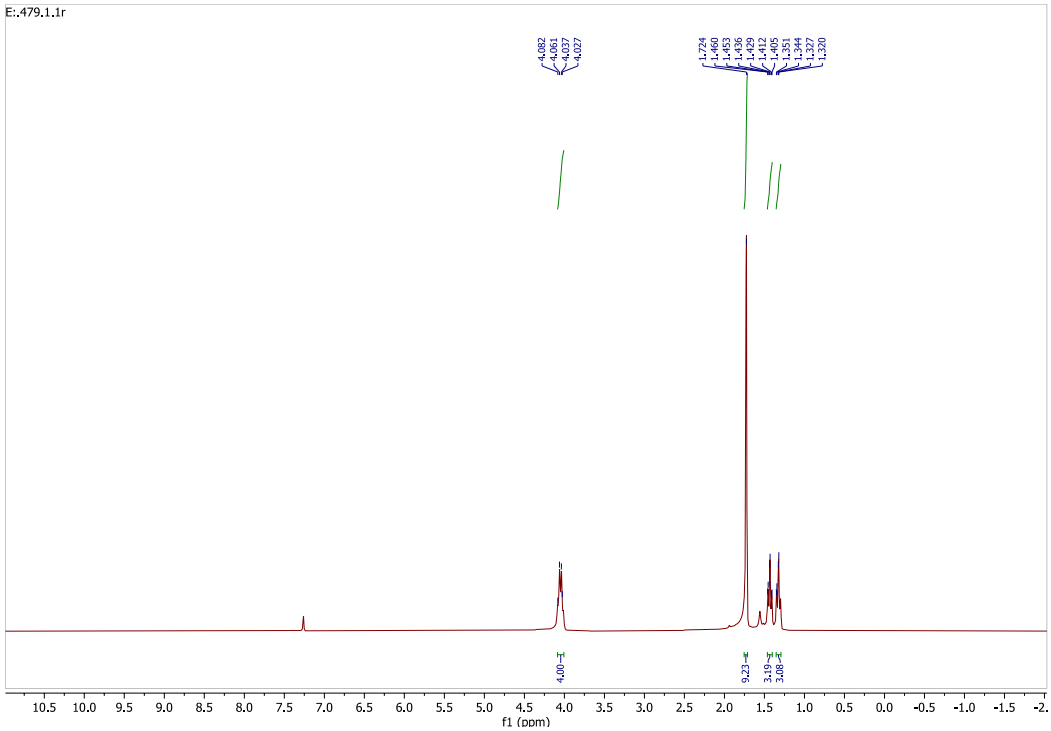
E:.479.1.1r
4.082
4.065
4.037
4.027
1.724
1.460
1.453
1.436
1.429
1.419
1.412
1.405
1.351
1.344
1.327
1.320
4.00
9.23
3.19
3.08
f1 (ppm)

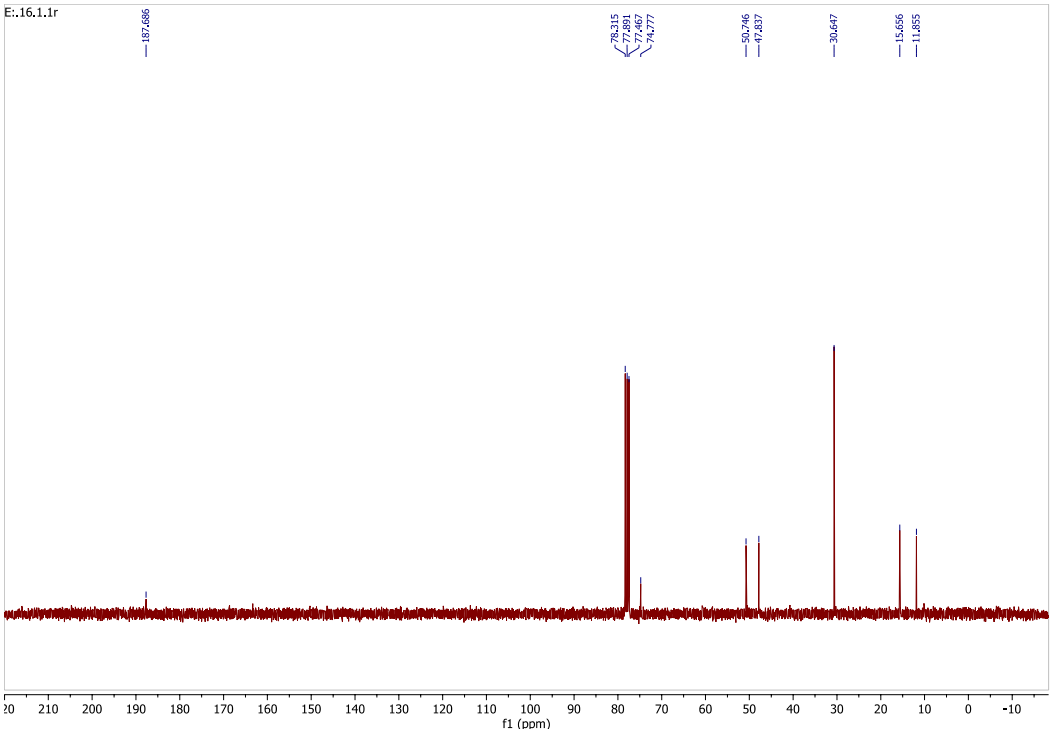
E:.16.1.1r
187.686
78.315
77.891
77.467
74.777
50.746
47.837
30.647
15.656
11.855
f1 (ppm)

[Cu•2$_2$]BF$_4$ (4)

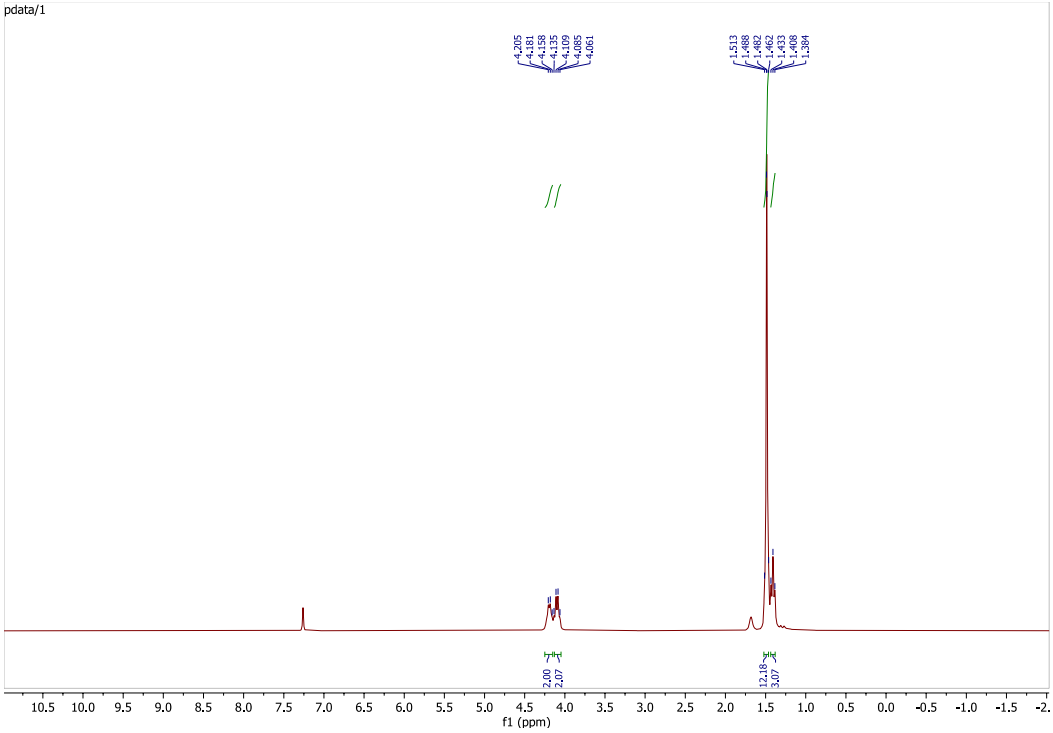
pdata/1
4.205
4.181
4.158
4.135
4.109
4.085
4.061
1.513
1.488
1.482
1.462
1.453
1.408
1.384
2.00
2.07
12.18
3.07
f1 (ppm)

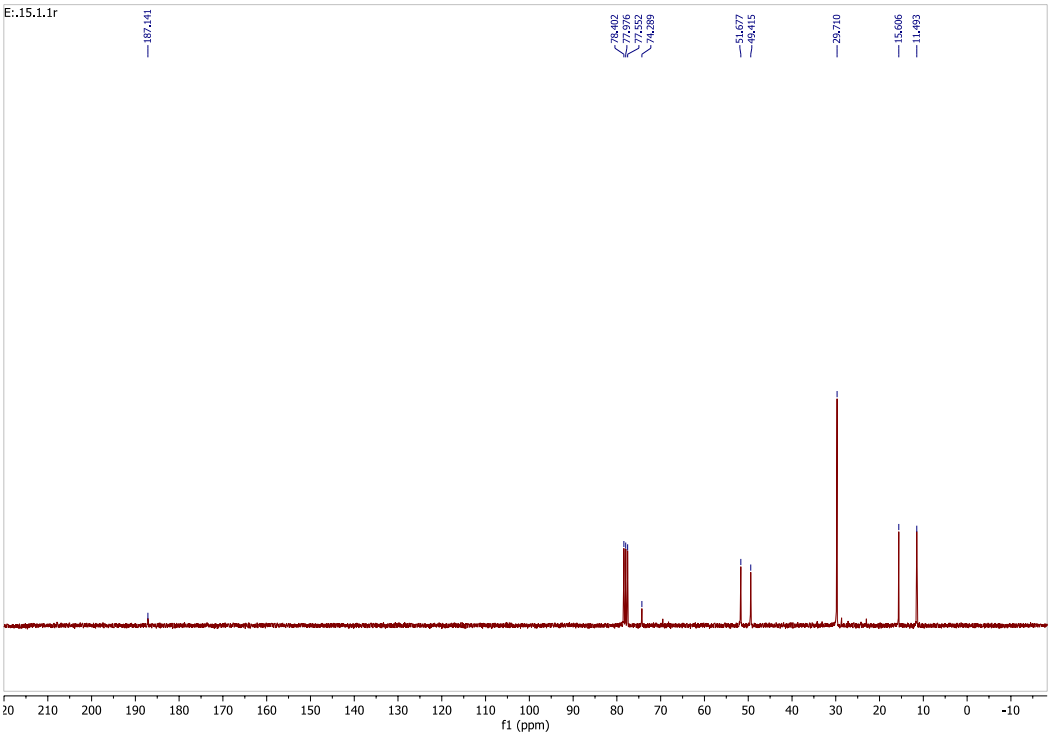
E:.15.1.1r
187.141
78.402
77.976
77.552
74.289
51.677
49.415
29.710
15.606
11.493
f1 (ppm)

X-Ray Crystal structural data

Experimental: Single crystals of **$C_9N_3SH_{19}$**. **N,N-diethyl-*t*-butylazothioformamide** (2), were collected at 298 K on a Bruker D8 Venture using microfocus Mo(Kα)-radiation (λ=0.71073 Å) source. Data have been corrected for absorption using SADABS[1] area detector absorption correction program. Using Olex2[2], the structure was solved with the SHELXT[3] structure solution program using Direct Methods and refined with the SHELXL[4] refinement package using least squares minimization. All non-hydrogen atoms were refined with anisotropic thermal parameters. Hydrogen atoms of the investigated structure were located from different Fourier maps but finally their positions were placed in geometrically calculated positions and refined using a riding model. Calculations and refinement of structures were carried out using APEX3[5], SHELXTL[6], and Olex2 software. The tert-butyl group is disordered due to the free rotation of the methyl groups, which was treated as positional disorders. The occupancies of the corresponding disordered carbon atoms were fixed to be 0.5 using the PART instruction. EADP command was also used to constrain these carbon atoms to have similar anisotropic displacement parameters.

Crystallographic Data for **N,N-diethyl-*t*-butylazothioformamide** (2): $C_9H_{4.5}N_3S$ (M =201.33 g/mol): monoclinic, space group $P2_1/n$ (no. 14), a = 6.8487(6) Å, b = 21.0316(18) Å, c = 8.7303(7) Å, β = 95.504(3)°, V = 1251.71(18) Å^3, Z = 4, T = 273.15 K, μ(MoKα) = 0.226 mm^{-1}, $Dcalc$ = 1.068 g/cm^3, 22025 reflections measured (5.072° ≤ 2Θ ≤ 49.506°), 2131 unique (R_{int} = 0.0296, R_{sigma} = 0.0138) which were used in all calculations. The final R_1 was 0.0678 (I > 2σ(I)) and wR_2 was 0.1822 (all data).

Table A2.1: Crystal data and structure refinement for (2).	
Identification code	C9N3SH19
Empirical formula	$C_9H_{4.5}N_3S$
Formula weight	201.33
Temperature/K	273.15
Crystal system	monoclinic
Space group	$P2_1/n$
a/Å	6.8487(6)
b/Å	21.0316(18)
c/Å	8.7303(7)
α/°	90
β/°	95.504(3)
γ/°	90
Volume/Å^3	1251.71(18)
Z	4
ρ_{calc}g/cm^3	1.068
μ/mm^{-1}	0.226
F(000)	440.0
Crystal size/mm^3	0.57 × 0.44 × 0.34
Radiation	MoKα (λ = 0.71073)

2Θ range for data collection/°	5.072 to 49.506
Index ranges	$-8 \leq h \leq 8$, $-24 \leq k \leq 24$, $-10 \leq l \leq 10$
Reflections collected	22025
Independent reflections	2131 [R_{int} = 0.0296, R_{sigma} = 0.0138]
Data/restraints/parameters	2131/0/123
Goodness-of-fit on F^2	1.084
Final R indexes [I>=2σ (I)]	R_1 = 0.0678, wR_2 = 0.1749
Final R indexes [all data]	R_1 = 0.0765, wR_2 = 0.1822
Largest diff. peak/hole / e $Å^{-3}$	0.44/-0.31

Table A2.2: Fractional Atomic Coordinates ($\times 10^4$) and Equivalent Isotropic Displacement Parameters ($Å^2 \times 10^3$) for N,N-diethyl-*t*-butylazothioformamide (2): U_{eq} is defined as 1/3 of of the trace of the orthogonalised U_{IJ} tensor.

Atom	***x***	***y***	***z***	**U(eq)**
S1	2960.8(12)	6010.1(5)	8259.9(9)	73.7(4)
N1	3191(4)	6418.1(13)	4788(3)	70.7(7)
N2	4318(4)	6570.6(12)	5833(3)	65.2(7)
N3	6358(3)	5797.4(11)	7089(3)	54.2(6)
C1	4631(4)	6081.1(13)	7033(3)	52.0(7)
C2	2809(5)	6933.4(15)	3604(3)	68.6(9)
C3A	3530(20)	7569(5)	4009(12)	122.0(16)
C3B	4584(19)	7358(5)	3404(12)	122.0(16)

C4A	3543(19)	6664(6)	2150(12)	122.0(16)
C4B	2169(19)	6570(5)	2206(12)	122.0(16)
C5A	523(18)	6981(5)	3375(12)	122.0(16)
C5B	1216(19)	7343(5)	4131(12)	122.0(16)
C6	7765(5)	5909.9(16)	5946(4)	66.6(8)
C7	7520(6)	5437(2)	4635(4)	89.6(11)
C8	6968(5)	5346.5(15)	8340(4)	67.3(8)
C9	7918(5)	5677.5(18)	9748(4)	78.2(10)

Table A2.3: Anisotropic Displacement Parameters ($Å^2 \times 10^3$) for N,N-diethyl-*t*-butyl azothioformamide (2). The Anisotropic displacement factor exponent takes the form: $-2\pi^2[h^2a^{*2}U_{11}+2hka^*b^*U_{12}+\ldots]$.

Atom	U_{11}	U_{22}	U_{33}	U_{23}	U_{13}	U_{12}
S1	62.5(5)	104.0(7)	55.7(5)	12.2(4)	10.7(4)	7.1(4)
N1	83.3(18)	71.2(17)	55.9(15)	-1.4(12)	-2.7(13)	-3.6(14)
N2	69.3(16)	70.2(16)	55.0(14)	-3.7(12)	0.5(12)	-2.7(13)
N3	53.5(13)	58.3(13)	49.9(13)	4.2(10)	0.3(10)	1.6(10)
C1	58.6(16)	54.5(15)	41.7(14)	2.5(11)	-2.1(11)	-0.9(12)
C2	95(2)	59.1(18)	49.9(16)	10.1(13)	-2.8(15)	4.9(16)
C3A	162(5)	107(3)	93(3)	31(2)	-8(3)	9(3)
C3B	162(5)	107(3)	93(3)	31(2)	-8(3)	9(3)
C4A	162(5)	107(3)	93(3)	31(2)	-8(3)	9(3)

C4B	162(5)	107(3)	93(3)	31(2)	-8(3)	9(3)
C5A	162(5)	107(3)	93(3)	31(2)	-8(3)	9(3)
C5B	162(5)	107(3)	93(3)	31(2)	-8(3)	9(3)
C6	53.6(17)	79(2)	67.3(19)	-2.0(15)	7.3(14)	-4.4(14)
C7	88(3)	106(3)	77(2)	-18(2)	21.7(19)	3(2)
C8	67.9(19)	61.8(17)	70.7(19)	11.9(15)	-1.0(15)	11.0(15)
C9	74(2)	96(2)	62.3(19)	16.2(17)	-9.2(16)	0.9(18)

Table A2.4: Bond Lengths for N,N-diethyl-*t*-butylazothioformamide (2).

Atom	**Atom**	**Length/Å**		**Atom**	**Atom**	**Length/Å**
S1	C1	1.647(3)		C2	C3B	1.532(13)
N1	N2	1.182(3)		C2	C4A	1.519(12)
N1	C2	1.503(4)		C2	C4B	1.471(11)
N2	C1	1.470(3)		C2	C5A	1.563(12)
N3	C1	1.321(4)		C2	C5B	1.497(12)
N3	C6	1.471(4)		C6	C7	1.513(5)
N3	C8	1.476(3)		C8	C9	1.505(4)
C2	C3A	1.457(12)				

Table A2.5: Bond Angles for N,N-diethyl-*t*-butylazothioformamide (2).

Atom	Atom	Atom	Angle/°		Atom	Atom	Atom	Angle/°
N2	N1	C2	113.1(3)		C3A	C2	N1	117.5(4)
N1	N2	C1	113.6(3)		C3A	C2	C4A	114.4(7)
C1	N3	C6	123.0(2)		C3A	C2	C5A	106.5(7)
C1	N3	C8	120.4(2)		C4A	C2	C5A	108.9(7)
C6	N3	C8	116.6(2)		C4B	C2	N1	102.3(4)
N2	C1	S1	117.6(2)		C4B	C2	C3B	112.7(7)
N3	C1	S1	127.6(2)		C4B	C2	C5B	112.7(7)
N3	C1	N2	114.3(2)		C5B	C2	N1	106.7(4)
N1	C2	C3B	114.3(4)		C5B	C2	C3B	108.0(7)
N1	C2	C4A	104.8(5)		N3	C6	C7	112.0(3)
N1	C2	C5A	103.9(4)		N3	C8	C9	112.1(3)

Table A2.6: Torsion Angles for N,N-diethyl-*t*-butylazothioformamide (2).

A	B	C	D	Angle/°		A	B	C	D	Angle/°
N1	N2	C1	S1	-79.3(3)		C1	N3	C8	C9	-86.2(3)
N1	N2	C1	N3	107.9(3)		C2	N1	N2	C1	177.3(2)
N2	N1	C2	C3A	-11.4(8)		C6	N3	C1	S1	-178.3(2)
N2	N1	C2	C3B	33.6(6)		C6	N3	C1	N2	-6.4(4)

N2	N1	C2	C4A	116.9(6)		C6	N3	C8	C9	93.5(3)
N2	N1	C2	C4B	155.6(6)		C8	N3	C1	S1	1.4(4)
N2	N1	C2	C5A	-128.8(5)		C8	N3	C1	N2	173.3(2)
N2	N1	C2	C5B	-85.7(6)		C8	N3	C6	C7	88.1(3)
C1	N3	C6	C7	-92.2(4)						

Table A2.7: Hydrogen Atom Coordinates (Å×10^4) and Isotropic Displacement Parameters (Å^2×10^3) for N,N-diethyl-*t*-butylazothioformamide (2).

Atom	***x***	***y***	***z***	**U(eq)**
H3AA	2933	7718	4894	183
H3AB	3203	7852	3161	183
H3AC	4928	7556	4240	183
H3BA	5068	7534	4382	183
H3BB	4199	7697	2701	183
H3BC	5596	7110	3004	183
H4AA	2978	6899	1275	183
H4AB	3168	6226	2042	183
H4AC	4946	6698	2214	183
H4BA	3053	6221	2105	183
H4BB	2167	6842	1323	183
H4BC	870	6409	2278	183

H5AA	23	7045	4353	183
H5AB	-8	6595	2920	183
H5AC	149	7333	2709	183
H5BA	1741	7602	4979	183
H5BB	188	7079	4453	183
H5BC	699	7612	3300	183
H6A	9089	5880	6446	80
H6B	7583	6337	5538	80
H7A	8474	5522	3925	134
H7B	6225	5476	4115	134
H7C	7704	5014	5034	134
H8A	7883	5042	7978	81
H8B	5828	5114	8612	81
H9A	9046	5909	9484	117
H9B	8315	5368	10524	117
H9C	6999	5967	10135	117

Table A2.8: Atomic Occupancy for N,N-diethyl-t-butylazothioformamide (2).

Atom	**Occupancy**		**Atom**	**Occupancy**		**Atom**	**Occupancy**
C3A	0.5		H3AA	0.5		H3AB	0.5

H3AC	0.5		C3B	0.5		H3BA	0.5
H3BB	0.5		H3BC	0.5		C4A	0.5
H4AA	0.5		H4AB	0.5		H4AC	0.5
C4B	0.5		H4BA	0.5		H4BB	0.5
H4BC	0.5		C5A	0.5		H5AA	0.5
H5AB	0.5		H5AC	0.5		C5B	0.5
H5BA	0.5		H5BB	0.5		H5BC	0.5

[Cu•2(μ-Br)]$_2$ (3a) CCDC 2034876: X-ray diffraction data for **[Cu•2(μ-Br)]$_2$** (3a) was collected at 105 K on a Bruker D8 Venture using MoKα-radiation (λ=0.71073 Å). Data have been corrected for absorption using SADABS[1] area detector absorption correction program. Using Olex2[2], the structure was solved with the SHELXT[3] structure solution program using Direct Methods and refined with the SHELXL[4] refinement package using least squares minimization. All non-hydrogen atoms were refined with anisotropic thermal parameters. Hydrogen atoms of the investigated structure were located from difference Fourier maps but finally their positions were placed in geometrically calculated positions and refined using a riding model. Isotropic thermal parameters of the placed hydrogen atoms were fixed to 1.2 times the *U* value of the atoms they are linked to (1.5 times for methyl groups). Calculations and refinement of structures were carried out using APEX3[5], SHELXTL[6], and Olex2 software.

Crystallographic Data for **[Cu•2(μ-Br)]$_2$** (3a) $C_{18}H_{38}Br_2Cu_2N_6S_2$ (M =689.56 g/mol): monoclinic, space group $P2_1/c$ (no. 14), a = 10.4646(4) Å, b = 9.9481(4) Å, c = 14.1626(5) Å, β = 110.5340(10)°, V = 1380.69(9) Å^3, Z = 2, T = 105 K, μ(MoKα) = 4.602

mm^{-1}, *Dcalc* = 1.659 g/cm^3, 2Θmax = 57.4°, 77945 reflections collected, 3574 unique (R_{int} = 0.0275, R_{sigma}= 0.0090), R_1 = 0.0168 (I > 2σ(I)), wR_2 = 0.0410 (all data).

Table A2.9: Crystal data and structure refinement for $[Cu•2(\mu\text{-}Br)]_2$ (3a)	
Identification code	**$[Cu•2(\mu\text{-}Br)]_2$** (3a)
Empirical formula	$C_{18}H_{38}Br_2Cu_2N_6S_2$
Formula weight	689.56
Temperature/K	105
Crystal system	monoclinic
Space group	$P2_1/c$
a/Å	10.4646(4)
b/Å	9.9481(4)
c/Å	14.1626(5)
α/°	90
β/°	110.5340(10)
γ/°	90
Volume/$Å^3$	1380.69(9)
Z	2
ρ_{calc}g/cm^3	1.659
μ/mm^{-1}	4.602
F(000)	696.0

Crystal size/mm^3	0.26 × 0.18 × 0.05
Radiation	MoKα (λ = 0.71073)
2Θ range for data collection/°	5.836 to 57.4
Index ranges	$-14 \leq h \leq 14$, $-13 \leq k \leq 13$, $-19 \leq l \leq 19$
Reflections collected	77945
Independent reflections	3574 [R_{int} = 0.0275, R_{sigma} = 0.0090]
Data/restraints/parameters	3574/0/141
Goodness-of-fit on F^2	1.080
Final R indexes [I>=2σ (I)]	R_1 = 0.0168, wR_2 = 0.0399
Final R indexes [all data]	R_1 = 0.0196, wR_2 = 0.0410
Largest diff. peak/hole / e $Å^{-3}$	0.83/-0.39

Table A2.10: Fractional Atomic Coordinates ($\times 10^4$) and Equivalent Isotropic Displacement Parameters ($Å^2 \times 10^3$) for $[Cu \bullet 2(\mu\text{-}Br)]_2$ (3a). U_{eq} is defined as 1/3 of of the trace of the orthogonalised U_{IJ} tensor.

Atom	***x***	***y***	***z***	**U(eq)**
Br1	3827.3(2)	6512.9(2)	4772.3(2)	20.27(4)
Cu1	6003.9(2)	5697.6(2)	5932.1(2)	15.63(4)
S1	7756.1(3)	7256.4(3)	6183.5(2)	15.91(7)
N1	6569.2(10)	5773.7(10)	7442.7(8)	11.34(19)
N2	7498.3(10)	6529.6(10)	7975.7(8)	11.43(19)
N3	8811.8(11)	8384.3(10)	8008.2(8)	12.71(19)

C1	8039.6(12)	7437.2(12)	7418.4(9)	11.2(2)
C2	6107.9(13)	4773.7(12)	8055.2(9)	14.3(2)
C3	7018.5(17)	3542.1(14)	8144.7(12)	26.4(3)
C4	6238(2)	5317.1(16)	9089.5(12)	31.1(4)
C5	4632.4(15)	4435.3(17)	7441.2(13)	30.1(3)
C6	8925.6(13)	8567.9(13)	9073.5(9)	15.4(2)
C7	10110.3(14)	7775.5(15)	9788.6(10)	21.5(3)
C8	9564.9(14)	9350.9(13)	7614.2(11)	18.4(3)
C9	8708.1(16)	10585.4(14)	7165.3(12)	24.9(3)

Table A2.11: Anisotropic Displacement Parameters ($Å^2 \times 10^3$) for $[Cu \bullet 2(\mu\text{-}Br)]_2$ (3a). The Anisotropic displacement factor exponent takes the form: $-2\pi^2[h^2a^{*2}U_{11}+2hka^*b^*U_{12}+\ldots]$.

Atom	**U_{11}**	**U_{22}**	**U_{33}**	**U_{23}**	**U_{13}**	**U_{12}**
Br1	17.53(7)	20.91(7)	17.56(7)	-7.08(5)	0.13(5)	6.04(5)
Cu1	15.65(8)	17.29(8)	11.35(7)	-3.39(6)	1.49(6)	-2.07(6)
S1	18.23(15)	19.70(15)	11.11(13)	-0.14(11)	6.79(11)	-4.01(12)
N1	11.1(4)	10.6(4)	12.9(5)	-1.0(4)	4.9(4)	-0.1(4)
N2	11.5(5)	11.4(5)	11.3(4)	0.6(4)	3.8(4)	-0.8(4)
N3	11.7(5)	12.7(5)	13.6(5)	0.1(4)	4.2(4)	-2.5(4)
C1	9.1(5)	11.5(5)	12.7(5)	1.3(4)	3.5(4)	0.7(4)
C2	17.1(6)	12.3(5)	15.7(6)	0.3(4)	8.4(5)	-3.4(4)

C3	35.9(8)	19.0(7)	29.6(8)	10.7(6)	18.3(7)	8.3(6)
C4	55.6(11)	25.2(7)	23.9(7)	-6.7(6)	28.0(7)	-16.9(7)
C5	19.0(7)	34.7(8)	35.8(8)	5.6(7)	8.7(6)	-10.7(6)
C6	15.5(6)	16.2(6)	13.1(6)	-4.2(4)	3.4(5)	-3.6(5)
C7	15.9(6)	30.7(7)	15.2(6)	-0.2(5)	2.3(5)	-0.4(5)
C8	16.1(6)	16.8(6)	23.3(6)	0.1(5)	8.3(5)	-6.8(5)
C9	26.4(7)	17.3(6)	29.4(7)	5.9(6)	7.9(6)	-5.6(5)

Table A2.12: Bond Lengths for $[Cu{\bullet}2(\mu\text{-}Br)]_2$ (3a).

Atom	**Atom**	**Length/Å**		**Atom**	**Atom**	**Length/Å**
Br1	Cu1	2.4329(2)		N3	C1	1.3285(16)
Br1	Cu1[1]	2.4466(2)		N3	C6	1.4825(16)
Cu1	Br1[1]	2.4466(2)		N3	C8	1.4715(16)
Cu1	S1	2.3314(4)		C2	C3	1.5298(19)
Cu1	N1	2.0111(10)		C2	C4	1.5220(18)
S1	C1	1.6778(12)		C2	C5	1.5204(19)
N1	N2	1.2514(14)		C6	C7	1.5177(18)
N1	C2	1.5063(15)		C8	C9	1.522(2)
N2	C1	1.4396(15)				

[1]1-X,1-Y,1-Z

Table A2.13: Bond Angles for [Cu•2(μ-Br)]$_2$ (3a).

Atom	Atom	Atom	Angle/°		Atom	Atom	Atom	Angle/°
Cu1	Br1	Cu1[1]	77.955(7)		C1	N3	C8	120.91(11)
Br1	Cu1	Br1[1]	102.045(7)		C8	N3	C6	116.28(10)
S1	Cu1	Br1[1]	119.652(11)		N2	C1	S1	123.00(9)
S1	Cu1	Br1	112.412(11)		N3	C1	S1	125.27(9)
N1	Cu1	Br1[1]	115.55(3)		N3	C1	N2	111.69(10)
N1	Cu1	Br1	124.20(3)		N1	C2	C3	105.10(10)
N1	Cu1	S1	83.71(3)		N1	C2	C4	112.40(10)
C1	S1	Cu1	94.16(4)		N1	C2	C5	106.45(11)
N2	N1	Cu1	122.73(8)		C4	C2	C3	111.20(12)
N2	N1	C2	112.81(10)		C5	C2	C3	110.38(12)
C2	N1	Cu1	123.62(8)		C5	C2	C4	111.06(12)
N1	N2	C1	114.71(10)		N3	C6	C7	111.74(10)
C1	N3	C6	122.77(10)		N3	C8	C9	111.74(11)

[1]1-X,1-Y,1-Z

Table A2.14: Hydrogen Atom Coordinates (Å×10^4) and Isotropic Displacement Parameters (Å^2×10^3) for [Cu•2(μ-Br)]$_2$ (3a).

Atom	*x*	*y*	*z*	U(eq)
H3A	6933	3228	7469	40

H3B	6735	2825	8503	40
H3C	7970	3784	8519	40
H4A	7199	5511	9474	47
H4B	5899	4646	9450	47
H4C	5701	6144	9010	47
H5A	4074	5250	7343	45
H5B	4294	3762	7801	45
H5C	4578	4075	6784	45
H6A	8067	8272	9155	18
H6B	9054	9534	9249	18
H7A	9943	6812	9661	32
H7B	10199	7976	10486	32
H7C	10954	8027	9681	32
H8A	9842	8908	7090	22
H8B	10404	9634	8167	22
H9A	7889	10311	6606	37
H9B	9243	11208	6916	37
H9C	8441	11032	7685	37

[Cu•2(μ-I)]$_2$ 3b CCDC 203487: Single crystals of $C_{18}H_{38}Cu_2I_2N_6S_2$ **[Cu•2(μ-I)]$_2$** 3b were collected at 298 K on a Bruker D8 Venture using microfocus Mo(Kα)-radiation (λ=0.71073 Å) source. Data have been corrected for absorption using SADABS[1] area detector absorption correction program. Using Olex2[2], the structure was solved with the SHELXT[3] structure solution program using Direct Methods and refined with the SHELXL[4] refinement package using least squares minimization. All non-hydrogen atoms were refined with anisotropic thermal parameters. Hydrogen atoms of the investigated structure were located from difference Fourier maps but finally their positions were placed in geometrically calculated positions and refined using a riding model. Calculations and refinement of structures were carried out using APEX3[5], SHELXTL[6], and Olex2 software.

Crystallographic Data for **[Cu•2(μ-I)]$_2$** 3b: $C_{18}H_{38}Cu_2I_2N_6S_2$ (M =783.58 g/mol): triclinic, space group P-1 (no. 2), a = 8.3789(6) Å, b = 9.8569(8) Å, c = 10.6800(9) Å, α = 63.012(2)°, β = 73.508(2)°, γ = 73.054(2)°, V = 739.89(10) Å^3, Z = 1, T = 273.15 K, μ(Mo Kα) = 3.680 mm^{-1}, *Dcalc* = 1.7585 g/cm^3, 28466 reflections measured (4.34° ≤ 2Θ ≤ 49.56°), 2544 unique (R_{int} = 0.0428, R_{sigma} = 0.0180) which were used in all calculations. The final R_1 was 0.0299 (I>=2u(I)) and wR_2 was 0.0601 (all data).

Table A2.15: Crystal data and structure refinement for [Cu•2(μ-I)]$_2$ (3b).

Identification code	**[Cu•2(μ-I)]$_2$** (3b)
Empirical formula	$C_{18}H_{38}Cu_2I_2N_6S_2$
Formula weight	783.58
Temperature/K	273.15

Crystal system	triclinic
Space group	P-1
a/Å	8.3789(6)
b/Å	9.8569(8)
c/Å	10.6800(9)
α/°	63.012(2)
β/°	73.508(2)
γ/°	73.054(2)
Volume/$Å^3$	739.89(10)
Z	1
ρ_{calc}g/cm^3	1.7585
μ/mm^{-1}	3.680
F(000)	384.2
Crystal size/mm^3	0.3 × 0.2 × 0.15
Radiation	Mo Kα (λ = 0.71073)
2Θ range for data collection/°	4.34 to 49.56
Index ranges	$-9 \leq h \leq 9$, $-11 \leq k \leq 11$, $-12 \leq l \leq 12$
Reflections collected	28466
Independent reflections	2544 [R_{int} = 0.0428, R_{sigma} = 0.0180]
Data/restraints/parameters	2544/0/141

Goodness-of-fit on F^2	1.044
Final R indexes [I>=2σ (I)]	R_1 = 0.0299, wR_2 = 0.0538
Final R indexes [all data]	R_1 = 0.0385, wR_2 = 0.0601
Largest diff. peak/hole / e $Å^{-3}$	0.80/-0.56

Table A2.16: Fractional Atomic Coordinates ($\times 10^4$) and Equivalent Isotropic Displacement Parameters ($Å^2 \times 10^3$) for $[Cu \bullet 2(\mu\text{-}I)]_2$ (3b). U_{eq} is defined as 1/3 of of the trace of the orthogonalised U_{IJ} tensor.

Atom	***x***	***y***	***z***	**U(eq)**
I1	3173.6(4)	10702.0(4)	6558.1(3)	56.57(11)
Cu1	4877.8(8)	8334.8(6)	5953.8(6)	55.19(17)
S1	6417.8(16)	6240.0(14)	7585.5(14)	57.1(3)
N1	3504(4)	6690(4)	6375(4)	42.3(8)
N2	3871(5)	5312(4)	7210(4)	48.2(9)
N3	5627(5)	3441(4)	8715(4)	49.1(9)
C1	5320(5)	4938(5)	7857(4)	43.7(10)
C2	1903(6)	7025(5)	5825(5)	51.8(11)
C3	1680(8)	5670(7)	5632(8)	92(2)
C4	482(6)	7419(7)	6935(6)	77.0(16)
C5	2002(7)	8445(7)	4419(6)	77.6(17)
C6	4673(7)	2312(5)	8851(6)	62.1(13)
C7	3142(7)	2148(7)	10021(6)	78.8(17)

C8	6948(6)	2825(6)	9588(5)	62.9(13)
C9	8635(7)	2248(7)	8841(7)	87.0(19)

Table A2.17: Anisotropic Displacement Parameters ($Å^2 \times 10^3$) for $[Cu \bullet 2(\mu\text{-}I)]_2$ (3b). The Anisotropic displacement factor exponent takes the form: $-2\pi^2[h^2a^{*2}U_{11}+2hka^*b^*U_{12}+\ldots]$.

Atom	**U_{11}**	**U_{22}**	**U_{33}**	**U_{12}**	**U_{13}**	**U_{23}**
I1	67.2(2)	42.19(17)	54.07(19)	-16.55(14)	-1.71(15)	-15.81(14)
Cu1	59.1(4)	40.7(3)	60.1(4)	-15.4(3)	-10.5(3)	-12.0(3)
S1	55.7(7)	47.1(7)	67.4(8)	-18.3(6)	-21.6(6)	-11.0(6)
N1	38.0(19)	38(2)	50(2)	-7.7(15)	-7.0(16)	-17.5(17)
N2	48(2)	38(2)	57(2)	-10.0(17)	-13.1(18)	-15.1(18)
N3	53(2)	38(2)	49(2)	-10.2(17)	-8.6(17)	-10.7(17)
C1	43(2)	40(2)	44(2)	-9.8(19)	-6.2(19)	-14(2)
C2	45(3)	48(3)	63(3)	-7(2)	-18(2)	-19(2)
C3	100(5)	74(4)	135(6)	-8(3)	-61(4)	-50(4)
C4	46(3)	82(4)	99(4)	-14(3)	-7(3)	-35(4)
C5	63(4)	83(4)	76(4)	-12(3)	-32(3)	-13(3)
C6	74(3)	36(2)	74(3)	-13(2)	-16(3)	-17(2)
C7	78(4)	69(4)	90(4)	-40(3)	-1(3)	-25(3)
C8	62(3)	56(3)	54(3)	-10(2)	-20(2)	-3(2)
C9	64(4)	86(4)	96(5)	4(3)	-28(3)	-27(4)

Table A2.18: Bond Lengths for [Cu•2(μ-I)]$_2$ (3b).

Atom	Atom	Length/Å		Atom	Atom	Length/Å
I1	Cu1	2.6079(7)		N3	C1	1.330(5)
I1	Cu1[1]	2.6209(7)		N3	C6	1.484(6)
Cu1	Cu1[1]	3.0089(11)		N3	C8	1.464(6)
Cu1	S1	2.3288(13)		C2	C3	1.510(7)
Cu1	N1	2.071(3)		C2	C4	1.523(7)
S1	C1	1.667(4)		C2	C5	1.520(7)
N1	N2	1.244(5)		C6	C7	1.503(7)
N1	C2	1.505(5)		C8	C9	1.504(7)
N2	C1	1.439(5)				

[1]1-X,2-Y,1-Z

Table A2.19: Bond Angles for [Cu•2(μ-I)]$_2$ (3b).

Atom	Atom	Atom	Angle/°		Atom	Atom	Atom	Angle/°
Cu1[1]	Cu1	I1	55.071(19)		C8	N3	C1	120.7(4)
Cu1[1]	Cu1	I1[1]	54.67(2)		C8	N3	C6	116.5(4)
S1	Cu1	I1	119.91(4)		N2	C1	S1	123.7(3)
S1	Cu1	I1[1]	109.77(4)		N3	C1	S1	125.1(3)
N1	Cu1	I1	115.78(10)		N3	C1	N2	111.2(4)

N1	Cu1	I1[1]	116.98(10)		C3	C2	N1	112.5(4)
N1	Cu1	S1	82.60(10)		C4	C2	N1	104.7(4)
C1	S1	Cu1	95.97(15)		C4	C2	C3	111.6(5)
N2	N1	Cu1	122.2(3)		C5	C2	N1	106.6(4)
C2	N1	Cu1	125.0(3)		C5	C2	C3	111.2(5)
C2	N1	N2	112.6(3)		C5	C2	C4	109.9(4)
C1	N2	N1	115.5(3)		C7	C6	N3	112.8(4)
C6	N3	C1	122.9(4)		C9	C8	N3	112.3(4)

[1]1-X,2-Y,1-Z

Table A2.20: Hydrogen Atom Coordinates (Å×10^4) and Isotropic Displacement Parameters (Å^2×10^3) for [Cu•2(μ-I)]$_2$ (3b).

Atom	***x***	***y***	***z***	**U(eq)**
H3a	2650(30)	5390(30)	5000(40)	138(3)
H3b	1570(60)	4806(19)	6541(10)	138(3)
H3c	680(30)	5957(19)	5230(50)	138(3)
H4a	410(30)	6512(14)	7814(14)	115(2)
H4b	710(30)	8220(30)	7090(30)	115(2)
H4c	-574(10)	7770(40)	6600(20)	115(2)
H5a	2170(50)	9279(15)	4567(10)	116(3)
H5b	2930(30)	8202(15)	3737(14)	116(3)

H5c	960(20)	8750(30)	4060(20)	116(3)
H6a	4314(7)	2644(5)	7952(6)	74.5(16)
H6b	5420(7)	1308(5)	9042(6)	74.5(16)
H7a	2390(30)	3136(12)	9830(20)	118(3)
H7b	2570(30)	1420(40)	10060(30)	118(3)
H7c	3493(8)	1790(50)	10919(9)	118(3)
H8a	7062(6)	3632(6)	9821(5)	75.5(16)
H8b	6609(6)	1981(6)	10476(5)	75.5(16)
H9a	9000(30)	3092(13)	7990(30)	131(3)
H9b	9453(15)	1830(50)	9460(19)	131(3)
H9c	8527(15)	1450(40)	8600(40)	131(3)

[Cu•2$_2$]BF$_4$ (4) CCDC 2034878: X-ray diffraction data for **[Cu•2$_2$]BF$_4$ (4)** were collected at 100 K on a Bruker D8 Venture using MoKα-radiation (λ=0.71073 Å). Data have been corrected for absorption using SADABS[1] area detector absorption correction program. Using Olex2[2], the structure was solved with the ShelXT[3] structure solution program using Direct Methods and refined with the ShelXL[4] refinement package using least squares minimization. All non-hydrogen atoms were refined with anisotropic thermal parameters. Hydrogen atoms of the investigated structure were located from difference Fourier maps but finally their positions were placed in geometrically calculated positions and refined using a riding model. Isotropic thermal parameters of the placed hydrogen atoms were fixed to 1.2 times the *U* value

of the atoms they are linked to (1.5 times for methyl groups). Calculations and refinement of structures were carried out using APEX3[5], SHELXTL[6], and Olex2 software.

Crystallographic Data for **[Cu•2$_2$]BF$_4$ (4)** $C_{18}H_{38}BCuF_4N_6S_2$ (*M* =553.01 g/mol): monoclinic, space group $P2_1/c$ (no. 14), *a* = 12.4780(3) Å, *b* = 13.9347(4) Å, *c* = 15.4857(5) Å, *β* = 97.5560(10)°, *V* = 2669.23(13) Å^3, *Z* = 4, *T* = 100 K, μ(MoKα) = 1.020 mm^{-1}, *Dcalc* = 1.376 g/cm^3, 2Θmax = 52.742°, 30573 reflections collected, 5459 unique (R_{int} = 0.0488, R_{sigma} = 0.0321), R_1 = 0.0337 (I > 2σ(I)), wR_2 = 0.0797 (all data).

Table A2.21: Crystal data and structure refinement for [Cu•2$_2$]BF$_4$ (4)**.**

Identification code	UI_KW17 (RP-032 (t-butyl ATF-CuBF4))
Empirical formula	$C_{18}H_{38}BCuF_4N_6S_2$
Formula weight	553.01
Temperature/K	100
Crystal system	monoclinic
Space group	$P2_1/c$
a/Å	12.4780(3)
b/Å	13.9347(4)
c/Å	15.4857(5)
α/°	90
β/°	97.5560(10)
γ/°	90

Volume/Å^3	2669.23(13)
Z	4
ρ_{calc}g/cm^3	1.376
μ/mm^{-1}	1.020
F(000)	1160.0
Crystal size/mm^3	0.34 × 0.14 × 0.01
Radiation	MoKα (λ = 0.71073)
2Θ range for data collection/°	4.912 to 52.742
Index ranges	$-15 \leq h \leq 15$, $-17 \leq k \leq 17$, $-19 \leq l \leq 19$
Reflections collected	30573
Independent reflections	5459 [R_{int} = 0.0488, R_{sigma} = 0.0321]
Data/restraints/parameters	5459/0/299
Goodness-of-fit on F^2	1.033
Final R indexes [I>=2σ (I)]	R_1 = 0.0337, wR_2 = 0.0737
Final R indexes [all data]	R_1 = 0.0496, wR_2 = 0.0797
Largest diff. peak/hole / e Å^{-3}	0.64/-0.41

Table A2.22: Fractional Atomic Coordinates (×10^4) and Equivalent Isotropic Displacement Parameters (Å^2×10^3) for [Cu•2_2]BF_4 (4) . U_{eq} is defined as 1/3 of of the trace of the orthogonalised U_{IJ} tensor.

Atom	***x***	***y***	***z***	**U(eq)**
Cu1	4343.0(2)	2616.1(2)	4118.4(2)	13.66(8)

F1	670.5(15)	4326.5(13)	1969.5(12)	50.0(5)
F2	1165(3)	4719(2)	3344.5(18)	126.8(13)
F3	665.2(16)	3217.6(12)	3024.3(12)	53.2(5)
F4	-566.5(18)	4373.4(16)	2888(2)	92.0(9)
B1	482(2)	4172(2)	2813(2)	28.4(6)
S1A	4074.2(4)	3667.5(4)	5211.9(4)	18.55(13)
N1A	2299.1(14)	2525.0(12)	4752.1(12)	14.0(4)
N2A	2886.6(13)	2105.5(12)	4276.8(11)	12.8(4)
N3A	2009.0(14)	3939.2(12)	5436.2(12)	14.8(4)
C1A	2745.1(17)	3407.1(15)	5131.0(13)	13.8(4)
C2A	2452.5(17)	1147.5(15)	3948.2(14)	15.5(4)
C3A	3085.3(18)	410.3(16)	4546.6(15)	19.7(5)
C4A	2721(2)	1044.9(17)	3021.7(15)	22.8(5)
C5A	1244.5(18)	1050.6(17)	3979.8(18)	26.6(6)
C6A	2307.3(19)	4851.3(16)	5884.9(15)	19.8(5)
C7A	2356(2)	5667.7(17)	5239.1(17)	28.0(6)
C8A	839.4(17)	3693.5(16)	5319.1(15)	19.2(5)
C9A	531.4(19)	3130(2)	6084.6(17)	28.8(6)
S1B	5852.7(4)	1662.5(4)	4282.9(4)	15.86(12)
N1B	5834.8(14)	2883.0(12)	2883.3(12)	14.5(4)

N2B	4926.8(14)	3123.8(12)	3070.7(11)	12.7(4)
N3B	7355.1(14)	1972.7(13)	3232.0(12)	16.1(4)
C1B	6391.4(16)	2174.3(15)	3452.7(14)	13.6(4)
C2B	4358.7(17)	3847.1(15)	2448.3(14)	16.1(5)
C3B	3248.0(18)	3423.1(18)	2140.5(16)	23.8(5)
C4B	4260(2)	4754.7(17)	2979.7(17)	30.5(6)
C5B	4967(2)	4041.1(18)	1673.5(16)	26.2(6)
C6B	8028.8(18)	1217.3(16)	3690.0(16)	20.2(5)
C7B	8688.2(19)	1600.0(19)	4514.4(17)	28.5(6)
C8B	7828.6(19)	2484.7(17)	2529.5(16)	24.2(5)
C9B	7509(2)	2000(2)	1658.0(17)	35.7(7)

Table A2.23: Anisotropic Displacement Parameters ($Å^2 \times 10^3$) for $[Cu \bullet 2_2]BF_4$ (4). The Anisotropic displacement factor exponent takes the form: $-2\pi^2[h^2a^{*2}U_{11}+2hka^*b^*U_{12}+\ldots]$.

Atom	**U_{11}**	**U_{22}**	**U_{33}**	**U_{23}**	**U_{13}**	**U_{12}**
Cu1	10.95(13)	16.28(14)	14.43(14)	0.16(10)	4.22(10)	0.73(10)
F1	55.4(11)	49.2(11)	48.5(11)	19.4(9)	18.6(9)	14.6(9)
F2	168(3)	129(3)	78.8(19)	-39.1(17)	0.3(18)	-99(2)
F3	74.3(13)	39.0(10)	48.5(11)	17.8(8)	16.5(10)	17.7(9)
F4	66.8(15)	59.8(14)	166(3)	12.1(15)	78.1(16)	19.9(11)
B1	32.5(16)	22.1(14)	32.2(17)	-1.7(12)	10.0(13)	-2.1(12)

S1A	14.1(3)	21.5(3)	20.9(3)	-7.2(2)	4.9(2)	-3.9(2)
N1A	12.6(8)	13.6(9)	15.9(9)	1.5(7)	2.5(7)	1.2(7)
N2A	10.9(8)	14.2(9)	12.8(9)	2.1(7)	-0.2(7)	2.1(7)
N3A	15.4(9)	15.4(9)	14.2(9)	0.5(7)	4.0(7)	2.1(7)
C1A	15.6(11)	15.4(10)	10.5(10)	2.3(8)	2.5(8)	0.5(8)
C2A	14.8(11)	13.0(10)	18.1(12)	-1.1(8)	0.4(9)	-1.1(8)
C3A	25.1(12)	14.1(11)	19.5(12)	2.0(9)	1.5(9)	1.3(9)
C4A	31.6(14)	19.7(12)	16.3(12)	-2.4(9)	0.8(10)	-5.0(10)
C5A	16.1(12)	20.7(12)	42.9(16)	-5.5(11)	3.4(11)	-3.8(9)
C6A	22.9(12)	20.5(12)	15.9(12)	-5.4(9)	1.8(9)	4.1(9)
C7A	38.1(15)	15.0(12)	29.6(14)	-2.2(10)	-0.5(11)	0.8(10)
C8A	13.8(11)	21.8(12)	21.8(12)	-1.9(9)	1.4(9)	5.3(9)
C9A	18.0(12)	41.3(15)	28.3(15)	2.6(11)	7.6(10)	-4.6(11)
S1B	12.8(3)	17.9(3)	17.7(3)	5.0(2)	4.8(2)	2.9(2)
N1B	13.4(9)	14.2(9)	16.1(10)	-0.3(7)	3.0(7)	-1.5(7)
N2B	13.0(9)	12.8(9)	12.4(9)	-1.8(7)	1.5(7)	-1.6(7)
N3B	14.5(9)	15.1(9)	19.6(10)	-2.0(7)	5.3(8)	0.5(7)
C1B	13.5(10)	12.9(10)	14.7(11)	-3.5(8)	2.8(8)	-1.9(8)
C2B	15.8(11)	15.9(11)	16.4(11)	4.1(9)	2.0(9)	2.0(8)
C3B	18.8(12)	27.5(13)	23.5(13)	9.7(10)	-2.8(10)	-1.6(10)

C4B	45.5(16)	17.3(12)	26.3(14)	1.3(10)	-3.9(12)	9.9(11)
C5B	23.5(13)	30.2(13)	25.5(14)	14.0(11)	6.0(10)	1.4(10)
C6B	15.9(11)	17.8(11)	28.3(13)	0.2(9)	7.6(10)	6.5(9)
C7B	14.8(12)	37.1(15)	32.4(15)	-2.0(11)	-1.1(10)	4.5(10)
C8B	19.2(11)	25.0(13)	31.5(14)	6.3(10)	14.7(10)	1.0(10)
C9B	39.8(16)	46.7(17)	24.5(14)	4.8(12)	18.9(12)	5.0(13)

Table A2.24: Bond Lengths for [Cu•2_2]BF_4 (4).

Atom	**Atom**	**Length/Å**		**Atom**	**Atom**	**Length/Å**
Cu1	S1A	2.2970(6)		C2A	C4A	1.522(3)
Cu1	N2A	1.9965(17)		C2A	C5A	1.521(3)
Cu1	S1B	2.2920(6)		C6A	C7A	1.521(3)
Cu1	N2B	1.9935(17)		C8A	C9A	1.513(3)
F1	B1	1.374(3)		S1B	C1B	1.685(2)
F2	B1	1.343(4)		N1B	N2B	1.252(2)
F3	B1	1.381(3)		N1B	C1B	1.440(3)
F4	B1	1.358(4)		N2B	C2B	1.506(3)
S1A	C1A	1.686(2)		N3B	C1B	1.323(3)
N1A	N2A	1.250(2)		N3B	C6B	1.470(3)
N1A	C1A	1.442(3)		N3B	C8B	1.487(3)

N2A	C2A	1.504(3)		C2B	C3B	1.524(3)
N3A	C1A	1.316(3)		C2B	C4B	1.523(3)
N3A	C6A	1.473(3)		C2B	C5B	1.526(3)
N3A	C8A	1.487(3)		C6B	C7B	1.521(3)
C2A	C3A	1.531(3)		C8B	C9B	1.515(4)

Table A2.25: Bond Angles for [Cu•2_2]BF_4 (4).

Atom	**Atom**	**Atom**	**Angle/°**		**Atom**	**Atom**	**Atom**	**Angle/°**
N2A	Cu1	S1A	85.02(5)		N2A	C2A	C5A	112.48(17)
N2A	Cu1	S1B	121.86(5)		C4A	C2A	C3A	110.33(18)
S1B	Cu1	S1A	119.04(2)		C5A	C2A	C3A	110.82(19)
N2B	Cu1	S1A	118.55(5)		C5A	C2A	C4A	111.35(19)
N2B	Cu1	N2A	131.48(7)		N3A	C6A	C7A	111.39(18)
N2B	Cu1	S1B	85.03(5)		N3A	C8A	C9A	111.74(18)
F1	B1	F3	109.4(2)		C1B	S1B	Cu1	94.26(7)
F2	B1	F1	108.6(3)		N2B	N1B	C1B	114.85(17)
F2	B1	F3	109.2(3)		N1B	N2B	Cu1	122.16(14)
F2	B1	F4	111.8(3)		N1B	N2B	C2B	113.28(17)
F4	B1	F1	109.7(3)		C2B	N2B	Cu1	124.53(13)
F4	B1	F3	108.1(2)		C1B	N3B	C6B	120.61(18)

C1A	S1A	Cu1	92.61(8)		C1B	N3B	C8B	123.31(19)
N2A	N1A	C1A	114.42(17)		C6B	N3B	C8B	116.08(17)
N1A	N2A	Cu1	121.29(14)		N1B	C1B	S1B	123.27(15)
N1A	N2A	C2A	113.66(17)		N3B	C1B	S1B	125.06(17)
C2A	N2A	Cu1	124.61(13)		N3B	C1B	N1B	111.66(18)
C1A	N3A	C6A	120.71(18)		N2B	C2B	C3B	105.84(17)
C1A	N3A	C8A	123.15(18)		N2B	C2B	C4B	105.95(17)
C6A	N3A	C8A	116.07(17)		N2B	C2B	C5B	112.39(17)
N1A	C1A	S1A	122.47(15)		C3B	C2B	C5B	110.40(19)
N3A	C1A	S1A	125.34(17)		C4B	C2B	C3B	110.84(19)
N3A	C1A	N1A	112.10(18)		C4B	C2B	C5B	111.22(19)
N2A	C2A	C3A	104.87(17)		N3B	C6B	C7B	111.45(19)
N2A	C2A	C4A	106.74(17)		N3B	C8B	C9B	110.8(2)

Table A2.26: Hydrogen Atom Coordinates (Å×10^4) and Isotropic Displacement Parameters (Å^2×10^3) for [Cu•2_2]BF_4 (4).

Atom	***x***	***y***	***z***	**U(eq)**
H3AA	3861.17	492.9	4524.72	30
H3AB	2867.39	-238.69	4352.63	30
H3AC	2932.19	504.77	5145.47	30
H4AA	2335.36	1538.3	2651.49	34

H4AB	2499.37	407.99	2796.6	34
H4AC	3501.52	1122.45	3020.5	34
H5AA	864.34	1587.18	3665.37	40
H5AB	1103.95	1057.92	4587.71	40
H5AC	986.54	444.3	3706.78	40
H6AA	3021.14	4780.79	6242.63	24
H6AB	1769.67	5007.27	6280.2	24
H7AA	1673.09	5698.65	4847.25	42
H7AB	2952.29	5554.98	4898.02	42
H7AC	2474.3	6275.29	5555.95	42
H8AA	665.38	3310.4	4780.5	23
H8AB	408.32	4291.55	5250.8	23
H9AA	948.08	2532.29	6147.92	43
H9AB	-242.36	2980.11	5984.59	43
H9AC	688.82	3512.79	6617.07	43
H3BA	3332.65	2819.36	1832.04	36
H3BB	2829.02	3876.63	1746.88	36
H3BC	2868.25	3300.81	2644.62	36
H4BA	3849.75	4613.45	3462.75	46
H4BB	3882.44	5250.17	2606.56	46

H4BC	4982.52	4984.62	3211.71	46
H5BA	5694.38	4277.31	1883.53	39
H5BB	4576.73	4524.67	1294.55	39
H5BC	5020.39	3445.86	1344.81	39
H6BA	8523.54	955.76	3298.4	24
H6BB	7559.93	687.7	3843.63	24
H7BA	9152.91	2124.46	4363.86	43
H7BB	9137.08	1083.49	4798.5	43
H7BC	8199.24	1838.41	4911.99	43
H8BA	8626.3	2491.46	2665.91	29
H8BB	7572.81	3157.9	2498.55	29
H9BA	7768.13	1335.76	1687.35	54
H9BB	7832.86	2346.06	1205.52	54
H9BC	6720.29	2006.18	1517.35	54

UV-vis and binding isotherm titration data

All UV-Vis titration data has been uploaded to supramolecular.org and is freely accessible.

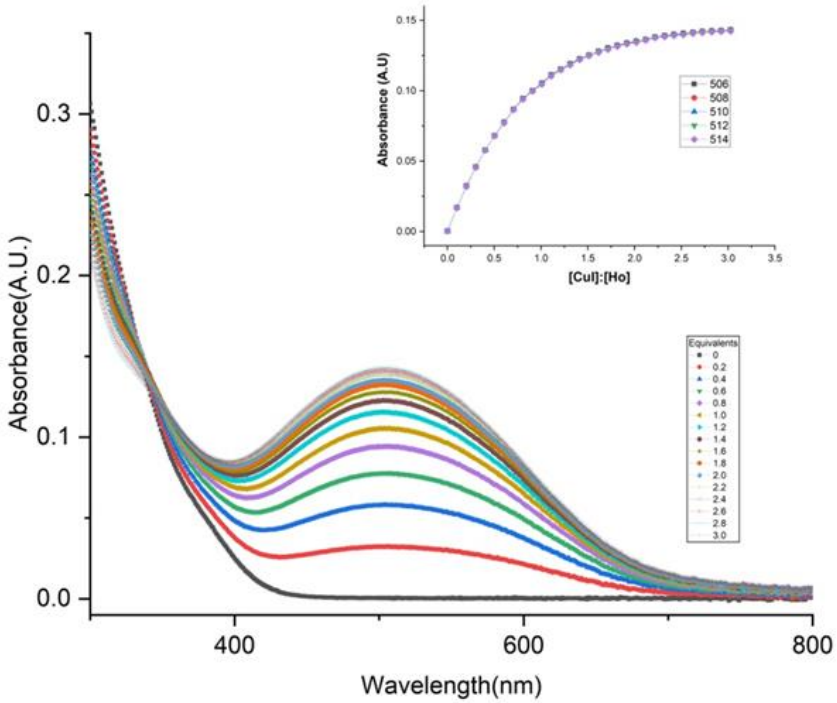

Figure A2.1: UV-Vis titration of Cu(I)I into ligand 2

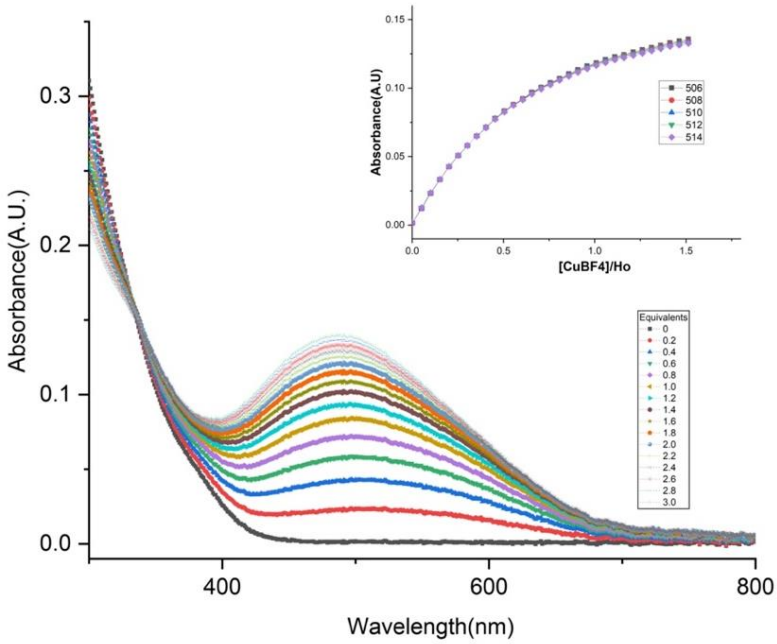

Figure A2.2: UV-Vis titration of Cu(I)I into ligand 2

Spill fill Images of 3a, 3b, 4 and phenyl analog

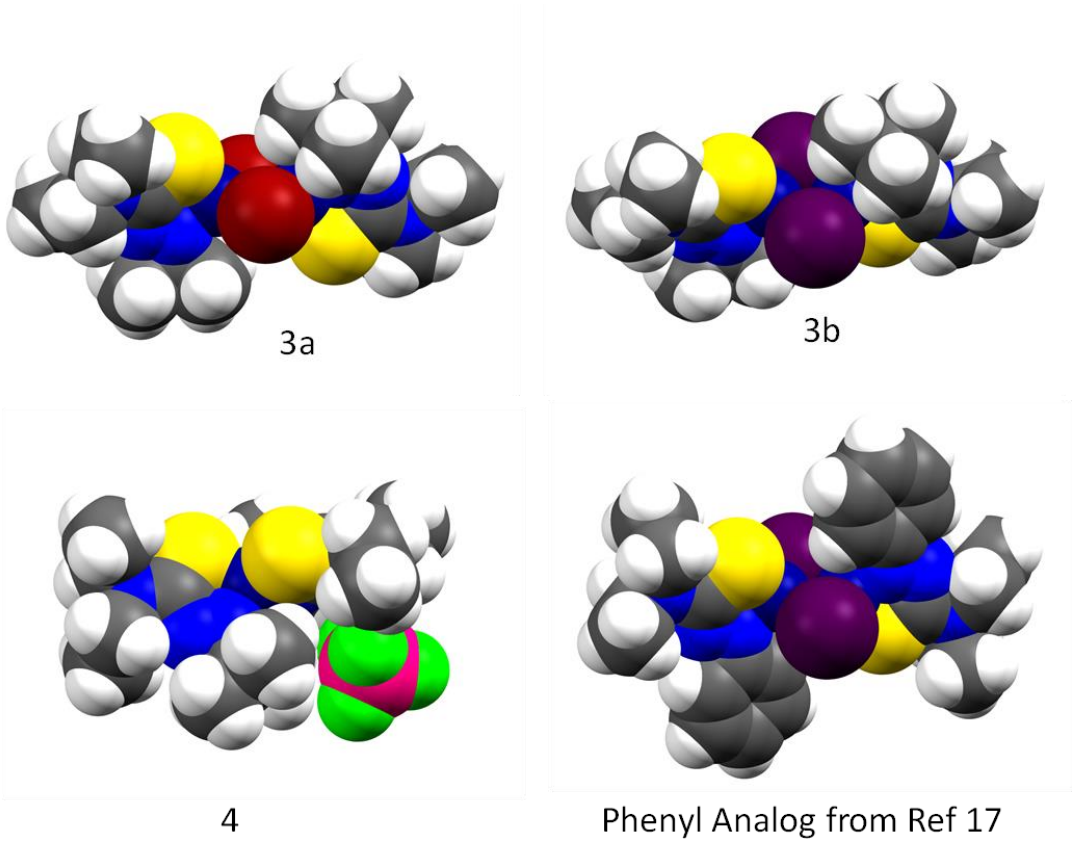

Figure A 2.3: Space fill models of 3a, 3b, 4 and a phenyl ATF analog to note is the steric interactions of the t-butyl group with cu(I)I in 3b are not present in phenyl analog.

References

1. Dolomanov, O. V.; Bourhis, L. J.; Gildea, R. J.; Howard, J. A. K.; Puschmann, H., OLEX2: a complete structure solution, refinement, and analysis program. *J Appl Crystallogr* **2009,** *42*, 339-341.
2. Bourhis, L. J.; Dolomanov, O. V.; Gildea, R. J.; Howard, J. A.; Puschmann, H., The anatomy of a comprehensive constrained, restrained refinement program for the modern computing environment - Olex2 dissected. *Acta Crystallogr A Found Adv* **2015,** *71* (Pt 1), 59-75.
3. Sheldrick, G. M., SHELXT - Integrated space-group and crystal-structure determination. *Acta Crystallogr A* **2015,** *71*, 3-8.
4. Sheldrick, G. M., Crystal structure refinement with SHELXL. *Acta Crystallogr C Struct Chem* **2015,** *71* (Pt 1), 3-8.
5. Adam, M.; Hovestreydt, E.; Ruf, M.; Kaercher, J., Reaching a new highpoint with crystallography software-APEX3. *Acta Crystallogr A* **2015,** *71*, S194-S194.
6. Burshtein, I. F.; Campana, C. F., Modeling Crxstal Structures with Disorder Using the Shelxtl 5.0 Software Package. *Acta Crystallogr A* **1996,** *52*, C44-C44.

Appendix III

Supporting Information for Chapter 4: Evaluating Coordinative Binding Mechanisms through an Experimental and Computational Study of Methoxy-substituted Arylazothioformamide Copper(I) Complexes.

General Methods

^{1}H and ^{13}C NMR experiments were performed on a Bruker AVANCE 500 MHz or 300 MHz instrument and samples were obtained in $CDCl_3$ (referenced to 7.26 ppm for ^{1}H and 77.16 ppm for ^{13}C) unless stated otherwise. Coupling constants (*J*) are in Hz. The multiplicities of the signals are described using the following abbreviations: s = singlet, br s = broad singlet, d = doublet, t = triplet, dd = doublet of doublets, dq = doublet of quartets, m = multiplet, app = apparent. Infrared spectra were obtained on a Thermo Scientific Nicolet 380 FT-IR spectrometer with attenuated total reflectance (ATR) as thin films on ZnSe disks and peaks are reported in cm^{-1}. Reaction progress was monitored by thin-layer chromatography on silica gel plates (60-F254), observed under UV light. Column chromatography was performed using silica gel (particle size 40–63 μm). Methyl iodide was purchased from EMD Millipore, 4-methoxyphenylhydrazine hydrochloride, 2-methoxyphenylhydrazine hydrochloride, 3-methoxyphenylhydrazine hydrochloride were purchased from AK Scientific, N,N-Diethylamine and CS_2 were purchased from Alfa-Aesar and used without further purification. Cu(I) halides and salts were purchased from Acros, Sigma–Aldrich, Alfa–Aesar, and AK Scientific and used without further purification.

Computational Details

All structures were fully optimized without symmetry constraints using the B3LYP functional as implemented in Gaussian 09 using the 6-31G** basis set for C, H, N, S, Br, B,

F, and P and the Stuttgart basis set with effective core potentials for all metal and iodine atoms. To verify the validity of the chosen method, other DFT functionals were used: B3LYP-D3, B3P86, B3PW91, M11, and wB97XD, but B3LYP gave structural parameters that best matched the experimental structures. The ultrafine integration grid was employed in all calculations, which ensured the stability of the optimization procedure for the investigated molecules. Each stationary point was confirmed by a frequency calculation at the same level of theory to be a real local minimum on the potential energy surface. More accurate electronic energies were computed for the optimized geometries using the larger 6-311++G(d,p) basis set. All reported free energies are for tetrahydrofuran solution at the standard state (T = 298 K, P = 1 atm, 1 mol/L concentration of all species in THF) as modeled by a polarized continuum model. The energy values given in the manuscript correspond to solvent-corrected Gibbs free energies that are based on B3LYP/6-311++G(d,p) electronic energies and all corrections calculated at the B3LYP/6-31G(d) level.

Synthesis and Characterization of Ligands and Coordination Complexes

N,N-diethyl-2-(4-methoxyphenyl)diazothioformamide (6): Ethanol (75 mL) was degassed for one hour under nitrogen flow in a flame-dried round bottom fitted with a magnetic stirrer. 4-methoxyphenylhydrazine•HCl (5.821 g, 30.00 mmol) was then added and allowed to solvate forming a dark purple solution. Carbon disulfide (2.06 mL, 34.2 mmol) was added dropwise by needle and allowed to stir for an hour. Potassium hydroxide (2.36 g, 42.0 mmol) dissolved in degassed ethanol (25 mL) was then quickly poured into the mixture and the solution was stirred for 30 minutes. Methyl iodide (2.09 mL, 33.60 mmol) was then added in one portion by needle and the solution was allowed to stir for one hour before concentration with a rotary evaporator producing an orange solid. The flask was then fitted to a reflux condenser and put

under nitrogen flow. Diethylamine (40 mL, 368.7 mmol) was added by cannula and the solution was refluxed for 48 hours. The resulting dark red solution was then cooled to room temp. and stirred under air for 2 hours. The solution was then washed with brine and extracted with ethyl acetate to afford a dark red oil. Flash column chromatography using 7:3 hexane: ethyl acetate gave 4.69 g (62 %) of orange solid. The resulting solid could be crystallized with slow evaporation of 7:3 hexane: ethyl acetate. ^{1}H NMR (300 MHz, Chloroform-*d*): δ 7.89 (d, *J* = 9.0 Hz, 2H), 6.99 (d, *J* = 9.0 Hz, 2H), 4.03 (q, *J* = 7.1 Hz, 2H), 3.90 (s, 3H), 3.55 (q, *J* = 7.1 Hz, 2H), 1.40 (t, *J* = 7.1 Hz, 3H), 1.18 (t, *J* = 7.1 Hz, 3H). ^{13}C NMR (75.4 MHz, $CDCl_3$): δ 195.1, 164.3, 147.0, 126.7, 115.3, 78.5, 78.0, 77.6, 56.6, 48.7, 46.0, 14.6, 12.3. FTIR (cm^{-1}): n 2974, 1579, 1419, 1259, 1145, 775. Elemental Analysis: $C_{12}H_{17}N_3OS$ (251.35) (Calculated) C, 57.74; H, 6.756; N, 16.42 (Found) C, 57.34; H, 6.82; N, 16.72; mp: 93 ˚C.

N,N-diethyl-2-(2-methoxyphenyl)diazothioformamide (8): To a flame-dried round-bottom flask equipped with a magnetic stirrer was added 20 mL of ethanol and 2-methoxyphenylhydrazine • HCl (1.8 g, 6.17 mmol) and allowed to degas for 1.5 hours under nitrogen flow. While under nitrogen, CS_2 (0.42 ml, 7.03 mol) was added dropwise and allowed to stir under ambient conditions for an hour. Potassium hydroxide (0.48 g, 8.64 mol) dissolved in degassed ethanol (5 mL) was then added and allowed to stir under nitrogen for an additional 30 minutes. Methyl iodide (0.43 ml, 6.91 mmol) was then added to the solution and stirred under nitrogen for 1 hour. The mixture was then concentrated with a rotary evaporator. The flask containing the resulting paste was then equipped with condenser column and put under nitrogen flow. Diethylamine (10 mL) was added via cannula and the solution refluxed under nitrogen for 48 hours. The solution was cooled to ambient temperature, opened to air and

allowed to stir for 2 hours. The resulting orange liquid was concentrated via rotary evaporator and purified using flash column chromatography 7:3 hexane: ethyl acetate providing .797 g (51% yield) of orange solid. The resulting solid was subjected to recrystallization using cyclohexane and tetrahydrofuran. ^{1}H NMR (300 MHz, Chloroform-*d*): δ 7.56 (d, *J* = 7.9 Hz, 1H), 7.48 (t, *J* = 7.9 Hz, 1H), 7.07 (d, *J* = 8.5 Hz, 1H), 6.98 (t, *J* = 7.6 Hz, 1H), 4.07 – 3.96 (m, 5H), 3.51 (q, *J* = 7.1 Hz, 2H), 1.39 (t, *J* = 7.0 Hz, 3H), 1.19 (t, *J* = 7.0 Hz, 3H). ^{13}C NMR (75 MHz, $CDCl_3$): δ 195.44 (C=S), 158.66, 142.22, 135.02, 121.42, 118.51, 113.82, 57.10, 48.53, 45.92, 14.48, 12.31. FTIR (cm^{-1}): n 2978, 1591, 1432, 1283, 1165, 852, 763. Elemental Analysis: $C_{12}H_{17}N_3OS$ (251.35) (Calculated) C, 57.74; H, 6.756; N, 16.42 (Found) C, 57.72; H, 6.77; N, 15.79; Melting point: 75˚ C. **CCDC 2169102**

N,N-diethyl-2-(3-methoxyphenyl)diazothioformamide (10): Ethanol (20 mL) was degassed under nitrogen flow in a flame-dried round bottom flask fitted with a magnetic stirrer for one hour. 3-methoxyphenylhydrazine•HCl (6.17 mmol, 1.078 g) was then added. Carbon disulfide (7.03 mmol, 0.42 mL) was added dropwise by needle and left to stir for an hour. Potassium hydroxide (0.48 g, 8.64 mmol) dissolved in degassed ethanol (5 mL) was then quickly poured into the mixture and the solution was stirred for 30 minutes. Methyl iodide (6.91 mmol, 0.43 mL) was added by needle. The solution was stirred for and additional hour and then carbon disulfide and ethanol were removed by rotary evaporator producing an orange solid. The flask was then fitted to a reflux condenser and put under nitrogen flow. Diethylamine (10 mL) was added by canula and allowed to reflux for 48 hours. The resulting dark red solution was then cooled to room temperature, opened to air, and stirred under ambient conditions for 2 hours. The solution was then washed with brine and extracted with ethyl acetate to afford a dark red oil. The resulting red liquid was concentrated via rotary evaporator and purified using flash

column chromatography 7:3 hexane: ethyl acetate forming 0.87 g (56 % yield) of dark red oil. ^{1}H NMR (300 MHz, Chloroform-*d*) δ 7.51 (d, *J* = 6.4 Hz, 1H), 7.44 – 7.38 (m, 2H), 7.12 – 7.06 (m, 1H), 4.01 (q, *J* = 7.1 Hz, 2H), 3.50 (q, *J* = 7.1 Hz, 2H), 1.40 (t, *J* = 7.1 Hz, 3H), 1.17 (t, *J* = 7.1 Hz, 3H). ^{13}C NMR (75.4 MHz, $CDCl_3$) δ 195.01, 161.27, 153.89, 130.83, 120.35, 118.41, 107.44, 56.40, 48.61, 45.98, 14.58, 12.29. FTIR (cm^{-1}): n 2975, 1594, 1430, 1280, 1154, 756. Elemental Analysis: $C_{12}H_{17}N_3OS$ (251.35) (Calculated) C, 57.74; H, 6.76; N, 16.42 (Found) C, 57.76; H, 6.74; N, 15.70.

NMR Spectral Data

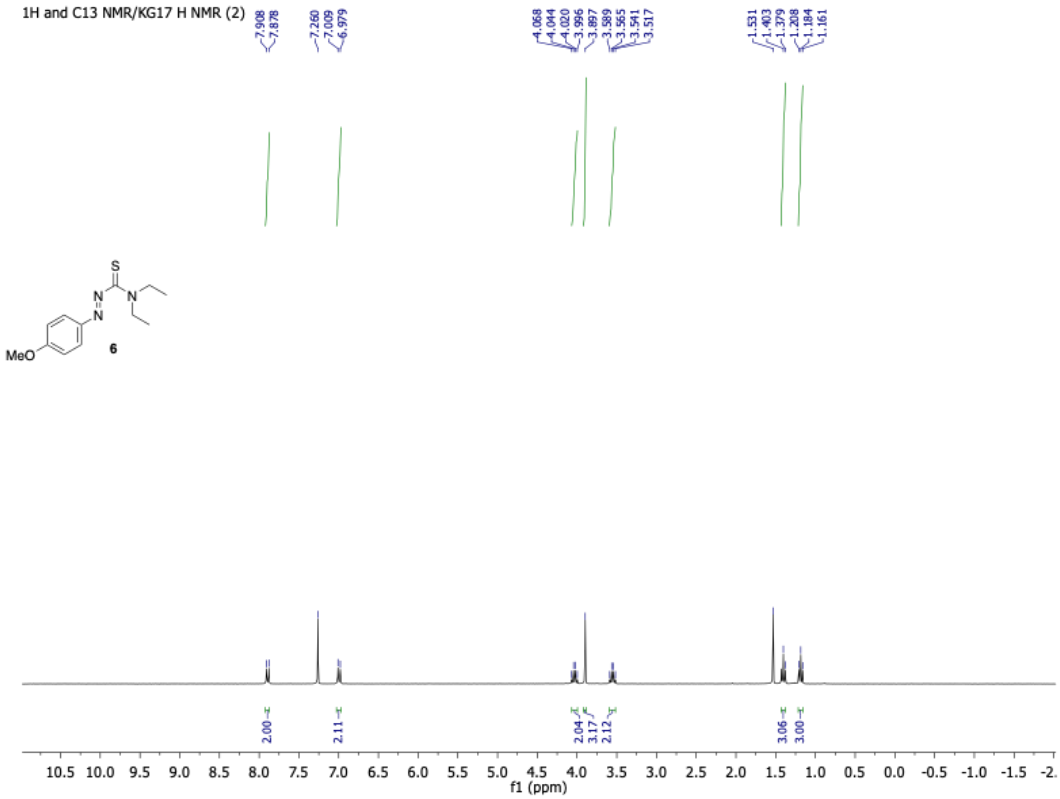

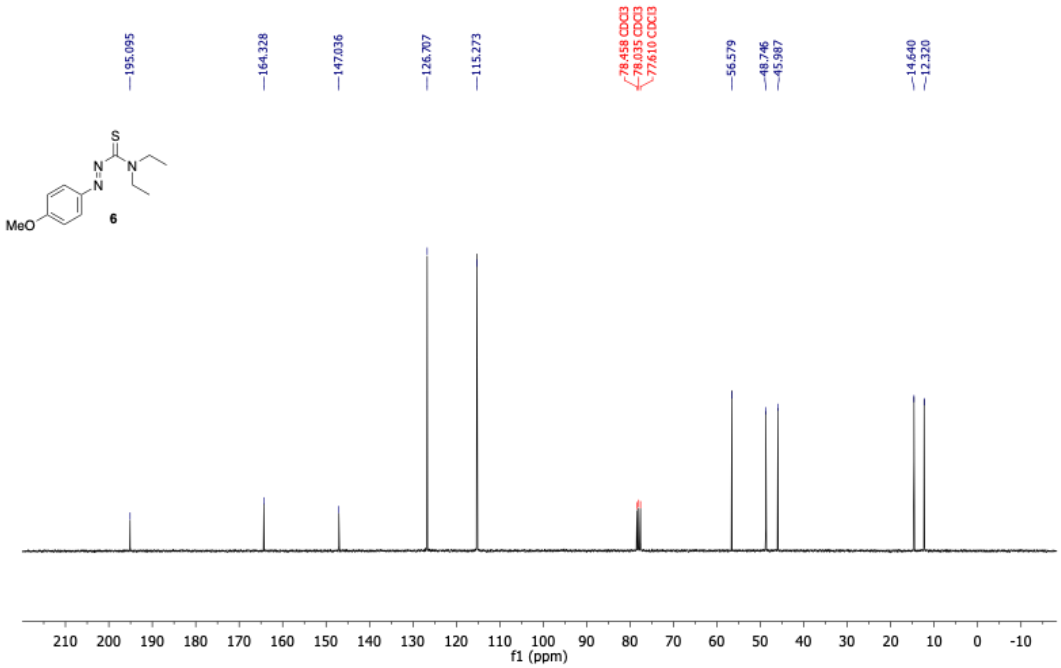
195.095
164.328
147.036
126.707
115.273
78.458 CDCl3
78.035 CDCl3
77.610 CDCl3
56.579
48.746
45.987
14.640
12.320
MeO
6
f1 (ppm)

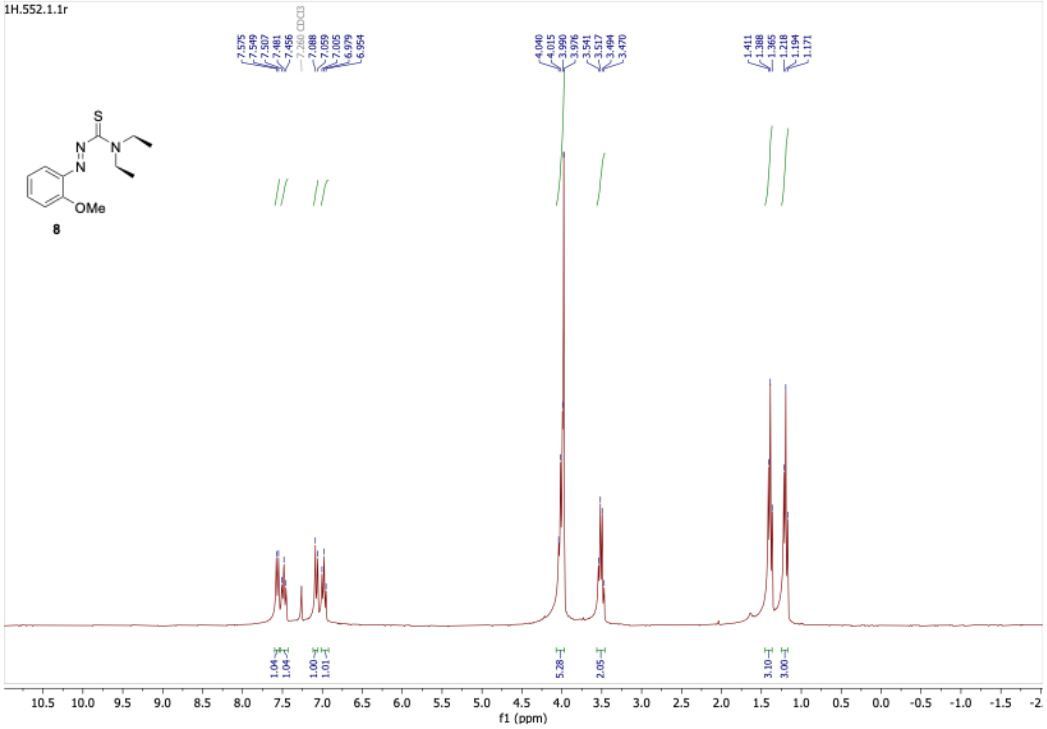
1H.552.1.1r
7.575
7.549
7.507
7.481
7.456
7.260 CDCl3
7.088
7.059
7.005
6.979
6.954
4.040
4.015
3.990
3.976
3.541
3.517
3.494
3.470
1.411
1.388
1.365
1.218
1.194
1.171
OMe
8
1.04
1.04
1.00
1.01
5.28
2.05
3.10
3.00
f1 (ppm)

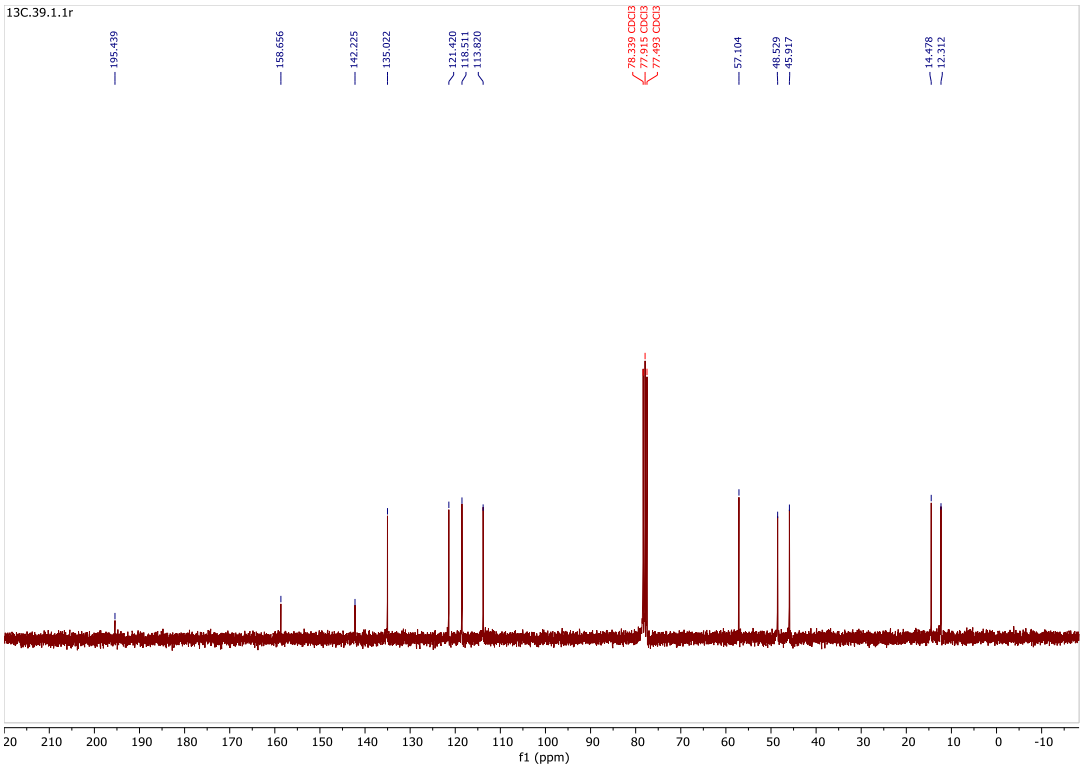
13C.39.1.1r
195.439
158.656
142.225
135.022
121.420
118.511
113.820
78.339 CDCl3
77.915 CDCl3
77.493 CDCl3
57.104
48.529
45.917
14.478
12.312
f1 (ppm)

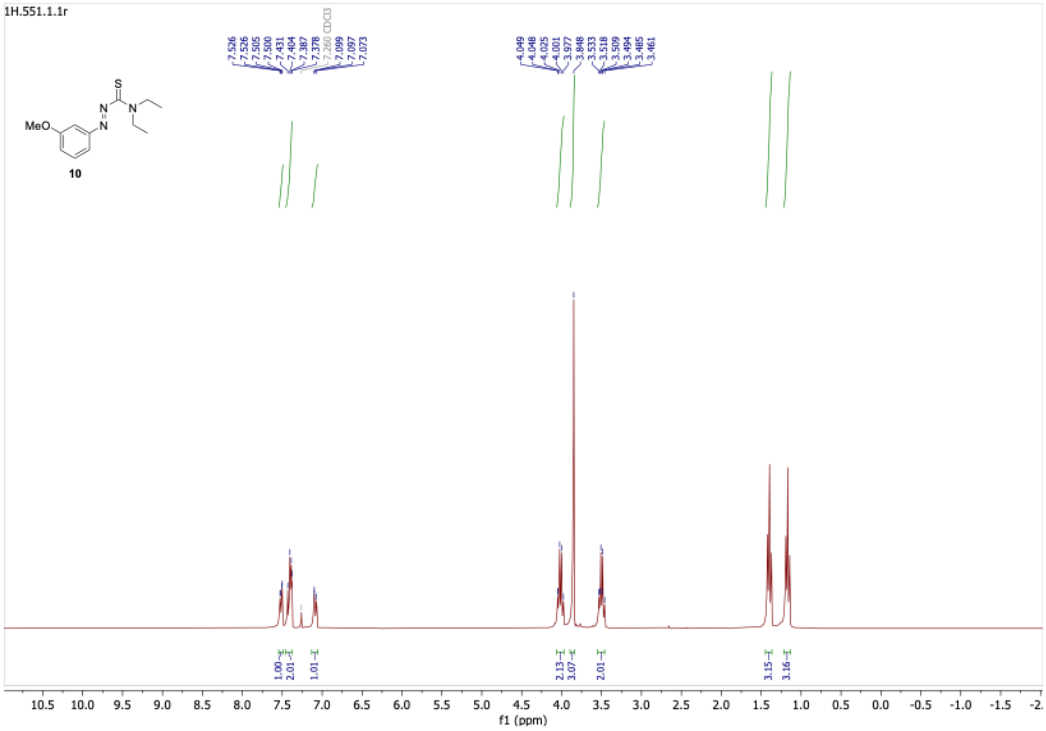
1H.551.1.1r
MeO
10
7.526
7.505
7.500
7.431
7.404
7.387
7.375
7.260 CDCl3
7.099
7.097
7.073
4.049
4.048
4.025
4.001
3.977
3.848
3.533
3.518
3.509
3.494
3.465
3.461
1.00
2.01
1.01
2.13
3.07
2.01
3.15
3.16
f1 (ppm)

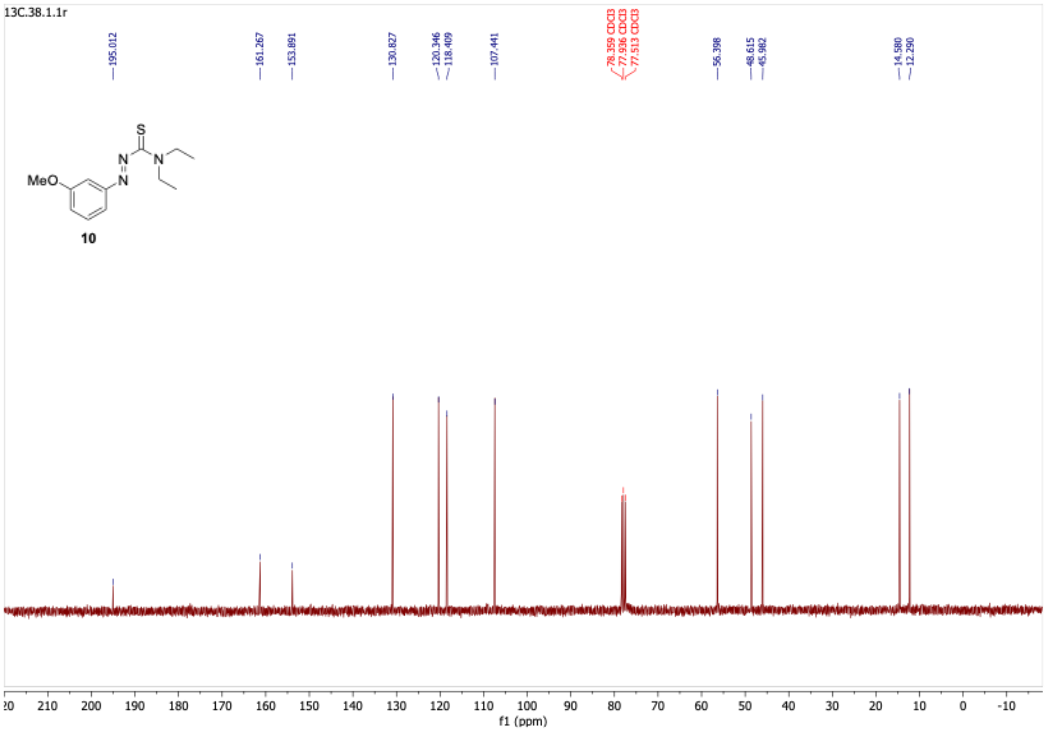
13C.38.1.1r
195.012
161.267
153.691
130.827
120.346
118.409
107.441
79.359 CDCl3
77.936 CDCl3
77.513 CDCl3
56.398
48.615
45.982
14.580
12.290
MeO
10
f1 (ppm)

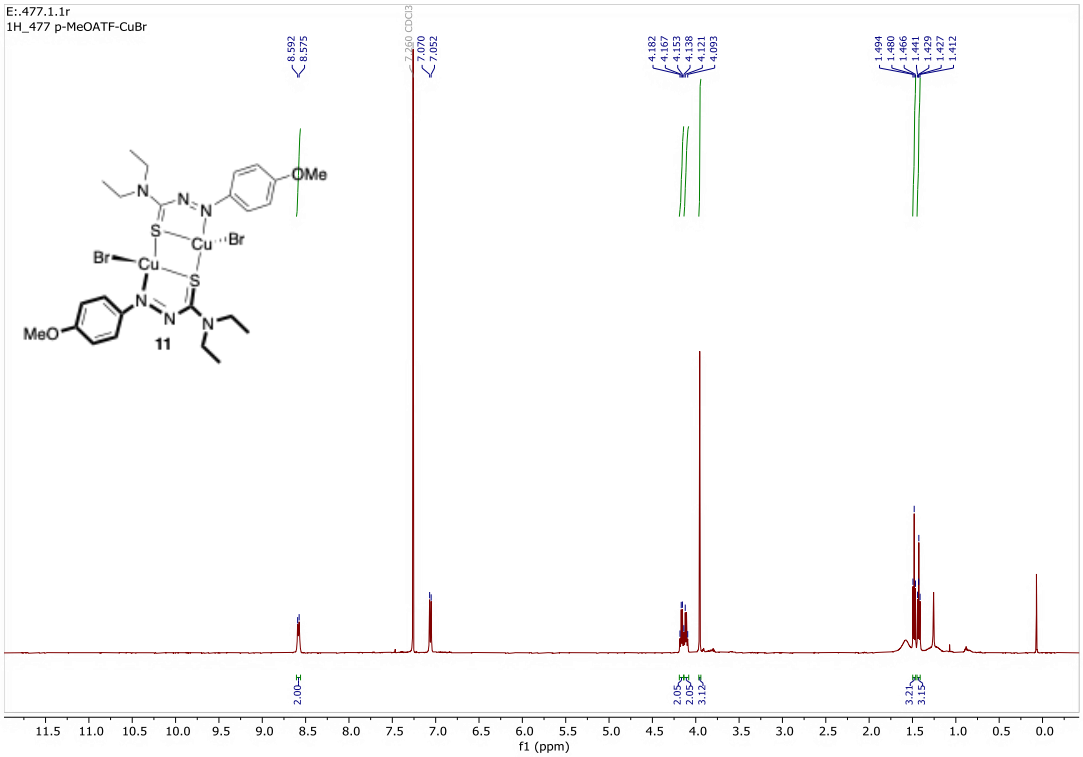
E:.477.1.1r
1H_477 p-MeOATF-CuBr
8.592
8.575
7.260 CDCl3
7.070
7.052
4.182
4.167
4.153
4.138
4.121
4.093
1.494
1.480
1.466
1.441
1.429
1.427
1.412
OMe
Br
Cu
S
N
MeO
11
2.00
2.05
2.05
3.12
3.21
3.15
f1 (ppm)

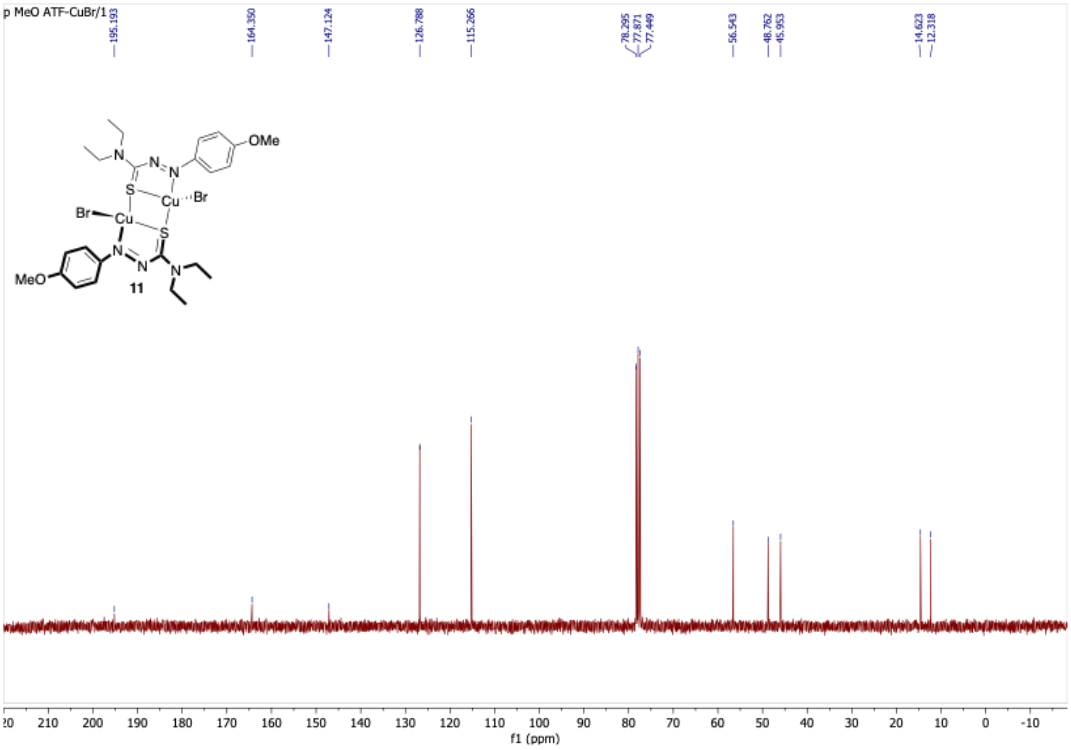
p MeO ATF-CuBr/1
195.193
164.350
147.124
126.788
115.266
78.295
77.871
77.449
56.543
48.762
45.953
14.623
12.318
OMe
Br
Cu
Cu
Br
S
S
N
N
N
N
N
MeO
11
f1 (ppm)

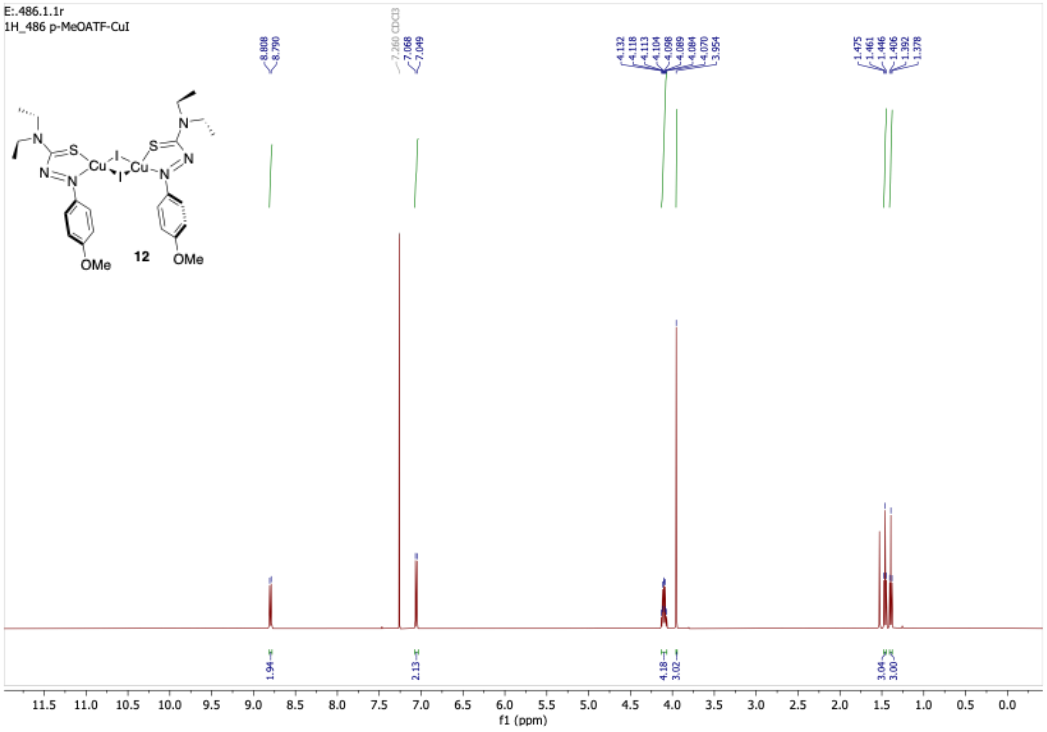
E:.486.1.1r
1H_486 p-MeOATF-CuI
8.808
8.790
7.260 CDCl3
7.068
7.049
4.132
4.118
4.113
4.104
4.098
4.089
4.084
4.070
3.954
1.475
1.461
1.446
1.406
1.392
1.378
Cu
Cu
I
I
S
S
N
N
N
N
OMe
12
OMe
1.94
2.13
4.18
3.02
3.04
3.00
f1 (ppm)

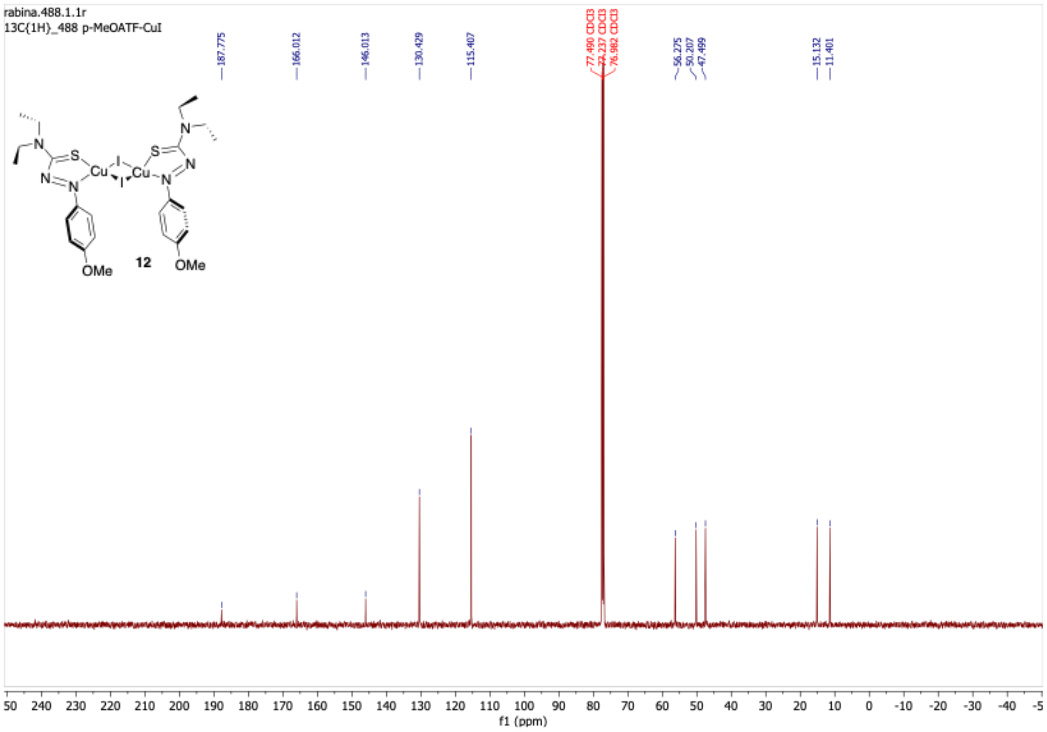
rabina.488.1.1r
13C{1H}_488 p-MeOATF-CuI
187.775
166.012
146.013
130.429
115.407
77.496 CDCl3
77.237 CDCl3
76.982 CDCl3
56.275
50.207
47.499
15.132
11.401
12
OMe
OMe
f1 (ppm)

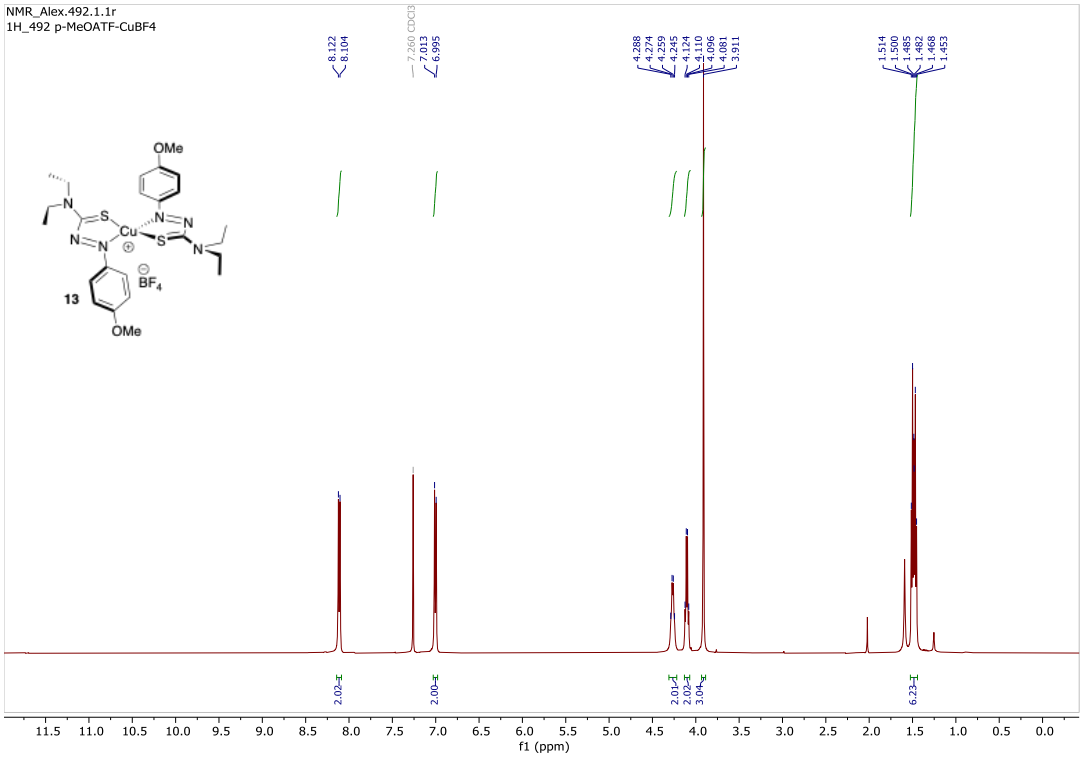
NMR_Alex.492.1.1r
1H_492 p-MeOATF-CuBF4
8.122
8.104
7.260 CDCl3
7.013
6.995
4.288
4.274
4.259
4.245
4.124
4.110
4.096
4.081
3.911
1.514
1.500
1.485
1.469
1.468
1.453
13
OMe
OMe
BF4
2.02
2.00
2.01
2.02
3.04
6.23
f1 (ppm)

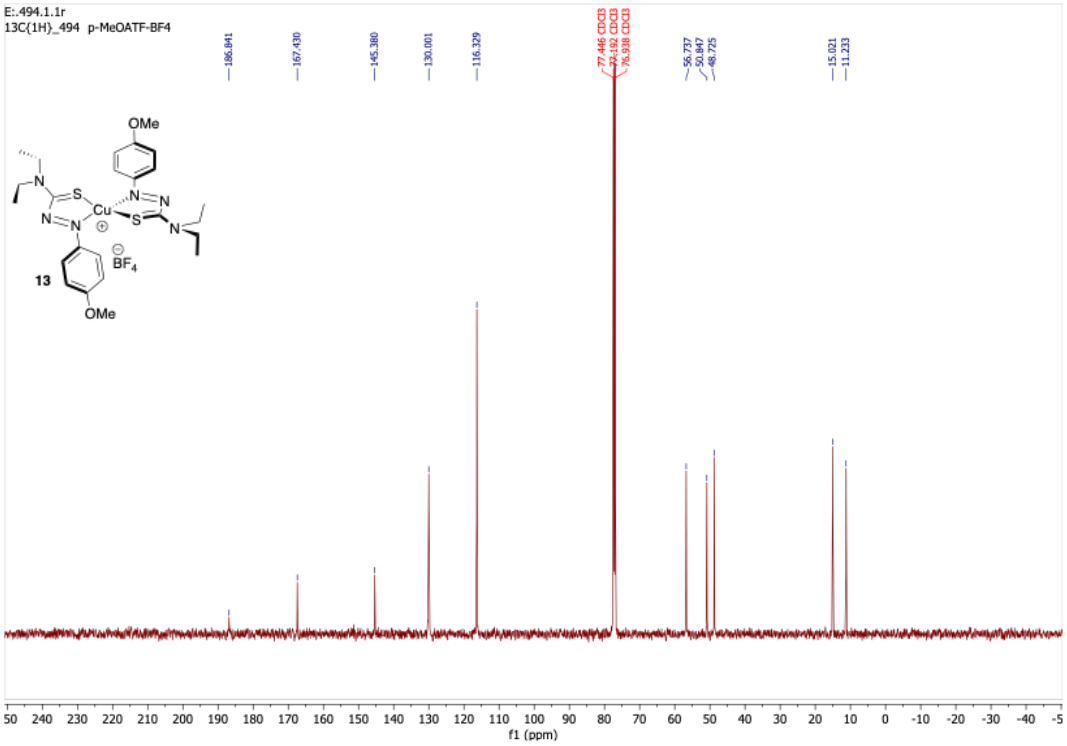
E:.494.1.1r
13C{1H}_494 p-MeOATF-BF4
186.841
167.430
145.380
130.001
116.329
77.446 CDCl3
77.192 CDCl3
76.938 CDCl3
56.737
50.947
48.725
15.021
11.233
OMe
Cu
BF4
13
OMe
f1 (ppm)

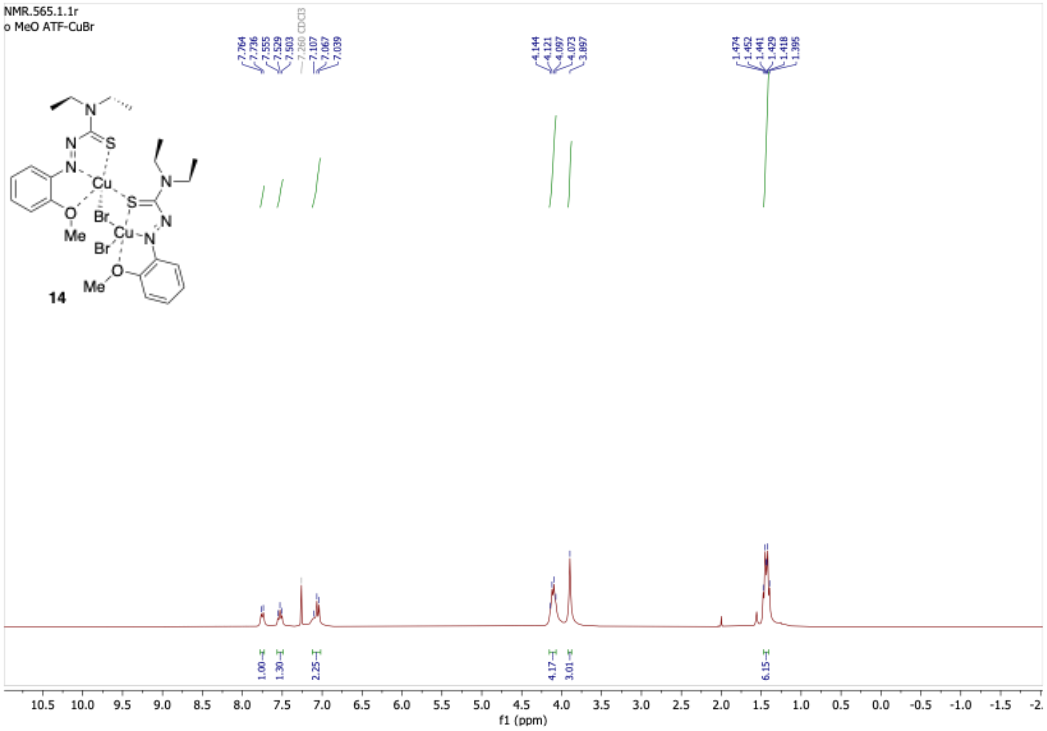
NMR.565.1.1r
o MeO ATF-CuBr
7.764
7.736
7.555
7.529
7.503
7.260 CDCl3
7.107
7.067
7.039
4.144
4.121
4.097
4.073
3.897
1.474
1.453
1.441
1.429
1.418
1.395
Cu
Br
Me
14
1.00
1.30
2.25
4.17
3.01
6.15
f1 (ppm)

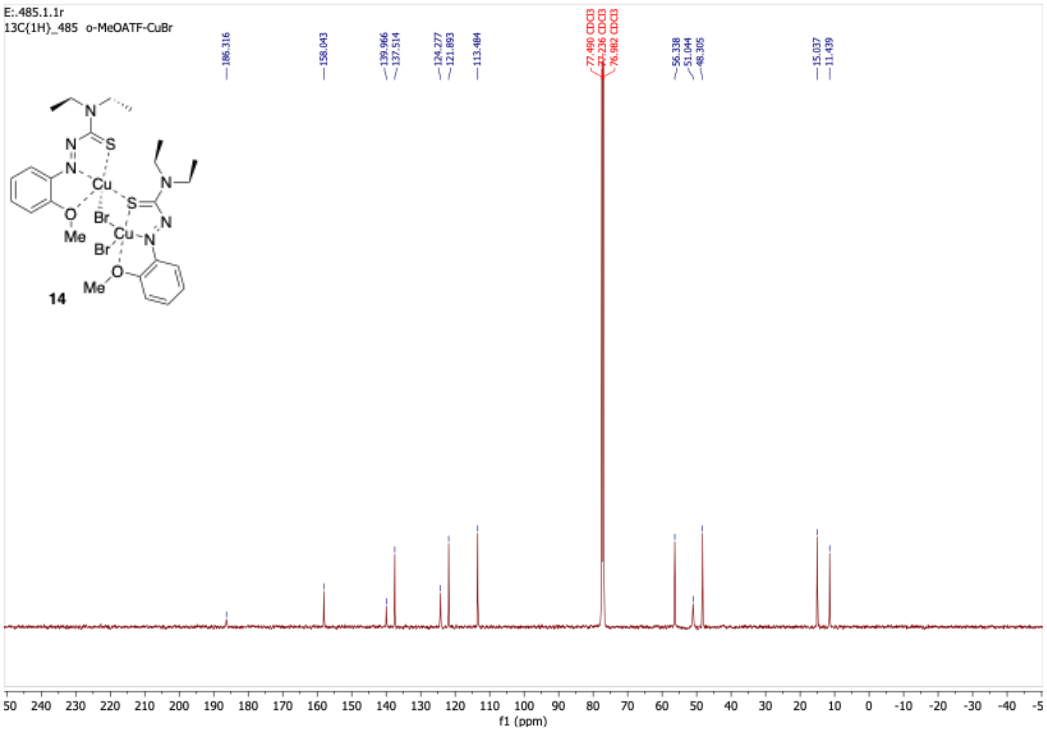
E:.485.1.1r
13C{1H}_485 o-MeOATF-CuBr
186.316
158.043
139.866
137.514
124.277
121.893
113.484
77.490 CDCl3
77.236 CDCl3
76.982 CDCl3
56.338
51.044
48.305
15.037
11.439
14
f1 (ppm)

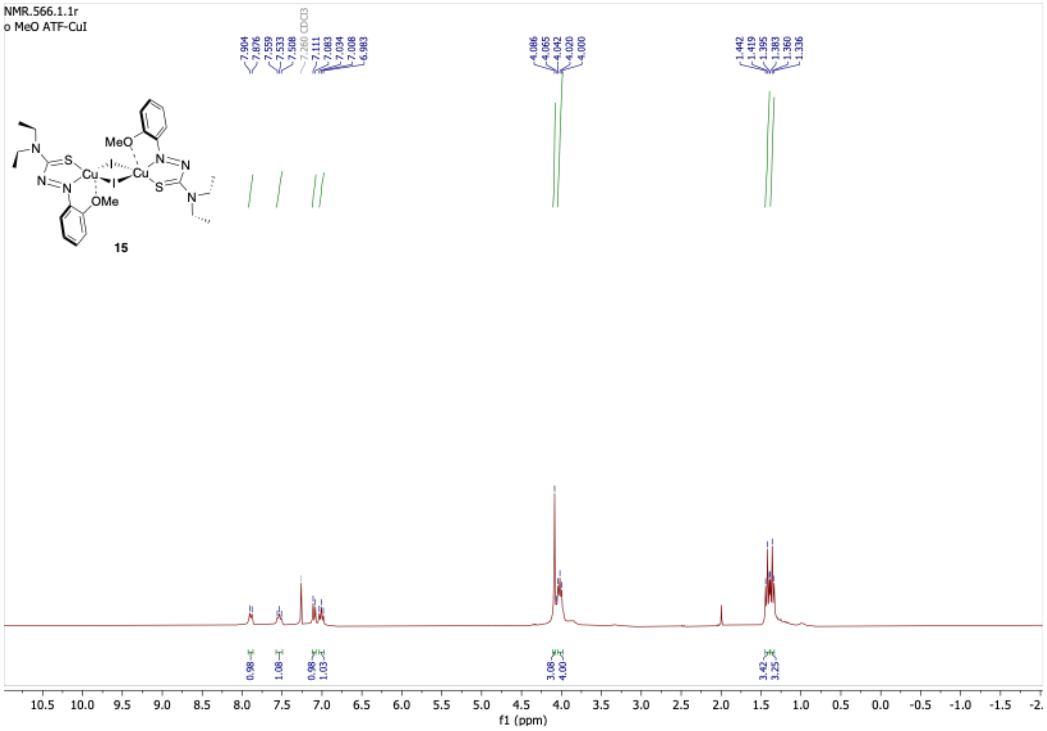
NMR.566.1.1r
o MeO ATF-CuI
7.904
7.876
7.559
7.533
7.508
7.260 CDCl3
7.111
7.069
7.034
7.008
6.983
4.086
4.065
4.042
4.020
4.000
1.442
1.419
1.395
1.383
1.360
1.336
15
0.98
1.08
0.98
1.03
3.08
4.00
3.42
3.25
f1 (ppm)

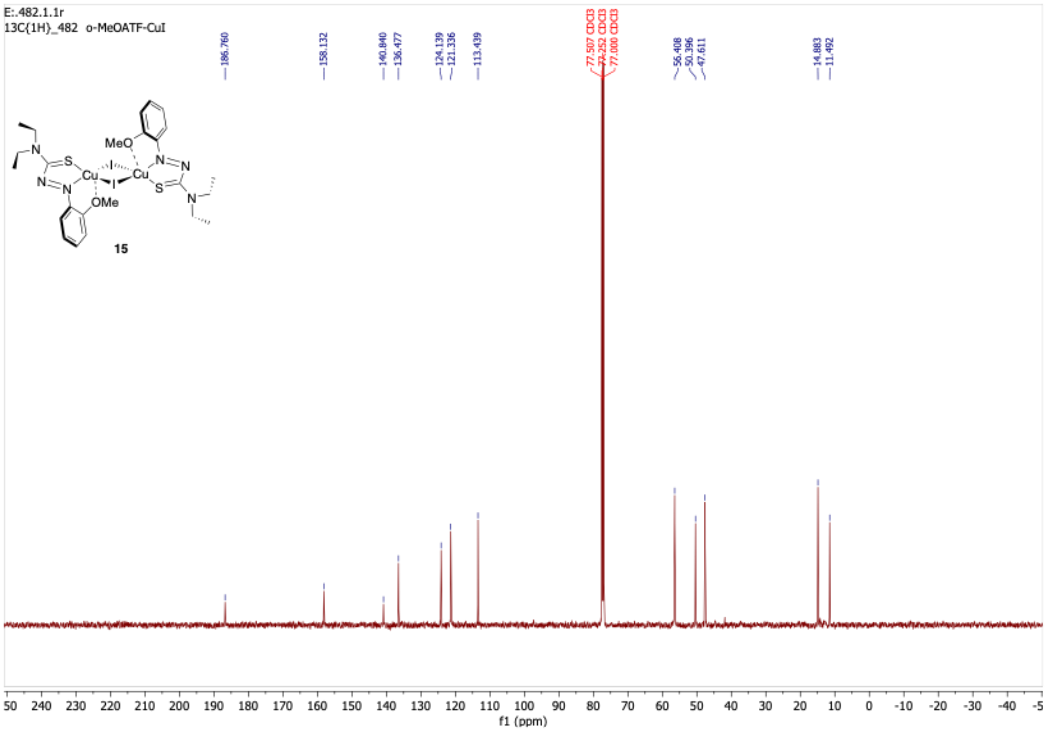
E:.482.1.1r
13C{1H}_482 o-MeOATF-CuI
186.760
158.132
140.840
136.477
124.139
121.336
113.439
77.507 CDCl3
77.252 CDCl3
77.000 CDCl3
56.408
50.396
47.611
14.883
11.492
MeO
OMe
15
f1 (ppm)

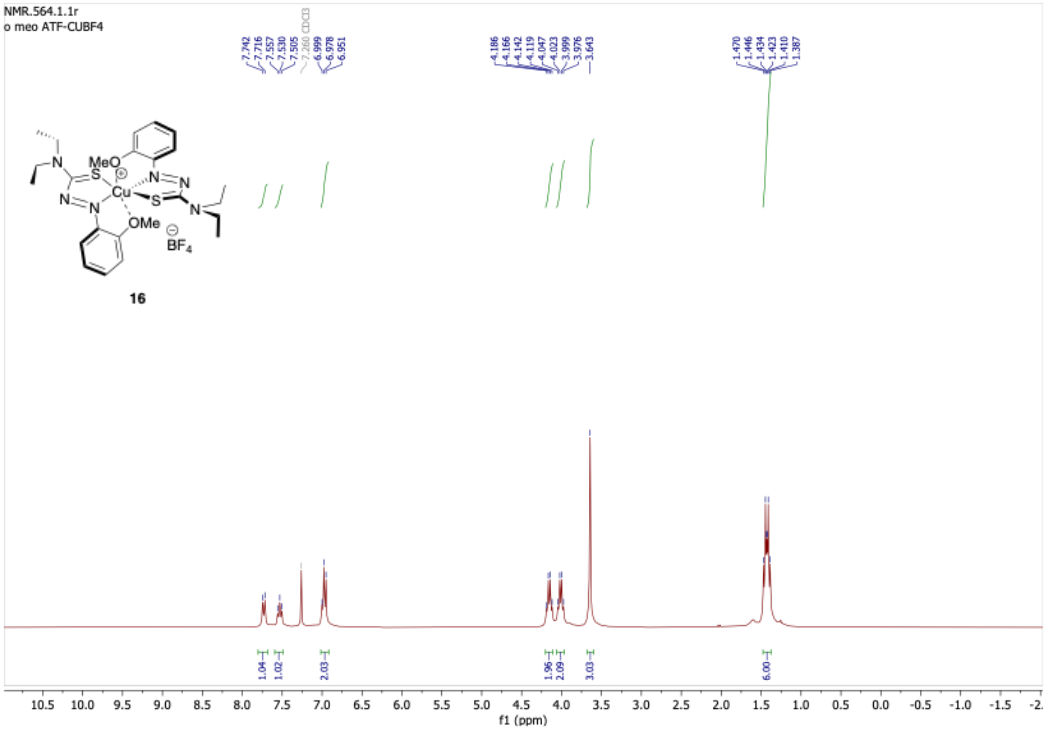
NMR.564.1.1r
o meo ATF-CUBF4
7.742
7.735
7.557
7.530
7.505
7.260 CDCl3
6.999
6.978
6.951
4.186
4.166
4.142
4.119
4.047
4.023
3.999
3.976
3.643
1.470
1.454
1.434
1.423
1.410
1.387
MeO
OMe
BF4
16
1.04
1.02
2.03
1.96
2.09
3.03
6.00
f1 (ppm)

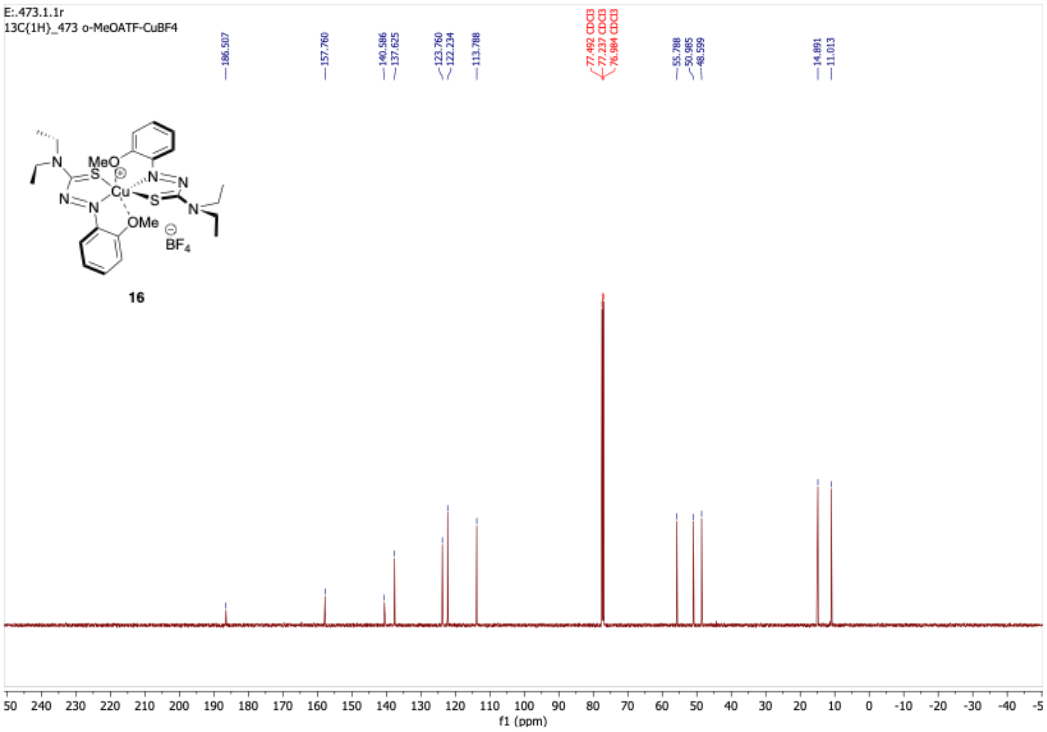
E:.473.1.1r
13C{1H}_473 o-MeOATF-CuBF4
186.507
157.760
140.586
137.625
123.760
122.234
113.788
77.492 CDCl3
77.237 CDCl3
76.984 CDCl3
55.788
50.985
49.599
14.891
11.013
16
f1 (ppm)

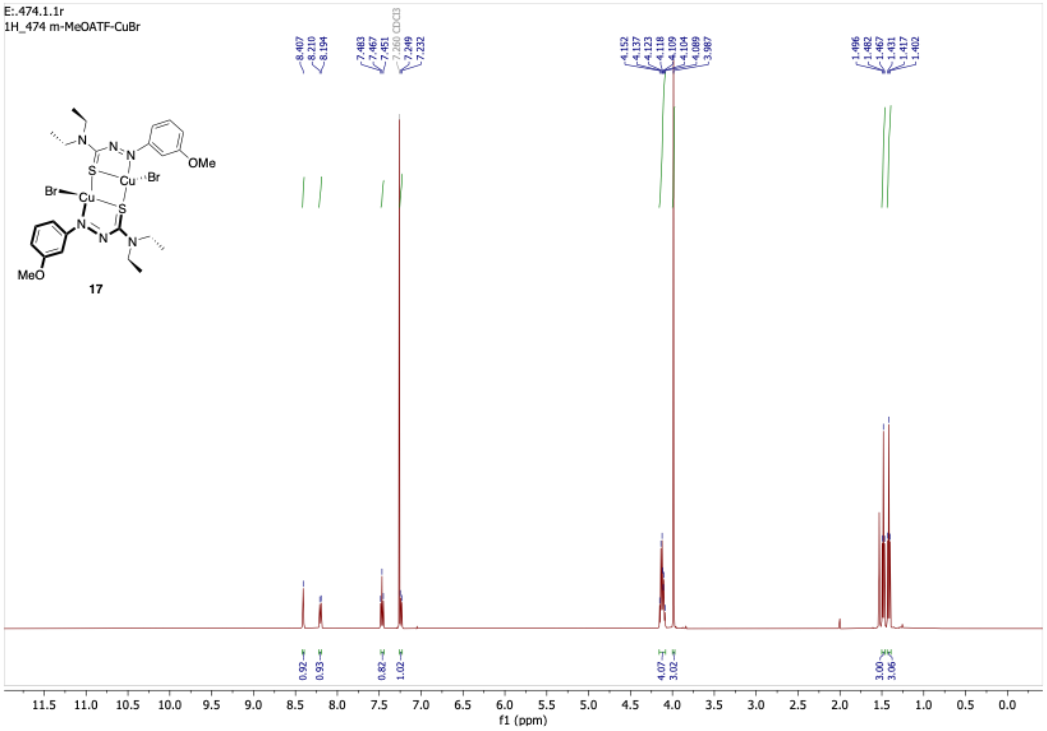
E:.474.1.1r
1H_474 m-MeOATF-CuBr
8.407
8.210
8.194
7.483
7.467
7.451
7.249
7.232
CDCl3
4.152
4.137
4.123
4.118
4.109
4.104
4.089
3.987
1.496
1.482
1.467
1.431
1.417
1.402
17
0.92
0.93
0.82
1.02
4.07
3.02
3.00
3.06
f1 (ppm)

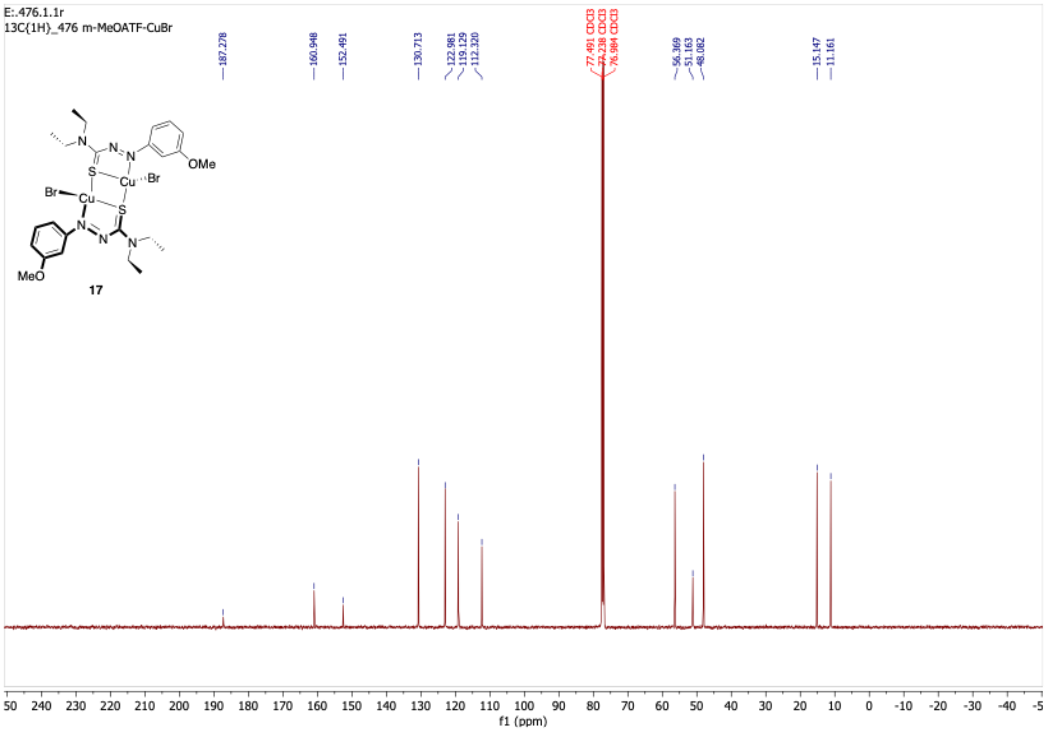
E:.476.1.1r
13C{1H}_476 m-MeOATF-CuBr
17
f1 (ppm)

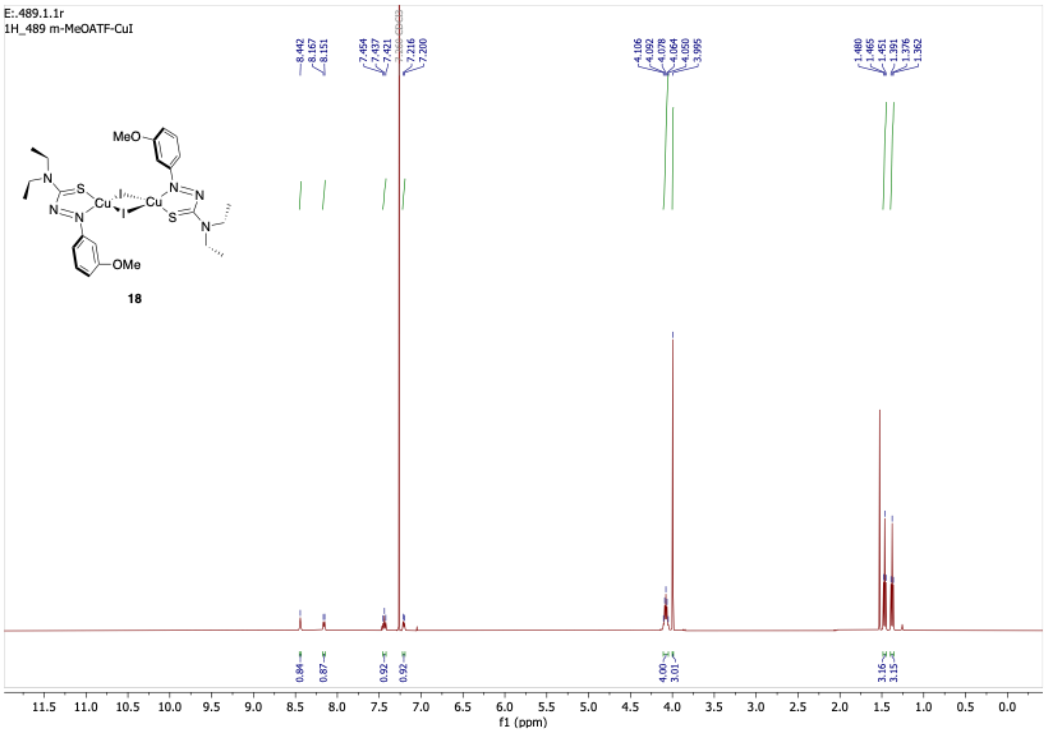
E:.489.1.1r
1H_489 m-MeOATF-CuI
18
f1 (ppm)

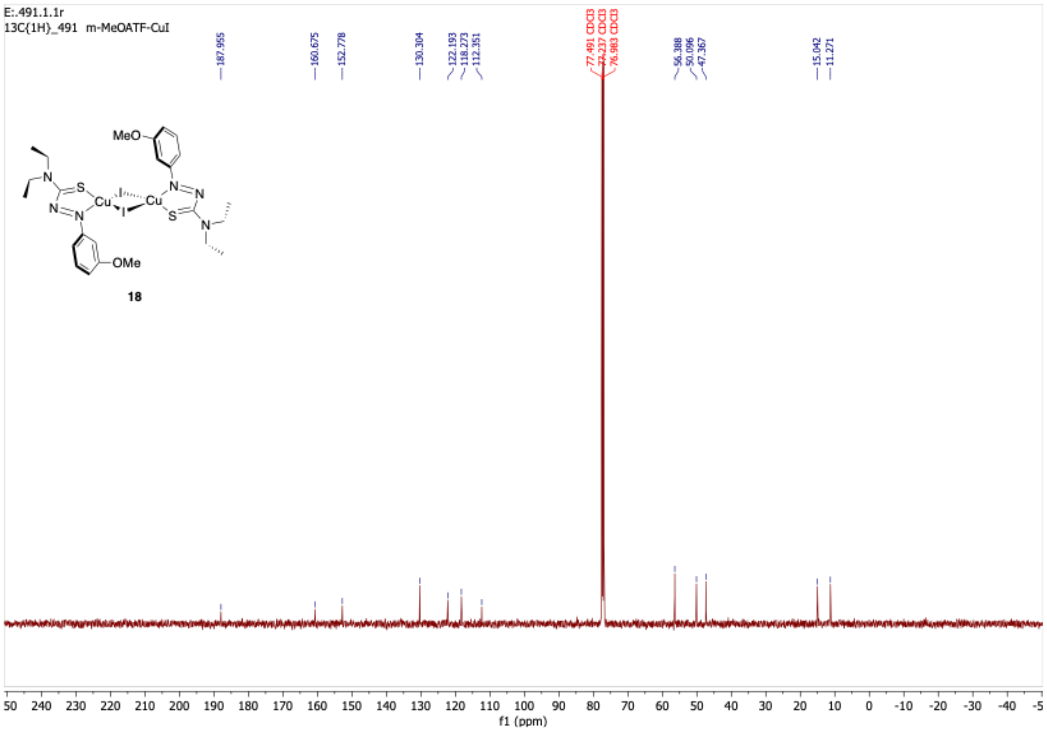
E:.491.1.1r
13C{1H}_491 m-MeOATF-CuI
187.955
160.675
152.778
130.304
122.193
118.273
112.351
77.491 CDCl3
77.237 CDCl3
76.983 CDCl3
56.388
50.096
47.367
15.042
11.271
MeO
OMe
18
f1 (ppm)

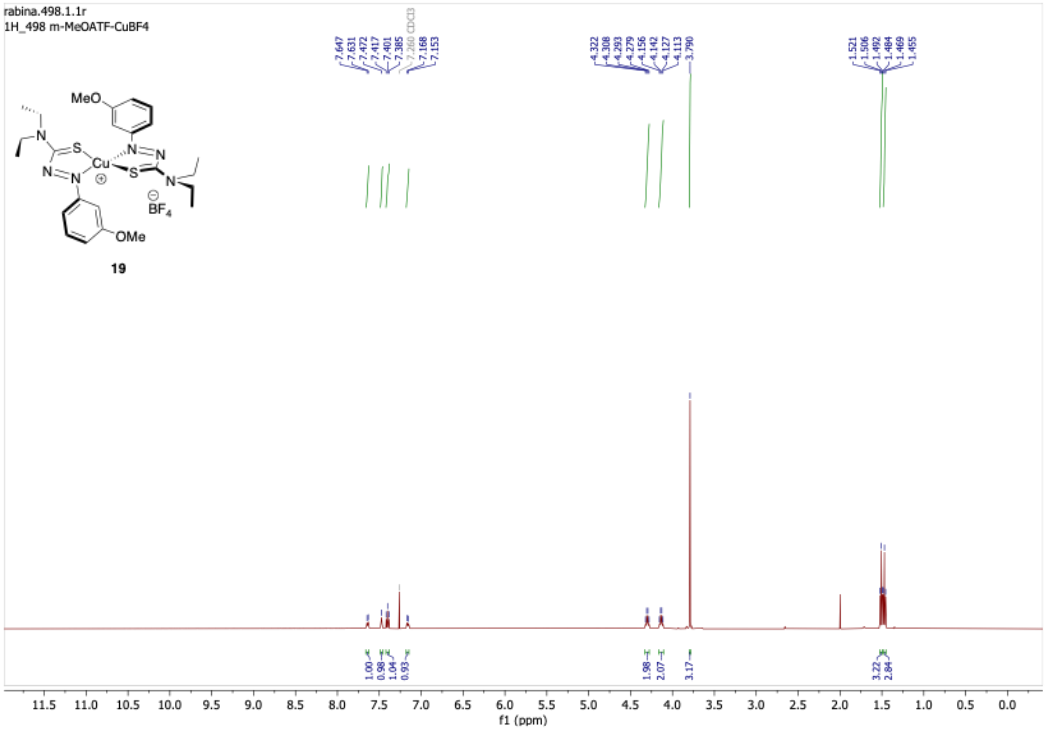
rabina.498.1.1r
1H_498 m-MeOATF-CuBF4
7.647
7.631
7.472
7.417
7.401
7.385
7.168
7.153
CDCl3
4.322
4.308
4.293
4.279
4.156
4.142
4.127
4.113
3.790
1.521
1.506
1.492
1.464
1.449
1.435
MeO
OMe
BF4
19
1.00
0.98
1.04
0.93
1.98
2.07
3.17
3.22
2.84
f1 (ppm)

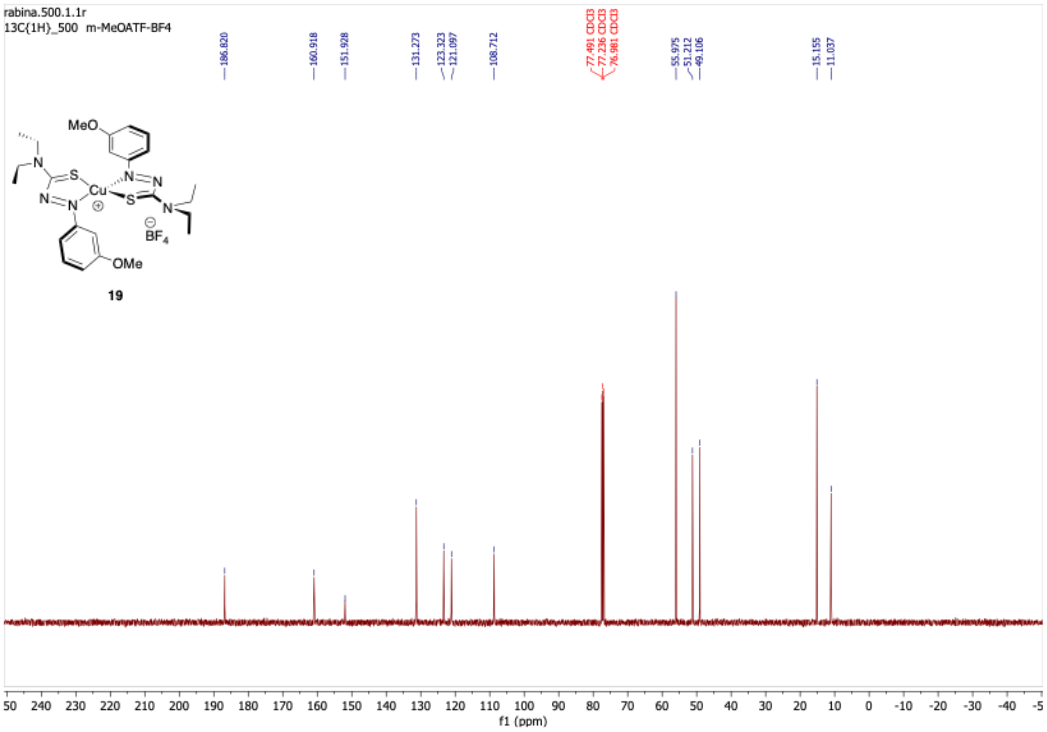

Energetics and Frontier Molecular Orbitals for *para*-MeOATF complexes

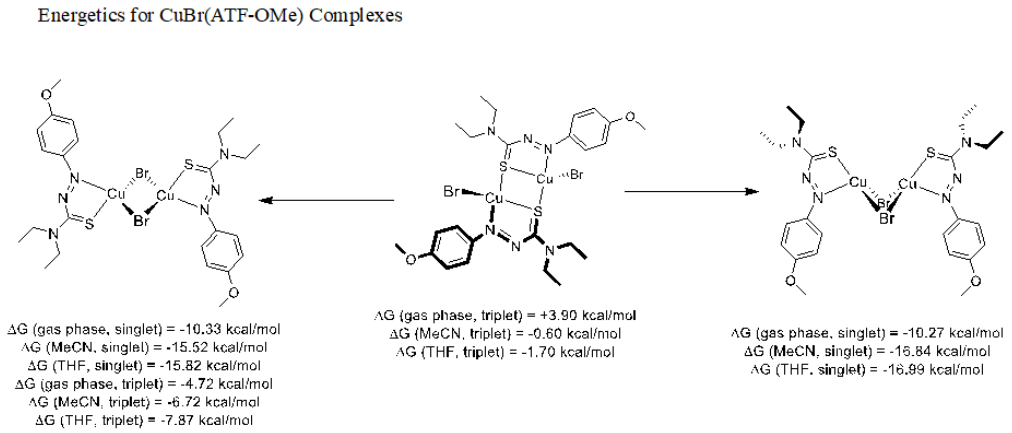

Figure A3.1: Calculated Energy values for various orientations with found crystal structure as middle structure. As *exo-halogen*, halogen-bridged (μ-X) and halogen-bridged "butterfly" structures were formed, the free energy of each orientation was modeled and compared.

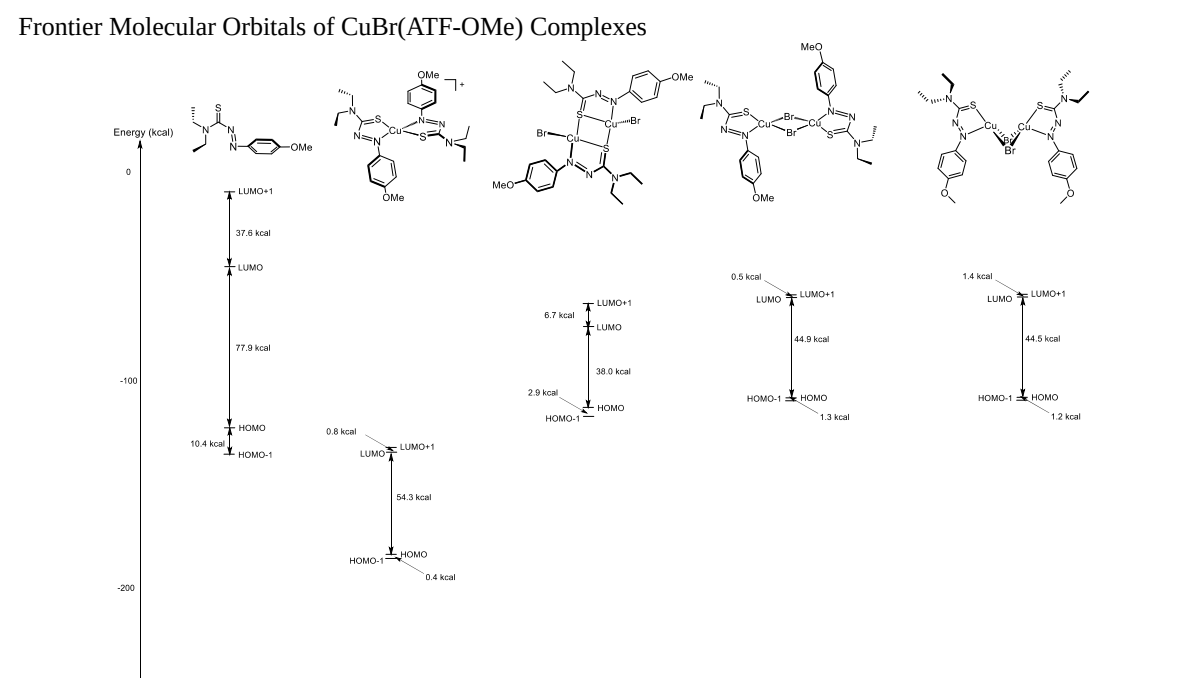

Figure A3.2: Frontier Molecular Orbital Diagram of the energy gaps for the various *para*-MeOATF•Cu^{I}Br dimer complexes compared to 2:1 complex and ligand.

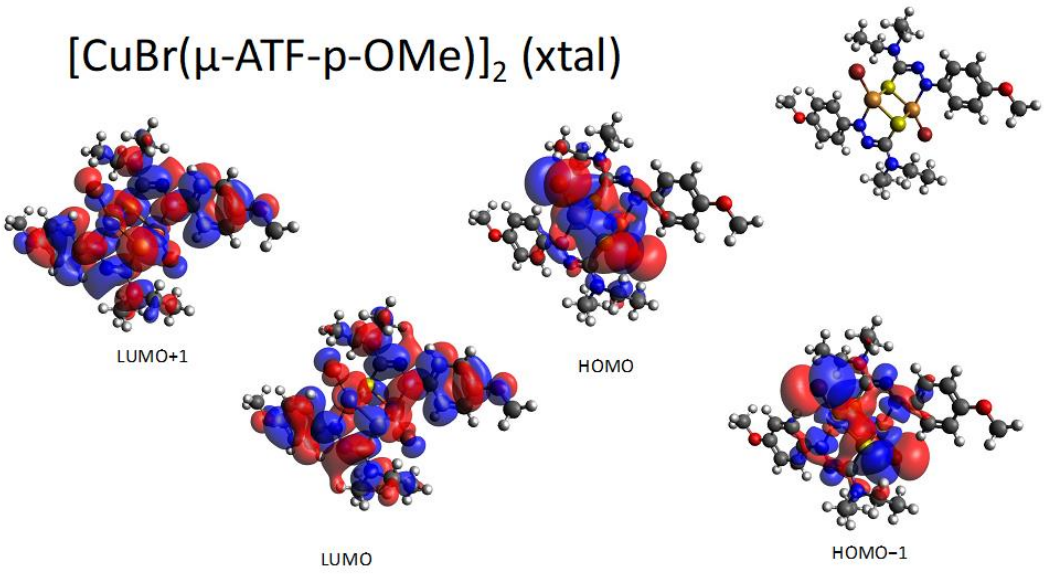

Figure A3.3: Computationally derived orbital diagram of the found crystal structure for the *para*-MeOATF-Cu^{I}Br complex in *exo*-Br dimeric orientation.

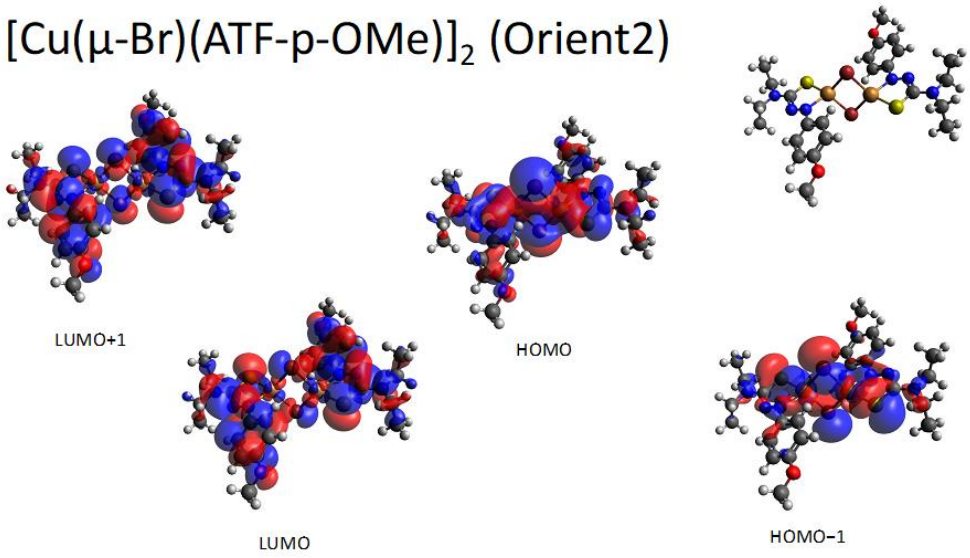

Figure A3.4: Computationally derived orbital diagram of the *para*-MeOATF-Cu^{I}Br complex in the halogen bridged μ-Br dimeric orientation.

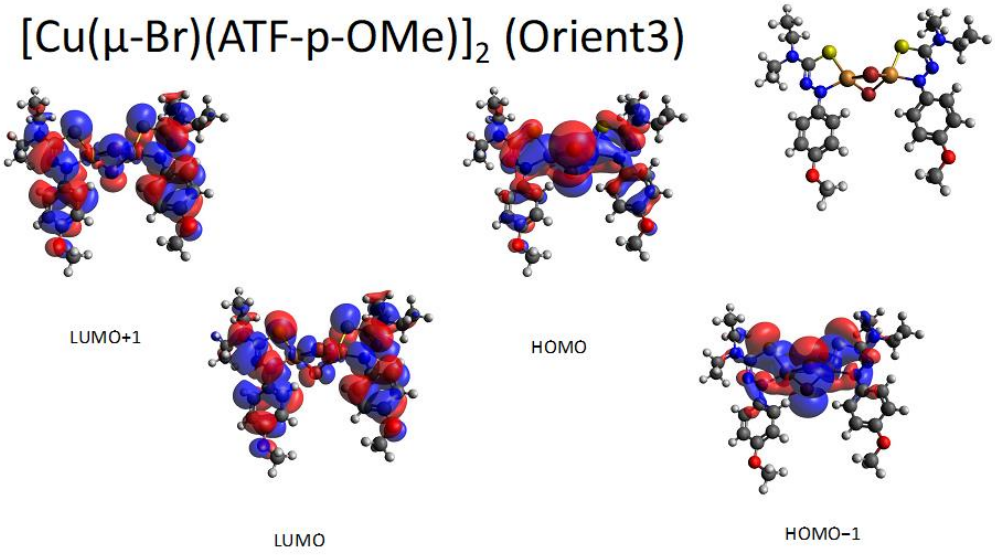

Figure A3.5: Computationally derived orbital diagram of the μ-Br halogen-bridged *para*-MeOATF-Cu^{I}Br complex in the "butterfly" dimeric orientation.

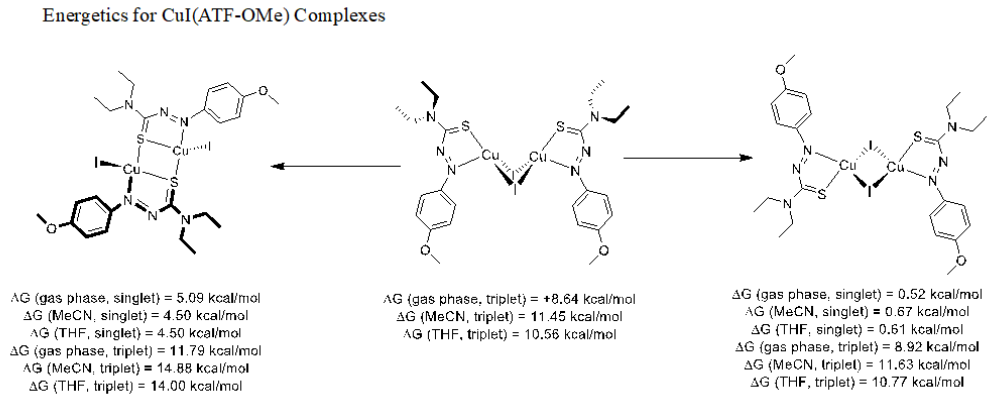

Figure A3.6: Calculated Energy values for three potential orientations against found crystal structure (middle structure) for *para*-MeOATF-Cu^{I}I dimeric complex. As *exo-halogen*, halogen-bridged (μ-X) and halogen-bridged "butterfly" structures were formed, the free energy of each orientation was modeled and compared.

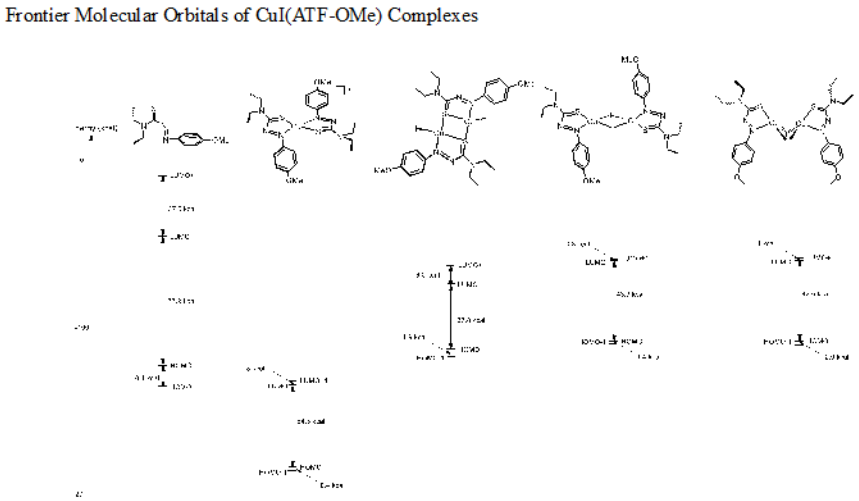

Figure A3.7: Frontier Molecular Orbital Diagram of the energy gaps for the various para-MeOATF•Cu^{I}I dimer complexes and compared to 2:1 complex and ligand by itself.

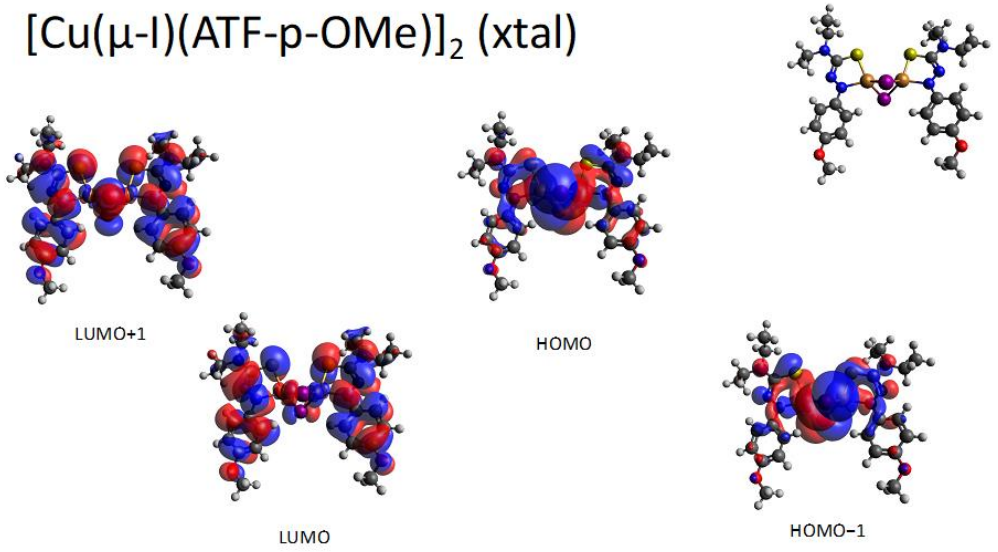

Figure A3.8: Computationally derived orbital diagram of the found *para*-MeOATF•$Cu^{I}I$ dimer crystal structure.

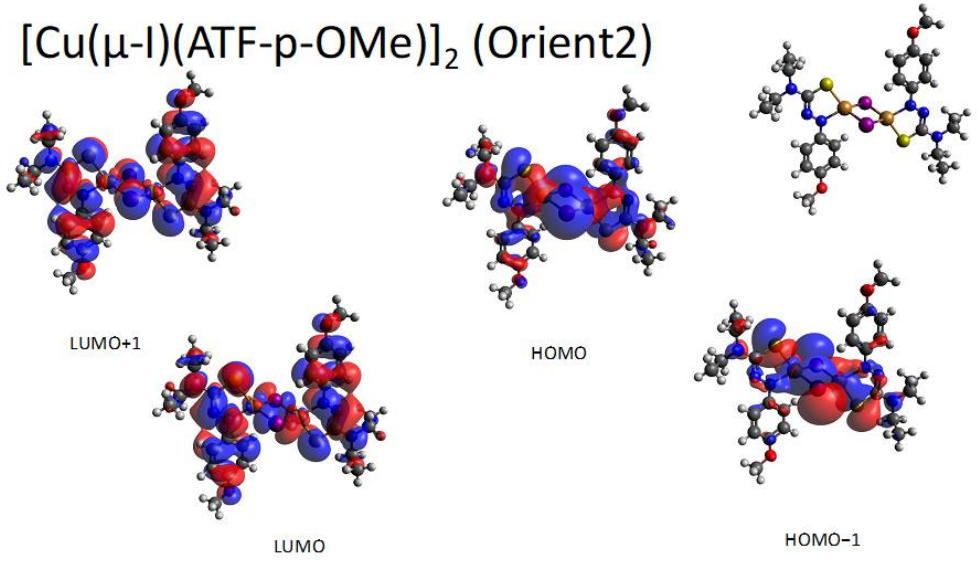

Figure A3.9: Computationally derived orbital diagram of the μ-I dimeric orientation.

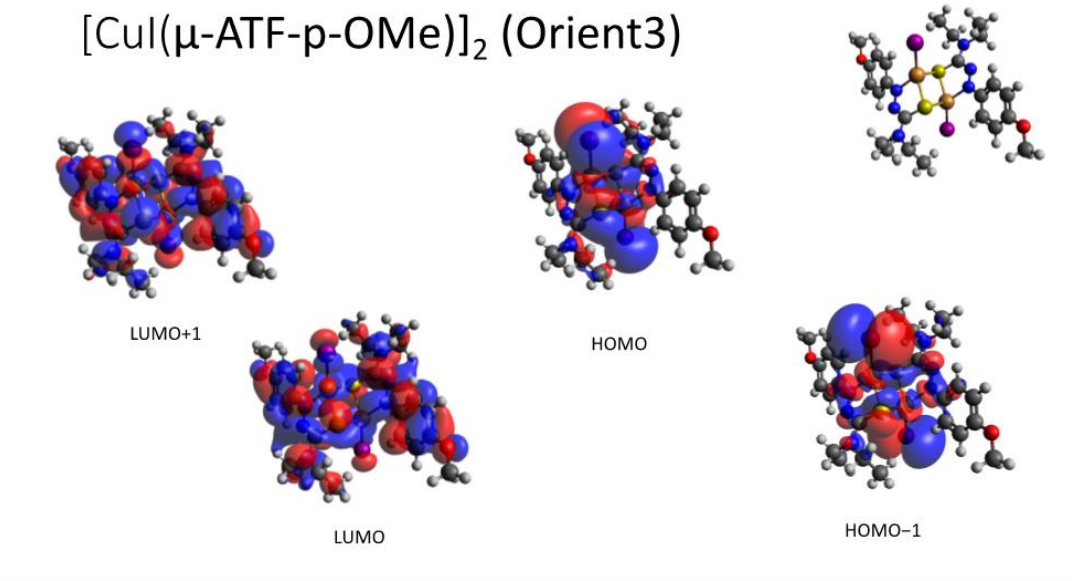

Figure A3.10: Computationally derived orbital diagram of the *exo*-I dimeric orientation.

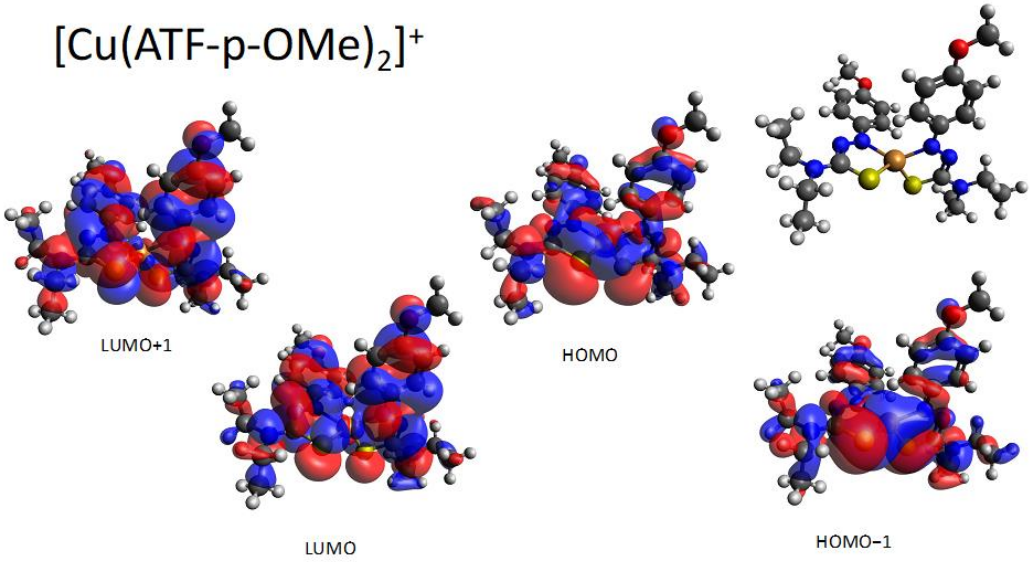

Figure A3.11: Computationally derived orbital diagram of the found crystal structure.

Computational Energies of Predicted Mechanistic Pathways

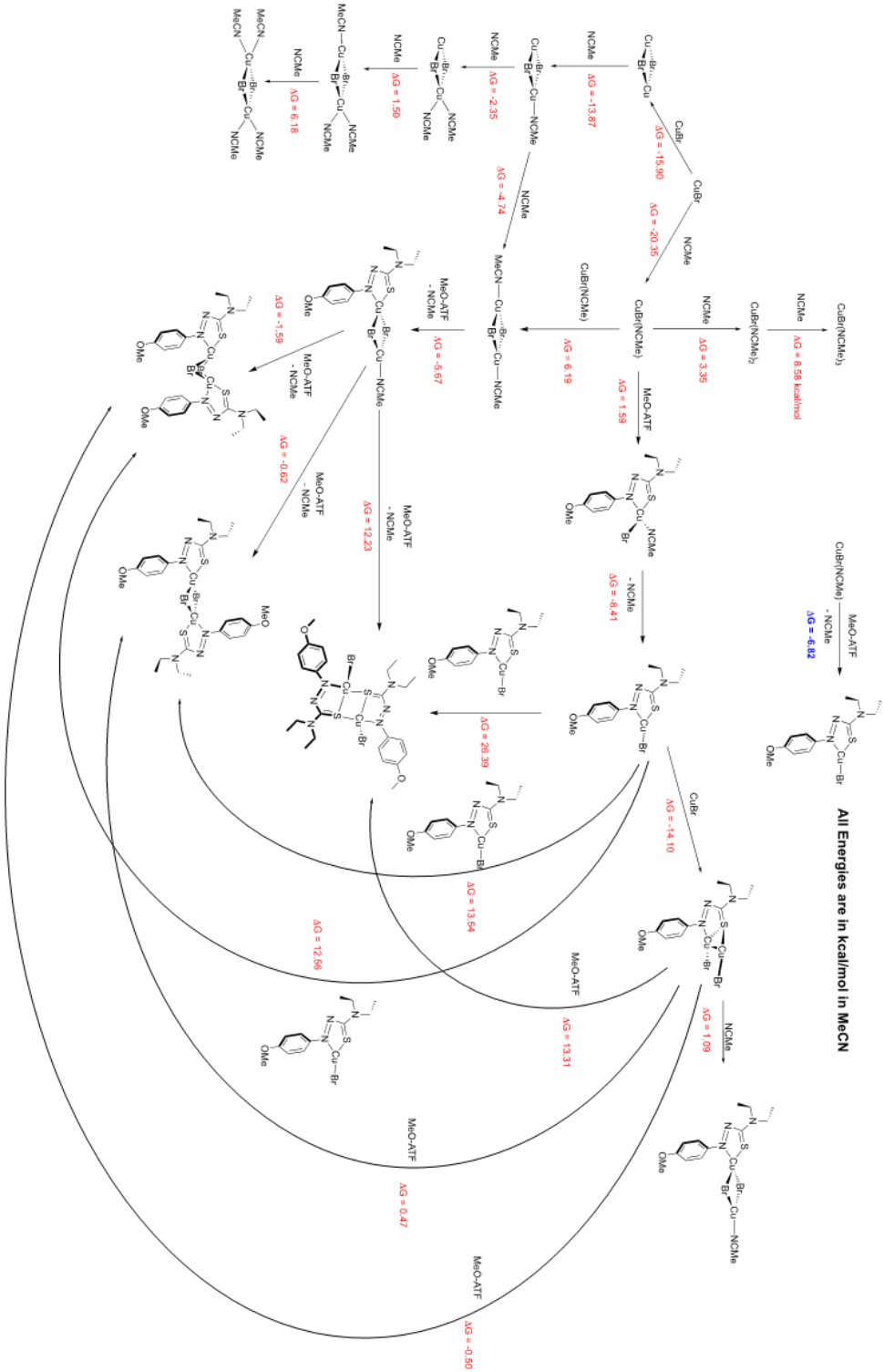

Figure A3.12: Overview of the computational mechanistic evaluation of the potential complex orientations of *para*-MeOATF (**6**) and $Cu^{I}Br$.

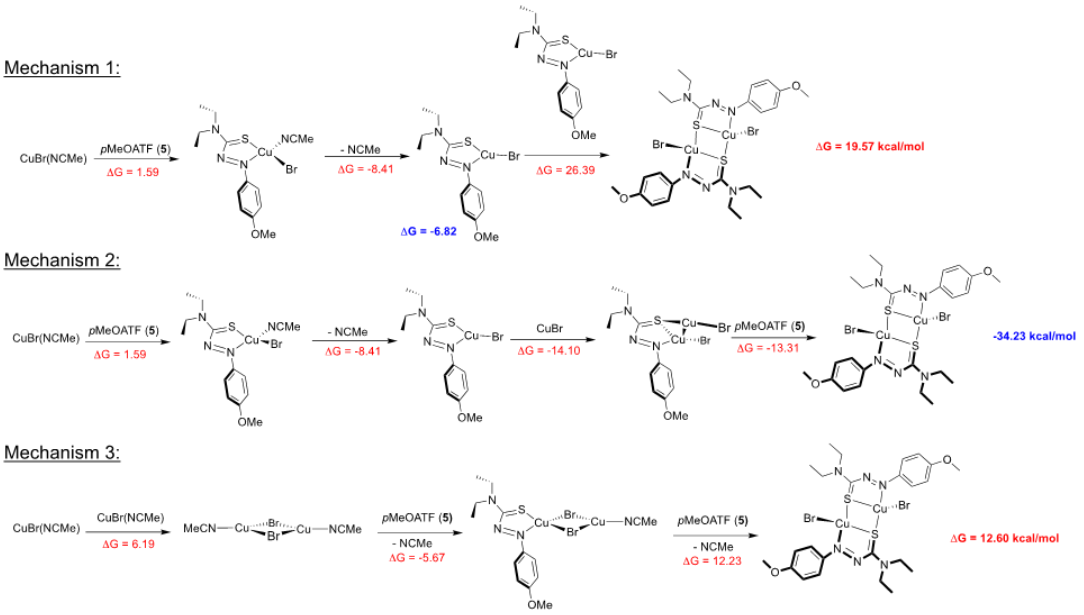

Figure A3.13: Comparison of binding association mechanisms for $Cu^{I}Br$ with *para*-MeOATF (**6**) based off the values found in Figure **A3.12** and crystalline (**11**).

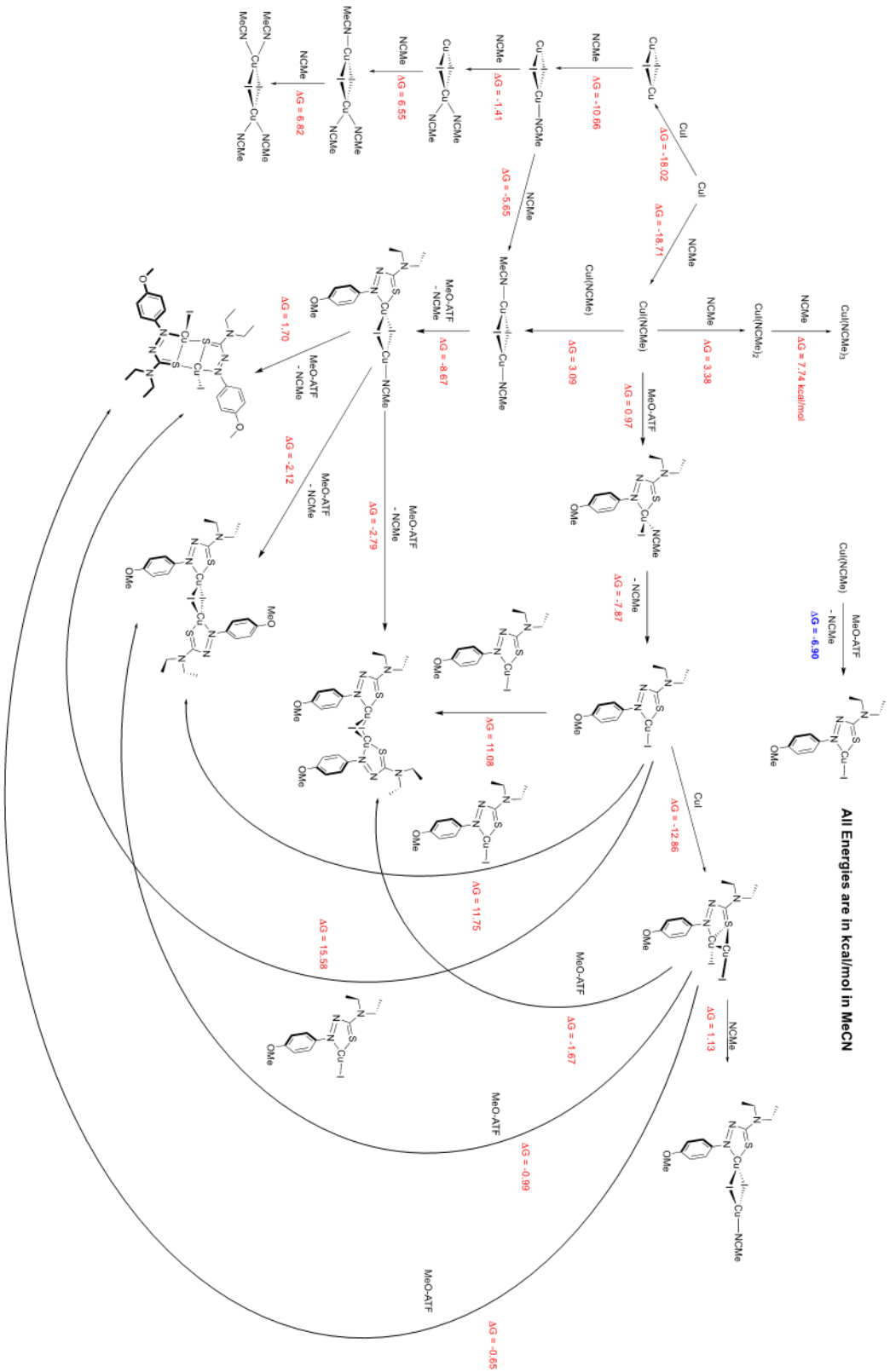

Figure A3.14: Overview of the computational mechanistic evaluation of the potential complexes of *para*-MeOATF (**6**) and $Cu^{I}I$.

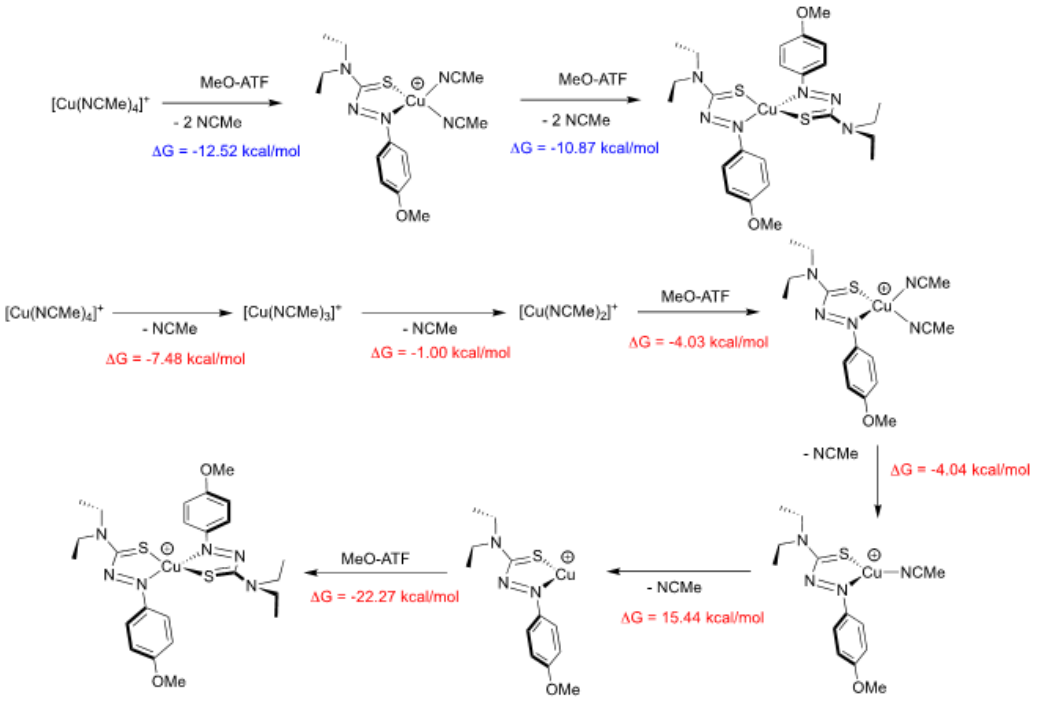

Figure A3.15: Computational mechanistic mvaluation of the potential complexes of *para*-MeOATF (**6**) and $[(CH_3CN)_4Cu^I](BF_4)$ based on crystalline (**13**).

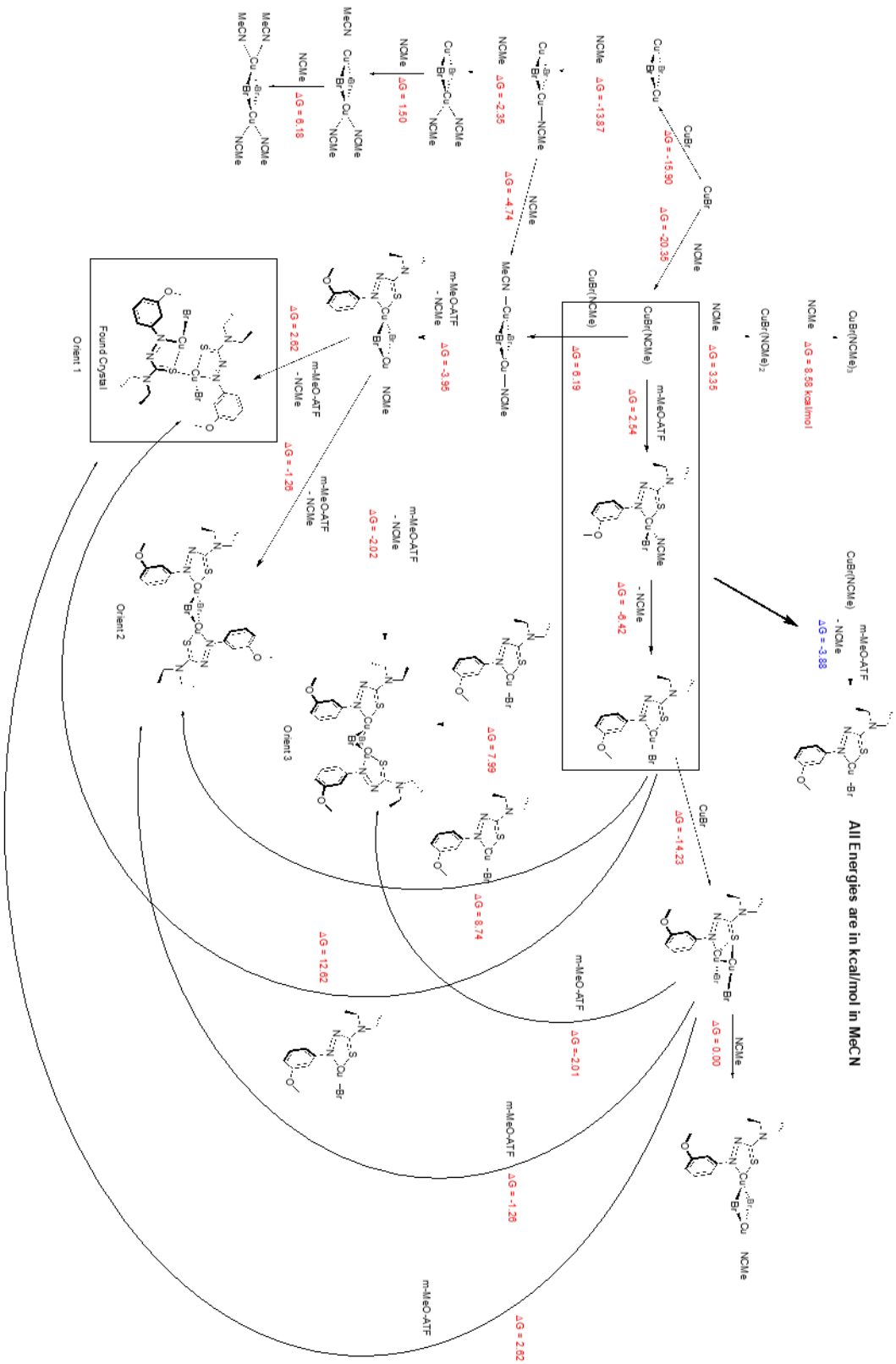

Figure A3.16: Overview of the computational mechanistic evaluation of the potential complexes of *meta*-MeOATF (**10**) and $Cu^{I}Br$

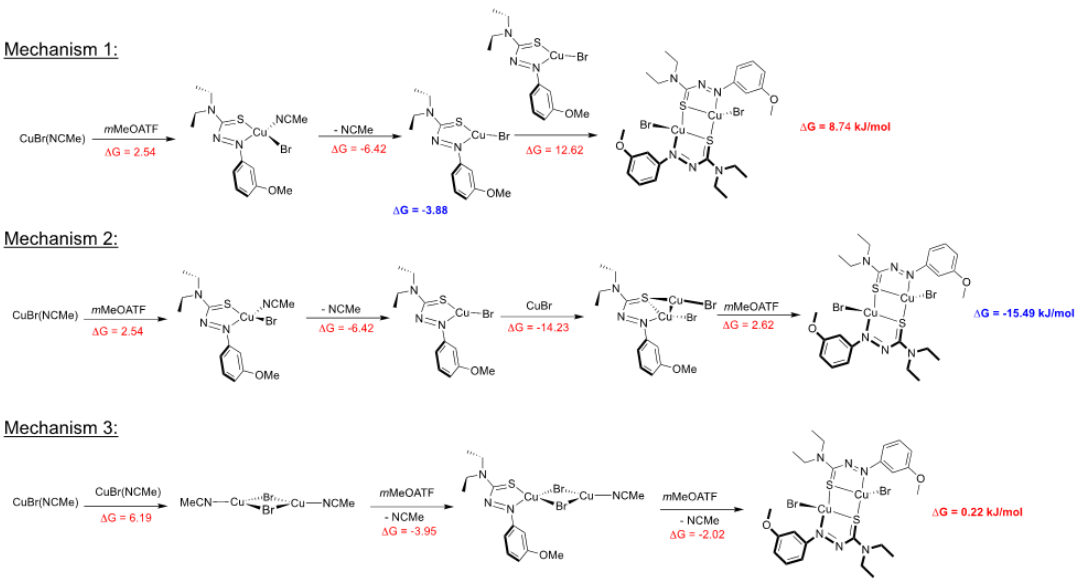

Figure A3.17: Comparison of Binding Association Mechanisms for $Cu^{I}Br$ with *meta*-MeOATF (**10**) based on the values found in Figure **A3.16** and crystalline (**17**).

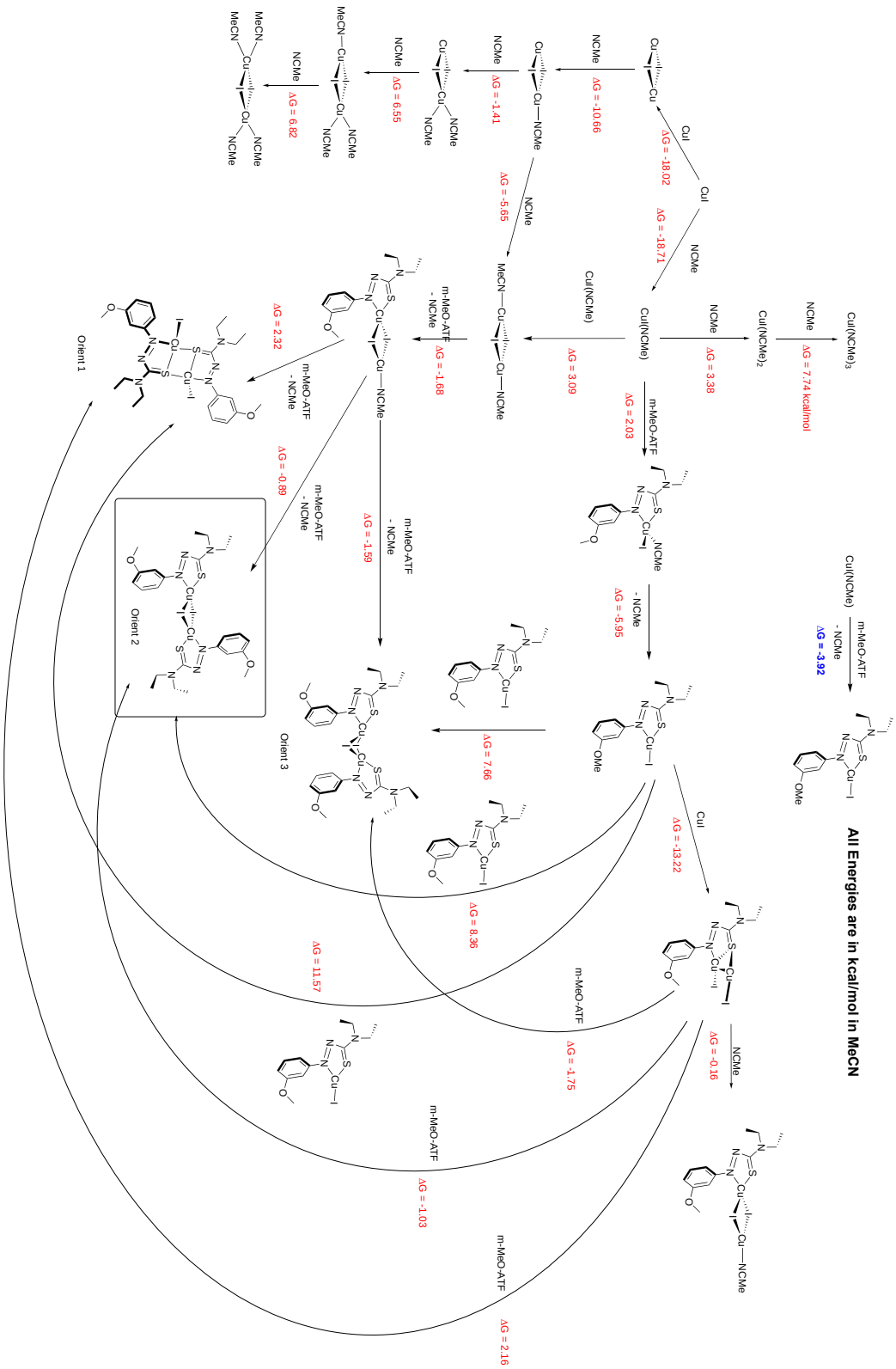

Figure A3.18: Overview of the computational mechanistic evaluation of the potential complexes of *meta*-MeOATF (**10**) and $Cu^{I}I$.

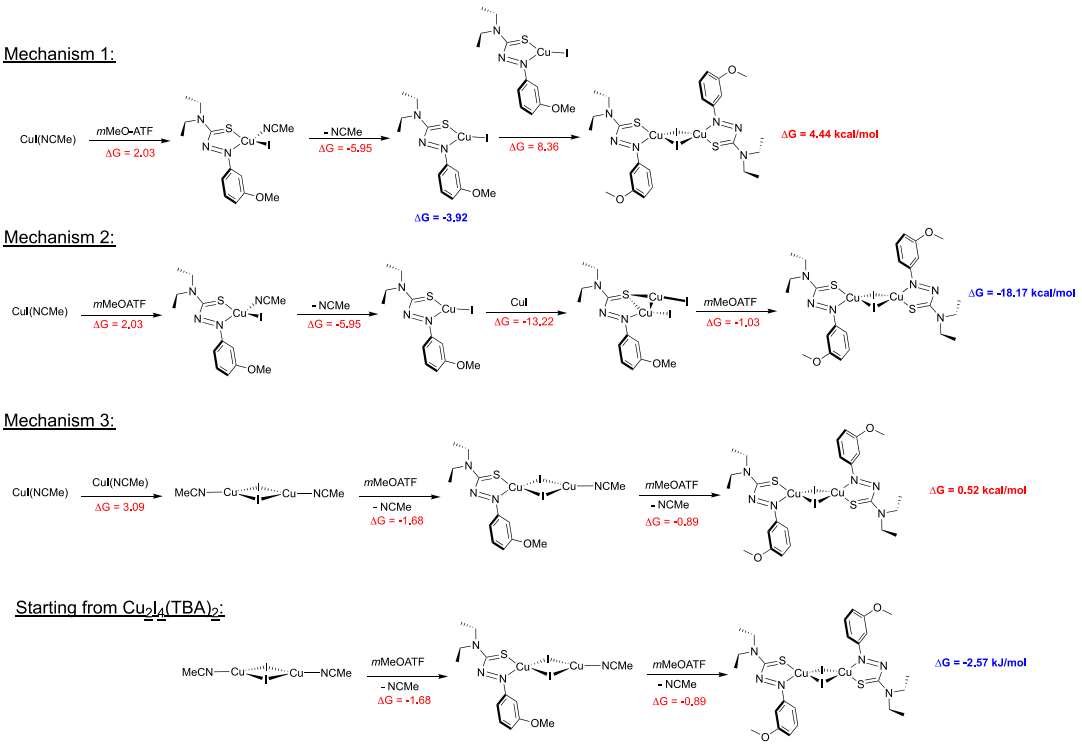

Figure A3.19: Comparison of Binding Association Mechanisms for $Cu^{I}I$ with *meta*-MeOATF (**10**) based on the values found in Figure **A3.18** and crystalline (**18**).

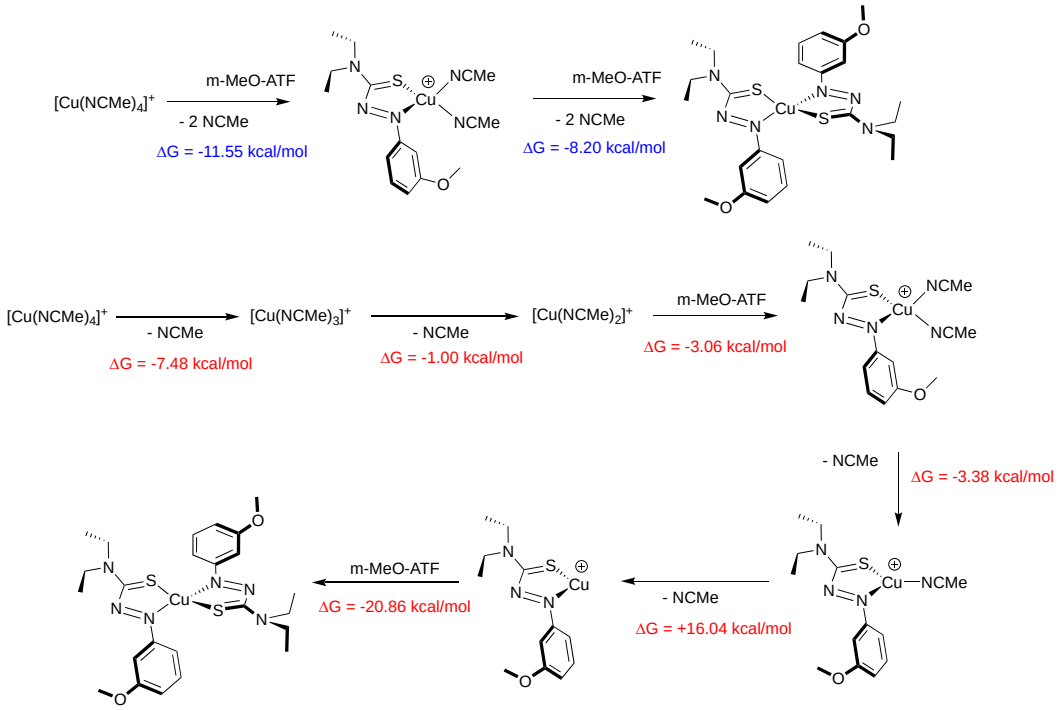

Figure A3.20: Computational mechanistic evaluation of the potential complexes of *meta*-MeOATF (**10**) and $[(CH_3CN)_4Cu^{I}](BF_4)$ and crystalline (**19**).

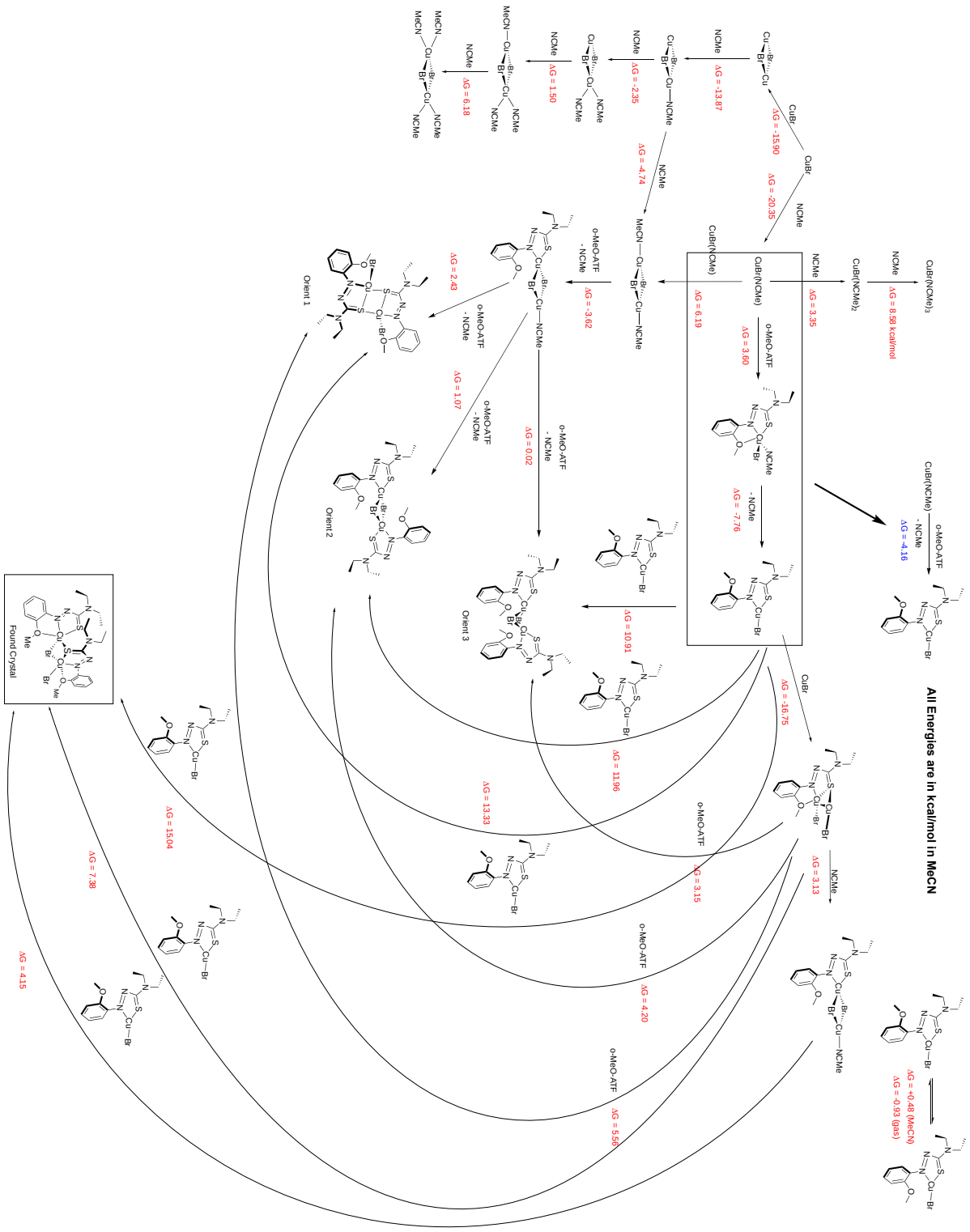

Figure A3.21: Overview of the computational mechanistic evaluation of the potential complexes of *ortho*-MeOATF (**8**) and $Cu^{I}Br$.

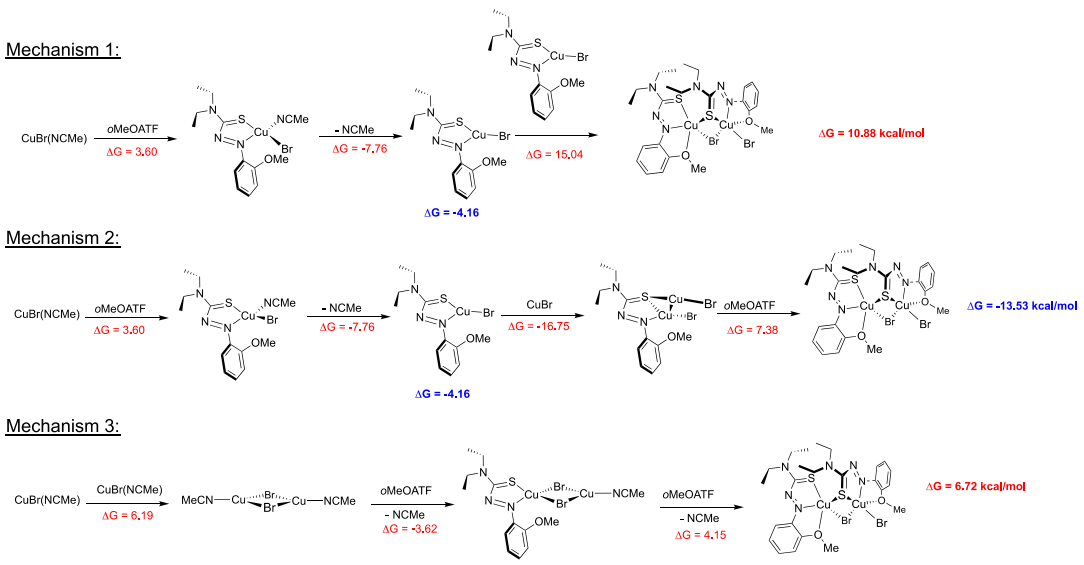

Figure A3.22: Comparison of Binding Association Mechanisms for $Cu^{I}Br$ with *ortho*-MeOATF (**8**) based on the values found in Figure **A3.21** and crystalline (**14**).

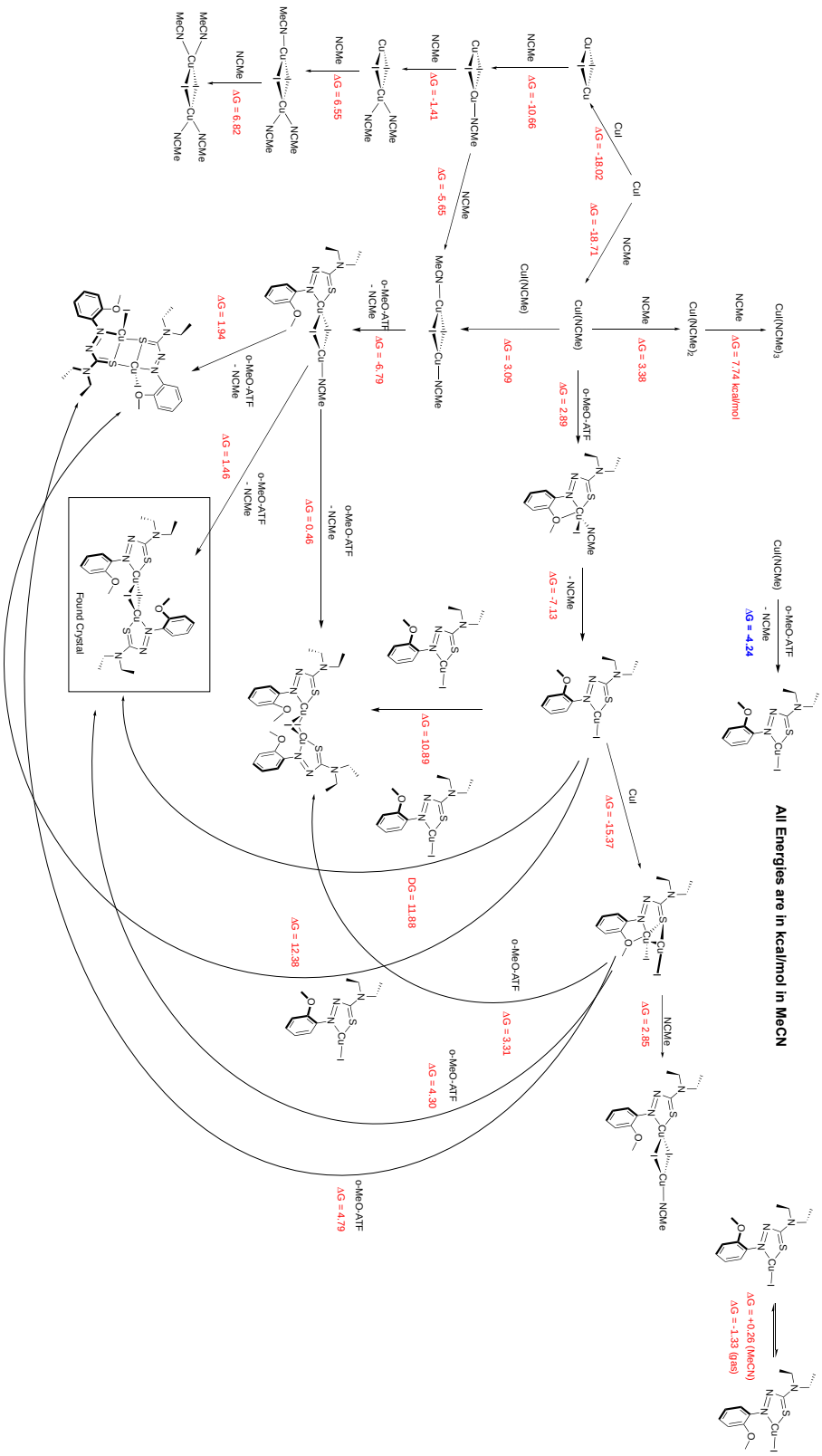

Figure A3.23: Overview of the computational mechanistic evaluation of the potential complexes of *ortho*-MeOATF (**8**) and $Cu^{I}I$

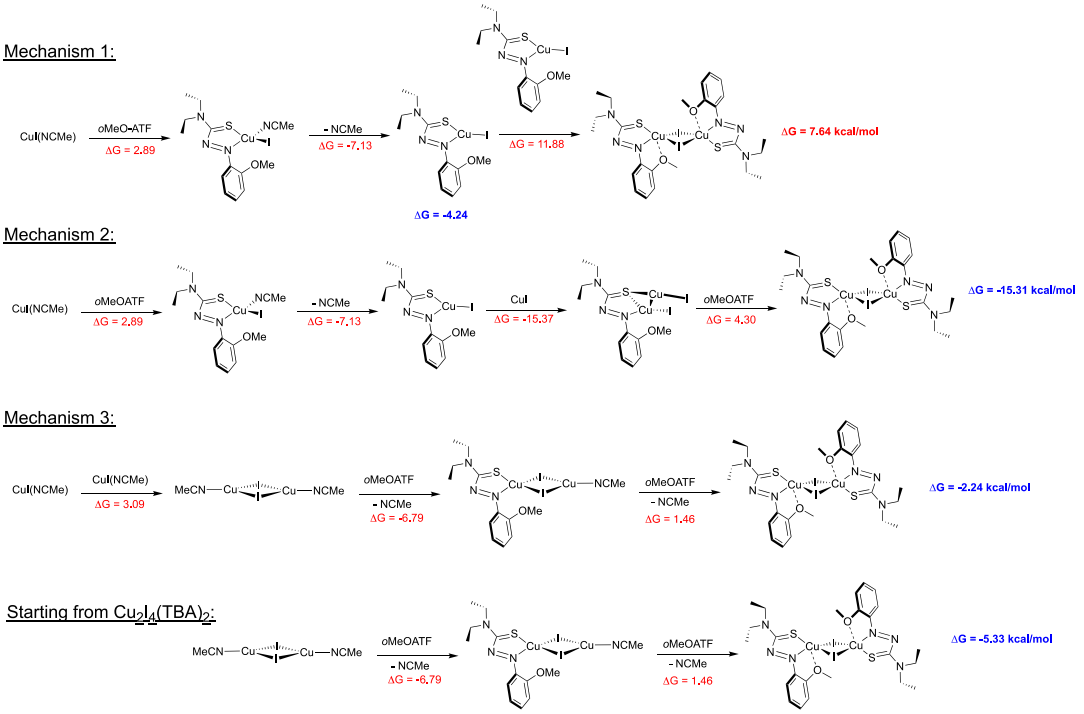

Figure A3.24: Comparison of binding association mechanisms for $Cu^{I}I$ with *ortho*-MeOATF (**8**) based on the values found in Figure **A3.23** and crystalline (**15**).

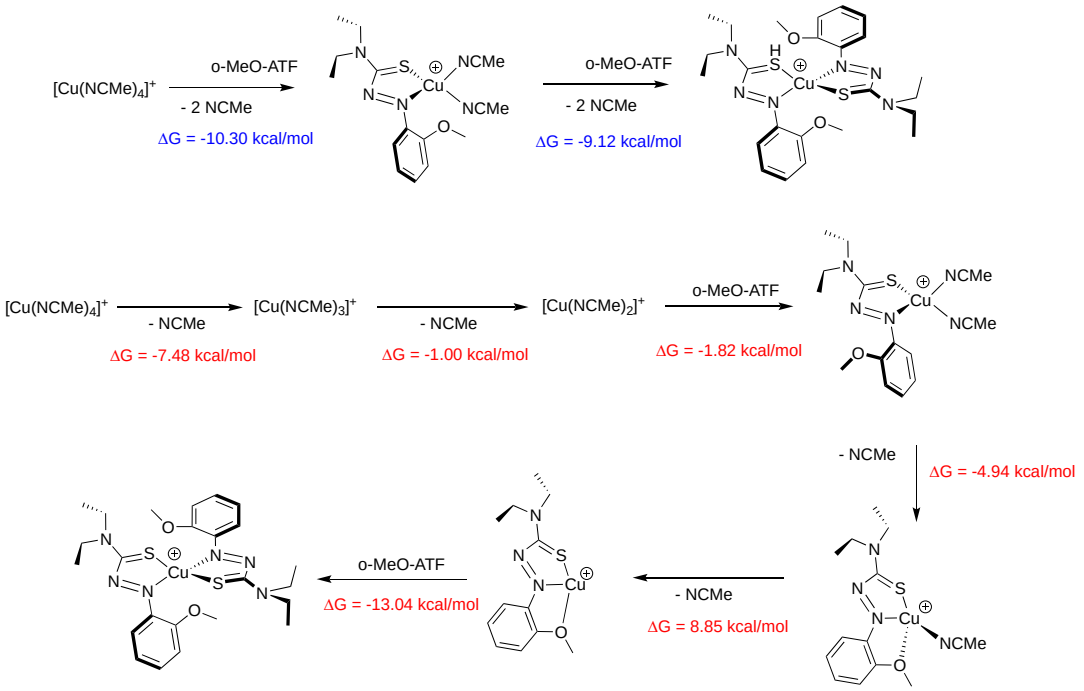

Figure A3.25: Computational mechanistic evaluation of the potential complexes of *ortho*-MeOATF (**8**) and $[(CH_3CN)_4Cu^{I}](BF_4)$ and crystalline (**16**).

UV-Vis Spectra data

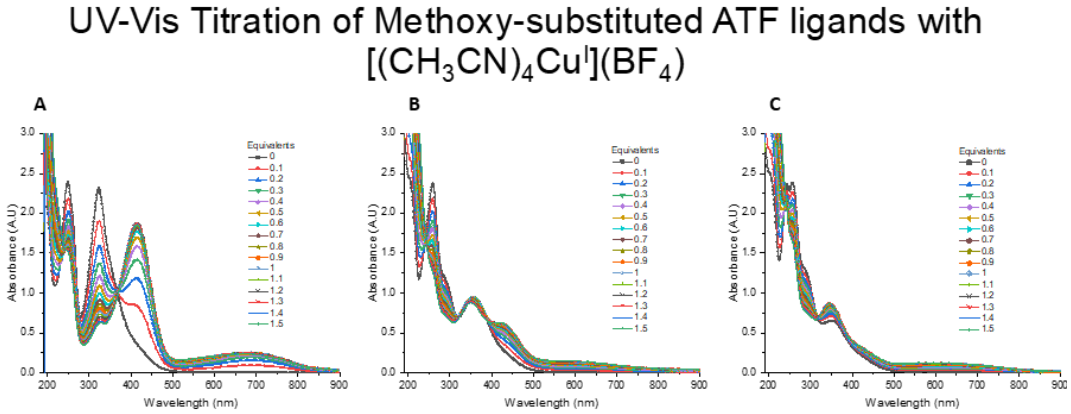

Figure A3.26: Representative examples of UV-Vis

X-ray Crystal Structure Experimental Protocols

Crystallographic Data for **11**: $C_{24}H_{35}Br_2Cu_2N_6O_{2.5}S_2$ (*M* =798.60 g/mol): monoclinic, space group C2/c (no. 15), *a* = 24.2339(13) Å, *b* = 8.1296(4) Å, *c* = 17.3573(9) Å, *β* = 117.842(2)°, *V* = 3023.7(3) Å^3, *Z* = 4, *T* = 100 K, μ(MoKα) = 4.223 mm^{-1}, *Dcalc* = 1.754 g/cm^3, 2Θmax =57.392°, 110818 reflections measured, 3893 unique (R_{int} = 0.0291, R_{sigma} = 0.0080), R_1 was 0.0165 (I > 2σ(I)), wR_2 was 0.0427 (all data).

X-ray diffraction data for **11** were collected at 100 K on a Bruker D8 Venture using MoKα-radiation (λ=0.71073 Å). Data have been corrected for absorption using SADABS[1] area detector absorption correction program. Using Olex2[2], the structure was solved with the SHELXT[3] structure solution program using Direct Methods and refined with the SHELXL[4] refinement package using least squares minimization. All non-hydrogen atoms were refined with anisotropic thermal parameters. Within the structure there is a partially occupied water located on a twofold axis. Upon freely refining the sight occupancy factor the occupancy returned near 0.5 (0.51) therefore for model simplicity the occupancy factor was fixed to 0.5. After refinement hydrogen atoms attached to a partially occupied water were found from the

residual density maps, placed, and refined resulting in chemically unreasonable shortening. Therefore, a bond length restraint (DFIX 0.85 0.02) was employed. All other hydrogen atoms of the investigated structure were located from difference Fourier maps but finally their positions were placed in geometrically calculated positions and refined using a riding model. Isotropic thermal parameters of the placed hydrogen atoms were fixed to 1.2 times the *U* value of the atoms they are linked to (1.5 times for methyl groups). Calculations and refinement of structures were carried out using APEX3[5], SHELXTL[6], and Olex2 software.

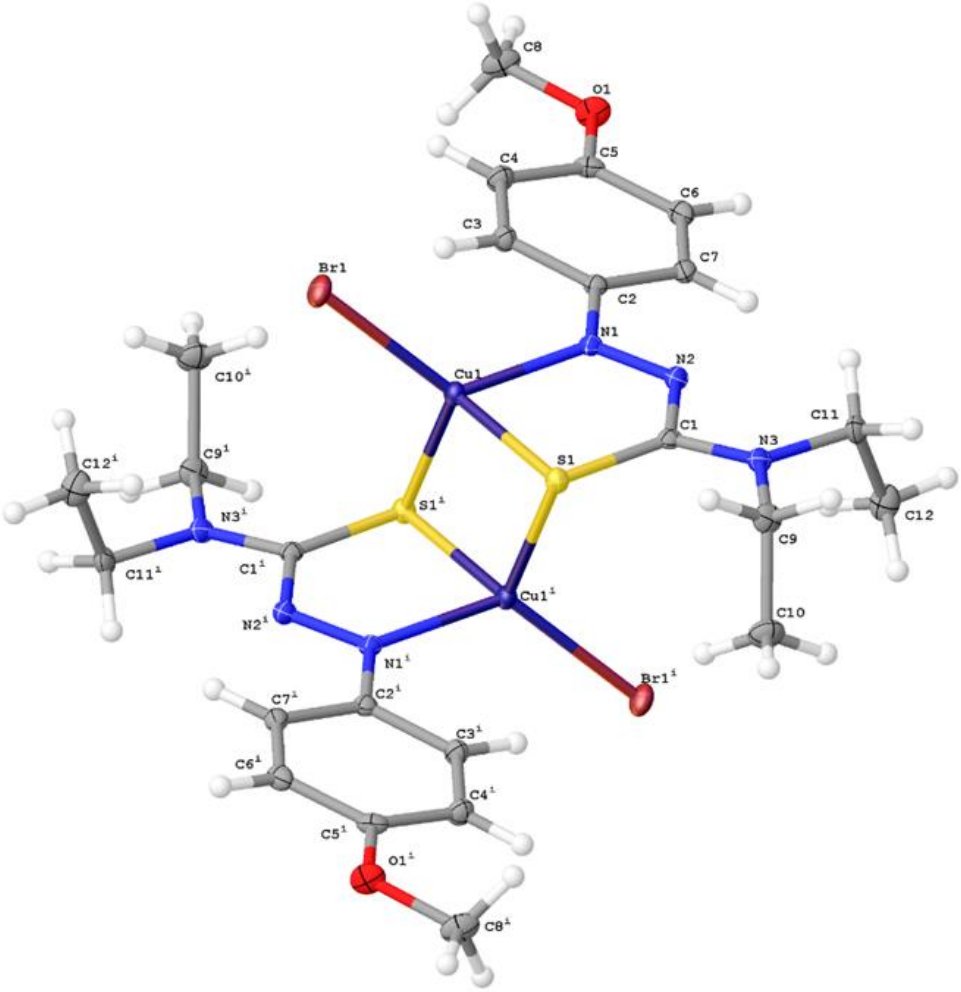

Crystallographic Data for **12**: $C_{24}H_{34}Cu_2I_2N_6O_2S_2$ (*M* = 883.57): orthorhombic, space group Pbca. *a* = 17.0538(19) A, b = 10.9415(12) A; c = 33.394(4) A; α = 90, β = 90, γ = 90, V = 6231.2(12) $Å^3$ Z = 8, T = 100K, MoKα (λ = 0.71073); ρ_{calc} = 1.884g/cm^3 , 2Θ range = 6.058 to 52.73; 169462 reflections collected, 6365 unique [R_{int} = 0.0700, R_{sigma} = 0.0234]

X-ray diffraction data for **12** were collected at 100 K on a Bruker D8 Venture using MoKα-radiation (λ=0.71073 Å). Data have been corrected for absorption using SADABS[1] area detector absorption correction program. Using Olex2[2], the structure was solved with the SHELXT[3] structure solution program using Direct Methods and refined with the SHELXL[4] refinement package using least squares minimization. All non-hydrogen atoms were refined with anisotropic thermal parameters. Hydrogen atoms of the investigated structure were located from difference Fourier maps but finally their positions were placed in geometrically calculated positions and refined using a riding model. Isotropic thermal parameters of the placed hydrogen atoms were fixed to 1.2 times the *U* value of the atoms they are linked to (1.5 times for methyl groups). Calculations and refinement of structures were carried out using APEX3[5], SHELXTL[6], and Olex2 software. After initial solution and refinement of the structure there were residual electron density peaks in the difference Fourier maps suggesting possible whole molecule disorder or a small twin component. However, the disordered positions of only the copper and the sulfur atoms are observed due to the small contribution of the disorder. Modeling the second position of these atomic sites (copper and sulfur) indicates a minor contribution of roughly 5%. Modeling these sites does not provide additional information, thus for simplicity the model presented is absent of disorder modeling. Modeling of the whole molecule disorder in this case would be troublesome and would require an

excessive amount of restraints and constraints to obtain a model stable for refinement. Two other data sets were collected and exhibited similar residual electron density during workup.

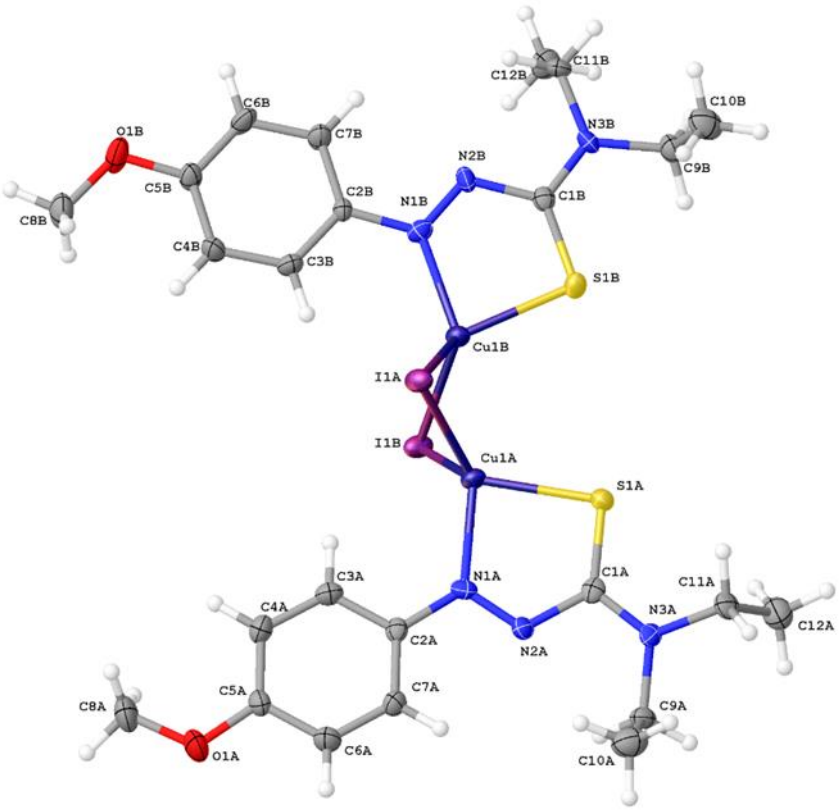

Crystallographic Data for **13**: $C_{28}H_{42}BCuF_4N_6O_3S_2$ (M =725.14 g/mol): triclinic, space group P-1 (no. 2), a = 10.3187(8) Å, b = 12.2882(9) Å, c = 13.9203(11) Å, α = 80.482(3)°, β = 86.348(3)°, γ = 76.307(3)°, V = 1690.7(2) Å^3, Z = 2, T = 100 K, μ(MoKα) = 0.830 mm^{-1}, $Dcalc$ = 1.424 g/cm^3, 2Θmax = 52.81°, 36525 reflections collected, 6924 unique (R_{int} = 0.0358, R_{sigma} = 0.0286), R_1 = 0.0328 (I > 2σ(I)), wR_2 = 0.0778 (all data).

X-ray diffraction data for **13** were collected at 100 K on a Bruker D8 Venture using MoKα-radiation (λ=0.71073 Å). Data have been corrected for absorption using SADABS[1] area detector absorption correction program. Using Olex2[2], the structure was solved with the SHELXT[3] structure solution program using Direct Methods and refined with the SHELXL[4]

refinement package using least squares minimization. All non-hydrogen atoms were refined with anisotropic thermal parameters. Hydrogen atoms of the investigated structure were located from difference Fourier maps but finally their positions were placed in geometrically calculated positions and refined using a riding model. Isotropic thermal parameters of the placed hydrogen atoms were fixed to 1.2 times the *U* value of the atoms they are linked to (1.5 times for methyl groups). Upon initial solution distal portions of one ligand, the tetrafluoroborate, and the tetrahydrofuran all displayed elongated thermal ellipsoids, suggesting disorder of these components data. These sections have been modeled as disordered over two positions. Calculations and refinement of structures were carried out using APEX3[5], SHELXTL[6], and Olex2 software.

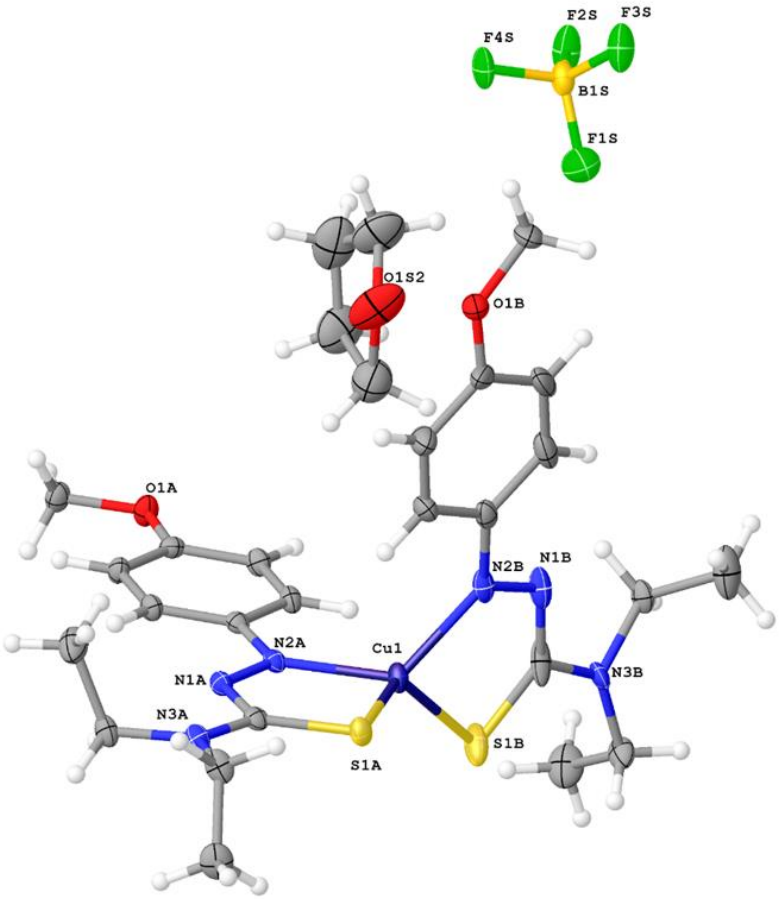

Crystallographic Data for **8**: $C_{12}H_{17}N_3OS$ (M =251.34 g/mol): monoclinic, space group $P2_1/c$ (no. 14), a = 10.9545(4) Å, b = 13.2160(4) Å, c = 8.7762(3) Å, β = 97.4780(10)°, V = 1259.76(7) Å^3, Z = 4, T = 100 K, μ(MoKα) = 0.245 mm^{-1}, $Dcalc$ = 1.325 g/cm^3, 2Θmax = 66.486°, 34915 reflections measured, 4845 unique (R_{int} = 0.0292, R_{sigma} = 0.0216), R_1 = 0.0371 (I > 2σ(I)), wR_2 = 0.0967 (all data).

X-ray diffraction data for **8** were collected at 100 K on a Bruker D8 Venture using MoKα-radiation (λ=0.71073 Å). Data have been corrected for absorption using SADABS[1] area detector absorption correction program. Using Olex2[2], the structure was solved with the SHELXT[3] structure solution program using Direct Methods and refined with the SHELXL[4] refinement package using least squares minimization. All non-hydrogen atoms were refined with anisotropic thermal parameters. The hydrogen atoms of the investigated structure were located from difference Fourier maps but finally their positions were placed in geometrically calculated positions and refined using a riding model. Isotropic thermal parameters of the placed hydrogen atoms were fixed to 1.2 times the U value of the atoms they are linked to (1.5 times for methyl groups). Calculations and refinement of structures were carried out using APEX3[5], SHELXTL[6], and Olex2 software.

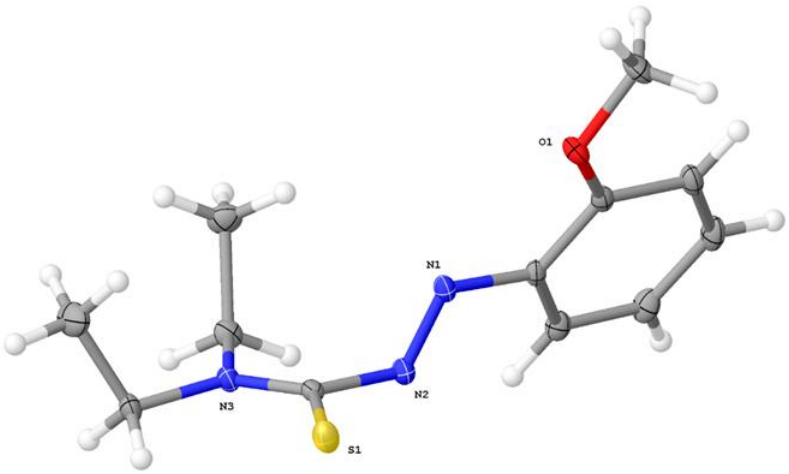

Crystallographic data for **14**: $C_{24}H_{34}Br_2Cu_2N_6O_2S_2$, ($M$=789.59 g/mol): triclinic, space group $P\bar{1}$, a = 11.0638(6) Å, b = 12.0978(6) Å, c = 13.3597(7) Å, 72.648(2), β = 69.917(2), 72.150(2), V = 1560.90(14) Å^3, Z = 2, T = 298 K, μ(MoKα) = 4.088 mm^{-1}, $Dcalc$ = 1.680 g/cm^3, 2Θ range = 4.026 to 52.83, 75034 reflections measured, 6393 unique (R_{int} = 0.0246, R_{sigma} = 0.0115), R_1 = 0.0238 (I > 2σ(I)), wR_2 = 0.0635 (I > 2σ(I)).

X-ray diffraction data for **14** were collected at 298 K on a Bruker D8 Venture using MoKα-radiation (λ=0.71073 Å). Data have been corrected for absorption using SADABS[1] area detector absorption correction program. Using Olex2[2], the structure was solved with the SHELXT[3] structure solution program using Intrinsic Phasing method and refined with the SHELXL[4] refinement package using least squares minimization. All non-hydrogen atoms were refined with anisotropic thermal parameters. Hydrogen atoms of the investigated structure were located from difference Fourier maps but finally their positions were placed in geometrically calculated positions and refined using a riding model. Isotropic thermal parameters of the placed hydrogen atoms were fixed to 1.2 times the U value of the atoms they are linked to (1.5 times for methyl groups). C21 and C22 are both disordered due to the thermal motion of the ethyl group. Both C21 and C22 were split into two parts and the occupancies were freely refined and found to be 86% and 14% split. Equal anisotropic displacement parameters were used for the disordered C21 and C22 atoms. Calculations and refinement of structures were carried out using APEX3[5], SHELXTL[6], and Olex2 (version 1.5) software.

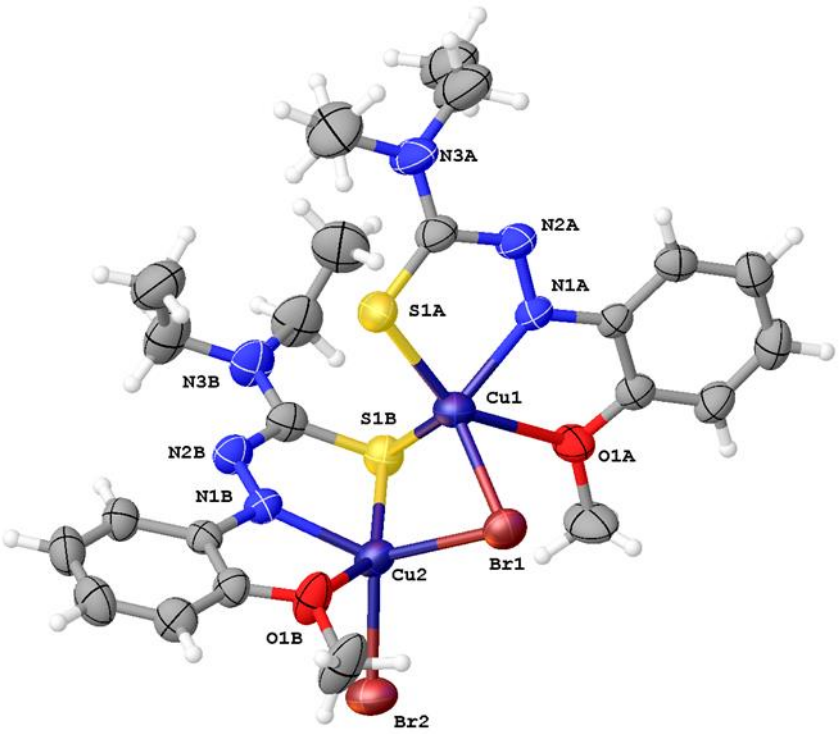

Crystallographic data for **15**: $C_{24}H_{34}Cu_2I_2N_6O_2S_2$, (2 $CHCl_3$) (M=1122.31 g/mol): monoclinic, space group P21/c, a = 8.6376(6) Å, b = 10.2700(7) Å, c = 22.8392(16) Å, β = 98.510(3)°, V = 2003.7(2) Å^3, Z = 2, T = 298 K, μ(MoKα) = 3.140 mm^{-1}, $Dcalc$ = 1.860 g/cm^3, 2Θ range = 5.362 to 49.488, 33233 reflections measured, 3414 unique (R_{int} = 0.0345, R_{sigma} = 0.0166), R_1 = 0.0253 (I > 2σ(I)), wR_2 = 0.0557 (I > 2σ(I)).

X-ray diffraction data for **15** were collected at 298 K on a Bruker D8 Venture using MoKα-radiation (λ=0.71073 Å). Data have been corrected for absorption using SADABS[1] area detector absorption correction program. Using Olex2[2], the structure was solved with the SHELXT[3] structure solution program using Intrinsic Phasing method and refined with the SHELXL[4] refinement package using least squares minimization. All non-hydrogen atoms were refined with anisotropic thermal parameters. Hydrogen atoms of the investigated structure were located from difference Fourier maps but finally their positions were placed in geometrically calculated positions and refined using a riding model. Isotropic thermal

parameters of the placed hydrogen atoms were fixed to 1.2 times the *U* value of the atoms they are linked to (1.5 times for methyl groups). The Cu–Cu distance in compound **15** is 3.024 Å, which is considered a metal-metal bond by the Olex2 program, however, this interaction is very weak, the bond is not included in the refinement. Calculations and refinement of structures were carried out using APEX3[5], SHELXTL[6], and Olex2 (version 1.5) software.

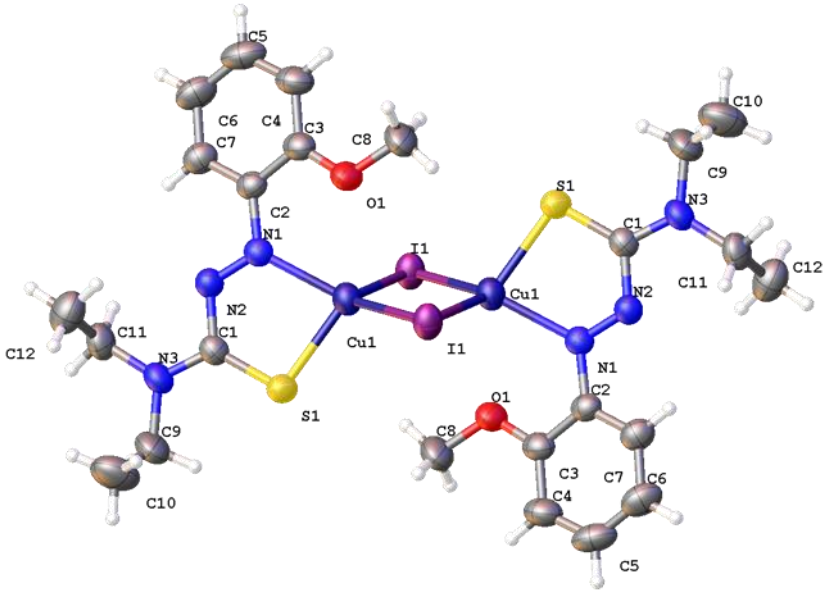

Crystallographic Data for **16**: $C_{24}H_{34}BCuF_4N_6O_2S_2$ (*M* =653.04 g/mol): monoclinic, space group C2/c (no. 15), *a* = 22.385(3) Å, *b* = 21.694(2) Å, *c* = 25.044(3) Å, *β* = 101.127(3)°, *V* = 11933(2) Å^3, *Z* = 16, *T* = 100 K, μ(MoKα) = 0.930 mm^{-1}, *Dcalc* = 1.454 g/cm^3, 2Θmax = 55.236°, 191762 reflections measured, 13838 unique (R_{int} = 0.0634, R_{sigma} = 0.0329), R_1 = 0.0438 (I > 2σ(I)), wR_2 = 0.1004 (all data).

X-ray diffraction data for **16** were collected at 100 K on a Bruker D8 Venture using MoKα-radiation (λ=0.71073 Å). Data have been corrected for absorption using SADABS[1] area detector absorption correction program. Using Olex2[2], the structure was solved with the SHELXT[3] structure solution program using Direct Methods and refined with the SHELXL[4]

refinement package using least squares minimization. All non-hydrogen atoms were refined with anisotropic thermal parameters. The hydrogen atoms of the investigated structure were located from difference Fourier maps and were finally placed in geometrically calculated positions and refined using a riding model. Isotropic thermal parameters of the placed hydrogen atoms were fixed to 1.2 times the *U* value of the atoms they are linked to (1.5 times for methyl groups). Calculations and refinement of structures were carried out using APEX3[5], SHELXTL[6], and Olex2 software.

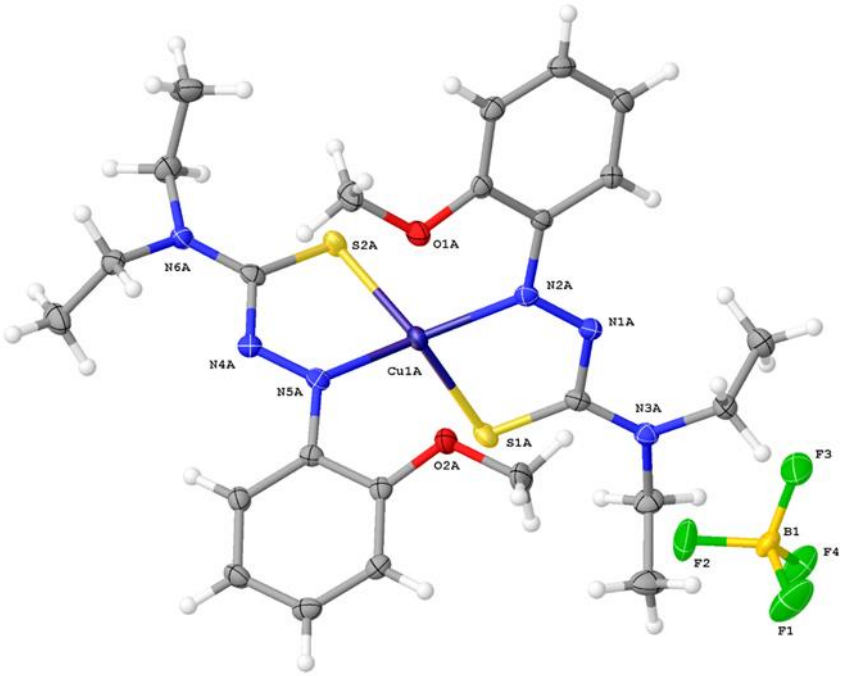

Crystallographic Data for **17**: $C_{24}H_{34}Br_2Cu_2N_6O_2S_2$ (*M* =789.59 g/mol): monoclinic, space group $P2_1/c$ (no. 14), *a* = 8.7342(3) Å, *b* = 14.4518(4) Å, *c* = 11.9733(4) Å, *β* = 98.1030(10)°, *V* = 1496.24(8) Å^3, *Z* = 2, *T* = 100 K, μ(MoKα) = 4.265 mm^{-1}, *Dcalc* = 1.753 g/cm^3, 2Θmax = 55.002°, 18723 reflections measured, 3437 unique (R_{int} = 0.0459, R_{sigma} = 0.0311) R_1 = 0.0261 (I > 2σ(I)), wR_2 = 0.0525 (all data).

X-ray diffraction data for **17** were collected at 100 K on a Bruker D8 Venture using MoKα-radiation (λ=0.71073 Å). Data have been corrected for absorption using SADABS[1] area detector absorption correction program. Using Olex2[2], the structure was solved with the SHELXT[3] structure solution program using Direct Methods and refined with the SHELXL[4] refinement package using least squares minimization. All non-hydrogen atoms were refined with anisotropic thermal parameters. The hydrogen atoms of the investigated structure were located from difference Fourier maps but finally their positions were placed in geometrically calculated positions and refined using a riding model. Isotropic thermal parameters of the placed hydrogen atoms were fixed to 1.2 times the *U* value of the atoms they are linked to (1.5 times for methyl groups). Calculations and refinement of structures were carried out using APEX3[5], SHELXTL[6], and Olex2 software.

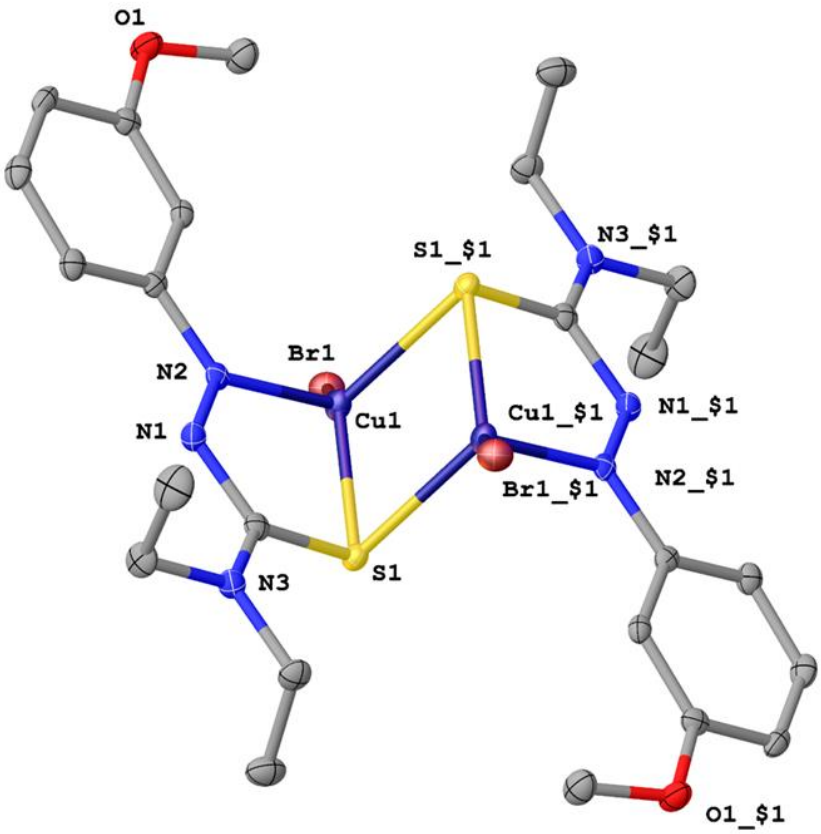

Crystallographic Data for **18**: $C_{24}H_{34}Cu_2I_2N_6O_2S_2$ (M =883.57 g/mol): monoclinic, space group $P2_1/n$ (no. 14), a = 9.5928(3) Å, b = 16.0571(6) Å, c = 11.1190(3) Å, β = 113.1340(10)°, V = 1574.97(9) Å^3, Z = 2, T = 100 K, μ(MoKα) = 3.475 mm^{-1}, $Dcalc$ = 1.863 g/cm^3, 2Θmax = 63.13°, 31054 reflections measured, 5269 unique (R_{int} = 0.0412, R_{sigma} = 0.0356), R_1 = 0.0349 (I > 2σ(I)), wR_2 = 0.0714 (all data).

X-ray diffraction data for **18** were collected at 100 K on a Bruker D8 Venture using MoKα-radiation (λ=0.71073 Å). Data have been corrected for absorption using SADABS[1] area detector absorption correction program. Using Olex2[2], the structure was solved with the SHELXT[3] structure solution program using Direct Methods and refined with the SHELXL[4] refinement package using least squares minimization. All non-hydrogen atoms were refined with anisotropic thermal parameters. The hydrogen atoms of the investigated structure were located from difference Fourier maps but finally their positions were placed in geometrically calculated positions and refined using a riding model. Isotropic thermal parameters of the placed hydrogen atoms were fixed to 1.2 times the U value of the atoms they are linked to (1.5 times for methyl groups). Calculations and refinement of structures were carried out using APEX3[5], SHELXTL[6], and Olex2 software.

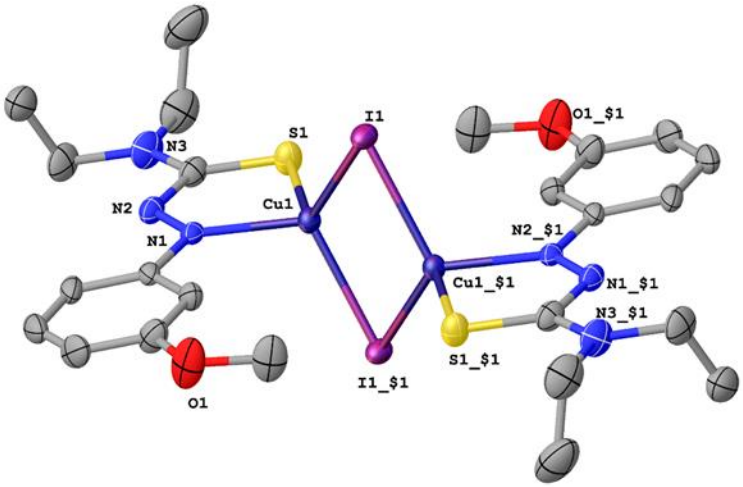

Crystallographic Data for **19**: $C_{24}H_{34}BCuF_4N_6O_2S_2$ (M =653.04 g/mol): triclinic, space group P-1 (no. 2), a = 8.7607(5) Å, b = 12.9094(7) Å, c = 13.3212(7) Å, α = 96.348(2)°, β = 99.280(2)°, γ = 100.252(2)°, V = 1447.99(14) Å^3, Z = 2, T = 105 K, μ(MoKα) = 0.958 mm^{-1}, $Dcalc$ = 1.498 g/cm^3, 2Θmax = 54.33°, 45779 reflections measured, 6429 unique (R_{int} = 0.0621, R_{sigma} = 0.0448), R_1 = 0.0365 (I > 2σ(I)), wR_2 = 0.0737 (all data).

X-ray diffraction data for **19** were collected at 105 K on a Bruker D8 Venture using MoKα-radiation (λ=0.71073 Å). Data have been corrected for absorption using SADABS[1] area detector absorption correction program. Using Olex2[2], the structure was solved with the SHELXT[3] structure solution program using Direct Methods and refined with the SHELXL[4] refinement package using least squares minimization. All non-hydrogen atoms were refined with anisotropic thermal parameters. The hydrogen atoms of the investigated structure were located from difference Fourier maps but finally their positions were placed in geometrically calculated positions and refined using a riding model. Isotropic thermal parameters of the placed hydrogen atoms were fixed to 1.2 times the U value of the atoms they are linked to (1.5 times for methyl groups). Calculations and refinement of structures were carried out using APEX3[5], SHELXTL[6], and Olex2 software.

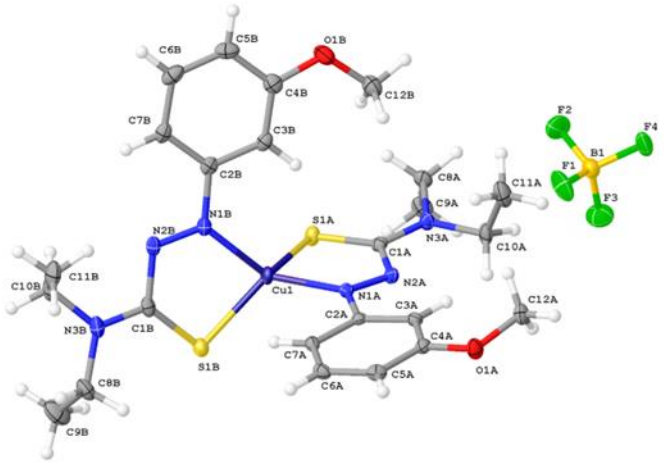

Data Tables

Table A3.1: X-ray crystal experimental data for compounds 11-13.			
Compound	**11•H_2O**	**12**	**13**
Empirical formula	$C_{24}H_{35}Br_2Cu_2N_6O_{2.5}S_2$	$C_{24}H_{34}Cu_2I_2N_6O_2S_2$	$C_{28}H_{42}BCuF_4N_6O_3S_2$
Formula weight	798.6	883.57	725.14
Temperature/K	100	100	100
Crystal system	monoclinic	orthorhombic	triclinic
Space group	C2/c	Pbca	P-1
a/Å	24.2339(13)	17.0538(19)	10.3187(8)
b/Å	8.1296(4)	10.9415(12)	12.2882(9)
c/Å	17.3573(9)	33.394(4)	13.9203(11)
α/°	90	90	80.482(3)
β/°	117.842(2)	90	86.348(3)
γ/°	90	90	76.307(3)
Volume/$Å^3$	3023.7(3)	6231.2(12)	1690.7(2)
Z	4	8	2
ρ_{calc}g/cm^3	1.754	1.884	1.424
μ/mm^1	4.223	3.513	0.830
F(000)	1604	3456	756.0
Crystal size/mm^3	0.56 × 0.54 × 0.23	0.16 × 0.12 × 0.05	0.18 × 0.14 × 0.06

Radiation	MoKα (λ = 0.71073)	MoKα (λ = 0.71073)	MoKα (λ = 0.71073)
2Θ range for data collection/°	5.308 to 57.392	6.058 to 52.73	5.884 to 52.81
Index ranges	$-32 \leq h \leq 32$, $-10 \leq k \leq 10$, $-23 \leq l \leq 23$	$-21 \leq h \leq 21$, $-13 \leq k \leq 13$, $-41 \leq l \leq 41$	$-12 \leq h \leq 12$, $-15 \leq k \leq 15$, $-17 \leq l \leq 17$
Reflections collected	110818	169462	36525
Independent reflections	3893 [R_{int} = 0.0291, R_{sigma} = 0.0080]	6365 [R_{int} = 0.0700, R_{sigma} = 0.0234]	6924 [R_{int} = 0.0358, R_{sigma} = 0.0286]
Data/restraints/parameters	3893/1/184	6365/0/349	6924/102/532
Goodness-of-fit on F^2	1.07	1.252	1.025
Final R indexes [I>=2σ (I)]	R_1 = 0.0165, wR_2 = 0.0414	R_1 = 0.0577, wR_2 = 0.1356	R_1 = 0.0328, wR_2 = 0.0715
Final R indexes [all data]	R_1 = 0.0191, wR_2 = 0.0427	R_1 = 0.0663, wR_2 = 0.1387	R_1 = 0.0481, wR_2 = 0.0778
Largest diff. peak/hole/e $Å^{-3}$	0.46/-0.17	3.02/-0.97	0.63/-0.29

Table A3.2: X-ray crystal experimental data for structures 17-19

Identification code	17	18	19
Empirical formula	$C_{24}H_{34}Br_2Cu_2N_6O_2S_2$	$C_{24}H_{34}Cu_2I_2N_6O_2S_2$	$C_{24}H_{34}BCuF_4N_6O_2S_2$
Formula weight	789.59	883.57	653.04
Temperature/K	100	100	105
Crystal system	monoclinic	monoclinic	triclinic
Space group	$P2_1/c$	$P2_1/n$	P-1
a/Å	8.7342(3)	9.5928(3)	8.7607(5)
b/Å	14.4518(4)	16.0571(6)	12.9094(7)

c/Å	11.9733(4)	11.1190(3)	13.3212(7)
α/°	90	90	96.348(2)
β/°	98.1030(10)	113.1340(10)	99.280(2)
γ/°	90	90	100.252(2)
Volume/Å^3	1496.24(8)	1574.97(9)	1447.99(14)
Z	2	2	2
ρ_{calc}g/cm^3	1.753	1.863	1.498
μ/mm^1	4.265	3.475	0.958
F(000)	792.0	864.0	676.0
Crystal size/mm^3	0.18 × 0.04 × 0.02	0.41 × 0.12 × 0.06	0.2 × 0.09 × 0.01
Radiation	MoKα (λ = 0.71073)	MoKα (λ = 0.71073)	MoKα (λ = 0.71073)
2Θ range for data collection/°	5.49 to 55.002	5.268 to 63.13	5.23 to 54.33
Index ranges	$-10 \leq h \leq 11$, $-18 \leq k \leq 18$, $-15 \leq l \leq 15$	$-11 \leq h \leq 14$, $-23 \leq k \leq 23$, $-16 \leq l \leq 16$	$-11 \leq h \leq 11$, $-16 \leq k \leq 16$, $-17 \leq l \leq 17$
Reflections collected	18723	31054	45779
Independent reflections	3437 [R_{int} = 0.0459, R_{sigma} = 0.0311]	5269 [R_{int} = 0.0412, R_{sigma} = 0.0356]	6429 [R_{int} = 0.0621, R_{sigma} = 0.0448]
Data/restraints/parameters	3437/0/175	5269/0/175	6429/0/367
Goodness-of-fit on F^2	1.039	1.064	1.052
Final R indexes [I>=2σ (I)]	R_1 = 0.0261, wR_2 = 0.0487	R_1 = 0.0349, wR_2 = 0.0652	R_1 = 0.0365, wR_2 = 0.0664
Final R indexes [all data]	R_1 = 0.0430, wR_2 = 0.0525	R_1 = 0.0575, wR_2 = 0.0714	R_1 = 0.0652, wR_2 = 0.0737
Largest diff. peak/hole / e Å^{-3}	0.49/-0.34	1.06/-0.51	0.42/-0.27

Table A3.3: X-ray crystal experimental data for structures 14 - 16

Identification code	14	15 • $2CHCl_3$	16
Empirical formula	$C_{24}H_{34}Br_2Cu_2N_6O_2S_2$	$C_{26}H_{36}Cl_6Cu_2I_2N_6O_2S_2$	$C_{24}H_{34}BCuF_4N_6O_2S_2$
Formula weight	789.59	1122.31	653.04
Temperature/K	298	298.15	100
Crystal system	triclinic	monoclinic	monoclinic
Space group	P-1	P2 1/c	C2/c
a/Å	11.0630(6)	8.6376(6)	22.385(3)
b/Å	12.9064(6)	10.2700(7)	21.694(2)
c/Å	13.3587(7)	22.8392(16)	25.044(3)
α/°	72.648	90	90
β/°	69.916	98.510(3)	101.127(3)
γ/°	72.151	90	90
Volume/$Å^3$	1560.49	2003.7(2)	11933(2)
Z	2	2	16
ρ_{calc}g/cm^3	1.680	1.86	1.454
μ/mm^1	4.089	3.14	0.930
F(000)	792	1096	5408.0
Crystal size/mm^3	0.3 x 0.2 x 0.2	0.42 × 0.2 × 0.06	0.19 × 0.14 × 0.09
Radiation	MoKα (λ = 0.71073)	MoKα (λ = 0.71073)	MoKα (λ = 0.71073)

2Θ range for data collection/°	4.036 to 52.83	5.362 to 49.488	5.01 to 55.236
Index ranges	$-13 \leq h \leq 13$, $-15 \leq k \leq 15$, $-16 \leq l \leq 16$	$-10 \leq h \leq 10$, $-12 \leq k \leq 12$, $-26 \leq l \leq 26'$	$-29 \leq h \leq 29$, $-28 \leq k \leq 28$, $-32 \leq l \leq 32$
Reflections collected	75034	33233	191762
Independent reflections	6393 [R_{int} = 0.0246, R_{sigma} = 0.0115]	3414 [R_{int} = 0.0345, R_{sigma} = 0.0166]	13838 [R_{int} = 0.0634, R_{sigma} = 0.0329]
Data/restraints/parameters	6393/0/351	3414/0/211	13838/0/734
Goodness-of-fit on F^2	0.961	1.057	1.115
Final R indexes [I>=2σ (I)]	R_1 = 0.0238. wR_2 = 0.0635	R_1 = 0.0253, wR_2 = 0.0557	R_1 = 0.0438, wR_2 = 0.0928
Final R indexes [all data]	R_1 = 0.0263, wR_2 = 0.0650	R_1 = 0.0303, wR_2 = 0.0600	R_1 = 0.0681, wR_2 = 0.1004
Largest diff. peak/hole / e $Å^{-3}$	0.80/-0.63	0.54/-0.60	0.44/-0.26

Table A3.4: Statistical evaluation of MeOATF Binding Associations with Cu^I salts

p-MeO ATF	**Binding Model**		**K11**	**% error**	**K12**	**% error**	**RMS**	**Cov**	**SSR**	**MLL**	**BIC**
Cu^IBr	1 to 1		278531.98 M^{-1}	± 20.6032 %			0.1506	0.1376	10.5492	-237.9	-259.23816
	2 to 1	Full	4723.85 M^{-1}	± 0.8361 %	27112.68 M^{-1}	± 0.2503 %	9.81E-03	1.07E-03	4.47E-02	313.69	251.00773
		Additive	14993.60 M^{-1}	± 2.4613 %	17568.57 M^{-1}	± 0.7819 %	1.67E-02	3.07E-03	0.1289	206.87	164.186949
		Non-Cooperative	20440.72 M^{-1}	± 0.3516 %	5110.18 M^{-1}	-	1.68E-02	3.12E-03	0.1311	205.16	143.805956
		Statistical	30735.30 M^{-1}	± 0.5608 %	7683.83 M^{-1}	-	1.99E-02	4.38E-03	0.1836	171.15	129.804082

	Binding Model		K11	% error	K12	% error	RMS	Cov	SSR	MLL	BIC
$Cu^{I}I$	1 to 1		689405.00 M^{-1}	± 40.5777 %			0.1681	0.1559	13.1326	-260.02	-281.35617
	2 to 1	Full	13126.67 M^{-1}	± 0.9403 %	7552.09 M^{-1}	± 0.2332 %	1.22E-02	1.36E-03	0.0687	270.41	207.722414
		Additive	30541.81 M^{-1}	± 4.0668 %	12614.38 M^{-1}	± 1.0236 %	2.71E-02	6.79E-03	0.3427	108.13	65.453223 5
		Non-Cooperative	17816.70 M^{-1}	± 0.2093 %	4454.18 M^{-1}	-	1.27E-02	1.50E-03	0.0755	260.88	199.525916
		Statistical	39504.32 M^{-1}	± 0.8176 %	9876.08 M^{-1}	-	2.76E-02	7.00E-03	0.3532	105.09	63.739667 7
	Binding Model		**K11**	**% error**	**K12**	**% error**	**RMS**	**Cov**	**SSR**	**MLL**	**BIC**
$Cu^{I}BF_4$	1 to 1		66766.44 M^{-1}	± 13.6073 %			0.1632	0.3031	12.386	-254.11	-295.452
	2 to 1	Full	12098.58 M^{-1}	± 2.3260 %	19799.35 M^{-1}	± 0.5936 %	1.84E-02	3.85E-03	0.1573	186.76	124.075428
		Additive	31974.03 M^{-1}	± 7.9417 %	28291.84 M^{-1}	± 1.9562 %	2.97E-02	1.01E-02	0.4113	89.71	47.028852 8
		Non-Cooperative	20483.30 M^{-1}	± 0.3363 %	5120.83 M^{-1}	-	2.20E-02	5.52E-03	0.2256	150.35	88.997242 4
		Statistical	57224.20 M^{-1}	± 1.0159 %	14306.05 M^{-1}	-	3.11E-02	1.10E-02	0.4507	80.47	39.125622
	Binding Model		**K11**	**% error**	**K12**	**% error**	**RMS**	**Cov**	**SSR**	**MLL**	**BIC**
Cu_2I_4	1 to 1		5408089 6.88 M^{-1}	± 1685.2241 %			0.1535	0.1591	3.6513	-43.59	-55.636507
	2 to 1	Full	15871.37 M^{-1}	± 1.3644 %	3722.74 M^{-1}	± 0.3206 %	1.05E-02	7.42E-04	1.70E-02	137.13	118.514471

		Additive	32459.75 M^{-1}	± 5.7839 %	10203.96 M^{-1}	± 1.4665 %	2.28E-02	3.52E-03	0.0807	84.72	71.575310 9
		Non-Cooperative	15556.41 M^{-1}	± 0.2385 %	3889.10 M^{-1}	-			1.70E-02	137.1	119.579958
		Statistical	36706.32 M^{-1}	± 0.9867 %	9176.58 M^{-1}	-			0.0816	84.34	72.297188 4
m-MeO ATF	**Binding Model**		**K11**	**% error**	**K12**	**% error**	**RMS**	**Cov**	**SSR**	**MLL**	**BIC**
$Cu^{I}Br$	1 to 1		157697.07 M^{-1}	± 5.4820 %	-	-	2.83E-03	3.17E-02	3.72E-03	564.73	523.386596
	2 to 1	Full	1418.05 M^{-1}	± 0.2944 %	3982.44 M^{-1}	± 0.0964 %	3.77E-04	5.64E-04	6.62E-05	971.61	908.928773
		Additive	54469.77 M^{-1}	± 4.8601 %	538.47 M^{-1}	± 4.9191 %	1.42E-03	8.02E-03	9.41E-04	703.63	660.949363
		Non-Cooperative	2735.67 M^{-1}	± 4.0005e-2 %	683.92 M^{-1}	-	4.27E-04	7.21E-04	8.47E-05	946.78	885.425227
		Statistical	8793.17 M^{-1}	± 0.3409 %	2128.30 M^{-1}	-	1.60E-03	1.01E-02	1.19E-03	680.13	638.785158
	Binding Model		**K11**	**% error**	**K12**	**% error**	**RMS**	**Cov**	**SSR**	**MLL**	**BIC**
$Cu^{I}I$	1 to 1		149537.77 M^{-1}	± 5.0859 %	-	-	3.35E-03	2.90E-02	5.23E-03	530.54	489.199416
	2 to 1	Full	1476.64 M^{-1}	± 0.2752 %	3701.18 M^{-1}	± 0.0914 %	4.21E-04	4.56E-04	8.23E-05	949.7	887.015071
		Additive	52990.51 M^{-1}	± 4.3409 %	591.14 M^{-1}	± 4.5873 %	1.61E-03	6.66E-03	1.20E-03	679.05	636.36905
		Non-Cooperative	2721.59 M^{-1}	± 3.7289e-2 %	680.40 M^{-1}	-	4.89E-04	6.16E-04	1.11E-04	919.35	858.001888
		Statistical	9242.72 M^{-1}	± 0.3401 %	2310.68 M^{-1}	-	1.88E-03	9.09E-03	1.64E-03	647.65	606.308006

	Binding Model		K11	% error	K12	% error	RMS	Cov	SSR	MLL	BIC
$Cu^{I}BF_4$	1 to 1		88717.53 M^{-1}	± 11.0861 %	-	-	7.23E-03	3.44E-01	2.43E-02	375.2	333.85569
	2 to 1	Full	2652.34 M^{-1}	± 0.7534 %	6254.28 M^{-1}	± 0.2373 %	5.93E-04	2.31E-03	1.63E-04	880.41	817.727574
		Additive	13133.65 M^{-1}	± 2.9201 %	4192.37 M^{-1}	± 0.9389 %	9.42E-04	5.83E-03	4.13E-04	786.9	744.224893
		Non-Cooperative	6739.31 M^{-1}	± 0.0917 %	1684.83 M^{-1}	-	6.38E-04	2.67E-03	1.89E-04	865.67	804.317802
		Statistical	14896.28 M^{-1}	± 0.2289 %	3724.07 M^{-1}	-	9.43E-04	5.84E-03	4.14E-04	786.61	745.260452
	Binding Model		**K11**	**% error**	**K12**	**% error**	**RMS**	**Cov**	**SSR**	**MLL**	**BIC**
Cu_2I_4	1 to 1		107237.14 M^{-1}	± 4.8724 %	-	-	1.75E-03	1.46E-02	4.76E-04	257.5	245.451367
	2 to 1	Full	1622.30 M^{-1}	± 0.2655 %	2.71e-6 M^{-1}	± 0.0837 %	1.95E-04	1.81E-04	5.89E-06	405.29	386.673682
		Additive	64166.09 M^{-1}	± 5.7526 %	292.29 M^{-1}	± 11.6645 %	1.21E-03	6.98E-03	2.28E-04	282.31	269.172724
		Non-Cooperative	1461.93 M^{-1}	± 2.4703e-2 %	365.48 M^{-1}	-	1.97E-04	1.85E-04	6.04E-06	404.5	386.973742
		Statistical	8128.91 M^{-1}	± 0.7655 %	2032.23 M^{-1}	-	1.90E-03	1.71E-02	5.58E-04	252.13	240.080582
o-MeO ATF	**Binding Model**		**K11**	**% error**	**K12**	**% error**	**RMS**	**Cov**	**SSR**	**MLL**	**BIC**
$Cu^{I}Br$	1 to 1		146361.96 M^{-1}	± 7.3297 %			7.39E-03	4.57E-02	2.54E-02	371.01	329.661911
	2 to 1	Full	1281.99 M^{-1}	± 0.7436 %	15707.54 M^{-1}	± 0.3083 %	1.29E-03	1.40E-03	7.75E-04	723.29	660.606946
		Additive	4319.70 M^{-1}	± 1.6570 %	6507.18 M^{-1}	± 0.8368 %	1.76E-03	2.61E-03	1.45E-03	660.22	617.539736

		Non-Cooperative	6285.25 M^{-1}	± 0.1561 %	1571.31 M^{-1}	-	1.79E-03	2.67E-03	1.48E-03	657.67	609.654685
		Statistical	9851.01 M^{-1}	± 0.2450 %	2462.75 M^{-1}	-	2.04E-03	3.47E-03	1.93E-03	631.27	589.919481
	Binding Model		**K11**	**% error**	**K12**	**% error**	**RMS**	**Cov**	**SSR**	**MLL**	**BIC**
$Cu^{I}I$	1 to 1		154936.78 M^{-1}	± 6.7723 %	-	-	7.19E-03	3.63E-02	2.41E-02	376.34	334.99905
	2 to 1	Full	1443.92 M^{-1}	± 0.4499 %	9270.11 M^{-1}	± 0.1696 %	9.64E-04	6.52E-04	4.33E-04	782.13	719.443415
		Additive	5550.10 M^{-1}	± 2.1252 %	4770.45 M^{-1}	± 1.1114 %	2.14E-03	3.20E-03	2.13E-03	621.37	578.686045
		Non-Cooperative	4667.01 M^{-1}	± 0.0880 %	1166.75 M^{-1}	-	1.35E-03	1.28E-03	8.51E-04	713.8	665.783157
		Statistical	10017.34 M^{-1}	± 0.2568 %	2504.34 M^{-1}	-	2.28E-03	3.64E-03	2.41E-03	608.5	567.151335
	Binding Model		**K11**	**% error**	**K12**	**% error**	**RMS**	**Cov**	**SSR**	**MLL**	**BIC**
$Cu^{I}BF_4$	1 to 1		73454.45 M^{-1}	± 8.6378 %			1.77E-02	0.2202	0.1456	194.56	153.21946
	2 to 1	Full	4518.40 M^{-1}	± 0.4474 %	5219.07 M^{-1}	± 0.1708 %	6.10E-04	2.62E-04	1.73E-04	874.65	811.969137
		Additive	12348.34 M^{-1}	± 1.4723 %	5782.66 M^{-1}	± 0.6148 %	9.09E-04	5.81E-04	3.84E-04	794.19	751.511085
		Non-Cooperative	10442.25 M^{-1}	± 0.0523 %	2610.54 M^{-1}	-	6.98E-04	3.43E-04	2.27E-04	847.44	799.428031
		Statistical	17189.80 M^{-1}	± 0.1020 %	4297.45 M^{-1}	-	9.74E-04	6.67E-04	4.41E-04	780.21	738.868311

	Binding Model		K11	% error	K12	% error	RMS	Cov	SSR	MLL	BIC
Cu_2I_4	1 to 1		198617.99 M^{-1}	± 14.2398 %			6.05E-03	3.67E-02	5.66E-03	174.13	162.084936
	2 to 1	Full	1528.73 M^{-1}	± 0.6286 %	7690.48 M^{-1}	± 0.2175 %	6.94E-04	4.84E-04	7.46E-05	319.87	301.255751
		Additive	6370.88 M^{-1}	± 4.2620 %	4553.17 M^{-1}	± 2.1431 %	1.99E-03	3.99E-03	6.15E-04	248.85	235.709792
		Non-Cooperative	4225.69 M^{-1}	± 0.1243 %	1056.42 M^{-1}	-	9.89E-04	9.83E-04	1.52E-04	296	278.477599
		Statistical	10603.46 M^{-1}	± 0.5076 %	2650.87 M^{-1}	-	2.08E-03	4.37E-03	6.74E-04	245.8	233.749017

Legend: RMS = root mean square; Cov = Covariance of fit; SSR = sum of squared residuals; MLL = log of marginal likelihood; BIC = Bayesian Information Criterion

References

1. Sheldrick, G. M. (1996). SADABS: Area Detector Absorption Correction; University of Göttingen, Germany.
2. Dolomanov, O.V.; Bourhis, L.J.; Gildea, R.J.; Howard, J.A.K.; Puschmann, H., (2009). J. Appl. Cryst., 42, 339-341.
3. Sheldrick, G. M. (2015). *Acta Cryst.* A71, 3-8.
4. Sheldrick, G. M. (2015). *Acta Cryst.* C71, 3-8.
5. Bruker (2016). APEX3. Bruker AXS Inc., Madison, Wisconsin, USA.
6. Sheldrick, G.M. (2008). Acta Cryst. A64, 112-122.

Appendix IV

Supporting Information for Chapter 5: Evaluation of Azothioformamides and Their Copper(I) and Silver(I) Complexes for Biological Activity.

General Methods

^{1}H and ^{13}C NMR experiments were performed on a Bruker AVANCE 500 MHz instrument and samples were obtained in in d-chloroform, $CDCl_3$, referenced to 7.26 ppm for ^{1}H and 77.16 ppm for ^{13}C or Acetonitrile-d_3, CD_3CN, referenced to 1.93 ppm for ^{1}H and 1.4 and 117.7 ppm for ^{13}C. Coupling constants (*J*) are in Hz. The multiplicities of the signals are described using the following abbreviations: s = singlet, br s = broad singlet, d = doublet, t = triplet, dd = doublet of doublets, dq = doublet of quartets, dsep =doublet of septets; tt = triplet of triplets, m = multiplet, app = apparent. Infrared spectra were obtained on a Thermo Scientific Nicolet 380 FT-IR spectrometer as thin films on ZnSe disks and peaks are reported in cm^{-1}. Elemental Analysis was performed on a Vario micro-Cube elemental analyzer for (C, H, N). Reaction progress was monitored by thin-layer chromatography on silica gel plates (60-F254), observed under UV light. Column chromatography was performed using silica gel (particle size 40–63 μm). Methyl iodide was purchased from EMD Millipore, 4-cyanophenylhydrazine hydrochloride, 4-sulfonamidephenylhydrazine hydrochloride, were purchased from AK Scientific, N, N-Diethylamine and CS_2 were purchased from Alfa-Aesar and used without further purification. Cu(I) halides and salts were purchased from Acros, Sigma–Aldrich, Alfa–Aesar, and AK Scientific and used without further purification.

Biological Data

A

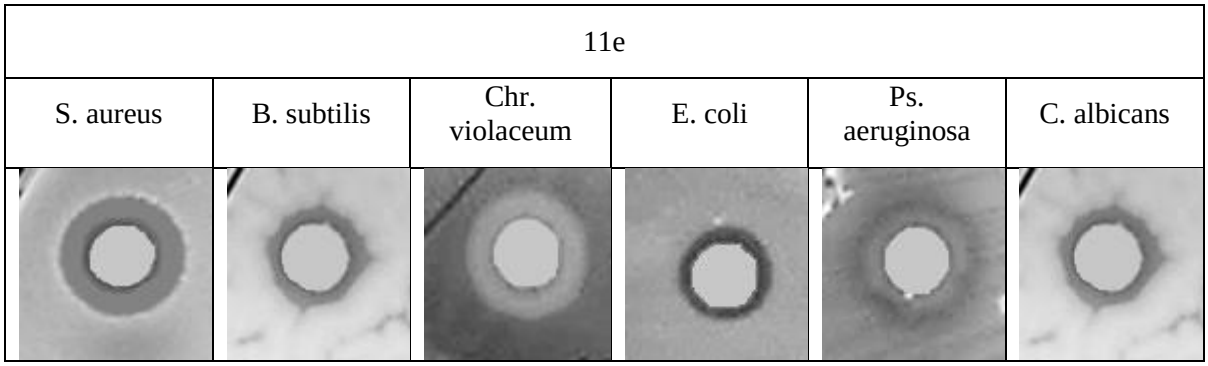

B

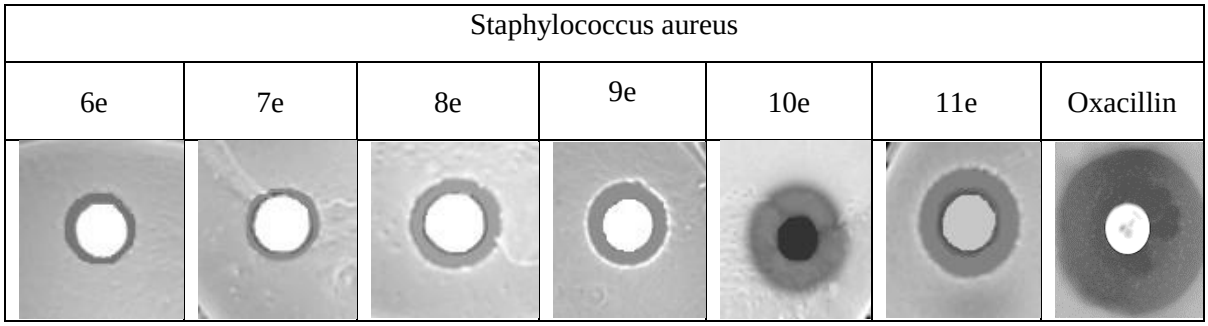

Figure A4.1: A: Effect of compound 11e against an array of gram-positive bacteria (Staphylococcus aureus, Bacillus subtilis), gram negative bacteria (Chromobacter violaceum, Escherichia coli, Pseudomonas aeruginosa), and yeast (Candida albicans). B: Effect of 6e ATF metal-chelating complex series showing the influence of coordinating atoms on antimicrobial activity against Staphylococcus aureus.

Table A4.1: Zone of Inhibition Results

Drug	**B. subtilis**	**S. aureus**	**C. violaceum**	**E. coli**	**Ps. aeruginosa**	**C. albicans**
6c	+/-	+	-	-	-	++
7c	++	++	+/-	-	-	+/-
8c	+	++	-	-	-	+/-
9c	++	++	+/-	+/-	-	+/-

10c	+	++	-	-	-	+/-
11c	+/-	++	+	+/-	+	+/-
6e	-	+/-	-	-	-	++
7e	+/-	++	+/-	-	-	+/-
8e	-	+	-	-	-	-
9e	+/-	++	+/-	-	-	-
10e	+	++	+/-	-	-	+
11e	+/-	++	+	+/-	+	++
6f	-	-	-	-	-	+/-
7f	-	+/-	-	-	-	+/-
8f	+/-	+	-	-	-	-
9f	-	+/-	-	-	-	-
10f	-	-	-	-	-	-
11f	+	++	+	+/-	+	++
6g	-	-	-	-	-	-
7g	+/-	+	+/-	-	-	+/-
8g	+/-	++	+	-	-	+/-
9g	+/-	+/-	+/-	-	-	-
10g	+/-	+	+/-	-	-	-
11g	+/-	+	+	+/-	+/-	++

Amp	+/-	++	-	-	-	-
Oxa	-	++	+	-	-	-
Zone of Inhibition Diameter: - = < 8 mm, +/- = 8-10 mm, + = 11-15 mm, ++ = > 15 mm. Amp = Ampicillin, Oxa = Oxacillin.						

Table A4.2: MIC values

Drug	B. subtilis	S. aureus	E. coli	Chr. violaceum	Ps. aeruginosa	C. albicans
6a	>50	>50	>50	>50	>50	>50
6b	>50	>50	>50	>50	>50	>50
6c	>50	>50	>50	>50	>50	>50
6d	>50	>50	>50	>50	>50	>50
6e	>50	>50	>50	>50	>50	>50
6f	>50	>50	>50	>50	>50	>50
6g	>50	>50	>50	>50	>50	>50
6h	>50	>50	>50	>50	>50	>50
7c	**10**	**10**	>50	>50	>50	**10**
7e	>50	**25**	>50	>50	>50	>50
7f	>50	>50	>50	>50	>50	>50
7g	**50**	**25**	>50	>50	>50	>50
8c	**25**	**25**	>50	>50	>50	**25**
8e	**50**	**10**	>50	>50	>50	>50

8f	**50**	**10**	>50	>50	>50	>50
8g	>50	>50	>50	>50	>50	>50
9c	**25**	**10**	>50	>50	>50	**25**
9e	>50	**25**	>50	>50	>50	>50
9f	>50	>50	>50	>50	>50	>50
9g	**50**	**25**	>50	>50	>50	>50
10c	**25**	**10**	>50	>50	>50	>50
10e	**50**	**10**	>50	>50	>50	>50
10f	>50	>50	>50	>50	>50	>50
10g	**50**	**25**	>50	>50	>50	>50
11c	**10**	**25**	**50**	**50**	**50**	>50
11e	**25**	**50**	**25**	**25**	**50**	>50
11f	**10**	**25**	**25**	**25**	**25**	>50
11g	**25**	**10**	**25**	**25**	**50**	**50**

NMR Spectral Data for Azothioformamide Ligands

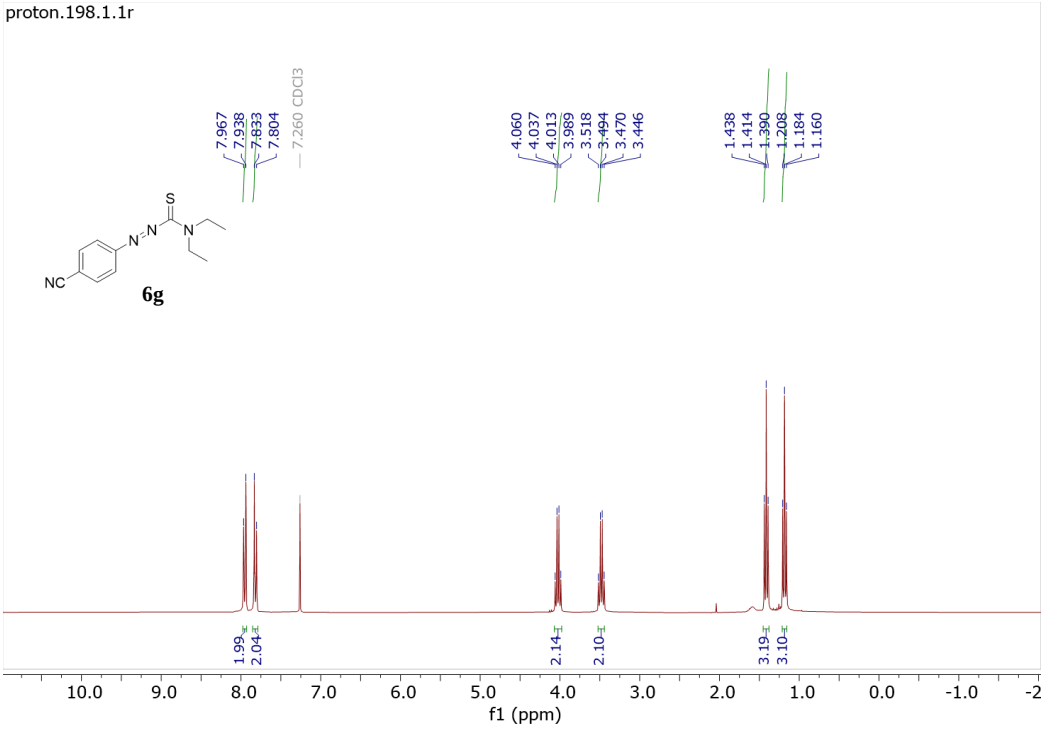

Figure A4.2: ^{1}H NMR spectrum of **6g** (N,N-diethyl-2-(4-cyanophenyl) diazothioformamide) in $CDCl_3$

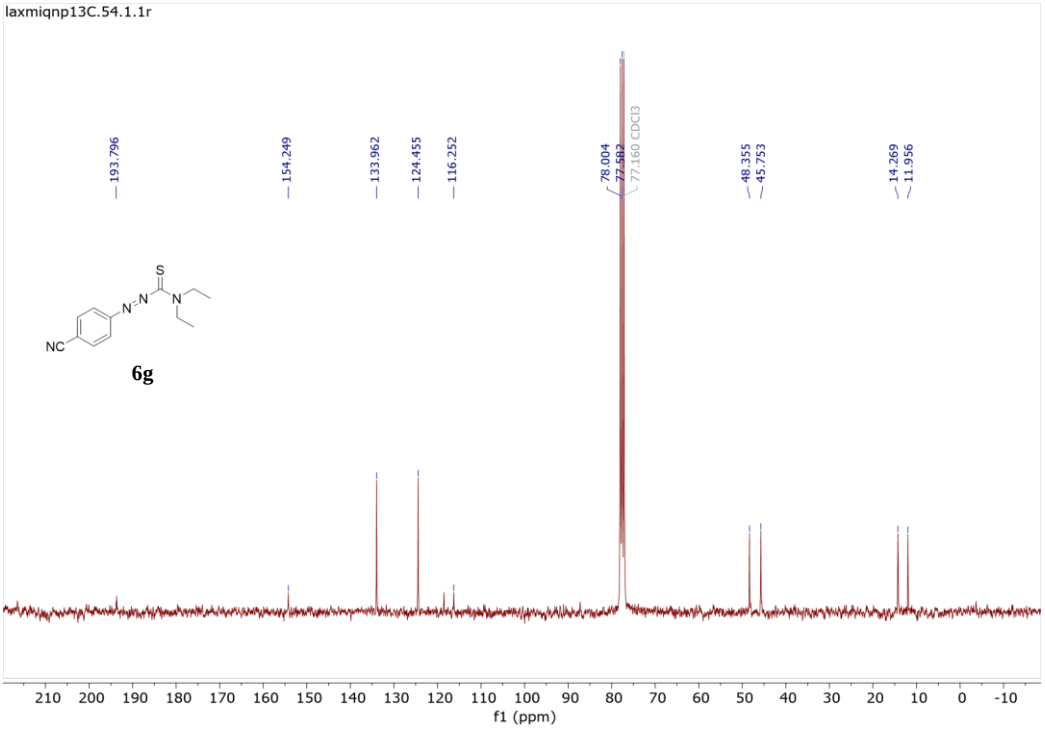

Figure A4.3: ^{13}C NMR spectrum of **6g (**N,N-diethyl-2-(4-cyanophenyl) diazothioformamide) in $CDCl_3$

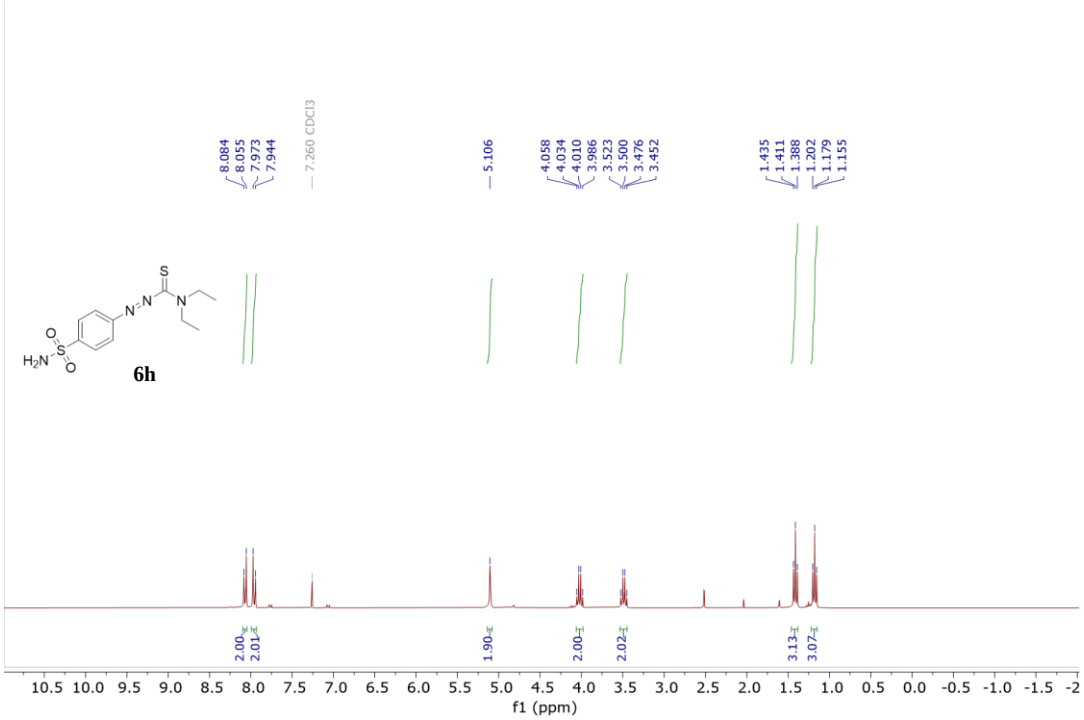

Figure A4.4: ^{1}H NMR spectrum of **6h** N,N-diethyl-2-(4-Sulfonamidephenyl) diazothioformamide in $CDCl_3$

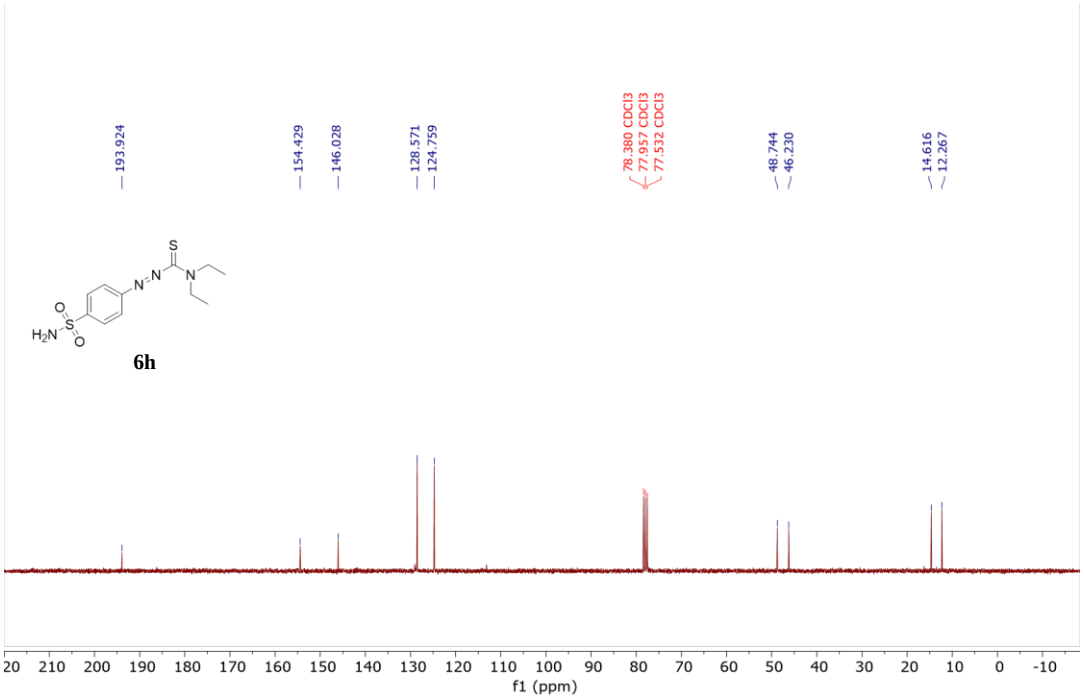

Figure A4.5: ^{13}C NMR spectrum of **6h** (N,N-diethyl-2-(4-Sulfonamidephenyl) diazothioformamide) in $CDCl_3$

NMR Spectral Data for metal Coordination complexes

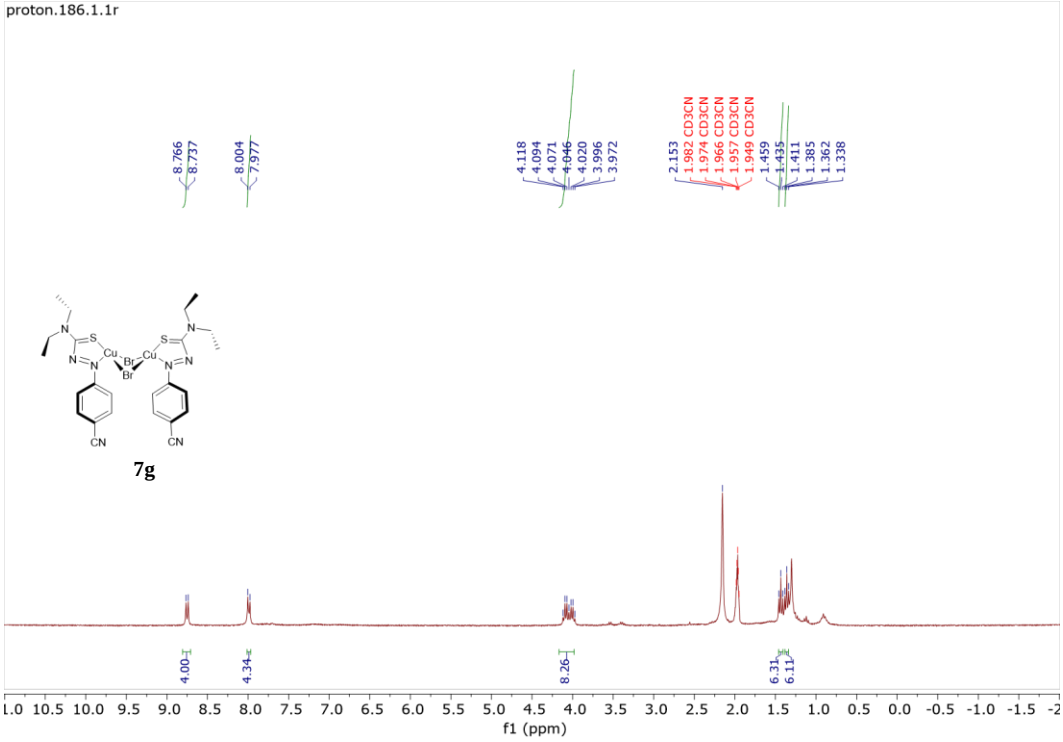

Figure A4.6: ^{1}H NMR spectrum of **7g** Bis[(N,N-diethyl-2-(4-cyanophenyl) diazothioformamide)CuBr] in CD_3CN

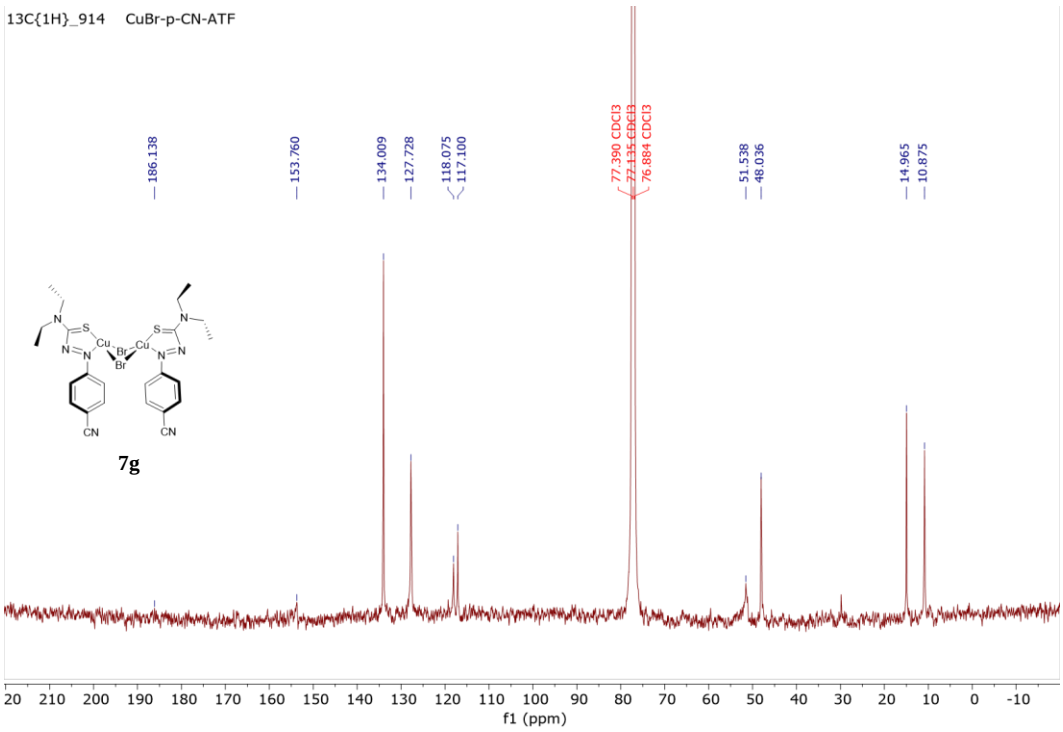

Figure A4.7: ^{13}C NMR spectrum of **7g** Bis[(N,N-diethyl-2-(4-cyanophenyl) diazothioformamide)CuBr] in $CDCl_3$

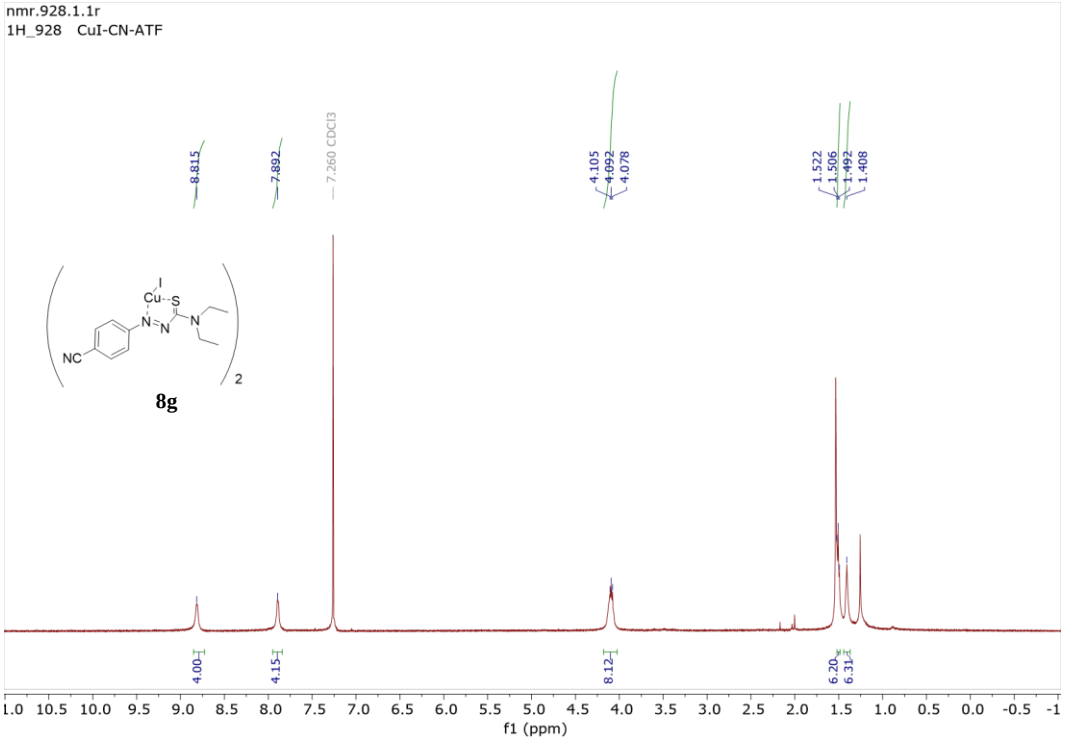

Figure A4.8: ^{1}H NMR spectrum of **8g** Bis[(N,N-diethyl-2-(4-cyanophenyl) diazothioformamide)CuI] in $CDCl_3$

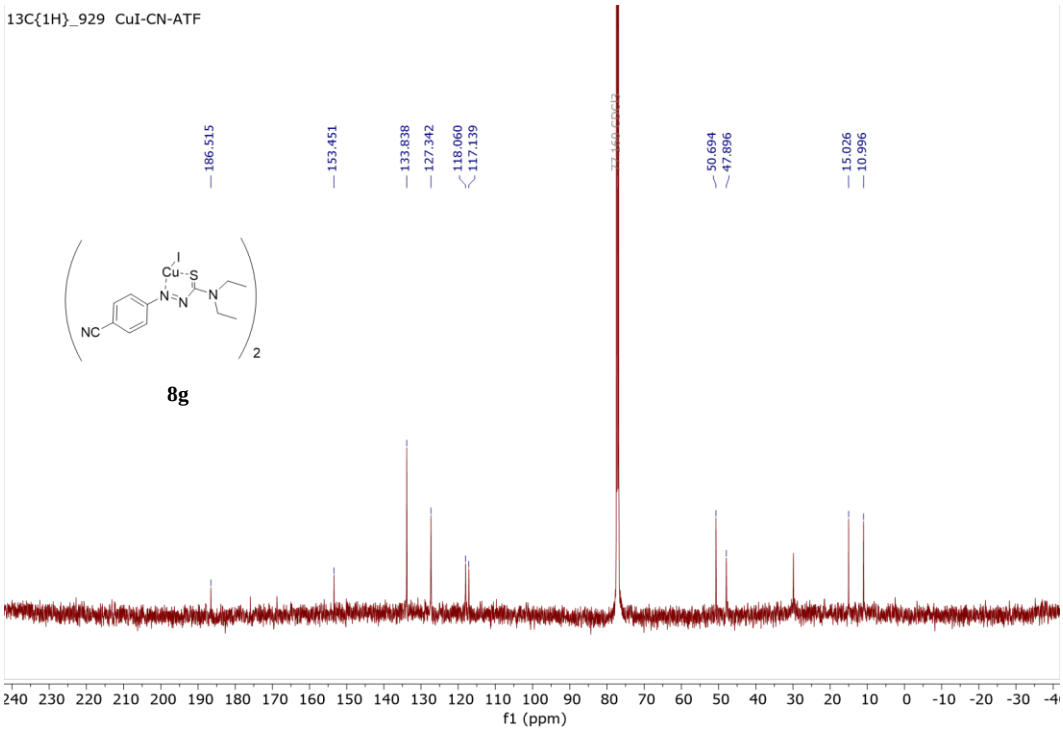

Figure A4.9: ^{13}C NMR spectrum of **8g** Bis[(N,N-diethyl-2-(4-cyanophenyl) diazothioformamide)CuI] in $CDCl_3$

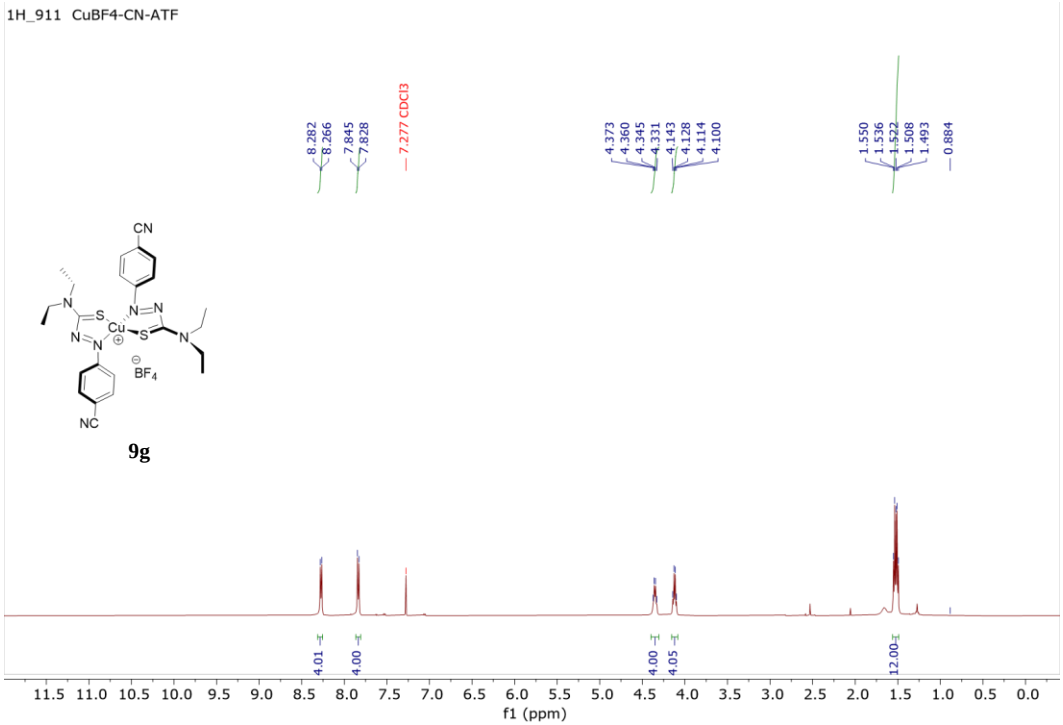

Figure A4.10: ^{1}H NMR spectrum of **9g** [(N,N-diethyl-2-(4-cyanophenyl) diazothioformamide)$_2$Cu](BF$_4$) in CDCl$_3$

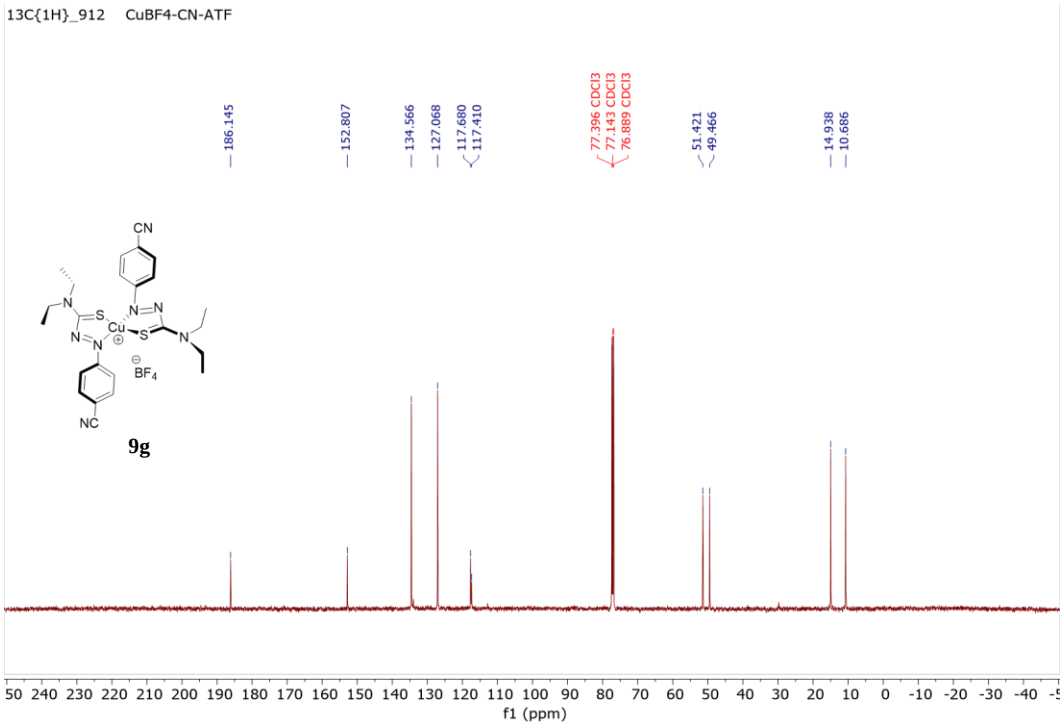

Figure A4.11: ^{13}C NMR spectrum of **9g** [(N,N-diethyl-2-(4-cyanophenyl) diazothioformamide)$_2$Cu](BF$_4$) in CDCl$_3$

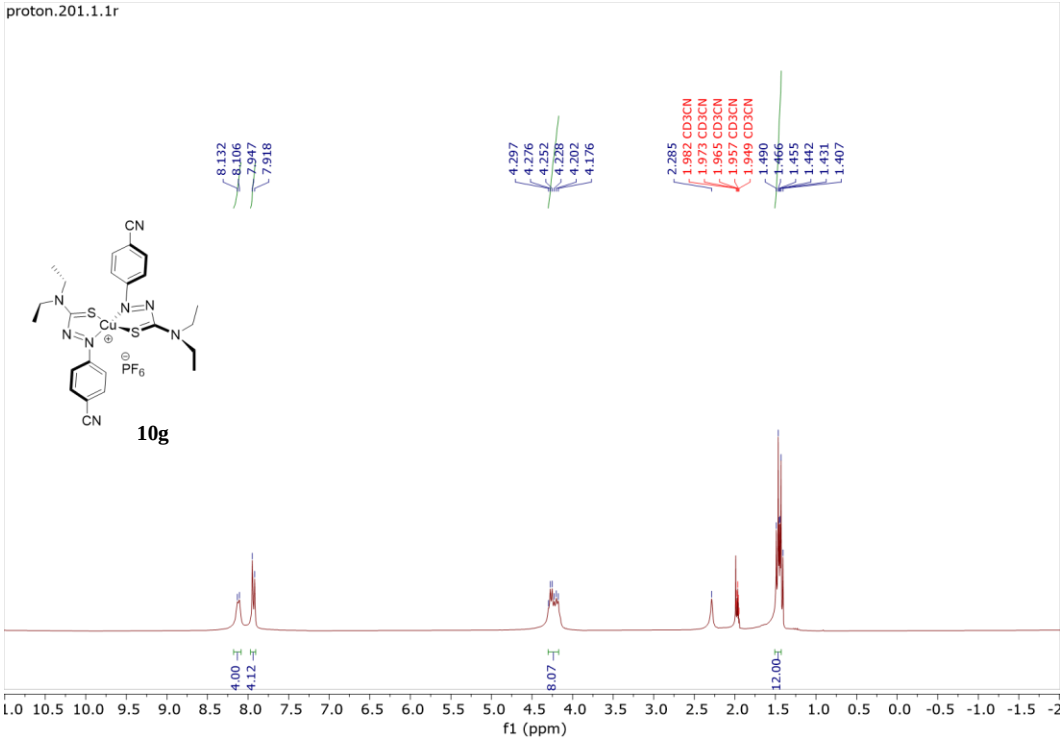

Figure A4.12: ^{1}H NMR spectrum of **10g** [(N,N-diethyl-2-(4-cyanophenyl) diazothioformamide)$_2$Cu](PF$_6$) in CD$_3$CN

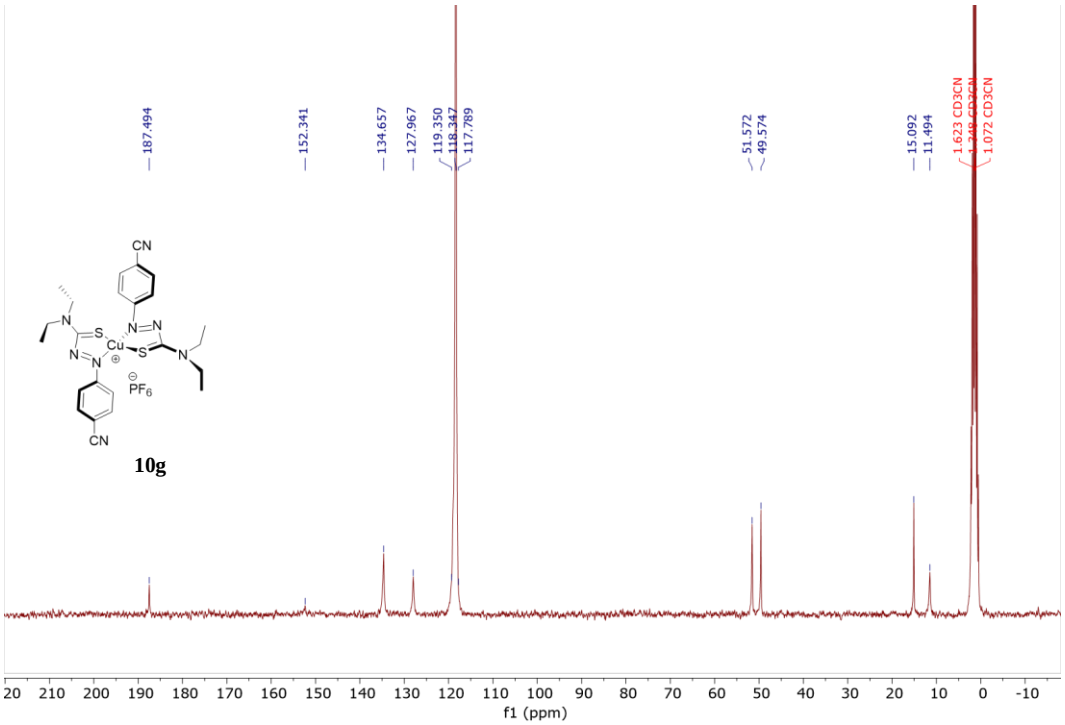

Figure A4.13: ^{1}H NMR spectrum of **10g** [(N,N-diethyl-2-(4-cyanophenyl) diazothioformamide)$_2$Cu](PF$_6$) in CD$_3$CN

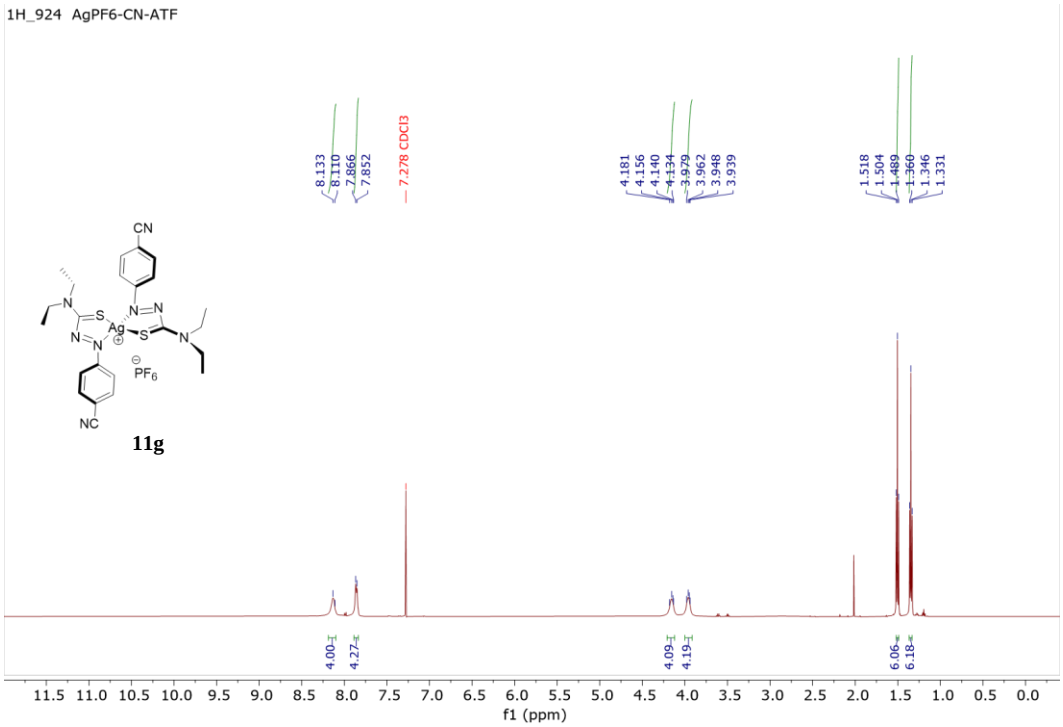

Figure A4.14: ^{1}H NMR spectrum of **11g** [(N,N-diethyl-2-(4-cyanophenyl) diazothioformamide)$_2$Ag](PF$_6$) in CDCl$_3$

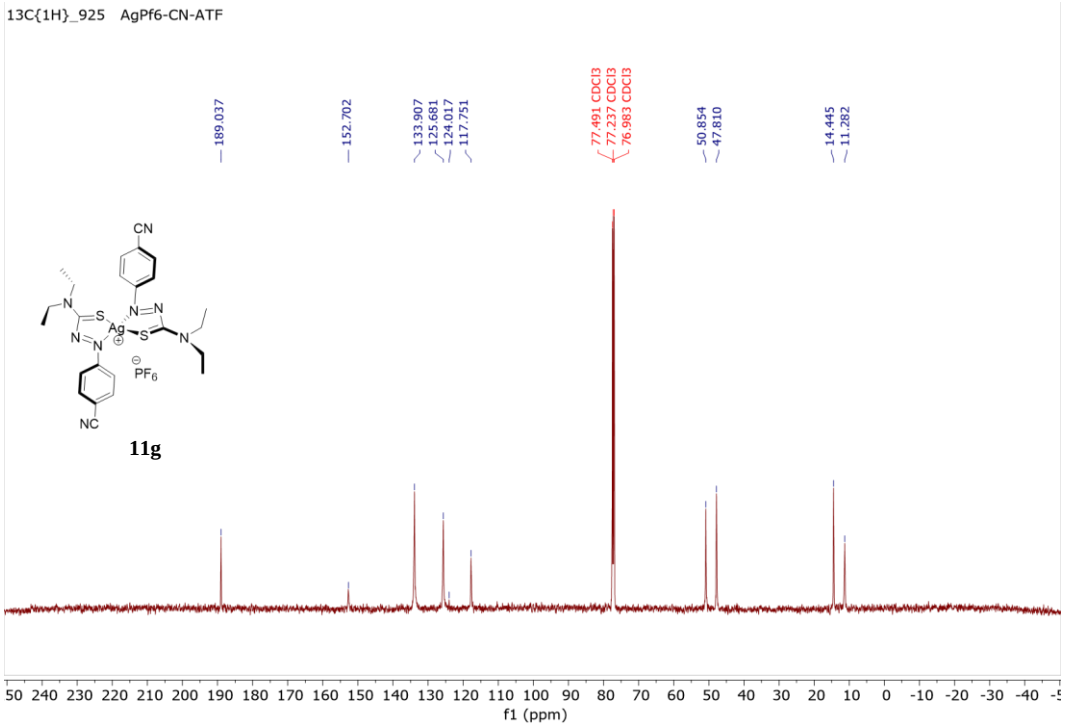

Figure A4.15: ^{13}C NMR spectrum of **11g** [(N,N-diethyl-2-(4-cyanophenyl) diazothioformamide)$_2$Ag](PF$_6$) in CDCl$_3$

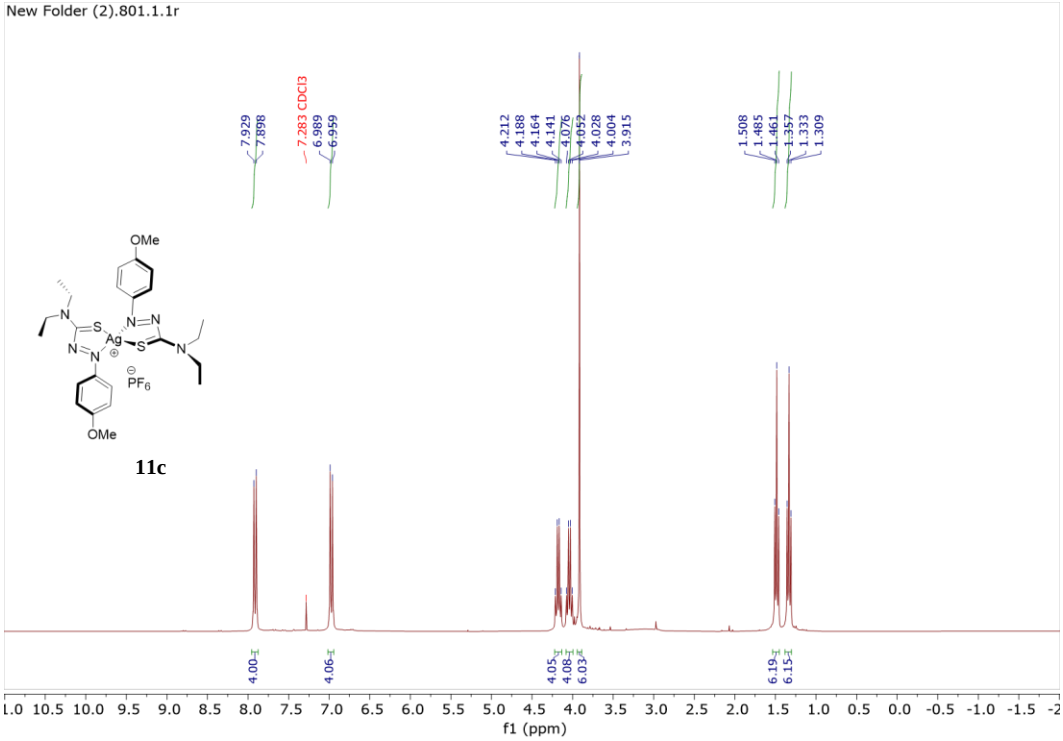

Figure A4.16: ^{1}H NMR spectrum of **11c**[(N,N-diethyl-2-(4-methoxyphenyl) diazothioformamide)$_2$Ag](PF$_6$) in CDCl$_3$

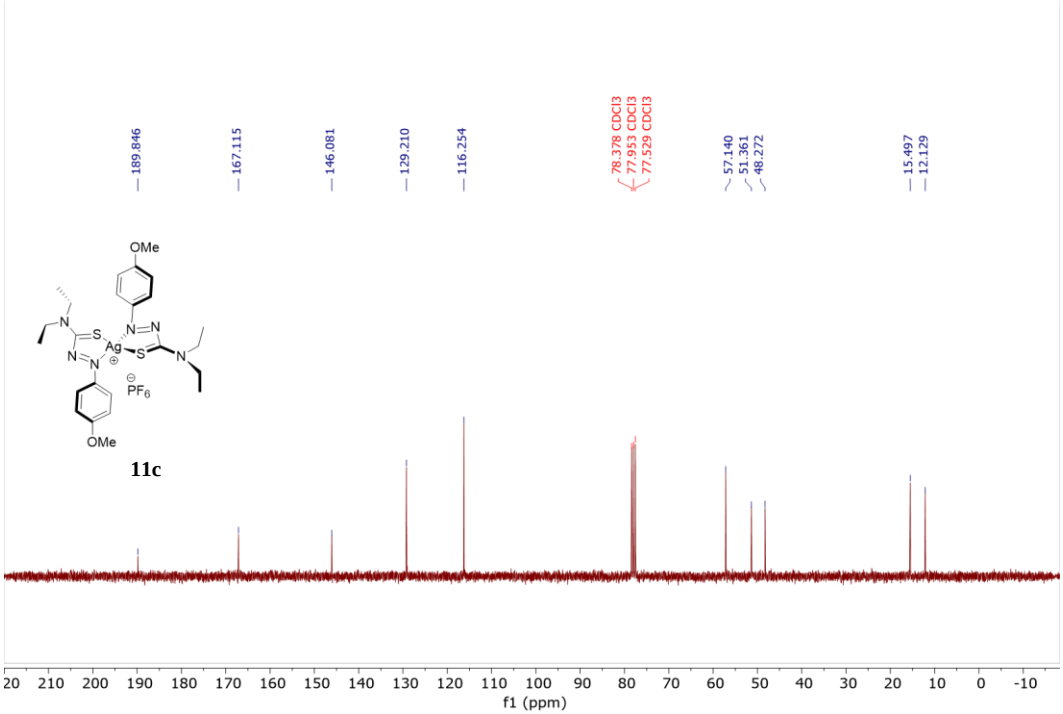

Figure A4.17: ^{13}C NMR spectrum of **11c**[(N,N-diethyl-2-(4-methoxyphenyl)diazothioformamide)$_2$Ag](PF$_6$) in CDCl$_3$

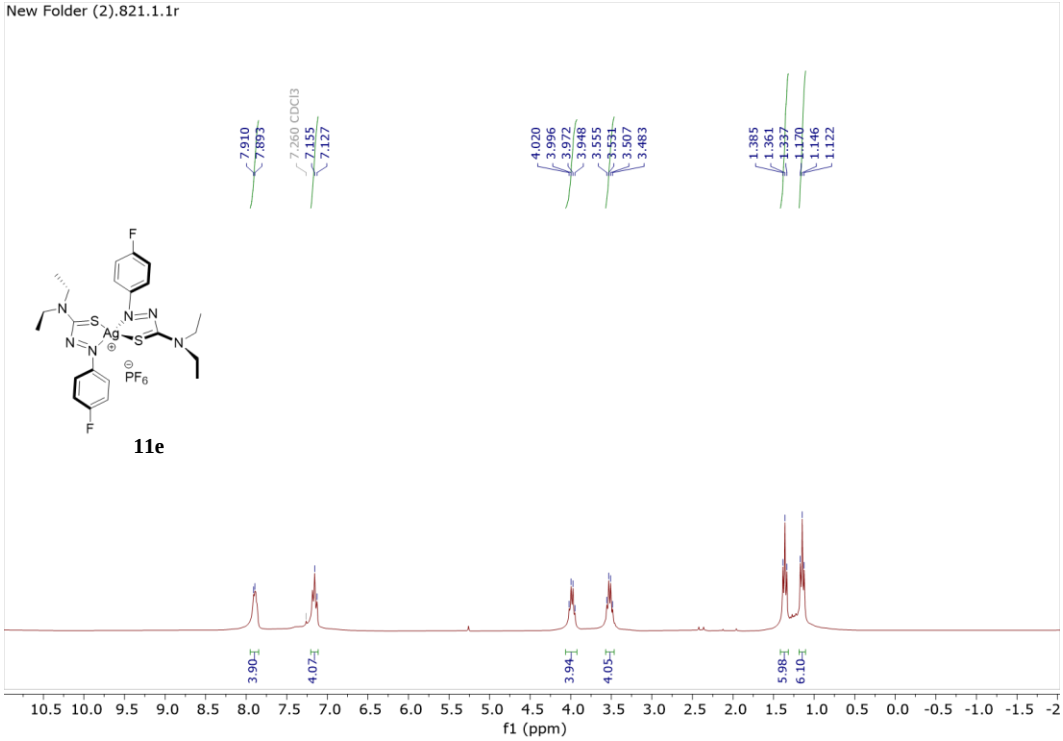

Figure A4.18: ^{1}H NMR spectrum of **11e** [(N,N-diethyl-2-(4-fluorophenyl) diazothioformamide)$_2$Ag](PF$_6$) in CDCl$_3$

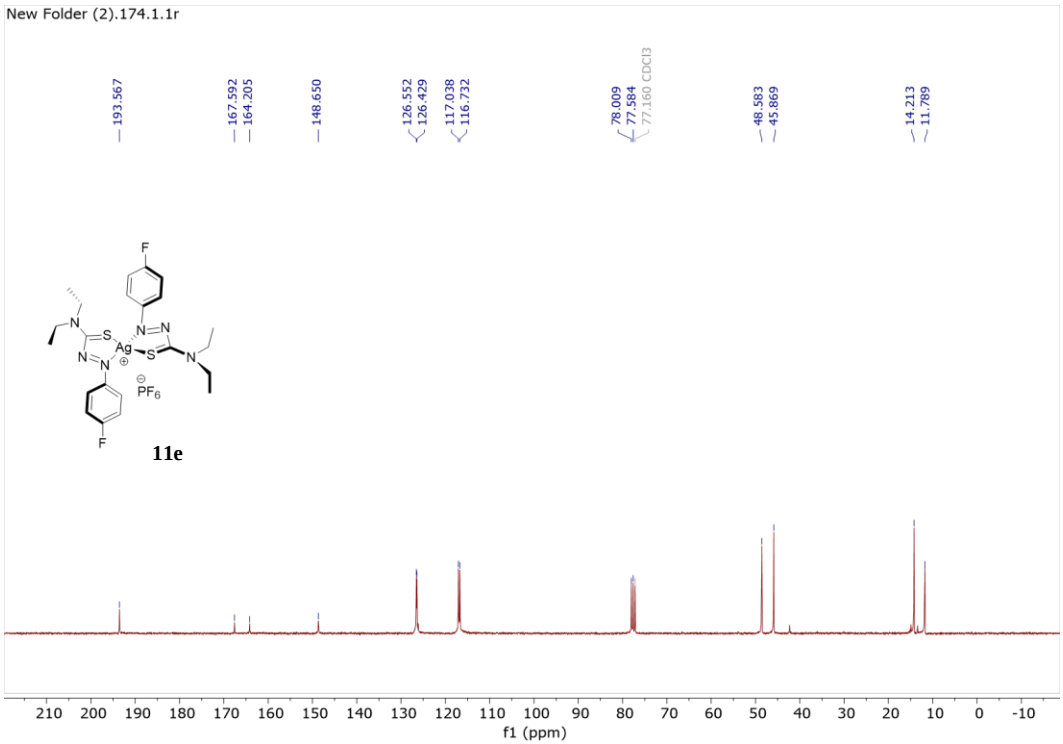

Figure A4.19: ^{13}C NMR spectrum of **11e** [(N,N-diethyl-2-(4-fluorophenyl) diazothioformamide)$_2$Ag](PF$_6$) in CDCl$_3$

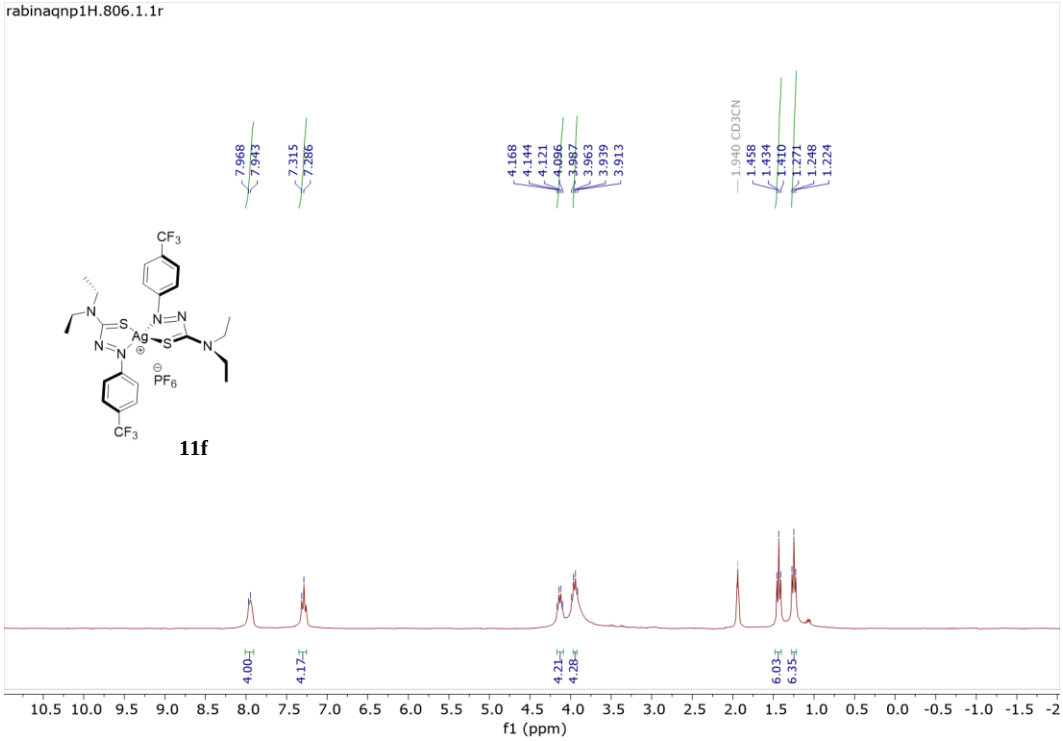

Figure A4.20: ^{1}H NMR spectrum of **11f** [(N,N-diethyl-2-(4-trifluoromethyl phenyl) diazothioformamide)$_2$Ag](PF$_6$) in CD$_3$CN

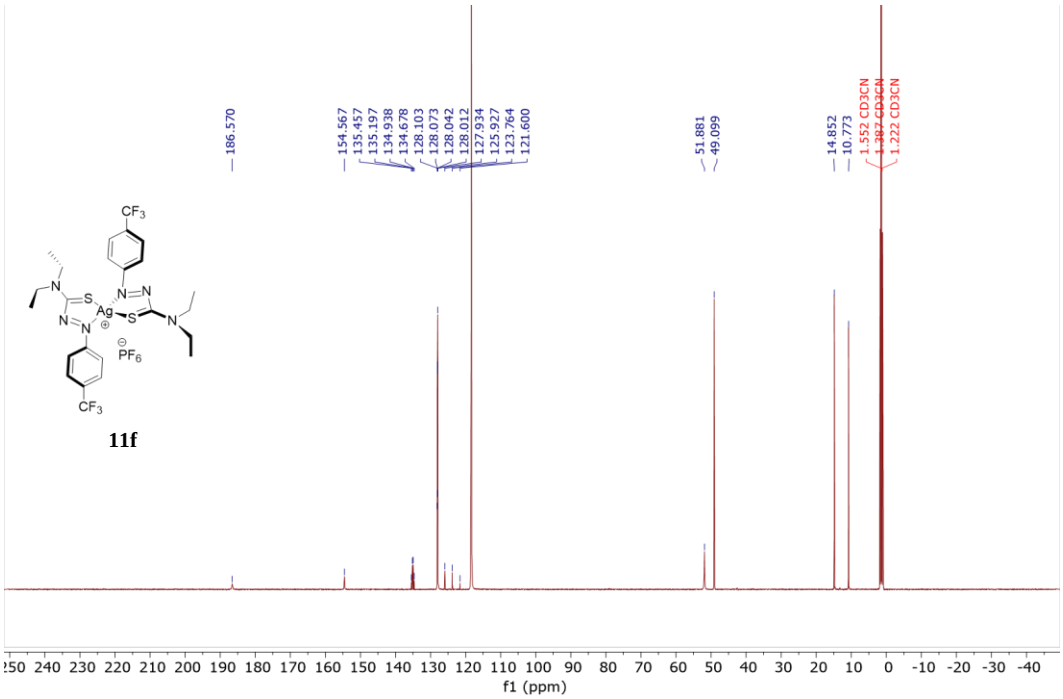

Figure A4.21: ^{13}C NMR spectrum of **11f** [(N,N-diethyl-2-(4-trifluoromethyl phenyl) diazothioformamide)$_2$Ag](PF$_6$) in CD$_3$CN

Experimental Data for X-ray Crystal Structures

Crystallographic Data for 6g: $C_{12}H_{16}N_4S$ (M =248.35 g/mol): monoclinic, space group $P2_1/c$ (no. 14), a = 18.2006(11) Å, b = 9.0898(5) Å, c = 17.1535(9) Å, β = 118.161(2)°, V = 2501.9(2) Å^3, Z = 8, T = 100 K, μ(MoKα) = 0.242 mm^{-1}, $Dcalc$ = 1.319 g/cm^3, 2Θmax = 61.164°, 86469 reflections measured, 7661 unique (R_{int} = 0.0592, R_{sigma} = 0.0328), R_1 = 0.0365 (I > 2σ(I)), wR_2 = 0.0791 (all data).

X-ray diffraction data for **6g** were collected at 100 K on a Bruker D8 Venture using MoKα-radiation (λ=0.71073 Å). Data have been corrected for absorption using SADABS[1] area detector absorption correction program. Using Olex2[2], the structure was solved with the SHELXT[3] structure solution program using Direct Methods and refined with the SHELXL[4] refinement package using least squares minimization. The structure was treated as a two-component pseudo-merohedral twin using the TwinRotMat package within the PLATON[5] program (twin law: 1 0 0 0 -1 0 0 0 -1) with the BASF parameter refining to 0.4039(7). All non-hydrogen atoms were refined with anisotropic thermal parameters. The hydrogen atoms of the investigated structure were located from difference Fourier maps. Hydrogen atoms bound to heteroatoms were placed and refined. All other hydrogen atoms were placed in geometrically calculated positions and refined using a riding model. Isotropic thermal parameters of the placed hydrogen atoms were fixed to 1.2 times the U value of the atoms they are linked to (1.5 times for methyl groups). Calculations and refinement of structures were carried out using APEX3[6], SHELXTL[7], and Olex2 software.

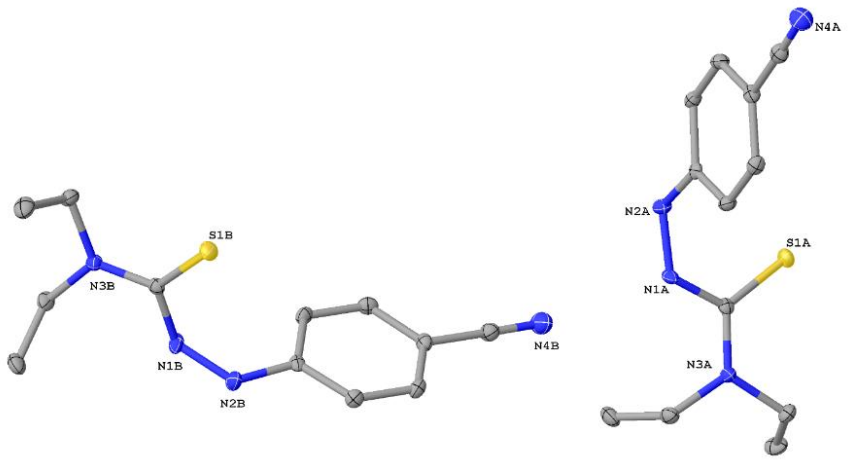

Crystallographic Data for 6h: $C_{11}H_{16}N_4O_2S_2$ (M =300.40 g/mol): monoclinic, space group $P2_1/c$ (no. 14), a = 21.0003(5) Å, b = 14.3450(4) Å, c = 9.7164(3) Å, β = 101.1170(10)°, V = 2872.13(14) Å^3, Z = 8, T = 100 K, μ(MoKα) = 0.374 mm^{-1}, *Dcalc* = 1.389 g/cm^3, 2Θmax = 54.21°, 110883 reflections measured, 6335 unique (R_{int} = 0.0846, R_{sigma} = 0.0313), R_1 was 0.0496 (I > 2σ(I)), wR_2 = 0.1045 (all data).

X-ray diffraction data for **6h** were collected at 100 K on a Bruker D8 Venture using MoKα (λ = 0.71073). Data have been corrected for absorption using SADABS[1] area detector absorption correction program. Using Olex2[2], the structure was solved with the SHELXT[3] structure solution program using Direct Methods and refined with the SHELXL[4] refinement package using least squares minimization. All non-hydrogen atoms were refined with anisotropic thermal parameters. Hydrogen atoms in the investigated structure were located from difference Fourier maps but finally their positions were placed in geometrically calculated positions and refined using a riding model. Isotropic thermal parameters of the placed hydrogen atoms were fixed to 1.2 times the U value of the atoms they are linked to (1.5 times for methyl groups). Hydrogen atoms connected to heteroatoms were located from the difference map, placed, and

refined. Calculations and refinement of structures were carried out using APEX4[5], SHELXTL[6], and Olex2 software.

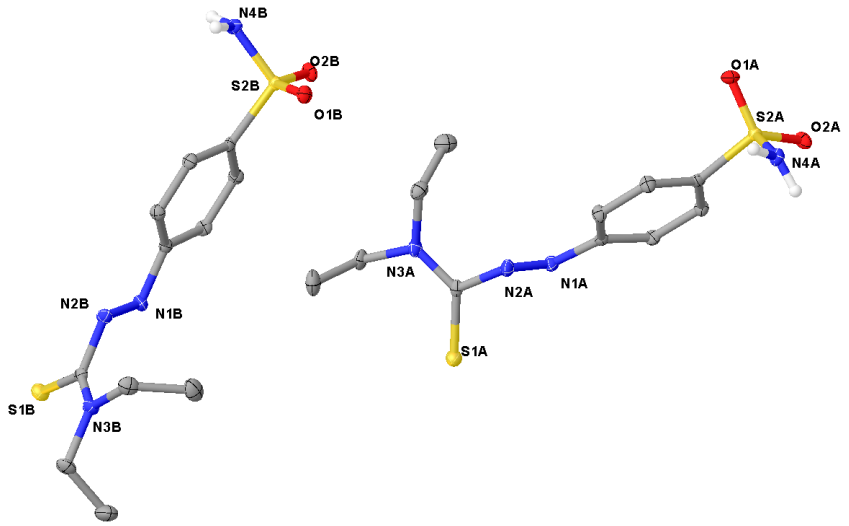

Crystallographic Data for 7g: $C_{24}H_{28}Br_2Cu_2N_8S_2$ (M =779.56 g/mol): triclinic, space group P-1 (no. 2), a = 10.6525(7) Å, b = 11.7310(7) Å, c = 13.2202(8) Å, α = 65.057(2)°, β = 89.469(2)°, γ = 87.626(2)°, V = 1496.62(16) Å^3, Z = 2, T = 100 K, μ(MoKα) = 4.260 mm^{-1}, *Dcalc* = 1.730 g/cm^3, 2Θmax = 50.188°, 77798 reflections measured, 5307 unique (R_{int} = 0.0604, R_{sigma} = 0.0232), R_1 = 0.0313 (I > 2σ(I)), wR_2 = 0.0826 (all data).

X-ray diffraction data for **7g** were collected at 100 K on a Bruker D8 Venture using MoKα-radiation (λ=0.71073 Å). Data have been corrected for absorption using SADABS[1] area detector absorption correction program. Using Olex2[2], the structure was solved with the SHELXT[3] structure solution program using Direct Methods and refined with the SHELXL[4] refinement package using least squares minimization. All non-hydrogen atoms were refined with anisotropic thermal parameters. The hydrogen atoms of the investigated structure were located from difference Fourier maps but finally their positions were placed in geometrically calculated positions and refined using a riding model. Isotropic thermal parameters of the

placed hydrogen atoms were fixed to 1.2 times the *U* value of the atoms they are linked to (1.5 times for methyl groups). Calculations and refinement of structures were carried out using APEX3[5], SHELXTL[6], and Olex2 software.

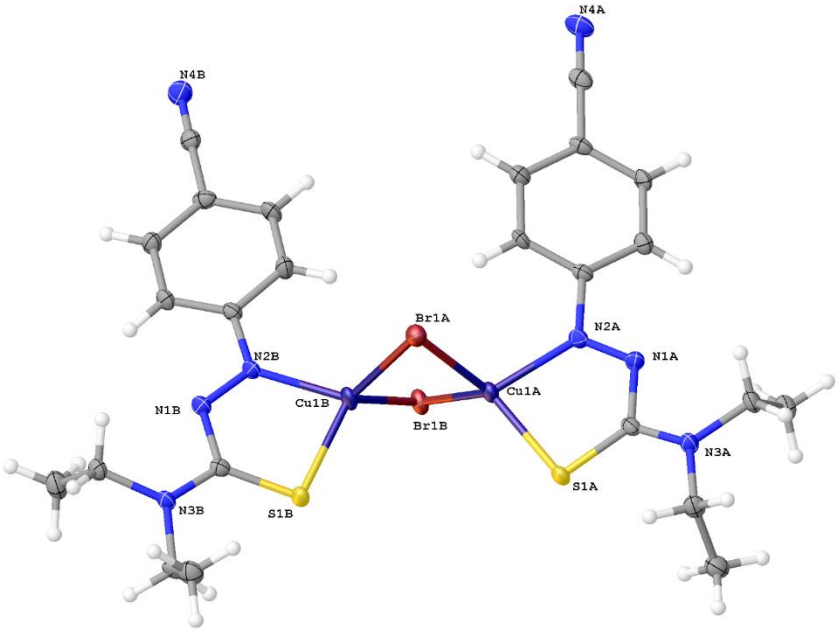

Crystallographic Data for 9g: $C_{24}H_{28}BCuF_4N_8S_2$ (*M* =643.01 g/mol): triclinic, space group P-1 (no. 2), *a* = 13.4025(10) Å, *b* = 15.2162(12) Å, *c* = 15.4943(12) Å, *α* = 89.380(3)°, *β* = 72.859(3)°, *γ* = 72.305(3)°, *V* = 2865.8(4) Å^3, *Z* = 4, *T* = 100 K, μ(MoKα) = 0.964 mm^{-1}, *Dcalc* = 1.490 g/cm^3, 2Θmax = 50.494°, 105444 reflections measured, 10201 unique (R_{int} = 0.0685, R_{sigma} = 0.0423), R_1 = 0.0714 (I > 2σ(I)), wR_2 = 0.1764 (all data).

X-ray diffraction data for **9g** were collected at 100 K on a Bruker D8 Venture using MoKα (λ = 0.71073). Data have been corrected for absorption using SADABS[1] area detector absorption correction program. Using Olex2[2], the structure was solved with the SHELXT[3] structure solution program using Direct Methods and refined with the SHELXL[4] refinement package using least squares minimization. All non-hydrogen atoms were refined with anisotropic

thermal parameters. Hydrogen atoms in the investigated structure were located from difference Fourier maps but finally their positions were placed in geometrically calculated positions and refined using a riding model. Isotropic thermal parameters of the placed hydrogen atoms were fixed to 1.2 times the *U* value of the atoms they are linked to (1.5 times for methyl groups). Calculations and refinement of structures were carried out using APEX4[5], SHELXTL[6], and Olex2 software. Diffraction images indicated that either the crystal was cracked or was a non-merohedral twin as many reflections were slightly split. This observation was consistent for over 10 crystals screened. Evaluation of the reflections within APEX4 suggested a second crystal domain. Efforts to treat the data as a non-merohedral twin were unsuccessful. The model presented treats the data as a single crystal.

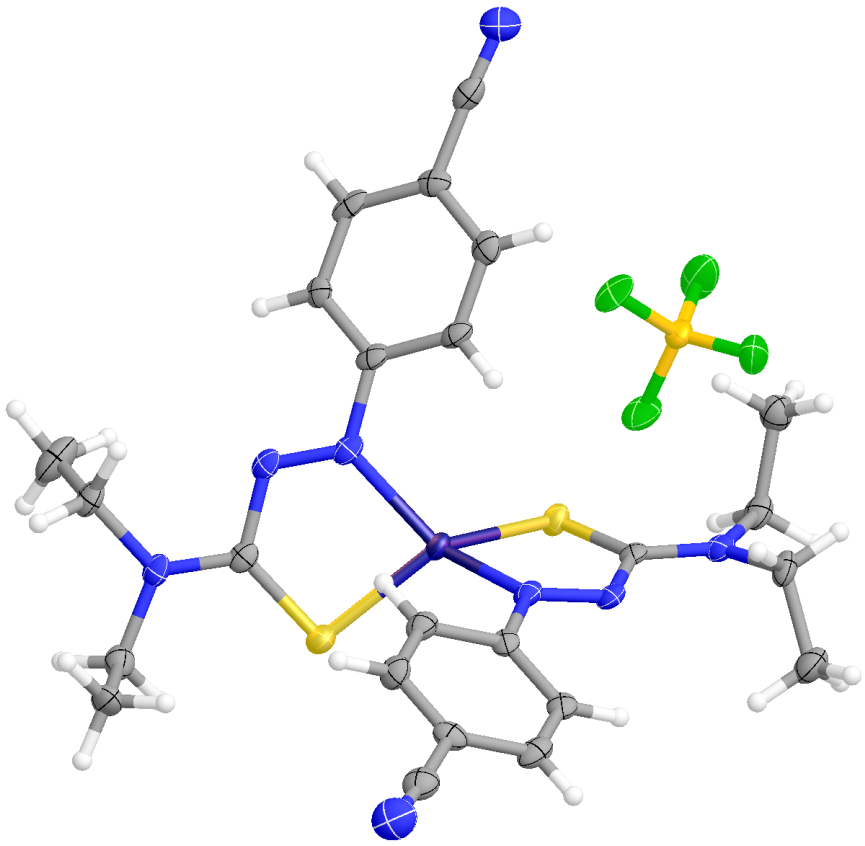

NMR spectra for Stability Test in DMSO- *d*6

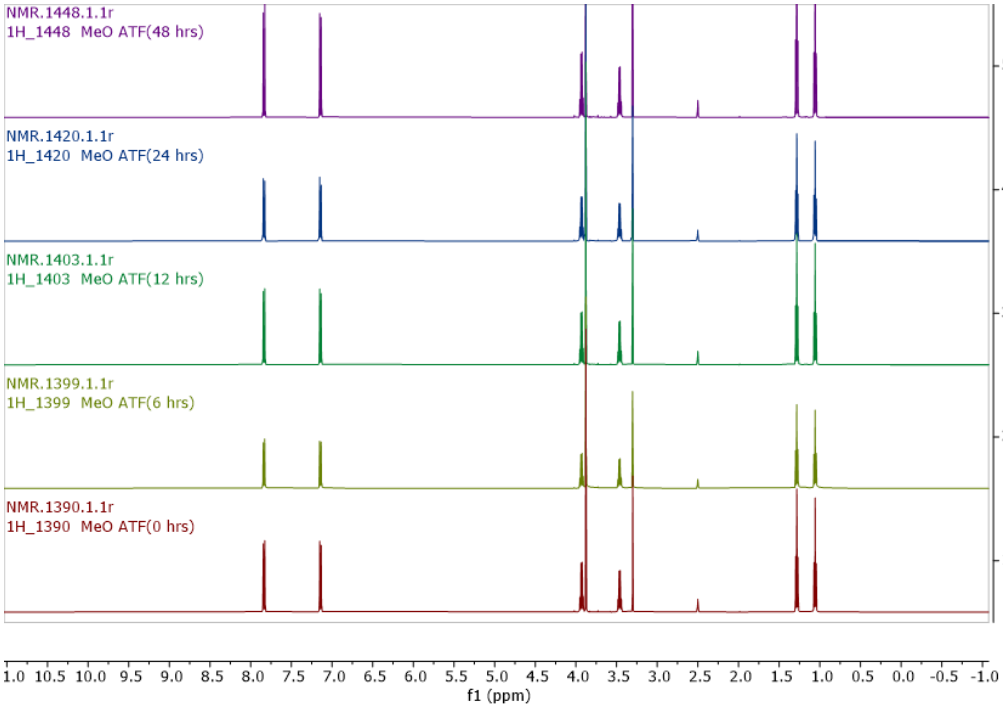

Figure A4.22: ^{1}H NMR spectrum of **6c** (N,N-diethyl-2-(4-methoxyphenyl) diazothioformamide) in DMSO-d_6 recorded for 48 hrs.

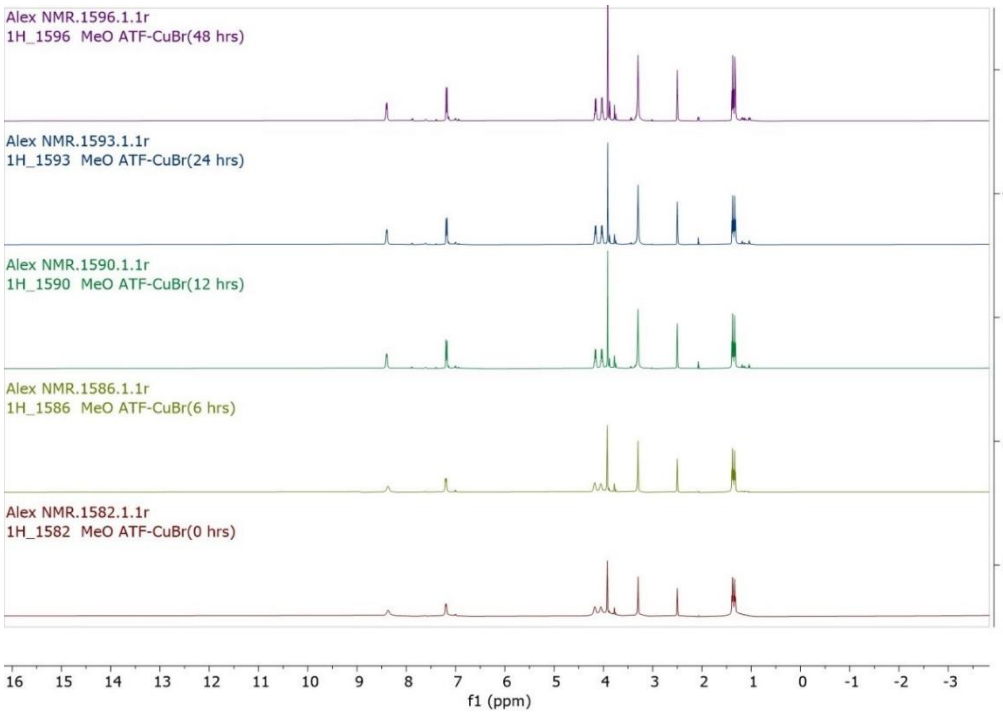

Figure A4.23: ^{1}H NMR spectrum of **7c** [(N,N-diethyl-2-(4-methoxyphenyl) diazothioformamide)CuBr] in DMSO-*d6* recorded for 48 hrs**.**

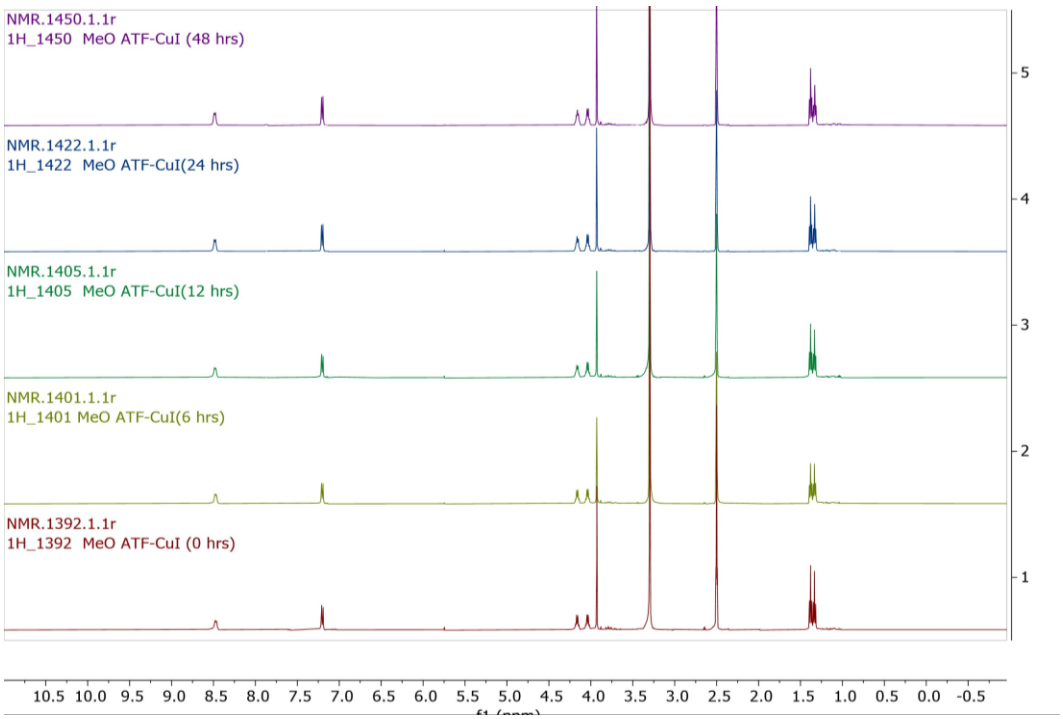

Figure A4.24: ^{1}H NMR spectrum of **8c** [(N,N-diethyl-2-(4-methoxyphenyl) diazothioformamide)CuI] in DMSO-*d6* recorded for 48 hrs.

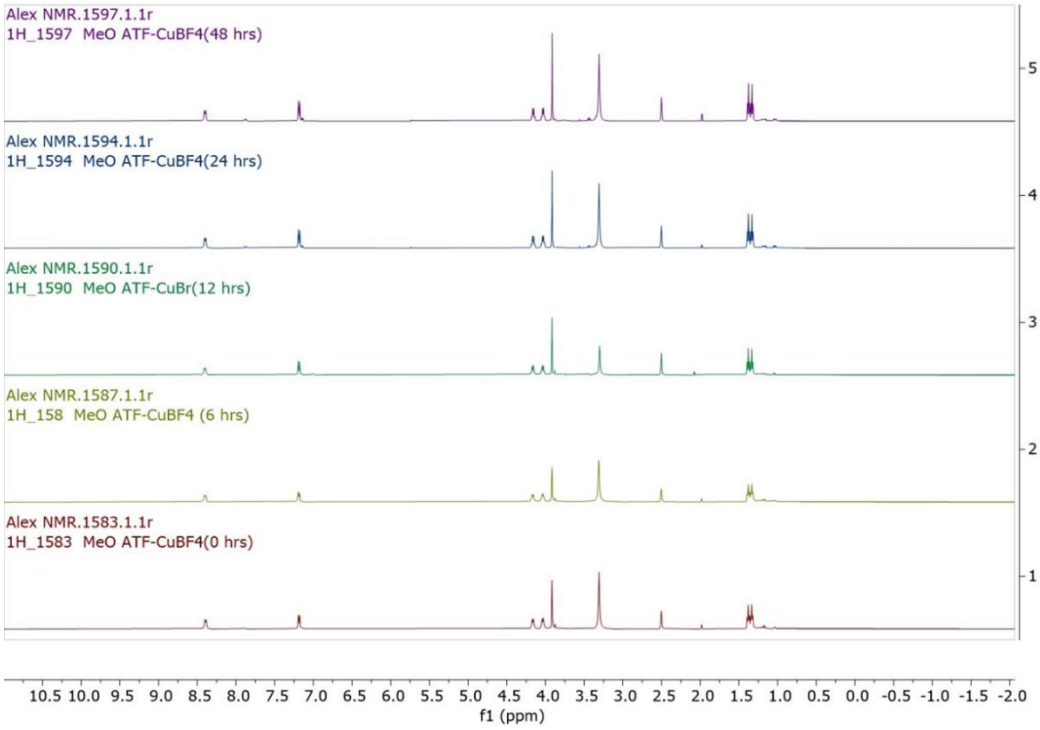

Figure A4.25: ^{1}H NMR spectrum of **9c** [(N,N-diethyl-2-(4-methoxyphenyl) diazothioformamide)$_2$Cu](BF$_4$) in DMSO-*d6* recorded for 48 hrs**.**

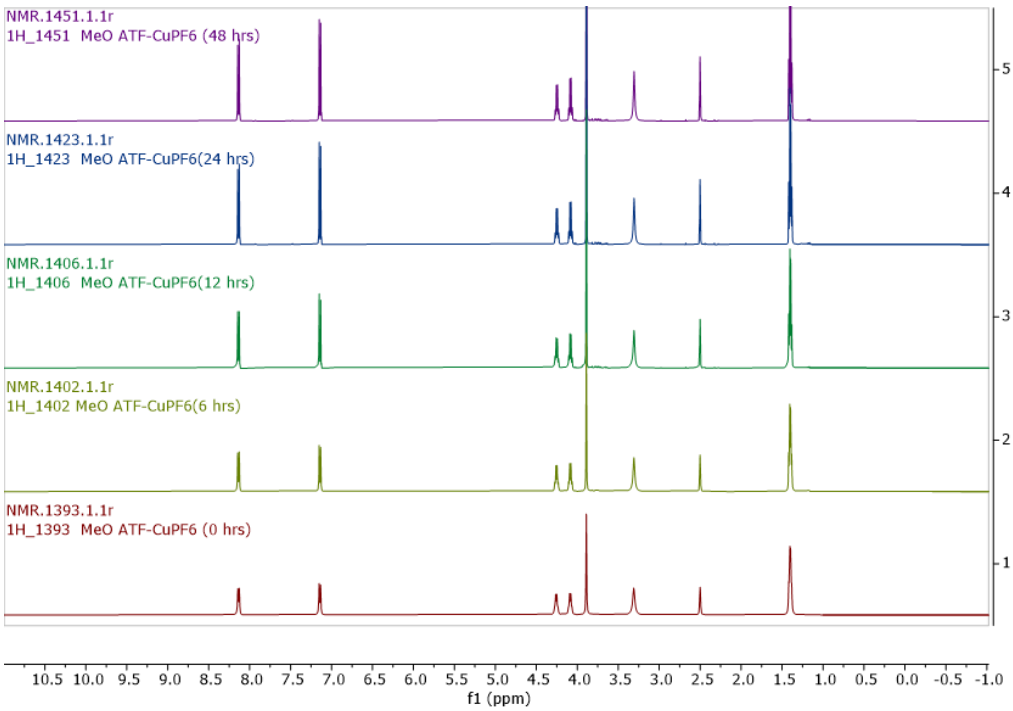

Figure A4.26: ^{1}H NMR spectrum of **10c** (N,N-diethyl-2-(4-methoxylphenyl) diazothioformamide)$_2$Cu](PF_6) in DMSO-*d6* recorded for 48 hrs**.**

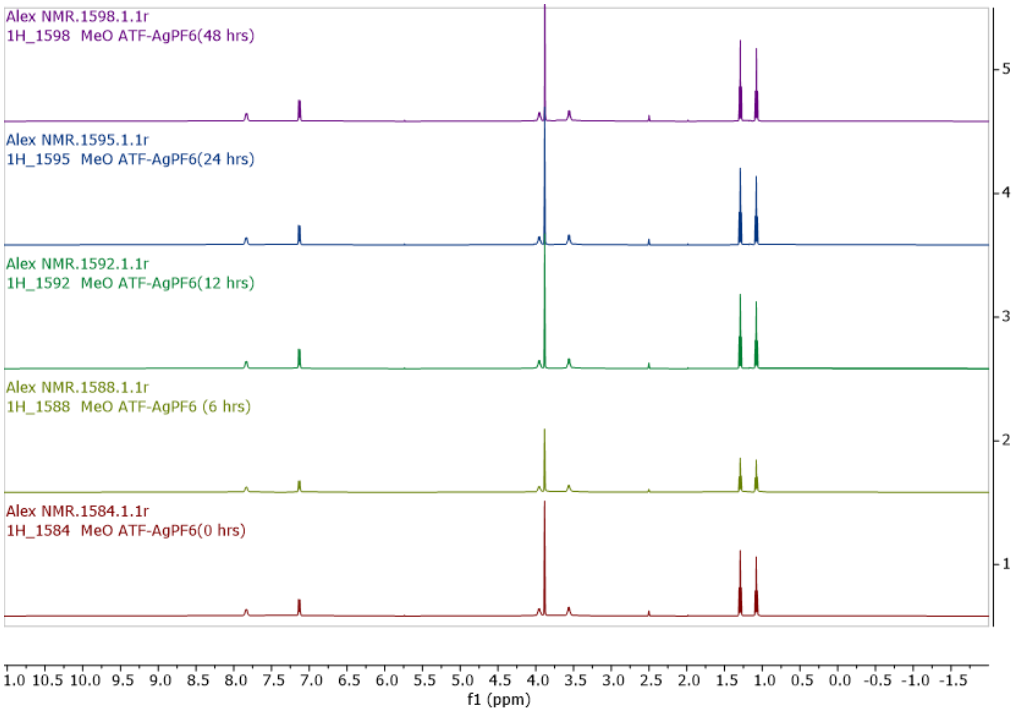

Figure A4.27: ^{1}H NMR spectrum of **11c** ((N,N-diethyl-2-(4-methoxylphenyl) diazothioformamide)$_2$Ag](PF_6) in DMSO-*d6* recorded for 48 hrs**.**

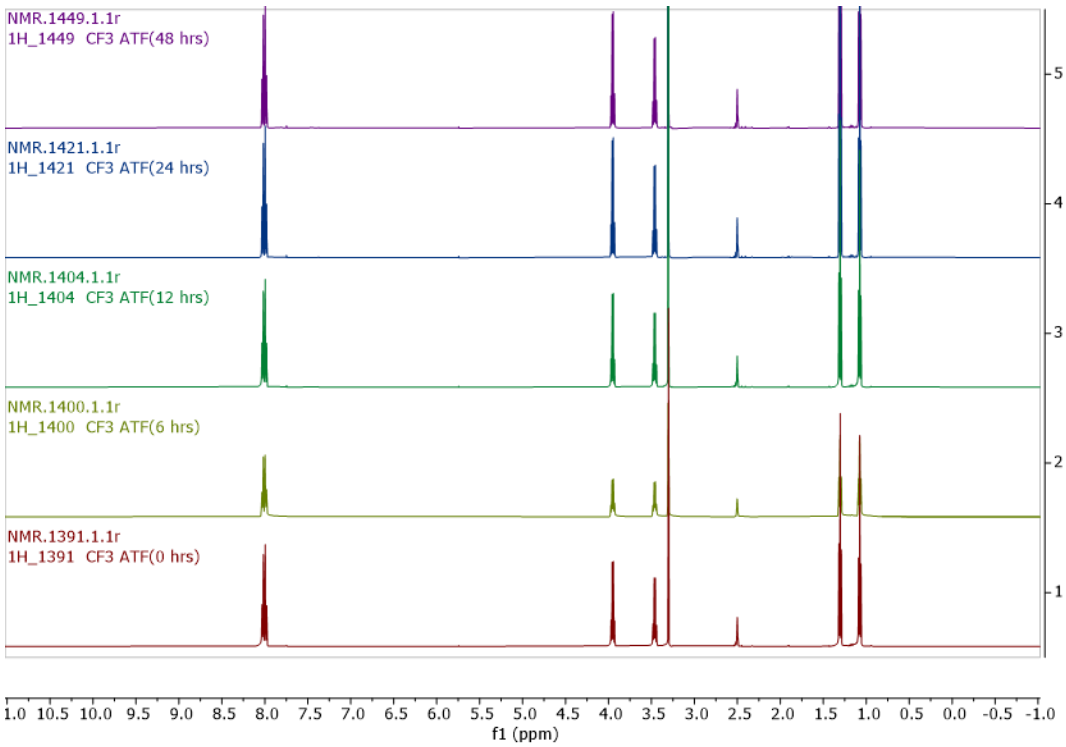

Figure A4.28: ^{1}H NMR spectrum of **6f** (N,N-diethyl-2-(4-trifluoromethylphenyl) diazothioformamide) in DMSO-*d6* recorded for 48 hrs**.**

NMR spectra for Stability Test in MeOH-*d*4

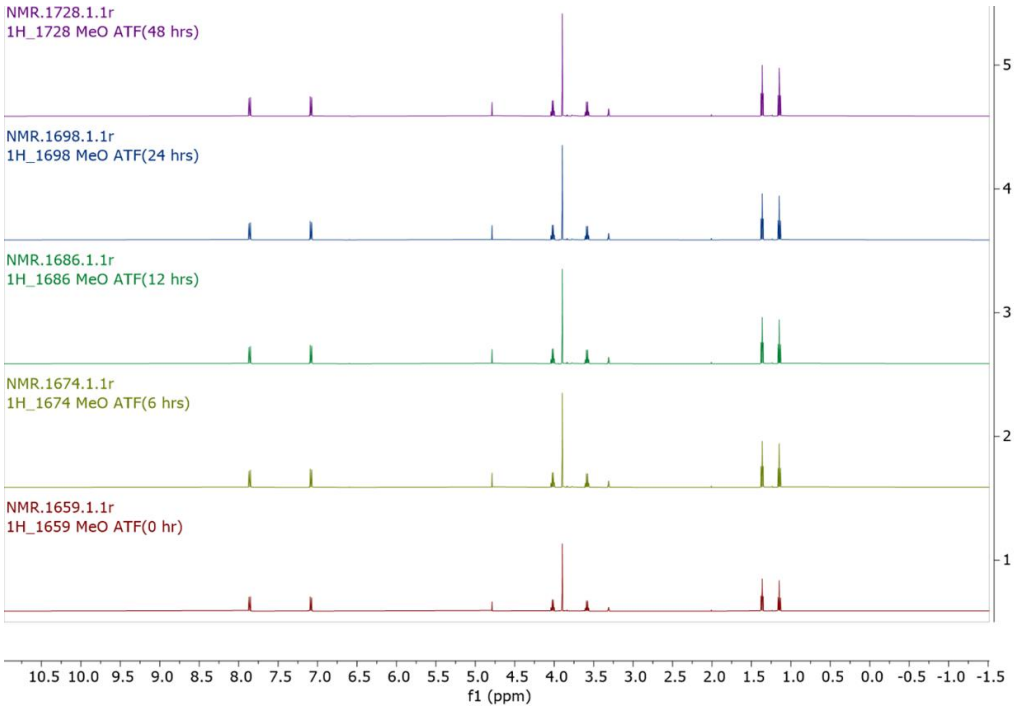

Figure A4.29: ^{1}H NMR spectrum of **6c** (N,N-diethyl-2-(4-methoxyphenyl) diazothioformamide) in MeOD recorded for 48 hrs.

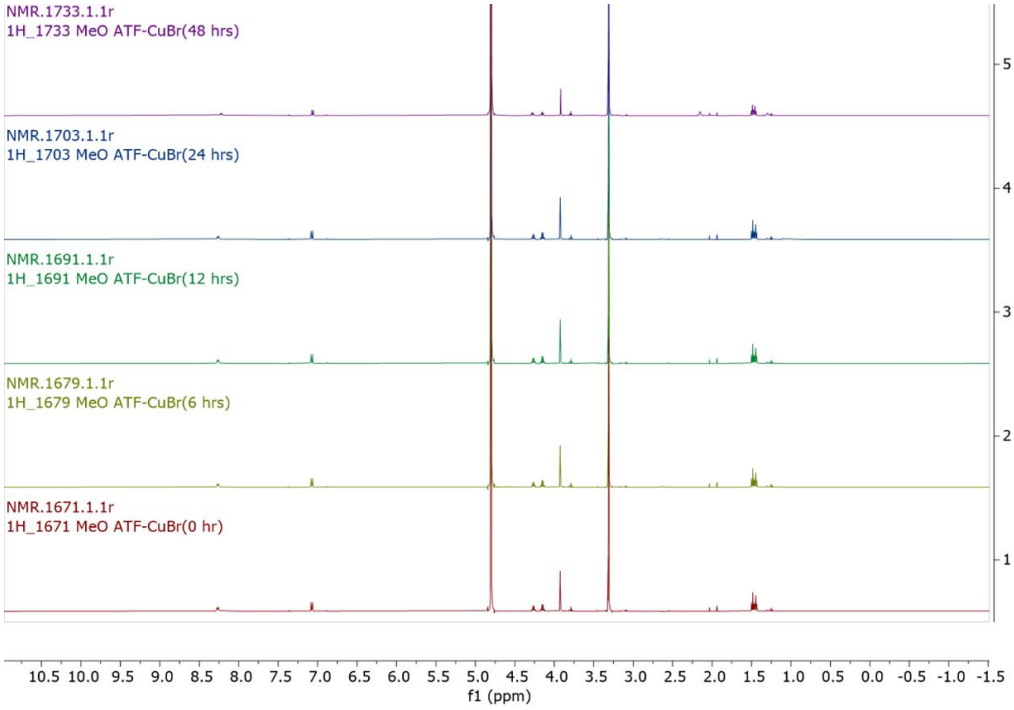

Figure A4.30: ^{1}H NMR spectrum of **7c** [(N,N-diethyl-2-(4-methoxyphenyl) diazothioformamide)CuBr] in MeOD recorded for 48 hrs**.**

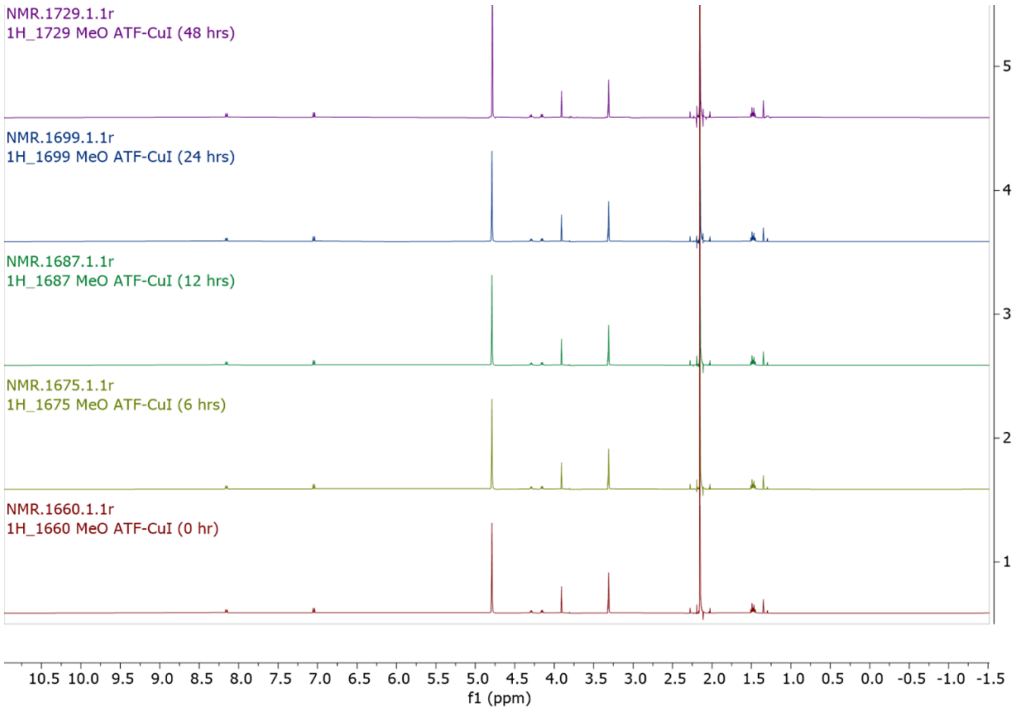

Figure A4.31: ^{1}H NMR spectrum of **8c** [(N,N-diethyl-2-(4-methoxyphenyl) diazothioformamide)CuI] in MeOD recorded for 48 hrs.

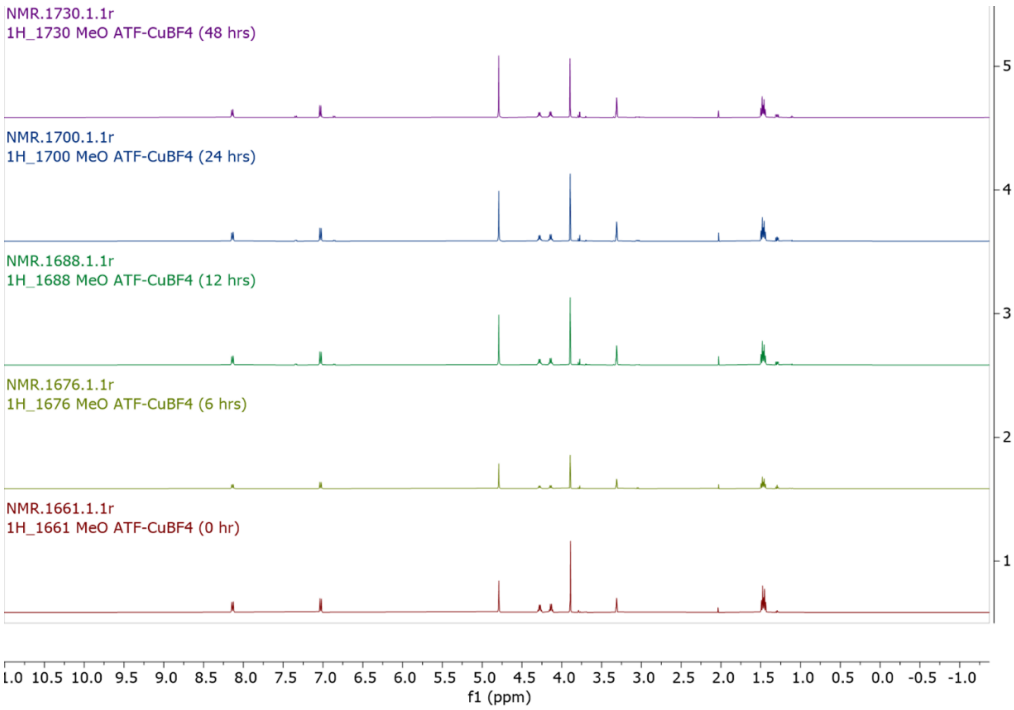

Figure A4.32: ^{1}H NMR spectrum of **9c** [(N,N-diethyl-2-(4-methoxyphenyl) diazothioformamide)$_2$Cu](BF$_4$) in MeOD recorded for 48 hrs**.**

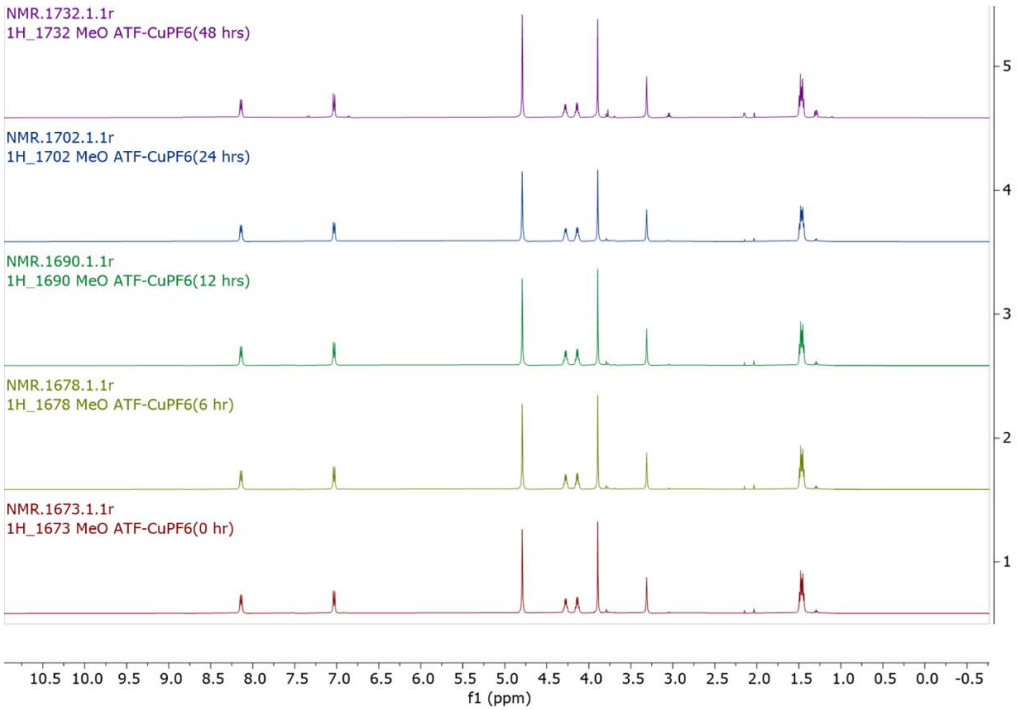

Figure A4.33: ^{1}H NMR spectrum of **10c** (N,N-diethyl-2-(4-methoxylphenyl) diazothioformamide)$_2$Cu](PF$_6$) in MeOD recorded for 48 hrs**.**

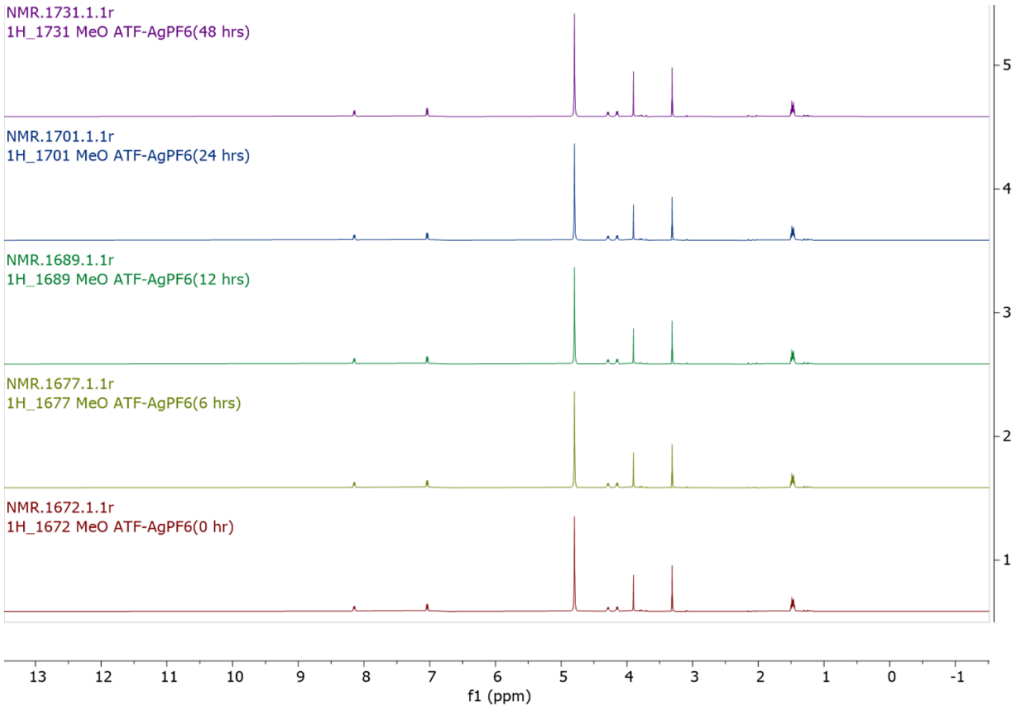

Figure A4.34: ^{1}H NMR spectrum of **11c** ((N,N-diethyl-2-(4-methoxylphenyl) diazothioformamide)$_2$Ag](PF$_6$) in MeOD recorded for 48 hrs**.**

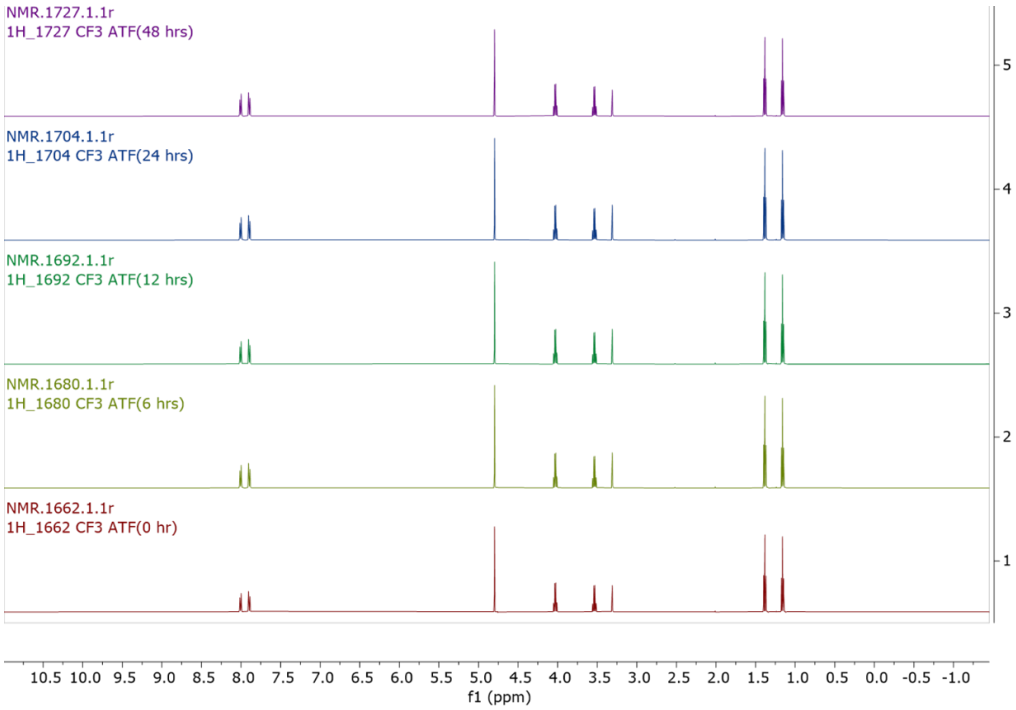

Figure A4.35: ^{1}H NMR spectrum of **6f** (N,N-diethyl-2-(4-trifluoromethylphenyl) diazothioformamide) in MeOD recorded for 48 hrs**.**

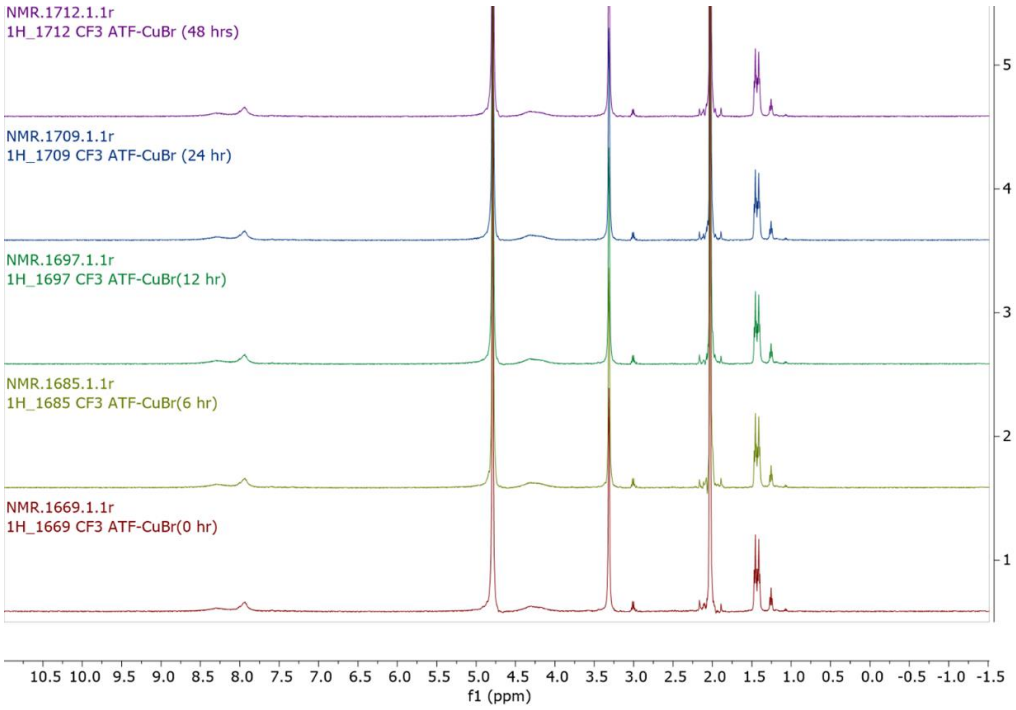

Figure A4.36: ^{1}H NMR spectrum of **8f** ([(N,N-diethyl-2-(4-trifluoromethylphenyl) diazothioformamide)CuBr] in MeOD recorded for 48 hrs.

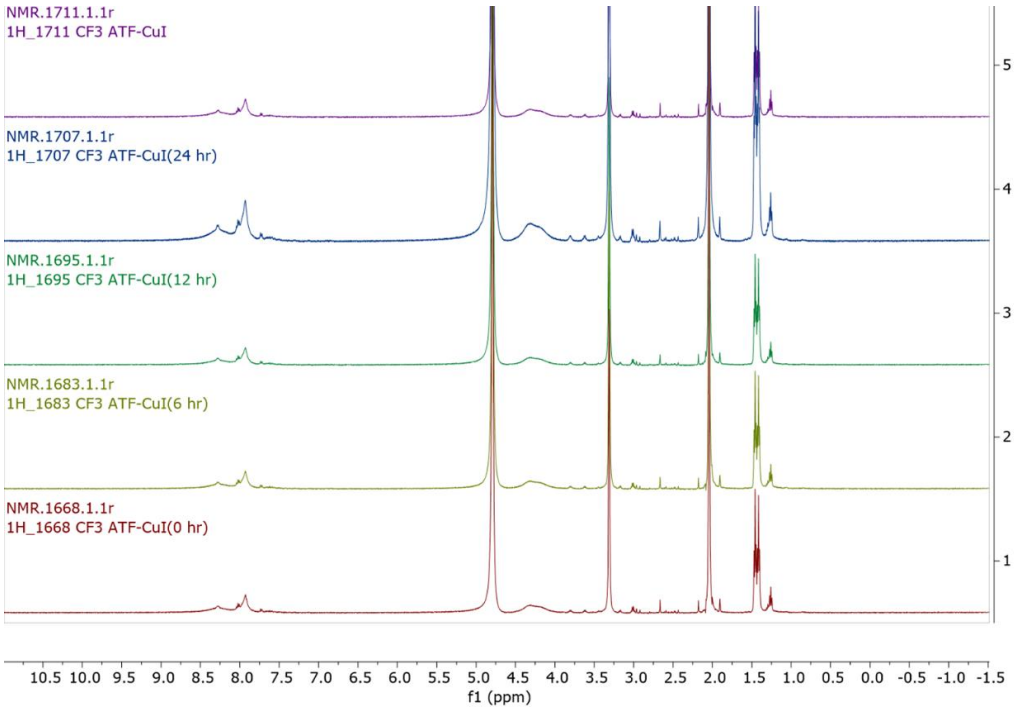

Figure A4.37: ^{1}H NMR spectrum of **8f** ([(N,N-diethyl-2-(4-trifluoromethylphenyl) diazothioformamide)CuI] in MeOD recorded for 48 hrs.

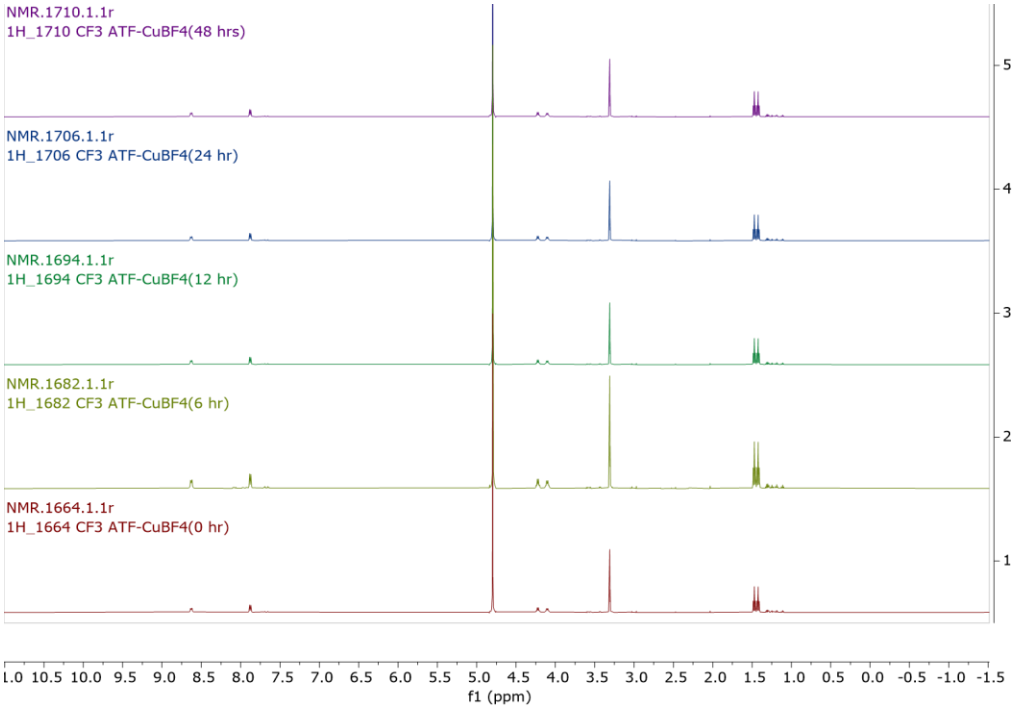

Figure A4.38: ^{1}H NMR spectrum of **9f** [(N,N-diethyl-2-(4-trifluoromethylphenyl) diazothioformamide)$_2$Cu](BF_4) in MeOD recorded for 48 hrs**.**

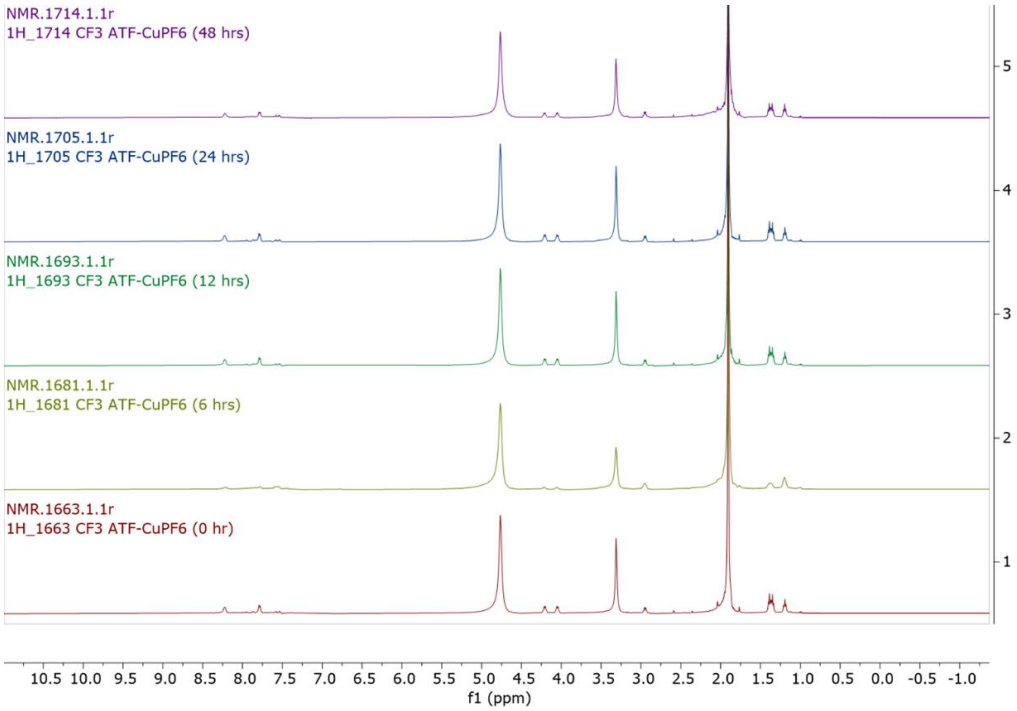

Figure A4.39: ^{1}H NMR spectrum of **9f** [(N,N-diethyl-2-(4-trifluoromethylphenyl) diazothioformamide)$_2$Cu](PF$_6$) in MeOD recorded for 48 hrs**.**

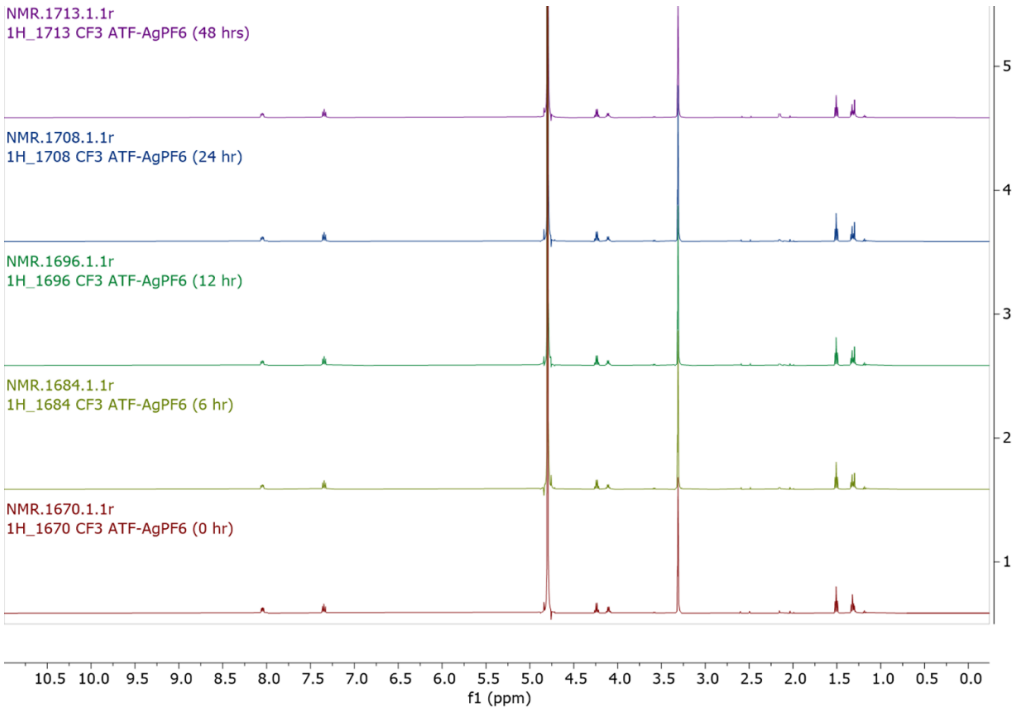

Figure A4.40: ^{1}H NMR spectrum of **11f** [(N,N-diethyl-2-(4-trifluoromethylphenyl) diazothioformamide)$_2$Ag](PF$_6$) in MeOD recorded for 48 hrs.

References

1. Sheldrick, G. M. (1996). SADABS: Area Detector Absorption Correction; University of Göttingen, Germany.
2. Dolomanov, O.V.; Bourhis, L.J.; Gildea, R.J.; Howard, J.A.K.; Puschmann, H., (2009). J. Appl. Cryst., 42, 339-341.
3. Sheldrick, G. M. (2015). *Acta Cryst.* A71, 3-8.
4. Sheldrick, G. M. (2015). *Acta Cryst.* C71, 3-8.
5. Bruker (2016). APEX3. Bruker AXS Inc., Madison, Wisconsin, USA.
6. Sheldrick, G.M. (2008). Acta Cryst. A64, 112-122.

Appendix V

Supporting Information for Chapter 6: Catalytic Carboxylation of Terminal Alkynes with Copper(I) Azothioformamide complexes.

General Methods

^{1}H and ^{13}C NMR experiments were performed on either a Bruker AVANCE 300 or 500 MHz instrument and spectral data were obtained in $CDCl_3$ (referenced to 7.26 ppm for ^{1}H and 77.16 ppm for ^{13}C), CD_3CN (referenced to 1.94 ppm for ^{1}H and 118.7 and 1.39 ppm for ^{13}C), d_6-DMSO (referenced to 2.49 ppm for ^{1}H and 39.52 ppm for ^{13}C), and d_4-MeOH (referenced to 3.31 ppm for ^{1}H and 49.3 ppm for ^{13}C). Coupling constants (*J*) are in Hz. The multiplicities of the signals are described using the following abbreviations: s = singlet, br s =broad singlet, d = doublet, t = triplet, q = quartet, dd = doublet of doublets, m = multiplet, app = apparent. Infrared spectra were obtained on a Thermo Scientific Nicolet FT-IR spectrometer with ZnSe ATR attachment and peaks are reported in cm^{-1}. Elemental Analysis was performed on a Vario micro-Cube elemental analyzer for (C,H,N). Reaction progress was monitored by thin-layer chromatography on silica gel plates (60-F254), observed under UV light. Column chromatography was performed using silica gel (particle size 40–63 μm).

Computational Details

Calculations were performed with the Gaussian16 software package.[1] The B3LYP functional was used in conjunction with the 6-31G(d,p) (H, C, N, O, and S) and SDD (Cu, with ECP) basis sets using ultrafine integration grids.[2] The CPCM solvation model was used to calculate thermodynamic parameters in DMSO.[3] Frequency calculations were performed on all minimized structures to confirm the absence of imaginary frequencies and evaluate thermodynamics.

Characterization of Propiolic acid products

General procedure for the Synthesis of Propiolic acids

[*Para*-MeOATF-CuI]$_2$ complex (35 mg, 0.04 mmol) and cesium carbonate (977 mg, 3.0 mmol) were added to a flame dried, carbon dioxide flushed round-bottom flask equipped with a magnetic stirrer. Under carbon dioxide atmosphere, terminal alkyne (1 mmol) and anhydrous DMSO (5 mL) were added to the flask. Carbon dioxide in the form of balloon was introduced at ambient pressure and the mixture was stirred at 40 ˚C for 24 h. The reaction was cooled to room temperature, quenched with water, and filtered. Filtrate was acidified with20 mL of 6M HCl and extracted with diethyl ether (4 x 10 mL). The combined organic layers were washed with brine and dried with anhydrous Na_2SO_4. The solvent was removed under reduced pressure giving target propiolic acid product. NMR spectral data matched that of known compounds.

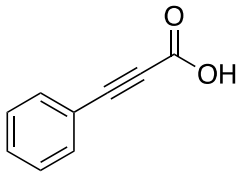

3-phenylpropiolic acid (28) (99% yield)

^{1}H NMR (300 MHz, Chloroform-*d*) δ 7.62 (d, *J* = 6.8 Hz, 2H), 7.49 (t, *J* = 7.4 Hz, 1H), 7.40 (t, *J* = 7.4 Hz, 2H). ^{13}C NMR (75 MHz, $CDCl_3$) δ 159.59, 134.16, 132.03, 129.54, 119.99, 90.03, 80.96.

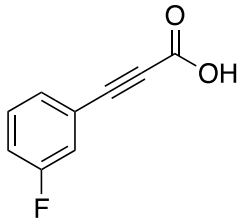

3-(3-fluorophenyl)propiolic acid (29) (71% yield)

^{1}H NMR (300 MHz, Chloroform-*d*) δ 7.43 – 7.35 (m, 2H), 7.34 – 7.27 (m, 1H), 7.23 – 7.16 (m, 1H). ^{13}C NMR (75 MHz, $CDCl_3$) δ 164.76 (d, $J_{C\text{-}F}$ = 249 Hz), 159.07, 131.36 (d, $J_{C\text{-}F}$= 8 Hz), 130.03 (d, $J_{C\text{-}F}$ = 3 Hz), 121.84 (d, $J_{C\text{-}F}$ = 10 Hz), 120.92 (d, $J_{C\text{-}F}$ = 24 Hz), 119.66 (d, $J_{C\text{-}F}$ = 20 Hz), 88.03 (d, $J_{C\text{-}F}$ =3 Hz), 81.37.

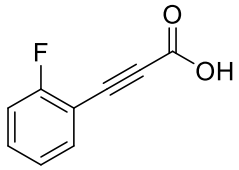

3-(2-fluorophenyl)propiolic acid (30) (72% yield)

^{1}H NMR (500 MHz, Chloroform-*d*) δ 7.62 – 7.55 (m, 1H), 7.51 – 7.43 (m, 1H), 7.21 – 7.15 (m, 1H), 7.18 – 7.10 (m, 1H). ^{13}C NMR (126 MHz, $CDCl_3$) δ 165.12 (d, $J_{C\text{-}F}$ = 260 Hz), 157.48, 135.02, 133.36 (d, $J_{C\text{-}F}$ = 8 Hz), 124.57 (d, $J_{C\text{-}F}$ = 3 Hz), 116.28 (d, $J_{C\text{-}F}$ = 20 Hz), 108.45 (d, $J_{C\text{-}F}$ = 15 Hz), 84.68, 82.41.

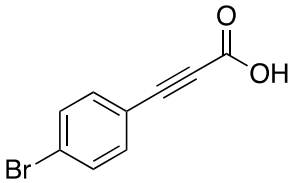

3-(4-bromophenyl)propiolic acid (31) (76% yield)

^{1}H NMR (500 MHz, DMSO-d_6) δ 7.66 – 7.65 (m, 1H), 7.64 – 7.63 (m, 1H), 7.56 – 7.55 (m, 1H), 7.54 – 7.53 (m, 1H). ^{13}C NMR (126 MHz, DMSO) δ 154.14, 134.38, 132.11, 124.66, 118.26, 83.20, 82.68.

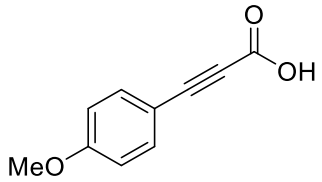

3-(4-methoxyphenyl)propiolic acid (32) (77% yield)

^{1}H NMR (500 MHz, Chloroform-*d*) δ 7.56 (d, *J* = 8.8 Hz, 2H), 6.90 (d, *J* = 8.8 Hz, 2H), 3.84 (s, 3H). ^{13}C NMR (126 MHz, $CDCl_3$) δ 162.18, 158.40, 135.56, 114.65, 111.18, 90.19,79.88,55.67.

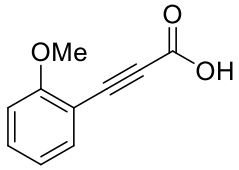

3-(2-methoxyphenyl)propiolic acid (33) (73% yield)

^{1}H NMR (500 MHz, Chloroform-*d*) δ 7.33 – 7.26 (m, 1H), 7.24 – 7.19 (m, 1H), 7.13 – 7.12 (m,

1H), 7.03 (m, 1H), 3.82 (s, 3H). ^{13}C NMR (126 MHz, $CDCl_3$) δ 159.64, 158.49, 130.02, 126.06, 120.23, 118.31, 117.89, 89.23, 79.95, 55.63

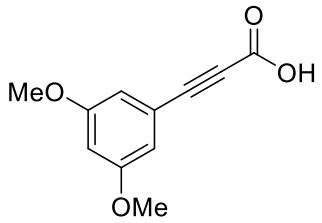

3-(3,5-dimethoxyphenyl)propiolic acid (34) (81% yield)

^{1}H NMR (500 MHz, Chloroform-*d*) δ 6.75 (d, *J* = 2.3 Hz, 2H), 6.58 (t, *J* = 2.3 Hz, 1H), 3.79 (s, 6H). ^{13}C NMR (126 MHz, $CDCl_3$) δ 160.90, 158.26, 120.50, 111.10, 104.98, 89.21, 79.57, 55.78.

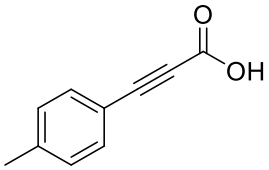

3-(*p*-tolyl)-propiolic acid (35) (85% yield)

^{1}H NMR (500 MHz, Chloroform-*d*) δ 7.51 (d, *J* = 7.9 Hz, 2H), 7.20 (d, *J* = 7.8 Hz, 2H), 2.39 (s, 3H). ^{13}C NMR (126 MHz, $CDCl_3$) δ 158.97, 142.18, 133.56, 129.70, 116.24, 89.97, 80.04, 21.98.

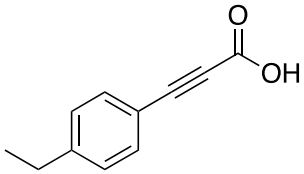

3-(4-ethylphenyl)propiolic acid (36) (83% yield)

^{1}H NMR (300 MHz, Chloroform-*d*) δ 7.54 (d, *J* = 7.7 Hz, 2H), 7.22 (d, *J* = 7.1 Hz, 2H), 2.69 (q, *J* = 6.7, 6.1 Hz, 2H), 1.25 (t, *J* = 7.6 Hz, 3H). ^{13}C NMR (75 MHz, $CDCl_3$) δ 159.91, 149.02, 134.32, 129.15, 117.09, 90.69, 80.72, 29.89, 15.92

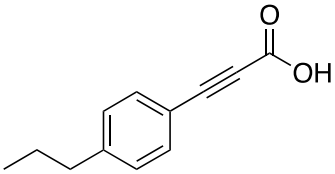

3-(4-propylphenyl)propiolic acid (37) (87% yield)

^{1}H NMR (500 MHz, Chloroform-*d*) δ 7.53 (d, *J* = 8.5 Hz, 2H), 7.20 (d, *J* = 8.3 Hz, 2H), 2.62 (t, *J* = 8.5, 6.8 Hz, 2H), 1.65 (h, *J* = 7.4 Hz, 2H), 0.94 (t, *J* = 7.3 Hz, 3H). ^{13}C NMR (126 MHz, $CDCl_3$) δ 158.57, 146.15, 132.86, 128.37, 115.74, 89.31, 79.42, 37.61, 23.63, 13.19.

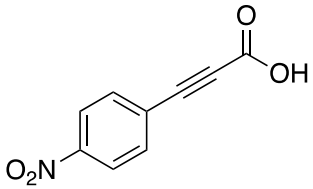

3-(4-nitrophenyl)propiolic acid (38) (70% yield)

^{1}H NMR (500 MHz, DMSO-d_6) δ 8.27 (d, J = 9.0 Hz, 2H), 7.89 (d, J = 9.0 Hz, 2H).

^{13}C NMR (126 MHz, DMSO) δ 153.79, 148.21, 133.81, 125.62, 123.95, 85.71, 85.04.

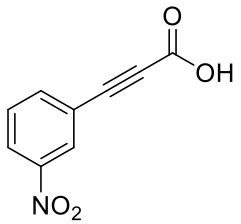

3-(3-nitrophenyl)propiolic acid (39) (67% yield)

^{1}H NMR (500 MHz, Acetonitrile-d_3) δ 8.41 – 8.37 (m, 1H), 8.30 (m, 1H), 7.95 (m, 1H), 7.67 (m, 1H). ^{13}C NMR (126 MHz, CD_3CN) δ 154.01, 149.33, 139.57, 131.34, 128.38, 126.50, 121.97, 83.80, 82.62.

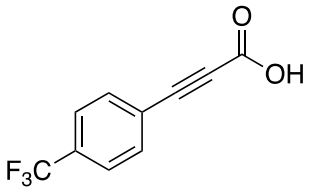

3-(4-trifluoromethylphenyl)propiolic acid (40) (72% yield)

^{1}H NMR (500 MHz, DMSO-d_6) δ 7.81 – 7.75 (m, 4H). ^{13}C NMR (126 MHz, DMSO) δ 153.89, 133.15, 130.86 (q, $J_{C\text{-}F}$ =32 Hz), 125.68 (q, $J_{C\text{-}F}$ = 4 Hz), 124.65, 122.48 (q, $J_{C\text{-}F}$ = 274 Hz), 83.37, 82.19.

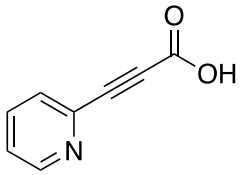

3-(pyridin-2-yl)propiolic acid (41) (29% yield)

^{1}H NMR (500 MHz, Methanol-d_4) δ 8.61 – 8.59 (m, 1H), 7.91 (td, J = 7.8, 1.7 Hz, 1H), 7.73 – 7.68 (m, 1H), 7.51 (ddd, J = 7.8, 4.9, 1.2 Hz, 1H). ^{13}C NMR (126 MHz, CD_3OD) δ 156.76, 151.30, 141.78, 138.99, 130.11, 126.45, 123.57, 82.57.

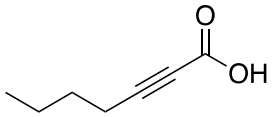

2- Heptynoic acid (42) (50% yield)

^{1}H NMR (300 MHz, Chloroform-*d*) δ 2.34 (t, *J* = 7.0 Hz, 2H), 1.55 (p, *J* = 7.1 Hz, 2H), 1.42 (p, *J* = 7.3 Hz, 2H), 0.90 (t, *J* = 7.2 Hz, 3H). ^{13}C NMR (75 MHz, $CDCl_3$) δ 159.47, 93.63, 73.48, 30.21, 22.71, 19.24, 14.19.

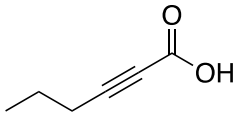

2- Hexynoic acid (43) (47% yield)

^{1}H NMR (300 MHz, Chloroform-*d*) δ 10.26 (s, 1H), 2.32 (t, *J* = 7.0 Hz, 2H), 1.60 (h, *J* = 7.3 Hz, 2H), 1.00 (t, *J* = 7.4 Hz, 3H). ^{13}C NMR (75 MHz, $CDCl_3$) δ 158.35, 92.41, 72.98, 21.06, 20.75, 13.45.

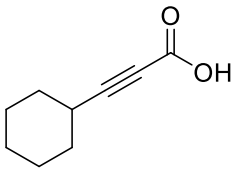

3-cyclohexylpropiolic acid (44) (94% yield)

^{1}H NMR (500 MHz, Chloroform-*d*) δ 10.77 (s, 1H), 2.54 (p, *J* = 9.1, 1H), 1.86 – 1.80 (m, 2H), 1.76 – 1.66 (m, 2H), 1.56 – 1.47 (m, 3H), 1.37 – 1.28 (m, 3H). ^{13}C NMR (126 MHz, $CDCl_3$) δ 158.98, 96.34, 72.82, 31.48, 29.12, 25.75, 24.75.

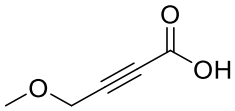

4-methoxybut-2-ynoic acid (45) (52% yield)

^{1}H NMR (500 MHz, Chloroform-*d*) δ 9.25 (s, 1H), 4.26 (s, 2H), 3.43 (s, 3H). ^{13}C NMR (126 MHz, $CDCl_3$) δ 156.87, 85.78, 78.00, 59.60, 58.35.

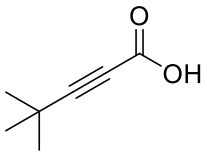

4,4 dimethylpent-2-ynoic acid (46) (55% yield)

^{1}H NMR (500 MHz, Chloroform-*d*) δ 1.29 (s, 9H). ^{13}C NMR (126 MHz, $CDCl_3$) δ 158.50, 99.80, 71.46, 30.02, 27.87

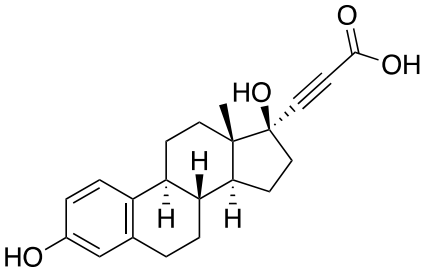

3-((8R,9S,13S,14S,17S)-3,17-dihydroxy-13-methyl-7,8,9,11,12,13,14,15,16,17-decahydro-6H-cyclopenta[a]phenanthren-17-yl)propiolic acid (47) (38% yield)

^{1}H NMR (300 MHz, Methanol-d_4) δ 7.09 (d, *J* = 8.6 Hz, 1H), 6.58 – 6.49 (m, 1H), 6.48 (s, 1H), 4.82 (s, 2H), 2.83 – 2.72 (m, 2H), 2.41 – 2.23 (m, 2H), 2.18 (q, *J* = 7.5, 5.8 Hz, 2H), 2.09 – 1.94 (m, 1H), 1.91 – 1.72 (m, 4H), 1.48 – 1.34 (m, 4H), 0.89 (s, 3H). ^{13}C NMR (75 MHz, MeOD) δ 156.53, 155.86, 138.75, 132.38, 127.25, 116.05, 113.76, 92.31, 80.39, 78.94, 51.10, 48.93, 44.81, 40.99, 39.54, 34.22, 30.61, 28.48, 27.59, 23.80, 13.27. IR (ATR, cm^{-1}); 3306, 2927, 2222, 1654, 1497. HRMS-ESI (m/z): $[M + H]^+$ $C_{21}H_{24}O_4$ Calculated 339.1596; Found 339.1583.

NMR Spectral Data for Cu(I) coordination complexes

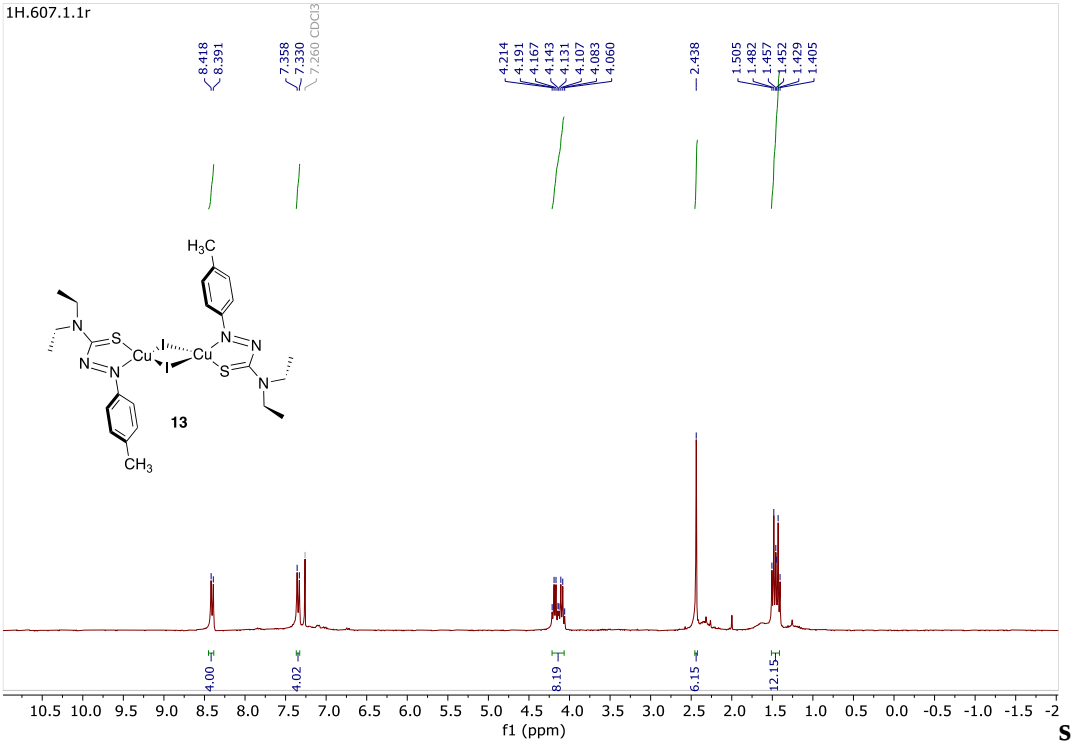

Figure A5.1: ^{1}H NMR spectrum of **13** (μ-I)-[Cu(*p*-tolyl-ATF)I]$_2$ in CDCl$_3$

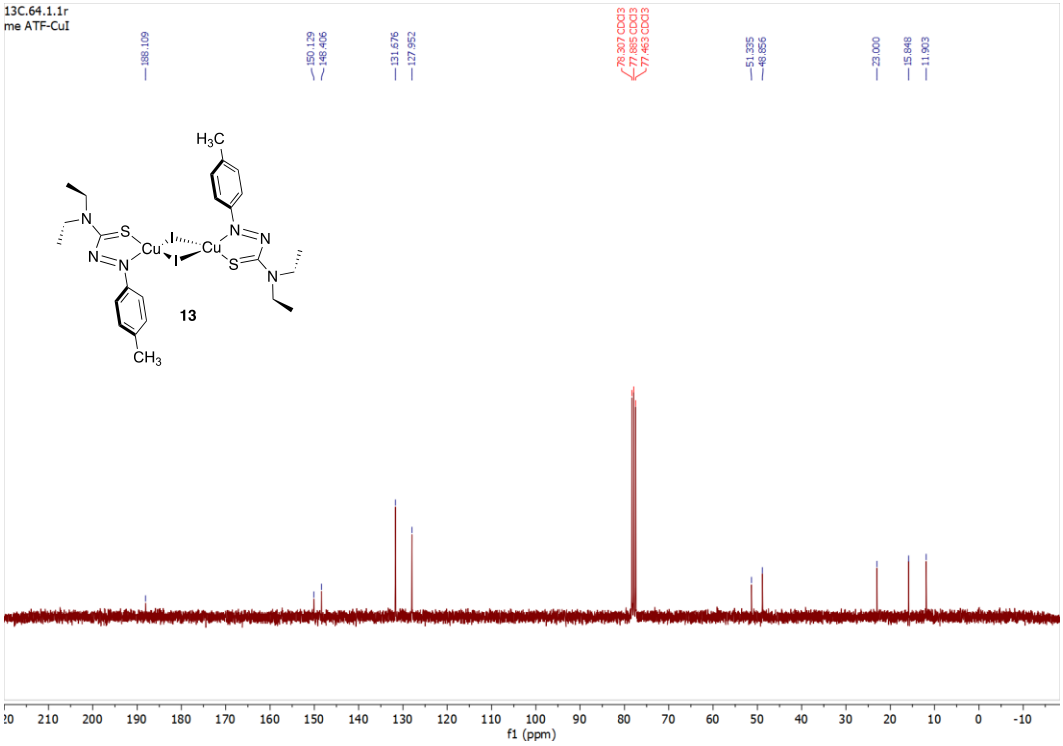

Figure A5.2: ^{13}C NMR spectrum of **13** (μ-I)-[Cu(*p*-tolyl-ATF)I]$_2$ in CDCl$_3$

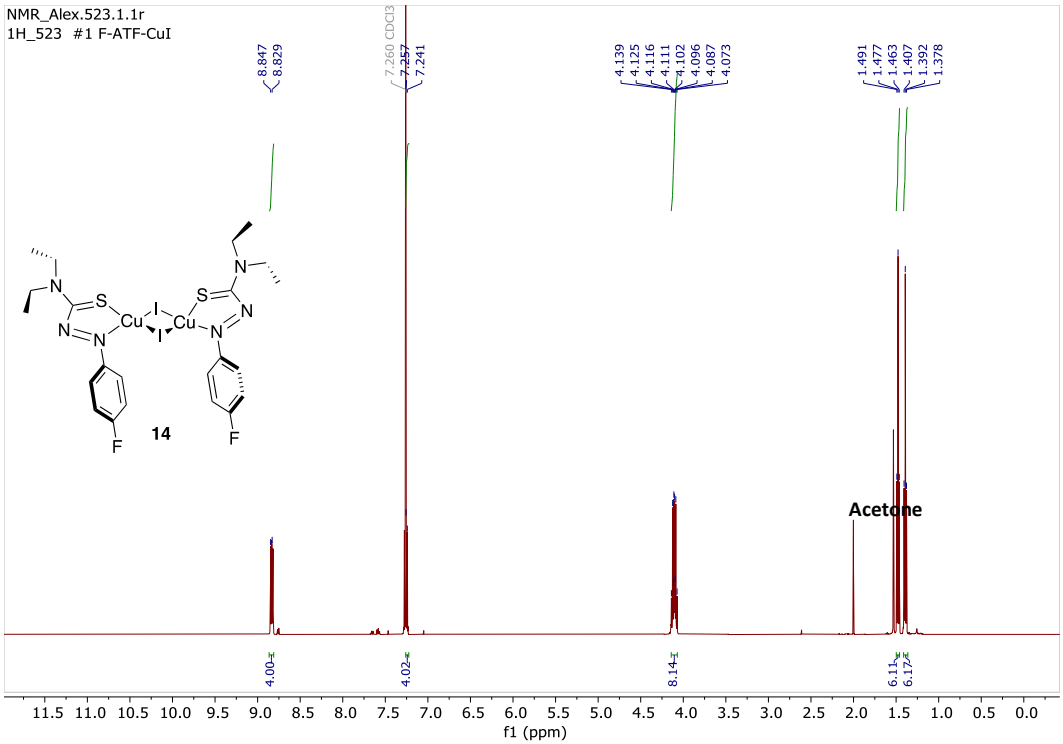

Figure A5.3: ^{1}H NMR spectrum of **14** (μ-I)-[Cu(*p*-fluorophenyl-ATF)I]$_2$ in $CDCl_3$

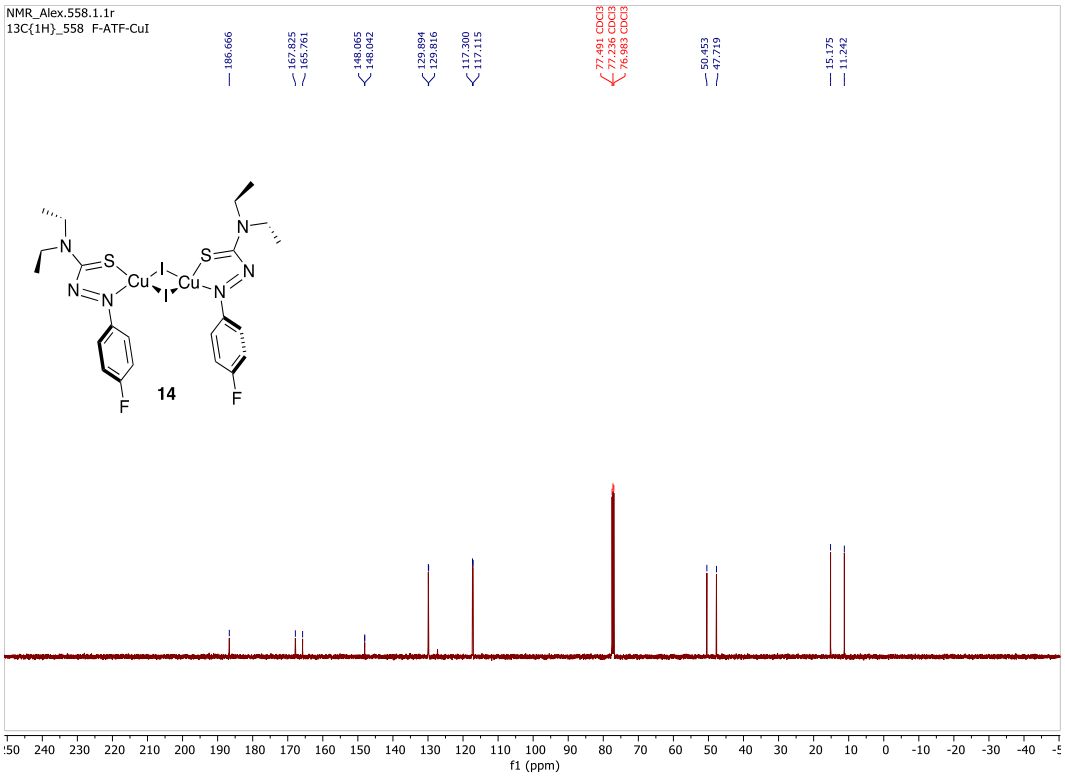

Figure A5.4: ^{13}C NMR spectrum of **14** (μ-I)-[Cu(*p*-fluorophenyl-ATF)I]$_2$ in $CDCl_3$

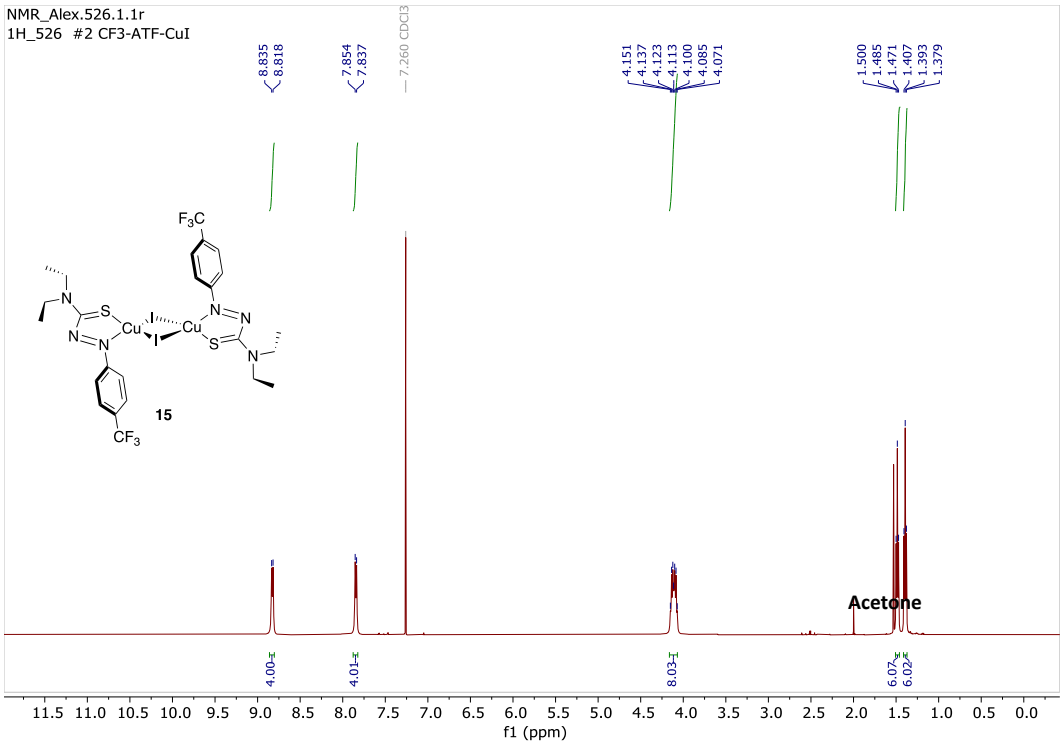

Figure A5.5: ^{1}H NMR spectrum of **15** (μ-I)-[Cu(*p*-trifluoromethylphenyl-ATF)I]$_2$ in CDCl$_3$

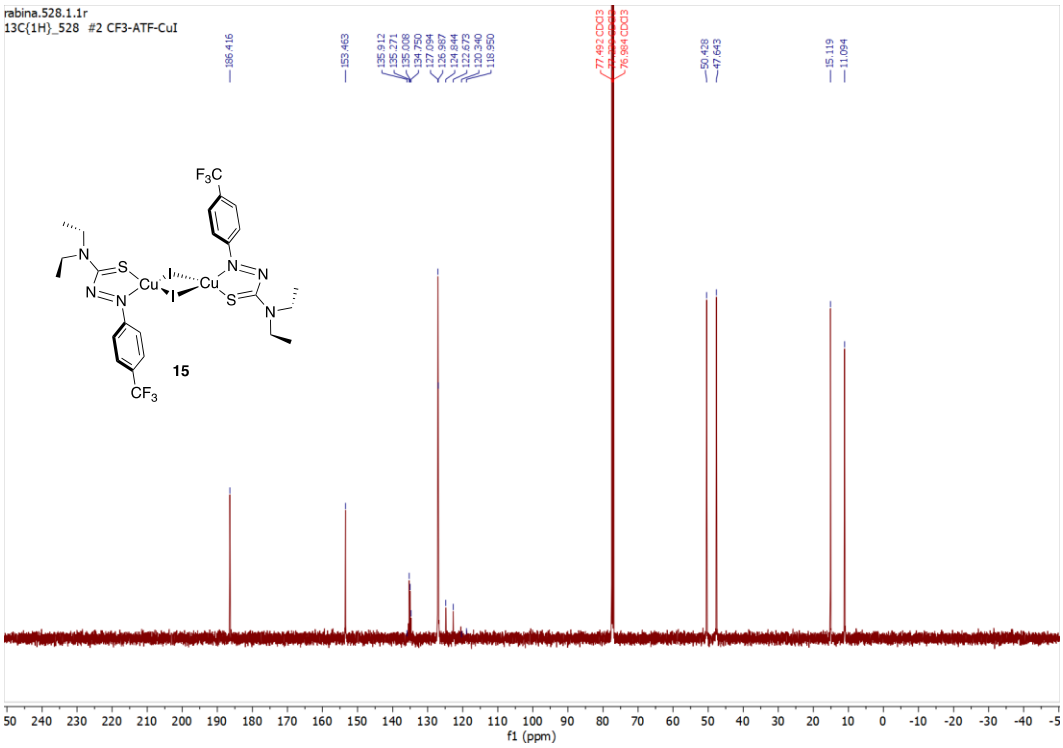

Figure A5.6: ^{13}C NMR spectrum of **15** (μ-I)-[Cu(*p*-trifluoromethylphenyl-ATF)I]$_2$ in CDCl$_3$

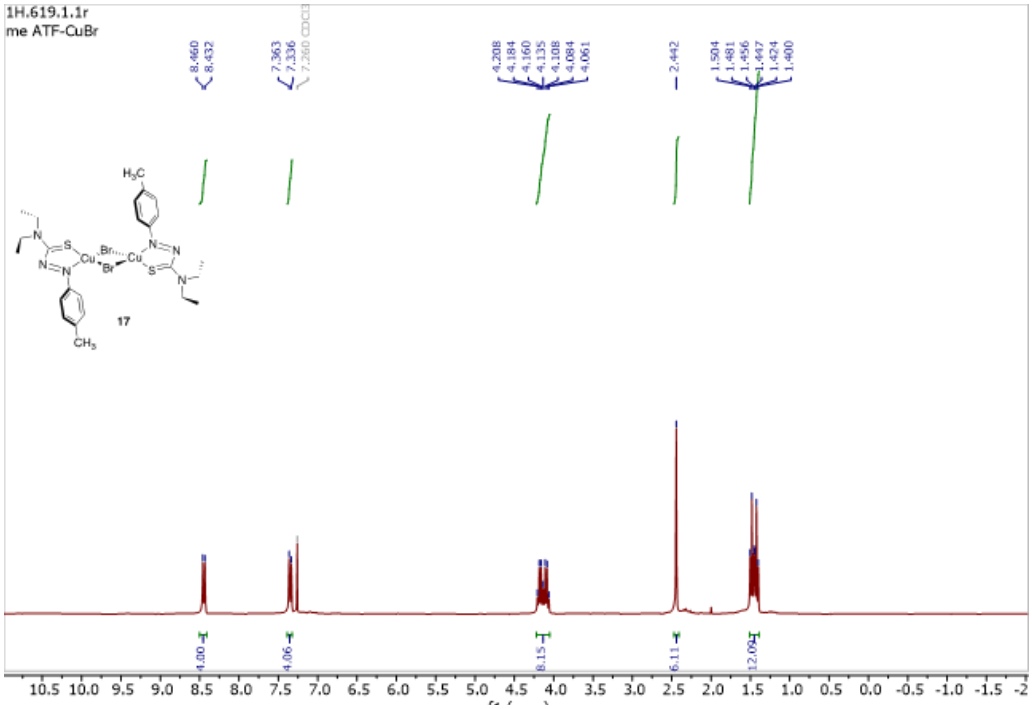

Figure A5.7: ^{1}H NMR spectrum of **17** (μ-Br)-[Cu(*p*-tolyl-ATF)Br]$_2$ in $CDCl_3$

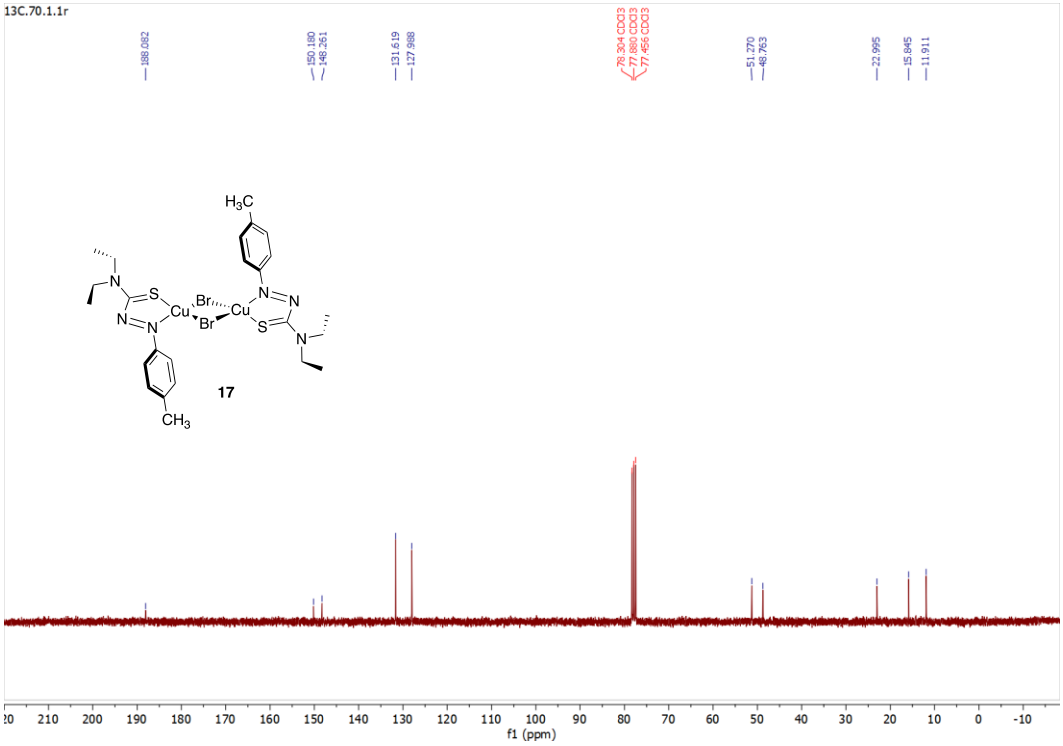

Figure 5.8: ^{13}C NMR spectrum of **17** (μ-Br)-[Cu(*p*-tolyl-ATF)Br]$_2$ in $CDCl_3$

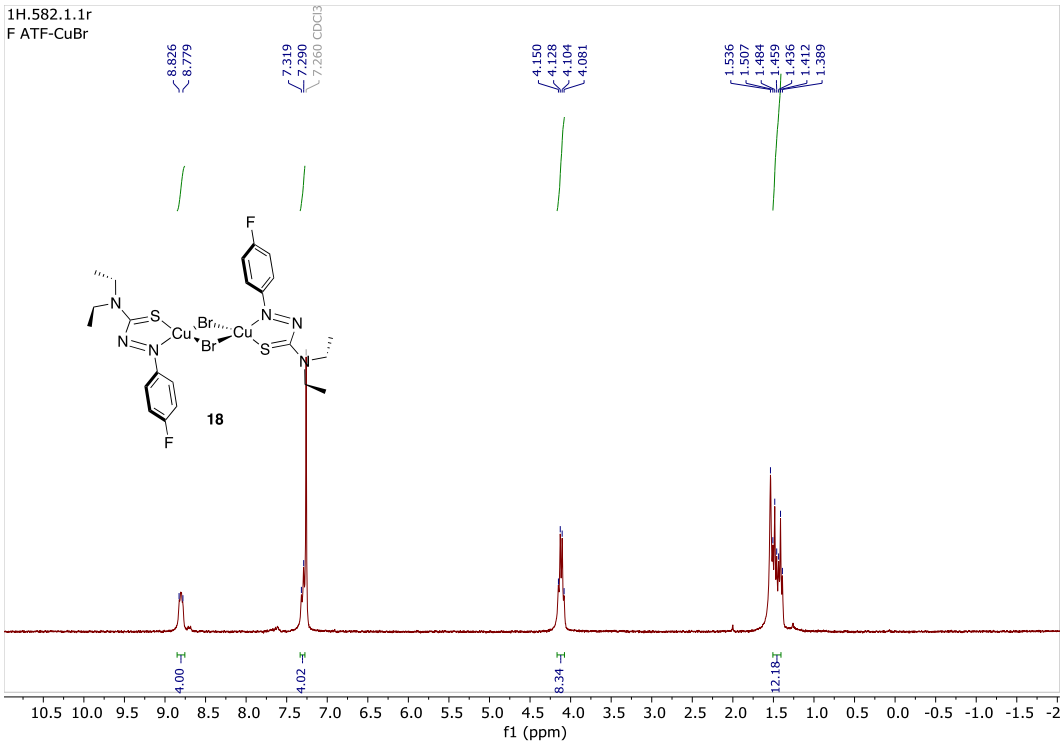

Figure A5.9: ^{1}H NMR spectrum of **18** (μ-Br)-[Cu(*p*-fluorophenyl-ATF)Br]$_2$ in CDCl$_3$

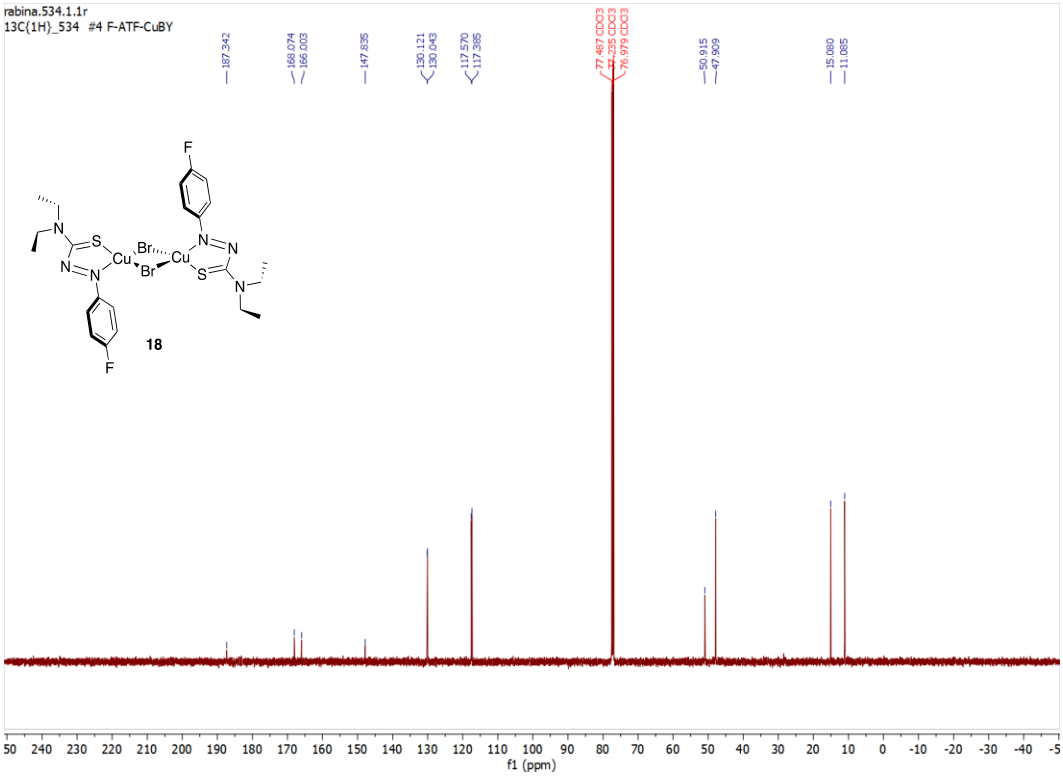

Figure A5.10: ^{13}C NMR spectrum of **18** (μ-Br)-[Cu(*p*-fluorophenyl-ATF)Br]$_2$ in CDCl$_3$

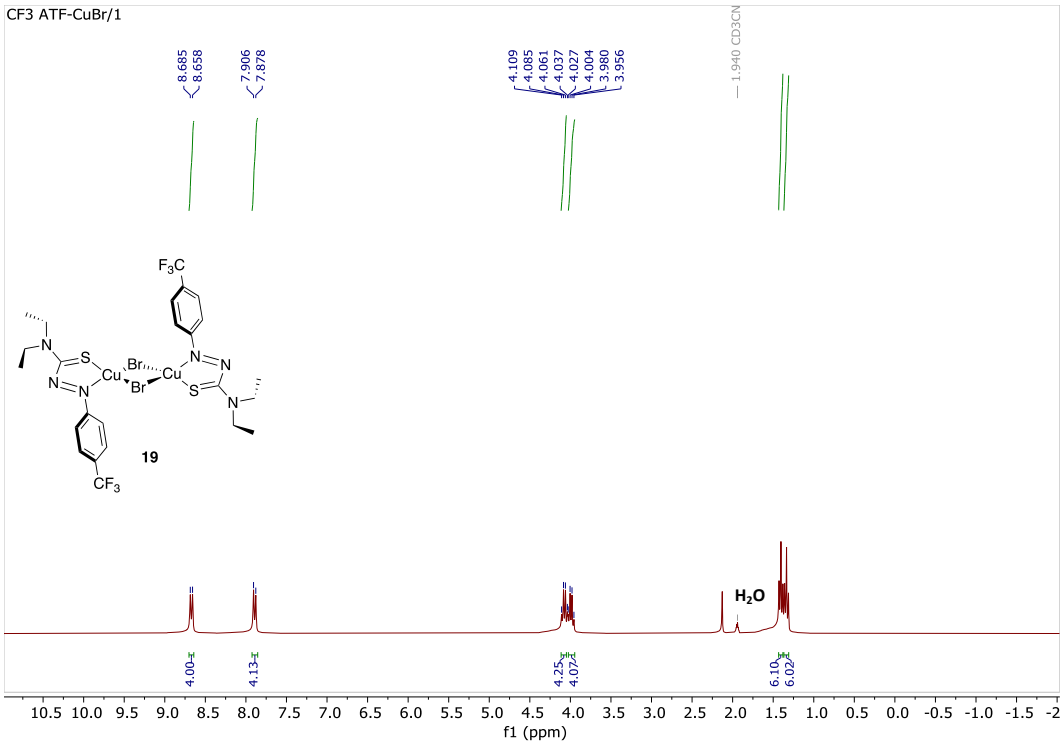

Figure A5.11: ^{1}H NMR spectrum of **19** (μ-Br)-[Cu(*p*-trifluoromethylphenyl-ATF)Br]$_2$ in CD_3CN

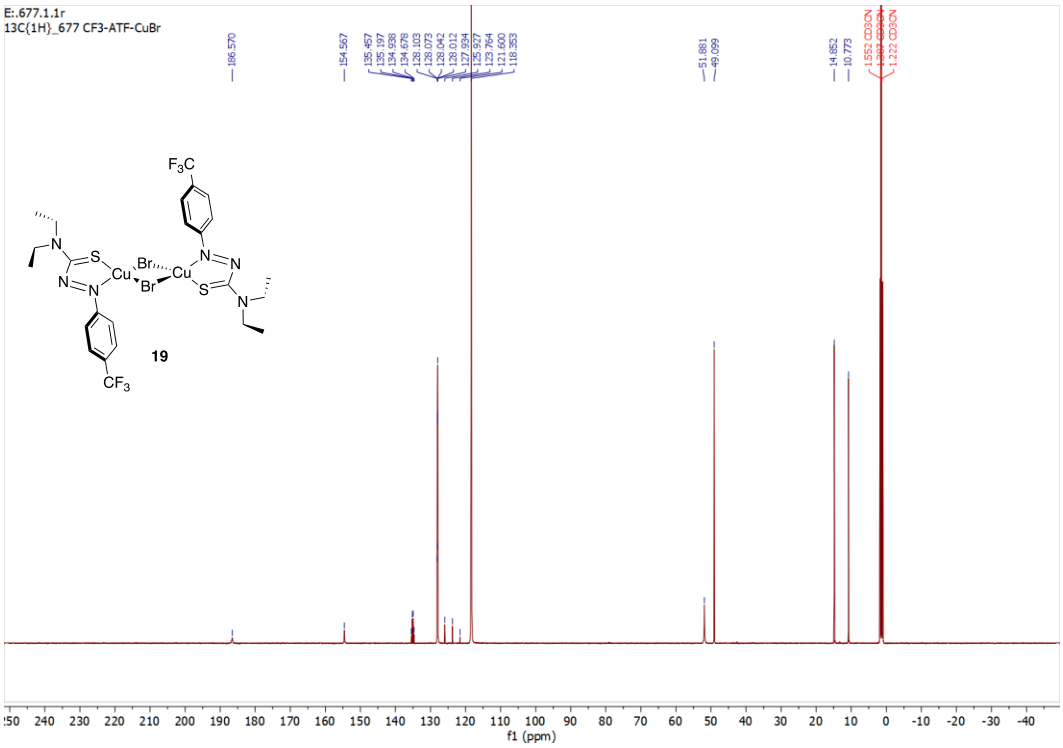

Figure A5.12: ^{13}C NMR spectrum of **19** (μ-Br)-[Cu(*p*-trifluoromethylphenyl-ATF)Br]$_2$ in CD_3CN

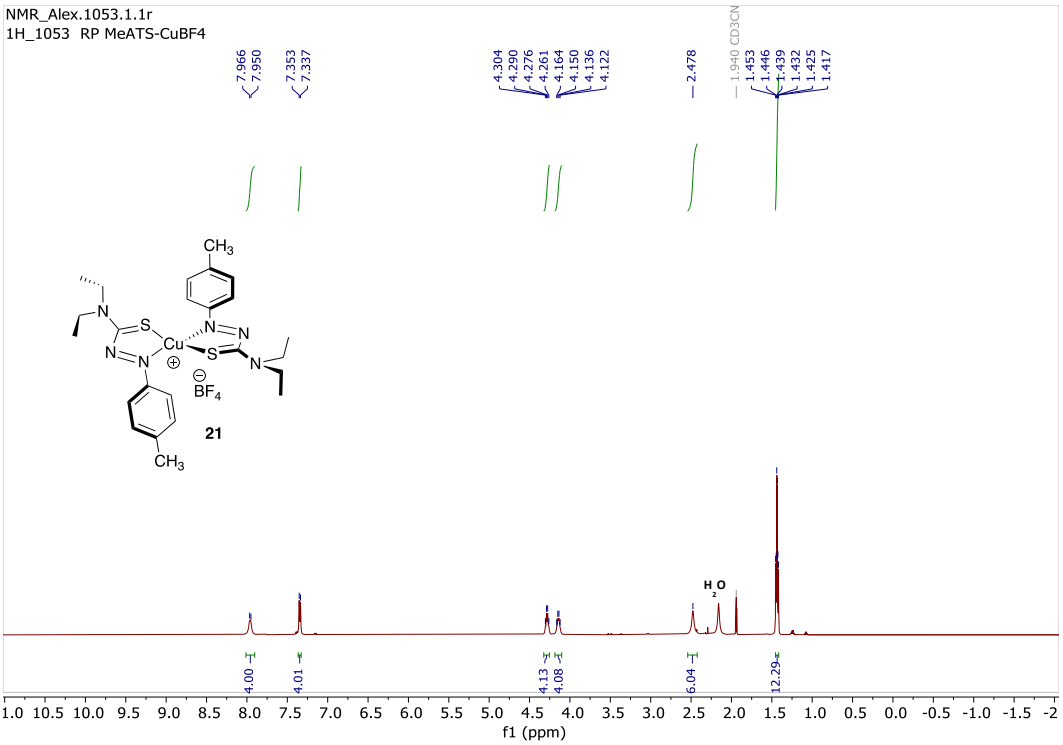

Figure A5.13: ^{1}H NMR spectrum of **21** [(*p*-tolyl-ATF)$_2$Cu](BF$_4$) in CD$_3$CN

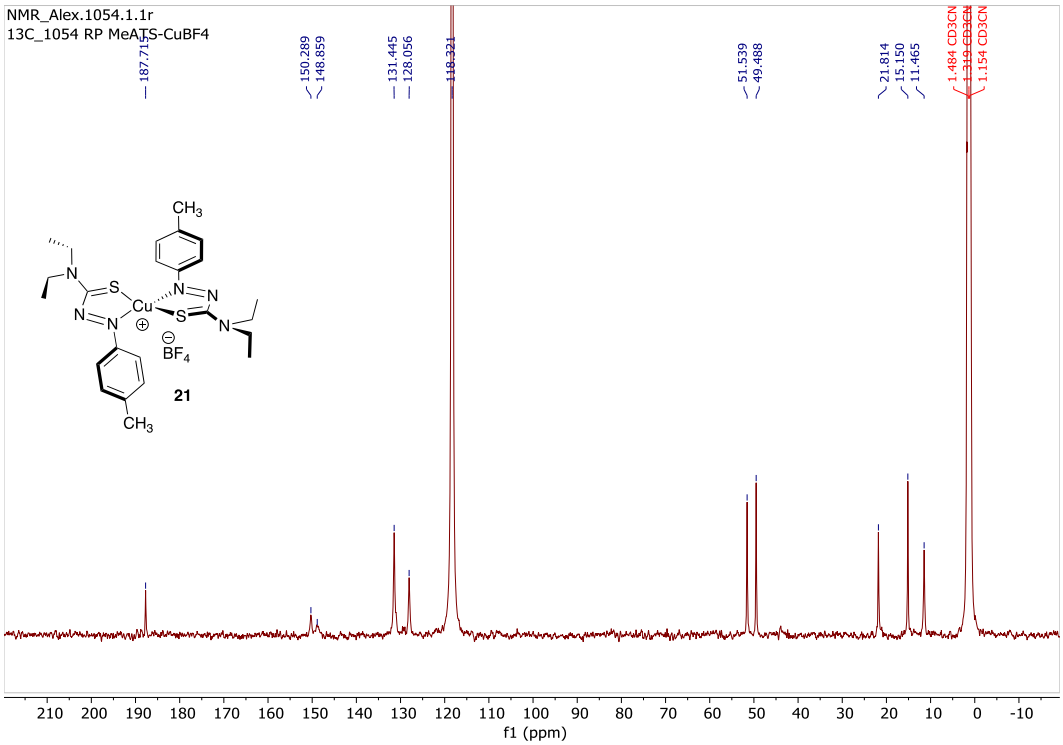

Figure A5.14: ^{13}C NMR spectrum of **21** [(*p*-tolyl-ATF)$_2$Cu](BF$_4$) in CD$_3$CN

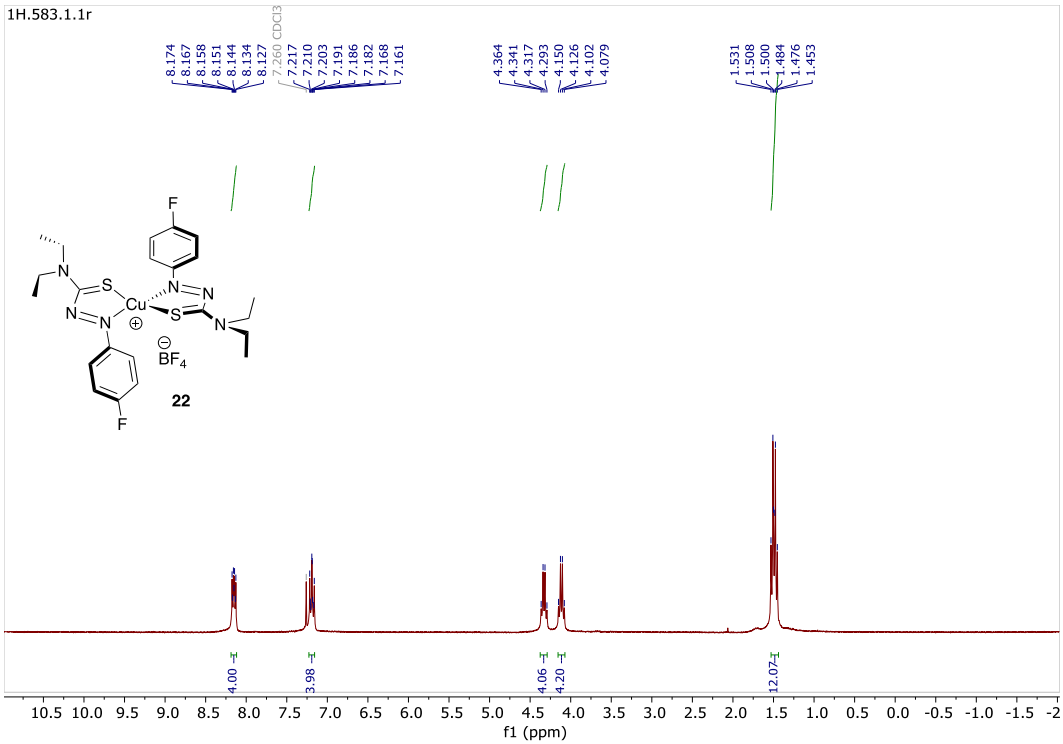

Figure A5.15: ^{1}H NMR spectrum of **22** [(*p*-fluorophenyl-ATF)$_2$Cu](BF$_4$) in CDCl$_3$

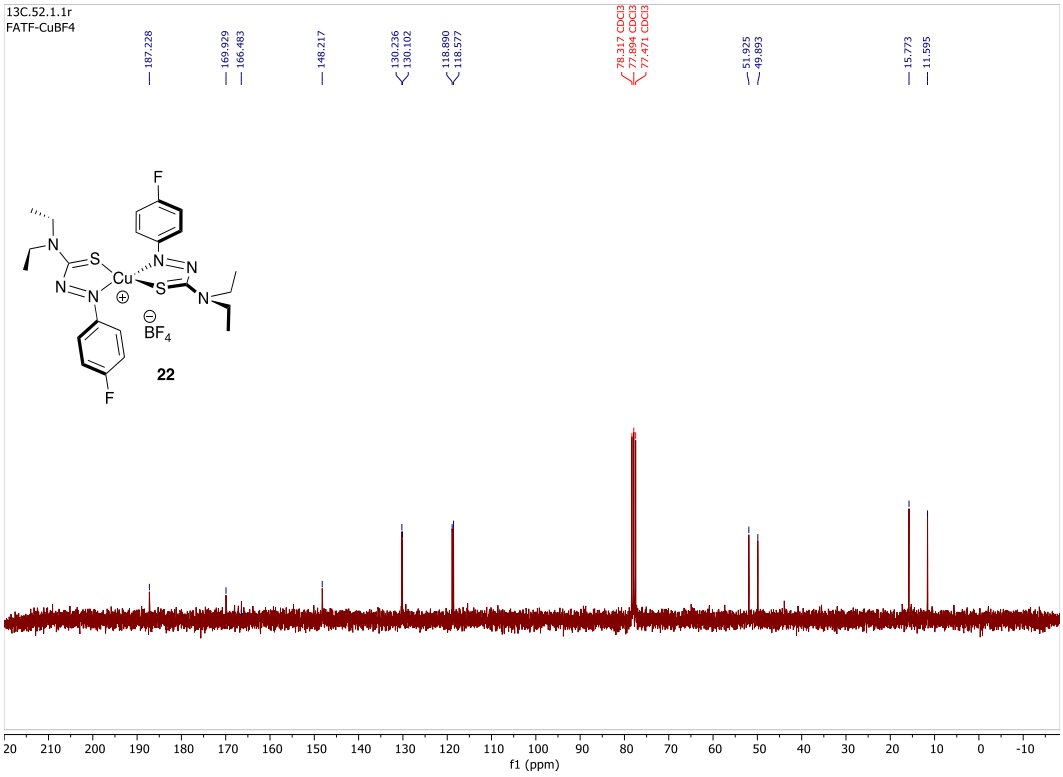

Figure A5.16: ^{13}C NMR spectrum of **22** [(*p*-fluorophenyl-ATF)$_2$Cu](BF$_4$) in CDCl$_3$

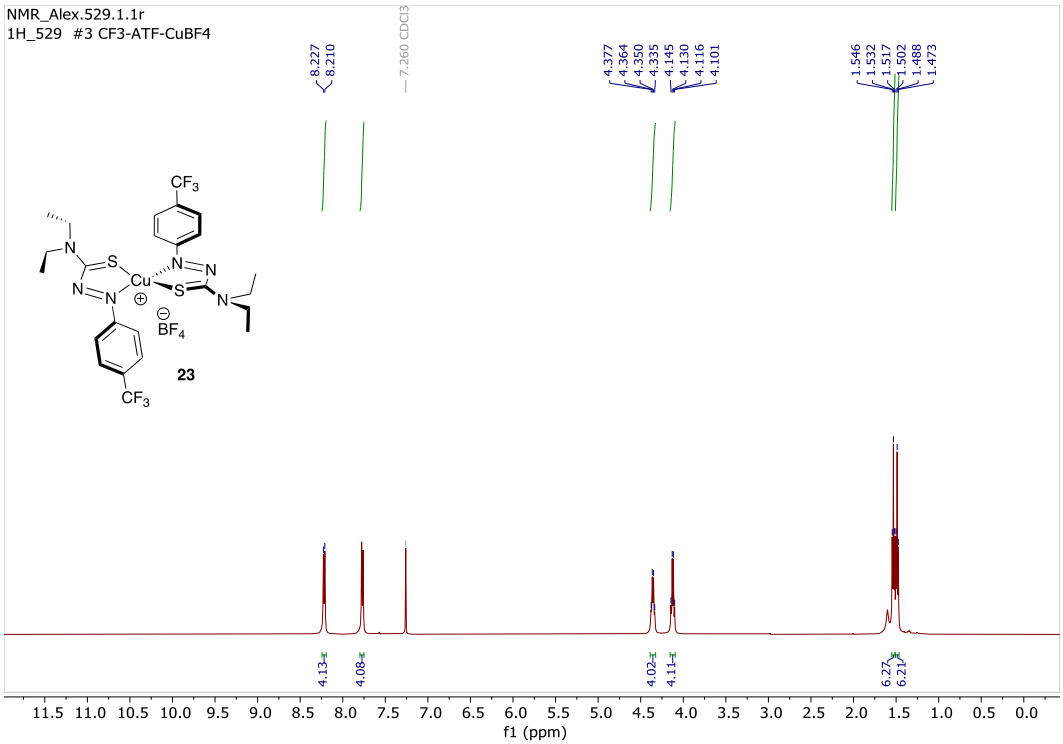

Figure A5.17: ^{1}H NMR spectrum of **23** [(*p*-trifluoromethylphenyl-ATF)$_2$Cu](BF$_4$) in CDCl$_3$

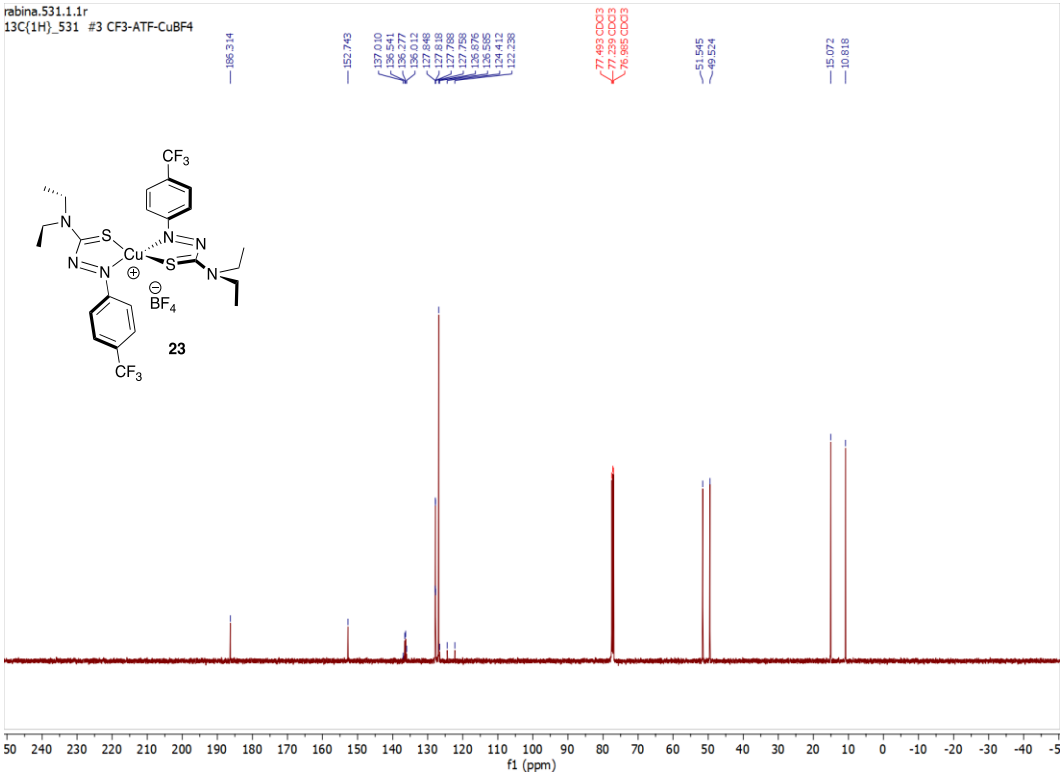

Figure A5.18: ^{13}C NMR spectrum of **23** [(*p*-trifluoromethylphenyl-ATF)$_2$Cu](BF$_4$) in CDCl$_3$

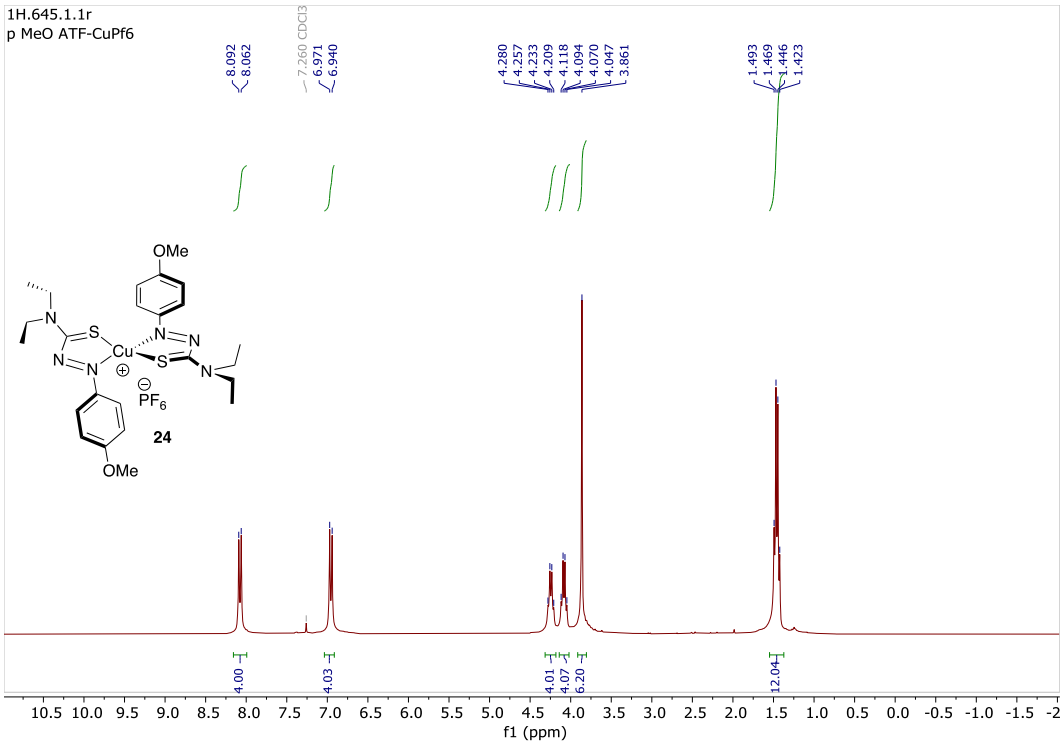

Figure A5.19: ^{1}H NMR spectrum of **24** [(*p*-methoxyphenyl-ATF)$_2$Cu](pF$_6$) in CDCl$_3$

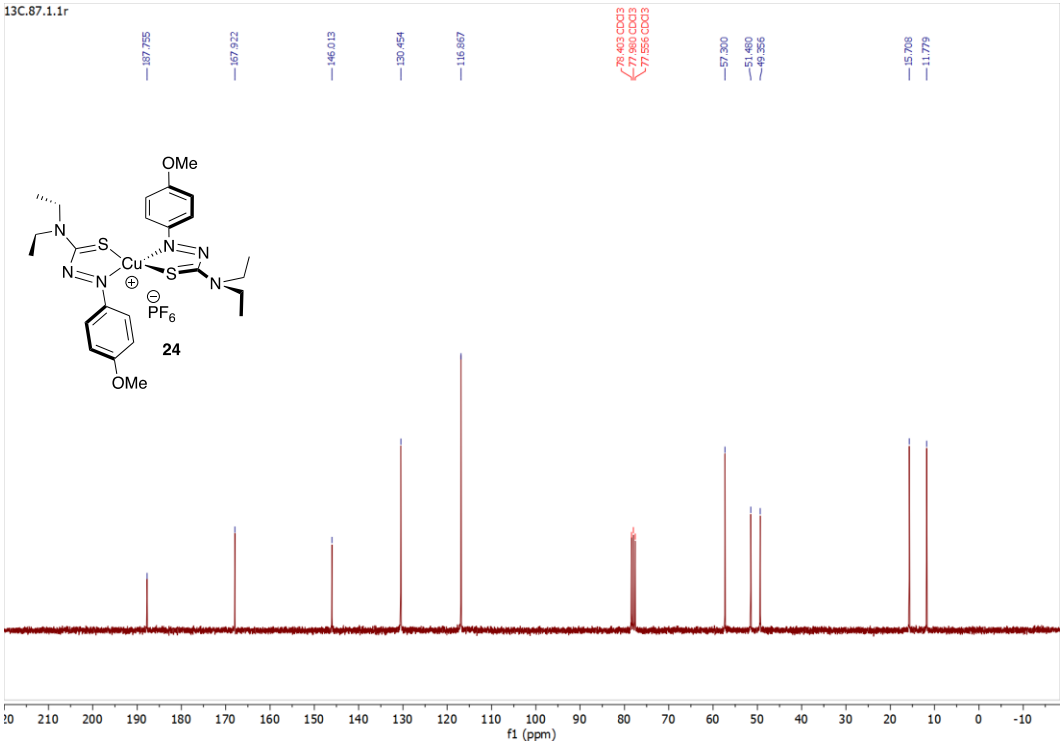

Figure A5.20: ^{13}C NMR spectrum of **24** [(*p*-methoxyphenyl-ATF)$_2$Cu](PF$_6$) in CDCl$_3$

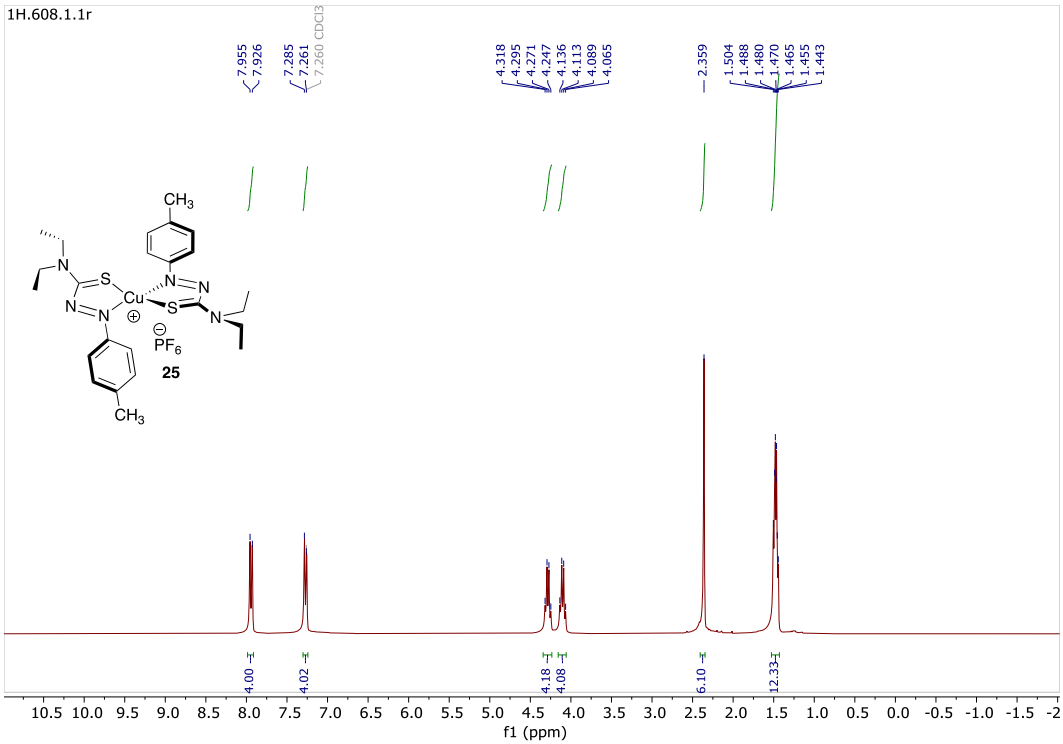

Figure A5.21: ^{1}H NMR spectrum of **25** [(*p*-tolyl-ATF)$_2$Cu](PF$_6$) in CDCl$_3$

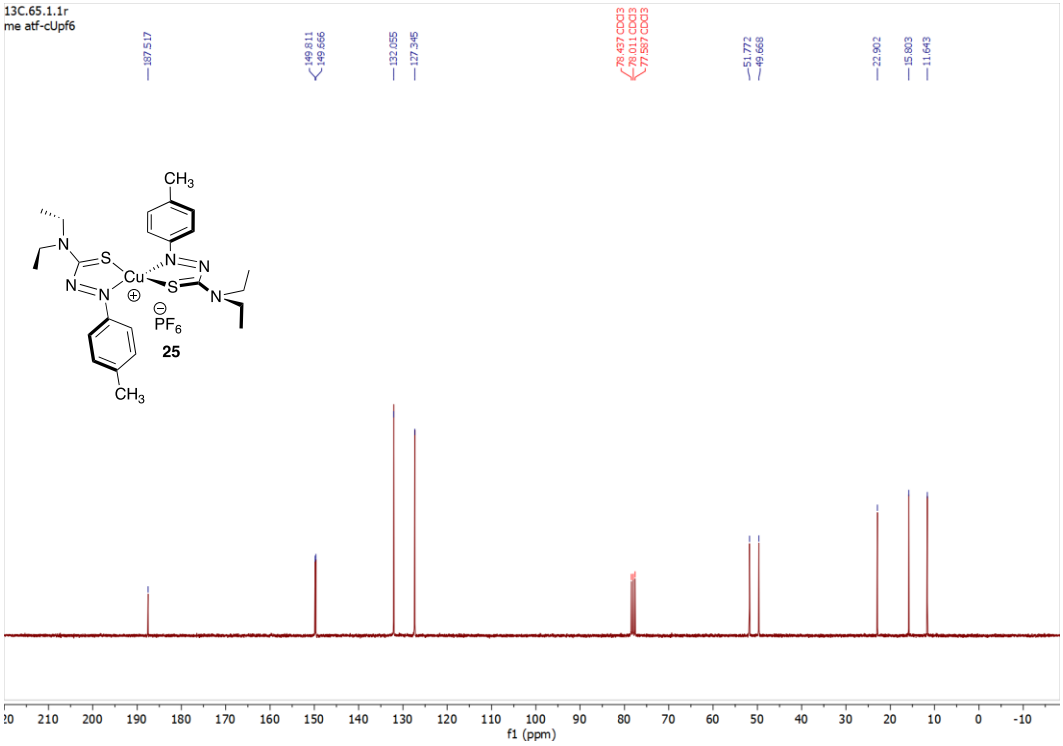

Figure A5.22: ^{13}C NMR spectrum of **25** [(*p*-tolyl-ATF)$_2$Cu](PF$_6$) in CDCl$_3$

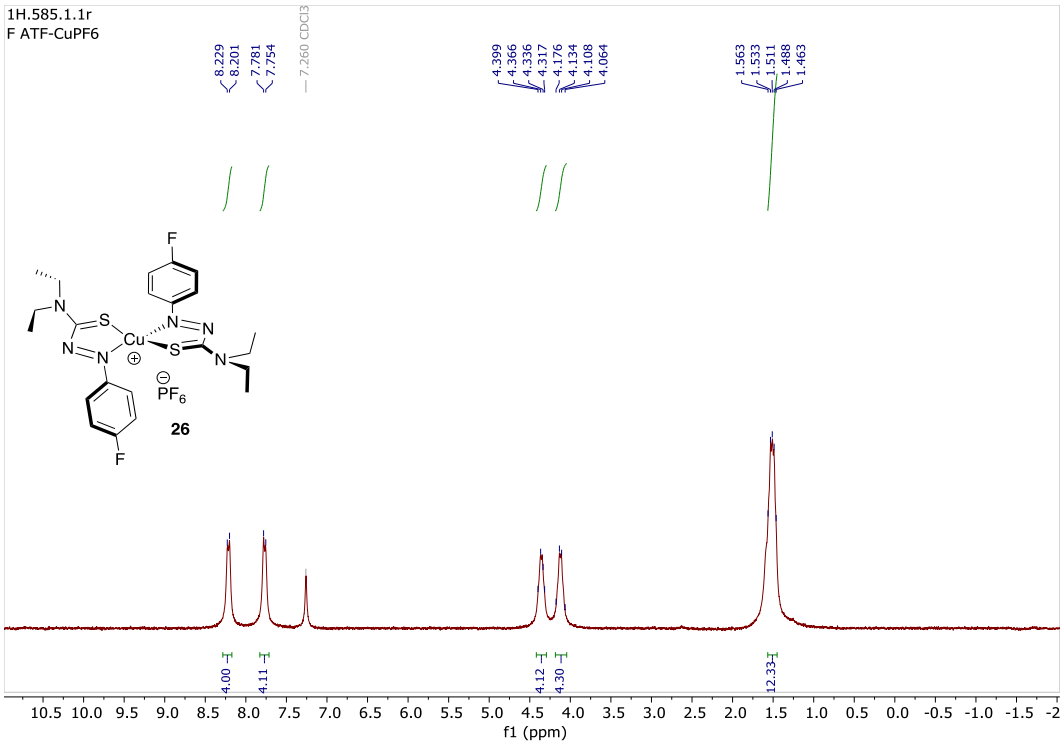

Figure A5.23: ^{1}H NMR spectrum of **26** [(*p*-fluorophenyl-ATF)$_2$Cu](PF$_6$) in CDCl$_3$

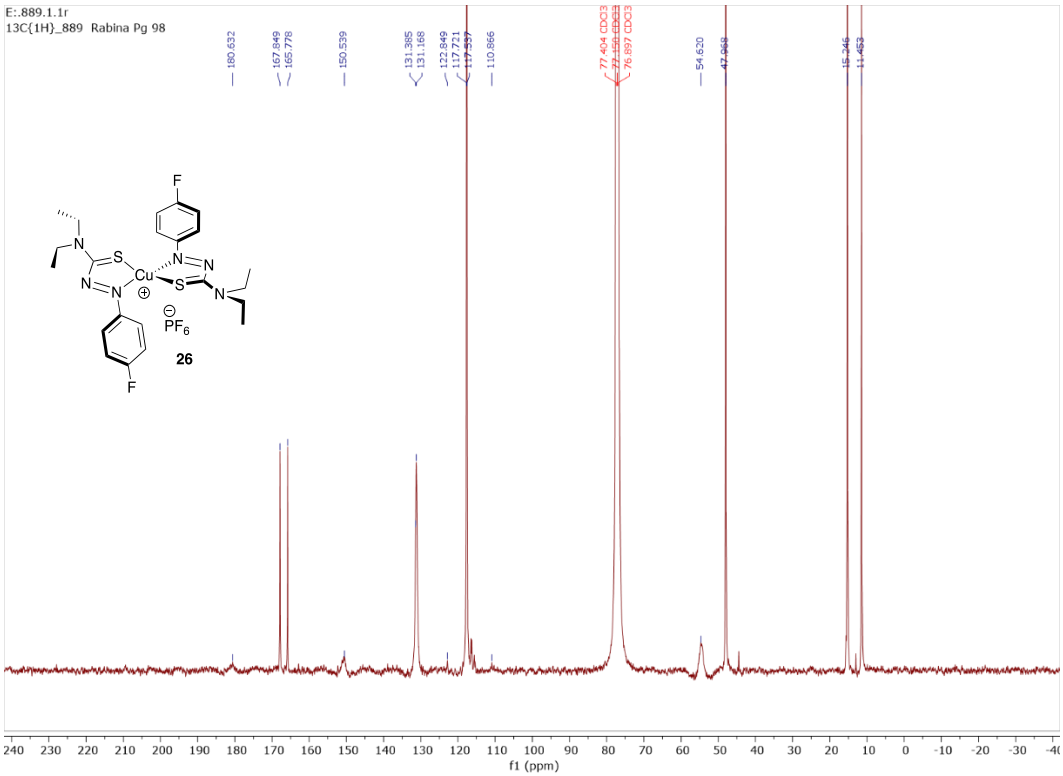

Figure A5.24: ^{13}C NMR spectrum of **26** [(*p*-fluorophenyl-ATF)$_2$Cu](PF$_6$) in CDCl$_3$

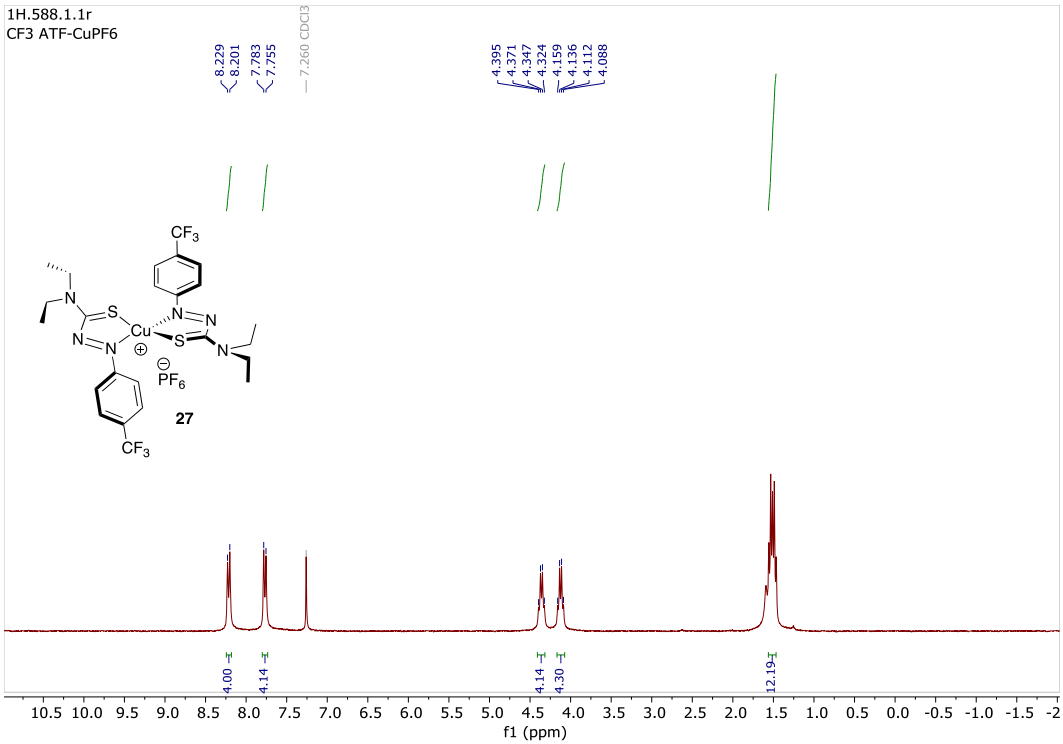

Figure A5.25: ^{1}H NMR spectrum of **27** [(*p*-trifluoromethylphenyl-ATF)$_2$Cu](PF$_6$) in CDCl$_3$

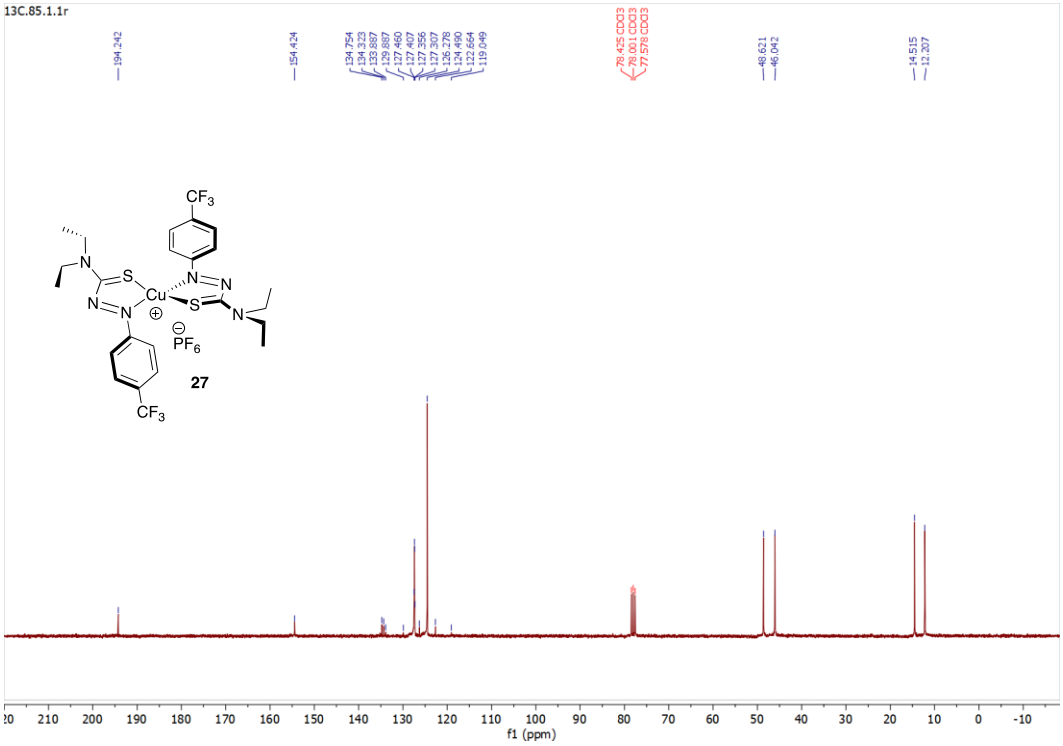

Figure 5.26: ^{13}C NMR spectrum of **27** [(*p*-trifluoromethylphenyl-ATF)$_2$Cu](PF$_6$) in CDCl$_3$

NMR Spectral Data for Propiolic acid Products

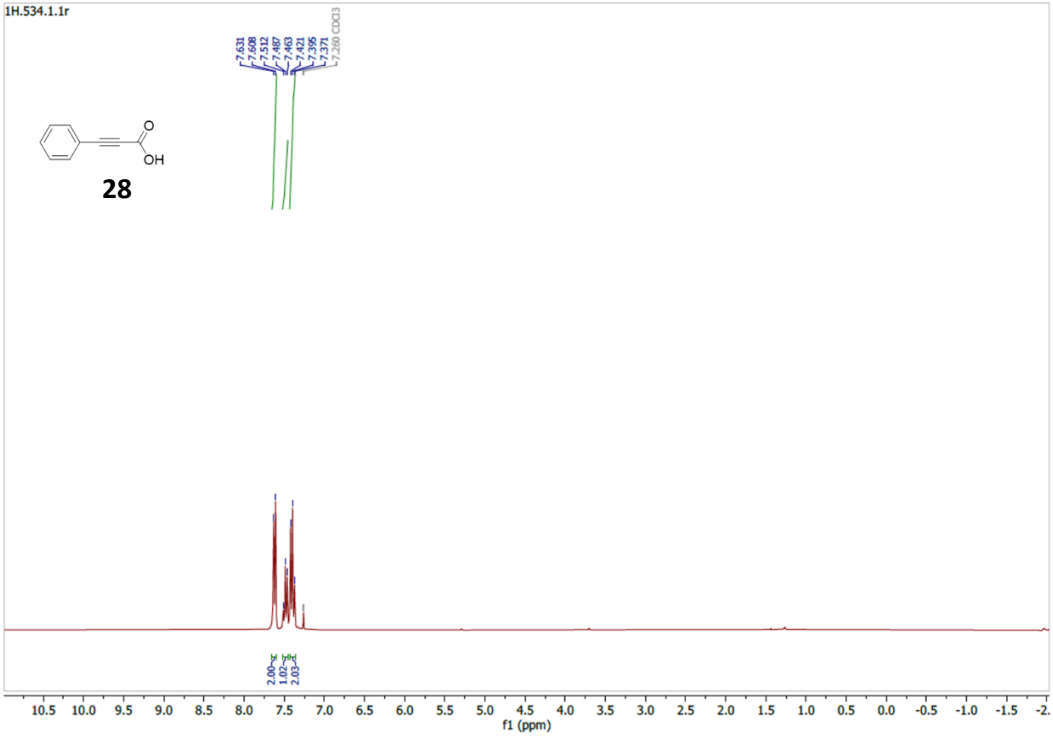

Figure A5.27: ^{1}H NMR spectrum of **28** (3-Phenyl propiolic acid) in $CDCl_3$

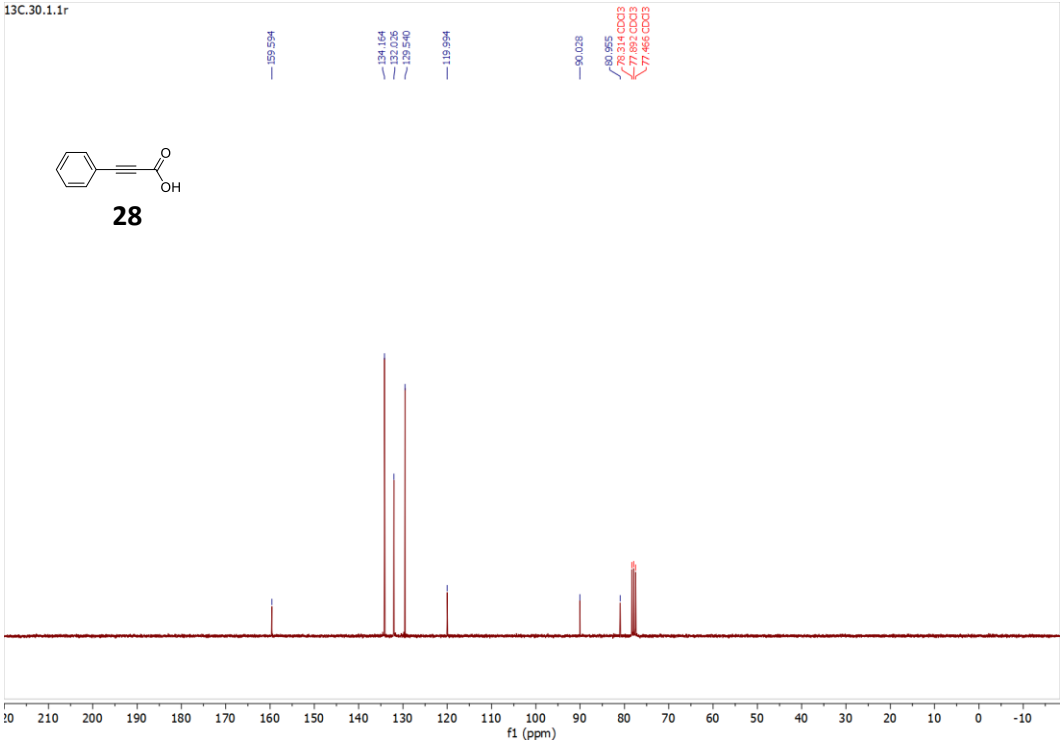

Figure A5.28: ^{13}C NMR spectrum of **28** (3-Phenyl propiolic acid) in $CDCl_3$

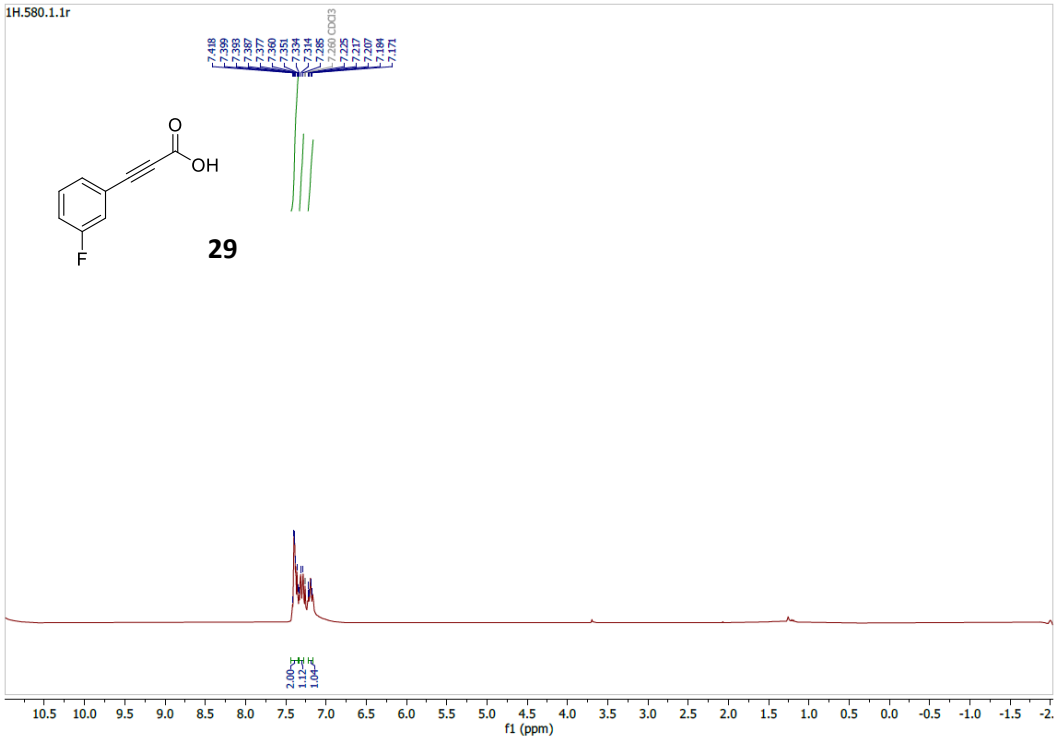

Figure A5.29: ^{1}H NMR spectrum of **29** [3-(3-fluorophenyl)propiolic acid] in $CDCl_3$

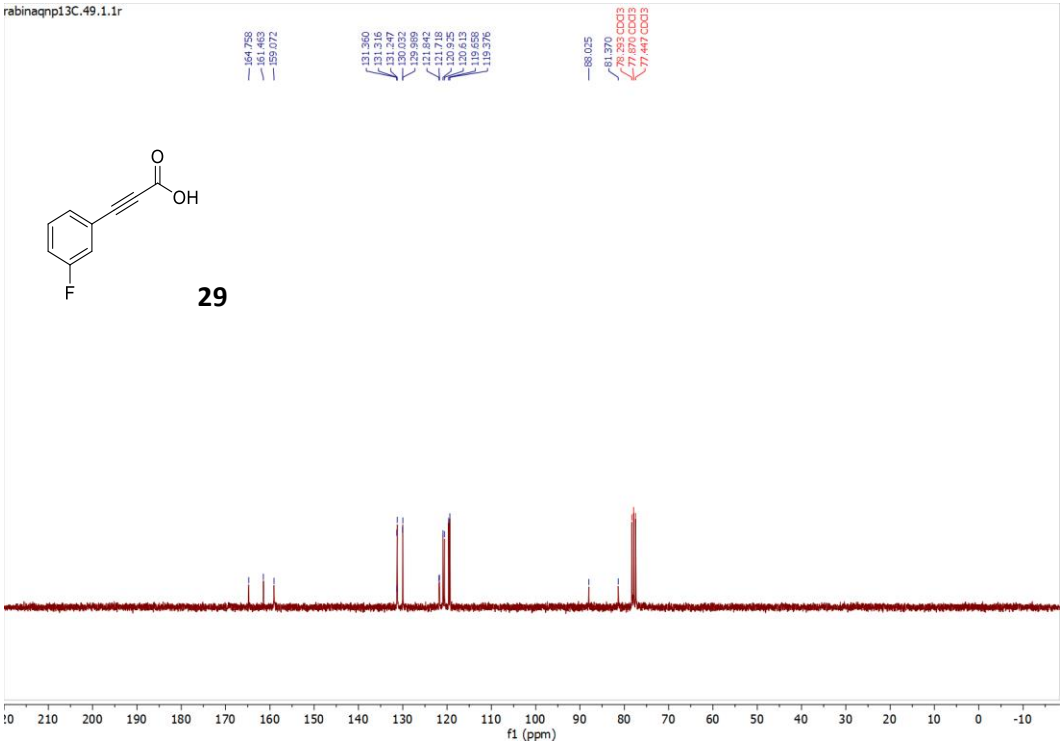

Figure A5.30: ^{13}C NMR spectrum of **29** [3-(3-fluorophenyl)propiolic acid]in $CDCl_3$

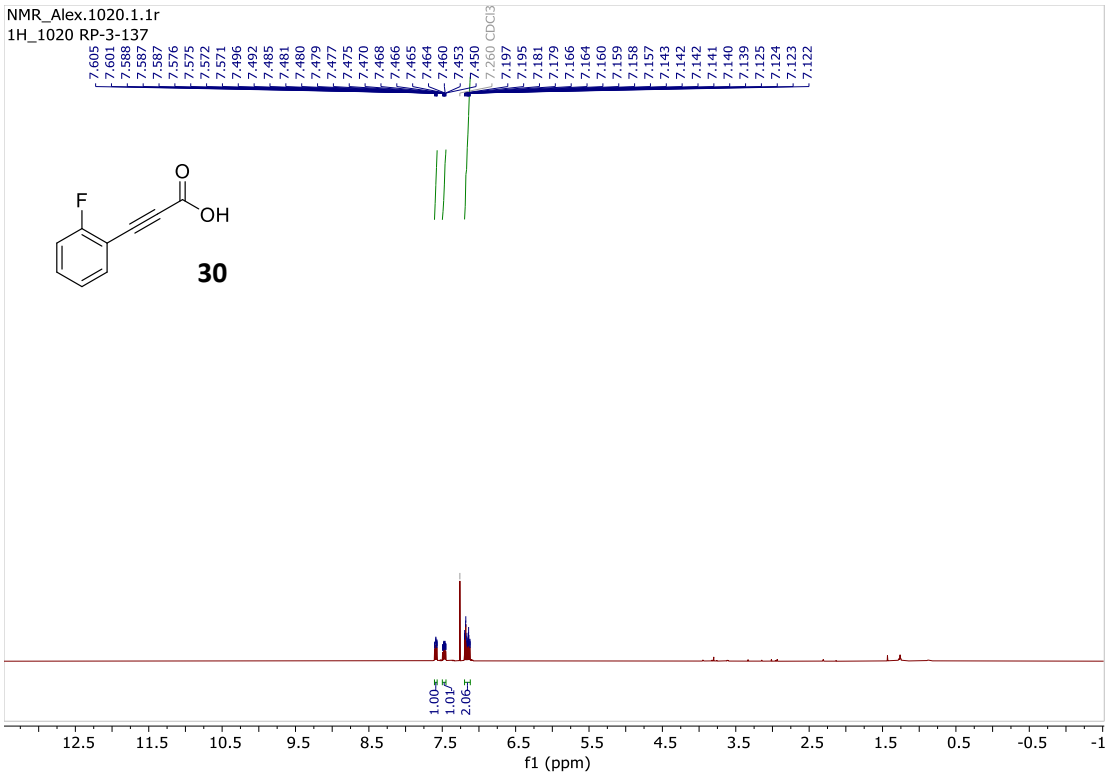

Figure A5.31: ^{1}H NMR spectrum of **30** [3-(2-fluorophenyl)propiolic acid]in $CDCl_3$

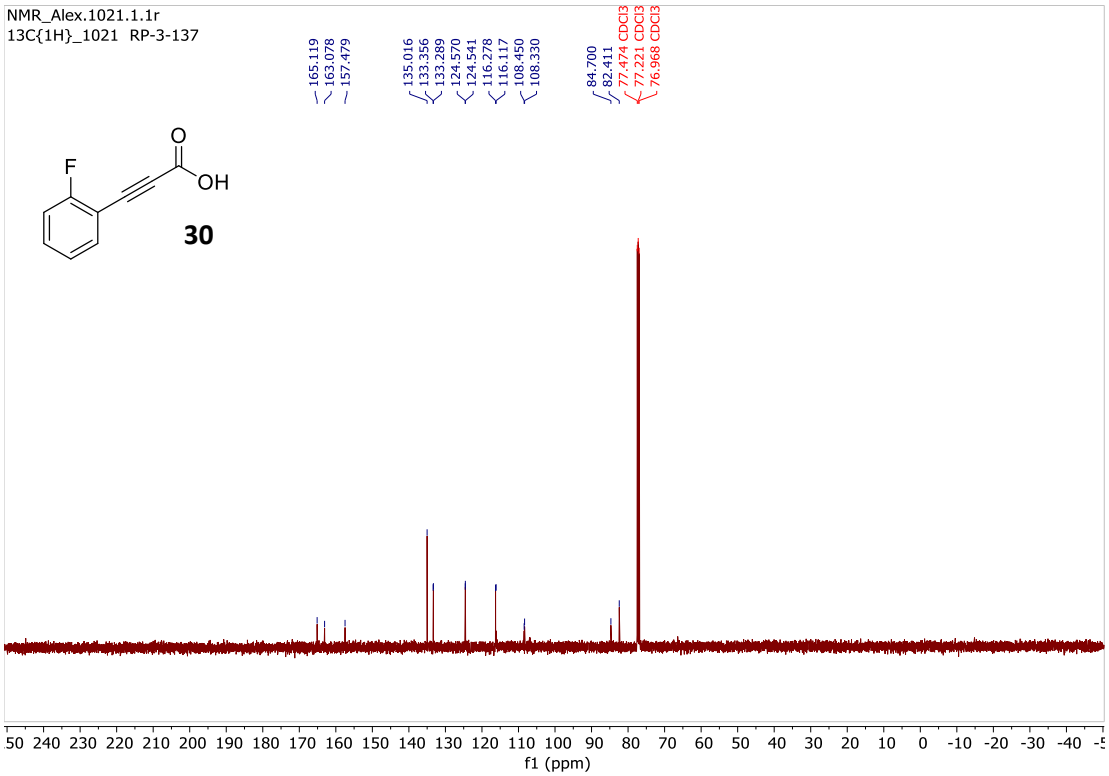

Figure A5.32: ^{13}C NMR spectrum of **30** [3-(2-fluorophenyl)propiolic acid]in $CDCl_3$

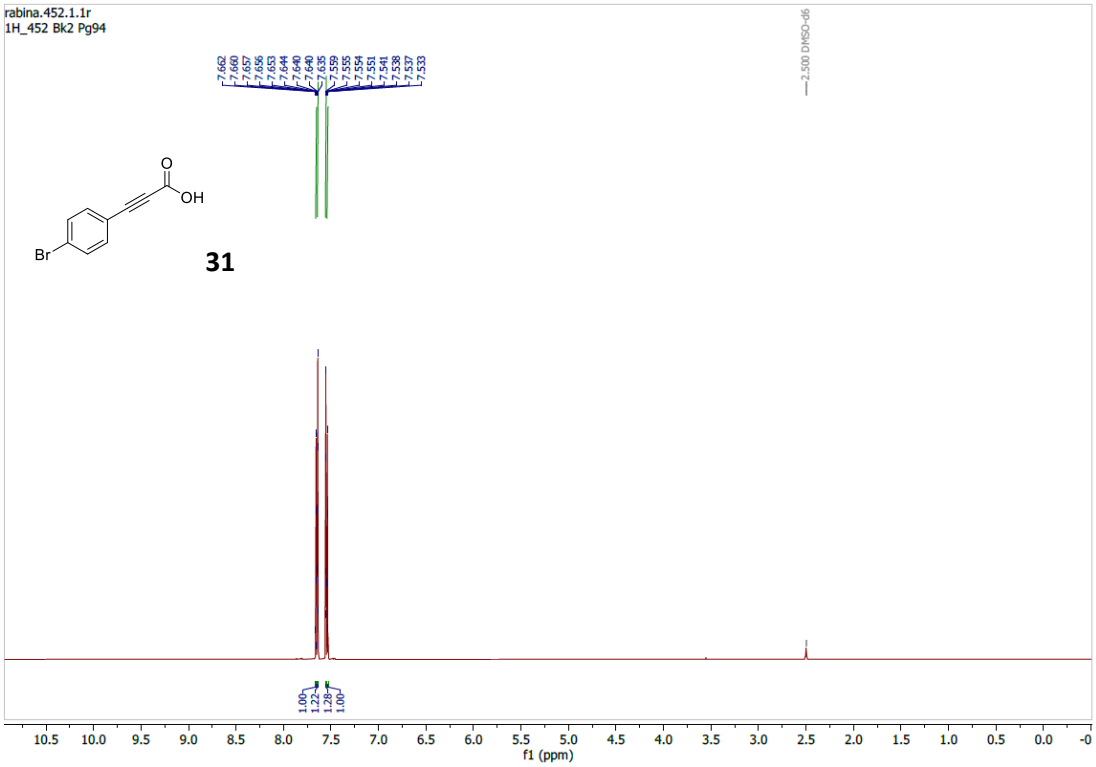

Figure A5.33: ^{1}H NMR spectrum of **31** [3-(4-bromophenyl)propiolic acid] in d_6-DMSO

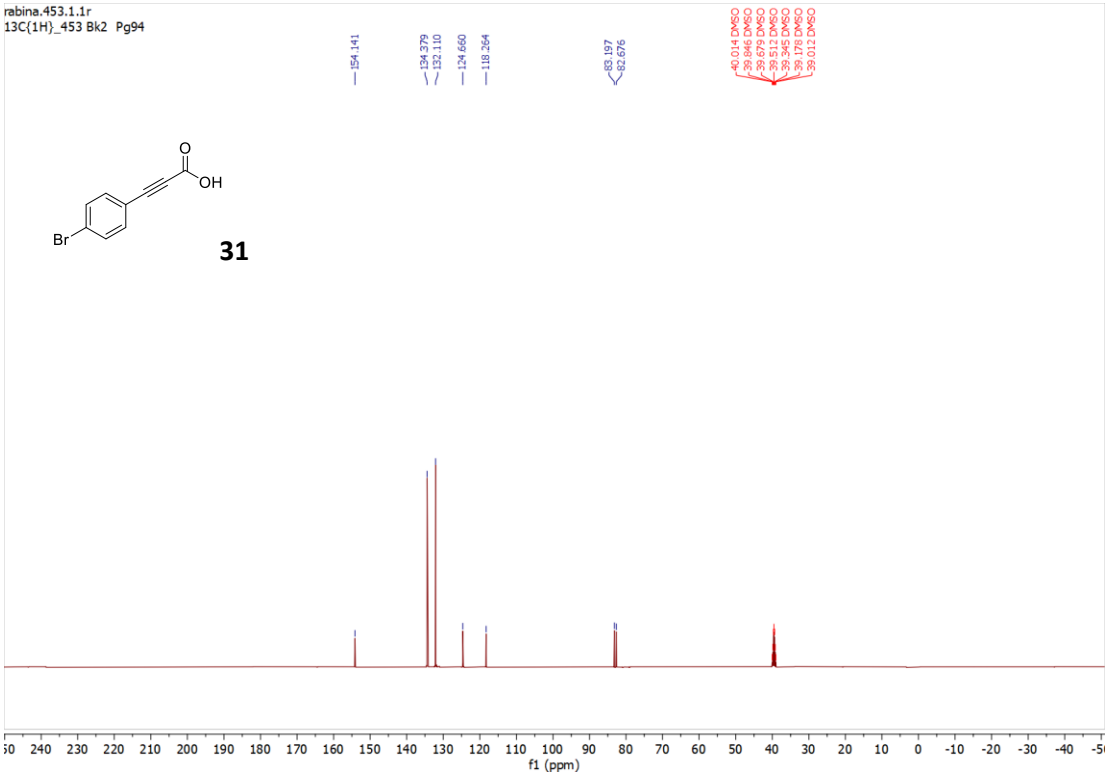

Figure A5.34: ^{13}C NMR spectrum of **31** [3-(4-bromophenyl)propiolic acid] in d_6-DMSO

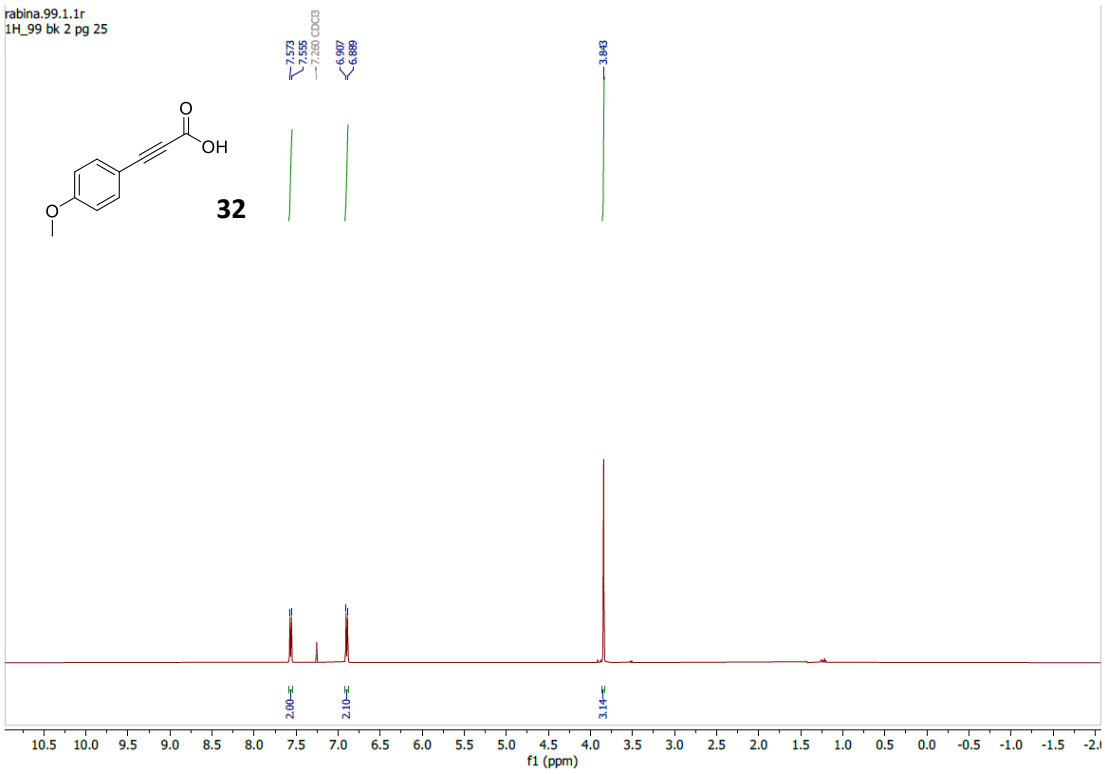

Figure A5.35: ^{1}H NMR spectrum of **32** [3-(4-methoxyphenyl)propiolic acid] in $CDCl_3$

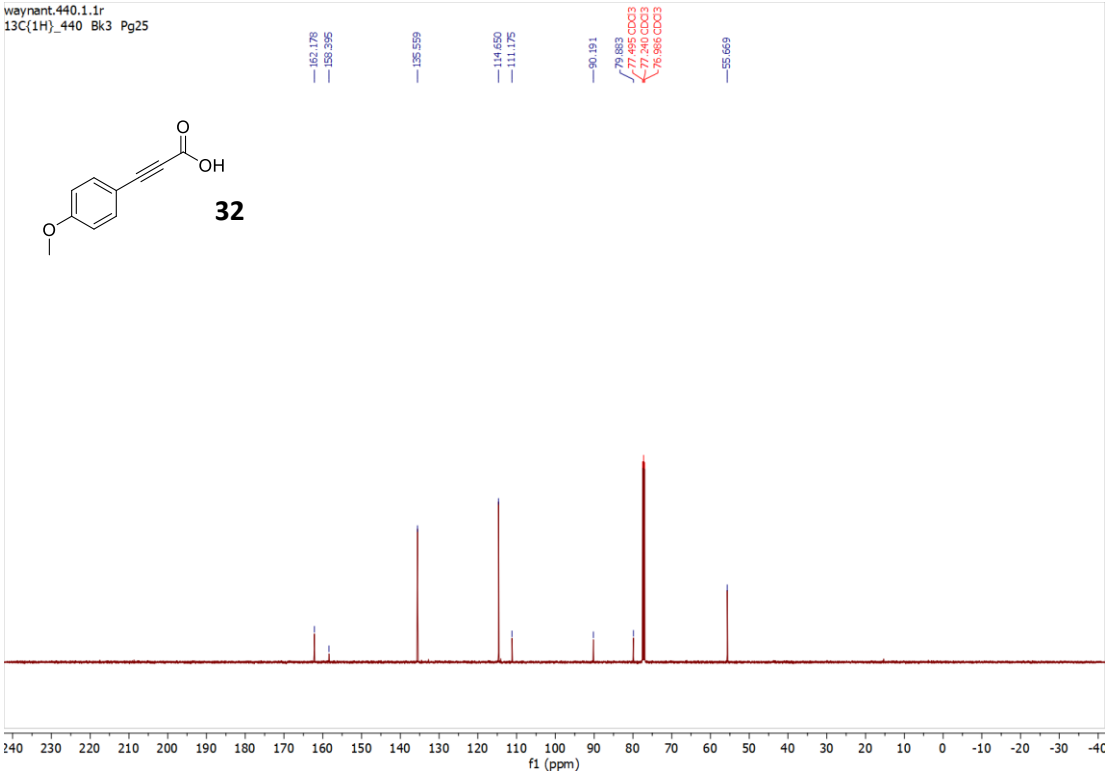

Figure A5.36: ^{13}C NMR spectrum of **31** [3-(4-methoxyphenyl)propiolic acid] in $CDCl_3$

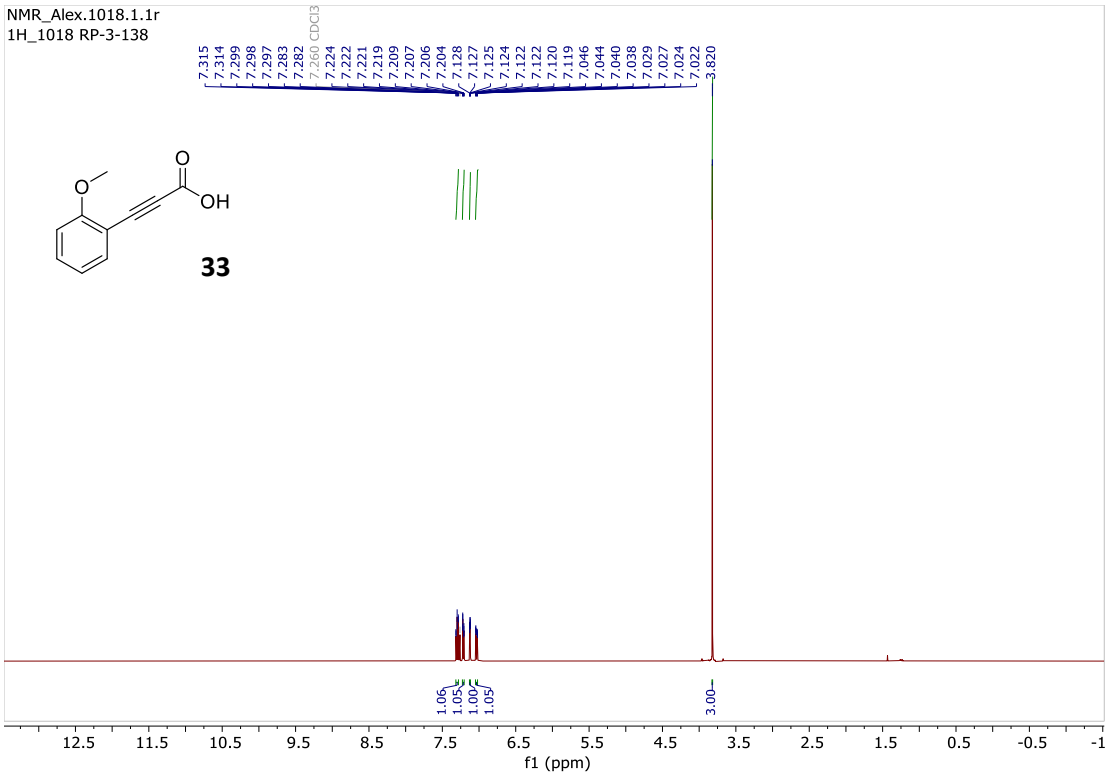

Figure A5.37: ^{1}H NMR spectrum of **33** [3-(2-methoxyphenyl)propiolic acid] in $CDCl_3$

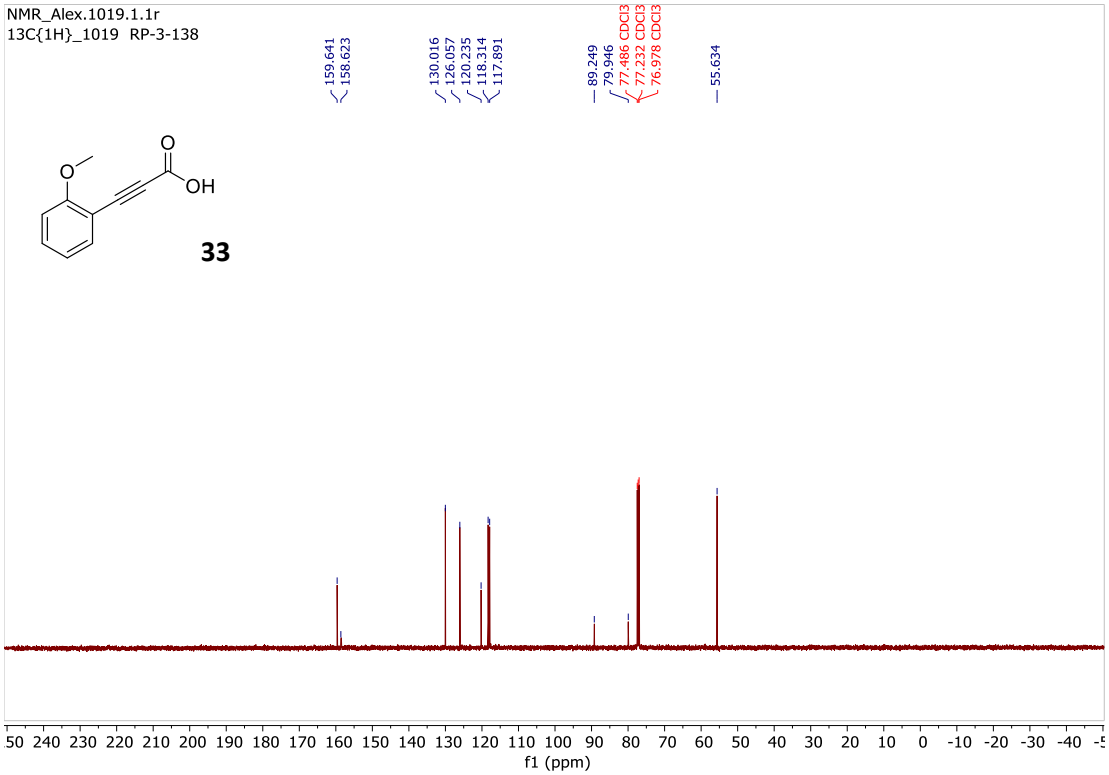

Figure A5.38: ^{13}C NMR spectrum of **33** [3-(2-methoxyphenyl)propiolic acid] in $CDCl_3$

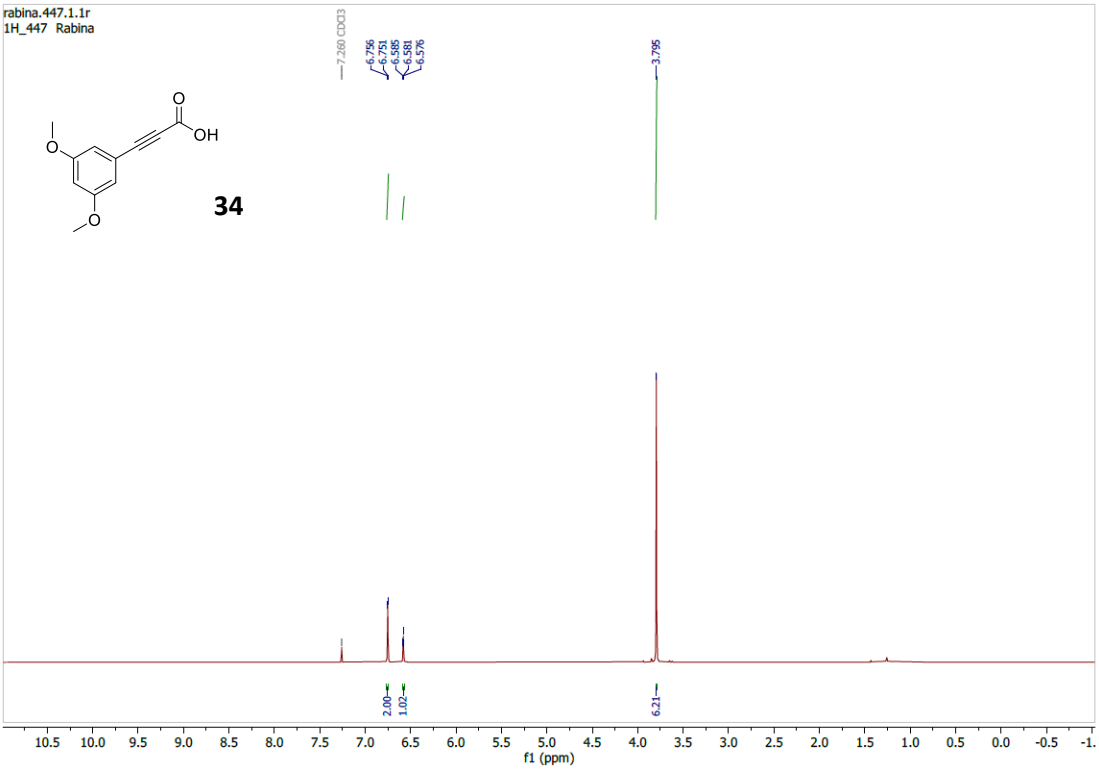

Figure A5.39: ^{1}H NMR spectrum of **34** [3-(3,5-dimethoxyphenyl)propiolic acid] in $CDCl_3$

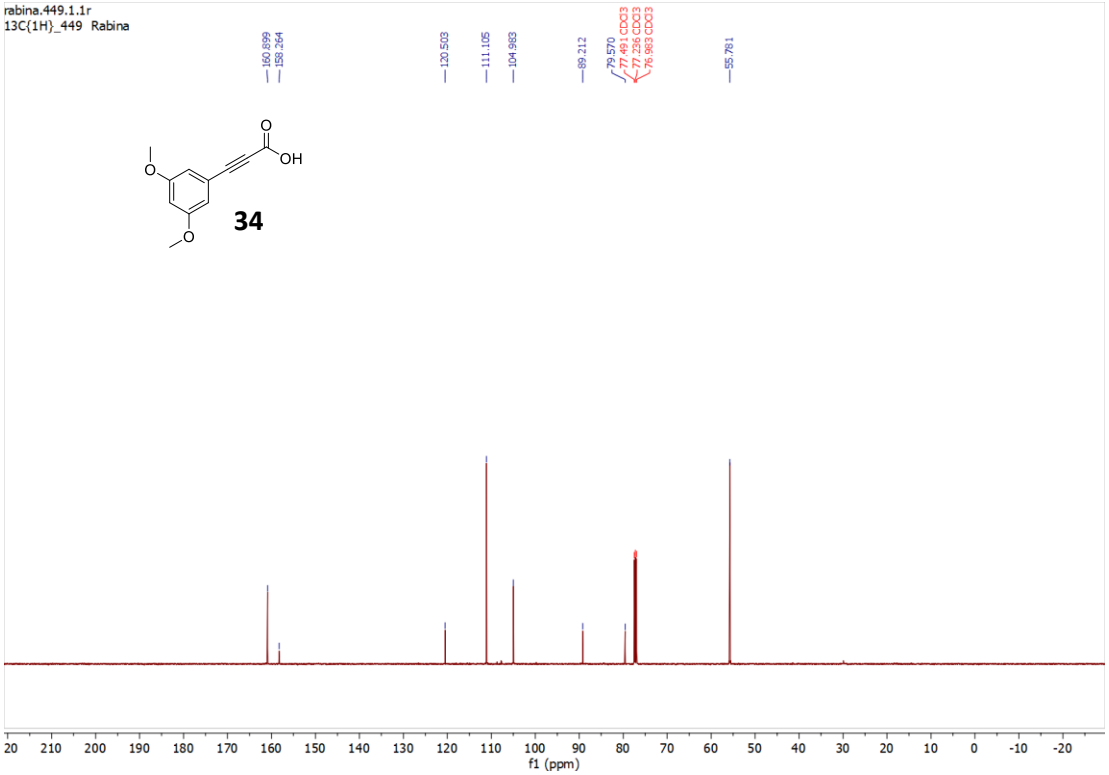

Figure A5.40: ^{13}C NMR spectrum of **34** [3-(3,5-dimethoxyphenyl)propiolic acid] in $CDCl_3$

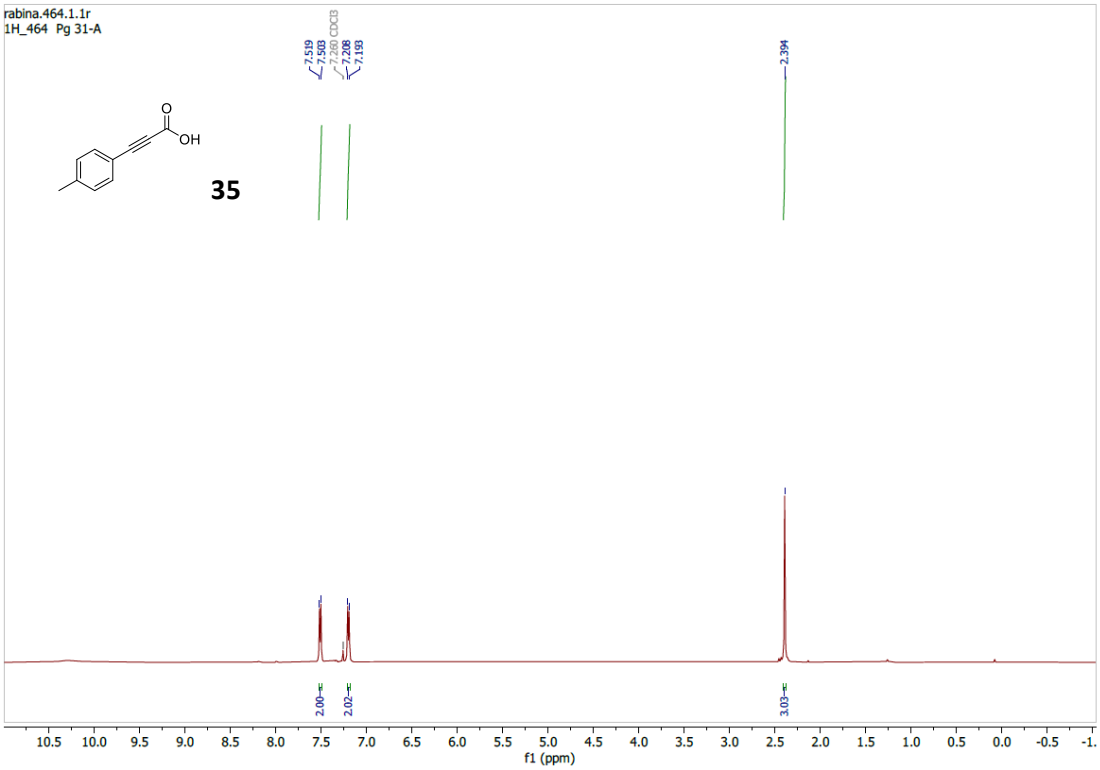

Figure A5.41: ^{1}H NMR spectrum of **35** [3-(*p*-tolyl)propiolic acid] in $CDCl_3$

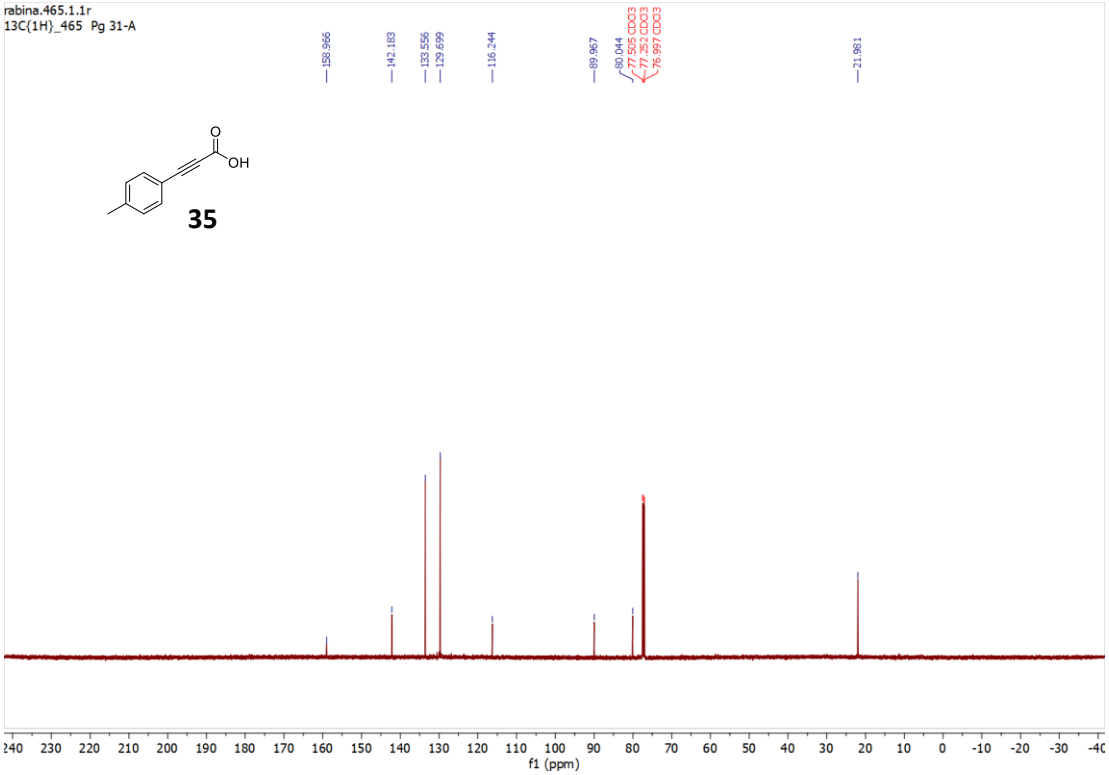

Figure A5.42: ^{13}C NMR spectrum of **35** [3-(*p*-tolyl)propiolic acid] in $CDCl_3$

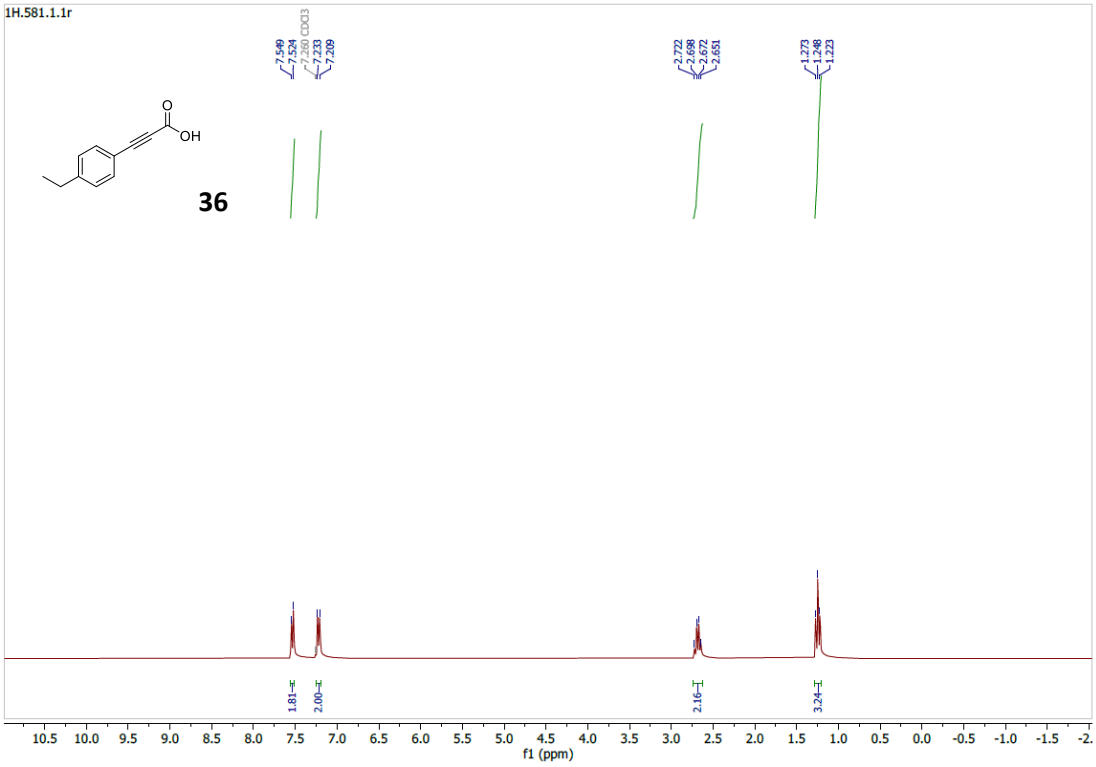

Figure A5.43: ^{1}H NMR spectrum of **36** [3-(4-ethyl phenyl)propiolic acid] in $CDCl_3$

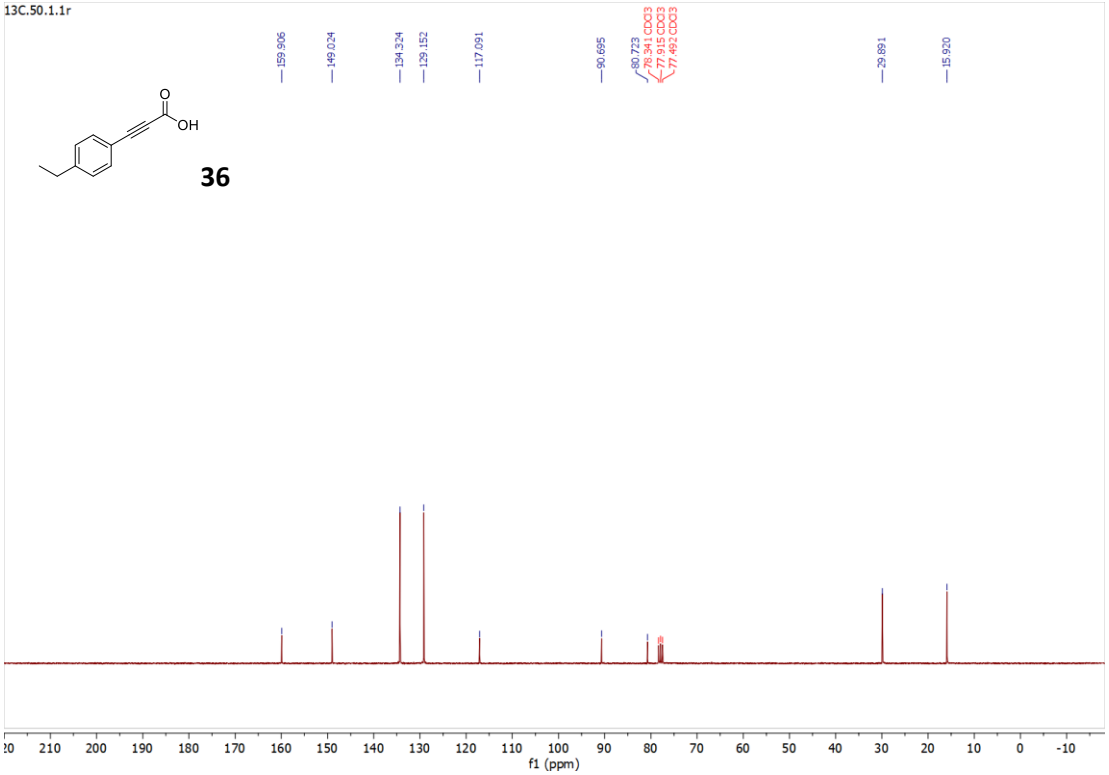

Figure A5.44: ^{1}H NMR spectrum of **36** [3-(4-ethylphenyl)propiolic acid] in $CDCl_3$

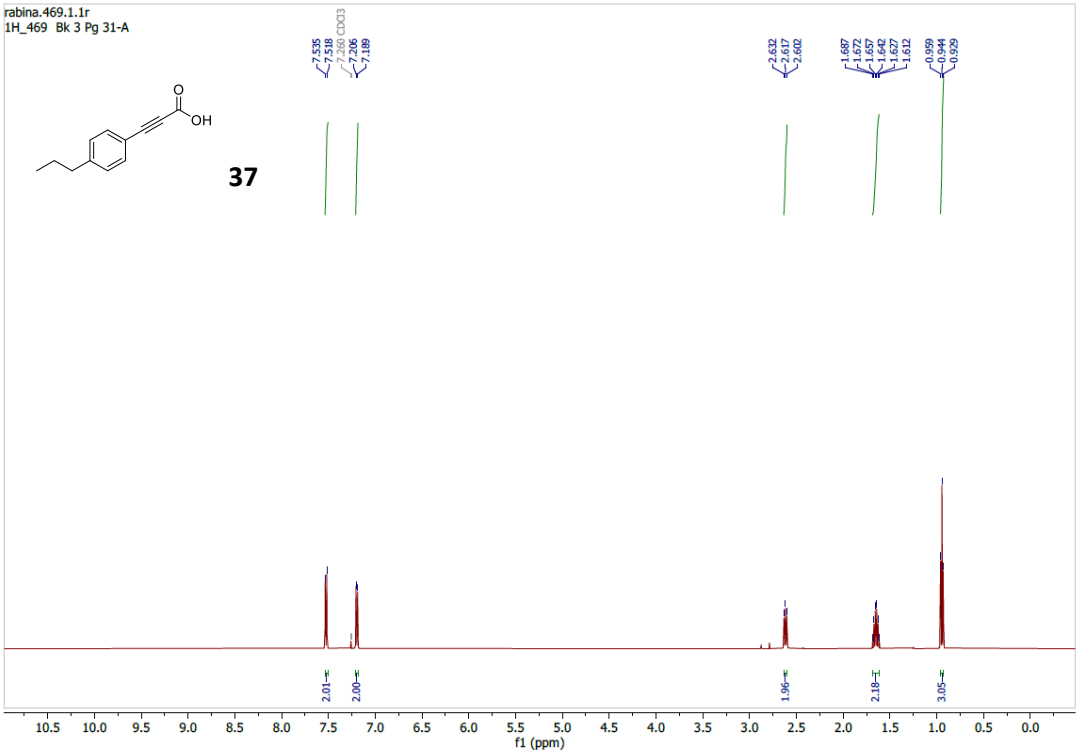

Figure A5.45: ^{1}H NMR spectrum of **37** [3-(4-propylphenyl)propiolic acid] in $CDCl_3$

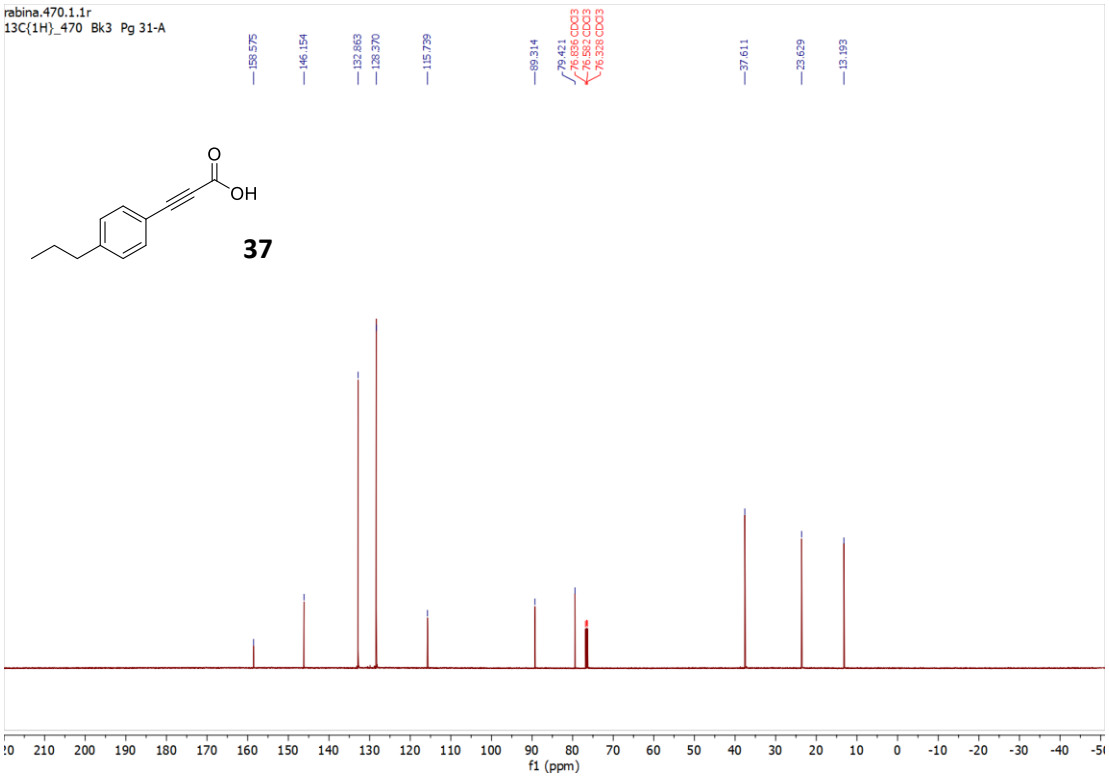

Figure A5.46: ^{13}C NMR spectrum of **37** [3-(4-propylphenyl)propiolic acid] in $CDCl_3$

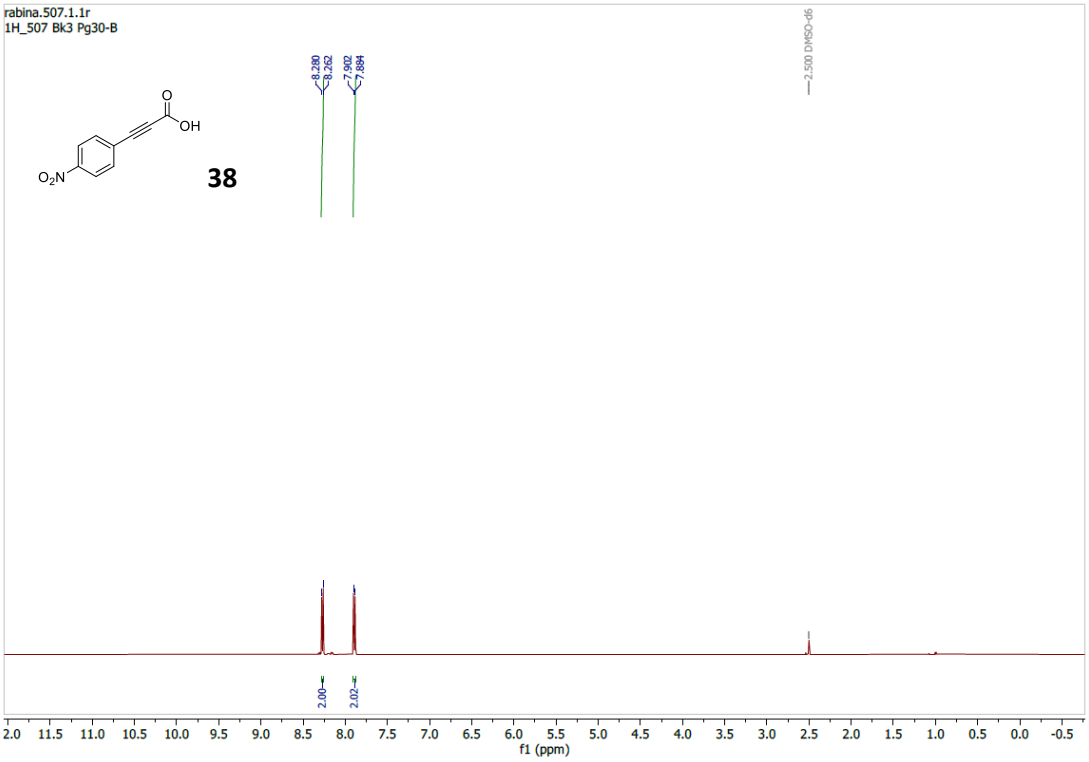

Figure A5.47: ^{1}H NMR spectrum of **38** [3-(4-nitrophenyl)propiolic acid] in DMSO

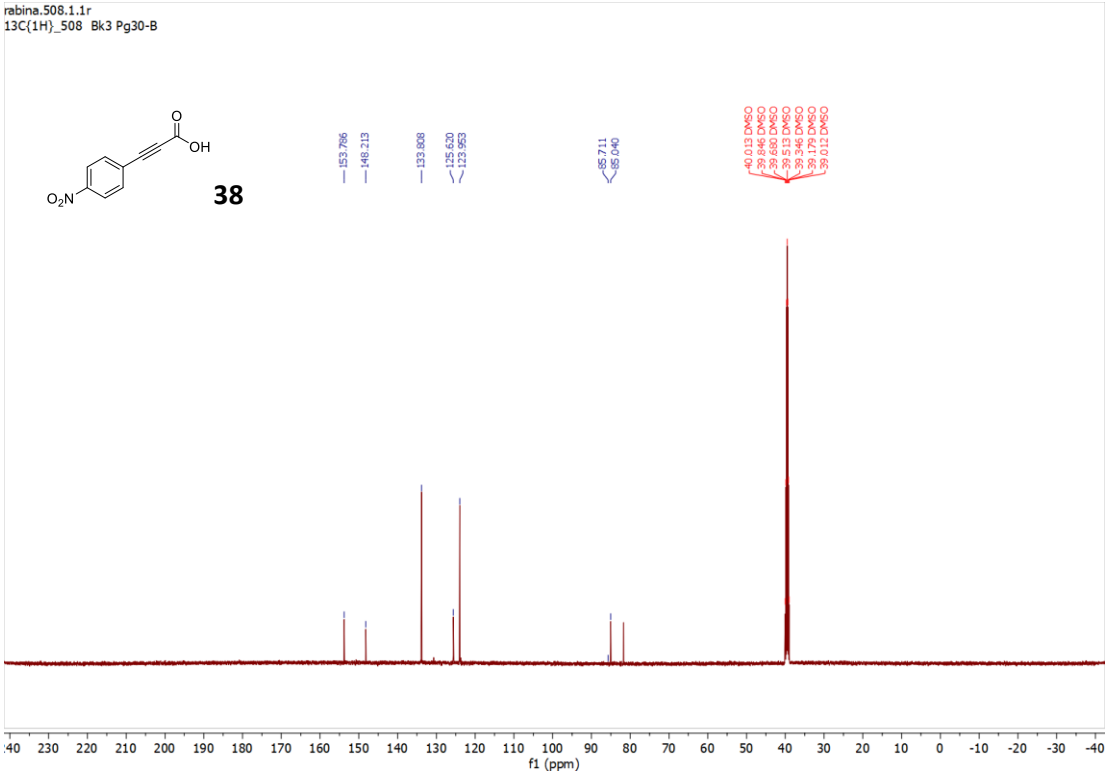

Figure A5.48: ^{13}C NMR spectrum of **38** [3-(4-nitrophenyl)propiolic acid] in DMSO

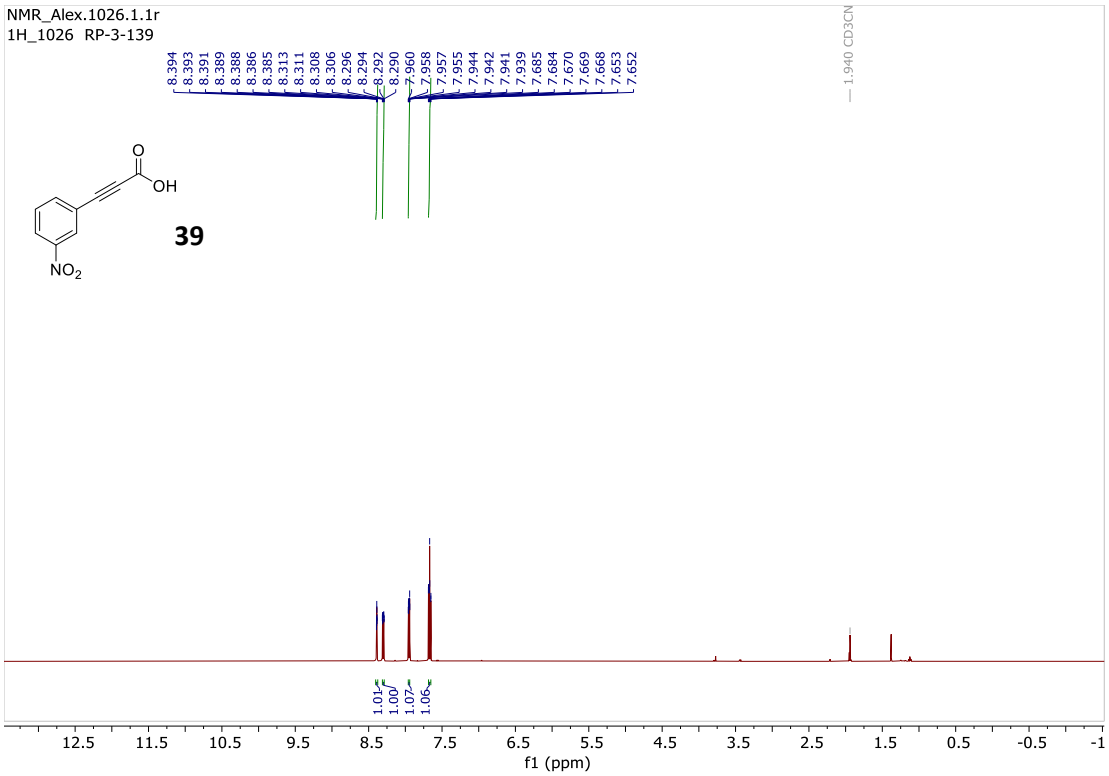

Figure A5.49: ^{1}H NMR spectrum of **39** [3-(3-nitrophenyl)propiolic acid] in CD_3CN

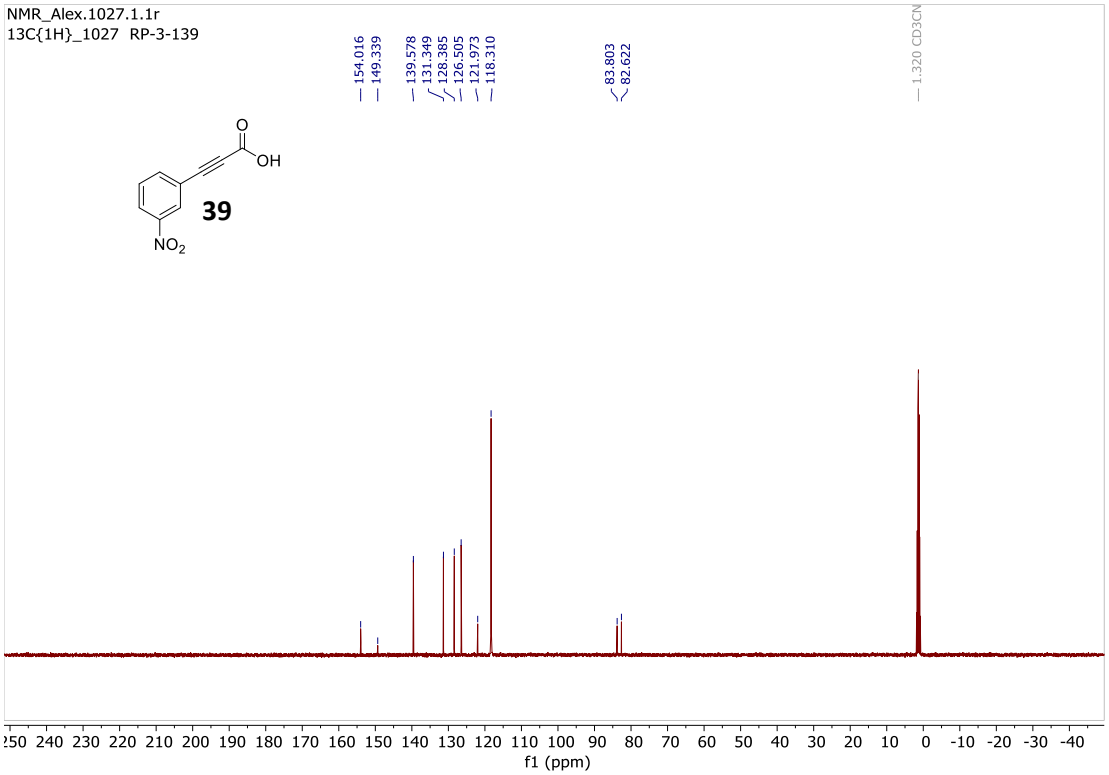

Figure A5.50: ^{1}H NMR spectrum of **39** [3-(3-nitrophenyl)propiolic acid] in CD_3CN

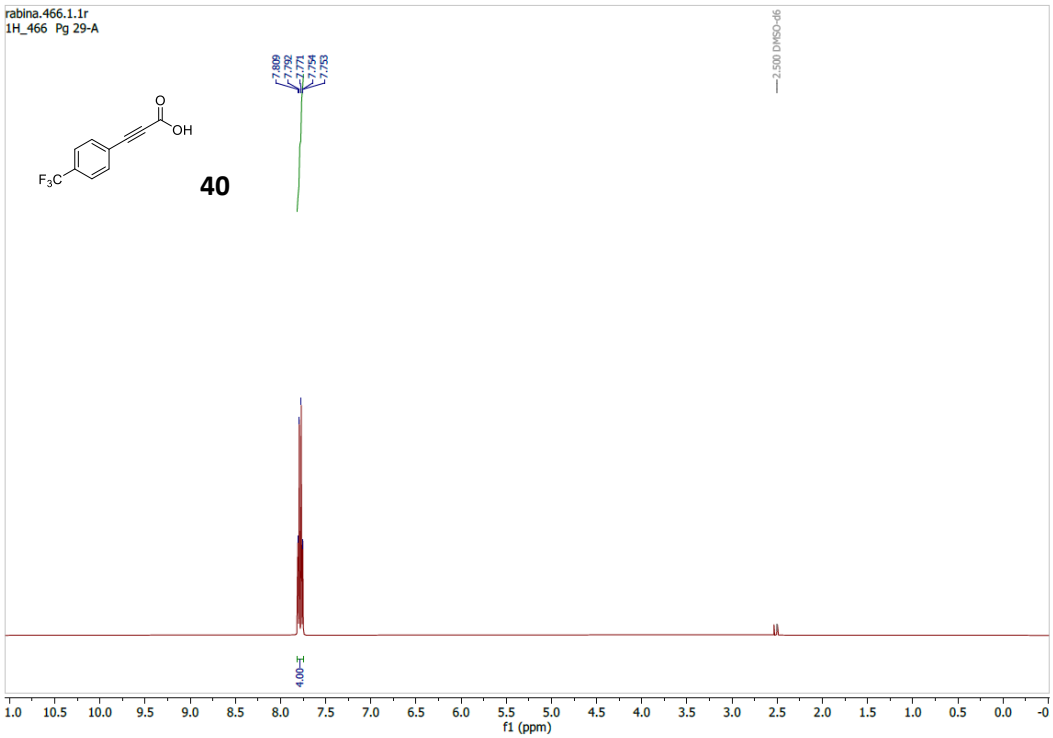

Figure A5.51: ^{1}H NMR spectrum of **40** [3-(4-trifluoromethylphenyl)propiolic acid] in *d*$_6$-DMSO

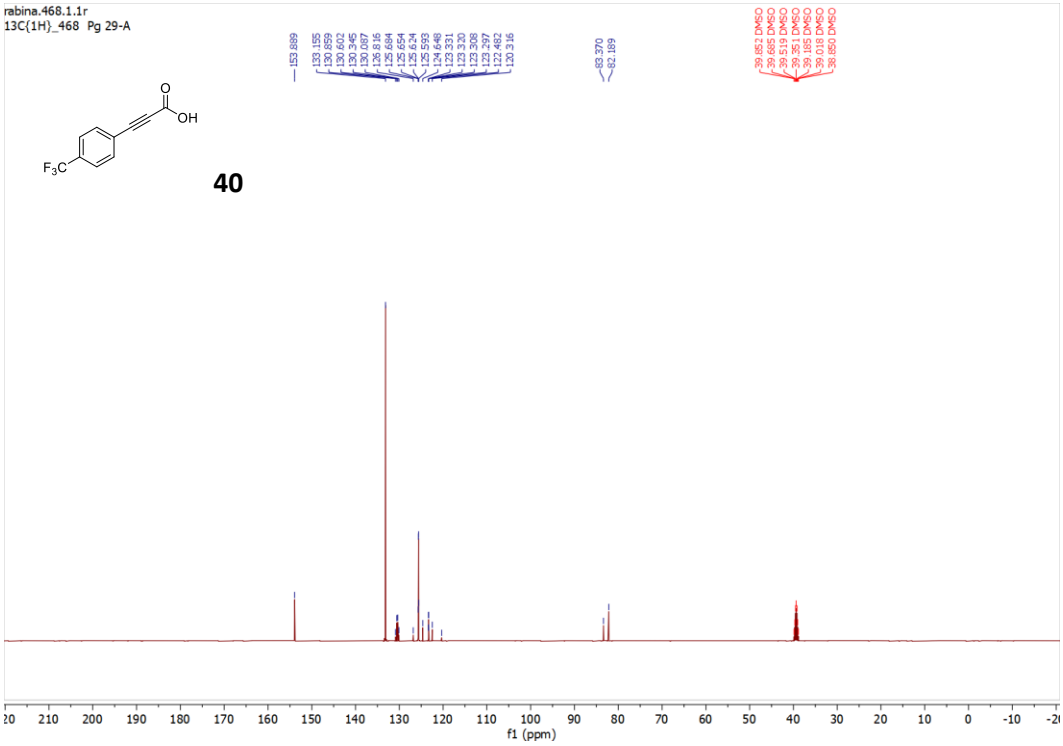

Figure A5.52: ^{13}C NMR spectrum of **40** [3-(4-trifluoromethylphenyl)propiolic acid] in *d*$_6$-DMSO

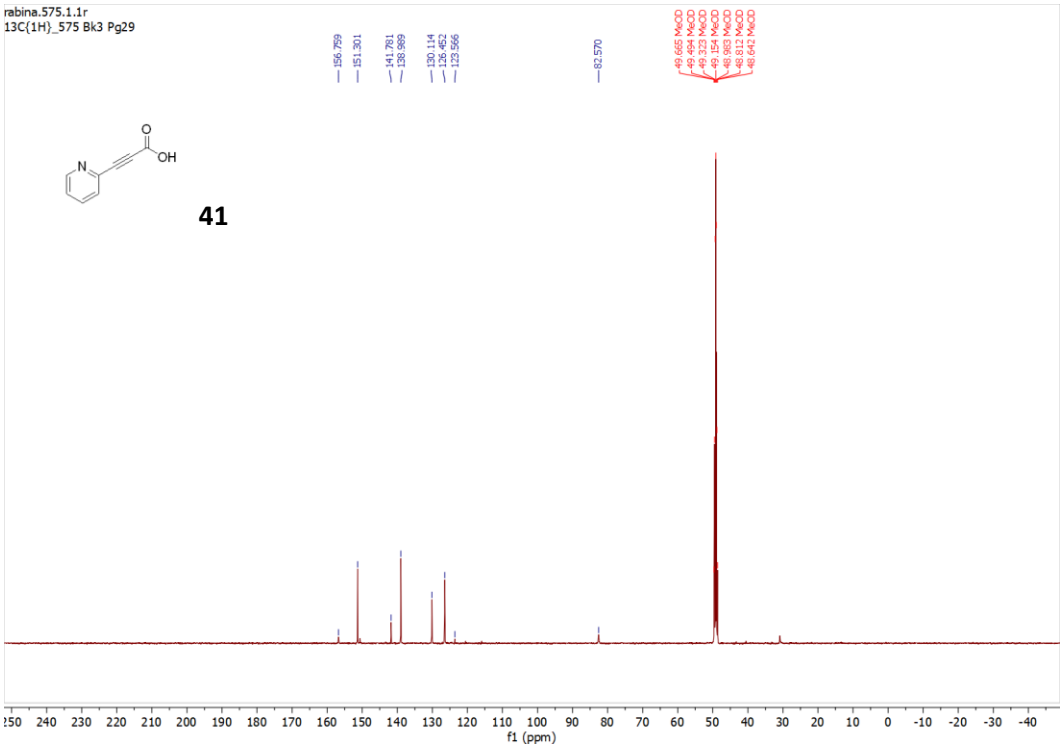

Figure A5.53: ^{1}H NMR spectrum of **41** [3-(pyridine-2-yl)propiolic acid] in d_6-DMSO

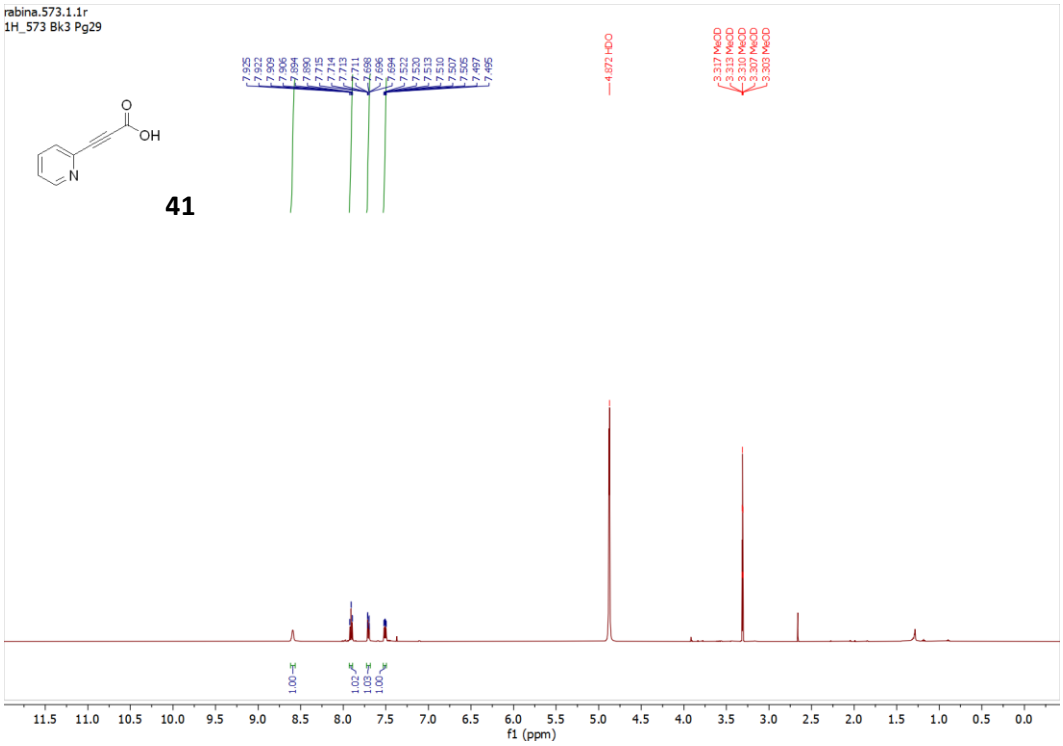

Figure A5.54: ^{13}C NMR spectrum of **41** [(3-(pyridin-2-yl)propiolic acid] in d_6-DMSO

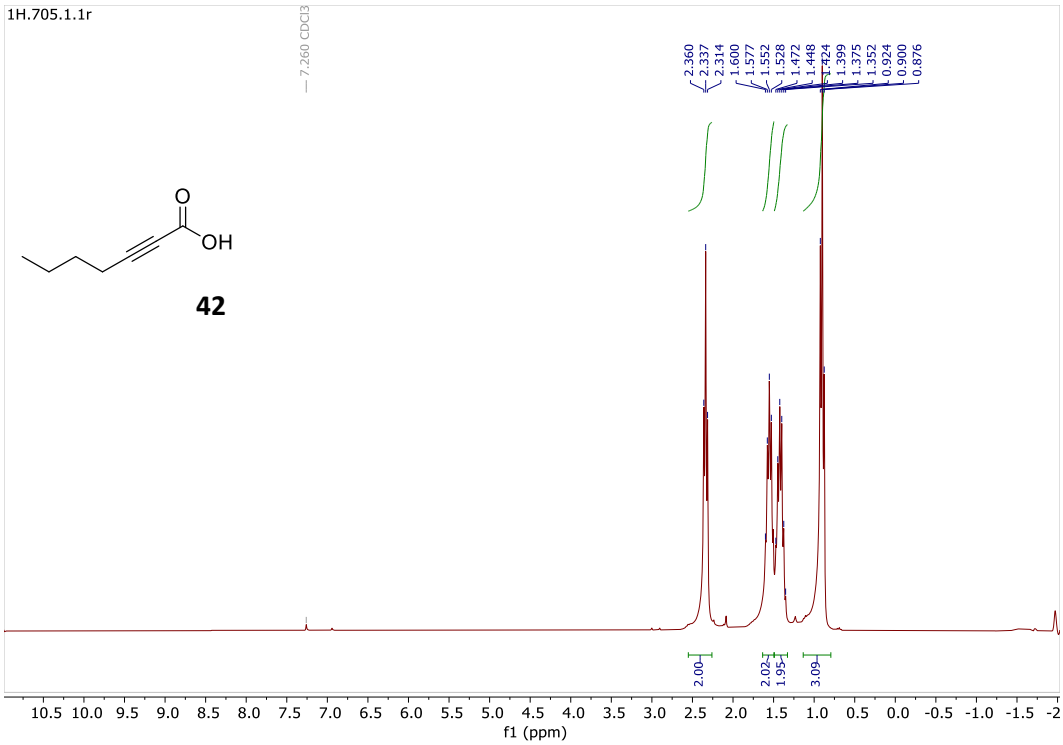

Figure A5.55: ^{1}H NMR spectrum of **42** [2-heptynoic acid] in $CDCl_3$

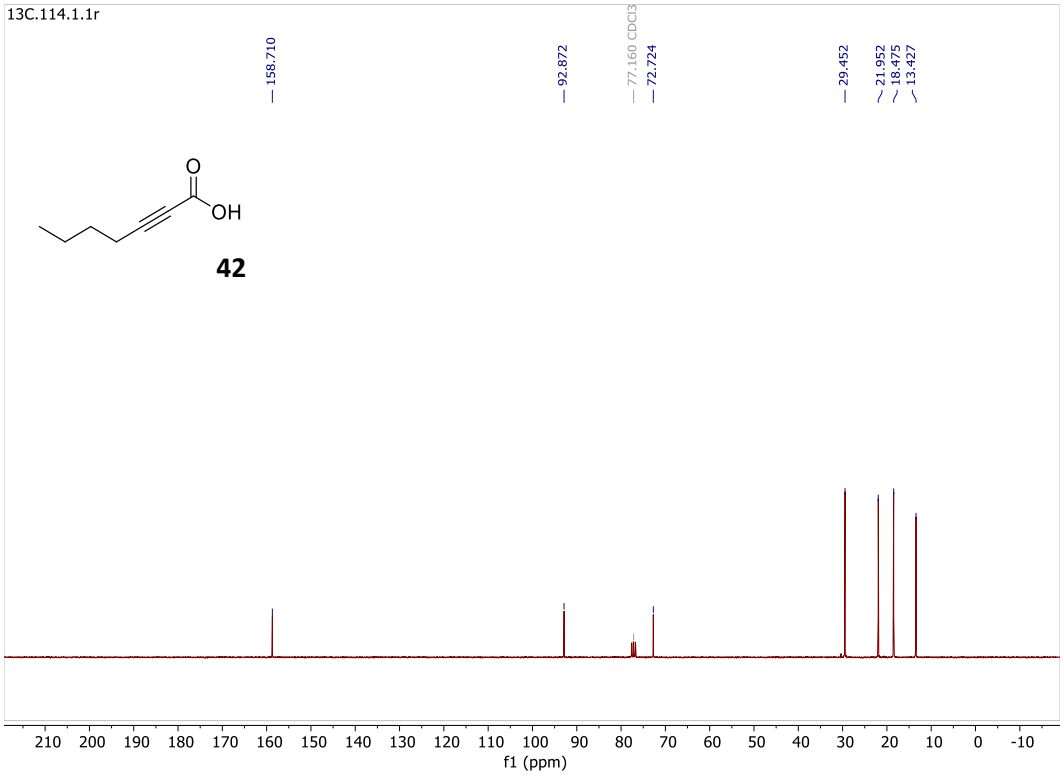

Figure A5.56: ^{13}C NMR spectrum of **42** (2-heptynoic acid) in $CDCl_3$

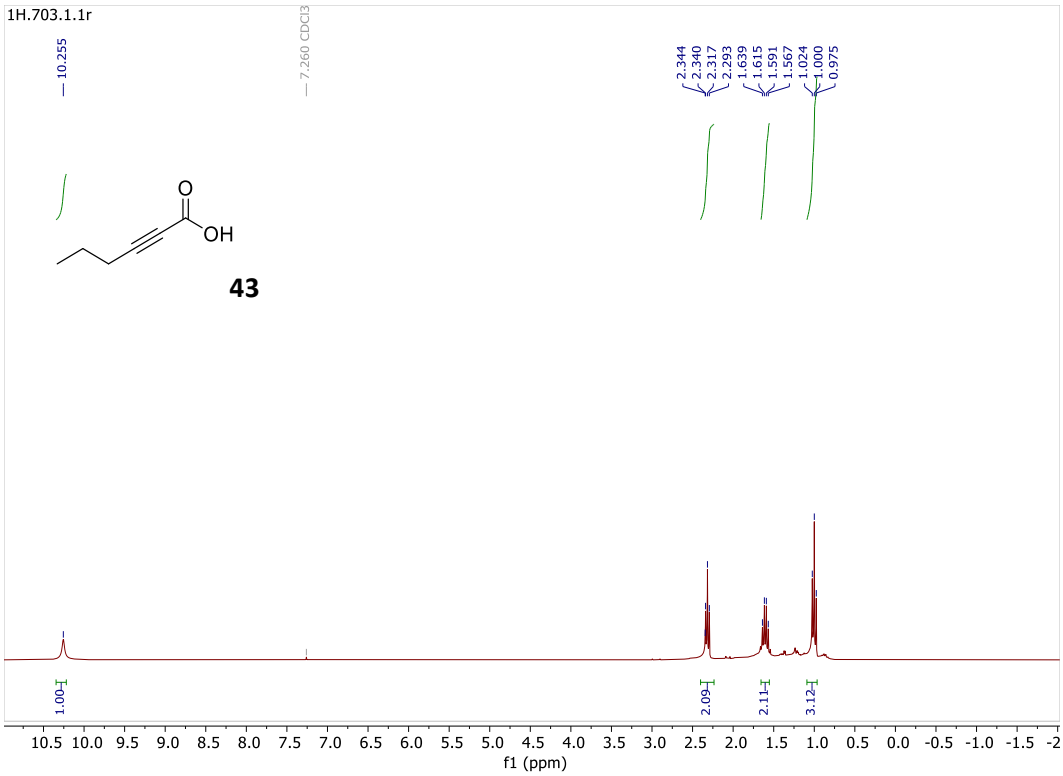

Figure A5.57: ^{1}H NMR spectrum of **43** (2-hexynoic acid) in $CDCl_3$

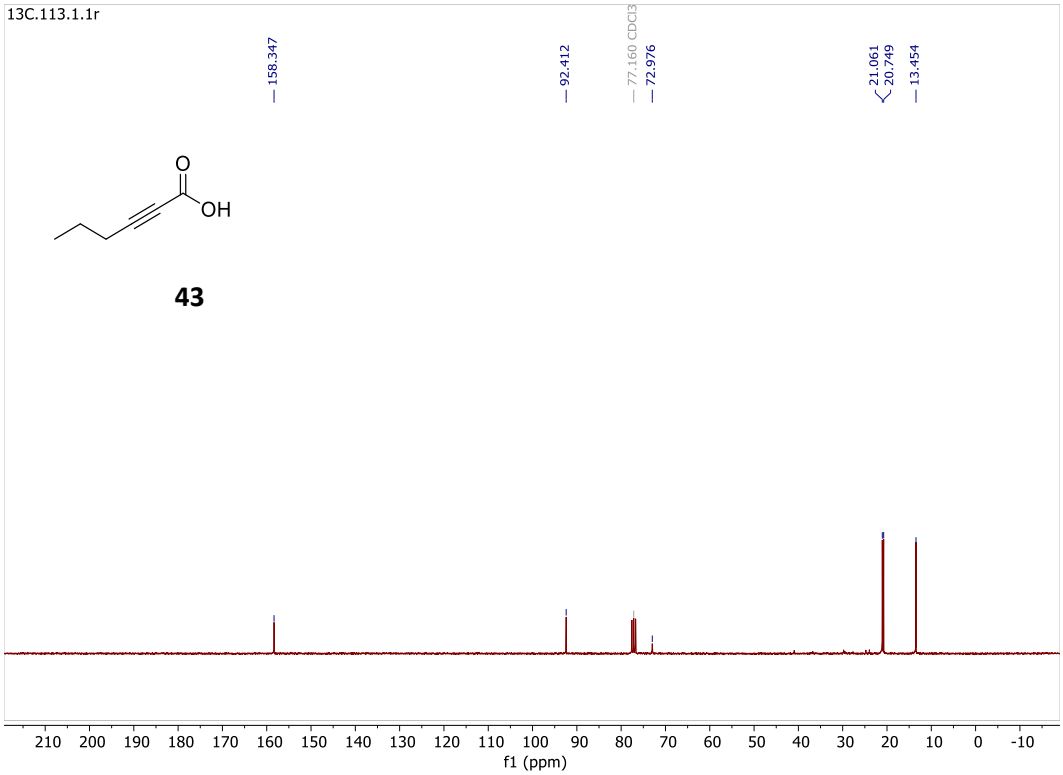

Figure A5.58: ^{13}C NMR spectrum of **43** (2-hexynoic acid) in $CDCl_3$

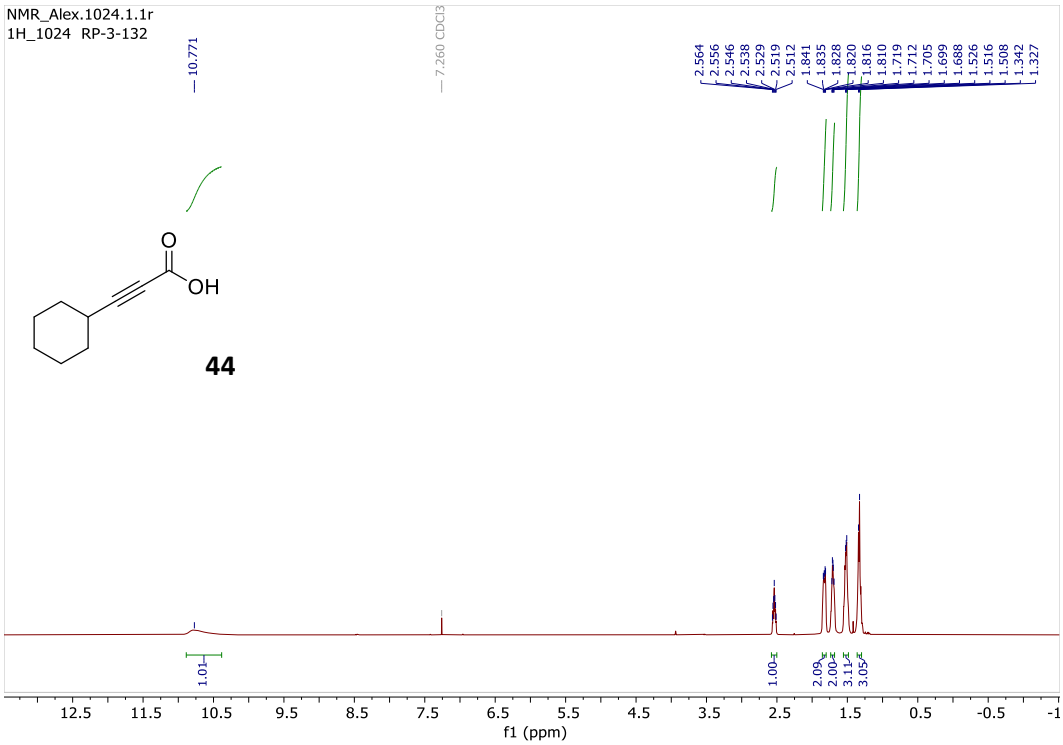

Figure A5.59: ^{1}H NMR spectrum of **44** (3-cyclohexylpropiolic acid) in $CDCl_3$

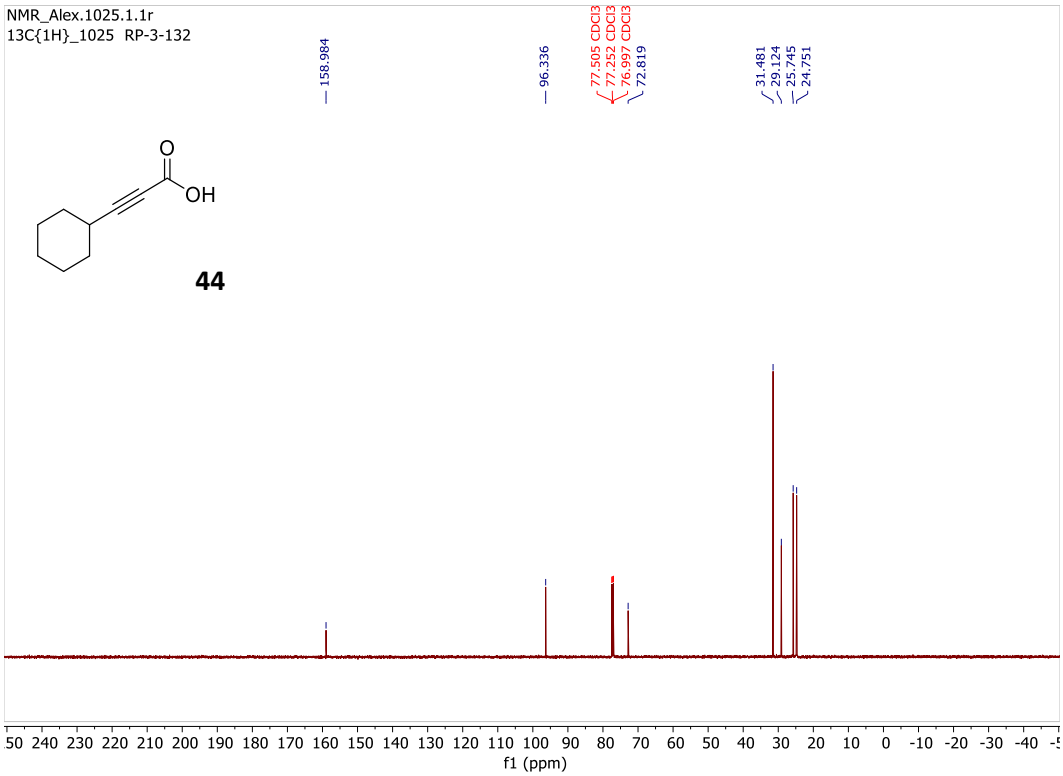

Figure A5.60: ^{13}C NMR spectrum of **44** (3-cyclohexylpropiolic acid) in $CDCl_3$

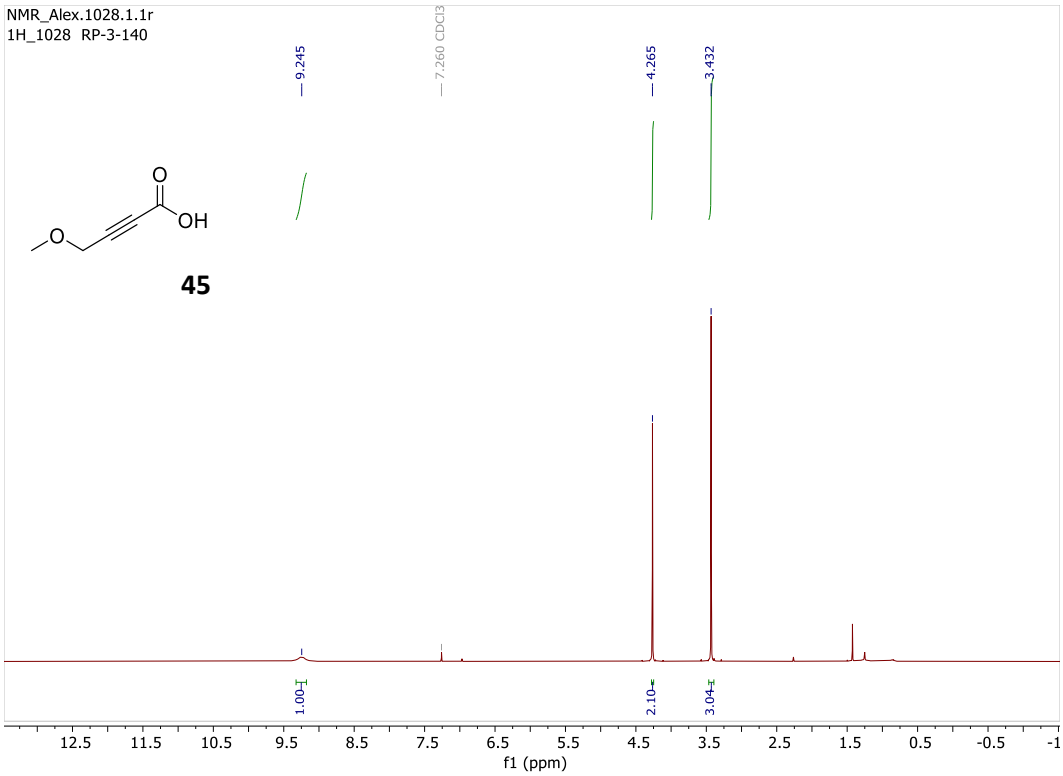

Figure A5.61: ^{1}H NMR spectrum of **45** (4-methoxybut-2-yonic acid) in $CDCl_3$

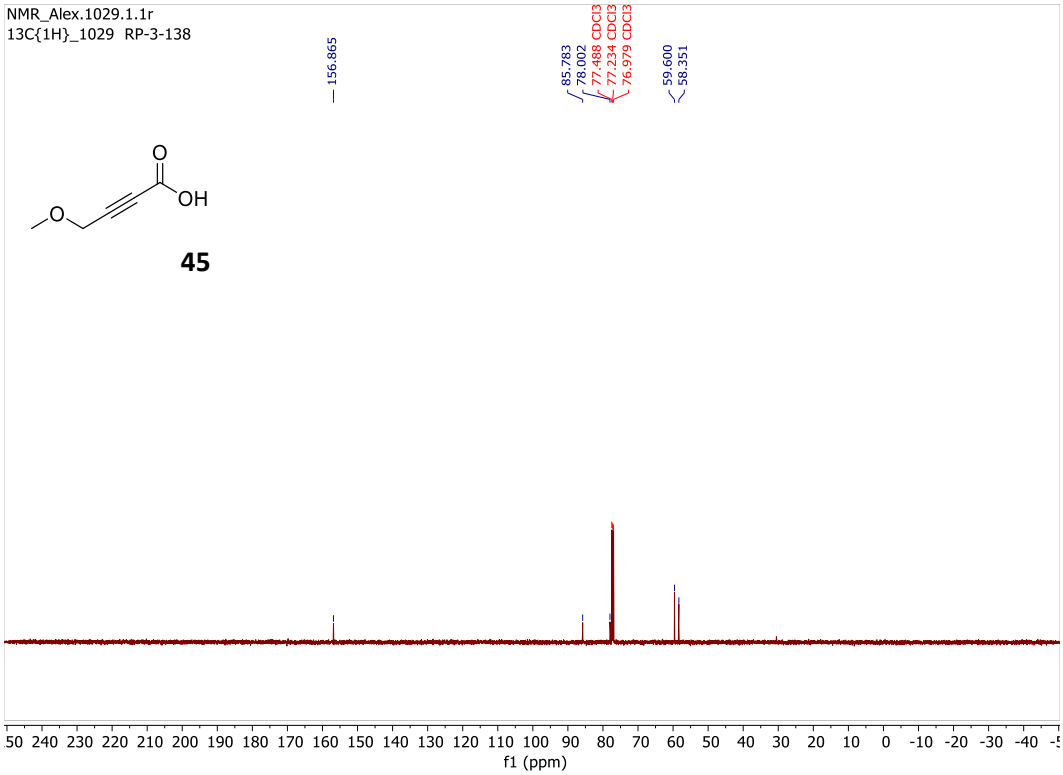

Figure A5.62: ^{13}C NMR spectrum of **45** (4-methoxybut-2-yonic acid) in $CDCl_3$

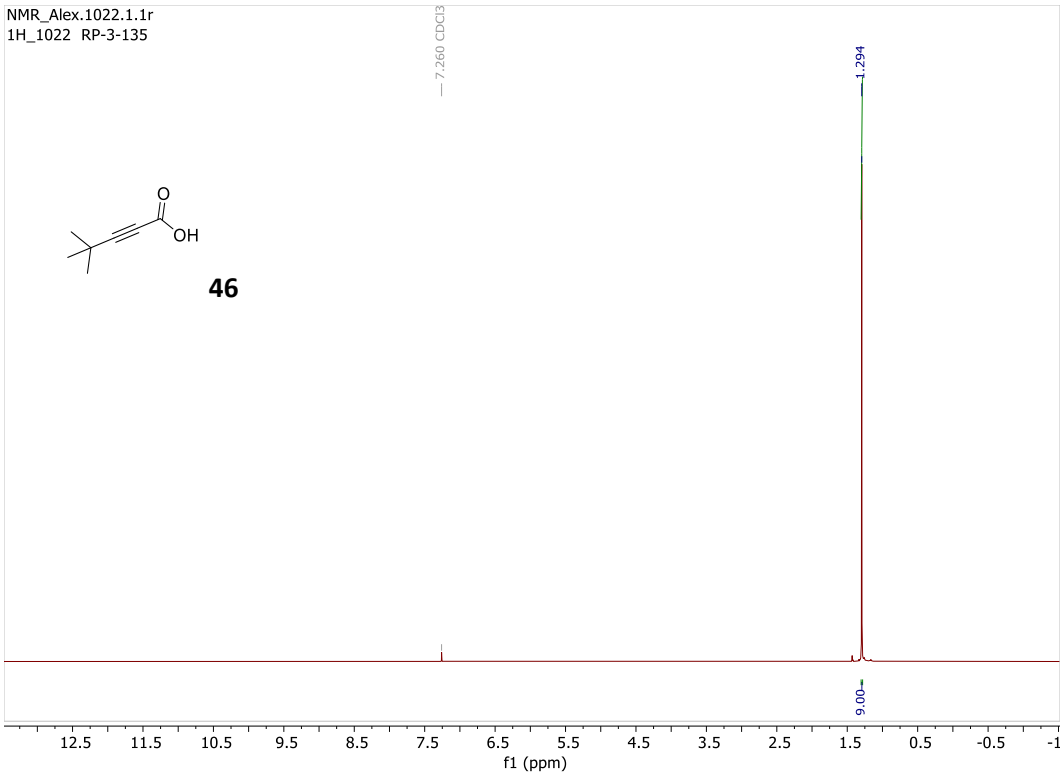

Figure A5.63: ^{1}H NMR spectrum of **46** (4,4 dimethylpent-2-ynic acid) in $CDCl_3$

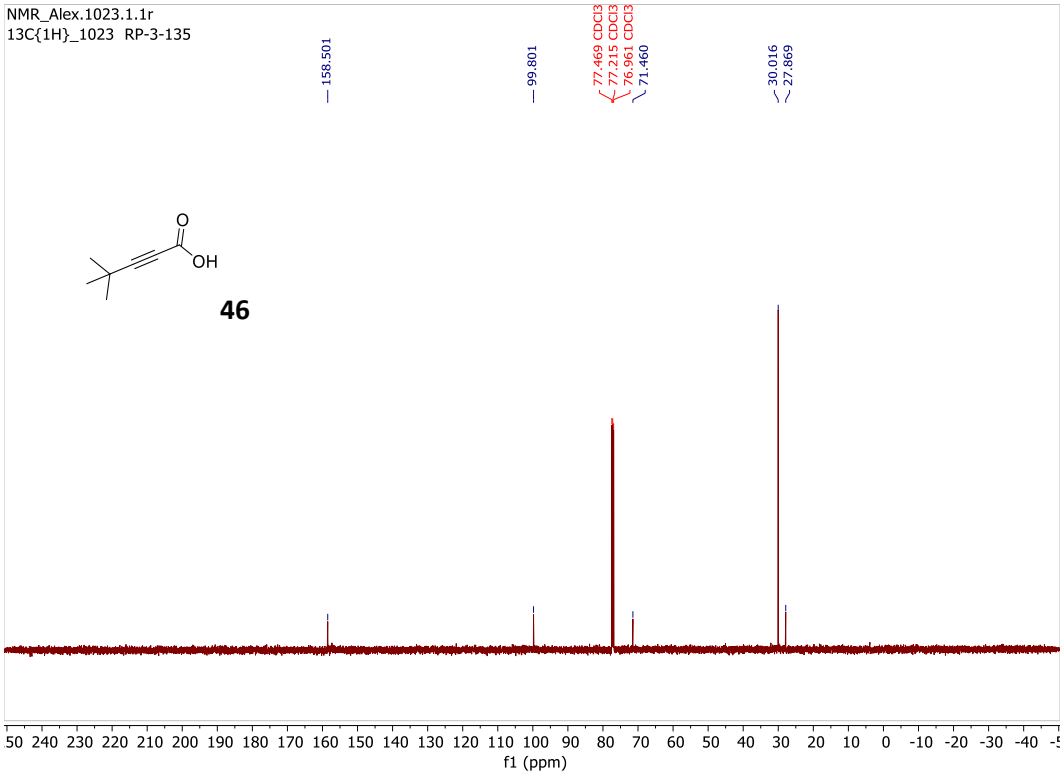

Figure A5.64: ^{13}C NMR spectrum of **46** (4,4 dimethylpent-2-ynic acid) in $CDCl_3$

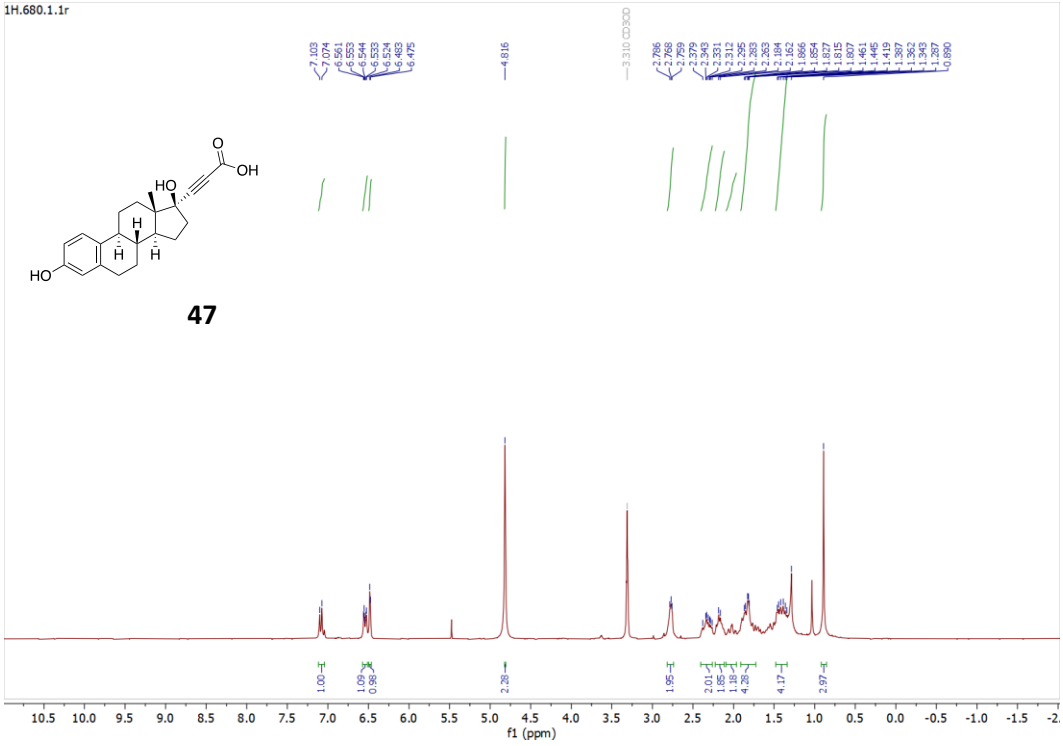

Figure A5.65: ^{1}H NMR spectrum of **47** (3-((8R,9S,13S,14S,17S)-3,17-dihydroxy-13-methyl-7,8,9,11,12,13,14,15,16,17-decahydro-6H-cyclopenta[a]phenanthren-17-yl)propiolic acid) in CD_3OD

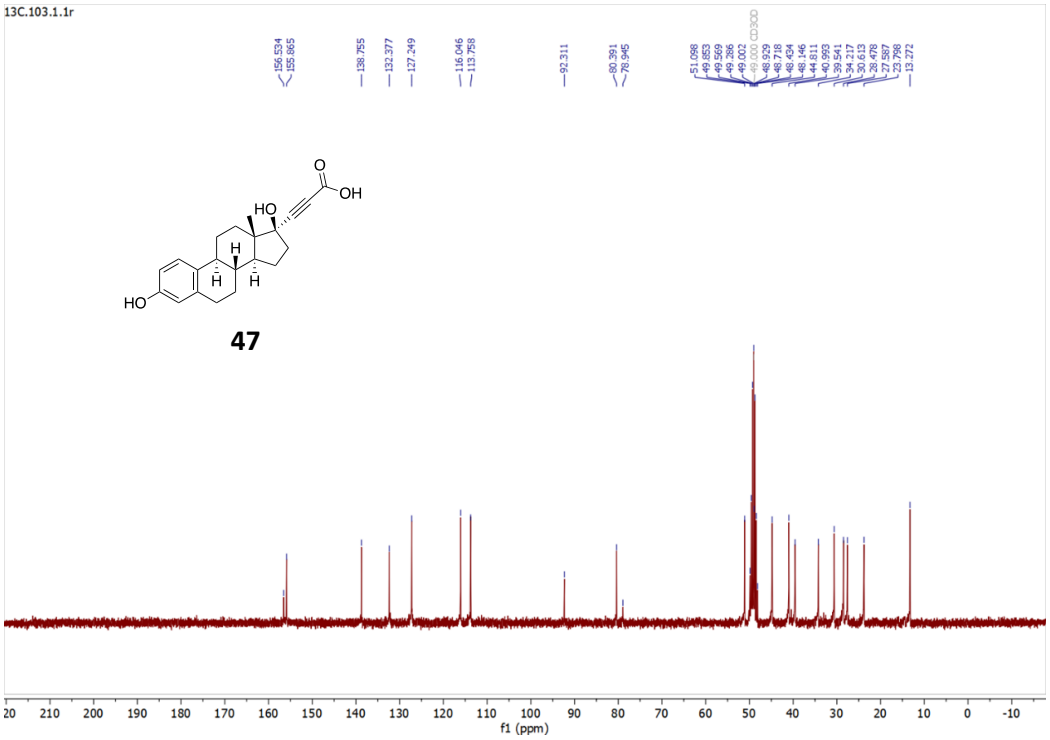

Figure A5.66: ^{13}C NMR spectrum of **47** (3-((8R,9S,13S,14S,17S)-3,17-dihydroxy-13-methyl-7,8,9,11,12,13,14,15,16,17-decahydro-6H-cyclopenta[a]phenanthren-17-yl)propiolic acid) in CD_3OD

Experimental Data for X-ray Crystal Structures

Crystallographic Data **(μ-I)-[Cu(*p*-tolyl-ATF)I]$_2$ (13),** $C_{24}H_{34}Cu_2I_2N_6S_2$ (*M* =851.57 g/mol): triclinic, space group P-1 (no. 2), *a* = 8.6944(5) Å, *b* = 9.7741(5) Å, *c* = 10.6577(5) Å, *α* = 115.600(2)°, *β* = 102.940(2)°, *γ* = 98.527(2)°, *V* = 764.48(7) Å^3, *Z* = 1, *T* = 100.0 K, μ(MoKα) = 3.571 mm^{-1}, *Dcalc* = 1.850 g/cm^3, 2Θmax = 56.596°, 22738 reflections measured, 3765 unique (R_{int} = 0.0619, R_{sigma} = 0.0471) R_1 = 0.0422 (I > 2σ(I)), wR_2 =0.0999 (all data).

X-ray diffraction data for **(μ-I)-[Cu(*p*-tolyl-ATF)I]$_2$ (13)** were collected at 100 K on a Bruker D8 quest using Mo Kα-radiation (λ= 0. 71073Å). Data have been corrected for absorption using SADABS[1] area detector absorption correction program. Using Olex2[2], the structure was solved with the SHELXT[3] structure solution program using Direct Methods and refined with the SHELXL[4] refinement package using least squares minimization. All non-hydrogen atoms were refined with anisotropic thermal parameters. The hydrogen atoms of the investigated structure were located from difference Fourier maps but finally their positions were placed in geometrically calculated positions and refined using a riding model. Isotropic thermal parameters of the placed hydrogen atoms were fixed to 1.2 times the *U* value of the atoms they are linked to (1.5 times for methyl groups). After initial refinement there was some residual electron density near the iodide and the iodide displayed an elongated ellipsoid. This iodide disorder has been modeled over two positions using a PART instruction and tied to a free variable. Refinement of the free variable shows and approximate 92:08 disorder. The iodide disorder model incorporates bond similarity restraints (SADI 0.02) and a thermal ellipsoid constraint (EADP). Calculations and refinement of structures were carried out using APEX4[5], SHELXTL[6], and Olex2 software.

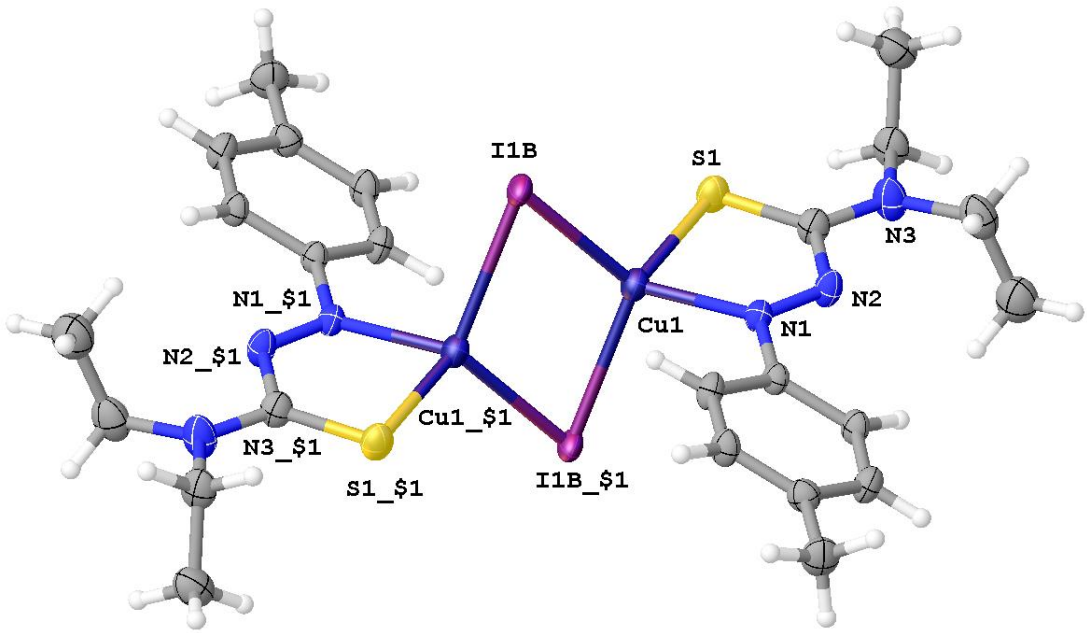

Crystallographic Data for **(μ-I)[Cu(*p*-fluorophenyl-ATF)I]$_2$ (14),** $C_{26}H_{36}Cu_2F_2I_2N_6OS_2$ (M =931.61 g/mol): orthorhombic, space group Pnma (no. 62), a = 15.9143(7) Å, b = 17.2551(7) Å, c = 12.2004(5) Å, V = 3350.3(2) Å^3, Z = 4, T = 100 K, μ(MoKα) = 3.278 mm^{-1}, *Dcalc* = 1.847 g/cm^3, 2Θmax = 57.4°, 164605 reflections measured, 4471 unique (R_{int} = 0.0549, R_{sigma} = 0.0144), R_1 = 0.0246 (I > 2σ(I)), wR_2 = 0.0603 (all data).

X-ray diffraction data for **(μ-I)[Cu(*p*-fluorophenyl-ATF)I]$_2$ (14)** were collected at 100 K on a Bruker D8 Venture using MoKα-radiation (λ=0.71073 Å). Data have been corrected for absorption using SADABS[1] area detector absorption correction program. Using Olex2[2], the structure was solved with the SHELXT[3] structure solution program using Direct Methods and refined with the SHELXL[4] refinement package using least squares minimization. All non-hydrogen atoms were refined with anisotropic thermal parameters. The hydrogen atoms of the investigated structure were located from difference Fourier maps (except for the tetrahydrofuran solvent molecule) but finally their positions were placed in geometrically

calculated positions and refined using a riding model. Isotropic thermal parameters of the placed hydrogen atoms were fixed to 1.2 times the *U* value of the atoms they are linked to (1.5 times for methyl groups). The tetrahydrofuran molecule exhibits disorder about a mirror plane. The disorder has been treated using a negative PART value and fixing the site occupancy factor to 0.5. After refinement there was residual electron density near I2 (≈ 3.6 e $Å^{-3}$) suggesting a small component of disorder. This iodide disorder has been modeled over two positions using a PART instruction and tied to a free variable. Refinement of the free variable shows and approximate 91:09 disorder. The iodide disorder model incorporates bond similarity restraints (SADI 0.02) and a thermal ellipsoid constraint (EADP). Calculations and refinement of structures were carried out using APEX3[5], SHELXTL[6], and Olex2 software.

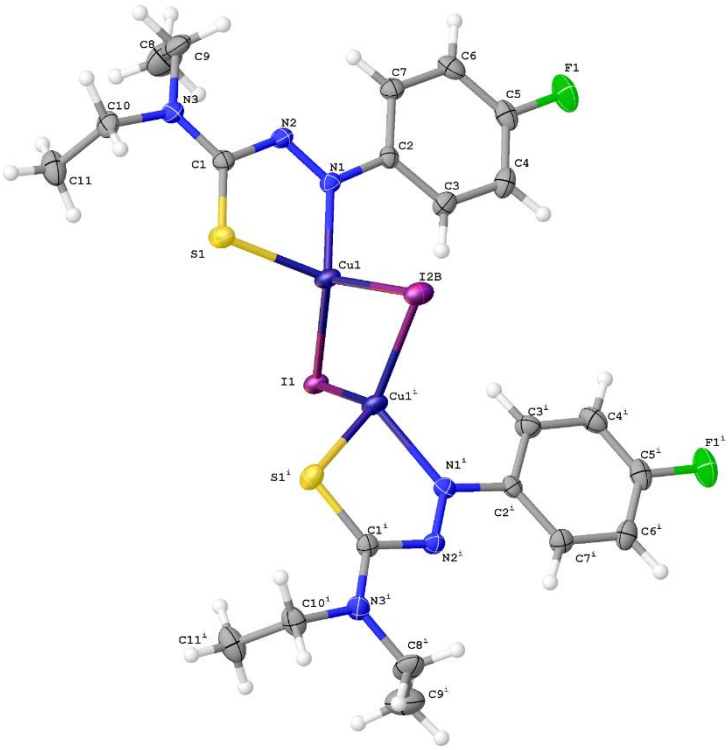

Crystallographic Data for **(μ-I)[Cu(*p*-trifluoromethylphenyl-ATF)I]$_2$ (15),** $C_{24}H_{28}Cu_2F_6I_2N_6S_2$ (*M* =959.52 g/mol): triclinic, space group P-1 (no. 2), *a* = 8.3142(3) Å, *b* = 9.8732(4) Å, *c* = 11.1984(5) Å, *α* = 69.9860(10)°, *β* = 73.3630(10)°, *γ* = 84.2700(10)°, *V* = 827.58(6) Å^3, *Z* = 1, *T* = 100 K, μ(MoKα) = 3.336 mm^{-1}, *Dcalc* = 1.925 g/cm^3, 2Θmax = 57.496°, 48360 reflections collected, 4312 unique (R_{int} = 0.0252, R_{sigma} = 0.0119), R_1 = 0.0155 (I > 2σ(I)), wR_2 = 0.0362 (all data).

X-ray diffraction data for **(μ-I)[Cu(*p*-trifluoromethylphenyl-ATF)I]$_2$ (15)** were collected at 100 K on a Bruker D8 Venture using MoKα-radiation (λ=0.71073 Å). Data have been corrected for absorption using SADABS[1] area detector absorption correction program. Using Olex2[2], the structure was solved with the ShelXT[3] structure solution program using Direct Methods and refined with the ShelXL[4] refinement package using least squares minimization. All non-hydrogen atoms were refined with anisotropic thermal parameters. Hydrogen atoms of the investigated structure were located from difference Fourier maps but finally their positions were placed in geometrically calculated positions and refined using a riding model. Isotropic thermal parameters of the placed hydrogen atoms were fixed to 1.2 times the *U* value of the atoms they are linked to (1.5 times for methyl groups). Calculations and refinement of structures were carried out using APEX3[5], SHELXTL[6], and Olex2 software.

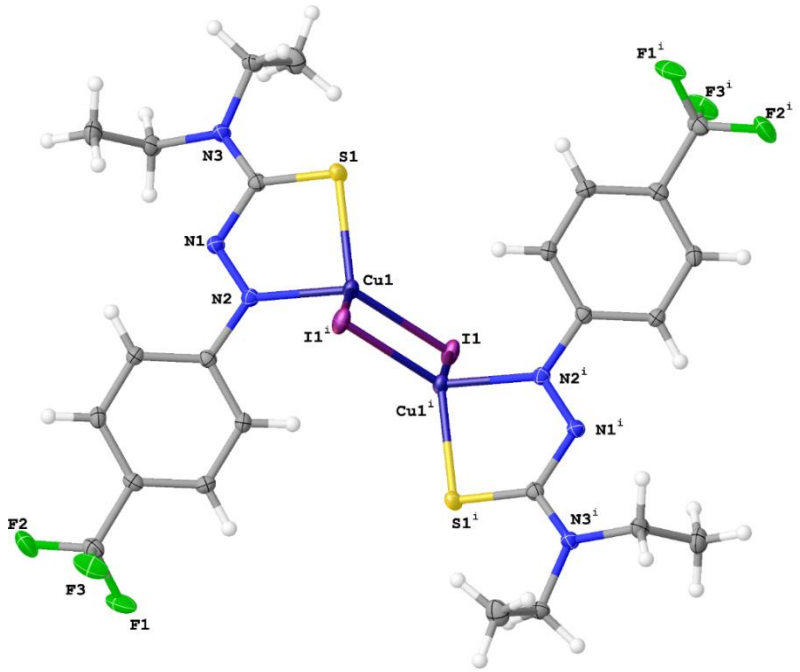

Crystallographic Data **(μ-Br)-[Cu(*p*-tolyl-ATF)Br]$_2$ (17),** $C_{24}H_{34}Br_2Cu_2N_6S_2$: triclinic, space group *P*-1 (no. 2), *a* = 8.4658(7) Å, *b* = 9.4256(7) Å, *c* = 10.6204(9) Å, *α* = 115.524(3)°, *β* = 100.941(3)°, *γ* = 98.353(3)°, *V* = 725.77(10) Å^3, *Z* = 1, *T* = 100.0 K, μ(MoKα) = 4.387 mm^{-1}, *Dcalc* = 1.733 g/cm^3, 2Θmax = 56.566°, 18784 reflections measured, 3569 unique (R_{int} = 0.0632, R_{sigma} = 0.0519) R_1 = 0.0319 (I > 2σ(I)), wR_2 = 0.0705 (all data).

X-ray diffraction data for **(μ-Br)-[Cu(*p*-tolyl-ATF)Br]$_2$ (17)** were collected at 100 K on a Bruker D8 quest using Mo Kα-radiation (λ= 0. 71073Å). Data have been corrected for absorption using SADABS[1] area detector absorption correction program. Using Olex2[2], the structure was solved with the SHELXT[3] structure solution program using Direct Methods and refined with the SHELXL[4] refinement package using least squares minimization. All non-hydrogen atoms were refined with anisotropic thermal parameters. The hydrogen atoms of the investigated structure were located from difference Fourier maps but finally their positions were placed in geometrically calculated positions and refined using a riding model. Isotropic

thermal parameters of the placed hydrogen atoms were fixed to 1.2 times the *U* value of the atoms they are linked to (1.5 times for methyl groups). Calculations and refinement of structures were carried out using APEX4[5], SHELXTL[6], and Olex2 software.

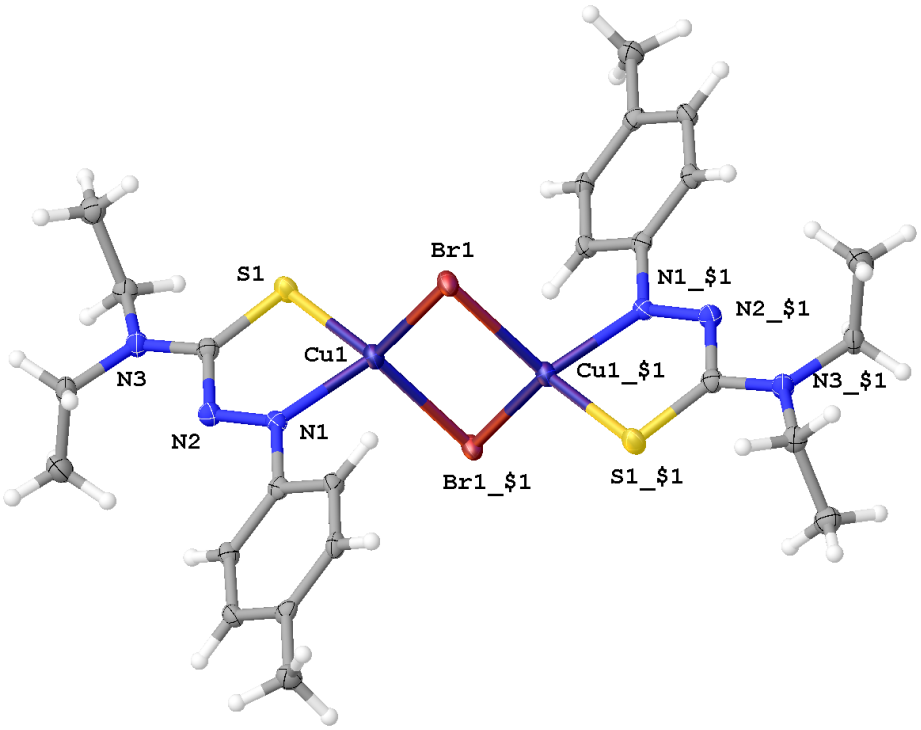

Crystallographic Data for **(μ-Br)[Cu(*p*-fluorophenyl-ATF)Br]$_2$ (18)**, $C_{22}H_{28}Br_2Cu_2F_2N_6S_2$ (*M* =765.52 g/mol): monoclinic, space group $P2_1/n$ (no. 14), *a* = 9.1685(5) Å, *b* = 14.1640(8) Å, *c* = 11.2096(6) Å, *β* = 109.781(2)°, *V* = 1369.81(13) Å^3, *Z* = 2, *T* = 100 K, μ(MoKα) = 4.660 mm^{-1}, *Dcalc* = 1.856 g/cm^3, 2Θmax = 47.522°, 58438 reflections collected, 3557 unique (R_{int} = 0.0509, R_{sigma} = 0.0201), R_1 was 0.0243 (I > 2σ(I)), wR_2 = 0.0531 (all data).

X-ray diffraction data for **(μ-Br)[Cu(*p*-fluorophenyl-ATF)Br]$_2$ (18)** were collected at 100 K on a Bruker D8 Venture using MoKα-radiation (λ=0.71073 Å). Data have been corrected for absorption using SADABS[1] area detector absorption correction program. Using Olex2[2], the

structure was solved with the ShelXT[3] structure solution program using Direct Methods and refined with the ShelXL[4] refinement package using least squares minimization. All non-hydrogen atoms were refined with anisotropic thermal parameters. Hydrogen atoms of the investigated structure were located from difference Fourier maps but finally their positions were placed in geometrically calculated positions and refined using a riding model. Isotropic thermal parameters of the placed hydrogen atoms were fixed to 1.2 times the *U* value of the atoms they are linked to (1.5 times for methyl groups). Calculations and refinement of structures were carried out using APEX3[5], SHELXTL[6], and Olex2 software.

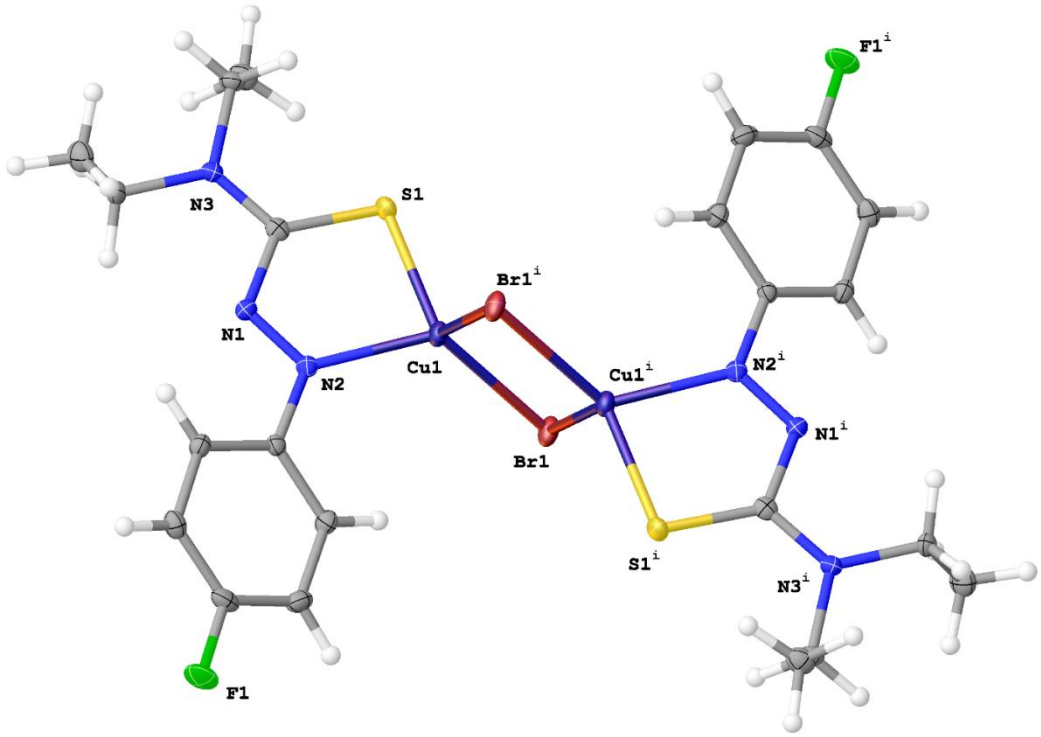

Crystallographic Data for **(μ-Br)[Cu(*p*-trifluoromethylphenyl-ATF)Br]$_2$ (19),** $C_{24}H_{28}Br_2Cu_2F_6N_6S_2$ (*M* =865.54 g/mol): triclinic, space group P-1 (no. 2), *a* =

8.3354(4) Å, *b* = 9.4424(4) Å, *c* = 11.2544(5) Å, *α* = 69.302(2)°, *β* = 72.897(2)°, *γ* = 82.850(2)°, *V* = 791.77(6) Å^3, *Z* = 1, *T* = 100 K, μ(MoKα) = 4.060 mm^{-1}, *Dcalc* = 1.815 g/cm^3, 2Θmax = 55.056°, 36271 reflections collected, 3649 unique (R_{int} = 0.0382, R_{sigma} = 0.0197), R_1 = 0.0208 (I > 2σ(I)), wR_2 = 0.0499 (all data).

X-ray diffraction data for **(μ-Br)[Cu(*p*-trifluoromethylphenyl-ATF)Br]$_2$ (19)** were collected at 100 K on a Bruker D8 Venture using MoKα-radiation (λ=0.71073 Å). Data have been corrected for absorption using SADABS[1] area detector absorption correction program. Using Olex2[2], the structure was solved with the SHELXT[3] structure solution program using Direct Methods and refined with the SHELXL[4] refinement package using least squares minimization. All non-hydrogen atoms were refined with anisotropic thermal parameters. Hydrogen atoms of the investigated structure were located from difference Fourier maps but finally their positions were placed in geometrically calculated positions and refined using a riding model. Isotropic thermal parameters of the placed hydrogen atoms were fixed to 1.2 times the *U* value of the atoms they are linked to (1.5 times for methyl groups). Calculations and refinement of structures were carried out using APEX3[5], SHELXTL[6], and Olex2 software.

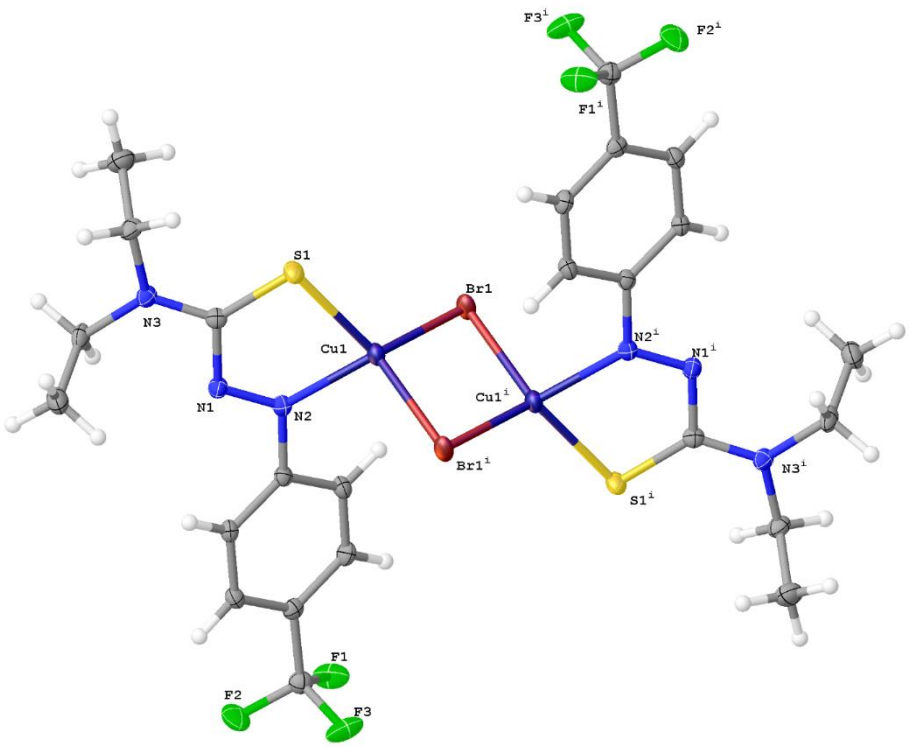

Crystallographic Data **[(*p*-tolyl-ATF)$_2$Cu](BF$_4$) (21),** $C_{24}H_{34}BCuF_4N_6O_{0.5}S_2$ (M =629.04 g/mol): triclinic, space group P-1 (no. 2), a = 7.7546(2) Å, b = 13.9577(4) Å, c = 14.5761(4) Å, α = 84.190(2)°, β = 83.596(2)°, γ = 75.324(2)°, V = 1512.29(7) Å^3, Z = 2, T = 100 K, μ(MoKα) = 0.911 mm^{-1}, *Dcalc* = 1.381 g/cm^3, 2Θmax = 50.052°, 41848 reflections measured, 5344 unique (R_{int} = 0.0375, R_{sigma} = 0.0208), R_1 = 0.0624 (I > 2σ(I)), wR_2 = 0.1222 (all data).

X-ray diffraction data for **[(*p*-tolyl-ATF)$_2$Cu](BF$_4$) (21)** were collected at 100 K on a Bruker D8 Venture using MoKα-radiation (λ=0.71073 Å). Data have been corrected for absorption using SADABS[1] area detector absorption correction program. Using Olex2[2], the structure was solved with the SHELXT[3] structure solution program using Direct Methods and refined with the SHELXL[4] refinement package using least squares minimization. All non-hydrogen atoms were refined with anisotropic thermal parameters. Most of the hydrogen atoms of the

investigated structure were located from difference Fourier maps but finally their positions were placed in geometrically calculated positions and refined using a riding model. Isotropic thermal parameters of the placed hydrogen atoms were fixed to 1.2 times the *U* value of the atoms they are linked to (1.5 times for methyl groups). Upon refinement it was apparent from the difference map there was disorder with the BF_4 anion. This disorder was modeled over two positions using a PART instruction and tied to a free variable. The model incorporates bond distance similarity restraints (SADI), 1,3 bond distances restraints (DANG) as well as thermal ellipsoid restraints (SIMU) and two thermal ellipsoid constraints (EADP). The crystal structure also incorporates a water molecule that is treated with half occupancy. The hydrogen atoms for this water have not been modeled as their location could not be observed from the difference map. Calculations and refinement of structures were carried out using APEX4[5], SHELXTL[6], and Olex2 software.

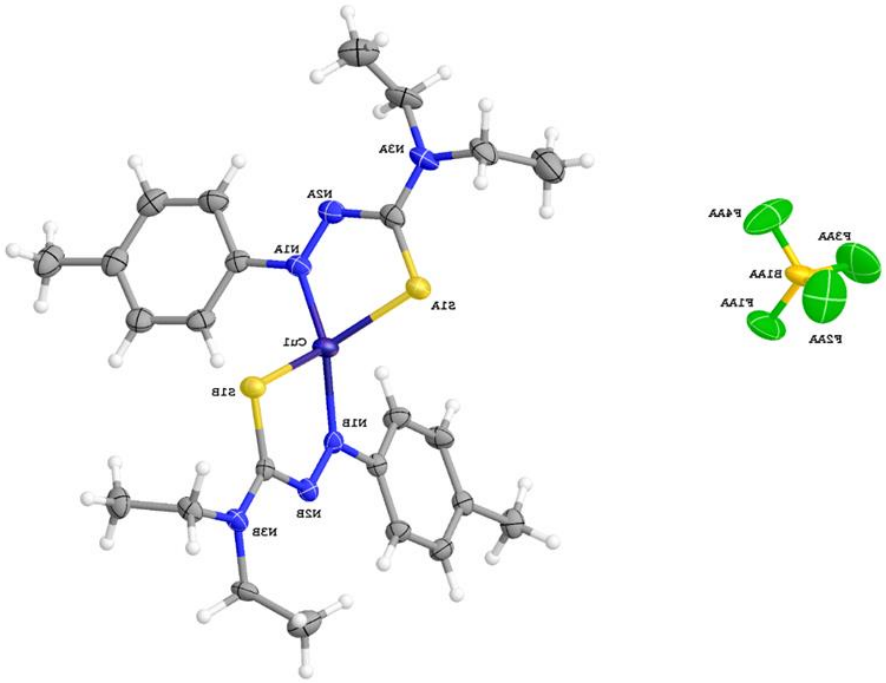

Crystallographic Data **[(p-fluorophenyl-ATF)$_2$Cu](BF$_4$) (22)**, $C_{26}H_{36}BCuF_6N_6OS_2$ (M =701.08 g/mol): monoclinic, space group C2/c (no. 15), a = 27.1057(19) Å, b = 13.5753(10) Å, c = 17.8231(13) Å, β = 108.127(3)°, V = 6232.8(8) Å3, Z = 8, T = 100 K, μ(MoKα) = 0.902 mm-1, Dcalc = 1.494 g/cm3, 2Θmax = 52.92°, 98033 reflections measured, 6404 unique (Rint = 0.0765, Rsigma = 0.0321), R1 = 0.0413 (I > 2σ(I)), wR2 = 0.0958 (all data).

X-ray diffraction data for **[(*p*-fluorophenyl-ATF)$_2$Cu](BF$_4$) (22)** were collected at 100 K on a Bruker D8 Venture using MoKα-radiation (λ=0.71073 Å). Data have been corrected for absorption using SADABS[1] area detector absorption correction program. Using Olex2[2], the structure was solved with the SHELXT[3] structure solution program using Direct Methods and refined with the SHELXL[4] refinement package using least squares minimization. All non-hydrogen atoms were refined with anisotropic thermal parameters. The hydrogen atoms of the investigated structure were located from difference Fourier maps (except for the tetrahydrofuran solvent molecule) but finally their positions were placed in geometrically calculated positions and refined using a riding model. Isotropic thermal parameters of the placed hydrogen atoms were fixed to 1.2 times the *U* value of the atoms they are linked to (1.5 times for methyl groups). After refinement, the data suggested some disorder of the tetrafluoroborate anion. The disorder has been modeled over two positions using a PART instruction and tied to a free variable. Refinement of the free variable shows and approximate 63:37 disorder. The tetrafluoroborate disorder model incorporates bond similarity restraints (SADI 0.02) and a thermal ellipsoid constraint (EADP). The tetrahydrofuran molecule in the crystal structure has enlarged thermal ellipsoids, and some residual electron density proximal to the molecule, suggesting some disorder. Attempts made to model the disorder of the

tetrahydrofuran were unsuccessful. Calculations and refinement of structures were carried out using APEX3[5], SHELXTL[6], and Olex2 software.

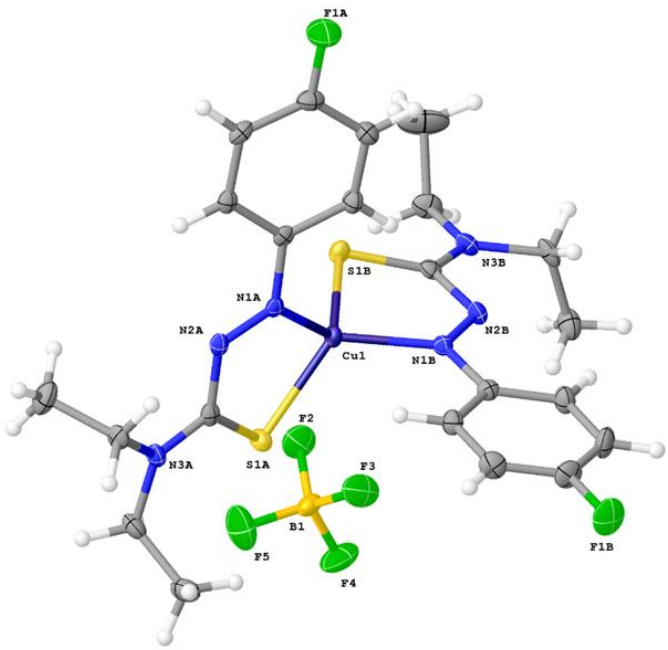

Crystallographic Data **[(*p*-trifluoromethylphenyl-ATF)$_2$Cu](BF$_4$) (23),** triclinic, space group P-1(no. 2), a =13.4542(3) Å, b = 15.6967(4) Å, c = 16.0532(4) Å, α = 89.4360(10)°, β = 72.1140(10)°, γ = 71.8000(10)°, V = 3051.04(13) Å^3, Z = 4, T = 100 K, μ(MoKα) = 0.941 mm^{-1}, *Dcalc* = 1.587 g/cm^3, 2Θmax = 52.744°, 145373 reflections measured, 12472 unique (R_{int} = 0.0728, R_{sigma} = 0.0384), R_1 = 0.0515 (I > 2σ(I)), wR_2 = 0.1449 (all data).

X-ray diffraction data for **[(*p*-trifluoromethylphenyl-ATF)$_2$Cu](BF$_4$) (23)** were collected at 100 K on a Bruker D8 Venture using MoKα-radiation (λ=0.71073 Å). Data have been corrected for absorption using SADABS[1] area detector absorption correction program. Using Olex2[2], the structure was solved with the SHELXT[3] structure solution program using Direct Methods and refined with the SHELXL[4] refinement package using least squares minimization. All non-hydrogen atoms were refined with anisotropic thermal parameters. The hydrogen

atoms of the investigated structure were located from difference Fourier maps but finally their positions were placed in geometrically calculated positions and refined using a riding model. Isotropic thermal parameters of the placed hydrogen atoms were fixed to 1.2 times the *U* value of the atoms they are linked to (1.5 times for methyl groups). Calculations and refinement of structures were carried out using APEX4[5], SHELXTL[6], and Olex2 software.

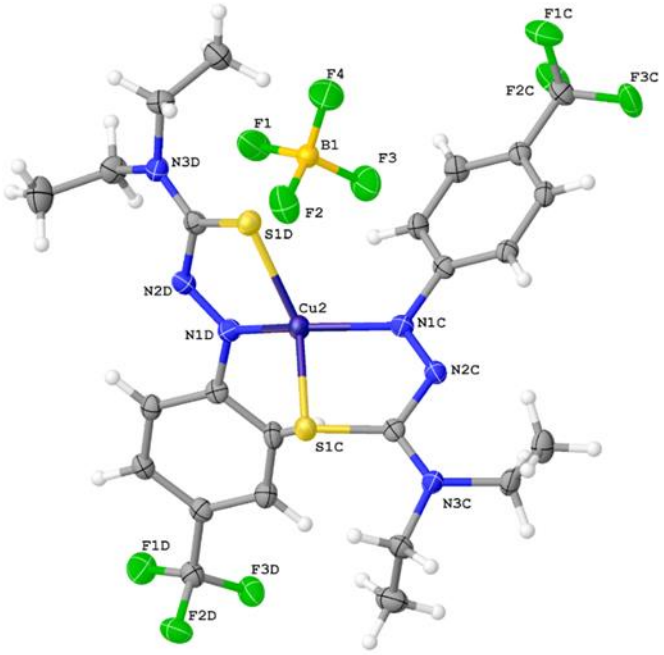

References

1. Sheldrick, G. M. (1996). SADABS: Area Detector Absorption Correction; University of Göttingen, Germany.
2. Dolomanov, O.V.; Bourhis, L.J.; Gildea, R.J.; Howard, J.A.K.; Puschmann, H., (2009). J. Appl. Cryst., 42, 339-341.
3. Sheldrick, G. M. (2015). *Acta Cryst.* A71, 3-8.
4. Sheldrick, G. M. (2015). *Acta Cryst.* C71, 3-8.
5. Bruker (2021). APEX4. Bruker AXS Inc., Madison, Wisconsin, USA.
6. Sheldrick, G.M. (2008). Acta Cryst. A64, 112-122.